PROCEEDINGS BOOK OF THE 7[TH] INTERCONTINENTAL GEOINFORMATION DAYS

18-19 NOVEMBER 2023

Peshawar, PAKISTAN

MERSIN UNIVERSITY-ENGINEERING FACULTY
DEPARTMENT OF GEOMATICS ENGINEERING

ISBN: 978-605-72800-6-0 https://igd.mersin.edu.tr/

The proceedings of the

7th Intercontinental Geoinformation Days

Editor-in-Chief

Prof. Dr. Murat Yakar

Editors

Prof. Dr. Shakeel Mahmood

Prof. Dr. Khalil Valizadeh Kamran

Res. Asst. Aydın Alptekin

ISBN: 978-605-72800-6-0

Peshawar, 2023

7th Intercontinental Geoinformation Days

I would like to thank all of the contributing authors and reviewers to the 7th Intercontinental Geoinformation (IGD) Symposium, 18-19 November 2023. In this international symposium, which has 76 papers, 37 papers are from Türkiye and the remaining 39 papers are from 11 different countries.

Best regards

Prof. Dr. Murat YAKAR

Honor Board

Ali Hamza PEHLİVAN – Governor of Mersin Province
Prof. Dr. Erol YAŞAR – Rector of Mersin University
Prof. Dr. Orhan AYDIN – Rector of Tarsus University
Prof. Dr. Ömer ARIÖZ – Rector of Toros University
Mehmet Zeki ADLI – Director of Turkish Land Registry and Cadastre
Prof. Dr. Diane DUMASHIE– FIG President
Prof. Dr. Lena Halounová – ISPRS President
Prof. Dr. Chryssy POTSIOU – FIG Honorary President
Prof. Dr. Haluk ÖZENER – Boğaziçi University Director of Kandilli Observatory
Dr. Orhan ERCAN – FIG Vice President

Organizing Committee

Mersin University – Faculty of Engineering – Department of Geomatics Engineering
Prof. Dr. Murat Yakar – Conference Chairman
Prof. Dr. Zakir Eminov – Director of Institute of Geography, Co-Chairman
Prof. Dr. Said Safarov – head of Caspian Sea hydrometeorology department
Assoc. Prof. Dr. Erdinç Avaroğlu
Assoc. Prof. Dr. Jalal Shiri
Prof. Dr. Behrouz Sari Sarraf
Prof. Dr. Khalil Valizadeh Kamran
Assoc. Prof. Dr. Bakhtiar Feizizadeh
Prof. Dr. Maryam Bayati Khatibi
Assoc. Prof. Dr. Aboulfazl Ghanbari
Asst. Dr. Sadra Karimzadeh
Asst. Dr. Iraj Teymouri
Asst. Dr. Husain Karimzadeh
Prof. Dr.Saeid Jahabakhsh
Prof. Dr. Shahram Rostaei
Assoc. Prof. Dr. Shahrivar Rostaei
Assoc. Prof. Dr.- Zaur Imrani
Asst. Dr. Mohsen Aghayari
Asst. Prof. Dr. Ali Ulvi
Asst. Prof. Dr. Fatma Bünyan Ünel
Asst. Prof. Dr. Lütfiye Kuşak
Dr. Behnam Khorrami
Dr. - Elnur Safarov
Dr. - Rovshan Kerimo
Dr. - Sabuhi Talibov
Dr. Hakan Doğan
Lect. Atilla Karabacak
Lect. Şafak Fidan
Res. Asst. Abdurahman Yasin Yiğit
Res. Asst. Aydın Alptekin
Eng. Engin Kanun
Eng. Mücahit Emre Oruç
Eng. Seda Nur Gamze Hamal
Eng. Huseynova Bayimkhanim
Eng. Emil Jabrayilov
Eng. Rasulzade Vusale

Executive Committee

IGD-7 Technical Program

18 November 2013

Time	Session 1: Geographic Information Systems
10.00-10.10	**A geostatistical analysis of soil salinity and its impact on wheat yield in Gujranwala District** Asma Javed, Shakeel Mahmood
10.10-10.20	**Seismicity analysis of the Eastern Hindu Kush Region using geospatial techniques** Mahnoor Qadir, Shakeel Mahmood
10.20-10.30	**Analysis and forecasting of coastline morphology in Pakistan using digital shoreline analysis** Mazhar Shakoor, Shakeel Mahmood
10.30-10.40	**Analysis of snow avalanche causes and damages in District Chitral, Pakistan** Ramsha Sohail, Shakeel Mahmood
10.40-10.50	**Mapping of frequently flood affected villages in Eastern Hindukush Region, Pakistan** Ramsha Sohail, Shakeel Mahmood

Time	Session 2: Remote Sensing
11.00-11.10	**Optical remote sensing application of Kızılcaören-Sivrihisar (Eskişehir) REE-Thorium Deposit** Cihan Yalçın, Orkun Turgay
11.10-11.20	**An application of remote sensing and GIS in geothermal alteration and potential in Ziga/Aksaray (Türkiye)** Hacer Bilgilioğlu
11.20-11.30	**Comparing land motion in Chiang Mai and Bangkok, Thailand, using Sentinel-1 InSAR time series** Kunlacha Inpai, Timo Balz
11.30-11.40	**Assessment of urbanization and different land use and land cover types on urban heat islands in growing cities, a case study: Tabriz, Iran** Khalil Valizadeh Kamran
11.40-11.50	**Performance evaluation of spectral indices and classification algorithms for built-up area extraction using PRISMA hyperspectral images** Seyed Hedayat Sheikhghaderi, Mostafa Mahdavifard, Ayub Mohammadi, Seyed Kazem Alavipanah

Time	Session 3: Geographic Information Systems
12.00-12.10	**Emerging trends in geographic information systems** Samir Ganili
12.10-12.20	**GIS-based soil loss estimation using revised universal soil loss equation** Ekundayo Adesina, Oluibukun Ajayi, Joseph Odumosu, Abel Illah
12.20-12.30	**Land use and land cover classes affected by possible sea level rise in Mersin city center** Onur Güven, Ümit Yıldırım, Cüneyt Güler, Mehmet Ali Kurt
12.30-12.40	**LULC change and CO_2 emissions in Shangai 2000-2020** Jianwen Zheng, Yishao Shi, Katabarwa Murenzi Gilbert
12.40-12.50	**Trend analysis of precipitation and temperature in the Western Black Sea region of Türkiye** Muhammed Zakir Keskin, Ahmad Abu Arra, Seyma Akca, Eyüp Şişman

Time	Session 4: Remote Sensing
13.00-13.10	**Spatio- Temporal Land use/ cover Changes Analysis Using Remote Sensing and Landscape Spatial Metrics, A Case Study of basin Liqvan** Khalil Valizadeh Kamran, Fatemeh Adimi
13.10-13.20	**Exploring the difference between Standard Precipitation Evapotranspiration Index (SPEI) from in-situ meteorological stations and SPEIbase** Ahmad Abu Arra, Seyma Akca, Muhammed Zakir Keskin, Eyüp Şişman
13.20-13.30	**Monitoring changes in air pollution using Sentinel-5 data** Behnaz Ghaderi, Payam Alemi Safaval, Zahra Azizi
13.30-13.40	**Evaluation of the application of the multi-temporal method in Sentinel 2 satellite images for the separation of agricultural products** Samira Asadnezhand Khormazard, Mir Masuod Kheirkhah Zarkesh, Bagher Ghermezcheshmeh
13.40-13.50	**Investigating the effects of land cover land use change on surface temperature using Landsat satellite images** Esra Şengün, Ugur Alganci, Dursun Zafer Şeker

Time	Session 5: Surveying and Geodesy
14.00-14.10	**Examination of earthquake effects in closed reinforced concrete structures** Muhammed Emin Işık, Nuri Erdem
14.10-14.20	**A tool for basic surveying and geodetic calculations** Muaz Ayran, Veli İlçi
14.20-14.30	**Time series analysis of Turkish National Sea Level Monitoring System (TUDES) level data for Amasra Station** Ahsen Çelen, Yasemin Şişman
14.30-14.40	**Examining PPP accuracy in relation to altitude** Emre Akman, Veli İlçi

Time	Session 6: Land Administration, Cadastre and Land Use
15.00-15.10	**Assessment of land use land cover changes through remote sensing data in Multan Tahsil** Sajjad Hussain
15.10-15.20	**Urban transformation applications** Muhammed Emin Işık, Nuri Erdem
15.20-15.30	**Comparison of machine learning regression methods for mass real estate valuation** Batuhan Kamil Sağlam, Muhammed Oğuzhan Mete, Ufuk Özerman, Reha Metin Alkan
15.30-15.40	**Spatial clustering of villages: a solution for agricultural area management: Case study of Aghmiyun agricultural area, east Azerbaijan province, Iran** Javad Ghasemi, Bahman Tahmasi
15.40-15.50	**The investigation of house value criteria in Atakum-Mimarsinan District Pre- and Post-Pandemic by multiple regression analysis** Simge Anaklı, Yasemin Sisman, Mehmet Emin Tabar

Time	Session 7: Remote Sensing
16.00-16.10	**Detection of collapsed buildings from post-earthquake imagery using mask region-based convolutional neural network** Esra Yildirim, Taskin Kavzoglu
16.10-16.20	**Waterbody change detection using Sentinel3 thermal imagery (Case study: Mighan Wetland, Iran)** Maryam Sadat Aghamiri, Azadeh Aghamohammadi, Zahra Azizi
16.20-16.30	**Impact of climate change on the assessment of the content of the indicator organic suspended matter and sea surface temperature of the Caspian Sea** Ismayil Zeynalov, Rena Achmedova
16.30-16.40	**The impact of climate change on the temperature regime of the Kelbajar and Lachin regions of the Republic of Azerbaijan** Said Safarov , Arzu Majidzade
16.40-16.50	**Applicability of satellite data in estimating Actual Evapotranspiration by SEBS algorithm (Mughan plain, Ardabil, Iran)** Mahmoud Sourghali, Samaneh Bagheri, Khalil Valizadeh Kamran
16.50-17.00	**The modeling and analysis of empirical systems with complex networks** Leyla Naghipour, Khalil Valizadeh Kamran, Mohammad Taghi Aalami, Vahid Nourani

19 November 2023

Time	Session 8: UAV Photogrammetry
10.00-10.10	**Assessing algae accumulation in an artificial pond using UAV-based orthophoto** Seyma Akca, Nizar Polat
10.10-10.20	**Classifying unmanned aerial vehicle images for urban vegetation mapping utilizing SVM** Zahra Azizi, Payam Alemi Safaval
10.20-10.30	**Crack detection for bridge inspection utilizing UAV photogrammetry technique** Abdurahman Yasin Yiğit, Murat Uysal
10.30-10.40	**Monitoring shoreline and areal change with UAV data** Adem Kabadayı, Yunus Kaya
10.40-10.50	**Assessing the contribution of RGB VIs in improving building extraction from RGB-UAV images** Richmond Akwasi Nsiah, Saviour Mantey, Yao Yevenyo Ziggah
10.50-11.00	**The effect of the Number and Distribution of Ground Control Points (GCP) on map production** Volkan İzci, Ali Ulvi

Time	Session 9: Geographic Information Systems
11.10-11.20	**Delineation of groundwater potential zone and mapping using GIS/Remote Sensing techniques and Analytic Hierarchy Process (AHP) for District Bhimber, Pakistan** Muhammad Shahid Usman, Ghani Rahman, Saira Munawar
11.20-11.30	**Spatial distribution of public services and facilities in the Sahand new city of Iran** Shiva Sattarzadeh Salehi, Firouz Jafari
11.30-11.40	**Geopark Potential of Osmaniye Province** Nuri Erdem
11.40-11.50	**Logging methodology decision-making with the new high-resolution DEM of Türkiye** Arif Oguz Altunel, Oytun Emre Sakici
11.50-12.00	**Spatial and regression-based missing precipitation data imputation: Western Black Sea region** Seyma Akca, Muhammed Zakir Keskin, Ahmad Abu Arra, Eyüp Şişman

Time	Session 10: Close-Range and Aerial Photogrammetry
12.10-12.20	**Monitoring gully erosion from UAV data** Yunus Kaya, Nizar Polat
12.20-12.30	**Evaluating the ground point classification performance of Agisoft Metashape Software** Nizar Polat, Abdulkadir Memduhoğlu, Yunus Kaya
12.30-12.40	**The effect of segmentation parameters on extracting the crown area of Tehran pine trees (Pinus eldarica)** Ali Hosingholizade, Seyed Kazem Alavipanah, Parviz Zeaiean Firouzabadi
12.40-12.50	**Digitization and archiving of Turkish motives by photogrammetric methods** Eda Menekşe, Ali Ulvi
12.50-13.00	**3D modeling of a stone sarcophagus at Kanlıdivane Ruins** Aydın Alptekin, Murat Yakar
13.00-13.10	**Use of photogrammetry in criminology** Muhammed Emin Bıyık, Murat Yakar

Time	Session 11: LiDAR - 3D Laser Scanning
13.20-13.30	**The accuracy evaluation of point cloud data generated with iPhone 15 Pro Next Gen LiDAR sensor** Ramazan Alper Kuçak
13.30-13.40	**Terrestrial photogrammetry and handheld laser scanning technique in 3D modeling of small objects** Zekeriya Kaçarlar, Ali Ulvi
13.40-13.50	**A comprehensive study on enhanced accuracy analysis of LiDAR data** Berkan Sarıtaş, Gordana Kaplan
13.50-14.00	**Investigating the utilization of iPhone lidar sensor in documenting cultural heritage** Emine Beyza Dörtbudak, Şeyma Akça
14.00-14.10	**Investigation of the usability of handheld laser scanners in reverse engineering applications** Yaren Doğdu, Murat Yakar
14.10-14.20	**Indoor mapping with wearable laser scanner and iPad lidar** Doğukan Sugölü, Abdurahman Yasin Yiğit
14.20-14.30	**Evaluation of point cloud software in terms of 3D architectural drawings** Ali Ulvi
14.30-14.40	**Incorrect use of wearable mobile LiDAR: Example of Mersin Soli Beach and Ankara National Library Underpass** Atilla Karabacak, Murat Yakar

Time	Session 12: Remote Sensing
14.50-15.00	**Assessing the vulnerability of residential lands against earthquakes and ways to reduce vulnerability using spatial analysis: Case study of Tabriz city** Sana Foroughi, Farzad Rezaei, Faezeh Khoshkhoy
15.00-15.10	**Evaluation of the quality of climate time series maps extracted from GEE (case study: Arasbaran region - Iran)** Sajjad Moshiri, Khalil Valizadeh Kamran, Omid Rafieyan, Ahmad Nikdel Monavvar, Mohammad Ebrahim Ramazani
15.10-15.20	**Estimation of land subsidence using DInSAR and SBAS techniques** Mojdeh Miraki, Hormoz Sohrabi, Siavash Bakhtiarvand Bakhtiari
15.20-15.30	**Comprehensive temperature analysis of Türkiye between 2013 and 2023 using Google Earth Engine and ERA5 Dataset** Abdullah Sukkar, Ugur Alganci, Dursun Zafer Seker
15.30-15.40	**PM10 air pollutant prediction using deep learning LSTM Model: A case study of Istanbul, Türkiye** Omar Wisam Alqaysi, Dursun Zafer Şeker
15.40-15.50	**Estimation of chlorophyll concentration on surface water bodies from hyperspectral satellite data** Martina Frezza, Valeria La Pegna, Davide De Santis, Dario Cappelli, Fabio Del Frate

Time	Session 13: Land Administration, Cadastre and Land Use
16.00-16.10	**Spatial analysis of the vulnerability of rural housing to earthquakes (case study: rural settlements in the Tehran metropolitan area)** Bahman Tahmasi, Hassan Ali Faraji Sabokbar, Seyed Ali Badri
16.10-16.20	**The effect of smart mobility performance in mitigation of climate change, the experiences of European cities** Parinaz Badamchizadeh, Iraj Teymuri, Ali Oskouee Aras, Fereidoun Babaie Aghdam
16.20-16.30	**Evaluating land use plans in line with climate change adaptation policies in the Semnan Urban Region** Vahid Isazade, Abdul Baser Qasimi, Taher Parizadi, Esmail Isazade
16.30-16.40	**Preventive measures in disaster management can make the difference** Lucrezia Vittoria Natale, Donato Abruzzese
16.40-16.50	**Utilizing photogrammetry for forest rehabilitation assessment: Remote sensing techniques applied to Mt Rubavu in Rubavu District, Rwanda** Sabato Nzamwita, Isaac Nzayisenga, Patience Manizabayo

Time	Session 14: Geographic Information Systems
17.00-17.10	**Groundwater analysis and management plan using integrated community perception and geo-spatial techniques in Wana, South Waziristan** Saddam Hussain, Shakeel Mahmood
17.10-17.20	**Mapping Covid-19 incidence hotspots in Pakistan using spatial-statistical approach** Shakeel Mahmood, Zara Tariq
17.20-17.30	**Flood Vulnerability Assessment Using Geographical Information System: Case Study of Mpazi Sub-catchment, Kigali** Patience Manizabayo, Hyacinthe Ngwijabagabo, Isaac Nzayisenga, Sabato Nzamwita, Laika Amani, Eugene Uwitonze
17.30-17.40	**Multi-sensorial data-based assessment of artificial surfaces and vegetation index for the response to population expansion: A case study of Musanze Secondary City, Rwanda** Katabarwa Murenzi Gilbert, Yishao Shi, Isaac Nzayisenga
17.40-17.50	**Land surface temperature and urban heat island analysis using remote sensing and GIS: A case study in Mersin, Türkiye** Mehmet Özgür Çelik, Murat Yakar

Content	Page

7th Intercontinental Geoinformation Days

igd.mersin.edu.tr

A geostatistical analysis of soil salinity and its impact on wheat yield in Gujranwala District

Asma Javed *1, **Shakeel Mahmood** 1

1Government College University, Department of Geography, Lahore, Pakistan

Keywords
Physicochemical properties
Linear regression rate
IDW
Electrical Conductivity
Wheat Yield

Abstract

This study applies geostatistical analysis to examine how soil salinity affects wheat yield in the Gujranwala area in the context of changing rainfall patterns and climate change. The goal of the research is to determine the geographical and temporal patterns of soil salinity and how they affect agricultural productivity, with a particular emphasis on wheat cultivation. Despite the use of comprehensive geostatistical techniques and statistical analysis, the study finds a strong negative relationship between wheat production and soil salinity as determined by electrical conductivity (EC). As geostatistical techniques such as Linear Regression Rate (LLR) assess the influence of soil salinity on wheat yield, Inverse Distance Weighting (IDW) examines the distribution of salt in the soil. Finding hotspots for extremely salinized soil emphasizes the need for precise controls and thoughtful land management. Increasing soil salinity monitoring, encouraging targeted irrigation, looking into crops that can withstand salt, enhancing drainage, and teaching farmers how to manage soil salinity are some of the recommendations. This geostatistical analysis concludes that there is a notable negative link between Gujranwala wheat yield and soil salinity, which offers important information to land managers, policymakers, and agricultural experts. Understanding soil salinity dynamics enables proactive measures to enhance agricultural output.

1. Introduction

Worldwide, 20% of total cultivated land and 50% of irrigated areas are under salt stress. In Pakistan, about 14% of irrigated lands have deteriorated with salinity, while 64% yield losses are reported due to salinity. As a result, only roughly 23 Mha of land are left that may be used for agriculture (Irum and Ehetisham-ul-Haq, 2017). According to estimates, there are 14 billion ha of usable land on the planet, 6.5 billion ha of which are semi-arid and arid zones. This semi-arid and dry region has a 1 billion hectares salt-affected area (Balal et al., 2013). Salinity in soils is divided into primary and secondary salinity, with primary salinity resulting from the weathering of primary minerals or the parent material, and secondary salinity resulting from improper use of the soil and irrigation techniques that cause the rise of highly salinized ground water and its contribution to the salinization process.

The country's economy is dependent on the agricultural sector (Khan et al., 2013). Almost 20% of national income contributes in the gross domestic product (GDP) and 43.7% accounts for total employment. 66% of the population of the country resides in non-urban areas and their income depends directly or indirectly on the agriculture sector (Abdullah et al., 2015). The agriculture sector recorded a growth of 2.67% during the year 2019–2020. In Pakistan, the salt-affected area is 4.5 Mha (Aslam, 2016). This situation is particularly alarming, given Pakistan's reliance on the pressures put on regional food items by growing populations and farming exports. In Pakistan, salinity has impacted about 5.7 million hectares of land, including about 2 million hectares of abandoned agricultural land that could be extremely productive in the canal areas. In addition, a 62% decline in agricultural output has been connected to soil salinity. Salinity of the soil has significantly impacted Pakistan's agricultural sector, resulting in lower yields and lower farmer incomes. Due to its strong nutritional value, which includes providing carbohydrates, nutrient-rich fiber, and vitamins, wheat is a staple crop in many temperate regions and is in high demand. To do a geostatistical analysis of the Gujranwala district's soil salinity and its impacts on wheat yield from

* **Corresponding Author**

*(shakeelmahmoodkhan@gmail.com) ORCID ID 0000-0001-6909-0735

Cite this study

Javed, A., & Mahmood, S. (2023). A geostatistical analysis of soil salinity and its impact on wheat yield in Gujranwala District. Intercontinental Geoinformation Days (IGD), 7, 1-4, Peshawar, Pakistan

2000 to 2020 is the major objective of this work in light of the Gujranwala district's high soil salt content may be having a severe influence on wheat yields and quality, which might have significant consequences for the area's farmers as well as the general public.

2. Method

The data will be analyzed using statistical software and geostatistical tools. The study will also review relevant literature on soil salinity and wheat yield to provide context and support the analysis. To analyze Soil Salinity impact on wheat yield in District Gujranwala, a methodology based on GIS and remote sensing techniques was employed. The method include two criteria analysis of Soil Salinity. These criteria include; Impact of Soil Salinity on Wheat Yield. The following steps were taken in the analysis process: The Soil samples data of Physiochemical parameters of soil and Wheat Yield data from 2000 to 2020 taken from Principal Scientist of the Gujranwala Soil and Water Testing Laboratory and the Directorate of Crop Reporting Service, Agriculture Department Lahore. The Linear Regression Model and IDW analysis is performed. All the analysis are applied in spatial and temporal domains with in extent of Gujranwala district and years 2000 to 2020 of Gujranwala district.

To calculate the salinity levels of the soil samples, process them. This could include: Adjusting and utilizing instruments to gauge pH and electrical conductivity (EC). Steps consist of: GIS data importation into ArcGIS or QGIS software. Generating themed maps of the research area's various salinity levels. To evaluate the association between historical crop yield data and soil salinity, process and analyze the data. Typical actions include: Arranging the yield data according to the soil salinity levels at each location. Calculating various salinity ranges' mean, median, and variance statistical metrics. Finding the association between yield and salinity using statistical tests, such as correlation analysis. Correlation coefficients are calculated to express the direction and intensity of correlations. Regression analysis is used to model how salinity affects crop productivity. ANOVA should be used to compare crop yields at various soil salinity levels. Due to its applicability for investigating the linear correlations between variables, linear regression was selected for the study on the geo-spatial evaluation of soil salinity and its impact on wheat crop output in the Gujranwala District, Pakistan.

2.1. Study Area

Gujranwala is centrally located in Punjab, Pakistan, with geographical coordinates ranging from 31º to 32º N latitude and 73º to 74º E longitude (Figure. 1). The study area is bordered by Gujrat and Mandi Bahauddin to the north, Sheikhpura to the south, Hafizabad and Pindi Bhatian to the west, connecting it to Jhang, Chiniot, Sargodha, and Faisalabad to the southwest. Covering a total area of 3622 km² (1390 sq mi), Gujranwala is characterized by a typical altitude of 226 meters (744 feet) above sea level.

Positioned within the fertile plains of Punjab, Gujranwala benefits from irrigation through canals. The region is a part of Rachna Doab, which slopes from the northeast to the southwest and is traversed in its eastern portion by the Upper Chenab Canal. Throughout the year, the geographic area of Gujranwala witnesses' significant seasonal variations. The summer months, spanning from June to September, experience high temperatures ranging from 36 to 42 degrees Celsius (108 °F) (Kundu et al., 2018).

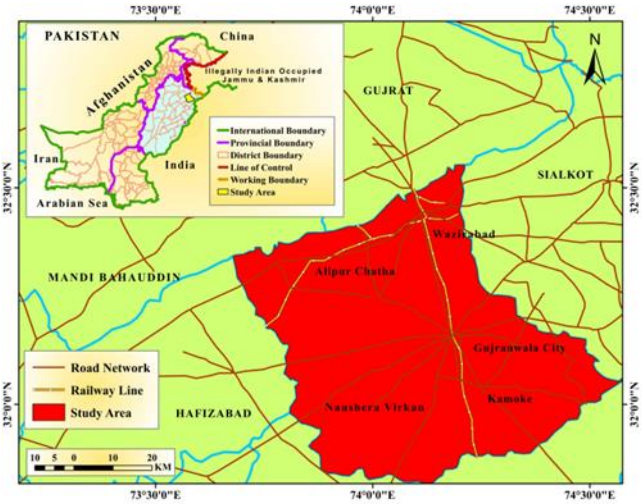

Figure 1. Location of study area.

3. Results

An adequate statistical linear regression analysis was run on the data to establish the association between crop yield and salinity (ECe) in a farming area. In this study, the linear regression analysis was computed using the statistical program SPSS. In this situation, wheat yield was the dependent variable, and linear regression was used to estimate its value based on the measured EC, which served as the independent variable. While the independent variable is sometimes referred to as the predictor variable, the dependent variable is sometimes called the outcome variable. It provides statistics that evaluate a regression model's performance. It evaluates how effectively the independent variables (predictors) provide explanation for variation in the dependent variable (wheat yield). The correlation coefficient (R) in the present study is -0.935a, showing a very significant negative correlation between the predictors and Wheat Yield. An R Square value of 0.875 indicates that the model's predictors can explain around 87.5% of the variation in wheat yield. In context of the complexity of the model and the size of the sample, the Adjusted R Square value of 0.871 indicates that the predictors represent around 87.1% of the variation in wheat yield. The difference between the estimated and actual Wheat Yield numbers in the present case is averaged out to be 1.434 standard errors of the estimate. The F Change statistic of 237.795 shows the model's overall significance, indicating that the variables jointly influence considerably to explaining Wheat Yield. The analysis revealed a strong negative correlation (r = .933) between EC and Wheat yield, and the regression model was able to account for 87% of the variance. This indicates that the model was well-suited for the data and statistically significant, as evidenced by a significant F-value of 55 and a p-value of less than .0005. Figure 3.10 illustrates a negative correlation between EC and wheat yield over the study period from 2000 to 2020. Specifically, electrical conductivity demonstrated an increasing trend, while wheat yield exhibited a decreasing trend.

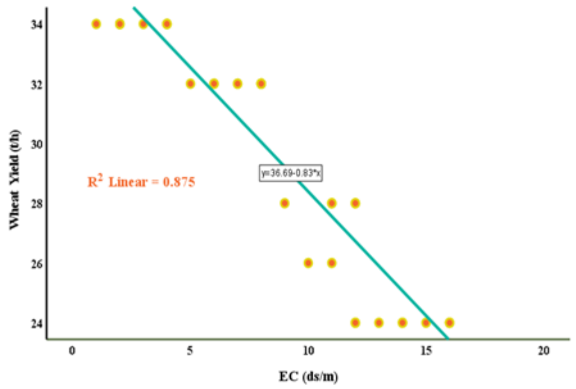

Figure 2. Scatter plot of EC and Wheat by year.

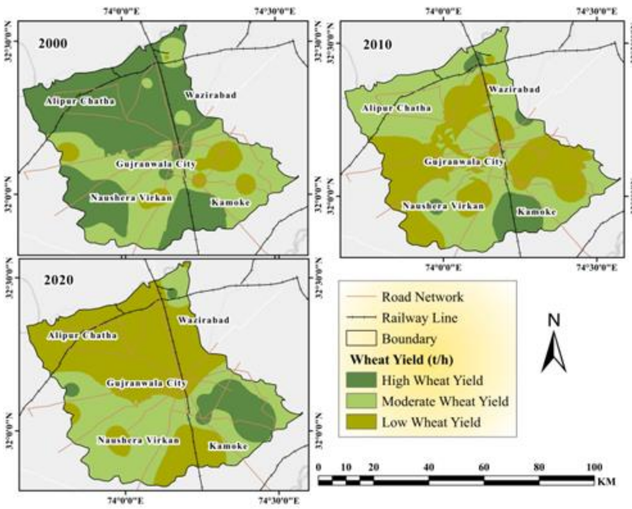

Figure 3. Wheat Productivity (2000-2020).

The analysis revealed a strong negative correlation (r = .933) between EC and Wheat yield, and the regression model was able to account for 87% of the variance. This indicates that the model was well-suited for the data and statistically significant, as evidenced by a significant F-value of 55 and a p-value of less than .0005. Figure 2 illustrates a negative correlation between EC and wheat yield over the study period from 2000 to 2020. Specifically, electrical conductivity demonstrated an increasing trend, while wheat yield exhibited a decreasing trend.

4. Discussion

The analysis and interpretation of the results from the geostatistical analysis of soil salinity and its effect on wheat yield in the Gujranwala District are presented in the discussion section. It examines the consequences of the findings, addressed the study's goals, highlights its most important results, and gives perspectives into the study's general worth. Wheat production and soil salinity: The investigation showed an alarming negative association between wheat yield and soil salinity, as assessed by electrical conductivity (EC). Salt has a negative effect on agricultural output as demonstrated by a correlation between higher soil salt levels and lower wheat production. The study evaluated the extent of the reduction in wheat yield caused to soil salinity in order to quantify the impact. Authorities and farmers can use this information to better understand the financial consequences and decide on appropriate soil salinity management techniques.

This knowledge can direct focused actions and techniques of land management. Identifying potential hazards and hotspots: the study found regions that need to be immediately targeted for salinity management measures because of their high soil salinity hotspots. Furthermore, it detected locations vulnerable to the development of salinity, contributing in preventing future growth and mitigating potential effects on agricultural productivity. Adaptation strategies: In order to mitigate the negative consequences of soil salinity in the Gujranwala District, the research proposes solutions for adaptation.

5. Conclusion

Understanding the relationship between soil salinity and agricultural productivity is made possible by the geostatistical analysis of soil salinity and its effect on wheat production in the Gujranwala District. The following conclusions and suggestions can be drawn from the data: In the Gujranwala District, soil salinity has a major negative effect on wheat yield. Wheat production is negatively correlated with increased soil salinity, as measured by electrical conductivity (EC). Areas with greater salt levels and variations in salinity status over time were identified by the geographical and temporal examination of soil salinity patterns. For focused treatments and methods of land management, this information is essential.

The study emphasizes how crucial it is to put adaptation measures into effect to lessen the negative consequences of soil salinity. These tactics can include enhanced irrigation systems, methods for reclaiming land, crop choices, and salinity-reduction-focused soil management techniques. The research has consequences for policy, underlining the necessity for the creation and application of laws that support sustainable land use, water conservation, and salinity control methods.

Acknowledgement

I would like to express my sincere appreciation to my co-author, Dr. Shakeel Mahmood, for his vital contributions and unflinching support during this project. His knowledge and commitment have made our joint work much more effective.

References

AbdelRahman, M. A. (2023). An overview of land degradation, desertification and sustainable land management using GIS and remote sensing applications. Rendiconti Lincei. Scienze Fisiche e Naturali, 1-42.

Abdennour, M. A., Douaoui, A., Piccini, C., Pulido, M., Bennacer, A., Bradaï, A., ... & Yahiaoui, I. (2020). Predictive mapping of soil electrical conductivity as a Proxy of soil salinity in south-east of Algeria. Environmental and Sustainability Indicators, 8, 100087.

Abdullah, D. Z., Khan, S. A., Jebran, K., & Ali, A. (2015). Agricultural credit in Pakistan: Past trends and future prospects. Journal of Applied Environmental and Biological Sciences, 5(12), 178-188.

Abdullah, D. Z., Khan, S. A., Jebran, K., & Ali, A. (2015). Agricultural credit in Pakistan: Past trends and future prospects. Journal of Applied Environmental and Biological Sciences, 5(12), 178-188.

Adamu, K. U., & Yusuf, B. L. (2023). Impact of Climate Change on Soil Salinity Along Irrigated Farmlands of Jakara River Downstream Minjibir Local Government Area, Kano State, Nigeria. In Climate Change Impacts on Nigeria: Environment and Sustainable Development (pp. 541-561). Cham: Springer International Publishing.

Corwin, D. L. (2021). Climate change impacts on soil salinity in agricultural areas. European Journal of Soil Science, 72(2), 842-862.

Dasgupta, S., et al. (2018). Climate change, salinization and high-yield rice production in coastal Bangladesh. Agricultural and Resource Economics Review, 47(1), 66-89.

Ehetisham-ul-Haq, M., Rashid, A., Kamran, M., Idrees, M., Ali, S., Irum, A., ... & Siddique, F. (2017). Disease forecasting model for newly emerging bacterial seed and boll rot of cotton disease and its vector (Dysdercus cingulatus). Archives of Phytopathology and Plant Protection, 50(17-18), 885-899.

Etinger, A., Balal, N., Litvak, B., Einat, M., Kapilevich, B., & Pinhasi, Y. (2013). Non-imaging MM-wave FMCW sensor for pedestrian detection. IEEE Sensors Journal, 14(4), 1232-1237.

Ge, X., Ding, J., Teng, D., Wang, J., Huo, T., Jin, X., ... & Han, L. (2022). Updated soil salinity with fine spatial resolution and high accuracy: The synergy of Sentinel-2 MSI, environmental covariates and hybrid machine learning approaches. Catena, 212, 106054.

Haj-Amor, Z., & Bouri, S. (2019). Use of HYDRUS-1D–GIS tool for evaluating effects of climate changes on soil salinization and irrigation management. Archives of Agronomy and Soil Science.

Haj-Amor, Z., Araya, T., Kim, D. G., Bouri, S., Lee, J., Ghiloufi, W., ... & Lal, R. (2022). Soil salinity and its associated effects on soil microorganisms, greenhouse gas emissions, crop yield, biodiversity and desertification: A review. Science of the Total Environment, 843, 156946.

Hoshan, M.N. (2022). Review of Reclamation of salinity affected soils by leaching and their effect on soil properties and plant growth. Tikrit journal for agricultural sciences.

Ivushkin, K., Bartholomeus, H., Bregt, A. K., Pulatov, A., Kempen, B., & De Sousa, L. (2019). Global mapping of soil salinity change. Remote sensing of environment, 231, 111260.

Jat, H. S., et al. (2019). Climate Smart Agriculture practices improve soil organic carbon pools, biological properties and crop productivity in cereal-based systems of North-West India. Catena, 181, 104059.

Machado, R. M. A., & Serralheiro, R. P. (2017). Soil salinity: effect on vegetable crop growth. management practices to prevent and mitigate soil salinization. Horticulturae 3:30. doi: 10.3390/horticulturae3020030.

Mandal, S. U. B. H. A. S. I. S., Raju, R., Kumar, A., Kumar, P., & Sharma, P. C. (2018). Current status of research, technology response and policy needs of salt-affected soils in India—A review. J. Indian Soc. Coast. Agric. Res, 36, 40-53.

Mohammad, Z. M., Taghizadeh-Mehrjardi, R., & Akbarzadeh, A. (2010). Evaluation of geostatistical techniques for mapping spatial distribution of soil pH, salinity and plant cover affected by environmental factors in Southern Iran. Notulae Scientia Biologicae, 2(4), 92-103.

Mukhopadhyay, R., Sarkar, B., Jat, H. S., Sharma, P. C., & Bolan, N. S. (2021). Soil salinity under climate change: Challenges for sustainable agriculture and food security. Journal of Environmental Management, 280, 111736.

Munns, R. (2009). Strategies for crop improvement in saline soils. Salinity and water stress: improving crop efficiency, 99-110.

7th Intercontinental Geoinformation Days

igd.mersin.edu.tr

Seismicity analysis of the Eastern Hindu Kush Region using geospatial techniques

Mahnoor Qadir *1, Shakeel Mahmood 1

1Government College University, Department of Geography, Lahore, Pakistan

Keywords
Seismicity
Depth
Magnitude
Spatial Interpolation
Hindu Kush

Abstract

This study presents a geo-statistical approach to analyze the seismicity of the Eastern Hindu Kush region using earthquake records from the past 200 years obtained from the USGS open-source geo-database. The study also utilized SRTM, Digital elevation model to visualize the spatial range, magnitude, and depth of earthquakes in the region. The IDW and Weighted Overlay Analysis approaches were employed to interpolate seismic data in a GIS environment. For seismic assessment in the Eastern Hindu Kush region, a Seismic Hazard Zonation Map (SHZM) based on fault density, seismic depth, and magnitude was developed. The map highlights that the north-eastern side of region is located in a zone with a high level of seismic activity. Western Chitral, the western part of Upper Dir, and Lower Dir fall under a moderate seismicity zone, while Swat, south-eastern Chitral, and the northern section of Upper Dir lie in a zone with strong seismic activity. The study findings revealed that the Hindu Kush Region is vulnerable to moderate and high-magnitude earthquakes, posing a risk to the region's residents, particularly given their socioeconomic status and the highly susceptible nature of their houses. As a result, the findings of this study can give significant insights to disaster management authorities in decision-making and policy planning to improve community resilience and minimize the potential negative effects of future earthquakes.

1. Introduction

Globally, over the past few decades, catastrophic events have caused significant damage to various communities (Bommer 2022). Among these, earthquakes are one of the devastating geological hazards causing human deaths, physical damage, and social disruption (Khurram et al. 2021). Rima, Tibet, experienced an earthquake on August 15, 1950, which resulted in the deaths of over 3000 people and the displacement of about 5,000,000 people (Siddiqui 2022). An earthquake that struck on May 31, 1970, off the coast of Peru claimed the lives of almost 70,000 people (Jiménez et al. 2023). Off the coast of central Chile, there was an earthquake that killed 525 people and caused multiple structures to collapse in 2010 (Bouih et al. 2022).

The Himalayan, Hindukush, and Karakoram Mountain ranges are among the world's most seismically active areas, due to the convergence of the Eurasian and Indian plates (Joshi and Thakur 2016). The rugged Hindu Kush region, in particular, is a tectonically complex area and likely the world's most active zone for intermediate-depth earthquakes (Mitrofan et al. 2022). The presence of several reverse and oblique strike-slip faults in the Hindukush region is responsible for the frequent intermediate to severe earthquakes. Moreover, due to lithospheric subduction within the sharply falling Hindukush region, several mantle earthquakes impact the northeast-trending plane zone beneath the area, with an average of more than five earthquakes of 5 Mw per year occurring. This zone is approximately 700 km long and stretches to around 300 km depth. Understanding the seismicity of regions like the Hindukush is critical for predicting and mitigating the impact of earthquakes and other natural disasters (Khalid et al. 2021).

This study is an attempt to model earthquake susceptibility. Geostatistical modeling adds a scientific and data-driven dimension to earthquake risk assessment. This can improve the efficiency of mitigation strategies by more precisely focusing on high-risk zones of the Eastern Hindu Kush region (Du et al. 2023). This research is an important contribution to the field of seismic hazard mitigation because it will help to update policies and encourage inter-disciplinary collaboration. The mapping provides important information for land-

* **Corresponding Author**

*(shakeelmahmoodkhan@gmail.com) ORCID ID 0000-0001-6909-0735

Cite this study

Qadir, M., & Mahmmod, S. (2023). Seismicity analysis of the Eastern Hindu Kush Region using geospatial techniques. Intercontinental Geoinformation Days (IGD), 7, 5-8, Peshawar, Pakistan

use planning, infrastructure development, and emergency preparedness.

Pakistan is situated in a seismically active and earthquake-prone region of the world, where the Arabian, Indian, and Eurasian tectonic plates interact at different rates, resulting in a complex seismo-tectonic environment (Khurram et al. 2021). The Hindu Kush region, in particular, is notorious for large earthquakes that can cause fatalities and infrastructure damage. On October 26, 2015, the Hindu Kush earthquake occurred, causing significant damage in northern areas of Pakistan and Afghanistan (Yariyan et al. 2020; Lantada et al. 2018; Aslam et al. 2018). The earthquake, which had a magnitude of 7.5, was caused by reverse faulting that occurred at a depth of 210 kilometers beneath the Hindu Kush region of Afghanistan. The earthquake struck 45 kilometers southwest of Jarm village in Afghanistan's Badakhshan Province and 150 kilometers northwest of Pakistan's Chitral region (Aslam and Naseer 2020). Mountain ranges are created by massive geological pressures, while deformations within restricted borders or active fault zones commonly cause earthquakes (Rehman and Burton 2020; Chen and Shearer 2016).

Given the high seismicity of the Hindu Kush region and its potential for devastating earthquakes, research in this area is critical for understanding the seismo-tectonic environment and seismic risk (Aslam et al. 2021). There is a need for comprehensive studies to identify the active faults, their characteristics, and the magnitude and frequency of earthquakes in the region (Hildebrandt et al. 2021). This research can help develop earthquake hazard maps, assess the potential impacts of earthquakes on the built environment and infrastructure, and develop effective strategies for disaster risk reduction and mitigation. Furthermore, research can help improve the understanding of earthquake ground motion characteristics and the response of structures to seismic loads in the region. This knowledge can inform the development of building codes and guidelines to improve the earthquake resistance of structures and reduce the potential for damage and loss of life in the event of an earthquake.

2. Method

The present study utilized geospatial approaches to analyze seismicity events primarily based on secondary data obtained from various sources. Spatial interpolation was applied to geo-visualize the spatial pattern of earthquake magnitude and depth. All spatial input layers were combined using weighted overlay analysis in GIS environment. The study employed earthquake data with magnitude 4 and above for the last 200 years from the United States Geological Survey (USGS) earthquake catalog. The data include location (latitude and longitude), depth, and magnitude. The Shuttle Radar Topographic Mission (SRTM), Digital Elevation Model (DEM) with a spatial resolution of 30 meters was also obtained from the USGS open-source geo-database. The geological map including geological formations and geological structures of the study region was acquired from the Geological Survey of Pakistan (GSP). Political map of Pakistan containing international and district boundaries was acquired from the Survey of Pakistan (SoP). The acquired data were processed and then Geo-database was created to store it. The earthquake location was geo-visualized in the form of point data in GIS environment. The earthquake depth and magnitude were linked to the location data in Geo-database. Then geological and political maps were digitized and .shp files of geological formations, geological structures particularly fault lines and pollical boundaries were created.

The spatial pattern of earthquake depth and magnitude was revisualized by utilizing Inverse Distance Weighted (IDW) technique of spatial interpolation. IDW technique was used for the set of points to identify the amount of surface variation required for analysis (Watson and Philip 1985). The study employed Weighted Overlay Analysis to create thematic maps for visualizing seismicity geographically. For Weighted Overlay Analysis, an important step was to reclassify layers of variables like seismic magnitude, seismic depth, and fault density. Depending on each input layer's relative significance to the analysis, each layer was assigned a weight. The Delphi technique was used to assign weights to the classes of each input layer. The study analyzed the geospatial patterns of earthquake hazards and identified areas of high and low seismic activity.

2.1. Study Area

The Hindu Kush extends southwestward from the Pamir Knot to Afghanistan and serves as a natural barrier separating South and Central Asia (Khan et al. 2021). Tirich Mir is the highest peak in the Hindu Kush Mountains with an elevation of 7,708 meters above mean sea level. In Pakistan, the districts of Chitral, Swat, Upper, and Lower Dir cover the Eastern Hindu Kush. The 700 km-long Hindu Kush Mountain range is located in northeast and central Afghanistan and northwest of Pakistan (Rusk et al. 2022). The Hindu Kush system has a median north-south dimension of around 240 km and a cross-sectional area of about 966 km (Joya et al. 2021).

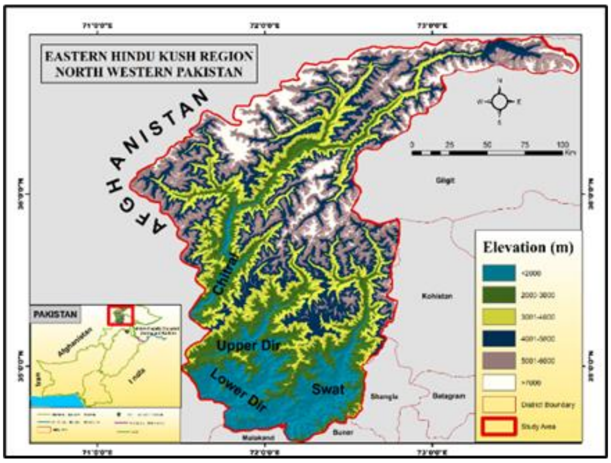

Figure 1. Location map of study area

The Eastern, middle, and Western are the three sections of the Hindu Kush (You et al. 2017). Administratively, the eastern Hindu Kush covers districts of Chitral, Dir Upper, Dir Lower, and Swat (Figure 1). Geographically, it extends from 34º34'11" to 36º54'30"N latitude and 71º11'56" to 73º52'5"E longitude (Mahmood and Atiq 2022). In this area, the Indian plate gradually rotates counterclockwise to encroach into the Eurasian plate. The region is seismically active. The focal depth of earthquakes ranges from 50 to 300 km (Mitrofan et al. 2022).

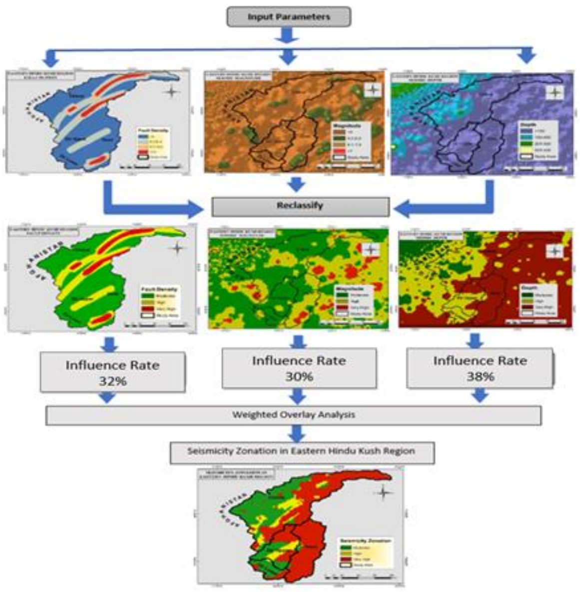

Figure 2. Seismic Magnitude in Eastern Hindu Kush

3. Results

3.1. Seismicity in Eastern Hindu Kush during 200 years span

The Hindu Kush region is characterized by a high degree of seismic activity, as demonstrated in Figure 3, which displays earthquakes with magnitudes of 4 and above over the past 200 years in the Eastern Hindu Kush.

3.2. Causes of Earthquake in Eastern Hindu Kush

Pakistan, located in South Asia, is situated in a highly seismically active region and holds significant importance within the Indian-Eurasian collision zone. The convergence of the Indian and Eurasian plates in the western Himalayas and the subduction of the Arabian plate beneath the Eurasian plate near Makran are two key factors responsible for the elevated seismicity of the region (Rehman et al. 2016). The country's seismic environment has a notable impact on the seismicity of Asia.

3.3. Seismic Magnitude

The area has been divided into different groups according to the seismic magnitude. The values of seismic magnitude vary from region to region. The brown color in the map shows the area where there is low seismic magnitude whereas the light brown color shows the areas with higher seismic magnitude. According to a study, earthquakes of magnitude 5.0 and above are frequent in the Hindu Kush region.

3.4. Seismicity Zonation

The approach of seismicity zoning of the Eastern Hindu Kush region has been depicted in Figure 9. The region is delineated into three zones based on fault density, seismic depth, and magnitude. The resulting seismic hazard map highlights that the north-eastern side of the region is located in a zone with a high level of seismic activity. On the other hand, the western Chitral, the western part of Upper Dir, and Lower Dir fall under a moderate seismicity zone, while Swat, south-eastern Chitral, and the northern section of Upper Dir lie in a zone with strong seismic activity (Figure 9). This area is highly vulnerable to earthquakes due to weak building codes and the susceptibility of existing structures. As a result, the region is at a high risk of being severely impacted by seismic events.

4. Discussion

The analysis revealed that the earthquakes in the Eastern Hindu Kush are caused by the collision of Indian and Eurasian tectonic plates (CUI et al. 2019). The findings indicate that the northeastern side of this region has quite active seismic activity. Swat, south-eastern Chitral, and the northern part of Upper Dir have strong seismic activity, compared to western Chitral, the western half of Upper Dir, and Lower Dir, which have moderate seismicity. The region's seismic hazard is undeniable, as shown by historical occurrences like the 2005 Kashmir Earthquake, which had an epicenter nearby the earthquake that occurred on October 26 and produced multiple aftershocks, and a much more recent earthquake of 5.2 magnitudes that occurred on November 22 (Basharat et al. 2021).

The analysis also revealed the cascading nature of disasters in the Hindu Kush region. It is essential to recognize that earthquakes can trigger secondary and tertiary hazards, such as landslides, landslide dams, and glacial lake outburst floods. As observed by Shafique (2020), landslides that were both widespread and disastrous were caused by the 2005 earthquake.

The study emphasizes that disaster resilience in the mountainous area requires making decisions based on the best Disaster Risk Reduction (DRR) and climate change adaptation studies available. A comprehensive framework is necessary for evaluating hazards' risks and recommending actions to make communities in the Eastern Hindu Kush region more resilient.

5. Conclusion

In conclusion, the study sheds light on the high seismicity and potential dangers posed by earthquakes in the Eastern Hindu Kush region. With the region being prone to secondary and tertiary hazards triggered by earthquakes, such as landslides and glacial lake outburst floods, it is crucial to adopt a multi-hazard approach to disaster risk reduction. By prioritizing initiatives that increase the population's resilience to catastrophic disasters, constructing earthquake-resilient buildings, avoiding construction on slopes, and addressing vulnerabilities found in socio-economic and political situations and processes, policymakers can significantly reduce disaster risk and protect the region's population.

Overall, the study highlights the importance of understanding the nature of disasters and adopting appropriate measures to ensure the safety and well-being of communities in the Eastern Hindu Kush region.

Acknowledgement

I want to express my gratitude to Dr. Shakil Mahmood for his consistent support, direction, and inspiration during this research.

References

Abers, G., Bryan, C., Roecker, S., & McCaffrey, R. (1988). Thrusting of the Hindu Kush over the southeastern Tadjik Basin, Afghanistan: Evidence from two large earthquakes. Tectonics, 7(1), 41-56.

Bahram, I. (2022). Analysis of Seismicity and Related Seismic Risk in Muslim Countries: Case Studies from Afghanistan and Pakistan (Doctoral dissertation, University of Arkansas).

Du, A., Wang, X., Xie, Y., & Dong, Y. (2023). Regional seismic risk and resilience assessment: Methodological development, applicability, and future research needs–An earthquake engineering perspective. Reliability Engineering & System Safety, 109104.

Hildebrandt, K. A., Burge-Beckley, T., & Sebok, J. (2019). Language documentation in the aftermath of the 2015 Nepal earthquakes: A guide to two archives and a web exhibit. Language Documentation & Description.

7th Intercontinental Geoinformation Days

igd.mersin.edu.tr

Analysis and forecasting of coastline morphology in Pakistan using digital shoreline analysis

Mazhar Shakoor [*1], **Shakeel Mahmood** [1]

[1]Government College University, Department of Geography, Lahore, Pakistan

Keywords
Remote sensing
Coastline detection
DSAS
Liner Regression Rate

Abstract
A sustainable protective strategy's design and informed coastal management depend on the assessment of coastal erosion and accretion. This study analyses Pakistani coastal dynamics from 1990 to 2020 using the Digital Shoreline Analysis System (DSAS) version 5.1 linked with ArcGIS software. The study, which focuses on erosion and accretion, uses metrics like Liner Regression Rate (LRR), End Point Rate (EPR), and Shoreline Change Envelope (SCE) to divide the area into four segments (a, b, c, and d) within the western zone. The findings show that the rates of erosion and accretion along Pakistan's coastline vary significantly. Maximum erosion rates are found on Transect Id 49, which reaches -42.28 m/yr; maximum accretion rates are found on Transect Id 105, which reaches 2.27 m/y to 2.77 m/y. Significantly, regions bordering Iran—segment d, in particular—accrete more than the original section between 1990 and 2020. The predominant process is erosion, which affects a large amount of Pakistan's coastline, especially in areas with a high concentration of industry and areas recently devastated by disasters. These results highlight the necessity of customized coastal management plans that take into account the intricate interactions between anthropogenic and natural elements in the area.

1. Introduction

Globally, coastal regions belong to the most valuable and vulnerable ecosystems (Kron, 2013; Hossain et al., 2020). According to researchers like, coastal regions are essential because they serve as transitional zones between terrestrial and aquatic ecosystems (Golla et al., 2020). By decreasing storm surges (Tognin et al., 2021), increasing carbon sinks (Lovelock and Reef, 2020, Ward et al., 2021), balancing sediment and nutrient cycling (Lonborg et al., 2021), and creating biodiversity conservation areas, they reduce exposure to natural hazards (such as coastal flooding and tsunamis) (Hopper et al., 2021). In contrast to 20% of the world's coastlines that are retreating at less than 10 meters per year and only 10% of the coasts that are either stable or advancing, over 70% of the world's coasts are retreating at rates of about 10 meters per year or more (INOC, 1991). Brunn's, (1962) rule says that, the near shore bottom adjusts in response to sea level rise to try and find a new equilibrium and restore the ratio between the distance offshore at which the waves hit the bottom (L) and the water depth at that distance (D). Equilibrium is created by the shore's erosion, which is equivalent to the sea level rise multiplied by the ratio (L/D).

Even though Pakistan's coastline is important, there haven't been many efforts to assess how erosion has affected it's roughly 1000 km of coastline. The majority of studies done to evaluate erosion and accretion along the Pakistani shoreline are small-scale and localized. In particular, Waqas et al. (2019) investigated the spatiotemporal variability of the offshore barrier islands (BIs) of the Sindh coast from 1974 to 2017, whereas Ijaz et al. (2017) examined the evolution of the main tidal creeks of the Islamic Republic of Pakistan (IDR) coastline from 1979 to 2017. As a result, reliable and efficient shoreline mapping is required for the implementation of proactive planning strategies for the future maintenance and control of coastal resources (Thomas et al., 2017). In order to accomplish this, extracting shoreline features from digital remote-sensing imagery is a potential and useful technique (Narayana, 2016).

In order to accomplish this, extracting shoreline features from digital remote-sensing imagery is a potential and useful technique (Narayana, 2016). With gratitude to enhanced sensor technology, open access data policies, and near real-time data collection, remote sensing has the unique feature of delivering geographically unlimited data at a lower cost than conventional ground-based evaluation (Szuster et al.,

* **Corresponding Author**

*(shakeelmahmoodkhan@gmail.com) ORCID ID 0000-0001-6909-0735

Cite this study

Shakoor, M., & Mahmood, S. (2023). Analysis and forecasting of coastline morphology in Pakistan using digital shoreline analysis. Intercontinental Geoinformation Days (IGD), 7, 9-12, Peshawar, Pakistan

2011). Remote sensing has greatly helped coastal observation for more than 40 years by supplying timely, cost-effective data at various geographic scales (Luijendijk et al., 2018). Furthermore, its abilities provide a rare window into past events to track the morphology of the shoreline over time and predict potential changes to the shoreline in the future using historical data.

2. Method

This study utilizes a combination of remote sensing data and existing databases for data collection. High-resolution satellite photos capture the research area at various times. Additionally, preexisting databases from governmental organizations, academic institutions, and prior studies supplement the data collection. The section provides a comprehensive overview of the Digital Shoreline Analysis System (DSAS) and its relevance to shoreline change analysis. DSAS, a widely-used tool employing GIS techniques, analyzes historical shoreline positions, quantifies erosion and accretion rates, and offers statistical tools for assessing significance. The section highlights DSAS's efficiency, accuracy, and ability to handle large datasets.

To digitize shorelines for different time periods, DSAS and GIS software will be used, and shoreline positions will be manually digitized based on visual indicators. The digitized shorelines will then be used to determine rates of shoreline change, erosion, and accretion. DSAS's statistical tools, including linear regression, will assess the scope and significance of shoreline changes over time. Spatial analysis approaches will identify hotspots of coastal change and vulnerable segments by superimposing shoreline change data on relevant spatial information. The analysis of shoreline change findings will unveil the primary causes and patterns of coastal erosion and accretion in the research area, presented through maps, charts, and statistical summaries to illustrate geographical and temporal changes in coastal dynamics.

Remote sensing data and pre-existing datasets will all be used in the data gathering for the Digital Shoreline Analysis System (DSAS) assessment of coastal erosion and accretion processes in Pakistan. For conducting a thorough research of shoreline dynamics and comprehending the coastal processes in the study area, precise and complete data gathering is essential.

A single database will be created from every piece of information that has been gathered, including remote sensing images, and existing datasets. Through this aggregation, the data may be easily managed and accessed throughout the analytical process. Georeferencing is an essential step in spatially aligning various datasets. Techniques for data resampling can be used to uniformly scale and standardize the spatial resolution of the datasets. By taking into account several elements that affect shoreline dynamics, this integration makes it possible to analyze patterns of coastal erosion and accretion in great detail. In order for the data to be used in the DSAS analysis, it may be necessary to convert or standardize it into a consistent format. In order to do this, data may need to be converted into GIS-compatible forms, like shape files or raster formats, while maintaining metadata and attribute information.

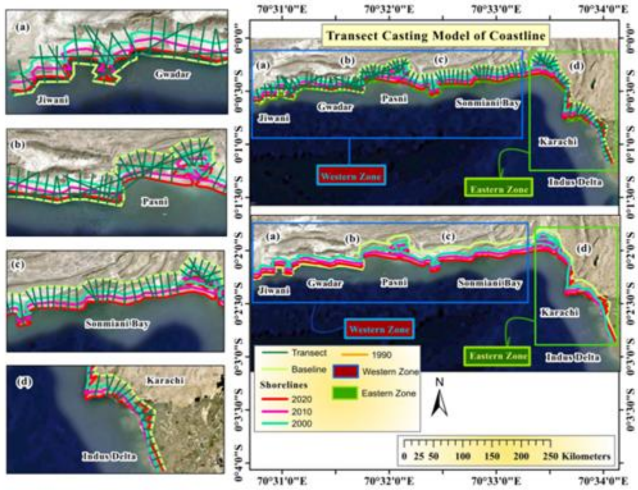

Figure 1. Transect generation for Study Area.

2.1. Study Area

Pakistan’s shoreline is about 1050 km-long coastline. This shoreline can be divided into two parts: the Sindh Coast (270 km) and the Makran Coast (720 km). The Exclusive Economic Zone (EEZ) of the nation is approximately 240,000 square kilometers in size, and its maritime zone, which includes the continental shelf, stretches up to 350 nautical miles from the shore. The Indus canyon, which covers the coastal shelf, is a notable feature of the region (Figure 1). Along the coasts of the two provinces, Sindh and Baluchistan, the extent of the continental shelf differs noticeably. The two provinces share authority over the seaward coastal zone up to 12 nautical miles (NM) from the coastline.

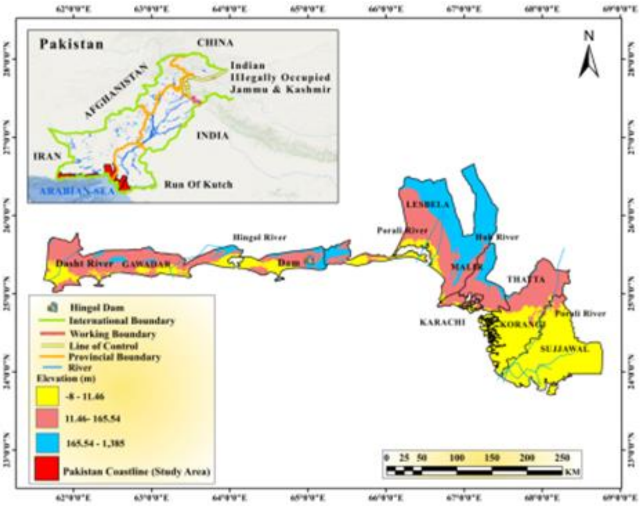

Figure 2. Location of study area.

The topography of Pakistan's coastline is heavily influenced by the nearby mountain ranges and the gradual deposition of sediments from the Indus River, resulting in a wide coastal plain in some areas. Overall, Pakistan's coastline varies significantly in elevation and topography, depending on the location. The central and eastern parts of Pakistan's coastline are typically flat and susceptible to flooding during monsoon season, with much of the land barely rising above sea level.

The weather is typically hot and humid all year long, reaching highs of up to 40 degrees Celsius (104 degrees Fahrenheit) in the summer. Heavy rainfall is brought to the maritime regions, especially in the east, during the monsoon season, which lasts from June to September. During the monsoon season, the Indus River delta is especially vulnerable to flooding, and the rains can seriously harm the area's infrastructure and crops.

3. Results

By fitting a regression line to all shoreline sites along a transect, the least squares regression (LRR) approach is used to calculate the rate of shoreline variation. Positions of the shoreline in the future and their corresponding confidence intervals can be predicted by this method, which considers all data points independent of changes in trend or accuracy. The overall average LRR rates for all segments exhibit a degradation tendency with values of -144.59 m/yr, -289.4 m/yr, -21.92 m/yr, and -84 m/yr, and an accumulation trend with values of 1.0 m/yr, 2.11 m/yr, 3.21 m/yr, and 8.48 m/yr for segments 1, 2, 3, and 4, accordingly. It shows more erosion along segment (b) and moderate to low along segment (c) to (d) while more accretion along segment (d). Segment (a) shows moderate erosion in Sky Blue colour,Segment (b) and (c) shows High to low erosion in Orange and Purple color respectively. Segment (d) show high accretion in Light Green color.

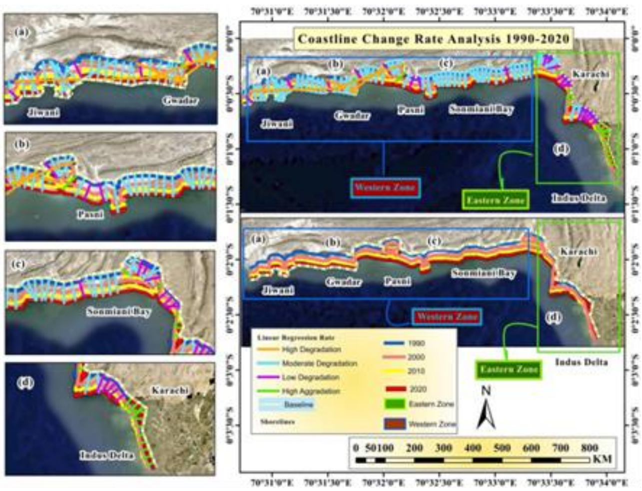

Figure 3. Coastline Change Analysis in terms of LRR.

The end point rate (EPR), a straightforward statistical metric, is calculated by dividing net shoreline movement (NSM) by the interval between the earliest and latest shoreline measurements. EPR average rate is shown in Figure 3 with the number of erosional transects at -6.15: 96% of all transects are subject to erosion of all transects with statistically significant erosion, 88.07%: highest value depreciation in 86.24%: While the average of all erosional rates is: -40.73 at transect ID: 49, -7.14. Number of accretions transects in an EPR 13 percent of all transects are incremental transects: Among all transects with statistically significant accretion, 11.93% are: 10.09%, 2.77 as the maximum value accretion at transect ID 105, and 1.16 as the average of all Accretion rates. The coastline is primarily subject to segment-wise degradation, as indicated in table 4.14, according to the rates of coastal position.

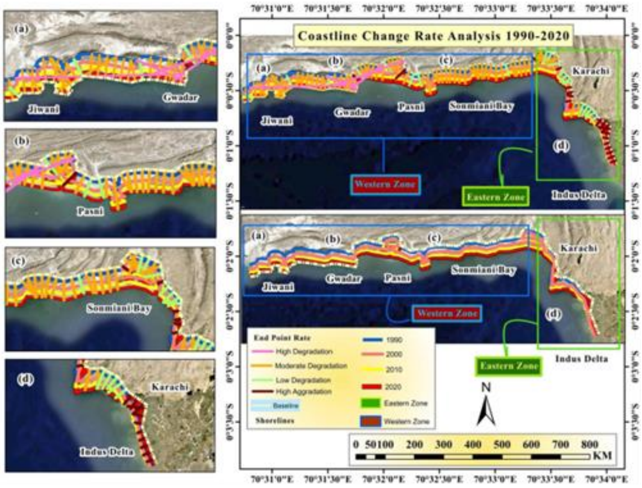

Figure 4. Coastline Change Analysis in terms of EPR.

4. Discussion

The Digital Shoreline Analysis System (DSAS) evaluation of coastal erosion and accretion trends in Pakistan has shed important light on the dynamics of the nation's coastline. The study has successfully identified rates of shoreline change and the primary hazards to the coastline by analyzing historical shoreline sites and using cutting-edge methods like DSAS version 5.1. The data point to segment-by-segment degradation as an important concern for Pakistani coastal communities. The study also identifies variances in the dynamics of other segments, highlighting the demand for specialized management approaches. This study utilized GIS and RS to evaluate 30 years (1990 to 2020) of data for the Pakistan coastline. Results indicate that erosion is noticeable along the coastline. The EPR approach is effective if the coastline experiences a steady movement whether toward the ocean or landward, but the LRR method is advantageous for segment-specific examination of coastal change.

5. Conclusion

Analyzing the spatiotemporal changes in the shoreline might be a useful non-structural strategy for coastal area decision-making. The current study may help in determining how susceptible the shoreline is. Human activity and environmental factors have significantly altered the coastline landscape over the past thirty years. The probable trends in shoreline alterations were predicted using the DSAS model, making it easier to create plans to reduce coastal risk. The shoreline in the western zone eroded significantly as a result of the development of Gwadar Port and its ancillary infrastructure, including breakwaters and jetties, whilst the shoreline in the eastern zone eroded comparatively little. Such constructions have the potential to interfere with natural coastal processes, change sediment transport and deposition patterns, and cause erosion and coastline retreat in the area. The results of the study indicate that natural coastal accretion, which entails sediment deposition and land creation along a coastline, is not a prominent process over Pakistan's entire coastline.

Acknowledgement

I would like to express my sincere appreciation to my co-author, Dr. Shakeel Mahmood, for his vital contributions and unflinching support during this project. His knowledge and commitment have made our joint work much more effective.

References

Addo, K. A., Walkden, M., & Mills, J. T. (2008). Detection, measurement and prediction of shoreline recession in Accra, Ghana. ISPRS Journal of Photogrammetry and Remote Sensing, 63(5), 543-558.

Anitha, P., & Natesan, U. (2014). Assessment of short term shoreline changes along Tuticorin, Southeast coast of India using Geospatial Techniques. Disaster Advances, 7(7), 1-7.

Arabadzhyan, A., Figini, P., García, C., González, M. M., Lam-González, Y. E., & León, C. J. (2020). Climate change, coastal tourism, and impact chains – a literature review. Current Issues in Tourism, 24, 2233 - 2268.

Baig, M. R. I., Ahmad, I. A., Shahfahad, Tayyab, M., & Rahman, A. (2020). Analysis of shoreline changes in Vishakhapatnam coastal tract of Andhra Pradesh, India: an application of digital shoreline analysis system (DSAS). Annals of GIS, 26(4), 361-376.

Beetham, E. P., & Kench, P. S. (2014). Wave energy gradients and shoreline change on Vabbinfaru platform, Maldives. Geomorphology, 209, 98-110.

Bera, R., & Maiti, R. (2019). Quantitative analysis of erosion and accretion (1975–2017) using DSAS—A study on Indian Sundarbans. Regional Studies in Marine Science, 28, 100583.

Blott, S. J., Pye, K., Van der Wal, D., & Neal, A. (2006). Long-term morphological change and its causes in the Mersey Estuary, NW England. Geomorphology, 81(1-2), 185-206.

Brantley, S. T., Bissett, S. N., Young, D. R., Wolner, C. W., & Moore, L. J. (2014). Barrier island morphology and sediment characteristics affect the recovery of dune building grasses following storm-induced overwash. PLoS One, 9(8), e104747.

Brooks, S. M., & Spencer, T. (2010). Temporal and spatial variations in recession rates and sediment release from soft rock cliffs, Suffolk coast, UK. Geomorphology, 124(1-2), 26-41.

Cabezas-Rabadán, C., Pardo-Pascual, J. E., Palomar-Vázquez, J., & Fernández-Sarría, A. (2019). Characterizing beach changes using high-frequency Sentinel-2 derived shorelines on the Valencian coast (Spanish Mediterranean). The Science of the total environment, 691, 216–231. https://doi.org/10.1016/j.scitotenv.2019.07.084

Chen, L. C. (1998). Detection of shoreline changes for tideland areas using multi-temporal satellite images. International journal of remote sensing, 19(17), 3383-3397.

Choung, Y., & Jo, M. (2016). Shoreline change assessment for various types of coasts using multi-temporal Landsat imagery of the east coast of South Korea. Remote Sensing Letters, 7, 100 - 91.

Cooper, J. A. G., Masselink, G., Coco, G., Short, A. D., Castelle, B., Rogers, K., ... & Jackson, D. W. T. (2020). Sandy beaches can survive sea-level rise. Nature Climate Change, 10(11), 993-995.

Mahmood, S., & Rahman, A. U. (2019). Flash flood susceptibility modeling using geo-morphometric and hydrological approaches in Panjkora Basin, Eastern Hindu Kush, Pakistan. Environmental earth sciences, 78, 1-16

Moore, L. J. (2000). Shoreline Mapping Techniques. Journal of Coastal Research, 16(1), 111–124. http://www.jstor.org/stable/4300016

Mukhopadhyay, A., Mukherjee, S., Mukherjee, S., Ghosh, S., Hazra, S., & Mitra, D. (2012). Automatic shoreline detection and future prediction: A case study on Puri Coast, Bay of Bengal, India. European Journal of Remote Sensing, 45(1), 201-213.

Tariq MAUR, Giesen VDN (2012) Floods and food management in Pakistan. Phys Chem Earth 47–48:11–20. https://doi.org/10.1016/j.pce.2011.08.014

7th Intercontinental Geoinformation Days

igd.mersin.edu.tr

Analysis of snow avalanche causes and damages in District Chitral, Pakistan

Ramsha Sohail [*1], **Shakeel Mahmood** [1]

[1]Government College University, Department of Geography, Lahore

Keywords
Avalanches
Chitral
DEM
Slope
Inventory Map

Abstract

Avalanches are a major problem in the Central Asian area, which includes the Karakorum, Hindu Kush, and Pamir ranges. Avalanches are frequently caused by the glaciers of Chiantar, Tirchmir, and Atrak near Chitral district. This study investigated the causes of avalanches in Chitral using data from the Digital Elevation Model (DEM) acquired from USGS. High-resolution Shuttle Radar Topography Mission (SRTM) DEM (30 m) from USGS was used to examine the causative factors such as elevation, slope, aspect, and hill shade. The objectives of the study were to determine the causes of natural avalanches, evaluate the amount of damage caused between 2010 and 2020, and provide a distribution map that shows the danger zones. Using GIS technology, it was discovered that the length and steepness of the slope, together with the lack of summit trees, were the main causes of large avalanches in Chitral. Avalanche hotspots throughout the last ten years were identified on the distribution map that resulted. Forecasters can identify danger areas and describe scenarios with the use of this information. The avalanche inventory map helps policymakers create preventative measures for risky locations in Chitral, which helps with risk management.

1. Introduction

Large glaciers that split off from their main bulk and tumble rapidly downward are typically the source of a snow avalanche. (Davies and McSaveney, 2002). In the winter, it is a serious hazard to individuals living in mountainous places and infrastructure i.e., buildings, roads (McClung and Schaerer 2006). Slope failure is controlled by the relationship between snow qualities and meteorological conditions (Mahboob et al. 2015). The structure and strength of snow layers, which are influenced by external variables such as wind, precipitation, and temperature, dictate the stability of an avalanche. Throughout the winter, the snowpack accumulates and is composed of several layers with highly changeable physical characteristics that are subject to variations in heat, water vapor concentration, and radiative fluxes brought on by shifting weather patterns. (Piacentini et al., 2020).

Snow avalanches in mountainous regions result in large financial losses and a high death toll. The kind of terrain, the weather, the presence of thick snowpacks over weak layers, and outside triggers are all factors that favor avalanche formation. These outside elements, which include explosions, earthquakes, passing skiers, and crumbling cornices, can add weight to the snowpack or cause it to break apart and trigger avalanches. (Podolskiy et al., 2010).

A secondary consequence of the destructive propagation of snow avalanches may be the massive deposition of surface rock and plant fragments that have traveled and piled alongside the debris from the avalanche. (Choubin et al., 2020). The accumulation of such snow-rock-debris and the mass wasting caused by snow avalanches have more detrimental long-term impacts. The accumulation of such snow-rock debris and the mass wasting brought on by snow avalanches result in more catastrophic long-term damage (Wesselink et al., 2017; Eckerstorfer and Malnes, 2015). The worldwide snow avalanche regime has been seen to be shifting during the past ten years (Oleinikov and Volodicheva, 2019). One of the main factors cited for raising the frequency and irregularity of occurrences as well as their risk and destruction is climate change. (Laute and Beylich, 2018).

In alpine regions around the world, avalanches represent a major risk to people, structures, and transportation systems. In Switzerland, avalanches claim the lives of 25 people on average every year; most of these deaths happen during winter sports activities and

* **Corresponding Author**

*(shakeelmahmoodkhan@gmail.com) ORCID ID 0000-0001-6909-0735

Cite this study

Sohail, R., & Mahmood, S. (2023). Analysis of snow avalanche causes and damages in District Chitral, Pakistan. Intercontinental Geoinformation Days (IGD), 7, 13-17, Peshawar, Pakistan

they regularly cause damage to infrastructure (Techel et al., 2015). In March 2012 and again in February 2015, a significant avalanche cycle hit mountain villages in Central Asia (Pakistan, Afghanistan, and Tajikistan), destroying towns, killing livestock, and killing hundreds of people. (Chabot and Kaba, 2016). Since 1950, Austria has seen almost 1,600 fatal avalanches, with an average of 30 fatalities year. In the past 55 years, the backcountry and off-piste have seen almost two thirds of all avalanche deaths (Höller 2007).

Around 172 people were killed and over 2 miles of road were buried in February 2010 when 17 avalanches that began in the southern approaches of the Salang Pass in the Hindu Kush Mountain range were caused by powerful winds and rain, according to World Atlas. A large number of cars were crushed by the avalanche and left to rot in frigid coffins, while other cars were forced into the valley's death jaws. A similar sequence of destructive avalanches struck four districts in the northeastern area of Afghanistan in February 2015. In the province of Panjshir, some 60 miles northeast of Kabul, over 100 houses were destroyed by avalanches. The trucks and rescue workers who were en route to the affected areas had difficulties due to heavy snowfall and fallen trees, which hindered their ability to reach the villages. A little over 310 persons lost their life in the accident (Ancey, 2016).

The biggest snow glacier in the world is located in Northern Pakistan, many hundred kilometers away from the glacier, across higher terrain and inside the severe shaking zone of the Hindu Kush. As of right present, there is no infrastructure in place to monitor seismic snow avalanches. (Khan et al., 2013).

2. Method

2.1. Data Collection

In this research, secondary data were used to achieve the desired objectives. The secondary data were acquired from concerned government departments and other private organizations. Digital Elevation Model (DEM), having 30m resolution, was obtained from the United States Geological Survey (USGS). The imagery data of the affected areas of Chitral were obtained by Landsat-8. The data related to damages by avalanches in the past were obtained from National Disaster Management Authority (NDMA) and, other sources. Some statistical data were acquired from other research articles, newspapers etc.

2.2. Data Processing

On the DEM of Chitral, analytical methods like as elevation, slope, aspect, and curvature were used to provide a visual result of the reasons of avalanche. Three rasters were required for the current study work flow. The pixel values in this DEM are in feet. In addition, the DEM values were used to derive the slope and aspect. Tables depicted the consequences of the avalanches in past years as well as the severity of the avalanches. A distribution map was created to depict the key avalanche hotspot regions in Chitral.

2.3. Study Area

Chitral is situated between 35°14′00′′ and 36°56′00′′ N and 71°11′00′′ and 73°42′00′′ E. Its surface area is 14,850 km^2. Geographically, Gilgit Baltistan's Ghizer District and the Swat District are located on the eastern side of Chitral. On the southern side of Chitral is Upper Dir; on the western side borders Afghanistan. Chitral is the largest of the districts that make up Khyber Pakhtunkhwa (KP), which is located in northwest Pakistan (Khan, 2013). Chitral stands at one of the highest elevations in the KP province. The Chitral area of Northern Pakistan traverses the Hindukush Range in the SW Pamir Syntaxis (Nusser, 2001).

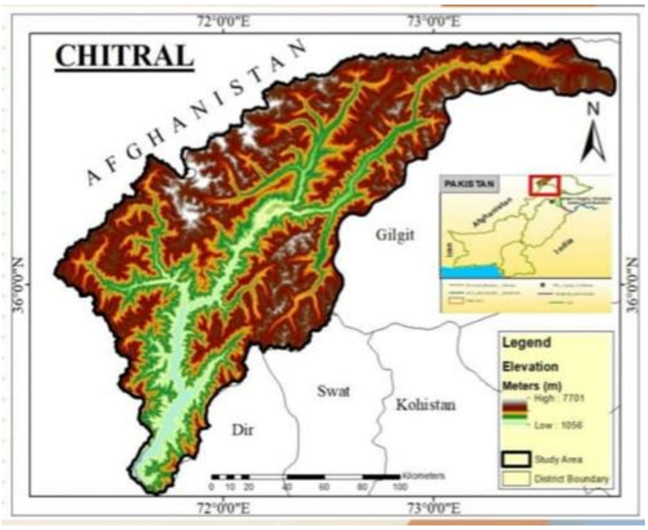

Figure 1. Location of the study area.

The climate in Chitral is moderate, with pleasant summers and extremely cold winters. Summer temperatures range from 22 to 24 degrees Celsius, while winter temperatures range from -4 to -6 degrees Celsius. Chitral has a moderate climate, with westerly winds that bring rain predominating from December to March throughout the winter. 16 degrees Celsius is the average annual temperature, with an average minimum temperature of 8 degrees and a high temperature of 24 degrees. Winters are cold, with January being the coldest, while summers are hot, with July being the hottest. (Ashraf et al., 2012).

3. Results

3.1. Analysis of Causative Factors

3.1.1. Slope

Slope angle is the principal factor that influences and causes avalanche release. To the second DEM raster, the Slope Function was appended. Specifically, a slope range of 30 to 50 degrees—that is, greater than 30 degrees and less than 50 degrees, respectively—was selected as the pixels-based value for essential slope-tolerance for this local function. Slope angles are one of the general parameters for avalanche vulnerability owing to slope. Avalanche initiation zones are systematically identified between 30 and 50 degrees (often even 60 degrees) as both wet and dry surfaces may be covered. The avalanche occurrence in this location is caused by the Chitral's slope degree, as indicated by the findings of the assessment's tilt study.

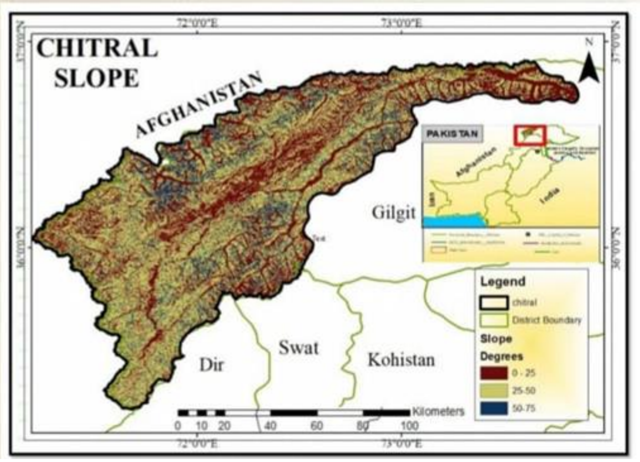

Figure 2. Slope of Chitral.

3.1.2. Elevation

While height doesn't directly affect the likelihood of snow avalanches, it does have an impact on the metrological factors that determine the stability of the snowpack. Consequently, height continues to be a crucial topographical factor in assessing avalanche danger in a spatial sense. Moreover, the wind speed increases in response to altitude changes, which increases the quantity of snowfall the wind produces. Elevation standards often include 4000 meters or above. It has been observed that most of the ice cover accumulates above 4000 m in Eastern Hindukush (between 4000 and 5500 m) since the study-area districts are in the HKH range. Therefore, in Chitral, height is a key factor in initiating the snow cover that leads to the Avalanche.

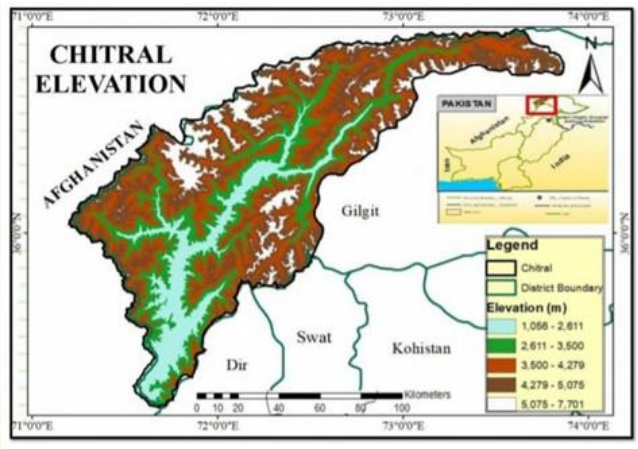

Figure 3. Elevation of Chitral.

3.1.3. Aspect

Using the Aspect Function, the original DEM raster was processed. Selected pixels were assigned an aspect of 112.5 to 202.5 (Aspect: Southeast & South), which means that they were greater than 112.5 degrees and less than 202.5 degrees, respectively. The values under investigation represent the Southeast aspect geographically because sun radiation rapidly focuses on certain aspect parts of the landscape, leading to the melting of ice.

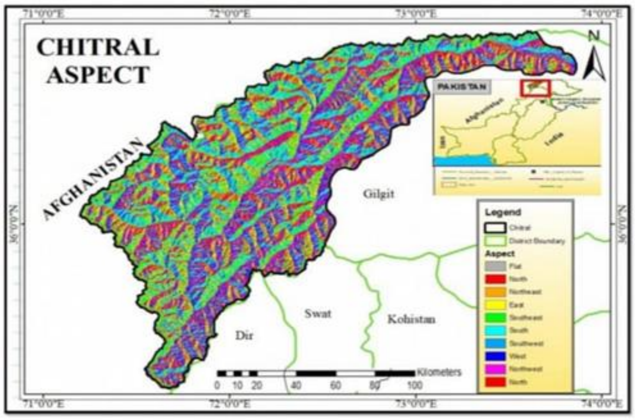

Figure 4. Aspect of Chitral.

3.1.4. Hillshade

The haded relief, or hillshading, technique adds a lighting effect to a map by taking into account variations in the studied area's height. To improve the visibility of the terrain, it mimics the sun's effects on hills and valleys, including shadows, shading, and lighting.

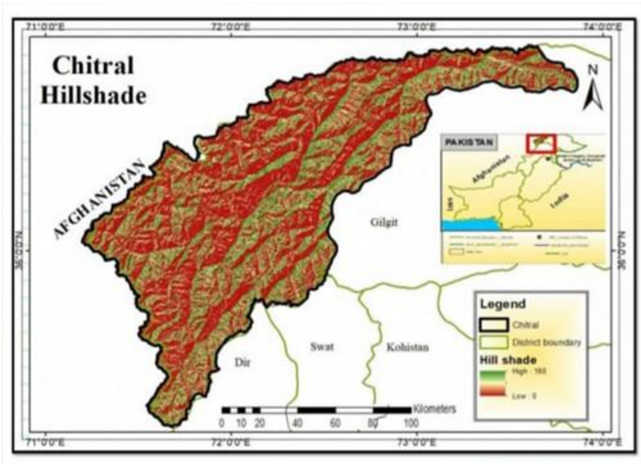

Figure 5. Hillshade of Chitral.

3.2. Analysis of Damages

Date of Avalanches	Locations	Effects
12-January-2011	Arkari Valley	12 people killed, 5 houses damaged
19-March-2016	Karimabad	19 people trapped, few vehicals were trapped because of the blockage of roads
22-March-2016	Susom Village	2 students killed
28-March-2016	Karimabad	6 injured, few cattles killed
27-January-2017	Sher shal village	15 people killed, many injured
05-February-2017	Karimabad	10 people killed
19-February-2017	Lowari tunnel	14 persons trapped 7 died
01-January-2017	Lowari top	2 persons killed
17- February-2017	Rech valley	1 death
18-February-2017	Reach valley	8 people killed, 10 injured,7 houses damaged
04-November-2018	Drosh	Four persons killed

Figure 6. Locations, dates and effects of avalanches.

There was insufficient data available on damages during the preceding 10 years. Google Scholars and

DAWN news provided the previously stated information of large-scale avalanche accidents in the Chitral area. The figures presented above indicate the timing and extent of the principal avalanche occurrence. Based on data, 2017 was the most catastrophic year in the preceding decade since most of the avalanches happened in Chitral.

3.3. Inventory map of Avalanches

The map below depicts the distribution of the key avalanche incidents and the regions in Chitral that are the biggest avalanche hotspots.

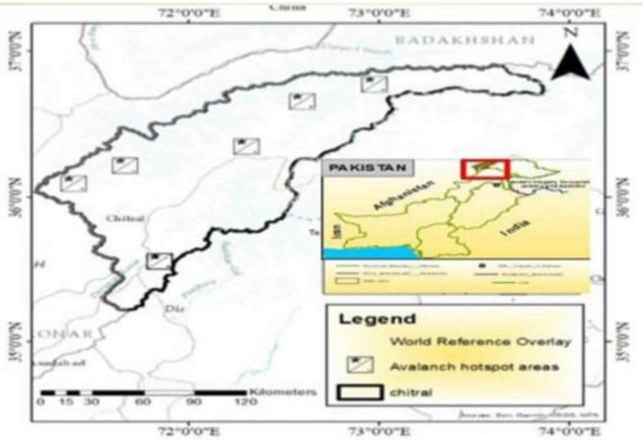

Figure 7. Main hotspot of Avalanches in Chitral.

4. Discussion

Records of avalanches from ranges including peaks over 7000 meters are not accessible. However, extreme altitudes and notable vertical relief above the terrain and snowline indicate certain common features. Near high mountain summits, winter weather with cold, dry snow is always predictable. The prolonged duration of snowpack instability is suggested by cold temperatures. Elevated altitudes indicate elevated solar radiation under clear sky conditions, which can rapidly exacerbate instability and potentially generate natural avalanches or increase the probability of human activation.

In some circumstances, there may be a greater chance for snow entrainment to generate bigger masses due to the steep vertical relief above the snowline. According to data from several sources, avalanches of significant size begin to deposit on slopes of around 10°, while snow avalanches begin to discharge on slopes between 25° and 55° (McClung, 2013).

Humans often misjudge avalanche instability, which leads to many accidents. (McClung and Schaerer, 2006). The results of icefalls are generally unpredictable. Risk management must be used if icefalls need to be crossed in order to avoid placing an excessive number of people in danger in one location at a time, including possible camp sites. The fact that snow avalanches caused by icefall have been a significant cause of fatalities makes forecasting more challenging. It may be argued that when the monsoon loads the accumulation zone, glacier mobility increases, even though there is no data to support this theory in terms of mortality rates.

5. Conclusion

In order to develop snow avalanche causes, the current study used a novel and integrative approach inside GIS by including crucial topography characteristics. The results show that there is a moderate to high risk of avalanche hazard in several areas of the study's target districts in Pakistan's northern zone. The analysis of avalanches in Chitral both geographically and temporally exposed a number of avalanche-related problems and damages. But the study also pinpointed the main natural avalanche sources in Chitral, and the main avalanche hotspot sites are shown on a map based on the majority of avalanche incidences in the region's districts. Additionally, elevation and related significant topographic data were extracted using SRTM DEM data with a 30-m spatial resolution used in this study; however, for optimal outcomes, high-resolution DEM is recommended.

Recommendations

- Non-structural methods
- Avalanche zoning
- Artificial Triggering
- Afforestation
- Structural Defenses

Acknowledgement

I would like to express my sincere appreciation to my co-author, Dr. Shakeel Mahmood, for his vital contributions and unflinching support during this project.

References

Ancey, C. (2016). Snow avalanches. In Oxford Research Encyclopedia of Natural Hazard Science.

Ashraf, A., Naz, R., & Roohi, R. (2012). Glacial lake outburst flood hazards in Hindukush, Karakoram and Himalayan Ranges of Pakistan: implications and risk analysis. Geomatics, Natural Hazards and Risk, 3(2), 113-132.

Chabot, D., & Kaba, A. (2016). Avalanche forecasting in the central Asian countries of Afghanistan, Pakistan and Tajikistan. Proc. 2016 Intl. Snow Sci. Wksp., Breckenridge, CO.

Choubin, B., Borji, M., Hosseini, F. S., Mosavi, A., & Dineva, A. A. (2020). Mass wasting susceptibility assessment of snow avalanches using machine learning models. Scientific Reports, 10(1), 1-13.

Davies T, McSaveney M (2002) Dynamic simulation of the motion of fragmenting rock avalanches. Can Geotech J 39(4):789–798

Eckerstorfer, M. & Malnes, E. Manual detection of snow avalanche debris using high-resolution Radarsat-2 SAR images. Cold Reg. Sci. Technol. 120, 205–218 (2015).

Fort M, Cossart E, Arnaud-Fassetta G (2010). Hillslope-channel coupling in the Nepal Himalayas and threat to man-made structures: the middle Kali Gandaki valley. Geomorphology, 124(3–4),178–199

Haq, I., 2007. Community response to climatic hazards in northern Pakistan. Mountain Research and Development 27 (4). http://dx.doi.org/10.1659/mrd.0947.

Hewitt, K. (2009) Rock avalanches that travel onto glaciers and related developments, Karakoram Himalaya. Inner Asia. Geomorphology, 103(1), 66–79

Höller, P. (2007). Avalanche hazards and mitigation in Austria: a review. Nat Hazards, 43, 81–101

Jessie Yeung, Sophia Saifi and Sajjad Qayyum, CNN; Updated 1309 GMT (2109 HKT) January 15, 2020; https://www.cnn.com/2020/01/15/asia/kashmir-pakistan-avalanche-intl-hnk/index.html

7th Intercontinental Geoinformation Days

igd.mersin.edu.tr

Mapping of frequently flood affected villages in Eastern Hindukush Region, Pakistan

Ramsha Sohail [*1], **Shakeel Mahmood** [1]

[1]Government College University, Department of Geography, Lahore, Pakistan

Keywords
Eastern Hindukush Region
Literature Review
Point Level Geocoding
Vulnerable villages Maps

Abstract

In order to locate and map the villages in the Eastern Hindu Kush region that are frequently affected by flooding, this research offers a rigorous analysis that combines point level geocoding techniques with an extensive literature assessment. In Eastern Hindu Kush region, flooding is a frequent and destructive natural calamity that affects infrastructure and populations. This study uses information from the literature and geospatial data to identify the communities that are most vulnerable in order to solve this problem. In order to precisely pinpoint these communities on digital maps, this research uses advanced geocoding techniques, which offers insightful information for activities aimed at mitigating and preparing for disasters. This study provides an integrated picture of the flood-prone regions in Eastern Hindu Kush region by merging historical flood data with academic research findings. This allows for targeted interventions and resource allocation for disaster management and community resilience.

1. Introduction

Floods are thought to be the most destructive hazard on a global scale (Rehman and Khan 2013; Qasim et al. 2016). Approximately half of all hydrometeorological disasters are related to flooding (Halgamuge and Nirmalathas 2017). The frequency and intensity of catastrophic floods have grown recently as a result of climate change, and they have become even more intense as a result of the encroachment of human activity along rivers (Khalid et al., 2018). In general, strong rains (Tariq and Giesen 2012; Mahmood et al. 2016a, b), dam breaches, river embankments, and the quickly melting of snow and glaciers (Jonkman et al. 2008; Sajjad et al. 2019) are the main causes of floods. Similarly, unexpected modifications to land cover and the fast expansion of communities inside floodplains aggravate floods even more (Syvitski and Brackenridge 2013; Iqbal et al. 2018).

The Eastern Hindukush region in Pakistan, characterized by its diverse topography and intricate river systems, faces the recurrent challenge of floods. This natural disaster often results from a combination of factors, including intense monsoon rains, glacial meltwaters and rapid snowmelt from the towering peaks (Gupta and Sah 2008). As watercourses navigate through steep terrains, the susceptibility to flash floods and riverine inundation increases, impacting both rural and urban communities (Hunter et al. 2005; Ali 2007). The socio-economic and environmental implications of floods in this region underscore the need for comprehensive understanding and effective mitigation strategies to safeguard lives and livelihoods.

2. Method

Frequently flooded villages in Pakistan's Eastern Hindukush region are mapped using an approach that incorporates information from a comprehensive literature assessment drawn from a variety of sources, including scholarly articles and newspapers. In order to pinpoint patterns, trends, and critical elements influencing a given village's susceptibility to periodic floods, a thorough analysis of past flood records, meteorological data, and scientific research was conducted in the first phase. This examination of the literature made it easier to identify high-risk areas, important environmental indicators, and socioeconomic variables that increase the impact of floods on nearby towns. Additionally, it gave rise to a basis for comprehending the dynamics of flood events, encompassing the part played by local topography, climate, and land use practices.

Point-level geocoding was used in the process to shift to a spatial analysis approach after the literature evaluation. This required converting textual data—like village names that are cited in the literature—into spatial coordinates, or latitude and longitude. The places that

* **Corresponding Author**

*(shakeelmahmoodkhan@gmail.com) ORCID ID 0000-0001-6909-0735

Cite this study

Sohail, R., & Mahmood, S. (2023). Mapping of frequently flood affected villages in Eastern Hindukush Region, Pakistan. Intercontinental Geoinformation Days (IGD), 7, 18-20, Peshawar, Pakistan

are commonly impacted by flooding were shown by plotting these geocoded points on a digital map using Geographic Information System (GIS) tools. A more precise identification and visualization of susceptible communities was made possible by the incorporation of geospatial data, which also let stakeholders and decision-makers evaluate the geographical distribution of flood-prone regions and rank intervention solutions.

2.1. Study Area

The districts of Chitral, Upper Dir, Lower Dir, and Swat make up Pakistan's Eastern Hindu Kush region. Geographically, it covers the area between 34°34'11" and 36°54'30" North Latitude and 71°11'56" to 73°52'5" East Longitude. A fourth region in Pakistan known as the Hindu Raj would be included in a comprehensive depiction of the Hindu Kush.

A long, twisting chain of mountains, including steep peaks like Mount Darkot and Buni Zom, which strike southward from the Lupsuk Peak in the Eastern region and continue to the Kabul River, forms this area. Hindu Kush includes this mountain range (Mahmood, 2019).

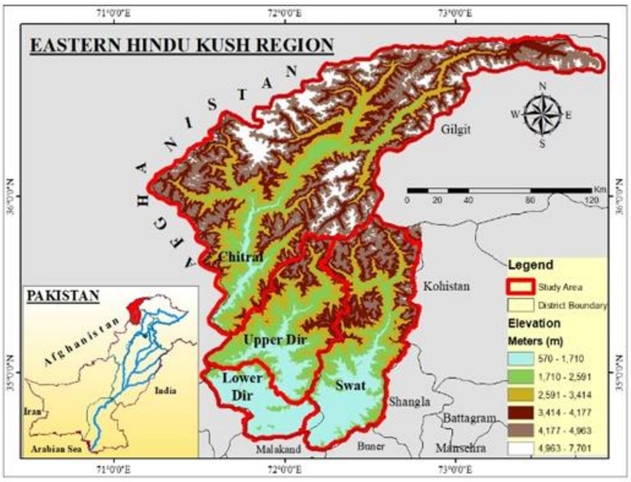

Figure 1. Location of study area.

The research region has cold to warm summer temperatures, with minimums of 16 °C and maximums of 32 °C. From December to February, the temperature drops below freezing. The hallmark of the winter season is the presence of snowfall. The difference between the minimum and greatest amounts of rainfall in December and March was 823 mm and 2149 mm, respectively. Snow usually begins to fall in November and moves southward when the temperature drops in December. Depending on the height, snow melting continues into March (Mahmood and Rahman, 2019).

3. Results

The Eastern Hindukush Region of Pakistan's inventory map of villages impacted by flooding shows a worrying pattern of repeated flood damage over the previous ten years, especially in tehsils like Kalkot, Chitral, Dir, Wari, Babuzai, Bahrain, and Timergara. These places are particularly vulnerable to floods due to a number of variables. First off, during periods of intense rainfall, the region is vulnerable to flash floods due to its geography, which is made up of steep hills and river valleys. The risk of riverbanks overflowing and surrounding settlements being inundated is increased by the mountainous topography, which speeds up water runoff. Furthermore, communities frequently settle in flood-prone locations since there are few other viable places to live, which makes the vulnerability worse owing to improper land-use planning and zoning rules.

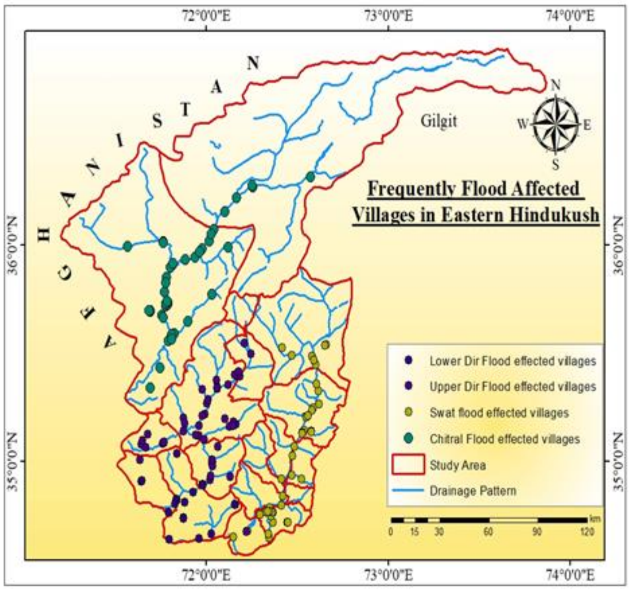

Furthermore, insufficient infrastructure in these tehsils exacerbates the effects of floods. Villages that lack sturdy drainage systems and flood prevention measures are vulnerable to harm during severe weather conditions. Older or badly maintained infrastructure frequently fails to resist the power of flooding, with disastrous results for the impacted populations. Moreover, soil erosion is a result of deforestation and poor land management, which lowers the ground's natural capacity to absorb excess water and raises the risk of floods. The confluence of these variables underscores the pressing requirement for all-encompassing flood alleviation tactics, encompassing the adoption of sustainable land-use methodologies, enhanced infrastructure, and community education initiatives, in order to protect the Eastern Hindukush Region against the catastrophic consequences of periodic flooding.

4. Discussion

Over the past ten years, the Eastern Hindukush Region of Pakistan—which includes tehsils like Kalkot, Chitral, Dir, Wari, Babuzai, Bahrain, and Timergara—has seen an alarming trend of recurring flood devastation. The creation of an inventory map that details the different elements that contribute to these places' susceptibility is crucial to comprehending the effects of floods on these settlements. The geology of the area, which is marked by rocky terrain and steep slopes, is one important component that enhances runoff during periods of heavy rainfall and speeds up the escalation of floods. The issue is made worse by the communities' poor construction of drainage systems and flood prevention measures, which makes them very vulnerable to flooding.

By itself, a hazard is not always disastrous. Any danger might have catastrophic effects on a population that is already vulnerable. One of the primary worldwide priorities is disaster resilience, which can only be achieved by reducing the vulnerability of vulnerable groups (Sarker et al., 2022). Vulnerability management helps communities that are vulnerable become resilient ones. According to Nasiri et al., (2016), vulnerability is a relationship that varies in both time and space between exposure and susceptibility of people, groups, structures, and objects. In addition to other demographic and environmental trends that have consistently exposed more people to natural hazards, the causes include population density, population growth, poverty, gender, age, and physical disability.

5. Conclusion

According to the research's findings, it will be easier to distinguish between high- and low-risk places by looking at the spatiotemporal pattern of flood-affected villages between 2010 and 2020. As a useful method for identifying flood risk from historical data, our analysis suggests using spatial statistics between 2010 and 2020. The spatial statistical approach is also demonstrated by the findings; with careful application, this method may be very helpful in identifying and analyzing flood mitigation strategies at the local level. The study has several limitations that should be noted, such as the fact that this analysis did not take into account anthropogenic or natural flood-influencing elements. On the basis of the categorical variables, the inquiry has been conducted. Within the subdivision, the risk zones are determined by how well the flood hotspots are identified. As such, mitigating actions must be considered in order to lower the danger of flooding hazards.

Acknowledgement

I would like to express my sincere appreciation to my co-author, Dr. Shakeel Mahmood, for his vital contributions and unflinching support during this project. His knowledge and commitment have made our joint work much more effective.

References

Ali, A. M. S. (2007) 2004 flood event in Southwestern Bangladesh: a study of its nature, causes, and human perception and adjustments to a new hazard. Nat Hazards 40:89–111

Gupta, V., & Sah, M. P. (2008) Impact of the trans-Himalayan Landslide Lake Outburst Flood (LLOF) in the Satluj catchment, Himachal Pradesh, India. Nat Hazards, 45, 379–390

Halgamuge, M. N., & Nirmalathas, A. (2017) Analysis of large food events: based on food data during 1985–2016 in Australia and India. Int J Disaster Risk Reduct, 24, 1–11

Hunter, N. M., Horritt, M. S., Bates, P. D., Wilson, M. D., & Werner, M. G. F. (2005). An adaptive time step solution for raster-based storage cell modeling of floodplain inundation. Adv Water Resour, 28, 975–991

Jonkman, S. N., Vrijling, J. K., & Vrouwenvelder, A. C. W. M. (2008). Methods for the estimation of loss of life due to foods: a literature review and a proposal for a new method. Nat Hazards 46:353–389. https://doi.org/10.1007/s11069-008-9227-5

Khalid, B., Cholaw, B., Alvim, D. S., Javeed, S., Khan, J. A., Javed, M. A., & Khan, A. H. (2018). Riverine food assessment in Jhang district in connection with ENSO and summer monsoon rainfall over Upper Indus Basin for 2010. Nat Hazards, 92, 971–993

Mahmood, S. (2019). Flood Risk Modelling and Management in Panjkora Basin, Eastern Hindu Kush, Pakistan. Doctoral dissertation, University of Peshawar, Peshawar.

Mahmood, S., & Rahman, A. U. (2019). Flash flood susceptibility modeling using geo-morphometric and hydrological approaches in Panjkora Basin, Eastern Hindu Kush, Pakistan. Environmental Earth Sciences, 78, 1-16.

Mahmood, S., Khan, A. H., & Ullah, S. (2016b). Assessment of 2010 fash food causes and associated damages in Dir Valley, Khyber Pakhtunkhwa Pakistan. Int J Disaster Risk Reduct, 16, 215–223

Mahmood, S., Rahman, A., & Sajjad, A. (2019). Assessment of 2010 food disaster causes and damages in district Muzafargarh, central Indus Basin. Pak Environ Earth Sci, 78,63

Nasiri, H., Mohd Yusof, M. J., & Mohammad Ali, T. A. (2016). An overview to flood vulnerability assessment methods. Sustainable Water Resources Management, 2, 331-336.

Qasim, S., Qasim, M., Shrestha, R. P., Khan, A. N., & Tun, K. (2016). Community resilience to food hazards in Khyber Pukhthunkhwa province of Pakistan. Int J Disaster Risk Reduct. https://doi.org/10.1016/j.ijdrr.2016.03.009

Rahman, A-u, & Khan, A. N. (2013) Analysis of 2010-food causes, nature and magnitude in the Khyber Pakhtunkhwa, Pakistan. Nat Hazards, 66, 887–904

Sajjad, A., Lu, J., Chen, X., Chisenga, C., & Mahmood, S. (2019). The riverine food catastrophe in august 2010 in south Punjab, Pakistan: potential causes, extent and damage assessment. Appl Ecol Environ Res, 17(6), 14121–14142

Sarker, M. N. I., Raihan, M. L., Parvin, G. A., Hossain, B., Alam, G. M., & Chumky, T. (2022). Urban vulnerability and resilience in the face of natural hazards: a critical conceptual review. Handbook on Climate Change and Disasters, 214-230.

Syvitski, J. P., & Brakenridge, G. R. (2013). Causation and avoidance of catastrophic fooding along the Indus River. Pakistan GSA Today, 23(1), 4–10

Tariq, M. A. U. R., & Giesen, V. D. N. (2012) Floods and food management in Pakistan. Phys Chem Earth, 47–48, 11–20. https://doi.org/10.1016/j.pce.2011.08.014

7th Intercontinental Geoinformation Days

igd.mersin.edu.tr

Optical remote sensing application of Kızılcaören-Sivrihisar (Eskişehir) REE-Thorium Deposit

Cihan Yalçın*[1], Orkun Turgay [2]

[1]Ministry of Industry and Technology, General Directorate of Industrial Zones, Worldbank PIU, Ankara, Türkiye
[2]Jeomodel, Ankara, Türkiye

Keywords
Remote sensing
REE-Th
Optical Remote Sensing
ASTER L1T data
Kızılcaören-Sivrihisar

Abstract

The Kızılcaören-Sivrihisar rare earth element (REE)-Thorium deposit is situated within the Eskişehir Province of Türkiye. The deposit in question represents the sole commercially viable rare earth element-thorium (REE-Th) source within Türkiye, thus rendering it a significant supplier of these crucial minerals. The Kızılcaören-Sivrihisar REE-Thorium deposit exhibits a captivating mineral assemblage that possesses the potential to unlock valuable resources. Within the geological composition, a complex interplay of minerals takes place, involving fluorite, bastnäsite, and barite. The Kızılcaören-Sivrihisar deposit can be effectively mapped using optical remote sensing techniques. This phenomenon can be attributed to the fact that the deposit exhibits several discernible characteristics that can be identified through the utilization of optical remote sensing techniques. This study demonstrates the presence of fluorite-bearing zones, which are characterized by the fluorite index. The present investigation provides evidence for the concurrent presence of divalent iron alongside fluorite. Quartz is also present within this ore-bearing zone. Magnesite and calcite are also found within the serpentinitic-mafic zone in the study area. In conclusion, the study area successfully identified the ore-bearing fluoritic zone through the application of remote sensing processing using ASTER L1T data. The aforementioned studies have demonstrated that optical remote sensing possesses significant potential as a valuable instrument for the examination and assessment of the Kızılcaören-Sivrihisar REE-Th deposit. The utilization of optical remote sensing enables the mapping of deposits, the identification of their extent, and the evaluation of their economic development potential.

1. Introduction

In the field of Earth sciences and mineral resource exploration, Optical Remote Sensing has emerged as a revolutionary technology, shedding light on novel approaches for detecting and characterizing crucial mineral deposits. Rare Earth Elements (REE) and Thorium deposits are of great importance due to their diverse applications in advanced technologies and sustainable energy systems. By harnessing the capabilities of light and electromagnetic radiation, Optical Remote Sensing offers a novel methodology for the non-invasive examination and evaluation of subterranean resources. This introduction explores the significant applications of Optical Remote Sensing in understanding the complexities of REE-Thorium deposits. It emphasizes the crucial role of Optical Remote Sensing in mapping geological characteristics, estimating the potential of resources, and informing strategic decision-making for a more efficient utilization of resources in the future. As we embark on this expedition, we will unveil the intricate relationship between technology and geology, which is reshaping the landscape of mineral resource management and fostering a new era of sustainable development.

With the development of remote sensing technology in recent years and the emergence of new methods accordingly, the separation of mineral deposits such as REE and radioactive raw materials can now be done successfully with ASTER data. In this article, the geological map of Kızılcaören Thorium-REE deposit and the mapping of minerals accompanying the ore minerals are explained. ASTER L1T is used for remote sensing

* **Corresponding Author**

*(cihan.yalcin@sanayi.gov.tr) ORCID ID 0000-0002-0510-2992
(orkun.turgay@aol.coml) ORCID ID 0000-0001-6958-3628

Cite this study

Yalçın, C., & Turgay, O. (2023). Optical remote sensing application of Kızılcaören-Sivrihisar (Eskişehir) REE-Thorium Deposit. Intercontinental Geoinformation Days (IGD), 7, 21-24, Peshawar, Pakistan

data for making mineralogical and geological mapping of the study area.

Despite considerable REE developments in Türkiye (e.g., Eskişehir-Kızılcaören, Malatya-Kuluncak, Sivas-Karaçayır), there is still no agreement on the petrogenesis of REE in these places due to a lack of previous investigations (Çimen et al., 2020).

The primary constituents of major and strategic radioactive elements include uranium and thorium. Applications are pursued in order to locate these elements due to their prevalence in numerous geological locations. Based on prior research (Şaşmaz, 2008), it has been determined that the primary sites for the enrichment of radioactive elements in Türkiye are situated in the western region of Anatolia.

The Eskişehir-Kızılcaören deposit is situated in the northwestern region of Türkiye and encompasses a mineral assemblage consisting of fluorite, bastnäsite, and barite. The Kızılcaören region has been recognized as a significant rare earth element (REE) deposit in Türkiye due to its average tenor weight of 2.78% and estimated REE content of approximately 4.67 million metric tons (Mt) (Kaplan, 1977; Öztürk et al., 2019). The area of the mineralization in question was first identified in 1959 using airborne gamma-ray spectrometry, as a result of the radioactivity emitted by thorium (Gültekin et al., 2003).

According to Nakoman (1979) four types Th-REE mineralization was identified. The classification primarily relies on the mineral paragenesis.

A study by Çimen et al., (2020) suggests that the rocks that host the REE-Th mineralization in the Eskişehir-Kızılcaören consist of hydrothermal metasomatized carbonatite and limestone, respectively.

The Kızılcaören-Sivrihisar REE-Thorium deposit in the Eskişehir region is noteworthy for its abundant concentration of Rare Earth Elements (REE) and Thorium, making it an intriguing topic for research. By harnessing the complex interaction between light and electromagnetic radiation, Optical Remote Sensing emerges as a pioneering approach, providing a non-intrusive and comprehensive understanding of the geological intricacies associated with this deposit. This paper delves into the specific application of Optical Remote Sensing in the context of the Kızılcaören-Sivrihisar REE-Thorium deposit.

2. Method

Pre-processing and image enhancement steps were employed in the remote sensing application of one of Türkiye's well-known REE-Thorium deposit.

Firstly preprocessing was applied to the ASTER L1T satellite imagery dataset of the deposit. In preprocessing, VNIR(Visible infrared bands) and SWIR(Shortwave infrared bands) clipped and radiometric calibration applied on these bands, later VNIR and SWIR bands stacked then IARR atmospheric correction applied on stacked VNIR and SWIR bands in ENVI Software. Radiometric calibration was also applied on TIR (Thermal Infrared bands), later Thermal Atmospheric correction (TAC) applied before Emissivity Correction in ENVI. All the preprocessing completed with atmospherically corrected VNIR and SWIR bands stacked to the atmospherically corrected and Emissivity corrected TIR data. Vegetation index (b3-b2)/(b3+b2) applied for vegetation mask created and applied to the final ASTER data for preprocessing is completed with masking on the final data for image processing (image enhancement) process for the discrimination of mineralogical and geological units of the study area.

2.1. Image Processing (Image Enhancement) Step

Image processing or image enhancement application is made for mineralogical mapping and alteration mapping, rock type mapping is the must. For this reason, Mafic Minerals detected by (b12/b13)*(b14/b13) Carbonaceous rocks (CI) were detected with (b13/b14) formulae for limestone and dolostone and Quartz (QI) detected with (b11/(b10+b12)*(b13/b12) for silicification Quartz bearing rocks (QRI) are detected with (b10/b12)*(b13/b12) formulae. Hydroxyl bearing (OH) minerals are detected with b4/b5 In addition Fluorite bearing zones detected by FI(Fluorite Index) with (b8/b6)*(b5/b3) from Hafez et al., (2021), Magnesite is detected by (b6+b8)/(b7+b9) formula and ferrous(II)Iron was detected by(b5/b3)+(b1/b2) and ferrous hydroxides is detected by (b6+b8)/b7, serpentine rich rocks is detected with (b7+b9)/b8 formulae with band arithmetic methods In ENVI software. Later these ratios were combined. And also decorrelation stretch was used for image processing step in the study area.

3. Results

Figure 1 represents the general geological situation of the study area. In Figure 2. Bluish zones contain ferrous iron (divalent iron) and light green zones represent carbonaceous (calcite) zones. In Figure 1 bright zones contain calcite, magnesite and few divalent irons.

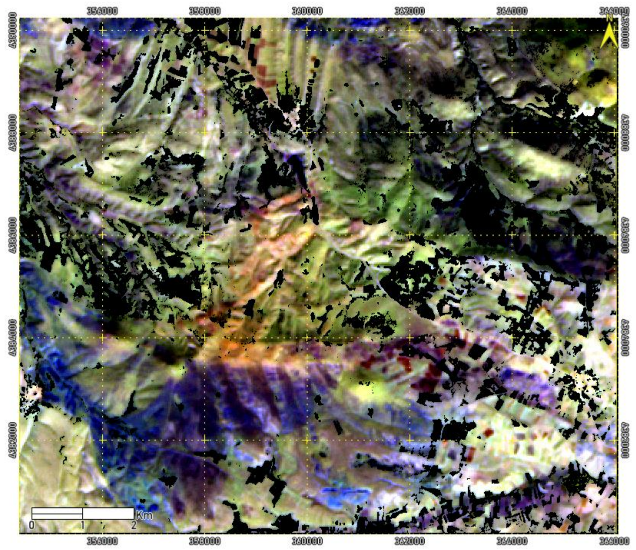

Figure 1. General rock discrimnation of the study area with RGB 7-4-2 combination

Figure 2 contains thorium bearing ore zones are represented by bluish zones. Bright green and greenish zones contain carbonates like calcite and magnesite. Pink and reddish zones contain divalent iron.

Figure 3 contains fluoritic zones in reddish and orange zones have the thorium related minerals and green areas represent the magnesite (magnesium carbonate) zones. In Figure 2, Hydroxyl bearing alteration minerals exist in the bluish and bright blue zones. Figure 3 contains fluoritic zones in reddish and orange zones have the thorium related minerals and green areas represent the magnesite (magnesium carbonate) zones.

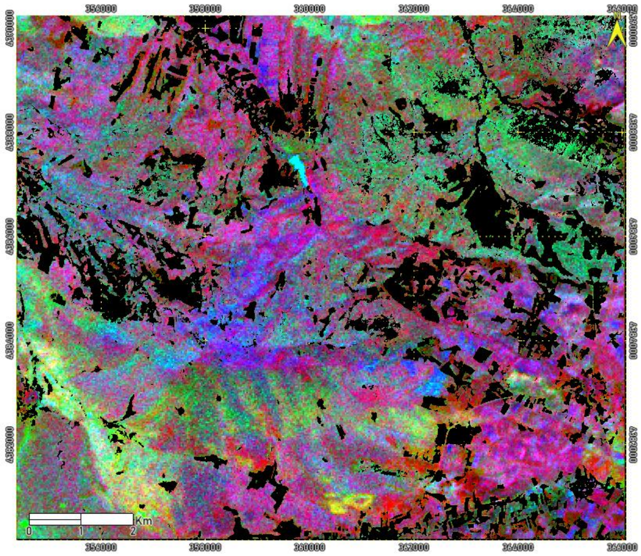

Figure 2. Magnesite-Calcite-Ferro(II)Iron in RGB band math combination image of study area

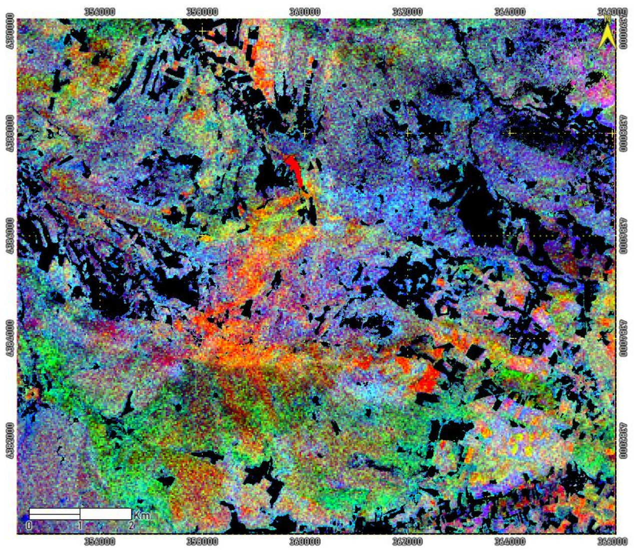

Figure 3. Fluorite-Magnesite-OH in RGB band math combination image of study area

Figure 4 contains fluoritic zones in reddish and orange zones have the thorium related minerals and blue zones represent the magnesite (magnesium carbonate) zones.

Figure 5 contains fluoritic zones in blue and bluish and orange zones have the thorium related minerals and green zones represent the magnesite (magnesium carbonate) zones. Blue zones represent Quartz bearing or quartzitic rocks.

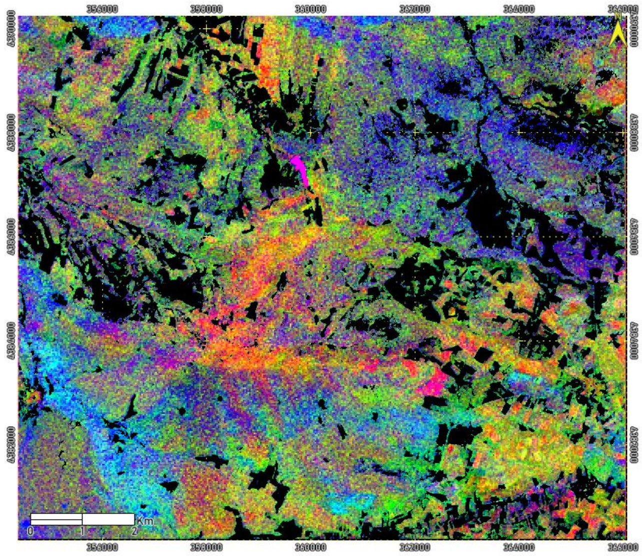

Figure 4. Fluorite-Magnesite-Serpentine RGB band math combination image of study area

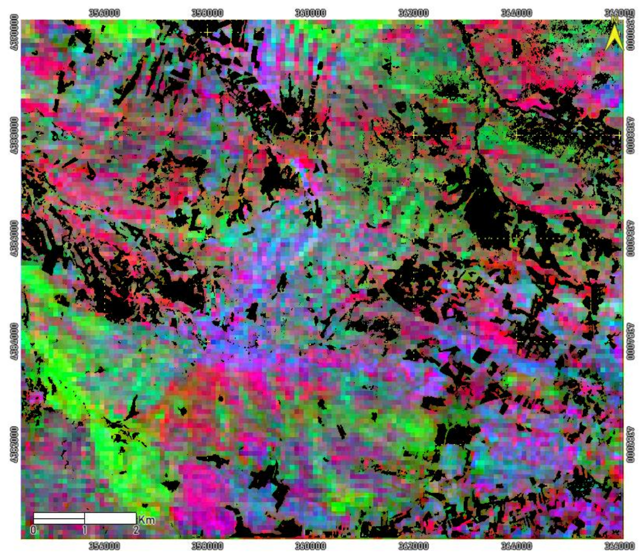

Figure 5. QRI-MRI-Fluorite in RGB band math combination image of the study area.

4. Discussion

The Kızılcaören-Sivrihisar REE-Thorium deposit exhibits a captivating mineral assemblage that possesses the potential to unlock its valuable resource. In the geological composition, a complex interplay of minerals takes place, involving fluorite, bastnäsite, and barite. The combination of these distinct minerals presents a compelling narrative regarding the origin and development of the deposit, providing invaluable knowledge about its historical context and economic importance.

The interdependent association among the three minerals, namely fluorite, bastnäsite, and barite, provides significant insights into the dynamic geological processes that influenced the formation of the Kızılcaören-Sivrihisar deposit. The utilization of Optical Remote Sensing, which possesses the capability to identify and differentiate minerals through their distinctive spectral characteristics, has emerged as a pivotal instrument in comprehending the complex dynamics of mineral interactions. The technology assists in the identification of the distribution, concentration, and potential economic significance of these minerals within the geological matrix of the deposit by capturing their distinct reflectance patterns. By examining the mineral composition of fluorite, bastnäsite, and barite, we can enhance our comprehension of the genesis of the deposit and establish a foundation for effective resource management strategies.

5. Conclusion

The previous studies have established a correlation between fluoritization and the presence of thorium and rare earth elements (REE) in the study area. This study demonstrated the presence of fluorite-bearing zones using the fluorite index. The study demonstrates the coexistence of divalent iron with fluorite. Quartz is also present within this zone containing ore. The study area also contains deposits of magnesite and calcite within the serpentinitic-mafic zone.

In summary, the study area has successfully identified ore-bearing fluoritic zones through the utilization of remote sensing techniques.

References

Çimen, O., Corcoran, Loretta., Kuebler, C., Simonetti, S., & Simonetti, A. (2020). Geochemical, stable (O, C, and B) and radiogenic (Sr, Nd, Pb) isotopic data from the Eskişehir-Kızılcaören (NW-Anatolia) and the Malatya-Kuluncak (E-central Anatolia) F-REE-Th deposits, Turkey: implications for nature of carbonate-hosted mineralization. Turkish Journal of Earth Sciences, 29, 5, Article 7. https://doi.org/10.3906/yer-2001-7.

Gültekin, A. H., Örgün, Y., & Suner, F. (2003). Geology, mineralogy and fluid inclusion data of the Kizilcaoren fluorite- barite- REE deposit, Eskisehir, Turkey. Journal of Asian Earth Sciences, 21, 365-376.

Hafez, M., Abu El-Leil, I., Soliman, N., & Abu Bakr, M. (2021). New Fluorite Index Using ASTER Data of Gabal Abu Diyab area, Central Eastern Desert, Egypt. *Al-Azhar Bulletin of Science*, *32*(Issue 2-D), 13-21. doi: 10.21608/absb.2021.94705.1136

Kaplan, H. (1977). Rare earth elements and thorium complex deposit of Kizilcaören village, Sivrihisar-Eskişehir, Turkey. Bulletin of Geological Engineering, 2, 69-76.

Nakoman, E., 1979, Radyoaktif hammaddeler jeolojisi: Ankara, M.T.A. Publ., Egitim Serisi No. 20, 575 p.

Öztürk, H., Hanilçi, N., Altuncu, S., & Kasapçı, C. (2019). Rare earth element (REE) resources of Turkey: An overview of their characteristics and origin. Bulletin of the Mineral Research and Exploration, 159, 129-143.

Şaşmaz, A. (2008). Determination of uranium occurrences from soil, water and plant samples and possible environmental effects around Köprübaşı (Manisa)uranium bed. Scientific and Technical Research Council of Turkey, Project no 107Y226, 82p

7th Intercontinental Geoinformation Days

igd.mersin.edu.tr

An application of remote sensing and GIS in geothermal alteration and potential in Ziga/Aksaray (Türkiye)

Hacer Bilgilioğlu [1]

[1]Aksaray University, Faculty of Engineering, Department of Geological Engineering, Aksaray, Türkiye

Keywords
Remote sensing
Geographic Information System
Geothermal
Alteration

Abstract

Where energy production is essential today, geothermal energy, one of the renewable energy sources, is of great importance. Ziga geothermal field, chosen as the study area, has an essential geothermal potential. Ziga Geothermal Area benefits from numerous sources, wells, thermal tourism, residential heating, greenhouse cultivation, and balneological practices. Hydrothermal alteration zones are one of the critical indicators for the exploration of geothermal fields. It contributes significantly to the exploration studies by narrowing the target areas in the feasibility studies of geothermal exploration studies. With remote sensing (UA) techniques in detecting hydrothermal alteration minerals spread over large areas, it is ensured that large areas can be evaluated holistically, and effective results can be obtained by saving time and economy. In the study, it was evaluated in a GIS environment by using ASTER satellite data to determine the hydrothermal alteration zones. The differences in the determined parameters of all alteration types in the study area were mapped with ASTER data. As a result of the data obtained by remote sensing and GIS methods, guiding data for the discovery of new potential areas in the rocks of Ziga and its surroundings are explained in detail in the study.

1. Introduction

Countries' energy needs are constantly increasing depending on their development and growth rate. Today, energy consumption is equated with the level of development. About 90% of the energy consumption in the world is met by coal, oil, and natural gas, which are called fossil fuels. Alternative energy sources are being researched due to the high carbon dioxide emissions of fossil energy sources and the fact that they are not renewable. Geothermal energy, one of the alternative sources, is significant because of its low carbon dioxide rate and renewable nature. Geothermal energy is preferred because it is uninterrupted compared to renewable energy sources such as the sun and wind (Arslan et al. 2000).

Geothermal energy can be defined as hot water and steam formed by the heat in various depths of the earth's crust, whose temperature is above the regional and atmospheric temperatures and contains molten minerals, salts, and gases. Since the waters that make up the geothermal fluid are generally of meteoric origin, geothermal resources are renewed as long as the atmospheric conditions continue (Kara, 2010). Parameters required for the formation of a geothermal system; The heat source deep in the earth's crust is the fluid that carries the heat (nutrition), the reservoir rock that contains the fluid, and the cover rock that prevents the loss of heat. Magma activities that reach shallow depths in the crust and/or the earth's surface from fractured and weak zones due to tectonism constitute the heat source of the geothermal system. Meteoric waters, which filter through cracks and cracks from the earth, accumulate in the reservoir rock, which is porous and permeable, after warming in the depths. Some of these waters rise along the fault lines and reach the earth's surface and form geothermal resources.

The criteria taken into account in geothermal resource exploration; are hot springs, steam outlets, geysers, and hydrothermal alteration zones. The most important of these is hydrothermal alteration, and potential geothermal areas have been determined by investigating hydrothermal alteration zones in many countries. Hydrothermal alteration is the chemical and mineralogical changes that occur in the rocks in the relatively shallow parts of the earth's crust by being affected by the heat-loaded fluids circulating in them. In this study, alteration types, distributions, and

* Corresponding Author

*(bilgiliogluhacer@gmail.com) ORCID ID 0000-0002-8629-1077

Cite this study

Bilgilioğlu H (2023). An application of remote sensing and GIS in geothermal alteration and potential in Ziga/Aksaray (Turkey) 5th Intercontinental Geoinformation Days (IGD), 25-28, Peshawar, Pakistan

interrelationships in the study area were examined (Burçak, 2006; 2009).

The kaolinization of feldspars is an example of this. In addition, the changes that occur in the rock with the elements added or withdrawn by the hydrothermal fluid (for example, silicification) can be considered in this context (Öngür, 1980). There are two types of hydrothermal alteration, active and inactive hydrothermal alteration. Active hydrothermal alteration is a continuous hydrothermal alteration and is used in the investigation of economically significant fluidized beds such as geothermal energy. On the other hand, inactive hydrothermal alteration is hydrothermal alteration; the activity gradually decreases over time and is used to investigate stable deposits of economic importance. This concept, which is examined in two parts as active and inactive hydrothermal alteration, depends on the rock composition, the composition of the geothermal fluid, and the physicochemical conditions (pressure and temperature) during the phase changes that develop. It is time-consuming and costly to prepare the alteration maps used to determine potential hydrothermal areas with classical field studies. Therefore, especially in recent years, remote sensing has been used frequently in the determination of alterations, and its success has been demonstrated by many researchers (Kratt et al., 2010; Calvin et al., 2015; Rodriguez-Gomez et al., 2021; Ramadhan et al., 2021; Canbaz et al., 2021; Şener and Şener, 2021; Uzun and Turgay, 2022).

This study aimed to determine the potential hydrothermal areas in and around Ziga thermal in Aksaray province by remote sensing. Advanced argillic, kaolinization, propylitization, sericitization and quartz alteration, and land surface temperature maps were produced and combined in this context. Finally, the geothermal suitability map was created.

2. Method

The Central Anatolian region tectonically forms an area where significant deformations are observed, bounded by the North Anatolian Fault and the East Anatolian Fault (Ketin, 1969). All these deformations are directly related to the volcanic activities in Central Anatolia. The volcanic activities that continued from the Miocene to the Quaternary created critical geothermal fields in the Central Anatolian region. One of these fields is the Aksaray Ziga field, located approximately 50 km southwest of Nevşehir.

The oldest unit, which cannot be observed in the study area but is stratigraphic, is the Bozçaldağ metamorphic schists and the Paleozoic age unit formed by the ultrabasic. Götük ignimbrite and Karakaya volcanic overlie this unit unconformably. Pink and yellow basalt, spilite obsidian, pumice, and Selime tuffs rich in andesite overlie these units. Kızılkaya ignimbrites with welded tuff are overlying the Selime tuff. It crops out in a wide area around the Ziga hot and mineral springs in the study area. Quaternary units overlie all these units (Afşin ve Yıldız, 1997; Duru, 2006).

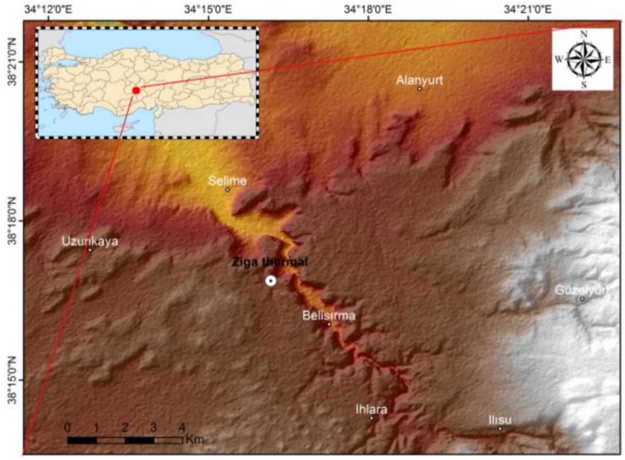

Figure 1. Study area

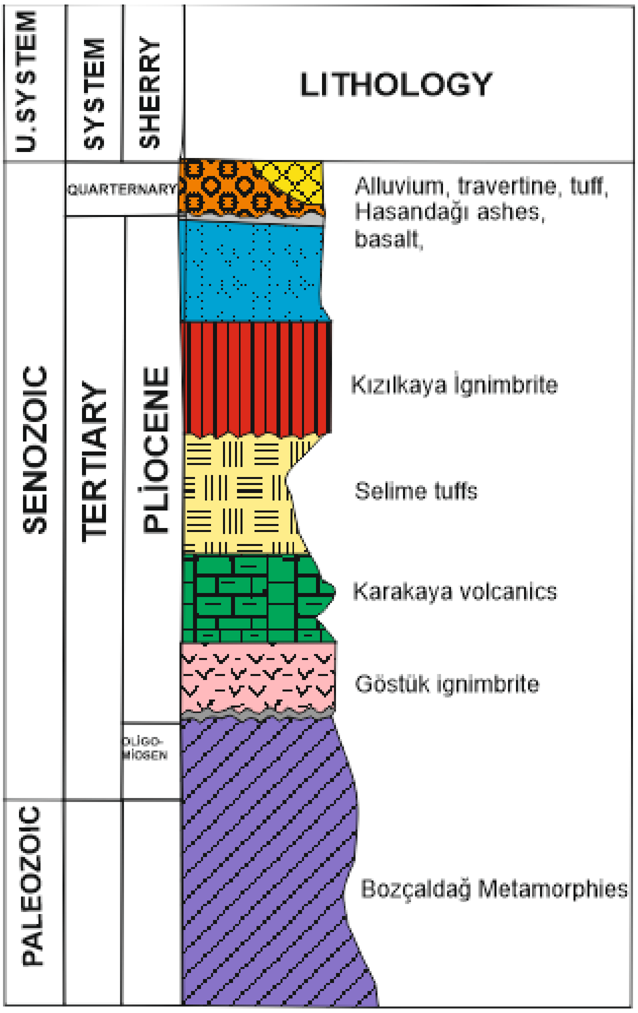

Figure 2. Stratigraphic section of the study area (Şimşek, 1993)

3. Results

ASTER (Advanced Spaceborne Thermal Emission and Reflection Radiometer) L1T dataset was used for creating alteration maps such as; advanced argillic, kaolinization, propylitization, sericitization, and quartz. The band ratios used in the determination of the relevant alterations as a result of the literature research are as follows;

- (B4+B6)/B5 band ratio for advanced argillic alteration (Fakhari et al., 2019; Uzun and Turgay, 2022),
- (B4/B5)(B8/B6) band ratio for Kaolenization (Ninomiya, 2003),
- (B6+B9)/(B7+B8) band ratio for Propylitization (Shahi and Kamkar-Rouhani, 2014),
- (B5+B7)/B6 band ratio for Sericitization (Fatima et al., 2017),
- ($B11^2$)/(B10*B12) band ratio for Quartz (Ninomiya, 2003).

After overlaying alteration and land surface maps using the ArcGIS raster calculation tool, the geothermal suitability map was created.

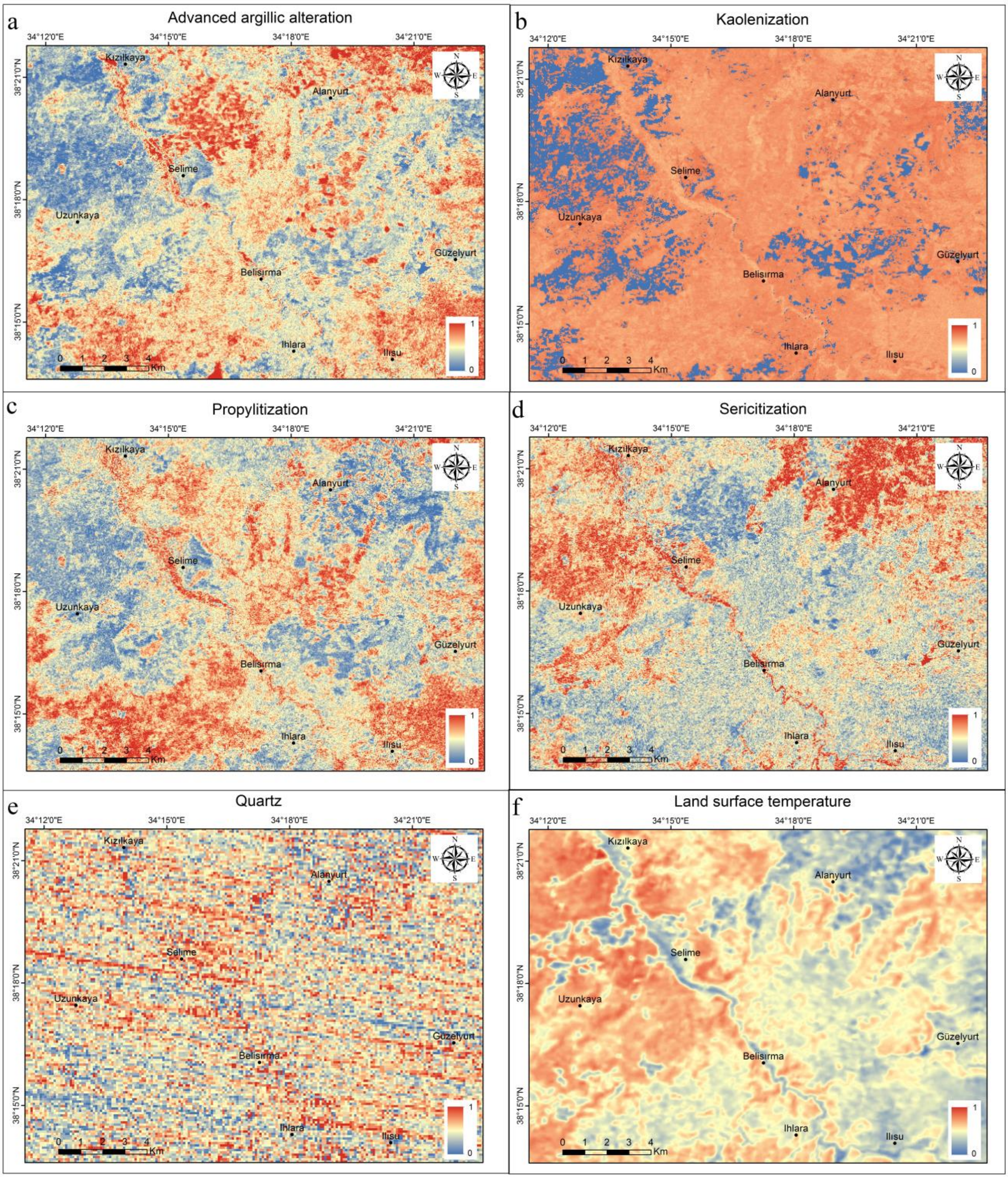

Figure 3. a: advanced argillic b: kaolinization c: propylitization d: sericitization e: quartz f: land surface temperature

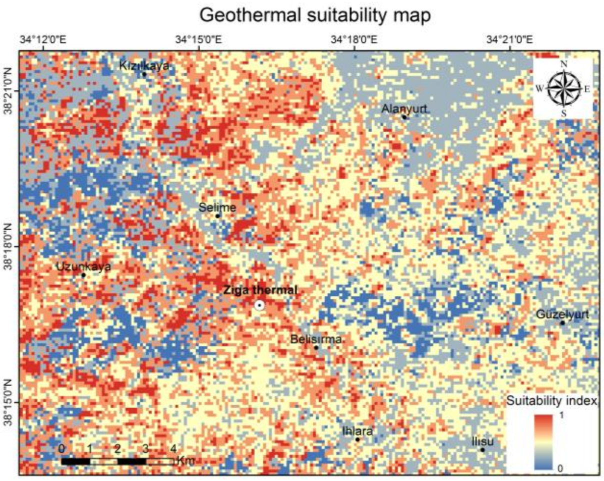

Figure 4. Geothermal suitability map

4. Conclusion

Alteration maps such as; advanced argillic, kaolinization, propylitization, sericitization, and quartz were produced by band combination with aster images. In addition, the land surface temperature was obtained with the help of thermal sensors. The obtained six different maps were combined by overlay analysis, and a geothermal suitability map was produced. According to the resulting map produced, "Ziga gothermal field", which are currently used as a thermal hotel and where hot water tourism is made, emerged in a suitable area, which shows the methodology's accuracy. This study is preliminary, and it is thought that candidate regions are determined this way. Laboratory studies are to be carried out with more detailed land and samples to be taken in suitable areas.

References

Afşin, M. & Yıldız, M. (1997). Ziga kaplıcası ve çevresinin jeolojik ve hidrojeolojik incelenmesi, N.Ü. Aksaray Mühendislik Fakültesi Jeoloji Mühendisliği Bölümü,10 s, (yayımlanmamış).

Arslan, S., Darıcı, M., & Karahan, Ç. (2000). Jeotermal Enerji Hizmet İçi Eğitim Seminer Notları, MTA Genel Müdürlüğü, Ankara.

Burçak, M. (2006). Aksaray jeotermal sahaları (Acıgöl-Ziga-Şahinkalesi) jeotermal ısı kaynaklarının araÇtırılması ve jeotermal sistemlerin kavramsal modellemesi, Yüksek Lisans Tezi,N.Ü. Fen Bilimleri Enstitüsü, Aksaray, 58-78.

Burçak, M. (2009). Aksaray jeotermal sahalarında (Acıgöl-Ziga-Şahinkalesi) su kimyası ve izotopik çalışmalar, MTA Dergisi, No: 138, Ankara, 45-68.

Calvin, W. M., Littlefield, E. F., & Kratt, C. (2015). Remote sensing of geothermal-related minerals for resource exploration in Nevada. Geothermics, 53, 517-526.

Canbaz, O., Gürsoy, Ö., Karaman, M., Çalışkan, A. B., & Gökce, A. (2021). Hydrothermal alteration mapping using EO-1 Hyperion hyperspectral data in Kösedağ, Central-Eastern Anatolia (Sivas-Turkey). Arabian Journal of Geosciences, 14(21), 1-23.

Duru, G. (2006). Ziga-Yaprakhisar (Aksaray) sıcak ve mineralli kaynak alanlarındaki traverten çökeliminde etkili olan faktörlerin su kimyası ve izotopik yöntemlerle belirlenmesi, Yüksek Lisans Tezi, N.Ü. Fen Bilimleri Enstitüsü Jeoloji Müh. ABD, 59-107, (yayımlanmamış).

Fakhari, S., Jafarirad, A., Afzal, P. & Lotfi, M. (2019), Delineation of hydrothermal alteration zonez for porphyry systems utilizing ASTER data in Jebal-Barez area, SE Iran, Iranian Journal of Earth Sciences, Vol.11, No.1, 2019, 80-92.

Kara, İ. (2010). Nevşehir / Acıgöl - Derinkuyu - Gülşehir sıcak ve mineralli sularının hidrojeokimyasal özellikler, MTA Dergisi, Ankara

Ketin, İ. (1969). Tectonic units of Anatolia. MTA Dergisi, 66, 24-33.

Kratt, C., Calvin, W. M., & Coolbaugh, M. F. (2010). Mineral mapping in the Pyramid Lake basin: Hydrothermal alteration, chemical precipitates and geothermal energy potential. Remote Sensing of Environment, 114(10), 2297-2304.

Ninomiya, Y. A. (2003). Stabilized Vegetation Index and Several Mineralogic Indices Defined for ASTER VNIR and SWIR Data. In Proceedings of the IEEE International Geoscience and Remote Sensing Symposium, Toulouse, France, 21–25 July 2003, 3, 1552–1554.

Ramadhan, R. F., Salsabila, G., Mogi, G. D., Ulhaq, H. D., & Saputra, R. A. (2021). Remote Sensing for Hydrothermal Alteration Zone Identification Using Landsat 8 OLI/TIRS Satellite Imagery on The Geothermal Prospect Area of Mountain Sirung, East Nusa Tenggara. Remote Sensing.

Rodriguez-Gomez, C., Kereszturi, G., Reeves, R., Rae, A., Pullanagari, R., Jeyakumar, P., & Procter, J. (2021). Lithological mapping of Waiotapu Geothermal Field (New Zealand) using hyperspectral and thermal remote sensing and ground exploration techniques. Geothermics, 96, 102195.

Şener, E., & Şener, Ş. (2021). Exploration of geothermal potential using integrated fuzzy logic and analytic hierarchy process (AHP) in Ağrı, Eastern Turkey. Turkish Journal of Earth Sciences, 30(9), 1134-1150.

Shahi, H. & Kamkar-Rouhami, A. (2014), A gis based weights of evidence model for mineral potential mapping of hydrothermal gold deposits in Torbat-e-Heydarieh area. Journal of Mining and Environment 5(2), 2014, 79-89.

Şimşek, Ş. (1993). Ihlara (Kapadokya) özel koruma bölgesinin ve bölgede yer alan termal kaynakların hidrojeolojik ve hidrojeokimyasal araştırması ve korumaya ilişkin öneriler, Özel Çevre Koruma Kurumu Teknik Raporu, No: 6, Ankara, 116 s.

Uzun, Ö. F., & Turgay, O. (2022). Investigation of the Hamamayağı/Ladik (Samsun, Turkey) geothermal field and it's surroundings by optical Remote Sensing with GIS methods. Turkish Journal of Geosciences, 3(2), 75-83.

Yıldırım, T. & Koçan, N. (2008). Nevşehir Acıgöl Kalderası Kalecitepe ve Acıgöl Maarlarının Jeoturizm Kapsamında Değerlendirilmesi . Ege Üniversitesi Ziraat Fakültesi Dergisi , 45 (2) , 135-143 . Retrieved fromhttps://dergipark.org.tr/tr/pub/zfdergi/issue/5091/69556

7th Intercontinental Geoinformation Days

igd.mersin.edu.tr

Comparing land motion in Chiang Mai and Bangkok, Thailand, using Sentinel-1 InSAR time series

Kunlacha Inpai[*1,2], **Timo Balz** [2]

[1]Burapha University, Faculty of Geoinformatics, Chon Buri, Thailand
[2]Wuhan University, State Key Laboratory of Information Engineering in Surveying, Mapping and Remote Sensing, Wuhan, China

Keywords
Chiang Mai and Bangkok
Land motion
Monitoring
PS-InSAR
Sentinel-1

Abstract

Bangkok, Thailand's capital, and Chiang Mai in northern Thailand are both susceptible to land motion due to natural and human influences. They differ significantly in geological settings: Bangkok is characterized by Neogene clay deposits prone to compaction-induced land subsidence, while Chiang Mai's motion is driven by factors like geological structure and morphology, leading to slope instability and subsidence. Sustainable development in these cities necessitates precise monitoring of geological hazard-prone areas. Radar interferometry, particularly the persistent scatterer interferometry (PS-InSAR) technique, offers a high-resolution, cost-effective solution. This study utilizes Sentinel-1 data to monitor land deformation in both cities, combining geological, morphological, and ground measurements to create deformation maps. Analysis of 61 images for Bangkok and 62 images for Chiang Mai from January 2020 to May 2023 reveals Bangkok's subsidence driven by the early Miocene geological evolution of the Thon Buri Basin, exacerbated by construction and groundwater extraction. Chiang Mai experiences vertical and horizontal motion influenced by factors like depositional environment, morphology, and lithology. Both cities face land subsidence challenges due to rapid urbanization, leading to structural damage and heightened flood risk. This research highlights the potential of PS-InSAR techniques for geological hazard and land deformation monitoring, addressing city-specific challenges and advantages.

1. Introduction

In the picturesque landscapes of northern Thailand, Chiang Mai and the bustling metropolis of Bangkok present captivating contrasts. Chiang Mai, nestled amidst mountains in a basin plain, is celebrated for its ancient temples, traditional festivals, and harmonious fusion of tradition and modernity. However, the very geological setting that makes it a tourist haven also exposes it to land motion hazards, including floods in lower plains and landslides during the monsoons. On the other hand, Bangkok, situated in a deltaic plain along the Chao Phraya River, dazzles with its royal history, iconic landmarks, and rapid modernization. Its skyline, adorned with futuristic structures, mirrors Thailand's economic ascent but is marred by rampant land subsidence, a consequence of unchecked urban development and groundwater overuse.

This study leverages Sentinel-1 satellite data and the Persistent Scatterer Interferometry Synthetic Aperture Radar (PS-InSAR) technique to monitor land motion in both cities. Its primary objectives encompass measuring land motion, dissecting its direction using ascending and descending orbits, and discerning the influence of varied geological and depositional settings. In a world where many capitals grapple with land subsidence, Bangkok's plight underscores the ramifications of unchecked urbanization. Conversely, Chiang Mai faces a different set of challenges rooted in its geological landscape. Through this research, the interplay of natural and human-induced factors shaping land motion in these critical economic centers will be unveiled, aiding in disaster preparedness and decision-making while showcasing the potential of advanced satellite technology for precision monitoring of land deformation.

* **Corresponding Author**

*(64910084@go.buu.ac.th) ORCID ID 0009 – 0003 – 3431 – 3566
(balz@whu.edu.cn) ORCID ID 0000 – 0002 – 1624 – 4697

Cite this study

Inpai, K., & Balz, T. (2023). Comparing land motion in Chiang Mai and Bangkok, Thailand, using Sentinel-1 InSAR time series. Intercontinental Geoinformation Days (IGD), 7, 29-32, Peshawar, Pakistan

2. Method

2.1. The study area and datasets

Bangkok is in a floodplain and deltaic plain and reaches towards the southern Gulf of Thailand. The research focuses on an area of about 1,385 square kilometers within Bangkok City, delineated by latitudes 13.634–13.916°N and longitudes 100.374–100.787°E. In parallel, the research encompasses an approximate expanse of 1,405 square kilometers within Chiang Mai City, demarcated by latitudes 18.824806–18.511480°N and longitudes 98.800152–99.181851°E. A distinctive NNE-SSW trending fault line prominently features in the rugged mountainous terrain of this area, residing at the basin's edge, and connects with tertiary extensional basins constituting the Chiang Mai basins, extending seamlessly from the western to the eastern stretches (Morley, 2009; Mankhemthong et al., 2019).

The Sentinel-1A images utilize Single Look Complex (SLC) data, featuring a wavelength of 5.547 centimeters and an interferometric wide swath spanning 250 kilometers. These images provide a resolution of 5x20 meters and include a comprehensive selection of both descending and ascending orbit. Specifically, there are 61 images covering the Bangkok City area and 62 images encompassing the Chiang Mai City area, spanning from January 2020 to May 2023. This comprehensive dataset, combined with geological insights, forms the foundation for precise monitoring and analysis of land motion in these diverse geological and depositional settings, aiding in disaster preparedness.

2.2. PS-InSAR time series technique

The SAR system transmits the phase and amplitude of a pulse, and the phase difference between two SAR images reveals land movement (Δϕ), but unwrapping this interferometric phase is crucial for measuring satellite line-of-sight land deformation as shown in Equation 1. This fundamental InSAR principle leverages differential SAR interferometry (DInSAR) using two images to process the phase difference. However, the accuracy of deformation readings is influenced by factors such as satellite positioning errors, topography, and atmospheric delay, all of which contribute to the observed phase difference (Δϕ) as shown in Equation 2 and must be accounted for in the analysis (Ferretti et al., 2001; Kampes et al., 2001).

$$\Delta\phi = \phi 1 - \phi 2 = \frac{4\pi}{\lambda} \Delta r \qquad (1)$$

where
ϕ1, ϕ2: the phase of each acquisition
Δr: the difference in range between two SAR acquisitions
λ: wavelength of the radar

$$\Delta\phi = \phi def + \phi orbit + \phi topo + \phi noise + \phi atm \qquad (2)$$

where
Δϕ: phase difference
ϕdef: phase contribution related to ground deformation
ϕorbit: Orbit Error
ϕtopo: Topographic Effect
ϕnoise: Noise
ϕatm: Atmospheric Delay

The PS-InSAR method uses the strong stable point to minimize the impact of the atmosphere and geometric correlation. This technique can detect land displacement with comparatively high precision in the line-of-sight velocity (Perissin, 2008). The approach entails pre-processing, processing (geocoding), and InSAR processing, as shown in Fig. 1. Moreover, SARPROZ software typically follows a well-defined methodology to monitor land displacement over time.

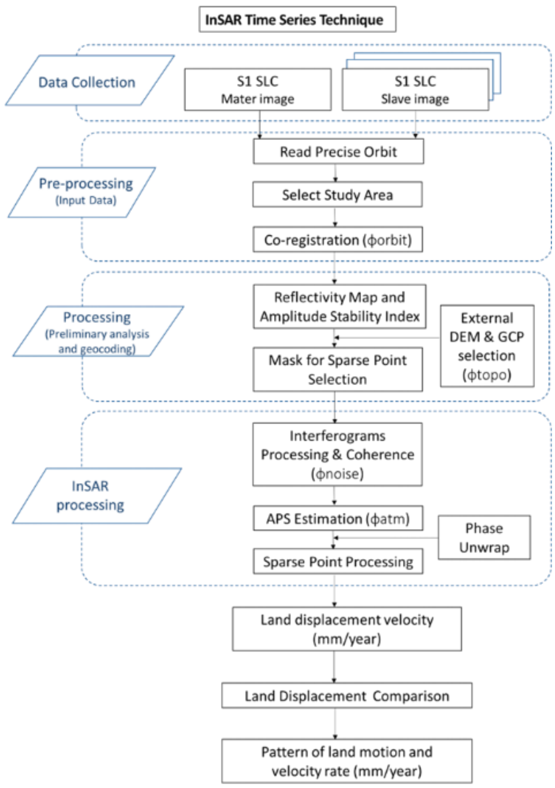

Figure 1. The method workflow

3. Results

The study examines land surface movement in both descending and ascending tracks of PS-InSAR in Bangkok. The findings highlight PS-InSAR data in both tracks, indicating a deficit range of 0.8 to 2.2 mm with standard deviations (SD) between 1 and 3. Notably, ascending time series have lower significant standard deviations than descending ones. Linear regression analysis shows a declining trend, suggesting subsidence. As shown in Table 1, surface displacement rates from PS-InSAR range from -11.3 mm/year to -24.4 mm/year. Furthermore, this study expands its investigation to evaluate land surface movement speed in Chiang Mai. Focusing on PS points on both descending and ascending tracks, the research identifies a range of -2.3 to -33 mm, with standard deviations from 1.5 to 2.7. Remarkably, descending time series exhibit lower standard deviations compared to ascending ones. Through thorough linear regression analysis, the study reveals a declining vertical motion trend in several areas, including San Patong, San Kamphang, and Muang Lamphun. Intriguingly, Hang Dong displays distinctive patterns: uplift in the descending track and subsidence in the ascending track, with horizontal motion. The PS-InSAR pairs in Table 1 display vertical displacement rates ranging between -7.8 mm/year and -14.7 mm/year. This meticulous analysis unveils the intricate vertical motion patterns in Chiang Mai, offering valuable insights into its geological factors.

Table 1. An association between the velocity of RSQ, which is equal to or higher than 0.8, and significant statistics of descending (DES) and ascending (AS) orbits in the Bangkok and Chiang Mai.

Study area	PS point	Velocity (mm/year)	SD	Motion pattern
Bangkok				
Phasi	DES152636	-24.4	3.0	Vertical
Charoen	AS339321	-22.2	1.6	
Lak Si	DES247645	-13.4	1.6	Vertical
	AS137679	-12.1	1.0	
Huai Khang	DES144500	-13.7	2.8	Vertical
	AS262611	-14.9	2.3	
Phra	DES66521	-12.1	1.9	Vertical
Khanong	AS355551	-11.3	2.2	
Lat Krabang	DES145019	-14.9	2.7	Vertical
	AS235791	-13.5	1.2	
Chiang Mai				
Hang Dong	DES39167	4.7	1.5	Horizontal
	AS93781	-28.3	2.7	
San Patong	DES111105	-12.4	2.3	Vertical
	AS23702	-14.7	2.5	
San	DES73824	-11.8	2.0	Vertical
Kamphang	AS30539	-7.8	2.4	
Muang	DES108573	-13.0	1.9	Vertical
Lamphun	AS10289	-10.0	2.2	

4. Discussion

The geological factors, namely tectonic settings, fault zones, rock type and strength, and sedimentary deposition and compaction, underpin the significant influence of land deformation patterns. Distinct geological characteristics within regions like Bangkok and Chiang Mai yield divergent land motion dynamics. Tectonic settings near plate boundaries produce pronounced deformation, exemplified by Chiang Mai's active tectonic boundaries and LANF, driving continuous crustal extension (Morley, 2009). In contrast, Bangkok's stability arises from its distance from tectonic zones. The presence of fault zones contributes to this disparity, with Chiang Mai exhibiting both vertical and horizontal land motion, while Bangkok predominantly experiences vertical motion. Moreover, the nature of rocks significantly dictates deformation, and Chiang Mai's resilient metamorphic rocks resist deformation, reducing subsidence. In contrast, Bangkok's softer sediments, prone to compaction, result in a higher rate of land subsidence (Sinsakul, 2000). In addition, sedimentary deposition and compaction also play a pivotal role, with Bangkok's extensive fine-grained sediment deposits susceptible to subsidence, while Chiang Mai's coarser-grained sediment exhibits less responsiveness to deformation. In conclusion, the profound effect of geology on land deformation is evident through these factors, offering valuable insights into the dynamic relationship between Earth's surface and its underlying geological foundation.

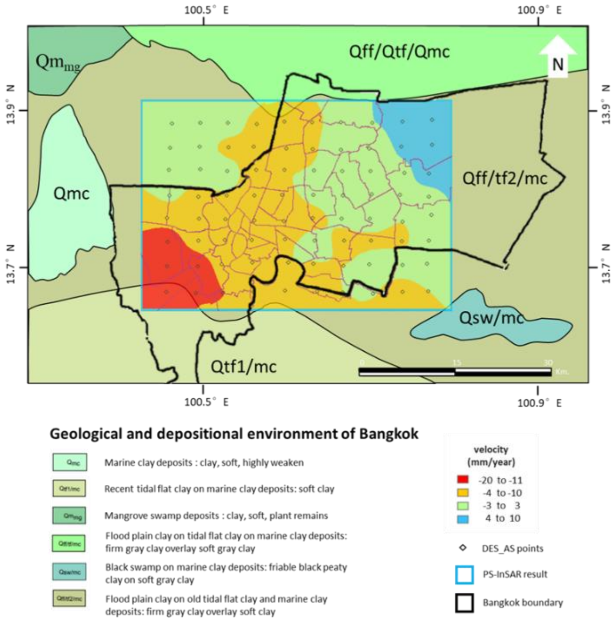

Figure 2. The vertical motion of Bangkok relates to a geological and depositional environment where the red area shows the high rate of subsidence and is flood plain clay and recent tidal flat clay on marine clay deposits; the yellow area shows the moderate rate of subsidence and is flood plain clay on old tidal flat clay and marine clay deposits; the green area shows the low to stable rate; and the blue area shows the uplift area where there is higher terrain and near the mountain on the east of Bangkok.

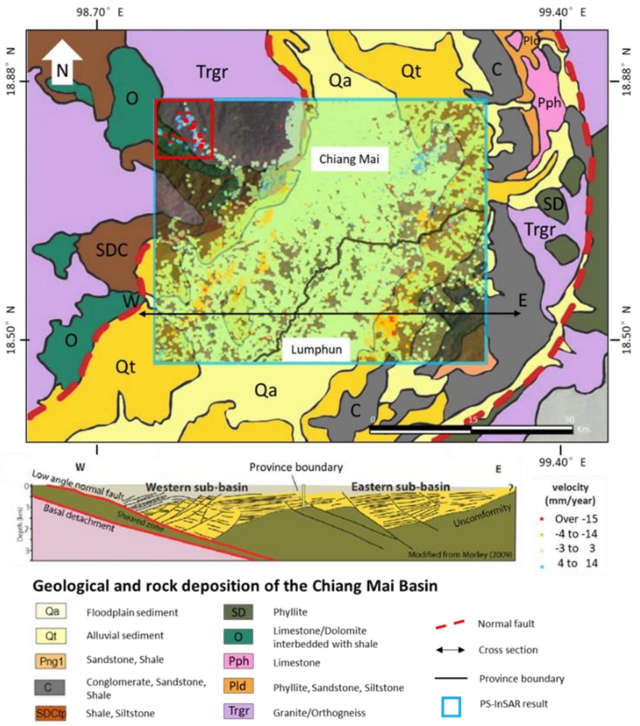

Figure 3. The land motion of Chiang Mai relates to a geological map and deposition environment where the small yellow area shows the subsidence is near the edge of the Chiang Mai basin and it's a floodplain-alluvial deposition, while a mountain area on the west of Chiang Mai is represented by the red (indicating subsidence from an ascending track) and blue (indicating uplift from a descending track), and the different directions of motion indicate horizontal motion

Furthermore, the influence of land deformation patterns is compounded by human activities, including groundwater extraction and construction, which have a significant impact in specific regions. For example, excessive groundwater extraction can induce land subsidence as it depletes underground aquifers, causing surrounding rocks or sediments to compress and the land surface to sink. Similarly, substantial construction can disrupt the stress distribution within the Earth's crust, leading to localized deformation. The population density and construction activity in cities like Bangkok and Chiang Mai are closely linked to the respective subsidence rates observed. In addition, natural factors such as heavy rainfall on steep slopes contribute to horizontal motion in Chiang Mai, particularly through landslides, which have been observed to damage both high-terrain and lower-plain areas. Sentinel-1's temporal data analysis has unveiled long-term trends in land motion, facilitating the monitoring of these patterns and the assessment of their environmental consequences. This study underscores the importance of community engagement and informed policymaking to mitigate the impacts of land motion in urban areas, with collaborative efforts essential for the judicious management of water resources and land utilization in response to the discernible trends influenced by geological traits and human activities in Bangkok and Chiang Mai.

5. Conclusion

Bangkok and Chiang Mai exhibit distinct land motion patterns due to their unique geological characteristics and local factors. Bangkok experiences primarily vertical subsidence driven by soft clay deposits and exacerbated by human activities, while Chiang Mai experiences a combination of vertical and horizontal motion influenced by geological structure, sediment deposition, mountainous terrain, rock type, and heavy rainfall that also trigger the land motion. Both cities face challenges related to land motion, but the scale and specific factors involved differ significantly between the two regions.

Acknowledgement

I extend my heartfelt gratitude to Asst. Prof. Dr. Sukonmeth Jitmahantakul and Dr. Kitsanai Charoenjit for their invaluable supervision and guidance. I am also deeply appreciative of my SCGI batch 4 classmates, fellow Master's and Ph.D. students, and the SAR team at the Faculty of Geoinformatics, Burapha University, as well as the State Key Laboratory of Information Engineering in Surveying, Mapping, and Remote Sensing, Wuhan University. The Department of Mineral Resources (DMR), the Department of Groundwater Resources (DGR), the City Planning Department Bangkok Metropolitan Administration, the Sentinel-1 website, and SARPROZ software were essential sources of data for this research. Thank you all for your support and contributions to this work.

References

Ferretti, A., Prati, C., & Rocca, F. (2001). Permanent scatterers in SAR interferometry. IEEE Transactions on Geoscience and Remote Sensing, 39(1), 8–20.

Kampes, B. M., Hanssen, R. F., & Swart, L. M. T. (2001). Strategies for non-linear deformation estimation from interferometric stacks. IGARSS 2001. Scanning the Present and Resolving the Future. Proceedings. IEEE 2001 International Geoscience and Remote Sensing Symposium (Cat. No. 01CH37217), 6, 2828–2831.

Mankhemthong, N., Morley, C. K., Takaew, P., & Rhodes, B. P. (2019). Structure and evolution of the Ban Pong Basin, Chiang Mai Province, Thailand. Journal of Asian Earth Sciences, 172, 208–220. https://doi.org/10.1016/j.jseaes.2018.09.010

Morley, C. K. (2009). Geometry and evolution of low-angle normal faults (LANF) within a Cenozoic high-angle rift system, Thailand: implications for sedimentology and the mechanisms of LANF development. Tectonics, 28, 1–30.

Perissin, D. (2008). Validation of the submetric accuracy of vertical positioning of PSs in C-band. IEEE Geoscience and Remote Sensing Letters, 5(3), 502–506.

Sinsakul, S. (2000). Late Quaternary geology of the Lower Central Plain, Thailand. Journal of Asian Earth Sciences, 18(4), 415–426. https://doi.org/10.1016/S1367-9120(99)00075-9

7th Intercontinental Geoinformation Days

igd.mersin.edu.tr

Assessment of urbanization and different land use and land cover types on urban heat islands in growing cities, a case study: Tabriz, Iran

Khalil Valizadeh Kamran[*1]

[1]University of Tabriz, Faculty of Planning and Environmental Sciences, Department of Remote sensing and GIS, Tabriz, Iran

Keywords
Urban heat islands
Thermal remote sensing
Land use
Land cover
Tabriz

Abstract

In this study, Landsat ETM+ and OLI images from 1984 to 2013 were selected to examine the relationship between land surface temperature and land use pattern in Tabriz, and to investigate the impact of land use changes on the urban heat islands. First, the mono-window algorithm was utilized to retrieve land surface temperature from thermal band of Landsat images. The zonal statistic was then carried out to evaluate the area proportion of land use classes in each LST category. Finally, the urban thermal characteristic was analyzed by investigating the relationships between the land surface temperature and land use types. The results suggest that the process of urbanization in Tabriz has significant effects on the surface temperature.

1. Introduction

Temperatures are gradually increasing globally due to a changing climate and have serious impacts on the health of human beings and other animal and plant species (Rinner and Hassain, 2011).

Urban heat island is a phenomenon caused by the increase of urbanization and air pollution. The city growth has changed the nature of surface reducing the presence of vegetation, with building structures and materials trapping solar radiation during the day, determining a significant temperature, differences between urban and rural areas (Bonafoni et al. 2016). Urban Heat Island, defined as the rise in temperature of any man-made area, result in a well-defined, distinct "warm island" among the "cool sea" represented by the lower temperature of the area's nearby natural landscape. When heat is radiated from surfaces of various land uses along with the presence of meteorological parameters such as wind speed and direction, an Urban Heat Island (UHI) can form (Taha et al. 2002). Beside high temperature, the thermal properties of land uses are playing significant role in producing heat islands (Streutker, 2003). When a land cover of buildings and roads replaces green space, the thermal, radiative, moisture and aerodynamic properties of the surface and the atmosphere are altered. In addition, the height of buildings and the way in which they are arranged affects the rate of escape of the sun's energy at night absorbed during the day by building materials. The result is that urban areas cool at a much slower rate than rural areas at night, thus maintaining comparatively higher air temperatures. Elevated temperatures from urban heat islands, particularly during the summer, can affect a community's environment and quality of life. While some impacts may be beneficial, such as lengthening the plant-growing season, the majority of them are negative. These impacts include: Increased energy consumption; Elevated emissions of air pollutants and greenhouse gases; Compromised human health and comfort; Impaired water quality

By using remote sensing techniques and data processing methodologies land surface temperature both in local and global scale can be acquired in order to analyze the relationship between temperatures, land use and land cover during different temporal intervals. In the present study satellite images of Landsat 7 ETM+ and Landsat 8 are used at 6 different dates from 1984 to 2013. The main objective is to examine the relationship between surface temperature and urban morphology and to interpret these relationships in terms of heat island processes and finally suggest some solution in order to make adjustment in UHI.

The Tabriz is the central city of Eastern Azerbaijan Province in Iran. Tabriz is Located in the Quru River valley between the long ridge of the volcanic cones of the Sahand and Eynali mountains (Figure 1).

* **Corresponding Author**

*(valizadeh@tabrizu.ac.ir) ORCID ID 0000 – 0003 – 4648 – 842x

Cite this study

Kamran, K. V. H. (2023). Assessment of urbanization and different land use and land cover types on urban heat islands in growing cities, a case study: Tabriz, Iran. Intercontinental Geoinformation Days (IGD), 7, 33-36, Peshawar, Pakistan

Tabriz is located in the coordinates of 38.0962° north latitudes and 46.2738° east longitudes with elevation ranges between 1,350 and 1,600 metres above sea level. The valley opens up into a plain that gently slopes down to the eastern shores of Lake Urmia, 60 kilometres (37 miles) to the west, with cold winters and temperate summers; the city is considered as summer resort (Tabriz, 2023).

2. Method

Two main datasets used in this study are: land use polygons of study area and remotely sensed thermal images. The land use data were obtained from Tabriz University, remote sensing laboratory. The dataset contained 62 types of land uses and Figure 1 shows the distribution of different land uses in Tabriz.

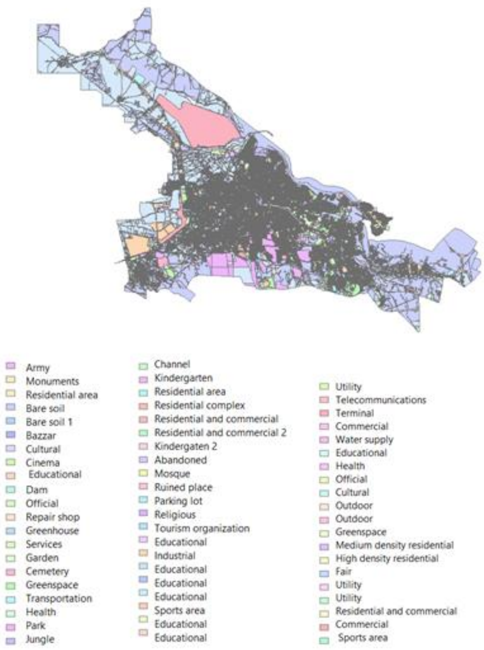

Figure 1. Distribution of land use categories in the city of Tabriz.

The satellite images were acquired from U.S. Geological survey's Earth Explorer database (http://earthexplorer.usgs.gov) including 5 Landsat 7 ETM+ and one Landsat 8 OLI images. The images were georectified to a Universal Transverse Mercator (UTM) coordinate system, using World Geodetic System (WGS) 1984 datum, assigned to Path 168 Row 34. Data set consists of six Landsat images belonging to years 1984,1990,2000, 2006,2011 and 2013 summer seasons, hence it is possible to evaluate the LST conditions in hot days (Table 1). Landsat 7 has 7 spectral bands with spatial resolution of 30 meters. Band 6 of Landsat 7 is thermal infrared band with 60 meters resolution but it can be resampled to 30 meters. Landsat OLI have 9 spectral band with 30 m spatial resolution for band 1-7 and 9, 1 panchromatic band with spatial resolution of 15 m for band 8 and 2infrared thermal bands with spatial resolution of 1oo m for band 10 and 11.

Table 1. Used data

Landsat	Date
7 ETM+	1984-08-27
7 ETM+	1990-08-28
7 ETM+	2000-08-23
7 ETM+	2006-08-24
7 ETM+	2011-08-22
8 TIRS	2013-08-27

In order to have accurate LST retrieval, estimation of land surface emissivity is important. Among lots of methods that have been proposed to obtain LSE drives NDVI threshold method proposed by Valor and Caselles (1996), is the most widely used method (Shi and Zhang, 2017).

$$P_V = [(NDVI - NDVI_{soil})/(NDVI_{veg} - NDVI_{soil})] \quad (1)$$

The NDVI is the normalized differential vegetation index; the $NDVI_{soil}$ and $NDVI_{veg}$ are set as empirical values of 0.05 and 0.7, respectively.

$$\mathcal{E} = P_V R_V \mathcal{E}_V + (1 - P_V) R_m \mathcal{E}_m + d_{\mathcal{E}} \quad (2)$$

Where $\mathcal{E}$ is ground emissivity; $\mathcal{E}_V$ *and* $\mathcal{E}_m$ are emissivity of vegetation and building surface, respectively, set as empirical values of 0.986 and 0.970; $d_{\mathcal{E}}$ is interaction of thermal radiation vegetation and building surface; R_V and R_m are temperature ratios of vegetation and building surfaces, calculated by the empirical equations:

$$R_V = 0.9332 + 0.0585 P_V \quad (3)$$

$$R_m = 0.9886 + 0.1287 P_V \quad (4)$$

By combination of equations (2) and (4), the ground emissivity can be estimated:

$$\mathcal{E} = 0.9589 + 0.086 P_V - 0.0671 {P_V}^2 \quad (5)$$

Ground emissivity of the study area was calculated by ENVI software using the above mentioned formulas.

2.1. Derivation of LST from Landsat 7 ETM+ and Landsat 8 TIRS

The land surface temperature (LST) was derived from Landsat 7 thermal band (band 6) and Landsat 8 TIRS thermal band (band 10) with the spatial resolution of 60 m and 100m, respectively.

First, the DN values were converted to spectral radiance by using the reflectance calibration process provided by ENVI program for all images and their metadata provided in the file with MTL extension.

The second step was to transform spectral radiance to at-sensor brightness temperature under the assumption of the uniform emissivity, using the following formula (Luo and Peng, 2016):

$$T_b = \frac{k_2}{\ln\left({k_1}/{L_\lambda} + 1\right)}$$

Where k_1 and k_2 are calibration constant. For Landsat 7 ETM+ k_1=666.09 k_2= 1282.71 mW cm-2 sr-1 μm-1

As a final step the surface temperature was calculated by the following formula;

$$T_s = \frac{T_b}{\varepsilon^{0.25}}$$

After completing the calculation part, the LST image map of the study area was created (Figure 2). Figure 3, showed the mean, maximum and minimum LST of the study area in different years.

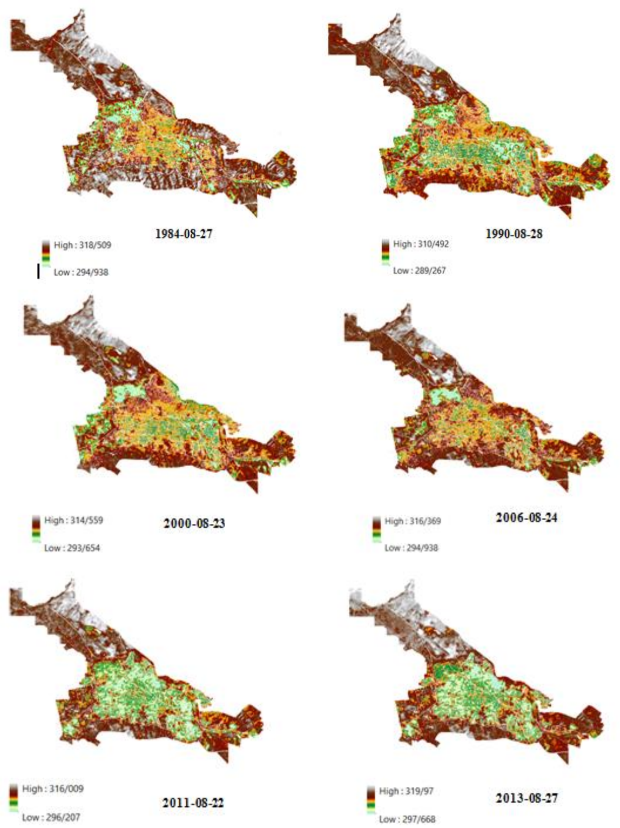

Figure 2. LST retrieval image map of Tabriz.

3. Results

3.1 Calculation of zonal statistics

After processing the Landsat images by ENVI software to get the land surface temperature, ArcGIS was put into use in order to identify tepmerature differences between land uses and also to assess the association between land use and land temperature. The thermal image was loaded in Arc GIS, and to get the detailed information about the land surface temperature of the study area, zonal statistics method was carried out. Zonal statistics, summerizes the values of the rasters within the zone of another dataset (either raster or vector) and reports the results in a table. The land use layer was used to define zonal boundries to obtain the mean surface temperature for each land use polygon. Zonal statistics on a thermal remote sensing image for the City of Tabriz revealed statistically significant differences between high average temperatures for commercial and resource/industrial land.

3.2 Calculation of NDVI

In this study, NDVI was used to present the relationship between LST and vegetation by linear regression correlation (Figure 3).

$$NDVI = \frac{(NIR - RED)}{NIR + RED}$$

Where;

NIR and RED are the reflectance in the near infrared and red bands respectively.

NDVI due to its simple calculation is largely used for the vegetation studies in a regional as well as global level. It is always advisable to combine the NDVI along with other parameters to get better results (Sruthi and Aslam, 2015).

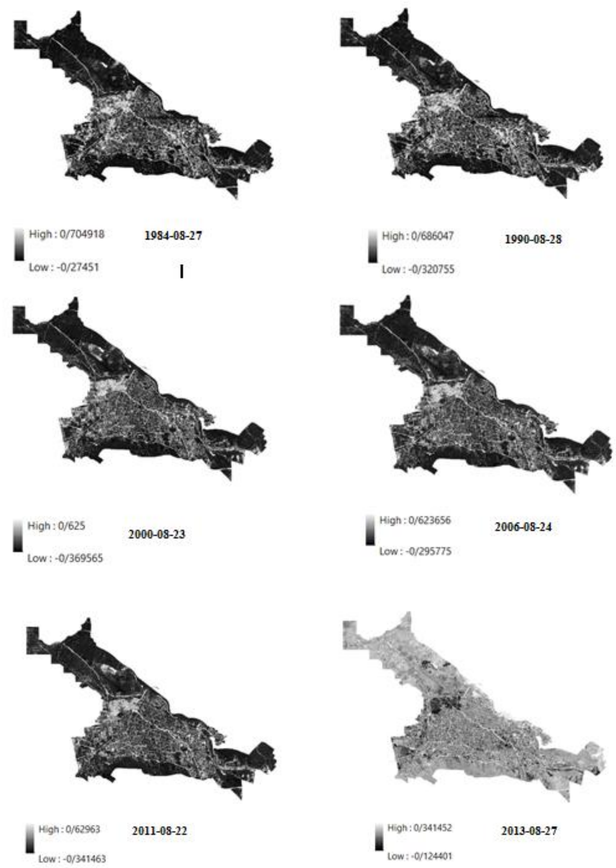

Figure 3: Normalized difference vegetation index (NDVI) of Tabriz.

3.3 Correlation analysis

In this part of the study, the correlation between NDVI and lands surface temperature is carried out to find the relationship between these variables. Table 2 shows the correlation results.

By calculating the correlation between LST and NDVI, From Table 2 it can be clearly noticed that, NDVI and LST show a high negative correlation in all years of study except 2013.

Table 2. Correlation between NDVI and LST.

Date		LST
1984	NDVI	-62%
1990	NDVI	-49%
2000	NDVI	-51%
2006	NDVI	-47%
2011	NDVI	-19%
2013	NDVI	56%

4. Discussion

The research includes spatial analysis of the standardized LST with regard to different land use types. Basic zonal statistics such as mean standardized LST and percentage share of hot and cold regions within 62 land use types were calculated. GIS was used for automated data processing through years 1984, 1990, 2000, 2006, 2011 and 2013. The values acquired from zonal statistics table are LST original raw values and should be converted from kelvin to celsius.

As shown in Table 3, among all the years highest temperature of lands surface belongs to Terminal except year 2000, which the highest degree is registered with bare soil. In 1984 the lowest temperature of land surface temperature is registered with green space while in both 1990 and 2000 the lowest degree belongs to the industrial region. In the next 3 years (2006, 2011 and 2013), min LST is allocated to Official, Residential and Utility categories, respectively.

Table 3. Result of LST in different years.

Year	Max temperature	Min temperature
1984	Terminal=44.85 ºC	Green space =20.85 ºC
1990	Terminal=36.85 ºC	Industrial=15.85 ºC
2000	Bare soil= 40.85 ºC	Industrial=19.85 ºC
2006	Terminal=42.85 ºC	Official=20.85ºC
2011	Terminal=42.85 ºC	Residential=22.85 ºC
2013	Terminal=45.85 ºC	Utility=23.85ºC

The results confirmed the most obvious dependence of the LST on different land use types and show that the land usage will influence urban temperature. According to the results obtained average temperatures is significantly higher for land uses like Bus terminal and lower for green spaces. The higher temperature in bus terminal of Tabriz is due to the fact that these areas are characterized by build up surfaces and the amount of asphalted areas. Concrete and metalic roofs in addition to the darker color of roofs and asphalt which have the low emissivity and higher heat capacity can be named as another relevant factors. Also, the heat emitting from the bus engines in terminal and lack of vegetation could affect the surface temperature. The size of land use area and surface temperatures are also relevant factors; as the size of land use increases, the temperature also tends to increase. The bus terminal covers a very vast area with 508409/1744 Km in comparison with other land uses

According to NDVI results, it can be clearly noticed that both the parameters are inversely Proportional to each other. It means that, when the temperature increase, the NDVI value decrease which points out the decrease in vegetation density in years from 1984 to 2011. However, in 2013 in can be seen that NDVI and LST show highly positive correlation.

5. Conclusion

UHI is usually observed between urban and rural land uses, and in few studies the intra-urban patterns are examined. In this study the land surface temperature of different land uses has been analyzed and several important findings are obtained. By using Landsat ETM+ and OLI and further the impact of land use change on land surface temperature is demonstrated. In other words, the change of land use is the important reason leading to increase in land surface temperature.

References

Bonafoni, S. Baldinelli, G. & Verducci, P. (2016). Sustainable strategies for smart cities: Analysis of the town development effect on surface urban heat islands through remote sensing methodologies. Department of Engineering, University of Perugia, via G.Duranti, 93, 06125 Perugia, Italy.

https://earthexplorer.usgs.gov

https://en.wikipedia.org/wiki/Tabriz

https://www.google.com/maps/place/Iran

Luo, X. & Peng, Y. (2016). Scale effects of the relationships between urban heat islands ad impact factors based on a geographically-weighted regression model. Institute of Computer Science and Technology, Chongqing university of Posts and Telecommunications, 2 Chongwen Road, Nan'an District, Chongqing400064, China.

Rinner, C., & Hassain, M. (2011). Toront's urban heat island-exploring the relationship between land use and surface temperaure." Department of Geography, Ryerson University, 350 Victoria Street, Toronto, ON M5B 2K3, Canada.

Shi, Y., & Zhang, Y. (2017). Remote sensing retrieval of urban land surface temperature in hot-humid region. State Key Laboratory of Subtropical Building Science, Department of Architecture, South China University of Technology, NO 381.Wushan road, Tianhe district, 510640 Guangzhou, PR China.

Sruthi,S.; Aslam, M.(2015) "Agricultural Drought Analysis Using the NDVI and Land Surface Temperature Data; a Case Study of Raichur District" Dept. of Geology, CUK-Kadaganchi, Gulbarga, Karnataka-58531.

Streutker, R. (2003). Satellite measured growth of the urban heat island of Houston, Texas. Remote sensing. Environmet. 2003. 85282-85289.

Taha, H., Hammer, H., & Akbari, H. (2002). Meteorological and Air Quality Impacts Of Increased Urban Surface Albedo and Vegetative Cover in the Greater Toronto Area, Canada. LBNL-49210; Lawrence Berkeley National Laboratory: Berkeley, CA, USA.

Valor, E., & Caselles, V. (1996). Mapping land surface emissivity from NDVI: application to European, African and south American areas. Remote Sensing Environment, 57(3),167-184

7th Intercontinental Geoinformation Days

igd.mersin.edu.tr

Performance evaluation of spectral indices and classification algorithms for built-up area extraction using PRISMA hyperspectral images

Seyed hedayat Sheikhghaderi [1], Mostafa Mahdavifard [*2], Ayub Mohammadi [3], Seyed Kazem Alavipanah [4]

1 University of Kharazmi, Department of Remote Sensing and GIS, Tehran, Iran
2 University of Tabriz, Department of Remote Sensing and GIS, Tabriz, Iran
3 University of Kurdistan, Department of Geomorphology, Sanandaj, Iran
4 University of Tehran, Department of Remote Sensing and GIS, Tehran, Iran

Keywords
Built-Up extraction
PRISMA
spectral indices
classification
threshold

Abstract

This article aims to evaluate and compare NDBI, NBI, PB1BI and HIBI spectral indices and SVM, ANN and MLC classification algorithms in order to identify and extract urban constructions using Prisma hyperspectral images. took The findings of this research indicate that the classification algorithms in both Tehran and Urmia have higher accuracy than the spectral indices; So, in Tehran city, PB1BI and HIBI indices have higher accuracy than NDBI and NBI indices with overall accuracy of 85% and 86% and kappa coefficient of 70% and 72% respectively from left to right. On the other hand, in Urmia city, NBI indices with 88% overall accuracy and 77% kappa coefficient and NDBI with 87% overall accuracy and 75% kappa coefficient showed better performance than PB1BI and HIBI indices. Also, in Urmia city, the overall accuracy and Kappa coefficient of SVM and ANN classification algorithms were more accurate than MLC with over 90%. Also, in the city of Tehran, SVM and ANN algorithms with overall accuracy and high Kappa coefficient of 90% and 83% performed better than the MLC algorithm. In general, according to the effectiveness of various factors including the scope of the study, the spectral range used, the type of roof of the buildings, the types of uses, etc., the combined and comparative use of indices and spectral algorithms improves the results.

1. Introduction

Urban areas usually cover a small portion of land around the world. However, the high population density and intensity of resource use compared to the surrounding environment make these areas very important areas of the earth (Firouzjaei et al. 2023). Population growth in urban areas leads to the expansion of built-up areas (Shahfahad et al, 2020).

Urbanization is increasing rapidly and it is predicted to increase to seven hundred to one million square kilometers by 2030 (Angel et al., 2005). In Iran, major changes in urban areas, especially big cities, have become more important due to the occurrence of fundamental changes (Eisizadeh et al. 2022).

Remote sensing technologies provide a reliable source of urban land cover/land use data collection. NASA's Landsat satellite data series (e.g., MSS, TM, and ETM+) have been widely used to map urban extent and monitor urban growth (Zhang et al., 2014).

Satellite data have also been used to calculate built-up extent, and these images are useful due to their historical availability and large-scale spatial coverage (Guindon et al. 2004).

In this study, data from the new Prisma hyperspectral satellite was used. In fact, using this new satellite, urban areas have been extracted to a limited extent. The purpose of the current study is to evaluate and compare new indicators of urban construction with classification algorithms in the extraction of urban construction.

2. Method

In this study, Prisma hyperspectral satellite images and a set of spectral indices and classification algorithms are used to extract and identify urban areas in the two cities of Tehran and Urmia in Iran.

2.1 Case Study

Tehran, as the capital of Iran, is located at 51° 6' to 51° 38' east longitude and 35° 34' to 35° 51' north latitude, and its height from the open water level is between 1800

* **Corresponding Author**

(hedayatp90@gmail.com) ORCID ID 0000-0003-4710-853X
*(mostafamahdavi842@gmail.com) ORCID ID 0000-0001-9811-5428
(ayubmohammadi1990@gmail.com) ORCID ID 0000-0001-8848-8917
(salavipa@ut.ac.ir) ORCID ORCID 0000-0002-3554-111X

Cite this study

Sheikhghaderi, S. H., Mahdavifard, M., Mohammadi, A & Alavipanah, S. K. (2023). Performance evaluation of spectral indices and classification algorithms for built-up area extraction using PRISMA hyperspectral images. Intercontinental Geoinformation Days (IGD), 7, 37-40, Peshawar, Pakistan

meters in the north to 1200 m in the center and 1050 m in the south is variable (Figure 2).

The city of Urmia is one of the metropolises of Iran, the capital of West Azarbaijan province and the city of Urmia in the northwest of Iran, which is located in the Azarbaijan region. This city is located on an orbit of 37 degrees and 32 minutes in the northern hemisphere from the equator. Also, this city is located on the meridian of 45 degrees and 2 minutes east of the Greenwich meridian, and the height of Urmia is 1,332 meters above sea level (Figure 1).

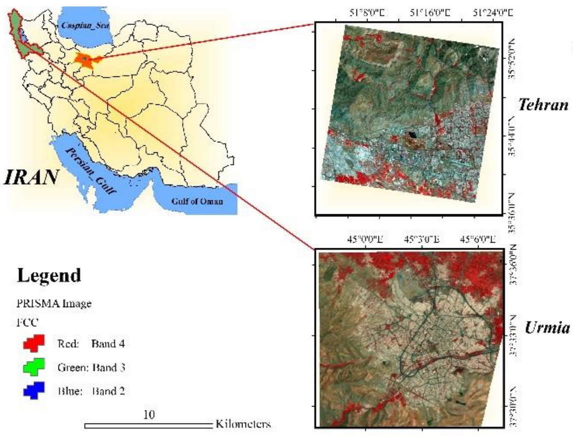

Figure 1. Geographical location of the study area

2.2 Datasets

PRISMA satellite or in other words (PRecursore IperSpettrale della Missione Applicativa) is a medium resolution hyperspectral satellite. This satellite was placed into Earth orbit in 2019 by the Italian Space Agency (ASI). The bands of this satellite include 250 bands that cover wavelengths from 400 to 2500 nm. Table (1) shows the complete specifications of the PRISMA satellite (Galeazzi et al, 2008 and Candela et al, 2016).

Table 1. Complete specifications of the PRISMA satellite

City	Spectral range (nm)	Spatial resolution (m)	Date of Acquisition
Tehran Urmia	VNIR:400-2505 PAN: 400-700	30 5	2020-8-2 2022-7-12

2.3. Data Processing

To extract and identify residential areas, Normalized Difference Built-up Index (NDBI), New Built-up index (NBI), powered B1 built-up index (PB1BI) and Hyperspectral Imagery-based Built-up Index (HIBI) (Jieli et al, 2010; Zha et al, 2010; Mukherjee et al, 2020; Gaur et al, 2023) and statistical classification algorithms, neural network and machine learning are used.

$$NBI = \frac{Red \times Swir2}{Nir}$$

$$NDBI = (SWIR - NIR) / (SWIR + NIR)$$

$$PB1BI = \frac{(Blue)^a}{(Red)^\beta \times (Nir)^y}; a, \beta, y > 0. \qquad a = 10.5,\ \beta = 5,\ y = 3.5$$

$$HIBI = \frac{BLUE(\lambda = 492.69nm) - NIR(\lambda = 959.52nm) - SWIR1(\lambda = 1626.78nm)}{BLUE(\lambda = 492.69nm) + NIR(\lambda = 959.52nm) + SWIR1(\lambda = 1626.78nm)}$$

In this regard, after applying the indices on the images of Tehran and Urmia cities, the threshold limit is used to separate the pixels related to Built-up areas from other pixels. The final output of indicators was classified into two classes: Built-up and No-Built up. On the other hand, to extract and identify residential areas using classification algorithms, 200 training data were taken on each of the images for Built-up and No-Built-up classes.

In the following, a number of ground control samples were taken from Google Earth's high spatial resolution photos to be used to evaluate the accuracy of the results of classification algorithms and indices using the Confusion matrix.

3 Results

Table (2) shows the thresholds extracted from spectral indices related to Built_up and NoBuilt_up classes for the cities of Tehran and Urmia.

Table 2. Spectral indices

Index	Tehran	Urmia
NBI	Built_up: 0.22 - 0.64 NoBuilt up: 0.00 - 0.85	Built up: 0.31 - 0.68 NoBuilt up: 0.00 - 0.84
HIBI	Built_up: -2.25 - 0.45 NoBuilt up: -60.31 - 0.87	Built_up: -2.61 - 0.48 NoBuiltup: -49.07 -0.48
PB1BI	Built_up: 0.00 - 12.02 NoBuilt up : 0.00 - 12.02	Built_up: 0.00 - 0.11 UnBuilt_up: 0.00 - 0.0048
NDBI	Built_up: -0.29 - 0.85 NoBuilt up: -2.36 - 0.94	Built_up: -0.01 - 0.91 UnBuilt_up: -3.31 - 0.91

The results of evaluating the accuracy of the results of spectral indices and classification algorithms in order to extract residential areas are given in Tables (3 and 4).

Table 3. Evaluation of accuracy of Tehran city results

Index/ Algorithm	Overall Accuracy (%)	Kappa (%)
NBI	69.87	38.49
HIBI	85.35	70.30
PB1BI	86.61	72.51
NDBI	65.69	37.36
SVM	92.46	84.52
ANN	91.63	83.63
MLC	89.95	79.41

The findings of this research indicate that in Tehran, PB1BI and HIBI indexes have higher accuracy compared to NDBI and NBI indexes, both visually and in terms of accuracy evaluation criteria. On the other hand, in Urmia, NBI, NDBI and PB1BI indices have the highest accuracy and HIBI index has lower accuracy than other indices. In this regard, as shown in Tables (3 and 4), in both Tehran and Urmia cities, SVM and ANN classification algorithms have the highest accuracy compared to MLC algorithm. In general, as can be cited from the results, the classification algorithms in both Tehran and Urmia have higher accuracy than the spectral indices, and the percentage of correct pixels assigned to the Built-up class and No-Built up is more in them. Figure (2 and 3) shows the results of spectral indices and classification algorithms for identifying and extracting urban areas.

Table 4. Evaluation of accuracy of Urmia city results

Index/ Algorithm	Overall Accuracy (%)	Kappa (%)
NBI	88.59	77.16
HIBI	84.21	65.90
PB1BI	85.96	70.70
NDBI	87.71	75.67
SVM	96.49	92.60
ANN	94.73	90.07
MLC	92.98	84.97

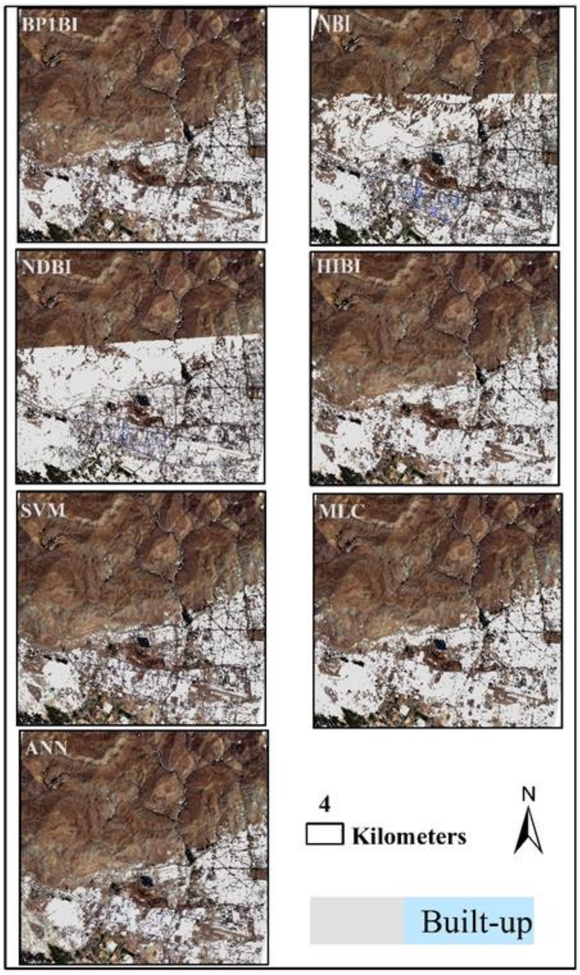

Figure 2. Map of built-up areas extracted from spectral indices and classification algorithms (Tehran)

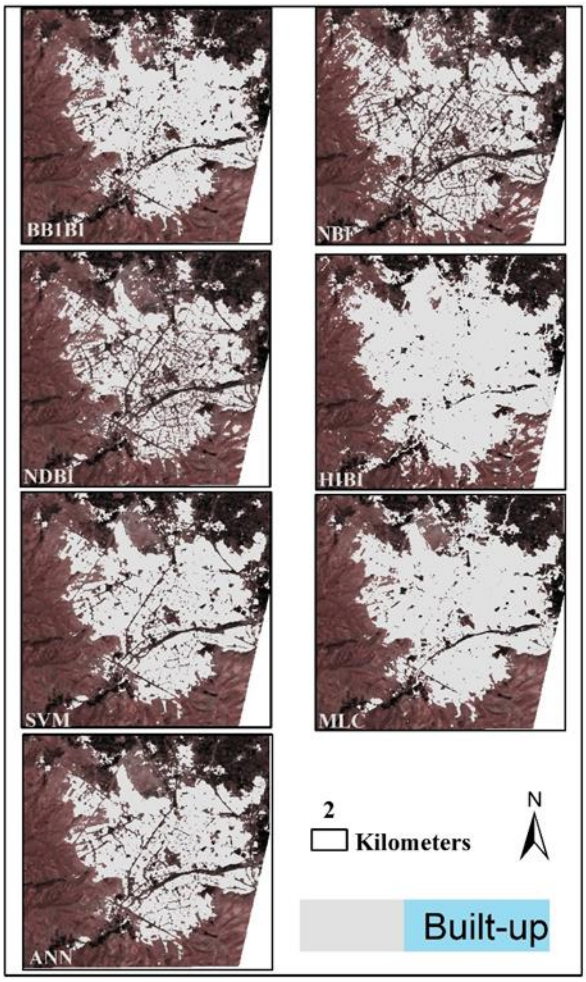

Figure 3. Map of built-up areas extracted from spectral indices and classification algorithms (Urmia)

4 Discussion

Due to continuous urbanization, land cover in urban areas is continuously developing in a short period of time compared to other areas. Therefore, the use of remote sensing, especially hyperspectral images, due to the multiplicity of its production bands, can be fruitful in order to identify and discover built-up areas. This article is done with the aim and comparative comparison of NDBI, NBI, PB1BI and HIBI production indices and SVM, ANN and MLC classification algorithms in order to identify and discover urban constructions using Prisma hyperspectral images.

As shown in Figure (2 nd 3), even though the Prisma images have a spatial resolution of 30 meters, in both Tehran and Urmia, the NDBI and NBI indices have been able to distinguish the built from the roads with high accuracy. In the meantime, although SVM and ANN classification algorithms are not very accurate in separating buildings from roads compared to other indicators and MLC classification algorithm, they perform well in separating buildings in places where the roads are wider. On the other hand, as seen in the center of the image in Tehran, there are gabled buildings with blue roofs, which the PB1BI and HIBI spectral indices were able to fully consider as built-up areas, while the NDBI and NBI indices performed poorly. In this regard, PB1BI and HIBI have not been able to separate the water area of the artificial lake from the built areas in the north of Tehran, which can be due to the presence of water area in the calculation of these indicators. In fact, areas with high reflectivity in the blue band range are considered as built-up areas. In this regard, one of the challenges faced by most indices, especially the NDBI and NBI indices, is the separation of bare soil and built-up areas; Since bare soil ranges are very similar to built up areas. Therefore, this has caused spectral integration between these two classes more than other complications. As seen in Figure (3), most of this spectral integration can be seen in the city of Tehran, and the reason for this is the presence of bare soil in the north and west of Tehran. In fact, these areas have a reflection similar to built-up areas. And the presence of high spectral integration has caused the results of Tehran city to be less accurate than the results of Urmia city. Meanwhile, the poor performance of NDBI and NBI indices compared to other indices is due to the greater influence of the SWIR band, where bare soil also has a high reflectance. In general, what is important from the findings of the research is that classification algorithms have performed better than spectral indices in identifying and extracting residential areas, and one of the important reasons is the direct participation of the user in the selection of training samples.

5 Conclusion

In this research, by using Prisma hyperspectral images and construction spectral indices as well as machine learning, statistical classification algorithms and artificial intelligence, urban built areas in Tehran and Urmia cities were separated from other complications. The findings of this research show that classification algorithms have performed better than spectral indices in identifying and extracting urban built-up area. In this regard, the findings indicate that each spectral index has strengths and weaknesses; So that each of these spectral indices will perform differently according to various factors such as the studied area, the spectral range used, the type of roof of the buildings, the types of uses, etc. Therefore, the combined use and comparison of spectral indices and classification algorithms together can greatly improve the results.

Acknowledgement

The authors of this article are extremely grateful to the Italian Space Agency for providing PRISMA hyperspectral images.

References

Angel, S., & Stephen, S. (2005). the dynamics of global urban expansion, Journal Transport and Urban, 1, 7-20.

Candela, L., Formaro, R., Guarini, R., Loizzo, R., Longo, F., & Varacalli, G. (2016, July). The PRISMA mission. In 2016 IEEE international geoscience and remote sensing symposium (IGARSS) (pp. 253-256). IEEE.

Galeazzi, C., Sacchetti, A., Cisbani, A., & Babini, G. (2008, July). The PRISMA program. In IGARSS 2008-2008 IEEE International Geoscience and Remote Sensing Symposium (Vol. 4, pp. IV-105). IEEE.

Gaur, S., Das, N., Bhattacharjee, R., Ohri, A., & Patra, D. (2023). A novel band selection architecture to propose a built-up index for hyperspectral sensor PRISMA. Earth Science Informatics, 16(1), 887-898.

Guindon B, Zhang Y, Dillabaugh C (2004) Landsat urban mapping based on a combined spectral– spatial methodology. Remote Sens Environ 92(2):218–232

Isazade, V., Ghanbari, A., & Kamran, K. V. (2022). Evaluation of spectral indices and extraction of constructed and non-constructed urban features and its comparison with ground surface temperature using Landsat 7 and 8 satellite images (Study area, Tehran). Geographical Planning of Space, 11(42),23-39.

Jieli, C., Manchun, L. I., Yongxue, L. I. U., Chenglei, S., & Wei, H. U. (2010, June). Extract residential areas automatically by new built-up index. In 2010 18th International Conference on Geoinformatics (pp. 1-5). IEEE.

Karimi Firozjaei, M., Mijani, N., Nadizadeh Shorabeh, S., Kazemi, Y., Ebrahimian Ghajari, Y., Jokar Arsanjani, J., ... & Alavipanah, S. K. (2023). Assessing the Effect of Urban Growth on Surface Ecological Status Using Multi-Temporal Satellite Imagery: A Multi-City Analysis. ISPRS International Journal of Geo-Information, 12(10), 406.

Mukherjee, A., Kumar, A. A., & Ramachandran, P. (2020). Development of new index-based methodology for extraction of built-up area from landsat7 imagery: Comparison of performance with svm, ann, and existing indices. IEEE Transactions on Geoscience and Remote Sensing, 59(2), 1592-1603.

Shahfahad., Mourya, M., Kumari, B., Tayyab, M., Paarcha, A., Asif. & Rahman, A., 2021, Indices based assessment of built-up density and urban expansion of fast growing Surat city using multitemporal Landsat data sets, GeoJournal., 86, 1607–1623.

Zha, Y.; Gao, J.; Ni, S. Use of normalized difference built-up index in automatically mapping urban areas from TM imagery. Int. J. Remote Sens. 2003, 24, 583–594.

Zhang, Jun, Peijun Li, and Jinfei Wang. 2014. "Urban Built-Up Area Extraction from Landsat TM/ETM+ Images Using Spectral Information and Multivariate Texture" Remote Sensing 6, 8, 7339-7359.

7th Intercontinental Geoinformation Days

igd.mersin.edu.tr

Emerging trends in geographic information systems

Samir Ganili

"Sukanal" Scientific-Research and Design Institute, Baku, Azerbaijan

Keywords
GIS Systems
New trends
Internet of Things (IoT)
Ethical considerations

Abstract
Geographic Information Systems (GIS) have undergone significant transformations in recent years, shaping the way we analyze and interpret spatial data. This paper explores the latest trends in GIS technology and their profound implications for various industries and society as a whole. We delve into five key trends: 1) the rise of location-based services, 2) the integration of GIS with Internet of Things (IoT), 3) advances in 3D GIS technology, 4) the increasing importance of GIS in disaster management, and 5) the ethical considerations in GIS data handling.

1. Introduction

Geographic Information Systems (GIS) have evolved from basic mapping tools to sophisticated spatial analytics platforms. As technology continues to advance, new trends in GIS are emerging, revolutionizing how we utilize and interact with spatial data. In this paper, we examine five prominent trends in the field of GIS, exploring their implications and potential impact on various industries.

1.1. The Rise of Location-Based Services

The proliferation of location-based services (LBS) is one of the most notable trends in GIS. LBS leverage GIS technology to provide users with location-specific information and services, transforming various sectors such as marketing, navigation, and social networking.

1.1.1. Personalized Marketing

GIS-powered LBS enable businesses to deliver highly targeted advertisements and promotions based on users' real-time locations. This trend enhances marketing effectiveness and customer engagement, while also raising concerns about privacy and data security.

1.1.2. Navigation and Transportation

The integration of GIS in navigation applications has revolutionized how people travel. Real-time traffic data, route optimization, and location-based alerts have become essential features of modern navigation systems, improving mobility and reducing congestion.

1.1.3. Social Networking

Social media platforms increasingly integrate GIS to enhance user experiences. Features like geotagged posts and location-based check-ins not only connect individuals but also contribute to the creation of spatially enriched user-generated content.

2. Integration of GIS with Internet of Things (IoT)

The synergy between GIS and the Internet of Things (IoT) represents a significant trend that enhances the capability to collect, analyze, and act upon real-time data from interconnected devices.

2.1. Smart Cities

GIS-IoT integration plays a pivotal role in the development of smart cities. Sensor networks and connected devices generate vast amounts of data, allowing city planners to optimize resource allocation, enhance public safety, and improve overall urban sustainability.

2.2. Environmental Monitoring

Environmental agencies leverage GIS and IoT to monitor ecosystems, air quality, and weather conditions

Samir Ganili
(ganili@gmail.com) ORCID ID 0009-0006-2089-4322

Ganili, S. (2023). Emerging Trends in Geographic Information Systems Intercontinental Geoinformation Days (IGD), 7, 41-43, Peshawar, Pakistan

in real-time. This integration aids in early detection of environmental issues, disaster management, and climate change mitigation.

3. Advances in 3D GIS Technology

The advancement of three-dimensional (3D) GIS technology opens new avenues for visualizing and analyzing spatial data in a more realistic and comprehensive manner.

3.1. Urban Planning and Architecture

3D GIS models aid urban planners and architects in creating accurate representations of cities and buildings. This technology enhances decision-making processes, enabling stakeholders to visualize the impact of proposed developments.

3.2. Emergency Response

3D GIS is invaluable in disaster management. Emergency responders can use 3D models to simulate disaster scenarios, identify potential hazards, and plan effective evacuation routes.

4. GIS in Disaster Management

GIS is increasingly vital in disaster management and emergency response. This trend reflects the growing importance of spatial data in mitigating, responding to, and recovering from natural and man-made disasters.

4.1. Early Warning Systems

GIS technology helps create early warning systems for natural disasters such as hurricanes, wildfires, and floods. These systems save lives by providing timely alerts and enabling efficient evacuation plans.

4.2. Post-Disaster Recovery

After a disaster, GIS assists in damage assessment, resource allocation, and recovery planning. Spatial data plays a crucial role in rebuilding infrastructure and communities.

5. Ethical Considerations in GIS Data Handling

The ethical aspects of GIS data handling have gained prominence as GIS technology continues to evolve. Data privacy, security, and responsible data usage are central to the ethical considerations in GIS.

5.1. Privacy Concerns

The collection of location data by GIS and LBS raises significant privacy concerns. Users' location information can be exploited for various purposes, necessitating robust privacy safeguards and legal regulations.

Privacy regulations and laws, such as the European Union's General Data Protection Regulation (GDPR) and the California Consumer Privacy Act (CCPA), have implications for spatial data. These regulations require organizations to obtain informed consent when collecting location data and to provide individuals with control over their data.

5.2. Data Security

The security of GIS data is paramount, particularly when it involves sensitive government, commercial, or personal information. Data breaches and unauthorized access pose serious threats to privacy and national security.

The security of spatial data is a growing concern. Unauthorized access to GIS databases can compromise sensitive information, including personal locations and critical infrastructure data. GIS professionals and organizations must prioritize data security measures to protect against cyber threats.

5.3. Ethical Data Usage

GIS professionals must adhere to ethical guidelines in data collection and analysis. This includes avoiding biases, ensuring data accuracy, and transparently communicating the implications of their work.

GIS professionals are increasingly confronted with ethical dilemmas related to data collection and usage. Questions about surveillance, profiling, and bias in spatial data analysis need to be addressed to ensure responsible and ethical GIS practices.

6. Conclusion

Geographic Information Systems have come a long way, driven by technological advancements and the increasing need for spatial data analysis. The trends discussed in this paper—the rise of location-based services, GIS-IoT integration, 3D GIS technology, the role of GIS in disaster management, and ethical considerations in GIS data handling—will continue to shape the future of GIS. As GIS technology evolves, it will play an increasingly integral role in addressing complex spatial challenges and enhancing decision-making processes across diverse industries and sectors. However, it is crucial to balance technological innovation with ethical and privacy considerations to ensure that GIS serves the greater good of society.

The trends discussed in this paper—cloud-based GIS, AI and ML integration, democratization of GIS, and spatial data privacy concerns—are shaping the future of GIS. These trends offer opportunities for innovation and collaboration while also requiring careful consideration of ethical and privacy implications. As GIS continues to advance, it will play an increasingly pivotal role in addressing complex spatial challenges and enhancing decision-making across a wide range of industries and sectors.

References

https://visitgis.com/10-emerging-gis-trends-2023-2024/

https://community.esri.com/t5/esri-young-professionals-network-blog/5-trends-in-gis-and-how-to-successfully-navigate/ba-p/1169616

7th Intercontinental Geoinformation Days

igd.mersin.edu.tr

GIS-based soil loss estimation using revised universal soil loss equation

Ekundayo Adesina*[1], Oluibukun Ajayi, [2], Joseph Odumosu[3], Abel Illah[1]

[1]Federal University of Technology, School of Environmental Technology, Surveying and Geoinformatics Department, Minna, Nigeria
[2]Namibia University of Science and Technology, Faculty of Engineering and the Built Environment, Department of Land and Spatial Sciences, Windhoek, Namibia
[3]Federal University of Oye Ekiti, Faculty of Environmental Science, Department of Surveying and Geoinformatics, Oye Ekiti, Nigeria

Keywords
Soil Erosion Estimation
GIS
RUSLE
Remote Sensing
Digital Elevation Models

Abstract

Soil loss estimation plays a vital role in the management and conservation of land and water resources, offering vital insights for watershed-level development in various regions. This study focuses on the development of a soil loss model for Bosso Local Government Area in Minna, Nigeria, utilizing the Revised Universal Soil Loss Equation (RUSLE). Integration of Landsat images, Digital Elevation Models (DEM), rainfall and precipitation records, and soil erodibility factors was employed to estimate the average annual soil erosion within the study area. The individual parameters of the RUSLE model were integrated into the ArcGIS environment using the raster calculator in the Arc toolbox. The results reveal that an alarming 6672.83 tonnes per hectare per year of soil are lost annually in the study area. This rate of soil erosion raises concerns about the sustainability of agricultural practices in the study area. The findings underscore a critical absence of conservation practices or plans to combat and mitigate soil erosion in the region. In light of these findings, it is imperative that local government authorities, in collaboration with various ministries, take immediate action to promote and enforce conservation measures aimed at combating soil erosion within the area.

1. Introduction

Soil erosion is a significant global issue influenced by natural and anthropogenic factors, causing land degradation and negative impacts on the economy and environment (Bakis *et al.,* 2021). Accurate assessment and estimation of soil loss are crucial for sustainable land and water resource management (Yusof *et al.,* 2019). The Universal Soil Loss Equation (USLE), modified by Wischmeier and Smith (1978), is a widely used empirical model for predicting long-term average yearly soil loss on agricultural land, with its improved and modified versions still widely used in studies (Wajesundara *et al.,* 2018).

The Revised Universal Soil Loss Equation (RUSLE) model, which forecasts erosion potential on a cell-by-cell level, is useful for ecosystem services related to soil erosion and protection (Yusof *et al.,* 2019). It finds the spatial distribution of yearly soil loss at catchment size and can be applied using GIS applications to determine individual variables contributing to erosion potential values (Ganasri and Ramesh, 2016). Numerous studies have been conducted on the estimation of long-term soil loss using geospatial techniques in different parts of the world, including the Fincha Catchment of Ethiopia (Wagari and Taimur, 2021), the Dolapha district of Nepal (Thapa, 2020), the Kalu Ganga River Basin (Panditharathne *et al.,* 2020), the Pabaragamuwa Province of Sri Lanka (Senanayake *et al.,* 2020), the tropical mountain river basin of the southern Western Ghats (Thomas *et al.,* 2018), the Padma River Basin, the Siruvani River watershed in Attapady valley, Kerala (Prasannakumar *et al.,* 2011), the Barakar River Basin of Jharkhand (Biswas and Pani, 2015) etc. Thus, this study is aimed at evaluating soil loss in the Bosso Local Government Area of Minna in North Central Nigeria using RUSLE and ArcMap interface. The findings can help in providing valuable information which can valuable for effective management of land and water resources, reduction of soil erosion, and for promoting environmental protection for policy and decision-makers.

* **Corresponding Author**

*(adesinageoworldsolutions@gmail.com) ORCID ID 0000-0001-9526-4540
(oajayi@nust.na) ORCID ID 0000-0002-9467-3569
(joseph.odumosu@fuoye.edu.ng) ORCID ID 0000-0003-1604-4924
(abelillah56@gmail.com) ORCID ID 0009-0002-6315-2821

Cite this study

Adesina E., Ajayi O, Odumosu J & Illah A (2023). GIS-based soil loss estimation using revised universal soil loss equation (RUSLE). Intercontinental Geoinformation Days (IGD), 7, 44-48, Peshawar, Pakistan

2. Materials and Methods

2.1. Study Area

Minna, the capital of Niger State, is the administrative centre for the Bosso and Chanchaga Local Government Areas. It covers about 72 km^2 and has a rocky landscape with a typical middle belt zone climate. The mean monthly temperature is 30-500C (830F) and the rainy season starts in April of every year. Literature suggests that gully development is influenced by the underlying geology, with rock types being key factors. The Niger State geological map reveals three types of lithology: porphyritic and biotite hornblende granite, fine-grained biotite granite, and undifferentiated schist (Abdulfatai *et al.,* 2014).

2.2. Method

RUSLE was used to estimate soil loss in the study area using primary and secondary data processed within GIS software environments. The following subsections describe some of the parameters integrated for the soil loss modelling.

2.2.1. Rainfall Erosivity Factor (R)

To calculate the quantity of rainfall experienced in the study area, equation (1) suggested by Morgan *et al.* (1984) was implemented and integrated ArcGIS software environment using the raster calculator tool.

$$R = 38.5 + 0.35P \qquad (1)$$

where, R= Rainfall erosivity factor, P = Mean annual rainfall in mm

2.2.2. Soil Erodibility Factor (K)

Soil erodibility factor k measures soil susceptibility to erosion, influenced by organic matter, texture, structure, and permeability. Higher values indicate higher sensitivity, with potential k-factor values listed in Table 1.

Table 1. Different ranges of the K factor and their meanings

Soil types	K factor	Meaning
Rocky soil/deserted land	0-0.2	Very low erodibility
Silt or clay loam	0.2-0.5	Low erodibility
Sandy loam	0.5-0.8	Moderate erodiblity
Sandy soil/gravelly soil	0.8-1.0	High erodibility

The study area's soil erodibility factor was calculated using Wischmeier and Smith's (1978) equation (see equation 2) in ArcGIS.

$$K = 0.2 + 0.3\exp\left(0.0256 * S_a * \left(1 - \left(\frac{S_i}{100}\right)\right) * \left(\frac{S_i}{C_i+S_i}\right)^{0.3} * \left(1.0 - \frac{0.25*C}{C+\exp(3.72-2.95C)}\right) * \left(1.0 - \frac{0.7*SN}{SN+\exp\left(-5.51+22.9SN\right)}\right)\right) \qquad (2)$$

where, Sa = Sand %; Si = Silt %; CL = Clay %; SN = 1-(Sa/100); C = Organic Carbon.

2.2.3. Slope length and steepness factor (LS)

Slope length, also known as slope steepness, measures a slope's inclination, while steepness is the ratio of its vertical rise to run. The slope's length and steepness, measured in meters and percentages/degrees, influence erosion which increases the likelihood of soil loss with each increase. This study used Wischmeier and Smith's (1978) slope length and steepness factor equation in ArcMap, incorporating parameters from Equation (3).

$$LS = \left(\frac{\lambda}{72.6}\right) m^{\times}[(65.41 \times \sin 2\theta) + (4.56 \times \sin\theta) + 0.065] \qquad (3)$$

where, λ= slope length in meters. θ= Angle of slope m= dependent on slope: (i) 0.5 if slope > 5% (ii) 0.4 if slope is between 3.5% and 4.5% (iii) 0.3 if slope is between 1% and 3% (iv) 0.2 if slope is less than 1%

2.2.4. Annual Soil Loss Map

The ArcMap toolbox was utilized to integrate the RUSLE model parameters, resulting in the mean yearly soil loss for the study area map, as shown in Equation (4).

$$A = R * K * LS * C * P \qquad (4)$$

3. Results and discussions

This section presents the obtained results and their analysis. The result of each of the component of the soil loss modelling as described in subsections 2.2.1 – 2.2.4 are discussed in subsections 3.1-3.6

3.1 Rainfall Erosivity Factor (R)

Figure 1 displays the study area's average annual rainfall erosivity factor.

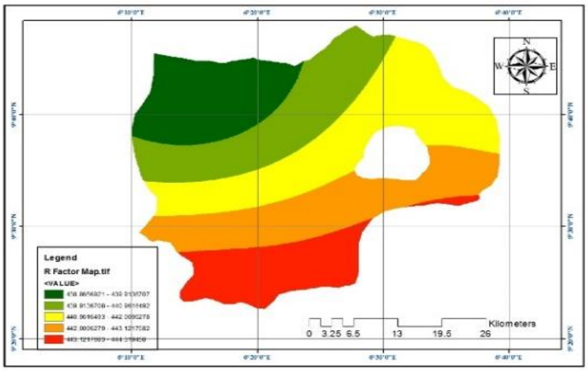

Figure 1. Rainfall erosivity factor map

The study area receives between 438.866 and 444.319 MJmmha1yr1 of annual rainfall, which can cause soil erosion. Intense rain can lead to more erosion, with significant damage resulting from sustained rainfall exceeding 25 mm per hour. Figure 1 shows that the study area experiences soil erosion due to 444.319 mm annual precipitation and four soil types, with a high k factor indicating soil susceptibility to erosion.

3.2 Soil Erodibility Factor (K)

Figure 2 shows the soil erodibility factor map of the study area, while Table 2 lists different soil types found in the study area.

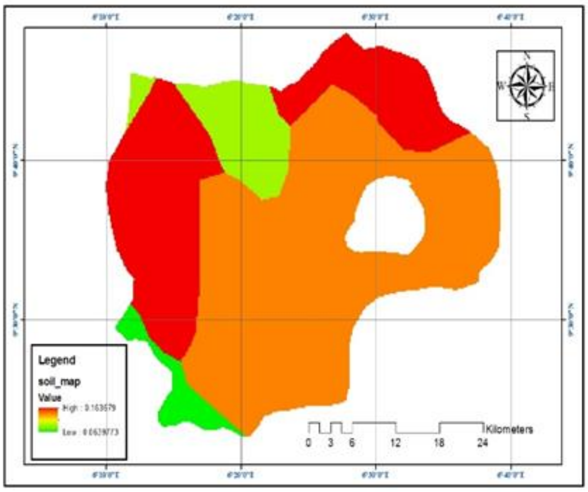

Figure 2. Soil erodibility factor map of Bosso local government Area

Table 2. Soil types found in the study region

Soil type	Sand %	Silt %	Clay %	OC %	(K) Factor
Distric Nitosol	38.9	17.6	43.6	1.57	0.06
Ferric Luvisol	74.6	9.6	15.9	0.39	0.16
Lithosol	58.9	16.2	24.9	0.97	0.12
Plinthic Luvisol	69.9	10.5	19.5	0.73	0.15

The digital soil map of the world (DSMW), a digital version of the FAO-UNESCO soil map, generated the erodibility factor k by displaying 4931 soil associations, a combination of different soil types. Soil erodibility in the study area, ranges from 0.064 to 0.016 m/h and comprises four distinct soil types, such as Distric Nitosol (73%), Ferric Luvisol (8%), Lithosol (9%), and Plinthic Luvisol (9%).

3.3 Slope Length and Slope Steepness Factor (LS)

Figure 3 displays the map of the study area's slope length and steepness factor.

The digital elevation model (DEM) of the study area with 12.5m resolution was used to generate the slope length and slope steepness factor. Table 3 describes various support practise variables for various conservation strategies. Figure 3 shows that topography influences soil erosion through slope length and steepness, with steeper slopes causing more intense runoff, with a more pronounced influence observed between 0 and 572.

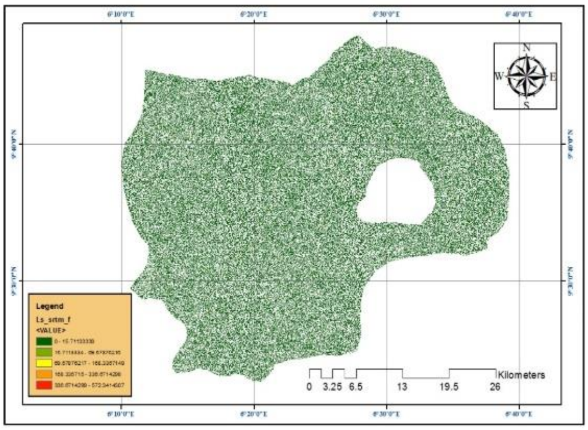

Figure 3. Slope length and steepness factor map of the study area

Table 3. Support practise elements for various conservation practises

Slope (%)	Contouring	Strip cropping	Terracing
0-7	0.55	0.27	0.2
7-11.3	0.66	0.3	0.12
11.3-17.6	0.8	0.4	0.16
17.6-26.8	0.9	0.45	0.18
26.8>	1	0.5	0.2

Source: (Shin, 1999)

The RUSLE model employs the Support Practise Element (SPE) to assess the effectiveness of conservation practices in reducing soil erosion, with 1 indicating greater success. Examples include terracing, contour farming, and cover crop application.

3.5 Conservation Factor (C)

The RUSLE model includes a conservation factor, which indicates the likelihood of soil erosion, the effectiveness of conservation measures, and land management strategies. The factor ranges from 0 to 1, with 1 indicating no conservation practice while 0 indicates a complete protection. Figure 4 displays the study area's conservation practise factor map.

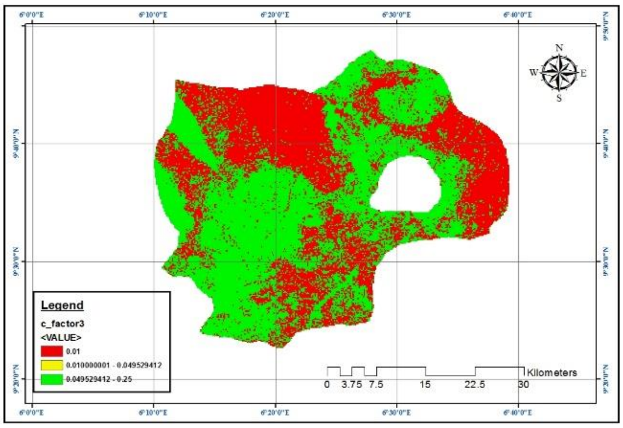

Figure 4. Conservation factor map

The conservation map shows that the area’s conservation factors ranges from 0.01 to 0.25 which indicates that while there are ongoing efforts to curb soil erosion in the area, the efforts are inadequate and not even distributed.

3.6. Mean Annual Soil Loss

The study area's mean annual soil loss was calculated using the RUSLE, summed up using relation and expressed as t/ha/yr. The annual soil loss map (figure 5) reveals a significant annual loss of 6672.83t/h/yr, which suggests a high erosion rate. Agricultural practice in the area, involving subsidence and large-scale farming, leads to soil loss which invariably impacts food production and environmental degradation.

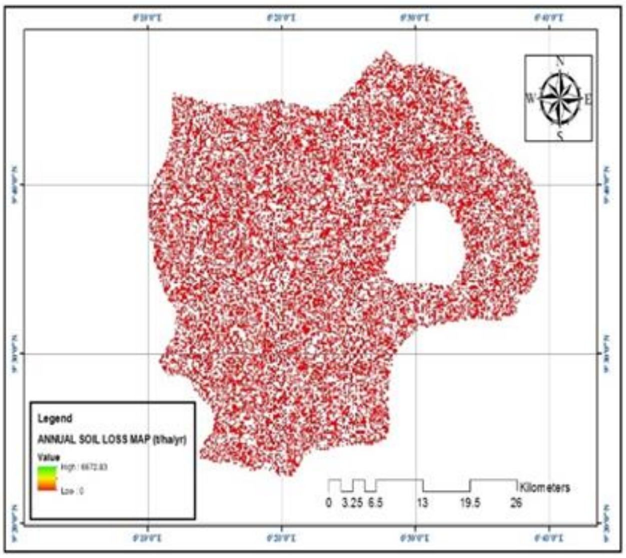

Figure 5. Mean annual soil loss map

Figure 5 shows that the mean annual soil loss in the study area, ranging from 0 to 6672.83 t/ha/yr, This means that the area exhibits considerable variability in terms of soil erosion rates. The range also indicates that there are likely different factors and conditions contributing to soil erosion in different parts of the area. It shows that while some areas are well-protected against erosion, other areas are more susceptible due to factors like topography, land use, vegetation cover, and climate. These high soil erosion rates can have negative environmental impacts, including sedimentation in water bodies, reduced soil fertility, and land degradation.

4. Conclusion

Soil erosion in the study area is primarily caused by varied topography, cover management, and land use practices. Excessive erosion occurs during rainy seasons, with an estimated rate of 6672.83 t/h/yr. The study suggests that using a GIS-based RUSLE model can simplify long-term estimation in an upland-lowland watershed, aiding in watershed management, resource planning, and identifying water harvesting sites to reduce soil erosion.

References

Abdulfatai, I. A, Okunlola, I. A, Akande, W. G, Momoh, L. O, & Ibrahim, K. O. (2014). Review of Gully Erosion in Nigeria: Causes, Impacts and Possible Solutions. Journal of Geosciences and Geomatics, 2(3), 125-129

Bakis, R., Bayajit, Y., Ahmady, D. M., & Cabuk, S. N. (2021). Analysis and comparison of spatial rainfall distribution applying different interpolation methods in the Porsuk River Basin, Turkey. *Eskisehir Technology University Journal SciTechnology B-Theoretical Science* 9(1):1–14. https://doi.org/10.20290/estubtdb.726491z

Biswas, S. S., & Pani, P. (2015). Estimation of soil erosion using RUSLE and GIS techniques: a case study of Baraka River Basin, Jharkhand, India. Model Earth System Environment 1(42):1–13. https://doi.org/10.1007/s40808-015-0040-3

Ganasri, B., & Ramesh, H. (2016). Assessment of soil erosion by RUSLE model using remote sensing and GIS-A case study of Nethravathi Basin. *Geoscience Frontier*7: https://doi.org/10.1016/j.gsf.2015.10.007

Morgan, R. P. C., morgan, D. D. V. & Finney, H. J. (1984). A predictive model for the assessment of soil erosion risk. Journal of Agricultural Engineering Research, 30,
245-253.

Panditharathne, D. I. D., Abeysingha, N. S., Nirmanee, K. G. S., & Mallawatantri, A. (2020). Application of revised Universal Soil loss equation (rusle) model to assess soil erosion in Kalu Ganga River Basin in Sri Lanka. Applied Environment Soil Science. https://doi.org/10.1155/2019/4037379

Prasannakumar, V., Shiny, R., Geetha, N., & Vijith, H. (2011). Spatial prediction of soil erosion risk by remote sensing, GIS and RUSLE approach: a case study of Siruvani river watershed in Attapady valley, Kerala, India. Environment Earth Science 64:965–972. https://doi.org/10.1007/s12665-011-0913-3

Senanayake, S., Pradhan, B., Huete, A., Brenan, J. (2020). Assessing soil Erosion hazards using land-use change and landslide frequency ratio Method: a case study of Sabaragamuwa Province, Sri Lanka. Remote Sensing 12:1483. https://doi.org/10.3390/rs12091483

Thapa, P. (2020). Spatial estimation of soil erosion using RUSLE modeling: a case study of Dolakha district, Nepal. Environment System Resource 9(15):1-10. https://doi.org/10.1186/s40068-020-00177-2

Thomas, J., Joseph, S., & Thrivikramji, K.P. (2018). Assessment of soil erosion in a tropical mountain river basin of the southern Western Ghats, India, using RUSLE and GIS. Geoscience Front 9:893–906. https://doi.org/10.1016/j.gsf.2017.05.011

Wagari, M., & Taimur, H. (2021). RUSLE model-based annual soil loss quantification for soil erosion protection: a case of Fincha Catchment, Ethiopia. Air Soil Water Resource 14:1–12. https://doi.org/10.1177/11786221211046234

Wajesundara, N. C., Abeysingha, N. S., Dissanayake, D. M. (2018). GIS-based soil loss estimation using RUSLE model: a case of Kirindi Oya river basin, Sri Lanka.

Model Earth System Environment 4(1):251–262. https://doi.org/10.1007/s40808-018-0419-z

Wischmeier, W. H., & Smith, D. D. (1978). Predicting rainfall erosion losses: a guide to conservation planning. Agriculture Handbook no 537. *US Department of Agriculture*, *Science and Education Administration*, *Washington, DC, USA*, p 163-176

Yusof, N. F., Lihan, T., Idris, W. M. R., Rahman, Z. A., Mustapha, M. A., Yusof, M. A. W. (2019). Prediction of soil erosion in Pansoon Sub-basin, Malaysia using RUSLE integrated in geographical information system. *Sains Malays* 48(11):2565–2574. https://doi.org/10.17576/jsm-2019-4811-26

7th Intercontinental Geoinformation Days

igd.mersin.edu.tr

Land use and land cover classes affected by possible sea level rise in Mersin city center

Onur Güven *1, **Ümit Yıldırım** 2, **Cüneyt Güler** 3, **Mehmet Ali Kurt** 4

[1]Bayburt University, Central Research Laboratory, Bayburt, Türkiye
[2]Bayburt University, Faculty of Applied Sciences, Department of Emergency Aid and Disaster Management, Bayburt, Türkiye
[3]Mersin University, Engineering Faculty, Department of Geological Engineering, Mersin, Türkiye
[4]Mersin University, Engineering Faculty, Department of Environmental Engineering, Mersin, Türkiye

Keywords
Sea level rise
Coastal area
Land use change
GIS
Mersin

Abstract

In this study, a sea level rise (SLR) investigation was carried out in an area representing the Mersin city center located in the south of Turkey. The study area covers an area of *ca*. 385 km^2. Future projections provided by the IPCC were used for the SLR assessment. These projections are for the years 2100, 2200, 2300, 2400, and 2500 and the SLR for these periods are 0.83 m, 2.03 m, 3.59 m, 5.17 m, and 6.63 m, respectively. It is aimed to determine the areas affected by the SLR that will occur according to these projections. In this context, land use and land cover (LULC) data were obtained from the CORINE 2018 dataset. The data obtained were adapted within the boundaries of the study area and processesed using various GIS analyses. The results have shown that all LULC classes are greatly affected by the SLR, but in varying degrees. Land losses as a result of SLR are as follows: 0.4% at 0.83 m SLR, 9.8% at 2.03 m SLR, 16.7% at 3.59 m SLR, 21.6% at 5.17 m SLR, and 25% at 6.63 m SLR.

1. Introduction

Coastal regions are areas of critical importance in terms of the possible effects of climate change. Sea level rise (SLR) is one of the most important consequences of climate change affecting people living in coastal regions. (Antonioli et al., 2020). It is inevitable that Turkey, which is surrounded by the sea on three sides and has a coastline of 8333 km (Demirkesen et al., 2008), will be affected by SLR. Sea water levels are rising due to two different parameters defined as increasing the water volume of the seas and cumulative expansion (EPA, 2016). The sea water level has increased by 98 mm from 1993 to the present (NASA, 2023) and has increased by 3.2 mm/yr over the last decades (Antonioli et al., 2020). According to data based on tide measurements, the SLR in the Mediterranean basin is 1.8 mm/yr (Antonioli et al., 2020).

Mersin is the city that has the longest coastline in Turkey, with a length of 321 km (MCT, 2023). The population of Mersin is 1,916432 as of the end of 2022, and it is one of the most populous cities in Turkey (TSI, 2023). 53% of the Mersin city consists of forests, 21% is agricultural lands, 22% is non-agricultural lands, and 4% is meadows and pastures (MTSO, 2023). In addition, Mersin, which ranks 1st in Turkey with a container business volume of 2.1 million TEU, has an essential economic infrastructure in maritime trade (MIP, 2021).

There are many studies on this subject in Turkey, but studies on micro-scale areas are limited (Demirkesen et al., 2008; Geymen and Dirican, 2016; Kuleli et al., 2009; Kurt and Li, 2020; Simav et al., 2015; 2016; Üstün, 2019; Zengin, 2023). In this study, Mersin city center was chosen, and the study area resides within the borders of three districts. In the study, LULC types affected by SLR was evaluated using GIS technology and climate projections.

2. Materials and Method

2.1. Study area

The study area, which covers an area of 385.4 km^2, constitutes the center of Mersin City, located on the Mediterranean coast in the south of Turkey (Fig. 1). While the study area is a narrow coastal plain in the west, it expands like a fan towards the east. Müftü Stream and

* **Corresponding Author**

*(onurguven@bayburt.edu.tr) ORCID ID 0000-0001-5608-7633
(umityildirim@bayburt.edu.tr) ORCID ID 0000-0002-7631-7245
(cguler@mersin.edu.tr) ORCID ID 0000-0001-8821-6532
(malikurt@mersin.edu.tr) ORCID ID 0000-0001-7255-2056

Cite this study

Güven, O., Yıldırım, Ü., Güler, C., & Kurt, M. A. (2023). Land use and land cover classes affected by possible sea level rise in Mersin city center. Intercontinental Geoinformation Days (IGD), 7, 49-52, Peshawar, Pakistan

Deliçay River are the important rivers of the study area. It is estimated that approximately 695,000 people live in this area. Transportation is provided by highways (O-51 and D400), railway (Adana-Mersin), and seaway. On the other hand, there is a marina and a port (MIP) where international trade takes place.

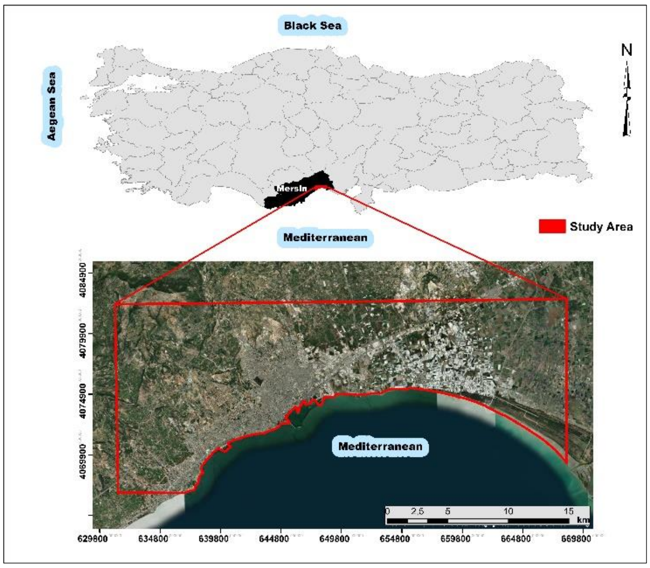

Figure 1. Map of the study area representing Mersin city center.

2.2. Sea level rise

A digital elevation model (DEM) was used to create a SLR database and determine future flood areas. Contour lines were taken as a basis when creating the DEM. DEM with a resolution of 10×10 m was obtained by digitizing 1:25000-scale topographic maps (Fig. 2) using ArcGIS 10.4 software. All data used in this study were georeferenced using the WGS 1984 UTM Zone 36N coordinate system.

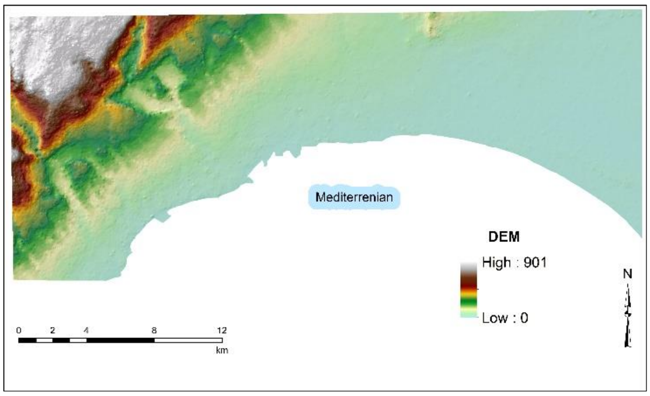

Figure 2. Digital elevation model (DEM) of the study area.

The scenarios in the Intergovernmental Panel on Climate Change (IPCC) report (IPCC, 2014) revealed the risk situation due to SLR in the study area. The report includes SLR scenarios for the years 2100, 2200, 2300, 2400, and 2500. SLR scenarios are divided into three categories based on low, medium, and high CO_2 concentrations (IPCC, 2014). In this study, the SLR scenario applied according to high CO_2 concentration is taken as a reference, and SLR values are presented by the years in Table 1.

Table 1. IPCC 5th Assessment Report SLR scenarios.

Scenario	2100	2200	2300	2400	2500
SLR (m)	0.83	2.03	3.59	5.17	6.63

2.3. Land use and land cover

This study aims to determine the LULC classes affected by the SLR for Mersin City. LULC data in grid format obtained from the CORINE dataset (EEA, 2018) was used to create the LULC layer for the study area. LULC parameters (Fig. 3) adapted to the study area are classified into 13 individual classes (Table 2).

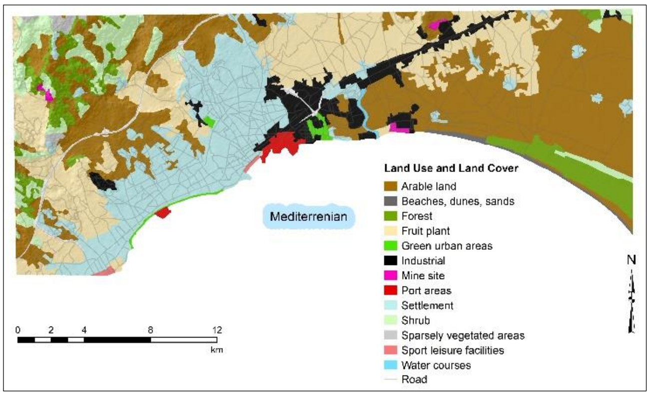

Figure 3. Map of the LULC classes of the study area.

Table 2. LULC types of the study area.

LULC	Area (km²)	LULC	Area (km²)
Arable land	145.0	Sparsely vegetated areas	2.1
Fruit plants	89.0	Green urban areas	2.1
Settlement	72.9	Beaches, dunes, sands	2.1
Forest	23.2	Mine site	1.1
Industrial	22.6	Sport-leisure facilities	0.6
Shrub	21.6	Water courses	0.6
Port areas	2.5	**Total**	**385.4**

3. Results

In this study, five different SLR scenarios (0.83 m, 2.03 m, 3.59 m, 5.17 m, and 6.63 m) were considered for the Mersin City. The areas most affected by these scenarios are located at the east of the study area (Fig. 4). This area is a coastal plain formed by alluvial deposits brought by the Deliçay and Tarsus rivers. This area's slope, characterized by a delta environment, varies between 0-10°. In addition, the city's important agricultural areas are located in the most sensitive area with respect to SLR.

LULC types affected by the combination of SLR and LULC were determined spatially (Table 3). Except for sparsely vegetated areas, all LULC classes were affected by different SLR scenarios. The most affected classes were arable land and forest. A section of the Adana-Mersin highway (D400) is inundated when sea levels rise by 6.63 m. LULC losses in SLR scenarios for 2100, 2200, 2300, and 2500 are 0.4%, 9.8%, 16.7%, 21.6%, and 25.0%, respectively.

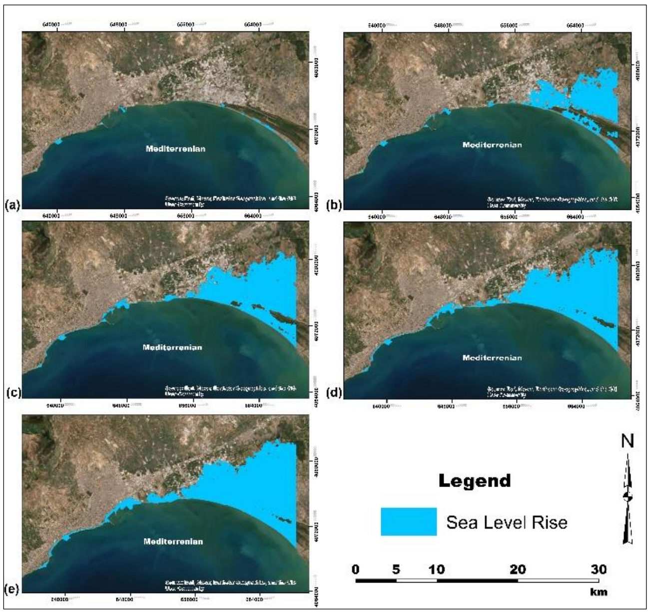

Figure 4. Map of SLR: (a) 0.83 m, (b) 2.03 m, (c) 3.59 m, (d) 5.17 m, (e) 6.63 m.

Table 3. LULC classes affected by SLR.

LULC	Effect on LULC (km²)				
	0.83 m	2.03 m	3.59 m	5.17 m	6.63 m
Arable land	0.3	30.8	49.2	61.3	68.1
Fruit plants	0.03	0.2	1.2	2.8	4.6
Settlement	0.07	0.3	1.1	2.4	3.6
Forest	0.09	3.8	7.8	9.4	10.2
Industrial	-	0.1	0.3	1.1	2.2
Shrub	-	0.02	0.2	1.0	1.7
Port areas	0.5	0.7	1.6	2.0	2.3
Sparsely vegetated areas	-	-	-	-	-
Green urban areas	0.03	0.1	0.4	0.5	0.7
Beaches, dunes, sands	0.7	1.6	2.0	2.1	2.1
Mine site	-	0.005	0.1	0.1	0.2
Sport-leisure facilities	0.02	0.1	0.2	0.3	0.4
Watercourses	0.01	0.1	0.1	0.1	0.2

4. Discussion

The Mersin city center, home to various LULC classes, was selected for the evaluation of the SLR effect. In addition, this city plays an important role in international trade.

Many studies conducted in Turkey are large-scale studies covering all coastal provinces. This study can be considered as a micro-scale when considered on a country basis. Studying smaller areas is essential in terms of climate change and water management. In this study, only global scenarios presented by IPCC are considered.

The delta region of the study area is in great danger due to rising sea levels. Economic activities here will be interrupted. These studies reveal the fact that SLR has socio-economic effects as well as ecological effects. With SLR, not only land loss but also population migration is inevitable. Therefore, branches of science such as climate change, economics, sociology, and ecology should be considered together.

5. Conclusion

To evaluate the SLR effect, the study area within the borders of Mersin city center and three districts was selected. 10×10 m resolution DEM data served as the basis for the SLR investigation. Contour lines were used to produce the DEM. CORINE 2018 LULC dataset was adapted to the study area to evaluate LULC types affected by SLR. A total of 13 LULC classes were defined in the study area. These LULC classes were combined with the SLR, and the affected areas were calculated.

According to data collected, arable land was the most impacted LULC class (6.63 m SLR). It was followed by forests, fruit plants, settlements, port areas, industrial, beaches-dunes-sands, shrubs, green urban areas, sports-leisure facilities, mine sites, water courses LULC types. Land losses as a result of SLR are as follows: 0.4% at 0.83 m SLR, 9.8% at 2.03 m SLR, 16.7% at 3.59 m SLR, 21.6% at 5.17 m SLR, and 25% at 6.63 m SLR.

References

Antonioli, F., De Falco, G., Lo Presti, V., Moretti, L., Scardino, G., Anzidei, M., … & Mastronuzzi, G. (2020). Relative Sea-Level Rise and Potential Submersion Risk for 2100 on 16 Coastal Plains of the Mediterranean Sea. Water, 12(8), 2173. https://doi.org/10.3390/w12082173

Demirkesen, A. C., Evrendilek, F., & Berberoğlu, S. (2008). Quantifying coastal inundation vulnerability of Turkey to sea-level rise. Environmental Monitoring and Assessment, 138(1-3), 101-106. https://doi.org/10.1007/s10661-007-9746-7

European Environment Agency (EEA). CORINE Land Cover 2018 (vector/raster 100 m), Europe, 6-yearly. Retrieved October 22, 2023 from https://land.copernicus.eu/pan-european/corine-land-cover/clc2018?tab=download

Geymen, A., & Dirican, A. Y. (2016). İklim değişikliğine bağlı deniz seviyesi değişiminin coğrafi bilgi sistemleri kullanılarak analiz edilmesi. Harita Teknolojileri Elektronik Dergisi, 8(1), 65-74. https://doi.org/10.15659/hartek.16.04.308

IPCC, (2014). Climate Change 2014: Synthesis Report. Contribution of Working Groups I, II, and III to the Fifth Assessment Report of the Intergovernmental Panel on Climate Change [Core Writing Team, R.K. Pachauri and L.A. Meyer (eds.)]. Geneva, Switzerland.

Kuleli, T., Şenkal, O., & Erdem, M. (2009). National assessment of sea level rise using topographic and census data for Turkish coastal zone. Environmental Monitoring and Assessment, 156(1-4), 425-434. https://doi.org/10.1007/s10661-008-0495-z

Kurt, S., & Li, X. (2020). Potential impacts of sea level rise on the coasts of Turkey. Journal of Environment and Earth Science, 10(5), 40-47. https://doi.org/10.7176/JEES/10-5-04

Mersin International Port Management INC. (MIP). (2021). Mersin Uluslararasi Limani Sürdürülebilirlik Raporu. Mersin, Türkiye: Author.

Mersin Chamber of Commerce & Industry (MTSO). (2023). 2022 Mersin Ekonomik Raporu. Mersin, Türkiye: Author.

Ministry of Culture and Tourism of the Republic of Turkey (KTB). (n.d.) Mersin. Retrieved October 10, 2023 from https://mersin.ktb.gov.tr/TR-73151/cografya.html

National Aeronautics and Space Administration (NASA). (2023). Sea Level. Retrieved from https://climate.nasa.gov/vital-signs/sea-level/

Simav, Ö., Şeker, D. Z., Tanık, A., & Gazioğlu, C. (2015). Kıyı etkilenebilirlik göstergesi ile Türkiye kıyıları risk alanlarının tespiti. Harita Dergisi, 153(81), 1-8.

Turkish Statistical Institute (TSI) (n.d.). İstatistikler. Retrieved October 10, 2023 from https://biruni.tuik.gov.tr/medas/?kn=95&locale=tr

U.S. Environmental Protection Agency (EPA). (2016). Climate change indicators in the United States. Fourth edition. Washington, United States: Author.

Üstün, Y. M. (2019). Antropojenik iklim değişikliğine bağlı deniz seviyesi değişiminin Sinop Yarımadası'na olası etkileri. Afet ve Risk Dergisi, 2(2), 64-79. https://doi.org/10.35341/afet.567218

Zengin, E. (2023). Inundation risk assessment of Eastern Mediterranean Coastal archaeological and historical sites of Türkiye and Greece. Environmental Monitoring and Assessment, 195(8), 1–25. https://doi.org/10.1007/s10661-023-11549-3

7th Intercontinental Geoinformation Days

igd.mersin.edu.tr

LULC change and CO_2 emissions in Shangai 2000-2020

Jianwen Zheng [1], Yishao Shi *[1], Katabarwa Murenzi Gilbert [1]

[1]Tongji University, College of Surveying and Geo-Informatics, Shanghai 200092, China

Keywords
Shanghai
Built-up
Land use change
Carbon emissions
Natural ecosystems

Abstract

The absorption and release of carbon dioxide by different types of land cover, with activities like deforestation or urbanization releasing CO^2, while afforestation or natural ecosystems act as carbon sinks, affecting the overall carbon balance in the atmosphere. This paper analyzes the spatial and temporal characteristics of land use and carbon emissions in Shanghai from 2000 to 2020 using the land use transfer matrix, the carbon emission estimation model, and the standardized error ellipse method. The results indicate that the total carbon emissions from land use in Shanghai have exhibited an upward trend from 2000 to 2020, with an average annual growth rate of 3.055%. The expansion of construction land has been identified as the main source of carbon emissions, while forests serve as the primary carbon sink. Spatial analysis reveals that areas with high-intensity carbon emissions are mainly concentrated in Pudong New Area, while regions with moderate carbon emissions are in Jiading and Minhang districts, gradually expanding towards the northeast. Based on these findings, it is recommended that carbon emission policies consider the characteristics of regional differences, control land use intensity appropriately, and guide low-carbon and efficient land utilization as the primary direction to achieve Shanghai's energy low-carbon transformation.

1. Introduction

With the severe global climate change situation, carbon reduction has become an important issue of common concern for countries worldwide. Land use change is one of the crucial factors influencing carbon emissions and carbon sequestration, indirectly affecting global climate change and regional ecological environments(Bryan et al., 2018; Jin et al., 2020). In response to climate change, China proposed the "dual carbon" goals in 2020(CAI et al., 2022). Emphasizing optimizing land use structure and improving green, low-carbon, and circular development in terms of carbon emissions reduction and carbon sinks. Therefore, conducting regional studies on carbon emissions from the land use perspective and analyzing the effects of different land use types within a region by constructing a scientifically sound accounting system for land use carbon emissions can contribute to formulating regional low-carbon spatial planning and carbon reduction decisions.

Many domestic scholars have analysed the spatial and temporal characteristics and trends of land use change and carbon emissions, carbon emission efficiency, and carbon reduction. (Pan et al., 2022; Wang et al., 2023; Xiao et al., 2022; Zhang et al., 2023; Zhu et al., 2022) Investigated the link between land use change and carbon emissions using a block approach at the national scale. Also, they explored the spatial correlation of carbon emissions at national and provincial levels by combining a model for assessing the hidden form of land use. Furthermore, they researched carbon emission efficiency, emission intensity, and spatial characteristics of different land use types at the provincial scale.

However, existing domestic literature mainly focuses on national macro-level, regional-level, and provincial-level analyses, with limited research on the relationship between land use and carbon emissions at the city level. Therefore, based on the land use changes in Shanghai from 2000 to 2020, this study investigates the spatiotemporal characteristics of carbon emissions among different regions, aiming to provide a more accurate and comprehensive scientific basis for urban planning and carbon reduction decision-making in Shanghai. Furthermore, it can be a reference and inspiration for carbon emission policy research in other cities and regions.

*Corresponding Authors

(hata2020@tongji.edu.cn) https://orcid.org/0009-0005-4789-275X
*(shiyishao@tongji.edu.cn)https://orcid.org/0000-0002-0048-6958
(zhengjianwen@tongji.edu.cn) https://orcid.org/0009-0009-3897-1025

Cite this study

Zheng, J., Shi, Y., & Gilbert, K. M. (2023). LULC change and CO_2 emissions in Shangai 2000-2020. Intercontinental Geoinformation Days (IGD), 7, 53-56, Peshawar, Pakistan

2. Method

2.1. Land use type transition matrix

The land use type transition matrix is a way to quantitatively express the inflow and outflow status of land use types in each parcel by creating a two-dimensional matrix. Its formula is as follows.

$$S_{ij} = \begin{vmatrix} S_{11} & S_{12} & \dots & S_{1n} \\ S_{21} & S_{22} & \dots & S_{2n} \\ \vdots & \vdots & \vdots & \vdots \\ S_{n1} & S_{n2} & \dots & S_{nn} \end{vmatrix}$$

Note: S_{ij} represents the total area of land type changes in Shanghai from 2010 to 2020. Here, i and j represent different land classes, and n represents the number of land use types.

2.2. Carbon emission estimation model

Carbon emissions from land use are composed of direct and indirect carbon emissions. Since the carbon emissions of cultivated land, garden land, forest land, grassland, water area and unused land remain stable for a long time, the direct carbon emission coefficient method is adopted to calculate their carbon emissions, and the calculation formula is as follows:

$$E_p = \sum_{i=1}^{n} e_i = \sum_{i=1}^{n} S_i \cdot \delta_i$$

Note: E_p represents the total carbon emissions; e_i represents the carbon emissions of each land use type; S_i represents the area of each land use type; δ_i represents the carbon emission coefficient of each land use type. Based on existing research, the carbon emission (absorption) coefficients for cultivated land, forest land, grassland, water areas, and unused land are 0.442, -0.644, -0.021, -0.298, and -0.005 tons per hectare ($t \cdot hm^{-2}$), respectively.

The carbon emission of construction land mainly comes from the energy consumed by human activities on impervious water areas. Since the construction land area cannot express the real carbon emissions well, the indirect carbon emission coefficient method is used to estimate the carbon emissions of construction land by calculating the consumption of various energy sources. The energy consumption data of each district in Shanghai is indirectly measured by the ratio of the district's GDP to the city's GDP. The types of energy involved in this study are shown in Table 2, and the calculation formula is as follows.

$$E_p = \sum_{i=1}^{n} a_i * b_i * c_i$$

Note: E_p represents the total carbon emissions from construction land; represents the consumption of various energy sources; represents the standard coal conversion coefficient for each energy source; represents the carbon emission coefficient for each energy source. The standard coal conversion coefficients and carbon emission coefficients for various energy sources can be found in Table 1.

Table 1. Standard coal conversion coefficient and carbon emission coefficient of energy

Energy Type	Raw Coal	Coke	Crude Oil	Gasoline
Standard Coal Conversion Coefficient(tce/t)	0.7143	0.9714	1.4286	1.4714
Carbon Emission Coefficient (tC/tce)	0.7559	0.855	0.5857	0.5538
Kerosene	Diesel	Fuel Oil	Natural Gas	Electricity
1.4714	1.4571	1.4286	1.33	0.1229
0.5714	0.5921	0.6185	0.4483	0.733

2.3. Ellipse analysis of standard errors

By using the Standard Deviation Ellipse Analysis feature in ArcGIS Pro 3.0.1 software, an analysis was conducted on the spatial distribution of carbon emissions in different regions of Shanghai. The major and minor axes of the ellipse represent the shape variation of carbon emission distribution, while the area indicates the concentration or dispersion of carbon emissions. The centroid coordinates represent the trajectory of the center of gravity of carbon emissions.

3. Results

According to Fig. 1 (a) and (b), it can be observed that the area of cultivated land in Shanghai has the highest proportion, averaging around 50%. The area of construction land and water bodies follows it. From 2000 to 2020, the most significant changes in Shanghai's land area were observed in cultivated land and construction land. The cultivated land area declined from 2000 to 2015, while the construction land area exhibited a continuous upward trend.

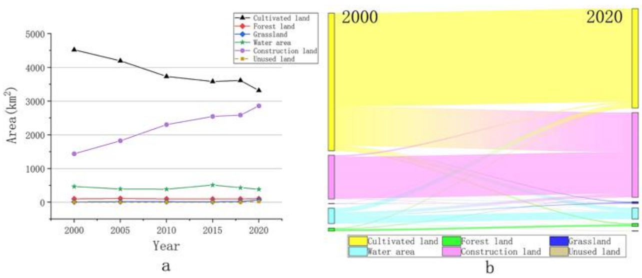

Figure 1. (a) Change of land use type area; (b) Land use transfer map

Between 2000 and 2020, the construction land area increased by 1419 km2, with the highest growth rate of 98%. On the other hand, the area of cultivated land decreased by 1200 km2, representing the highest decline rate of 26%. The areas of the remaining land types showed relatively stable changes.

According to Fig. 2 (a) and (b), the total carbon emissions in Shanghai have shown an increasing trend from 2000 to 2020. The carbon emissions have grown from 53.08 million tons in 2000 to 85.46 million tons in 2020, with an annual increase of 1.61 million tons. The growth trend can be divided into two phases: a rapid growth phase (2000-2010) with an increase of 64% and a slower phase (2010-2020) with a slightly reduced growth rate (the growth rate in 2020 was affected by the COVID-19 but still showed an overall increasing trend). From the perspective of the urban area (Hongkou, Huangpu, Jing'an, Putuo, Xuhui, Yangpu, Changning districts) and the suburban area (Minhang, Pudong New Area, Jiading, Jinshan, Qingpu, Songjiang districts), the carbon emissions in the urban area increased from 8.02 million tons in 2000 to 28.93 million tons in 2020, with an annual average increase of 1.05 million tons. On the other hand, the carbon emissions in the suburban area increased from 45.23 million tons in 2000 to 56.44 million tons in 2020, with an annual average increase of 0.57 million tons. From 2000 to 2020, the growth rate of carbon emissions in the urban area was higher than that in the suburban area. Still, the total carbon emissions in the suburban area have consistently exceeded those in the urban area.

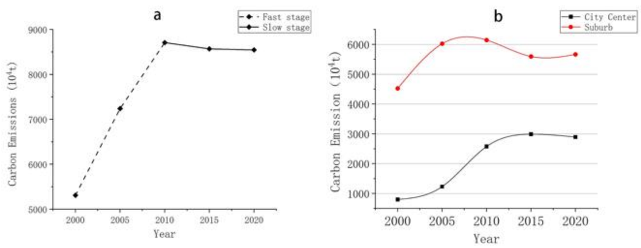

Figure 2. (a) Total carbon emissions of Shanghai; (b) Carbon emissions of urban and suburban areas of Shanghai

From 2000 to 2020, the total area of land use transfer in Shanghai was 1,850 km², accounting for 28% of the total land area of Shanghai. Generally, the land types that experienced more transfer out were arable land and water areas, with 1,466.866 km² and 268.119 km², respectively. The land type that experienced the most transfer was construction land, with an area of 1,422.017 km². The proportions of transfer in and out for forest land, grassland, and unused land were relatively low.

To visually demonstrate the spatial evolution of carbon emissions from land use in Shanghai from 2000 to 2020, this study standardized the data. It divided carbon emissions into four levels: slight, mild, moderate, and severe. As shown in Fig. 3, there are significant spatial differences in carbon emissions from land use in different periods in Shanghai. From 2000 to 2020, the heavy carbon emission zone expanded from the outer areas towards the inner areas.

Shanghai's severe carbon emission zone is mainly concentrated in the Pudong New Area. Pudong New Area, the special economic zone of Shanghai, is a highly active economic center. The region accommodates several industrial parks and bases that cater to diverse industries, including manufacturing, high-tech, and finance. However, it also houses energy-intensive and high-emission process industries. As a result, carbon emissions have rapidly increased from 23.77 million tons in 2000 to 29.5 million tons in 2020, and the emissions have remained consistently high.

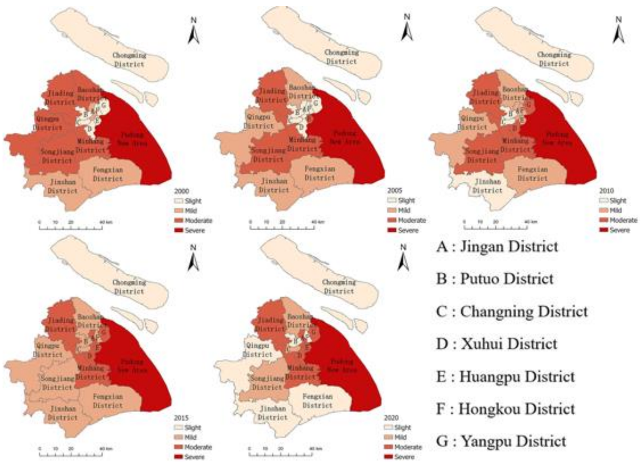

Figure 3. Spatial change of carbon emissions from land use in Shanghai from 2000 to 2020

The moderate carbon emission zone is mainly concentrated in Jiading District and Minhang District. In 2000, the carbon emissions in these districts accounted for 15% of the total emissions in Shanghai. In 2020, Jiading District and Minhang District had a total carbon emission of 11.29 million tons, accounting for 13.2% of the city's total. From 2000 to 2020, Songjiang District and Baoshan District transitioned from the moderate zone to the mild zone, and Qingpu District transitioned from the moderate zone to the mild zone and then to the slight zone. Jing'an District, Xuhui District, Huangpu District, and Yangpu District shifted from slight to moderate zones. As core commercial and bustling areas of the city, Jing'an District, Xuhui District, Huangpu District, and Yangpu District experience a significant population influx and transportation activities. They are also home to many energy-consuming industries, such as commerce, finance, and services, contributing to the increase in carbon emissions.

The mild and slight carbon emission zones are mainly concentrated in Putuo District, Baoshan District, Jinshan District, Fengxian District, and Chongming District. In 2000, the total carbon emissions in the slight zone were 7.56 million tons, accounting for 14.2% of the city's total. In 2020, the total carbon emissions in the slight zone were 13.52 million tons, accounting for 15% of the city's total. Chongming District, known for its ecological island tourism, has consistently remained in the slight zone. These areas have abundant forest land and superior ecological environments, reducing carbon emissions.

From the perspective of spatial differentiation characteristics in Fig. 4, carbon emissions in Shanghai are generally dominated by a northwest-southeast direction, and the spatial distribution range tends to contract from the outer areas to the inner areas. Looking at the distribution center, from 2000 to 2010, the spatial distribution center of carbon emissions in the city shifted from the internal center of Pudong New Area to the northwest boundary of Pudong New Area, with a displacement of 16 km. From 2010 to 2020, the distribution center moved 2.8 km northward to Huangpu District, then shifted 1.2 km southeast, and finally returned to the southwest boundary of Pudong New Area.

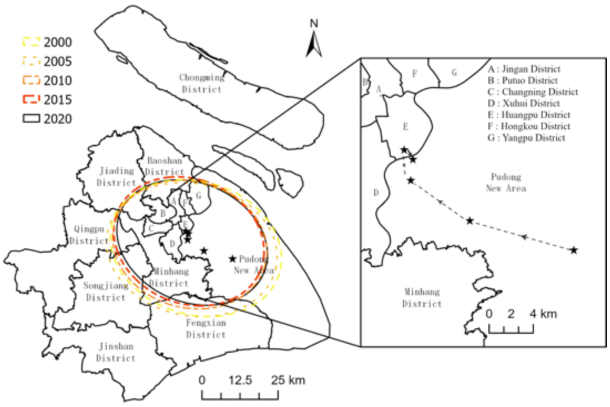

Figure 4. Ellipse of the standard deviation of total carbon emission in Shanghai from 2000 to 2020

Regarding the differentiation shape, the ratio of the minor axis to the major axis of the standard error ellipse of carbon emissions spatial distribution in the city showed a decreasing trend followed by an increasing trend from 2000 to 2020. The city's carbon emissions distribution was generally flattened, gradually developing along the major axis (northwest-southeast direction) while relatively slowing down along the minor axis (northeast-southwest direction). From the direction of divergence, the azimuth of the quasi-differential ellipse of the spatial distribution of carbon emissions in the city has been decreasing from 107.11° in 2000 to 105.55° in 2010, indicating that the influence of the southeast-oriented region of Shanghai on the spatial pattern of carbon emissions in the city has strengthened. The azimuth has increased by 7.85° from 2010 to 2020, indicating that the northwest region on the province's spatial pattern of carbon emissions.

4. Discussion

The research results indicate that the annual average growth rate of carbon emissions from land use in Shanghai from 2000 to 2020 was 3.055%, indicating a relatively fast growth rate. Carbon sources showed an increasing trend, while carbon sinks exhibited only slight fluctuations. The composition of carbon sources was dominated by construction land, while the composition of carbon sinks was dominated by forest land. Regarding the spatial differentiation of carbon emissions from 2000 to 2020, the heavy carbon emission areas were mainly concentrated in Pudong New Area, while the moderate carbon emission areas were concentrated in Jiading and Minhang districts, showing an expansion from the outer areas to the inner areas trend. Regions with carbon emissions above the moderate level accounted for a significant proportion. The center of carbon emissions gradually moved in the northeast direction. The spatial distribution of carbon emissions showed a shrinking trend from the outer to the inner areas. The influence of the northwestern region on the total carbon emissions in the city strengthened over time.

5. Conclusion

In summary, the pattern of carbon emissions from land use in Shanghai is not optimistic. The municipal government needs to optimize further and adjust the land use structure, formulate practical low-carbon emission reduction policies in line with the actual situation of Shanghai, and realize the low-carbon and efficient, sustainable use of regional land resources. To promote the sustainable development of land use and guide the development and utilization of land use in the direction of low-carbon intensification, it is recommended that the region carry out the regulation of low-carbon land use. In urban areas, low-carbon land use and compound utilization can be realized by increasing urban greening, promoting sustainable transportation, optimizing building energy efficiency, developing low-carbon industries, strengthening land planning control and promoting circular economy development; suburban areas carry out industrial structure adjustment, develop new energy by taking advantage of their geographical conditions and technology, gradually eliminate backward industries with high energy consumption, heavy pollution and low production capacity, and strictly control land use types to construction land, and reduce the conversion of land use types with low emission intensity.

References

Bryan, B. A., Gao, L., Ye, Y., Sun, X., Connor, J. D., Crossman, N. D., Stafford-Smith, M., Wu, J., He, C., & Yu, D. (2018). China's response to a national land-system sustainability emergency. *Nature*, *559*(7713), 193–204.

Caı, R., Zhu, H., Li, W., Xiao, Y., & Liu, Z. (2022). Development path of energy science and technology under "dual carbon" goals: Perspective of multi-energy system integration. *Bulletin of Chinese Academy of Sciences (Chinese Version)*, *37*(4), 502–510.

Jin, G., Guo, B., & Deng, X. (2020). Is there a decoupling relationship between CO2 emission reduction and poverty alleviation in China? *Technological Forecasting and Social Change*, *151*, 119856.

Pan, L., Yu, J., & Lin, L. (2022). The temporal and spatial pattern evolution of land-use carbon emissions in China coastal regions and its response to green economic development. *Frontiers in Environmental Science*, *10*, 1018372.

Wang, H., He, Y., Shi, W., Zeng, W., & He, Y. (2023). Spatiotemporal spillover effect and efficiency of carbon emissions from land use in China. *Environment, Development and Sustainability*, 1–39.

Xiao, P., Zhang, Y., Qian, P., Lu, M., Yu, Z., Xu, J., Zhao, C., & Qian, H. (2022). Spatiotemporal Characteristics, Decoupling Effect and Driving Factors of Carbon Emission from Cultivated Land Utilization in Hubei Province. *International Journal of Environmental Research and Public Health*, *19*(15), 9326.

Zhang, X., Zhang, J., & Yang, C. (2023). Spatio-Temporal Evolution of Agricultural Carbon Emissions in China, 2000–2020. *Sustainability*, *15*(4), 3347.

Zhu, L., Xing, H., & Hou, D. (2022). Analysis of carbon emissions from land cover change from 2000 to 2020 in Shandong Province, China. *Scientific Reports*, *12*(1), 8021.

7th Intercontinental Geoinformation Days

igd.mersin.edu.tr

Trend analysis of precipitation and temperature in the Western Black Sea region of Türkiye

Muhammed Zakir Keskin[*1], **Ahmad Abu Arra** [2], **Seyma Akca** [3] **Eyüp Şişman** [2]

[1]Bartın University, Engineering, Architecture and Design Faculty, Civil Engineering Department, Bartın, Türkiye
[2]Yıldız Technical University, Civil Engineering Department, İstanbul, Türkiye
[3]Harran University, Geomatic Engineering Department, Şanlıurfa, Türkiye

Keywords
Trend Analysis
Mann Kendall
Theil-Sen Slope
Temperature
Western Black Sea

Abstract

Climate change indicates alterations in climate parameters, involving both increases and decreases. Trend analysis enables the identification and direction of these changes. This study aims to conduct trend analysis in the Western Black Sea region of Türkiye. Non-parametric tests like Mann-Kendall and Theil-Sen Slope were employed to define temperature and precipitation changes in the region. In the analysis annual mean temperature (°C) and total annual precipitation (mm) data were used, collected from 15 different stations across the region. Mapping has been applied to visualize the results for better understanding of the findings. The results indicate an insignificant trend in precipitation across most of the region, while the temperature clearly demonstrates an upward trend.

1. Introduction

The detrimental impacts of climate change on both the Earth and human societies underscore the critical need for a comprehensive exploration of climate parameters. Among these investigations, trend analysis stands out as a pivotal approach, revealing the inclination of climate parameters to either rise or decline.

Mann Kendall and Theil-Sen's slope are frequently used methods in trend analysis. Mann-Kendall is a non-parametric statistical test used to detect trends in time series data. Theil-Sen's slope is a method for calculating the slope of a trend line. Kızılelma et al. (2015) conducted trend analysis of temperature and precipitation in the Central Anatolia region utilizing the Mann-Kendall and Theil Sen's slope methods. The results indicated notable temperature increases. Partal and Yavuz (2020) explored the presence of trends in drought indices within the Western Black Sea Region using trend analysis techniques. In their study, İrcan and Duman (2022) employed the Mann-Kendall and Theil Sen's slope methods to conduct trend analyses on minimum and maximum temperatures within the Van Lake Basin. Their investigation revealed an upward trend across all monitored stations.

In this research, data related to the annual average temperature (°C) and annual total precipitation (mm) were acquired from 15 meteorological measurement stations located in the Western Black Sea basin in the northern region of Türkiye. Comprehensive trend analysis was performed on this dataset utilizing the Mann-Kendall and Theil Sen's Slope methods. Subsequently, the obtained results were thoroughly interpreted and analyzed.

2. Method

2.1. Study Area and Stations

The Western Black Sea basin stands as one of Türkiye's regions with the most significant rainfall. Stretching from east to west, this area (Fig. 1), covers a rainfall territory spanning 28,855 km^2.

Monthly average temperature and monthly total precipitation data provided by the General Directorate of Meteorology were evaluated. Subsequently, 15 stations were selected that have good quality and continuity of data (Table 1). Annual average temperature and total annual precipitation data for the time period of 1990-2022 were derived from this selected dataset. Mann-Kendall Z statistics and Theil-Sen's Slope values were computed.

* **Corresponding Author**

*(mkeskin@bartin.edu.tr) ORCID ID 0009-0005-6724-491X
(ahmad.arra@std.yildiz.edu.tr) ORCID ID 0000-0001-8679-1752
(esisman@yildiz.edu.tr) ORCID ID 0000–0003–3696–9967
(seymakca@harran.edu.tr) ORCID ID 0000–0002–7888–5078

Cite this study

Keskin M.Z, Abu Arra A, Akca S, & Şişman E (2023). Trend analysis of precipitation and temperature in the Western Black Sea region of Türkiye. Intercontinental Geoinformation Days (IGD), 7, 57-60, Peshawar, Pakistan

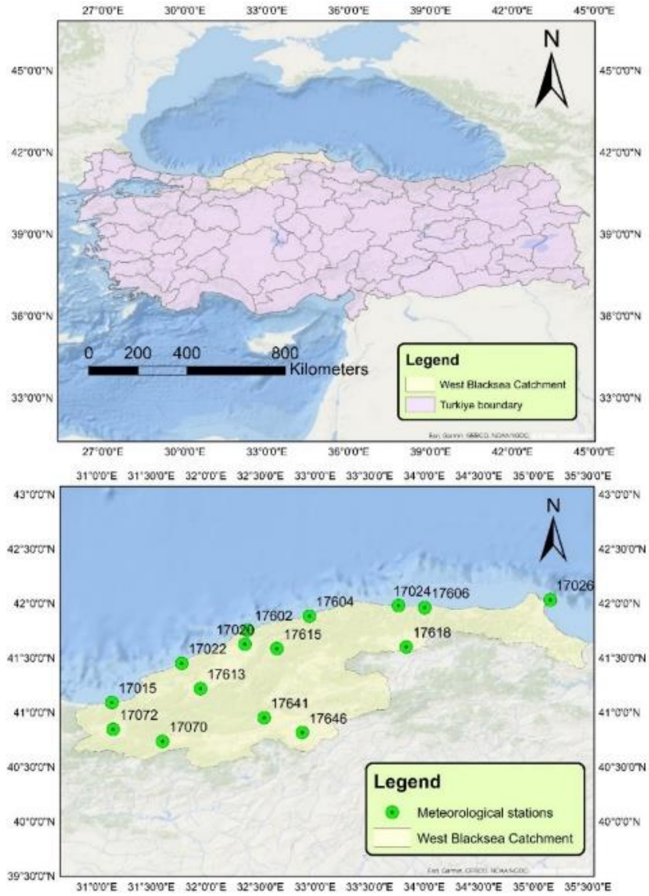

Figure 1. Study area

Table 1. Station details

Station Code	Station Name	Lat. (N)	Lon. (E)	Elev. (m)
17020	Bartın	41.62	32.36	33
17602	Amasra	41.75	32.38	73
696-17615	Ulus	41.58	32.64	162
17070	Bolu	40.73	31.60	743
17015	Akçakoca	41.09	31.14	10
17646	Çerkeş	40.82	32.88	1126
17072	Düzce	40.84	31.15	146
1397-17641	Eskipazar	40.94	32.53	757
17604	Cide	41.88	32.95	36
17618	Devrekani	41.60	33.83	1050
17024	İnebolu	41.98	33.76	64
17606	Bozkurt	41.96	34.00	167
17026	Sinop	42.03	35.15	32
962-17613	Devrek	41.23	31.97	100
17022	Zonguldak	41.45	31.78	135

The data used between 2005 and 2022 are from automatic observation stations as the stations had shifted to automatic measurement in 2005.

2.2. Trend analysis

Mann-Kendall is a statistical test that identifies trends in time series data without relying on specific parameters. It is specifically designed to detect monotonic trends, whether they are increasing or decreasing over time. S represents the number of pairs of data points with consistent trends (either both increasing or both decreasing). The sign of S denotes the direction of the trend. A notably positive S signifies an upward trend, while a significantly negative S implies a decreasing trend. S is calculated as;

$$S = \sum_{k=1}^{n-1} \sum_{j=k+1}^{n} sgn(x_j - x_k)$$

where x_i and x_j represent data values, the function 'sgn' operates as a sign function. It yields a value of +1 when $(x_j - x_i)$ is greater than 0, 0 when $(x_j - x_i)$ equals 0, and -1 when $(x_j - x_i)$ is less than 0.

In the context of the Mann-Kendall test, the Z statistics is used to assess the significance of the trend observed in a dataset. Z is estimated as;

$$Z = \begin{cases} \dfrac{S-1}{\sqrt{Var(S)}}; S > 0 \\ 0; S = 0 \\ \dfrac{S+1}{\sqrt{Var(S)}}; S < 0 \end{cases}$$

The Mann-Kendall test involves two hypotheses, H_0 and H_1. H_0 suggests that there is no trend, while H_1 suggests the presence of a trend. In other words, at a chosen significance level α, if $|Z| \leq Z(\alpha/2)$, then H_0 is accepted, indicating no trend. If $|Z| > Z(\alpha/2)$, H_1 is accepted, indicating a statistically significant trend. In this study, a confidence level of $\alpha = 0.1$ was chosen, and the z value is found to be 1.645 according to the Standard Normal Distribution table. Therefore, if the calculated Z value falls within the range [-1.645, 1.645], H_0 is accepted, signifying the absence of a trend. Otherwise, H_1 is accepted, indicating the presence of a statistically significant trend.

Theil-Sen slope is a method for estimating the slope of a trend line. It is resistant to outliers and does not assume any specific distribution for the data. The Theil-Sen slope is calculated by taking the median of all slopes between pairs of points in the dataset. For each pair of data points (x_n,y_n) and (x_m,y_m) where n<m, the slope is calculated as $(y_m-y_n)/(x_m-x_n)$.

3. Results

In the scope of the study annual datasets were derived by computing the average of monthly temperature data and the cumulative sum of monthly precipitation data. Trend analysis was conducted using station data spanning from 1990 to 2022, with a significance level set at 0.1. The outcomes of this analysis are presented in Fig. 2.

Mapping was used to make it easier to evaluate the results as shown in Fig. 3.

Upon analyzing the results, a declining trend in precipitation is evident across 11 stations, with two of them displaying a notably significant decrease. Conversely, an increasing trend in precipitation is observed in 4 stations. Examination of the map in Fig. 3 reveals a tendency of decreasing precipitation, particularly along the coastal regions, which gradually changes to increasing trend as one moves inland though they are insignificant. Notably, 3 out of the 4 stations displaying increased precipitation are located at elevations exceeding 750 meters, constituting the three highest points within the basin.

Both Mann-Kendall and Sen Slope methods consistently indicate the same direction of precipitation trends at the measurement stations. Sen Slope calculations reveal a decreasing trend in 11 stations and an increasing trend in 4 stations. The stations with an increasing or declining trend are the same in both methods. Bozkurt station exhibits the highest absolute values for both Mann-Kendall Z statistics and Sen Slope.

Regarding temperature trends, 13 stations exhibit an upward trend, while 2 stations demonstrate a declining trend according to both Mann-Kendall and Sen Slope calculations. Mann-Kendall results indicate a significant temperature increase in 12 out of the 13 stations. Correspondingly, these stations exhibit relatively high Sen Slope values. Upon inspection of the map, areas with decreasing temperatures are concentrated in the central region, whereas temperature rises are predominant, especially along the coastal areas.

		Bartin	Amasra	Ulus	Bolu	Akçakoca	Çerkeş	Düzce	Eskipazar	Cide	Devrakani	İnebolu	Bozkurt	Sinop	Devrek	Zonguldak
Total Annual Precipitation (mm)	Mean (mm)	1035.8	955.6	961.6	521.8	1117.5	407.4	804.2	435.4	1170.9	523.9	1039.3	1152.8	677.0	782.0	1201.7
	Median (mm)	1026.8	927.5	961.6	533.8	1099.3	399.0	790.2	435.4	1149.1	523.2	1058.1	1203.0	665.0	764.1	1140.6
	Std. Dev. (mm)	180.4	206.2	206.8	94.3	169.9	87.4	123.8	90.3	200.2	98.6	135.6	242.7	118.6	117.0	222.1
	MK-Z stat	→ -0.42	→ -0.82	→ -1.47	↓ -1.72	→ -1.19	→ 1.53	→ -0.67	→ 1.18	→ -1.36	→ 1.29	→ 0.08	↓ -3.21	→ -0.67	→ -0.23	→ -1.56
	Theil Sen Slope (mm/year)	-1.90	-3.19	-6.83	-2.94	-4.21	2.66	-1.48	1.83	-4.05	2.35	0.20	-12.6	-1.47	-0.60	-5.59
Annual Average Temperature (°C)	Mean (°C)	13.11	14.18	12.91	10.86	13.52	8.41	13.64	11.17	14.26	7.85	13.82	13.63	14.77	14.35	14.06
	Median (°C)	13.28	14.25	12.93	10.83	13.58	8.39	13.76	11.17	14.31	8.00	13.75	13.75	14.76	14.24	14.13
	Std. Dev. (°C)	0.80	0.80	0.56	0.82	0.98	0.93	0.93	0.65	0.77	0.84	1.07	0.79	0.93	0.64	0.84
	MK-Z stat	↑ 4.29	↑ 3.78	→ -1.44	↑ 2.49	↑ 5.07	↑ 3.01	↑ 4.23	→ 0.91	↑ 3.56	↑ 3.32	↑ 4.80	↑ 4.40	↑ 4.14	→ -1.08	↑ 4.23
	Theil Sen Slope (°C/year)	0.06	0.05	-0.02	0.04	0.09	0.05	0.07	0.01	0.05	0.05	0.08	0.05	0.07	-0.02	0.06

↓ Significant decrease ↑ Significant increase → Insignificant change

Figure 2. Mann Kendall and Theil-Sen slope results for total annual precipitation (mm) and annual average temperature (°C)

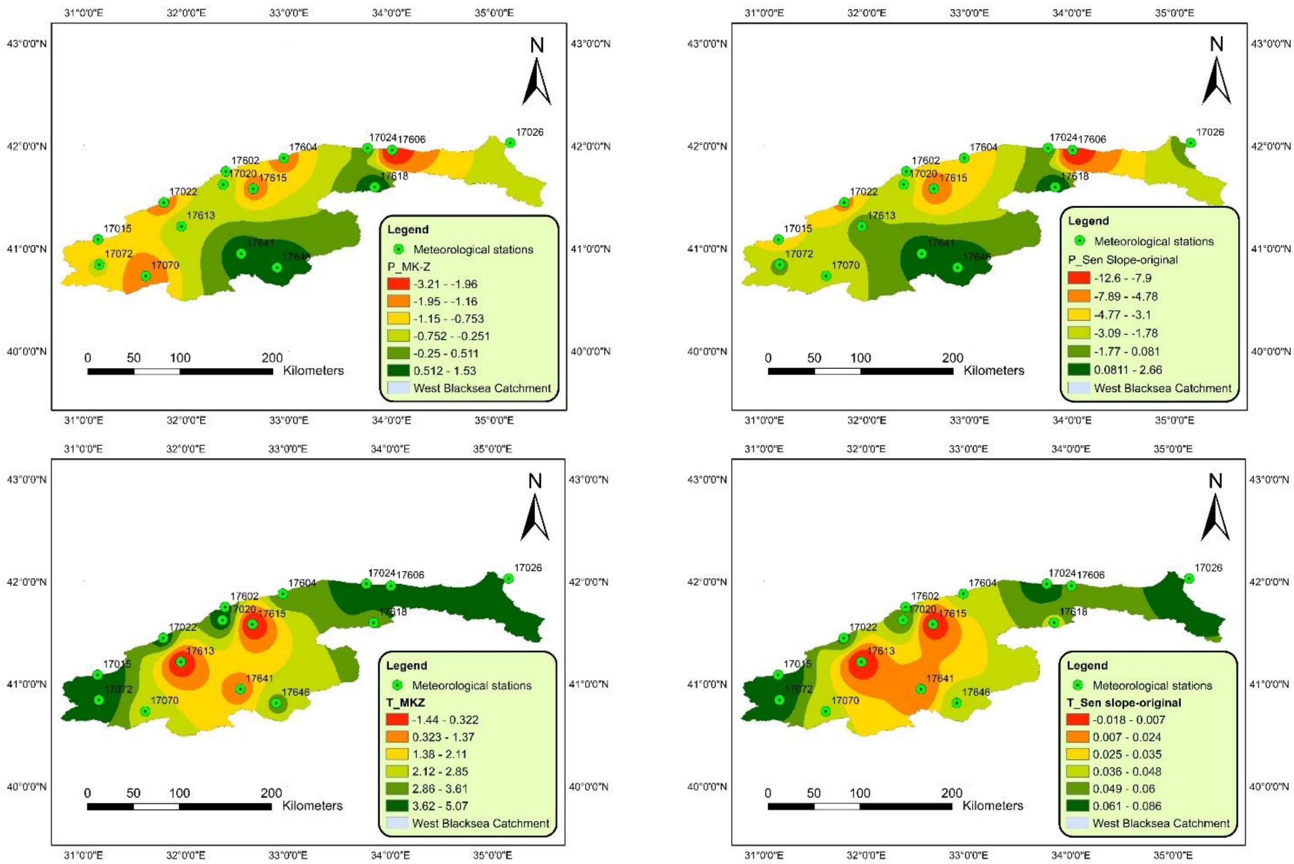

Figure 3. Mann Kendall Z statistics and Sen Slope of annual total precipitation (top left and top right respectively), Mann Kendall Z statistics and Sen Slope of annual average temperature (bottom left and bottom right respectively)

	Bartın	Amasra	Ulus	Bolu	Akçakoca	Çerkeş	Düzce	Eskipazar	Cide	Devrakani	İnebolu	Bozkurt	Sinop	Devrek	Zonguldak
Total Prec. change (mm)	-62.8	-105.3	-225.2	-96.9	-139.1	87.9	-48.8	60.3	-133.6	77.6	6.6	-417.3	-48.6	-19.9	-184.6
Total Temp. change (°C)	2.1	1.8	-0.5	1.2	2.8	1.5	2.2	0.3	1.5	1.5	2.6	1.8	2.3	-0.6	2.1

Figure 4. Changes in total precipitation (mm) and temperature (°C) based on Sen Slope calculations over the course of 33 years

4. Discussion

Several trend analysis studies conducted in the region provide valuable insights and contribute to the assessment of this study.

In his doctoral thesis, Çeribaşı (2015) applied the Mann-Kendall test at a 95% significance level to analyze precipitation data collected from the West Black Sea region between years from 1979 to 2012. Similar to this study's findings, Çeribaşı's research indicated that most stations exhibited no significant trends. However, this study identifies a decreasing trend in the Devrekani station, which was deemed insignificant in Çeribaşı's research. Interestingly, this study also identifies decreasing trends in the Bolu and Bozkurt stations, contrary to the absence of trends reported in the relevant study. It's important to note that this study extends the analysis beyond 2012, the endpoint of the previous study, suggesting that the observed decreasing trends in these two stations might have originated from the years after 2012.

In their research, Tokgöz and Partal (2020) employed the Mann-Kendall test at a 95% confidence level to analyze annual precipitation and temperature data from stations in the Black Sea region of Turkey. Their findings indicated that Bartın, Zonguldak, Bolu, and Düzce stations showed no trends, whereas Sinop exhibited an increasing trend. However, in our study, while Bartın, Zonguldak, and Düzce exhibited no trends, Bolu displayed a decreasing trend, and Sinop's trend was found insignificant. Moreover, in the previous study, Bartın, Sinop, and Bolu stations exhibited significant increasing trends in mean annual temperature, whereas Zonguldak and Düzce had insignificant trends. In our study, all five stations exhibited significant increasing trends in temperature analysis.

It is reasonable to assert that prior research in the region predominantly aligns with the findings of this study, particularly within the context of trend analysis.

5. Conclusion

As the results indicate in this study, precipitation and temperature trend analysis show concerning results.

Temperature in the region tends to increase especially in recent years.

As depicted in Fig. 4, the temperature in the region underwent significant changes over the 33-year period, reaching up to 2.8°C in some places based on Sen Slope calculations. Coastal stations like Akçakoca, İnebolu, and Sinop experienced the highest temperature changes (2.8°C, 2.6°C, and 2.3°C respectively). Given these observations, it is crucial to conduct a thorough assessment to determine if the observed rising trends in coastal areas are connected to increased sea water temperatures.

While precipitation trends are mostly insignificant, a negative trend is noticeable in most stations. The few stations that display insignificant increasing trends are located at the region's highest elevations. Over the 33-year span, certain stations experienced a decline in precipitation depth exceeding 20 centimeters (Fig 4). For instance, Sen Slope calculations indicate a loss of over 40 centimeters in Bozkurt station and above 20 centimeters in Ulus station, emphasizing the substantial decrease in precipitation levels. Overall, these trend results suggest the potential for more substantial changes in the region in the years ahead.

Acknowledgement

The authors express their gratitude to the General Directorate of Meteorology for providing the data.

References

Çeribaşı, G. (2015). Karadeniz ve Sakarya havzalarında yağış-akış-askıda katı madde verilerinin trend analizi ile incelenmesi. Doctoral Thesis, Sakarya University.

İrcan, M. R. & Duman, N. (2022). Van Gölü Havzası'ndaki maksimum ve minimum sıcaklıkların trend analizi. Türk Coğrafya Dergisi, (80), 39-52. https://doi.org/10.17211/tcd.1079628

Kızılelma, Y., Çelik, M. & Karabulut, M. (2015). İç Anadolu Bölgesinde sıcaklık ve yağışların trend analizi. Türk Coğrafya Dergisi, (64), 1-10.

Partal, Turgay & Yavuz, E. (2020). Batı Karadeniz Bölgesinde Kuraklık İndisleri Üzerine Trend Analizi Uygulanması. Doğal Afetler ve Çevre Dergisi. 6. 345-353. 10.21324/dacd.643161.

Tokgöz S, Partal T (2020). Karadeniz Bölgesinde Yıllık Yağış ve Sıcaklık Verilerinin Yenilikçi Şen ve Mann-Kendall Yöntemleri ile Trend Analizi. Iğdır Üniversitesi Fen Bilimleri Enstitüsü Dergisi, 10(2), 1107 - 1118. 10.21597/jist.633368

7th Intercontinental Geoinformation Days

igd.mersin.edu.tr

Spatio-temporal land use/ cover changes analysis using remote sensing and landscape spatial metrics: A case study of Basin Liqvan

Khalil Valizadeh Kamran *1, **Fatemeh Adimi** 1

1University of Tabriz, Department of Remote Sensing and GIS, Tabriz, Iran

Keywords
Land use/cover
Spatial metrics
Remote sensing
GIS
Liqvan

Abstract

Over time, patterns of land cover and land use change and subsequent changes are fundamental and human factor plays a most important role in this process. Ever, scientists have attempted to identify factors that cause land use changes and their impact on the environment. Therefore, in previous decades, researchers have different views collected from the field, as well as aerial photographs to detect land use changes resulting from the imposition of natural and human processes have been analyzed. Today, however, based on technological advances made in the field of remote sensing, satellite imagery can be used to more accurately evaluate the environmental changes during the process and the final results of the illustrated model. The main purpose of the ongoing monitoring of land use changes in river basins Liqvan is 1985-2006-2013. Accordingly, to explore the changes occurring in the study area, Landsat TM and ETM + Landsat images of the years 1985-2006-2013 were analyzed. Accordingly, after applying atmospheric and geometric correction, image enhancement operations performed using the maximum likelihood method of supervised classification algorithms similar actions and thematic maps of land use of the basin has been designed to Liqvan. Finally, moorland in the first place and then irrigated gardens and residential areas in the study area are eventually.

1. Introduction

Although urban areas currently cover only 3% of the earth's surface, these areas have significant effects at both local and global scales (Liu et al., 2002). In the current scenario, cities are becoming places Almost all are human activities (Rajeshwari, 2006). In the last 200 years, while the world's population has increased six times, the world's urban population has reached more than 100 times the initial number (Leo et al, 2004). And it is estimated that more than 5 million people will live in urban areas by 2025, and 80% of them will be in the cities of developed countries (Maser, 2001). In general, in a systemic approach, the development of cities can be divided into two processes: spontaneous and self-organizing (Wu, 2000, quoted by Mir Bagheri and colleagues, 2018).

Land surface gauges are land surface quantification tools, whose variety and variety have led to their wide application in planning related to land studies. These measurements are able to give us a lot of information about the structure and changes of the constituent parts of the landscape in a short period of time. In this research, the measures of spatial distribution and composition of spots were used at the level of the class and landscape of the land. With the aim of providing a rational analysis of land use changes in Liqvan Chai basin.

Remote sensing provides users with the necessary and sufficient facilities to extract and update land cover maps.

By using image processing techniques, it is possible to study more and more terrestrial phenomena and describe surface resources. Today, by using remote sensing images, it is possible to map land use/cover on a local to continental scale in the shortest time and at the lowest cost. The use of various classification methods of satellite images has made it possible to accurately extract the land use ratios of each geographical region (Fyzizadeh, 2016).

The change of land use includes the change of the type of uses and the change in the distribution and spatial patterns of activities and uses (Briasolis: 2000: 12). In other words, land use change means a change in the type of land use, which is not necessarily a change in the land surface, but also a change in land density and management (Pernoun, 2009: 40).

* **Corresponding Author**

*(valizadeh@tabrizu.ac.ir) ORCID ID 0000 – 0003 – 4648 – 842x
(f.adimy@yahoo.com)

Cite this study

Kamran, K. V., & Adimi, F. (2023). Spatio-temporal land use/ cover changes analysis using remote sensing and landscape spatial metrics: A case study of Basin Liqvan. Intercontinental Geoinformation Days (IGD), 7, 61-66, Peshawar, Pakistan

2. Method

In order to investigate the spatial structure and spatial analysis of different measures of land use spots, Fragstats software was used to quantify the measures. Fragstats is the title of a program that is used to quantify the structure and pattern of the land surface. This software is a complete set of land surface measurements.

This program has no limitation in scale (width or magnification) and it is suitable for analyzing the spatial pattern and different measures of the spots that make up the landscape of the land in heterogeneous environments and different conditions. It also expresses the calculated measures based on hectares or meters. For each input in the software, 3 output files are created: PATCH, CLASS, LAND. All files can be viewed as text files. This tool is used to analyze spatial patterns, especially in habitat modeling, wildlife protection and forest management. Some spatial metrics are described here:Indicator CA (Class Area) : The total area of built and unbuilt areas in an entire city. Usually, CA/TA ratio is used where TA is the total area of the region. This metric is an excellent mechanism for analyzing and comparing the development and changes in the area of constructed and unconstructed land, and its numerical value is greater than zero and has no maximum limit.Indicator NP: (Numbor of Patches) :

It measures the number of individual patches that make up a specific land use or land cover class. (Largest Patch Index) Indicator LPI

This metric shows the percentage of the user that is covered by the largest patch in a user class.

LPI= Indicator ED (Edge Density):

Border density measure: It is equivalent to the length of all borders divided by the area and is obtained from the following relationship.

ED= Indicator MPS (Mean Patch Size)

This metric shows the average size of spots that make up a specific user or class.

MPS= Indicator) pland (Land cover percentage: It measures the percentage ratio of each type of spot (class).

pi: is a ratio of the surface of the land occupied by the spot of type i aij = area (square meters) of spot ij A = the total area of the surface of the land, the sum of all the areas of the spots of type i, divided by the total surface area of the land, multiplied by 100 to convert to a percentage.

Spot density index (PD)

This measure shows the number of spots per unit area and allows comparison between different areas. This measure is used as habitat fragmentation index.

PD= ni/A (10000)(100) ni = number of spots type (class) i و A = The total surface area of the land

The number of spots of type i divided by the total surface area of the land multiplied by 1000 to convert to hectares (multiply by 100 to get the density of spots in 100 hectares.

Edge density index (Total edge): It is equal to the total length of all the edge segments that include the corresponding class type, the unit of which is meter.

Wang used measurement, shape, and size metrics to study the topography changes of the city of Wayne, Michigan, USA, between 1986 and 2000.Herold et al. (2002) used remote sensing and spatial metrics to study the spatial characteristics of the city of Santa Barbara. Herzog-Vlach (2002) used landscape metrics to monitor landscape changes in East Germany. The results showed that the land use spots have little diversity and the landscape of the land is becoming more and more fragmented. Chesia et al. (2009) investigated landscape dynamics in an abandoned rural environment in the Apennine Mountains. First, land use maps were prepared, and then the changes in land cover and landscape structure in three time periods were investigated through the shape, size, separation of spots based on CA, MPS, PSSD, LPI metrics. The results showed that forestry increased by 23.9%, pastures and wastelands decreased by 29.9%, and scattered urbanization and the dispersion of infrastructure such as roads and buildings also increased.

2.1. Study Area

Liqvan Chai basin is one of the sub-basins of Aji Chai and has an area of 76 square kilometers in the northern slope of Sahand between 46-30-20 east longitudes to 46-27-30 degrees and 55-55 north latitudes. - 42-˚37 to˚30-´49˚-37, has been expanded. From the north it leads to Spreh-Koh and Liqvan valley, from the south to Sahand heights, from the east to Saeedabadchai and Ojan watersheds and from the west to the Sardroud river watershed. The general map of Liqvan watershed is shown in Figure (1). (Hosseinzadeh, Hojjat, 1385).

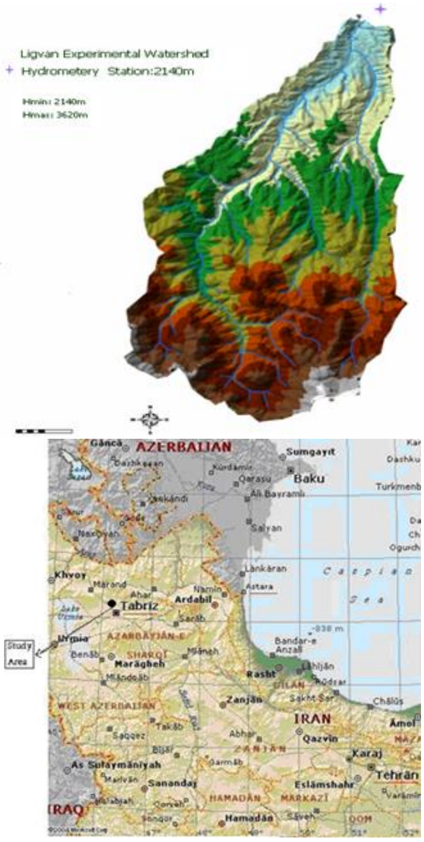

Figure 1. Map of Liqvan Chai catchment area materials and ways:

-Collecting and preparing maps

The data used in this project from the point of view of their source are as follows:

Landsat satellite images of three periods: 1985, 2006, 2013

Observations of field operations

- GPS impressions of points
- General data such as roads, residential areas, etc.
- Materials:

In this research, time series data of Landsat satellite images of 1985-2006-2013 of Liqvan Chai watershed were selected and analyzed.

1:50000 digital maps of Liqvan Chai basin

-software:

The software used in this research are: Arc GIS 10.2 software: In this software, analysis steps are performed and the change map is produced in this environment. ENVI 4.8 software: It is an image processing software, and all the stages of image preparation and processing were done in this environment. The research method in this research is descriptive-analytical. In this research, the desired information was first collected using library studies and field studies, then quantitative and qualitative methods were used to analyze this information. The used satellite images include TM satellite images of 1985, 2006 and 2013 from the area of Liqvan Chai catchment area.

3. Results

With exploitation from the existing maps and through field visits and visual interpretation and existing documents, the land uses were taken in the pre-classification and post-classification stages. At this stage, the Stack operation was performed on all bands of the images except thermal bands, and then, considering the resolution of the bands, appropriate bands (2, 3, 4 for the years 1985 and 2006 and bands 7, 5, 3 for 2013) was considered for classification.

Pre-processing: due to the fact that the images obtained from satellites, from the point of view of spatial, temporal and spectral resolution, always have the possibility of systematic and non-systematic errors, so preliminary processing should be done on the raw data through the imaging system. or the atmospheric conditions during the measurement (Jensen, 1996).

In this research, the maximum probability classification method was used. After evaluating the probabilities in each class, the pixels are assigned to the classes that have the most similarity, and if the probability values are lower than the introduced threshold, they are introduced as unclassified pixels. (Alavi Panah, 1382: 312). The desired maps were obtained using ENVI 4.8 software and the supervised classification method of the maximum probability type, image classification. In this regard, the images were divided into four classes, including built-up areas, barren areas, green spaces, and hydroponics.

No classification is complete until its accuracy is evaluated (Lylesend, 2001). Therefore, to ensure the accuracy of the classification, the classification accuracy is evaluated. The accuracy of the classification indicates the level of confidence in the extracted map, and in land use maps obtained from remote sensing images, it should be at least 85% (Anderson et al., 1976). The overall accuracy of the map extracted with the maximum likelihood algorithm in this research for 2013 (98.12%), 2006 (94.44%) and 1985 (94.75%) confirms this.

In this research, according to the region, the images were classified into 4 classes: built, gardens and green spaces, barren and irrigated agriculture. Below, the land use maps of three periods (1985, 2006 and 2013) can be seen. These maps were obtained after several operations mentioned above and field surveys as follows. Also, by using the methods available in ENVI software, the statistics and figures of each user can be seen as a percentage in the following tables.

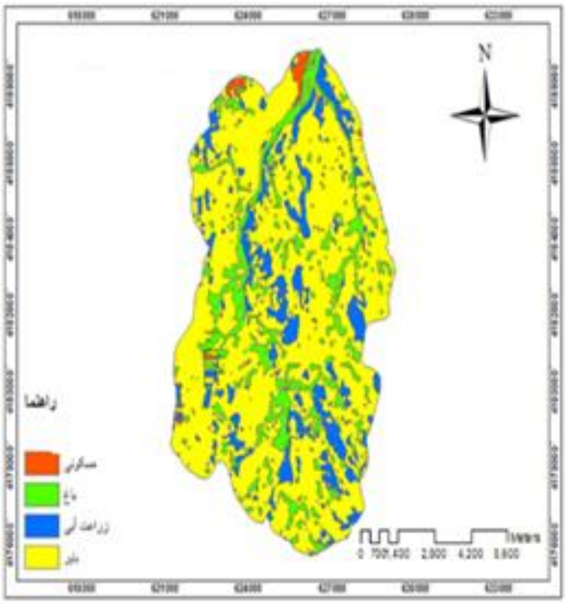

Figure 2. Land use related to the picture of 1985

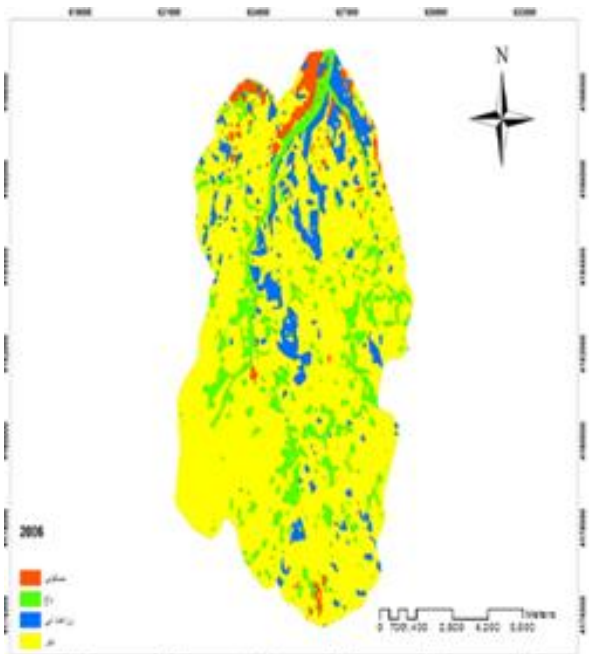

Figure 3. Land use related to the picture of 2006

Table 1. The land use area related to the 1985 picture

Class name	User	Area (hectares)	Area percentage
Residential	Residential	72.5	%0.96
Garden	Garden	1047..25	%13.87
Watery Agriculture	Watery Agriculture	1009.04	%13.37
barren	barren	5417.12	%71.78

Table 2. The land use area related to the 2006 picture

Class name	User	area (hectares)	Area percentage
Residential	Residential	217.92	%2.88
Garden	Garden	906.62	%12.02
Watery Agriculture	Watery Agriculture	690.61	%9.15
Barren	Barren	5730.26	%75.94

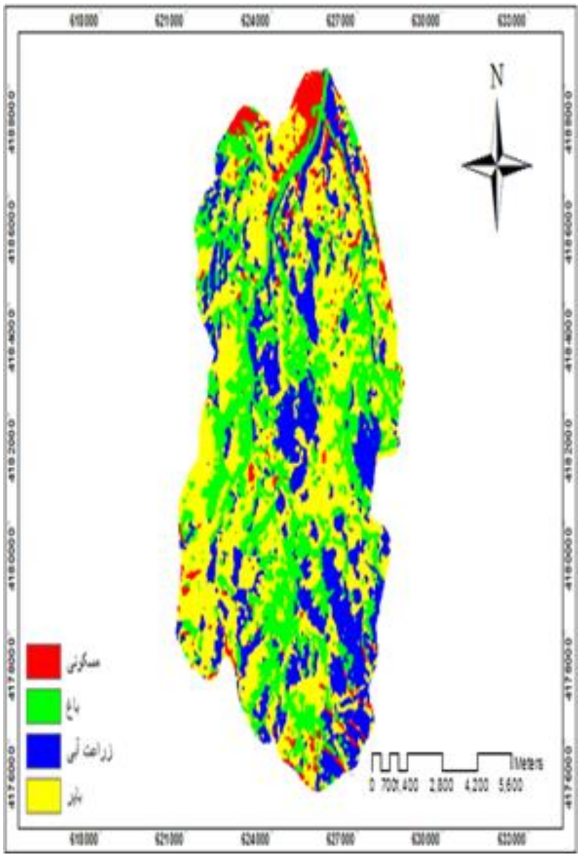

Figure 4. Land use related to the 2013 image

Table 3. The land use area related to the 2013 picture

Class name	User	Area (hectares)	Area percentage
Residential	Residential	362.85	%4.80
Garden	Garden	2175.8	%28.84
Watery Agriculture	Watery Agriculture	1756.6	%23.28
Barren	Barren	3249.3	%43.06

And according to the 2013 land use area table, it can be said that:

Residential areas in the years 1985-2013, although it occupies the least area of land use in the region, but it shows that residential areas are increasing, which is the reason for the expansion of the existing villages in the region, as well as the boom in villa construction. is in this area. The use of gardens shows a significant jump in 2013 compared to previous years. The use of irrigated agriculture has grown a lot in recent years, the reason for which can be the use of water from dams in the region that have been exploited in recent years in the field of irrigated agriculture. The use of barren lands shows that in the study area, the largest share of use during the study period belongs to this use.

Nature, extent and rate of land use/cover changes:

Using the accepted method in the research conceptual model, land use/land cover maps were produced for all three dates and the area of different land use classes in the region and the statistics indicating the change were calculated. The results obtained from these calculations in the different years studied are shown in Tables 3 and 4. There are different ways to quantify land cover changes. Among these different methods, the most basic method is to tabulate the total land cover changes for each land use/cover class and check the changes in different years. In order to determine the extent and rate of changes in land cover dynamics in the region, the following variables were developed and calculated. In order to determine the expansion and rate of changes in land cover dynamics in the region, variables were calculated as follows:

1) total area (Ta)
2) Change area (Ca)
3) Percentage of changes (Ce)
4) Annual rate of change (Cr)

These variables are calculated using the following relationships.

$$Ca = Ta\,(t2) - Ta\,(t1)$$
$$Ce = (Ca / Ta(t1)) * 100$$
$$Cr = Ce / (t2 - t1)$$

In these relationships, t1 and t2 are the beginning and end times of the studied time period. In the above tables, all the users have been calculated once and individual users have been studied once, and the results are given in the following tables.

Table 4. Changes in 1985-2006

Ca	Ce	Cr	Land cover in 1985-2006
145.42	200.58	9.55	Residential
140.63-	-13.42	0.64-	Gardens and green space
318.43-	31.56-	1.50-	Watery Agriculture
313.14	5.78	0.28	Barren lands
0.5-	161.38	7.69	Total

Table 5. Changes in 2006-2013

Ca	Ce	Cr	2006-2013 Land cover in
144.93	66.51	3.91	Residential
1269.18	139.99	8.23	Gardens and green space
1065.99	154.35	9.08	Watery Agriculture
2480.96-	43.29-	2.55-	Barren lands
0.86-	317.56	18.67	Total

Table 6. Changes in 1985-2013

Ca	Ce	Cr	Land cover in1985-2013
290.35	400.48	14.30	Residential
1128.55	107.76	3.85	Gardens and green space
747.56	74.08	2.64	Watery Agriculture
2167.82-	40.02-	1.43-	Barren lands
1.36-	54.23	19.36	Total

As seen in the above tables, the average annual rate of change in residential areas in the period of 2006-1985 was 9.55 and in the period of 2006-2013 it was 3.91 and in the whole period of 1985-2013 it was 14.30.

Spatial transformation analysis of land use/cover changes using spatial metrics:

In this research, the calculation of spatial metrics is based on land use/land cover maps resulting from the classification of satellite images and showing the appearance of the land consisting of spatial spots classified in different classes of spots. The landscape pattern analysis has been done at the level of user/coverage classes. For each cover class, the total area, the average size of the spot, the number of spots, the percentage of the class from the total landscape and the index of the largest spot are listed in table number (7).

Table 7. The metrics of the image of the land of the year 2013

The area of each user (CA) hectares	Percent coverage of each class (PLAN)	The number of spots (NP)	Measure the largest stain (LPI)	Total margin (TE)	Edge density (ED)	user name
370.53	3.47	192	0.88	123390	11.51	Residential
2174.04	20.39	253	6.25	432720	40.58	Gardens
1758.96	16.49	269	10.41	353520	33.16	Watery Agriculture
3244.5	30.43	281	3.32	571470	53.60	Barren ands
3098.16	29.06	4	10.20	91440	8.57	Study area

By comparing the NP metric and the TA metric, it can be seen that the highest number of spots belong to the barren land class, and the highest area and percent coverage belong to the barren land class, and the least number of spots belong to the residential land class, and the least area and percent coverage belong to the residential land. Is. Measuring the biggest spot related to irrigated agriculture and the smallest one related to residential lands, the density of the edge and the entire edge is the same. In general, from 1985 to 2013, it can be concluded that the percentage of vegetation and the LPI index have increased in parallel in these years. The number of residential spots has increased, but the residential area has decreased. And the largest area and the biggest stain in 1985 belongs to the gardens, which has been greatly reduced during these years, and the reason for this is the creation of villas that have been created.

4. Conclusion

Residential areas in the years 1985-2013, although it occupies the least area of land use in the region, but it shows that residential areas are increasing, which is the reason for the expansion of the existing villages in the region, as well as the boom in villa construction. is in this area. The use of gardens shows a significant jump in 2013 compared to previous years. The use of irrigated agriculture has grown a lot in recent years, the reason for which can be the use of water from dams in the region that have been exploited in recent years in the field of irrigated agriculture. The use of barren lands shows that in the study area, the largest share of use during the study period belongs to this use.According to the tables obtained from the measurement of land metrics, which were produced from the results of the classification of land cover for the years 2013-2006-1985, there have been many changes from 1985 to 2013. This shows the intensity of construction in this area. On the other hand, irrigated agriculture and gardens do not show drastic changes, and these areas do not show drastic changes except for the period of 2006-2013, in which the transformation of these areas into residential areas is also observed.

References

Alavi-Panah, Seyed Kazem, (2012). The application of remote sensing in earth sciences (soil sciences), Tehran, Tehran University Press.

Anderson, W. P., Kanaroglou, P. S., & Miller, E. J. (1996). Urban form, energy and the environment: a review of issues, evidence and policy. *Urban studies*, *33*(1), 7-35.

Briassoulls, H. (2000). Factors influencing land-use and land-cover change. land-use and land-cover change sciences. Vol.1.

Digital Image Classification, International Institue For Aerospace Survery and Earth Science, ITC,Enschede The Netherlands, Second Edition.

Faizizadeh, B. (2016). Comparison of pixel-based and object-oriented methods in the preparation of land use maps of the case study of the eastern floodplain of Lake Urmia". Master's thesis (RS&GIS). Faculty of Humanities and Social Sciences, Tabriz University

htpp://www.Earth Wathchers .org

http://www.Iranriver.ir

Jenssen L. L. F, & Gorte B. G. H. (2001). Principle Of Remote Sensing, chapter 12 Digital Image Classification, International Institue for Aerospace Survery and Earth Science, ITC, Enschede the Netherlands, Second Edition.

Jenssen, J. R. (1996). Introductory Digital Image Processing: A Remote Sensing Perspective, 2nd ed., Upper Saddle River, New Jersey:Prentic – Hall

Leao, S., Bishop, I., & Evans, D. (2004). Simulating urban growth in a developing nations region using a cellular automata-based model. ASCE-Journal of urban planning and development, 130, 3, 145-158

Lillesand, T. M. & Kiefer, R. W. (2000). Remote Sensing and Image Interpretation, 4th ed, John Wiley, and Sons, inc USA, 2001, ISBN: 0471255157

Liu, X. & Lathrop, R. G. (2002). Urban change detection based on an artificial neural network, International Gournal of Remote Se18.nsing, 23,2513-25

Masoumi, M. T. (2018). forecasting, modeling and forecasting of scattered urban development, case study of Ardabil city, doctoral dissertation in the field of geography and urban planning, Islamic Azad University, Tehran Science and Research Branch.

Masser, I. (2001). Managing our urban future: The roule of remote sensing and geographic infor mation systems, Habitat International 25:503-512

McGarical, K., Cushman, S. A., Neel, M. C., & Ene, E. (2002). FRAGSTATS: Spatial Pattern Analysis Program for Categorical Maps. URL.

Mirbagheri, Babak, Ali Akbar Metgan, (2018). Quantitative assessment of urban land concentration using the Ripley sk function in the GIS of the study area: the area of the cities of Islam Shahr, Rabat Karim, Nasim Shahr, Journal of Human Geography Research, No. 69.

Parnoun, Z. (2008). Study of the effects of immigration on land use change in Islamshahr city from 2008 to 2009, thesis for receiving a master's degree, Faculty of Geography, University of Tehran.

Rajeshwari. (2006). Management of the Urban Envirment Using Remote Sensing and Geographical Information Systems, J. Hum.Ecol., 20(4), 269-277.

www.umass.edu/landeco/research/fragstats/fragstats.html.

7th Intercontinental Geoinformation Days

igd.mersin.edu.tr

Exploring the difference between Standard Precipitation Evapotranspiration Index (SPEI) from in-situ meteorological stations and SPEIbase

Ahmad Abu Arra*[1], Seyma Akca[2], Muhammed Zakir Keskin[3], Eyüp Şişman [1]

[1]*Yildiz Technical University, Civil Engineering Department, Istanbul, Türkiye*
[2]*Harran University, Geomatic Engineering Department, Sanliurfa, Türkiye*
[3]*Bartin University, Civil Engineering Department, Bartin, Türkiye*

Keywords
SPEI
SPEIbase
Remote sensing
GIS
Istanbul

Abstract

Drought has destructive impacts on all sectors, such as environmental and agricultural sectors, as well as water resources management. The first step in drought evaluation and monitoring is determining the drought index. Because of its vital role, this research aims to investigate the difference between Standardized Precipitation Evapotranspiration Index (SPEI) at different timescales, 3, 6, 9, and 12-month, based on in-situ meteorological stations and SPEIbase, which is a satellite global product. They were compared in two ways: 1) using drought categorization and 2) drought index (SPEI values). The results showed a significant difference between the results obtained from each dataset. Based on the drought categorization, only 61% of the months were within the same categories. The dominant months were within the normal category (N) because of a wide range ranging between -1 and 1. Furthermore, SPEI values calculated using SPEIbase gave more extreme drought events (ED). However, SPEI using in-situ meteorological stations gave more severe drought events (SD) for all time scales. Also, a significant fluctuation can be noticed based on the difference between SPEI from the two datasets. These results can be attributed to many reasons, such as using different time periods, calculating potential evapotranspiration, and the reliability of the precipitation and potential evapotranspiration.

1. Introduction

As a natural disaster, drought globally poses substantial difficulties and challenges to water resources, societies, agriculture, and the environment (Wilhite, 2000 & Şen and Almazroui, 2021). In the 1990s, economic losses due to environmental hazards were more than 400 billion USD (Barbour et al. 2022). The high increase in frequency and intensity of drought events raised the concern of hydrologists, researchers, policymakers, and decision-makers (Mishra and Singh, 2010 & Abu Arra and Şişman, 2023). Monitoring and evaluating drought is pivotal for water resources management and developing drought mitigation plans. There are numerous drought indices, and each index has its parameters and methods. The Standardized Precipitation Evapotranspiration Index (SPEI) is one of the most widely used drought indices in the hydrology fields (Vicente-Serrano et al. 2010). The SPEI calculates the meteorological drought by considering precipitation and evapotranspiration (Vicente-Serrano et al. 2010). The drought indices have been proven to be a valuable approach to drought monitoring. They are used as a first step for monitoring and evaluation, enabling managers and decision-makers to understand and take action for drought impacts (Chong et al. 2022; Yong et al. 2023; Van Loon, 2015).

To calculate SPEI, both in-situ meteorological stations and satellite and remote sensing data such as SPEIbase (https://spei.csic.es/database.html) can be used. They are two distinct methods for collecting weather information. Each source has its advantages and disadvantages. For in-situ meteorological stations, the stations are physically situated on the ground at a specific geographic location. The collected data is real-time and on-site data. It is generally highly accurate, specifically for automated stations (Şen, 2). However, the main problem in in-situ stations is the spatial distribution of it and the data availability (Levizzani and Cattani, 2019). On the other side, the global products are

* **Corresponding Author**

*(ahmad.arra@std.yildiz.edu.tr) ORCID ID 0000-0001-8679-1752
(seymakca@harran.edu.tr) ORCID ID 0000 – 0002– 7888– 5078
(mkeskin@bartin.edu.tr) ORCID ID 0009 – 0005 – 6724 – 491X
(esisman@yildiz.edu.tr) ORCID ID 0000– 0003 –3696 – 9967

Cite this study

Abu Arra A, Akca S, Keskin, MZ, & Şişman E, (2023). Exploring the difference between Standard Precipitation Evapotranspiration Index (SPEI) from in-situ meteorological stations and SPEIbase. Intercontinental Geoinformation Days (IGD), 7, 67-70, Peshawar, Pakistan

collected instruments on aircraft. The data is collected using sensors. The accuracy can vary depending on the sensors and instruments used. These satellites and global products have a large scale, such as 0.5 degrees or 31 km spatial resolution (Copernicus Climate Change Service (C3S), 2017).

Some areas are covered by one or two grid data (remote sensing data). At the same time, the number of in-situ meteorological stations is limited. Subsequently, there is a huge need to investigate the difference between in-situ meteorological stations and satellite and remote sensing data regarding spatial distribution and small-scale areas for drought evaluation and monitoring. This research mainly aims to investigate the difference between SPEI at different timescales (3, 6, 9, and 12 months) calculated from in-situ meteorological stations and SPEIbase (satellite data) in terms of drought severity and drought categorization. Also, to compare the drought characteristics for each SPEI value.

2. Method

2.1. Data

To investigate the difference between SPEI from in-situ meteorological stations and SPEIbase, the application is conducted for the monthly precipitation and temperature records between 1951 and 2020 (70 years) from Florya meteorological station in Istanbul (**Figure 1**). The precipitation and temperature data were checked for consistency and continuity controls. **Table 1** summarizes the main information about Florya meteorological station.

2.2. SPEI from in-situ stations

The SPEI method was developed in 2010 by Vicente-Serrano et al. The difference between precipitation and evapotranspiration data is fitted to an appropriate probability density function (PDF), and the goodness-of-fit tests are controlled and checked by Kolmogorov-Simirnov and Chi-Square (Stephens, 1970). The last step is the normalization procedure of probabilities into normal PDFs. The evapotranspiration was calculated using the Thornthwaite method (Thornthwaite, 1948). Additional details regarding SPEI can be found in (Vicente-Serrano et al. 2010).

2.3. SPEI from SPEIbase

The SPEI values were taken directly from SPEIbase (https://spei.csic.es/database.html, accessed on 28 October, 2023). It provides data with 0.5 degrees resolution, and the time period started from 1901. The SPEI values were downloaded for 3, 6, 9, and 12-month timescales between 1951 and 2020 (70 years).

2.4. The difference between SPEI from in-situ meteorological stations and SPEIbase

The difference between SPEI values was evaluated using drought categorization defined by (McKee et al. 1993) and summarized in **Table 2.** Months with the same drought category were treated the same. Also, the comparison was done using SPEI severity values.

Table 1. Geographical and climatic information for Florya station.

Station's Name	Station ID	Latitude (N)	Longitude (E)
Florya	17636	40.97	28.78
	Mean Precipitation (P) - mm	Standard deviation (mm)	
	53.78	44.08	
	Mean Temperature (T) - °C	Standard deviation (°C)	
	14.42	6.74	

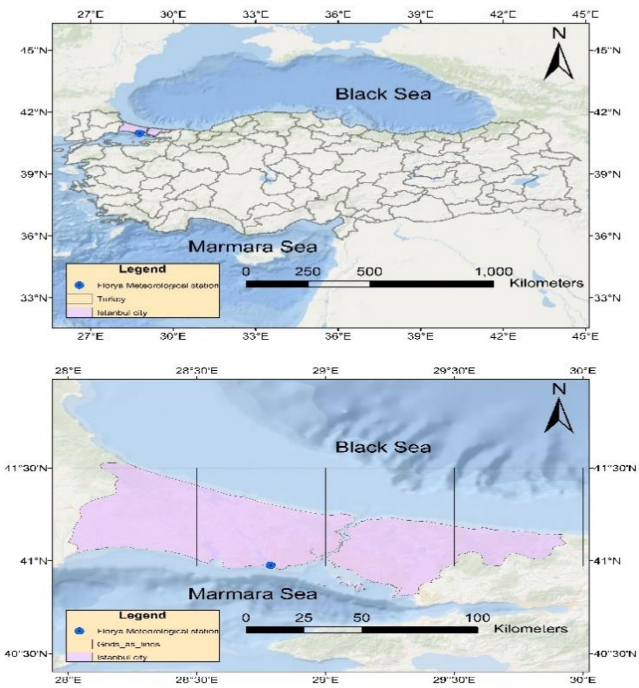

Figure 1. Location of Istanbul city, the Florya meteorological station, and the grid data obtained from the SPEIbase.

Table 2. Drought categorization for SPEI (McKee et al. 1993).

SPEI values (Drought Index_DI)	Drought categorization
2.00 ≤ DI	Extreme wet (EW)
1.50 ≤ DI <1.99	Severe wet (SW)
1.00 ≤ DI <1.50	Moderate wet (MW)
-0.99 ≤ DI <1.00	Normal (N)
-1.50 ≤ DI < -1.00	Moderate drought (MD)
-2.00 ≤ DI < -1.50	Severe drought (SD)
-2.00 > DI	Extreme drought (ED)

3. Results

The comparison process was done in two ways. The first way is drought categorization (**Table 2**). Each month was categorized based on in-situ meteorological stations and SPEIbase. The (SPEI_station) indicated the drought category based on the SPEI value from the in-situ station. And the (SPEIbase_grid) indicated the drought category based on SPEIbase. **Table 3**, **Table 4**, **Table 5**, and **Table 6** showed the number of months that fall within a specific drought categorization regarding SPEI3, SPEI6, SPEI9, and SPEI12 using in-situ meteorological stations and SPEIbase, respectively. The sum in these tables was the month's summation for each category. It can be noticed that the drought category was different based on SPEI data. The intersection in drought categories was about 530 months from about 840 months. The most dominant drought category was normal, which is between -1 and 1.

Increasing the timescale led to increasing the number of intersection months. For SPEI3, it was 501 months, and for SPEI12, it was 536 months. Also, in some months, according to in-situ stations, the drought category was dry, and according to SPEIbase, the drought category was wet. The empty values were the drought categories without any month. The number of extreme drought months for SPEI12 using in-situ stations was 24.

The second way for comparison was depending on the SPEI drought values. This comparison was conducted for the last 20 years, from 2000 to 2020. This way was essential to compare SPEI values by month scale and investigate the difference between them for each month. **Figure 2**, **Figure 3**, **Figure 4**, and **Figure 5** showed the difference between SPEI values for SPEI3, SPEI6, SPEI9, and SPEI12, respectively. The orange color was the SPEI values obtained from the in-situ meteorological station, the beige color was the SPEI values from SPEIbase, and the bronze color was the intersection months between SPEI calculated from in-situ meteorological stations and SPEIbase.

For short timescales like 3 and 6 months, the differences between in-situ stations and SPEIbase were observed and more considerable. In 2015, the SPEI values using the Florya station were about -1.0, and using SPEIbase, SPEI was about 2.0, which indicated a high difference between them. For more details, Fig. 2-5, showed the differences between them.

4. Discussion

The main objective of this research was to investigate the difference between SPEI from in-situ meteorological stations and SPEIbase. The difference between them was conducted in two ways: drought categorization and SPEI values. About 60% of the months were with the same drought category, which indicated a high disparity between them. Also, SPEI values calculated using SPEIbase gave more extreme dry events (ED) but less severe dry events (SD). This result can be attributed to three main reasons: 1) the different time periods that are used for each way. For stations, it was 70 years, and 120 years for SPEIbase. 2) PET may be different because the methods used were different. 3) The quality and consistency control for each data set. For SPEIbase, the area covered by one grid is large and was about 3000 km^2.

The high number of months with normal drought category (N) was because the normal category widely ranged between -1 and 1. Also, SPEIbase was more conservative for a short timescale because the drought months were more than in-situ data.

Table 3. The difference between SPEI from the in-situ meteorological station and SPEIbase at a 3-month timescale based on drought categorization.

		SPEIbase_Grid							
		EW	SW	MW	N	MD	SD	ED	sum
SPEI_Station	EW	9	6		1				16
	SW	10	17	14	3				44
	MW	7	20	25	42	1			95
	N	8	14	52	393	60	6	1	534
	MD				36	40	22	2	100
	SD		1		8	11	12	6	38
	ED				0	1	5	5	11
	sum	34	58	91	483	113	45	14	501

Table 4. The difference between SPEI from the in-situ meteorological station and SPEIbase at a 6-month timescale based on drought categorization.

		SPEIbase_Grid							
		EW	SW	MW	N	MD	SD	ED	sum
SPEI_Station	EW	12	7						19
	SW	6	17	8	1				32
	MW	9	20	19	46	1			95
	N	7	16	52	408	51	8		542
	MD		1	1	42	29	19	6	98
	SD				6	10	16	8	40
	ED					3	2	7	12
	sum	34	61	80	503	94	45	21	508

Table 5. The difference between SPEI from the in-situ meteorological station and SPEIbase at a 9-month timescale based on drought categorization.

		SPEIbase_Grid							
		EW	SW	MW	N	MD	SD	ED	sum
SPEI_Station	EW	5	7						12
	SW	7	22	14	2				45
	MW	7	17	21	23				68
	N	8	19	48	444	45	12		576
	MD			1	36	18	21	3	79
	SD			1	5	16	14	7	43
	ED					2	7	6	15
	sum	27	65	85	510	81	54	16	530

Table 6. The difference between SPEI from the in-situ meteorological station and SPEIbase at a 9-month timescale based on drought categorization.

		SPEIbase_Grid							
		EW	SW	MW	N	MD	SD	ED	sum
SPEI_Station	EW	10	4	1					15
	SW	6	24	13	2				45
	MW	7	16	13	30				66
	N	9	19	42	456	41	8		575
	MD		2		26	9	21	8	66
	SD			2	8	12	15	1	38
	ED						15	9	24
	sum	32	65	71	522	62	59	18	536

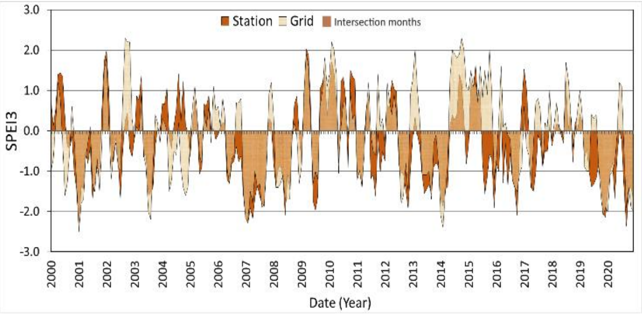

Figure 2. Comparison between SPEI3 from in-situ meteorological station and SPEIbase using DI for the last 20 years.

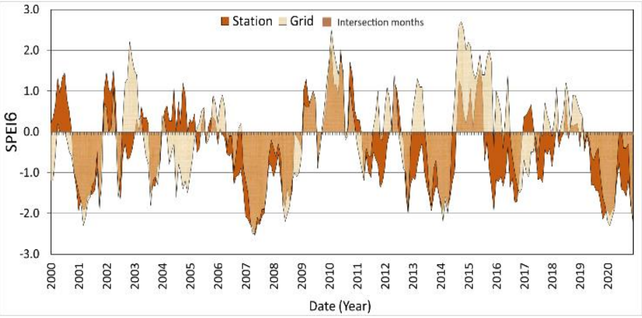

Figure 3. Comparison between SPEI6 from in-situ meteorological station and SPEIbase using DI for the last 20 years.

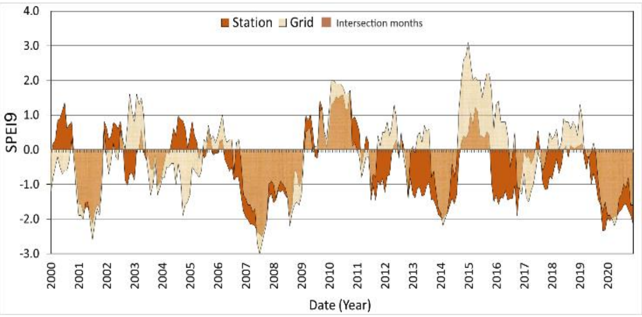

Figure 4. Comparison between SPEI9 from in-situ meteorological station and SPEIbase using DI for the last 20 years.

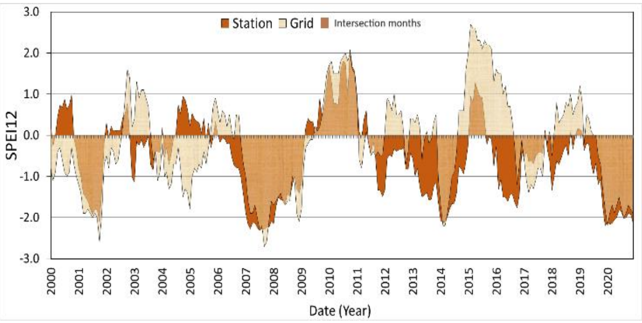

Figure 5. Comparison between SPEI12 from in-situ meteorological station and SPEIbase using DI for the last 20 years.

5. Conclusion

Drought is a critical issue for worldwide climate change adaptation and mitigation programs. Investigating the difference between SPEI from in-situ meteorological stations and SEPIbase is highly important because the drought index is the first step in drought analysis and evaluation processes.

The results proved a vital difference between SPEI using in-situ meteorological stations and SPEIbase. Based on drought categories, about 61% of the months were within the same drought category.

References

Abu Arra, A. & Şişman, E. (2023). Characteristics of Hydrological and Meteorological Drought Based on Intensity-Duration-Frequency (IDF) Curves. *Water*, *15*, 3142. https://doi.org/10.3390/w15173142

Barbour, E. J., Adnan, M. S. G., Borgomeo, E., Paprocki, K., Khan, M. S. A., Salehin, M. & Hall, J. W. (2022). The unequal distribution of water risks and adaptation benefits in coastal Bangladesh. Nat. Sustain., 5, 294–302.

Chong, K. L., Huang, Y. F., Koo, C. H., Ahmed, A. N. & El-Shafie, A. (2022). Spatiotemporal variability analysis of standardized precipitation indexed droughts using wavelet transform. J. Hydrol., 605, 127299.

Copernicus Climate Change Service (C3S). (2017). ERA5: Fifth generation of ECMWF atmospheric reanalyses of the global climate . Copernicus Climate Change Service Climate Data Store (CDS), *date of access*. https://cds.climate.copernicus.eu/cdsapp#!/home.

Levizzani, V. & Cattani, E. (2019). Satellite Remote Sensing of Precipitation and the Terrestrial Water Cycle in a Changing Climate. *Remote Sens.*, *11*, 2301. https://doi.org/10.3390/rs11192301

Mckee, T. B., Doesken, N. Y. & Kleist, Y. (1993). The relationship of drought frequency and duration to time scales. 8th Conference on Applied Climatology, Anaheim, CA, 179–184.

Mishra, A. K. & Singh, V. P. (2010). A review of drought concepts. J. Hydrol., 391, 202–216.

Şen, Z. & Almazroui, M. (2021). Actual precipitation index (API) for drought classification. Earth Systems and Environment 5: 59-70.

Stephens, M. A. (1970). Use of the Kolmogorov–Smirnov, Cramér–Von Mises and related statistics without extensive tables. J Roy Stat Soc 32B:115–122.

Thornthwaite, C. W. (1948). An approach toward a rational classification of climate. Geographical Review, 38(1), 55.

Vicente-Serrano, S. M., Beguería, S. & López-Moreno, J. I. (2010). A multiscalar drought index sensitive to global warming: The standardized precipitation evapotranspiration index. J. Clim., 23, 1696–1718.

Wilhite, D. A. (Ed.) (2000). Drought as a natural hazard: Concepts and definitions. In Drought: A Global Assessment; Routledge: London, UK, 2000; Chapter 1; Volume I, pp. 3–18.

Yong, S. L. S., Ng,, J. L., Huang, Y. F., Ang, C. K., Mirzaei, M. & Ahmed, A. N. (2023). Local and global sensitivity analysis and its contributing factors in reference crop evapotranspiration. Water Supply, 23, 1672–1683.

7th Intercontinental Geoinformation Days

igd.mersin.edu.tr

Monitoring changes in air pollution using Sentinel-5 data

Behnaz Ghaderi[1], Payam Alemi Safaval [2], Zahra Azizi [*1]

[1] Islamic Azad University, Science and Research Branch, Faculty of Natural Resources and Environment, Department of Remote Sensing and GIS, Tehran, Iran
[2] Remote Sensing and GIS, Geological Survey & Mineral Exploration of Iran, Iran

Keywords
Remote sensing,
Sentinel images-5
Air pollution,
Aerosol

Abstract

Today, air pollution is one of the most important issues in the field of environment and human health. In the last few years, remote sensing has helped a lot in the field of monitoring, measuring the concentration of pollutants. In this article, the monitoring of air pollution changes with Sentinel 5 satellite images in the southwest of Iran was discussed. Sentinel 5 images were received using the Google Earth Engine system in January 2022 to January 2023. After the detection of NO2, CO, UV-Aerosol and SO2, a map of atmospheric pollutants with color layers was obtained and then the one-year time changes of No2, Co, UV-Aerosol and SO2 were determined with a graph. The results of the graph of monthly changes showed that the concentration of NO2 and CO in spring and summer have the highest concentration, UV-Aerosol has the highest concentration in spring, and September and October have the highest concentration for SO2 in the center and southwest of Khuzestan province.

1. Introduction

Various factors are effective in producing air pollution that have adverse effects on the health of living organisms (Safarianzengir et al., 2020). Pollutants are classified in terms of physical state (solid, liquid and gas), emission source (mobile, fixed, natural, man-made) (Tiwary and Colls, 2009) and are one of the most important environmental issues, especially in advanced industrial countries and is developing (Meetham, 2016).

The most important air pollutants are carbon monoxide (CO), sulfur dioxide (SO_2), nitrogen dioxide (NO_2) and aerosol (AI) (WHO, 2010).

The World Health Organization (WHO-2020) reported that about 91% of the earth's population is exposed to air pollution with high levels of pollutants, which leads to the death of 7 million people annually.

In addition, air pollution threatens the health of all age groups, especially children (Vidotto et al., 2012), leads to cardiovascular diseases (Cesaroni, 2014), impaired fertility (Slama, 2013) and is a serious threat to It is the health of society.

Using remote sensing techniques is one of the most efficient methods to study pollution in the atmosphere (Duncan et al., 2014; Li, 2020).

In the past years, the western regions of Iran have been heavily affected by various air polluting phenomena, such as fine dust, due to their neighborhood with desert areas. One of the most damaged areas is Khuzestan province, which is in the danger zone for many days of the year. Therefore, in this study, air pollution in this area has been monitored using remote sensing (Ghaderi and Azizi, 2019).

2. Materials and methods

2.1. Study Area

The latitude and longitude of the study area is, 47°, 50° E and 30° 33° N respectively. It is the fifth most populous province of Iran with an area of 640057 square kilometers, it is located in the southwest of Iran on the shores of the Persian Gulf and the Arvand River. Due to the proximity to the Persian Gulf and the dry and burning winds of the Arabian Peninsula, it is a dry region and has a desert climate (Ghaderi and Azizi, 2021).

* **Corresponding Author**

*(zazizi@srbiau.ac.ir) ORCID ID 0000-0001-8572-7134
(Ghaderi6719@gmail.com) ORCID ID 0000 – 0003 – 8325 – 0776
(payam.alemi@srbiau.ac.ir) ORCID ID 0000 – 0003 – 4843 – 0782

Cite this study

Ghaderi, B., Safaval, A., P., & Azizi, Z. (2023). Monitoring changes in air pollution using Sentinel-5 data, Intercontinental Geoinformation Days (IGD), 7, 71-74, Peshawar, Pakistan

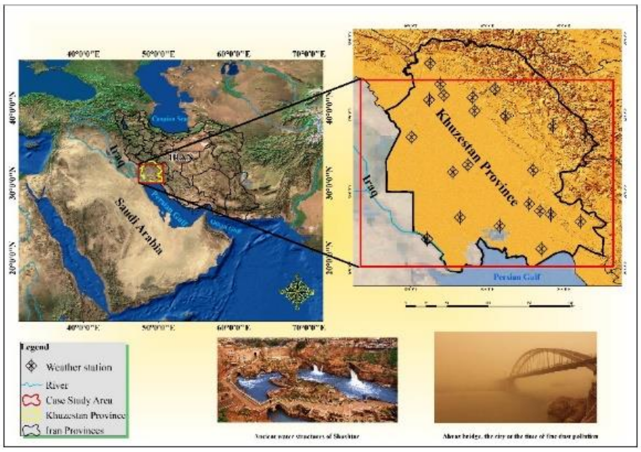

Figure 1. Study area

2.2 Method

This study is non-interventional and descriptive-analytical. Using the JavaScript programming language in the GEE environment, the products related to CO, SO2, NO2 and AI pollutants were called with Sentinel-5 images and the time period of 2022 to 2023 for monitoring atmospheric pollutants and determining polluted centers in the area of Khuzestan province of Iran was selected.

The required ground data was obtained from 22 meteorological stations (Figure 1). In the following, it was used to measure the changes in the concentration of different polluting gases. Then, the amount of air gases, carbon monoxide, nitrogen dioxide and sulfur dioxide in the atmosphere was checked and monitored. The required ground data was obtained from 22 meteorological stations.

In the following, it was used to measure the changes in the concentration of different polluting gases. Then, the amount of air gases, carbon monoxide, nitrogen dioxide and sulfur dioxide in the atmosphere was checked and monitored.

Using the Google Earth Engine Polygon system, the studied area was called, then the products related to the atmospheric pollutants UV-Aerosol, CO, NO2, and SO2 were received and analyzed during a ten-day time period, i.e. from November 1, 2022 to November 10, 2022.

Finally, the spatial map of air pollutants was obtained separately according to the average concentration of ten days and by the color combination method. and its concentration was displayed by Dataset Visualization parameters with color,

In order to monitor the temporal and spatial changes of pollutants, the monthly graph of changes during a one-year period was obtained from January 2022 to January 2023, and the average concentration of pollutant centers and aerosols was obtained.

The results obtained from the generated maps indicate the distribution of pollutant concentrations. (**Figure 2**).

3. Results

3.1. Slope of changes in air pollution

The average monthly changes of the amount of CO pollutant in 2022 to 2023 in different months are between 0.40-0.80 mol/m^2. The highest amount of CO gas started from May 2022 as an upward slope and continued until September, after which it had a downward slope.

According to the results, the decreasing trend of CO is in March and April and its lowest concentration is in November, so according to the graph, there is the highest concentration of carbon monoxide in spring and summer.

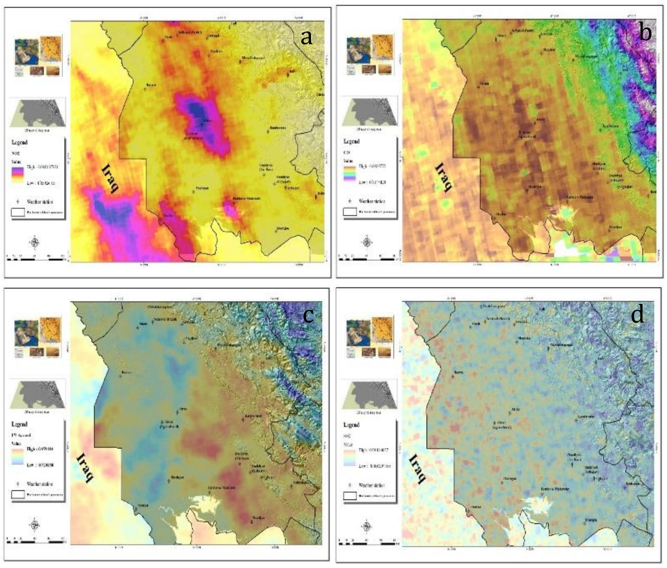

Figure 2. a) NO_2 pollutant distribution b) CO pollutant distribution c) UV-Aerosol pollutant distribution d) SO_2 pollutant distribution.

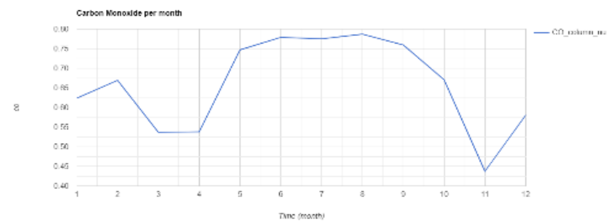

Figure 3. Chart of monthly CO changes from January 2022 to January 2023.

The graph of monthly changes of NO_2 pollutant shows that the trend of changes in February and March was at the lowest and constant .In spring and summer, NO_2 concentration has increased. With the change of season from summer to autumn, there has been a decreasing trend.

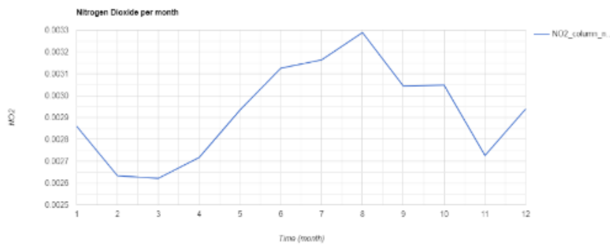

Figure 4. Chart of monthly NO2 changes from January 2022 to January 2023.

The graph of concentration changes for SO2 pollutant shows a lot of fluctuation. In the first month to the third month of the year, it had a downward slope and in the month of March, it had the minimum concentration. From the beginning of May, which means spring and summer, the amount of SO_2 is on the rise and shows a high concentration.

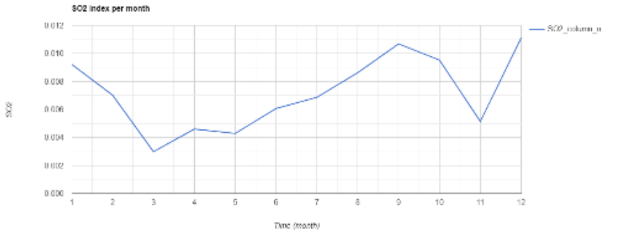

Figure 5. Chart of monthly SO2 changes from January 2022 to January 2023.

According to the chart of changes in the amount of aerosols in the atmosphere, it shows that the spring season had the maximum concentration of aerosols, and the highest concentration was in the month of May, which reduced the horizontal visibility to at least 100 meters (Figure 3).

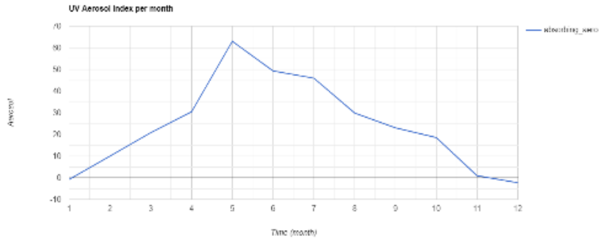

Figure 6. Chart of monthly SO_2 changes from January 2022 to January 2023.

The data of meteorological stations of Khuzestan province were used for validation in this research and the dust event was recorded in 5 stations of Ahvaz, Shadgan, Handijan, Abadan and Omidiyeh on October 1, 2022 to October 3, 2022 at 6, 9 and 12 hours with horizontal visibility of less than 100 meters.

In the Google Earth Engine environment, a three-day graph and a spatial map of aerosols were obtained and compared with the results at the stations. Finally, the results were correct (Figure 7).

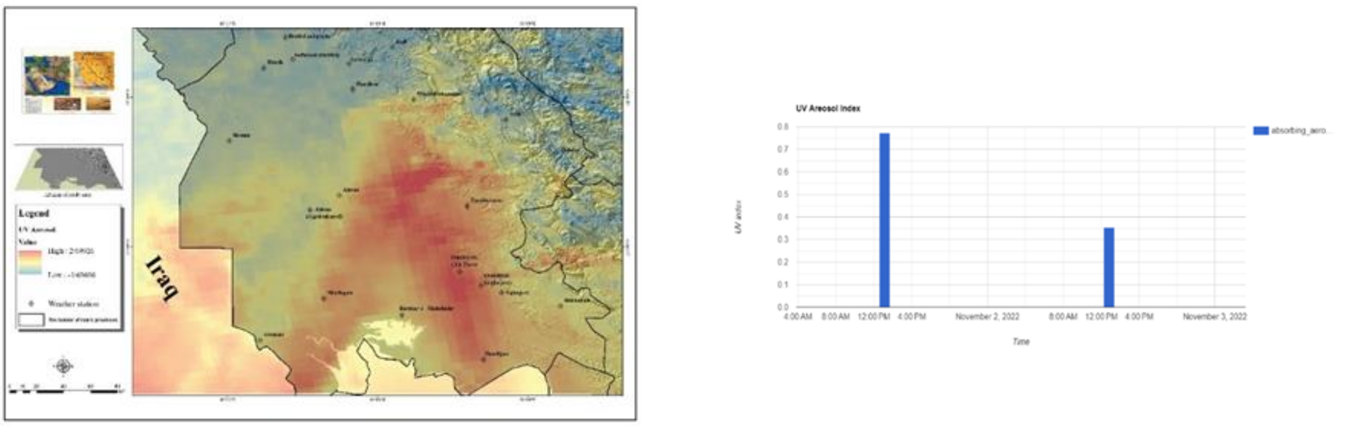

Figure 7. Validation results according to meteorological data

4. Discussion

When the concentration of gases exceeds a limit and is dangerous for human health, it is considered air pollution, so it causes environmental problems. Many studies have been done with different methods for monitoring, preventing and predicting air pollution, and remote sensing and GIS have greatly helped in pollutant monitoring.

Many studies have been done regarding the estimation of pollutant concentration with satellite images.

5. Conclusion

Iran is facing a decrease in the middle and upper levels of the troposphere during the hot seasons due to its location in the subtropical high-pressure dynamic currents.

With the continuation and vertical expansion of the high-pressure subtropical current, a hot and dry air mass is formed on the plateau of Iran. which, by affecting other atmospheric variables, leads to the dryness of large areas of Iran.

The main sources of dust for dust storms in southwestern Iran are a range between northern and central Iraq, northern Saudi Arabia and eastern Syria (Rivandi et al., 2013).

The phenomenon of dust in Khuzestan province has human and natural factors, among which the droughts of recent years can be mentioned as the most important. Also, dam construction, water transfer to dry areas, agriculture, Iraq and Iran war are human factors involved in increasing the severity of the crisis (Rshnv, 2009).

In the meantime, the storms that enter Khuzestan by the air currents of Saudi Arabia and Iraq have destructive effects on the air quality and environment of this region (Ghaderi, 2020).

The results of the present study showed that the distribution of atmospheric pollutants in the south and southwest of Khuzestan province, that is, in the weather stations of Ahvaz, Abadan, Shadgan, Omidiyeh, Handijan, had the highest concentration, it is abundantly clear on the map of the southwestern border of the country.

Therefore, according to the validation map of aerosol centers in the southwest of Iran, the eastern regions of Iraq were more.

The results of the graph of changes in the average concentration of atmospheric pollutants in 2022 to 2023 showed that the concentration of NO2 and CO in the months of May to October has the highest level and UV-Aerosol has the highest concentration in the months of May, June and July. Also, September and October show the highest concentration of SO_2 in the center of Khuzestan province and Ahvaz city.

References

Cesaroni, G., Forastiere, F., Stafoggia, M., et al. (2014). Long term exposure to ambient air pollution and incidence of acute coronary events: prospective cohort study and meta-analysis in 11 European cohorts from the ESCAPE Project." Bmj 348.

Duncan, B. N., Prados, I., Lamsal, N. L., Liu, Y., Streets, D. J., Gupta, P. (2014). Ernest Hilsenrath et al. "Satellite data of atmospheric pollution for US air quality applications: Examples of applications, summary of data end-user resources, answers to FAQs, and common mistakes to avoid." Atmospheric environment ,94, 647-662.

Ghaderi B., Azizi Z (2021). HYSPLIT algorithm in dust source Identifying and modeling. Intercontinental Geoinformation Days (IGD), Vol. 4: 239-241.

Ghaderi, B., Azizi, Z. (2019). Detecting and monitoring dust storm and studying the effect of temperature and relative humidity parameters using remote sensing. 2ND Conference of the Arabian journal of geosciences (CAJG) 25-28 November, Sousse, Tunisia.

Ghaderi, B., Azizi, Z. (2020). Monitoring of dust phenomenon and Investigate its correlation with temperature and humidity parameters (Case study: Khuzestan Province). Journal of Geomatics Science and Technology, 9(4), 51-60.

Li, J. (2020). Pollution trends in China from 2000 to 2017: A multi-sensor view from space, Remote Sensing, 12(2), 208.

Meetham, A. R., Bottom, D. W., Cayton, S., (2016). Atmospheric pollution: its history, origins and prevention. Elsevier Books.

Rivandi, A., Mirrokni, M., Mohammadiha, A. (2013). Investigation of Formation and Propagation of Dust Storms Entering to the West and Southwest of Iran Using Lagrangian Particle Diffusion Model, HYSPLIT, Journal of Climate Research, 1392(13), 1-16.

Rshnv, A. S. (2009). Dust phenomenon Ghbardr Khuzestan province, quarterly rainfall, Ahvaz, Khuzestan province meteorological Station.

Safarianzengir, V., Sobhani, B., Yazdani, M. H., Kianian, M., (2020). Monitoring, analysis and spatial and temporal zoning of air pollution (carbon monoxide) using Sentinel-5 satellite data for health management in Iran, located in the Middle East, Air Quality Atmosphere & Health, 13: https://doi.org/10.1007/s11869-020-00827-5.

Slama, R., Bottagisi, S., Solansky, I., Lepeule, J., Giorgis-Allemand, L., Sram, R., (2013). Short-term impact of atmospheric pollution on fecundability. Epidemiology, 871-879.

Vidotto, J. P., Pereira, L. A. A., Braga, A. L. F., Silva, C. A., Sallum, A. M., Campos, L. M., Martins, L.C., Farhat, S. C. L., (2012). Atmospheric pollution: influence on hospital admissions in paediatric rheumatic diseases, Lupus, 21(5), 526-533.

7th Intercontinental Geoinformation Days

igd.mersin.edu.tr

Evaluation of the application of the multi-temporal method in Sentinel 2 satellite images for the separation of agricultural products

Samira Asadnezhand Khormazard*[1], Mir Masuod Kheirkhah Zarkesh[2], Bagher Ghermezcheshmeh[2]

[1] Islamic Azad University, Specialized Department of Remote Sensing and GIS, Faculty of Natural Resources and Environment, Science and Research Unit, Tehran, Iran
[2] Soil Conservation and Watershed Research Institute, Agricultural Research, Education and Extension Organization, Tehran, Iran

Keywords
Sentinel 2
Maximum likelihood
Minimum distance
time series

Abstract

One of the ways to obtain information about the condition of the land is to produce land use maps. In this research, using different time series from Sentinel 2 satellite images, with the aim of choosing the appropriate classification method for the separation of land products in Ravansar city, Kermanshah province. Took based on the growing season, it was first prepared by referring to the agricultural calendar of different products of the region. By determining the time of planting, the peak of greenness, harvesting and plowing of different crops, information was collected and stored in the database for the necessary analysis to determine the time of the images based on the major crops of the study area, including (wheat, corn, barley, road, other-vegetation, other-plough-barren, water, peas, tomato) should be taken from Sentinel 2 images on two dates. By making the necessary corrections on the images, in the next step, the mentioned dates were done with the PCA method and then the classification was done with the maximum likelihood and minimum distance method. The results showed that the maximum likelihood classification was more accurate than the minimum distance method in multiple times with an overall accuracy of 94% and a kappa coefficient of 92%.

1. Introduction

Having regularly updated information on the state of the earth's surface phenomena, various activities can be carried out in the fields of agriculture, industry, animal husbandry, commercial services and transportation, etc.

Gaining awareness and knowledge regarding the cultivation pattern and the area under cultivation plays an important role in the management of agricultural lands and the estimation of the amount of net production (Immitzer et al., 2016).

In order to identify and separate the cultivated lands of different crops and prepare a map of regional crops in Africa, two images (related to the months of May and September) of digital data of Landsat satellite, ETM sensor from 2011 were used. In order to classify the image in each of these two months, the supervised classification method including maximum likelihood and artificial network was used. To compare the images obtained from the two methods, educational and experimental samples and the same working method were chosen for both methods. Electromagnetic waves used in remote sensing provide the possibility of extracting a variety of information from vegetation.

Separation of agricultural lands from other covers is always considered as a major challenge in remote sensing studies. However, one of the most valuable applications of remote sensing in this field is the production of maps of the type of cultivation and the estimation of its cultivated area (Ghazaryan et al., 2018, Lenco et al., 2019).

2. Method

The studied area in Ravansar city is located at longitude 46.39 degrees east and latitude 43.43 degrees

* **Corresponding Author**

*(nezhand6744@gmail.com) ORCID ID 0009 – 0008 – 3071 – 3921
(kheirkhahzarkesh96@gmail.com) ORCID ID xxxx – xxxx – xxxx – xxxx
(baghergh@gmail.com) ORCID ID xxxx – xxxx – xxxx – xxxx

Cite this study

Khormazard, S. A., Zarkesh, M. M. K., Ghermezcheshmeh, B. (2023). Evaluation of the application of the multi-temporal method of Sentinel 2 satellite images in the separation of agricultural products. Intercontinental Geoinformation Days (IGD), 7, 75-77, Peshawar, Pakistan

north, with an average altitude of 1380 meters and an area of 1140 square kilometers, on the slopes of Mount Shahu in the northwest and 47 kilometers from Kermanshah city (Figure 1).

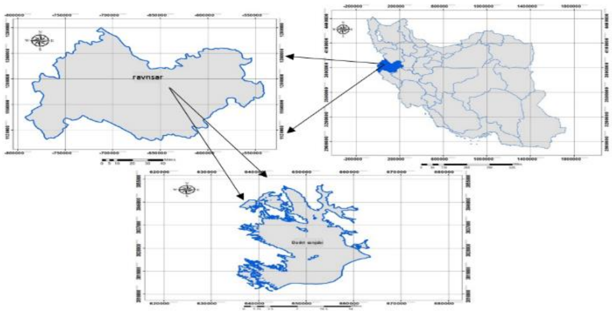

Figure 1. Study area

In this research, two Sentinel 2 images were received from the American Copernicus site on 02/15-11/06, 2016, and were prepared for classification after the necessary radiometric and atmospheric corrections. Then, with color band combination and PCA method (Principal Component Analysis) two images were done to separate the product by visual interpretation method. Layer stacking A new layer was created as a time series and was classified and evaluated for accuracy. The most common supervised classification algorithms are maximum likelihood classification and minimum distance classification

After that, the supervised classification was done using the methods of maximum likelihood and minimum distance according to the ground sample. The land cover classification is based on the spectral signature defined in the soil samples. In this way, the image classification software determines which class is most similar to which of the classes in the educational samples.

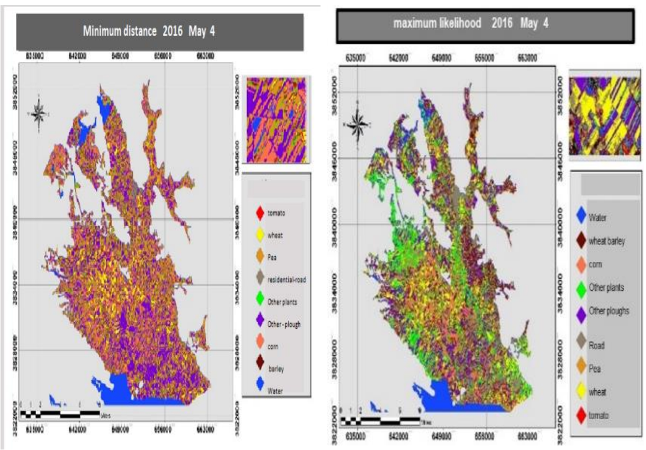

Figure 2. Classification map with the method of Maximum Locklihood and Minimum Distance in May 2016.

And one of the most common methods of expressing the classification accuracy is to prepare the classification error matrix. The error matrix compares the relationship between the known reference data (ground truths) and the relevant results of an automatic classification in a category-by-category manner.

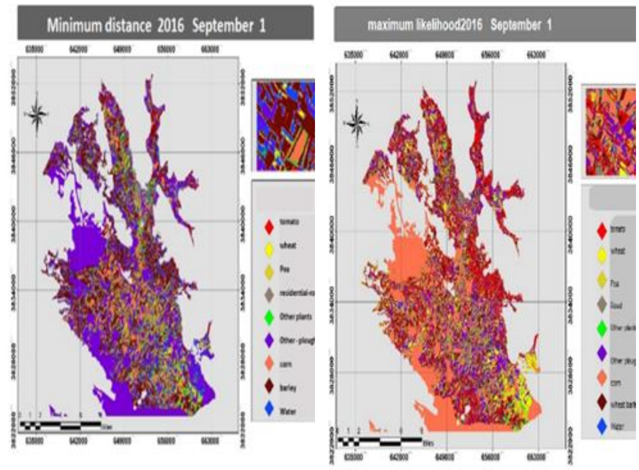

Figure 3. Classification map with Maximum Locklihood and Minimum Distance method in September 2016.

3. Discussion and Results

Investigating land use changes is one of the most important aspects of natural resource management and reviewing environmental changes (Bayatikhatibi and Amiriyan, 2022).

Accuracy evaluation results are usually presented in the form of an error matrix, in which case various parameters and values that indicate accuracy or some kind of error in the results are extracted from this matrix. This matrix is the result of a pixel-by-pixel comparison, and the known pixels are the corresponding pixels in the classification results.

Using 2 classification methods, maximum likelihood and minimum distance were done to analyze land use changes and evaluate the accuracy of classifications.

The most important stage of any research is its results. At this stage of the research, the results of image classification with the supervised classification method are used to evaluate the accuracy of the classification and review and separation.

By using the agricultural calendar of different crops in the region and the collected information and determining the time of planting, peak greenness, harvesting and plowing of different crops, this information was stored in the database and the necessary analyzes were made to determine the time of the images based on the major crops of the study area. (wheat, corn, barley, residential-road, other-vegetation, other-plough-barren, water, peas, tomato) on the date of images (May & September) of 2016 were taken from Sentinel 2 satellite images.

Then, each of the images was resized or resampled to make the size of all the pixels in the image bands the same.

The overall accuracy of the land use map extracted based on the agricultural calendar, for example, in May 2016, the corn plant species is in the stage of planting and sprouting.

Kappa coefficient of corn was mentioned in the date and in maximum likelihood classification, 69 pixels out of 90 pixels were identified And on September 2016, corn has reached its full growth The maximum likelihood classification has detected 80 pixels out of 90 pixels

Also, in the minimum distance classification, 55 pixels out of 90 pixels were detected on the first date and 63 pixels out of 90 pixels were detected on the second date.

4. Conclusion

Regarding the monitored methods, the maximum likelihood method has the highest accuracy compared to the minimum distance method in all dates

As well as knowing the agricultural calendar of any type of plant, better accuracy can be obtained in satellite images

And based on the research, it is suggested to use other images with high spatial and spectral resolution and appropriate time to select the image. And the maximum likelihood method should be investigated in different climatic conditions and multi-temporal data should be used more or less.

References

Bayati Khatibi, M., Amiriyan Yosef. (2022) Classification of land use and calculation of changes from 2931 to 2011 using Landsat 8 satellite data. Application of remote sensing and GIS in environmental sciences, 1 (3), 25-48.

Biro, K., Pradhan, B., Sulieman, H., & Buchroithner, M. (2013). Exploitation of TerraSAR-X data for land use/land cover analysis using object-oriented classification approach in the African Sahel Area, Sudan. Journal of the Indian Society of Remote Sensing, 41, 539-553.

Ghazaryan, G., Dubovyk, O., Löw, F., Lavreniuk, M., Kolotii, A., Schellberg, J., & Kussul, N. (2018). A rule-based approach for crop identification using multi-temporal and multi-sensor phenological metrics. European Journal of Remote Sensing, 51(1), 511-524.

Immitzer, M., Vuolo, F., & Atzberger, C. (2016). First experience with Sentinel-2 data for crop and tree species classifications in central Europe. Remote sensing, 8(3), 166.

Jędrych, M., Zagajewski, B., & Marcinkowska-Ochtyra, A. (2017). Application of Sentinel-2 and EnMAP new satellite data to the mapping of alpine vegetation of the Karkonosze Mountains. Polish Cartographical Review, 49(3), 107-119.

Kwang, C., Jnr, E. M. O., & Amoah, A. S. (2017). Comparing of landsat 8 and sentinel 2A using water extraction indexes over Volta River. Journal of Geography and Geology, 10(1), 1-7.

.

7th Intercontinental Geoinformation Days

igd.mersin.edu.tr

Investigating the effects of land cover land use change on surface temperature using Landsat satellite images

Esra Şengün[1], Ugur Alganci *[1], Dursun Zafer Şeker [1]

[1]Istanbul Technical University, Civil Engineering Faculty, Geomatics Engineering Department, Istanbul, Türkiye

Keywords
Land use / Land cover
Urban heat islands
Random Forest
Google Earth Engine
Change detection

Abstract

Global and local population growth and the rapid increase in urbanization affect nature negatively by the destruction on forests and natural lands. An additional problem can be considered as the increment of the land surface temperatures due to the heat island phenomenon. Thus, long-term monitoring of rapidly developing cities is important. In this study, Izmir, which ranks 3rd among the big cities of the country, was chosen to monitor the long-term effects of urbanization. For this purpose, a 20-year period from 2020 to the past has been examined with Landsat images. As a first step, historical land cover – land use maps were produced from satellite images using the Random Forest algorithm in the Google Earth Engine platform. Secondly, the urban thermal field variance index (UTFVI) was calculated from thermal bands of Landsat images to examine the effect of urban heat islands and their relation to urbanization progress. Results of these analyses indicated that both cities faced urbanization at the expense of forest and semi-natural area loss in this 20-year period, which is well correlated with an increase in the UTFVI values. Moreover, the increase in UTFVI values on already urbanized regions proposed that the intensity of the urban areas also increased.

1. Introduction

Rapid and uncontrolled urbanization is one of the most important factors affecting the habitat, climate and ecosystem. This unpredictable increase in urbanization, unplanned industrialization, excessive destruction of forested or green areas, and climate changes have a vital negative impact on the health of people living in cities (Çelik et al., 2019).

Remote sensing data and analysis based on these data are frequently used in order to see the degree of this negative impact, to manage the environment and to take precautions. The groundbreaking advances in satellite systems in recent years have positively affected the remote sensing discipline, and it is seen that satellite image-based approaches are increasingly used in the monitoring and evaluation of environmental disasters or climate events such as climate change, drought, flood, earthquake, fire, urban heat island, etc.

According to Oke (1982), urban heat island (UHI) formation occurs when the urban atmosphere is warmer than the surrounding rural areas. The main causes of this formation are roof surfaces, which are characterized as impermeable surfaces, and light absorbing surfaces covered with dark materials such as concrete and asphalt. These types of surfaces re-radiate the solar energy they absorb into the environment and reflect it poorly. This leads to an increase in urban temperatures not only during the day but also after the sun sets (US EPA, 2014).

In general, atmospheric heat islands are measured by networks of weather stations with air temperature sensors, while urban heat islands are determined by land surface temperature (LST). There are many different methods in the literature for calculating the LST. The most preferred of these methods are: Split window method (Sobrino et al, 1996), temperature/emissivity separation algorithm (Gillespie et al, 1998), mono window algorithm (Qin et al, 2001) and single channel method (Jiménez-Muñoz and Sobrino, 2003).

Several studies investigated the effects of urbanization on the urban heat islands in different cities of Türkiye (Kaya et al. 2012; Şekertekin et al. 2015; Ünal et al. 2019). However there no studies focused on this effect in Izmir city yet to our knowledge and very few studies correlated the relationship between urbanization

* Corresponding Author

(sengun16@itu.edu.tr) ORCID ID 0000 – 0002 – 4018 – 4639
*(alganci@itu.edu.tr) ORCID ID 0000-0002-5693-3614
(seker@itu.edu.tr) ORCID ID 0000-0001-7498-1540

Cite this study

Şengün, E., Algancı, U., & Şeker, D. Z. (2023). Investigating the effects of land cover land use change on surface temperature using Landsat satellite images. Intercontinental Geoinformation Days (IGD), 7, 78-81, Peshawar, Pakistan

and thermal field variance index (UTFVI) (Cevik Degerli et al., 2023).

This study focuses on the long-term land cover (LC) change analysis of Izmir city by use of LC classification results belonging to 2000 – 2009 and 2020 and correlate the findings with the changes in UHI conditions by use of UTFVI.

2. Method

The methodology of this study is consisting of two stages that are land cover mapping with use of Landsat images and random forest algorithm, LST derivation from thermal bands and urban thermal field variance index calculation respectively.

2.1. Land cover mapping

This study uses random forest (RF), one of the most current machine-learning based classifier, for land cover classification. It can be considered as a pixel-based algorithm since it analyzes pixels individually rather than taking them as a group like object-based approaches. Algorithm uses decision trees, which identify the classes of training data and determine which class the test data will be included in based on the results obtained from the training data (Erdem et al., 2018).

The classification schema was constructed according to CORINE LULC Level 1 class definitions. Algorithm is fed with around 800 samples for training and tested with around 200 test points for each year.

2.2. UTFVI retrieval

Zhang et al. (2006) UTFVI as a way to identify locations affected by UHI. Formula UTFVI is displayed in Eq. 1.

$$UTFVI = \frac{T_s - T_m}{T_s} \qquad (1)$$

where, Ts represents the LST of the pixel and Tm represents the average LST of the region. Higher values of this index show higher affect of UHI on the region. To calculate this index, first the LST was derived from the thermal bands of Landsat images similar with the procedure provided in Celik et al., (2019) study.

3. Results

The LC classification results for the three dates are provided in Fig. 1. According to accuracy assessment results, overall accuracies achieved 95%, 92% and 97%, while kappa values were observed as 0.93, 0.89, and 0,96 for the 2000, 2009 and 2011 dates respectively.

To perform a detailed LC change analysis, images from two different dates were combined to create a change image and the changing areas were identified from this change image. To create this change image, the pixel values of the previous year's LC map were multiplied by 10 and summed with the new dated image. The aim here is to generate new classes on a pixel basis. These classes are the combination of the transformations of the five classes used in the study (Table 1 and Table 2).

Between 2000 and 2009, there is an increase of 252.87 km² in the area of the city. 190.87 km² of the transformed areas is attributed to agriculture. It is followed by barren areas with 36 km² and forest areas with 26 km² as a result of excessive destruction. When the change areas between 2009-2020 are analyzed, the results show an increase in urban areas. The reason for this is the conversion of 122 km² from forest, about 5 km2 from wetlands, 85 km² from barren areas and finally 100 km² from agricultural areas to urban.

When the UTFVI maps are investigated, it can be asserted that the density and distribution of the extreme UHI Effect class (≥ 0.02) has increased in line with the increase in urbanization (Figure 2).

Table 1. Areal statistics of classes with change matrix for 2000 – 2009 period.

		2009 (sqkm)					
		Forest	Water	Urban	Bareland	Agriculture	Total
2000 (sqkm)	Forest	5782.67	5.30	43.55	45.99	807.70	6685.21
	Water	22.75	171.45	2.58	0.40	14.58	211.77
	Urban	54.28	5.06	266.89	17.67	238.80	582.70
	Bareland	34.22	2.57	24.22	12.28	33.57	106.85
	Agriculture	1308.46	8.39	297.98	69.36	2802.07	4486.25
	Total	7202.37	192.79	635.21	145.69	3896.72	

Table 2. Areal statistics of classes with change matrix for 2009 – 2020 period.

		2020 (sqkm)					
		Forest	Water	Urban	Bareland	Agriculture	Total
2009 (sqkm)	Forest	6262.53	24.95	88.46	31.39	828.82	7236.15
	Water	10.39	177.16	4.44	2.49	3.97	198.45
	Urban	44.19	4.03	326.03	27.13	235.40	636.78
	Bareland	54.92	0.59	28.20	13.33	48.64	145.68
	Agriculture	1234.31	7.58	300.44	47.34	2329.97	3919.63
	Total	7606.33	214.32	747.56	121.68	3446.80	

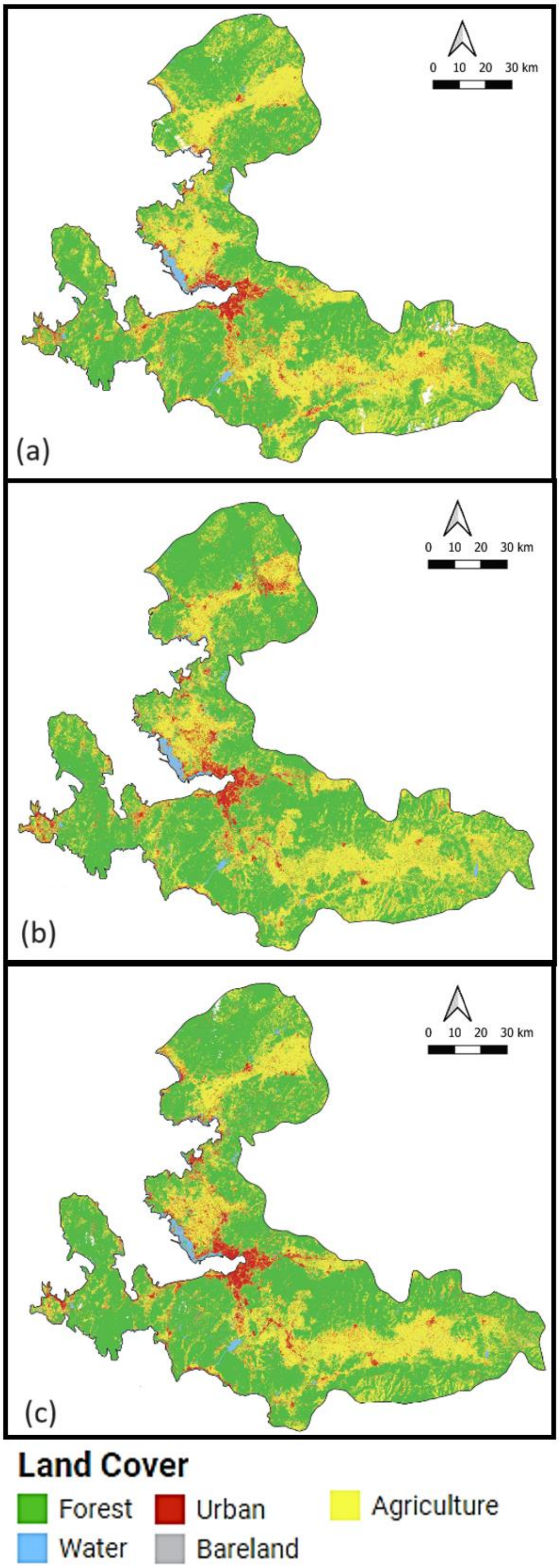

Figure 1. Land cover maps of Izmir city for (a) 2000, (b) 2009 and (c) 2020

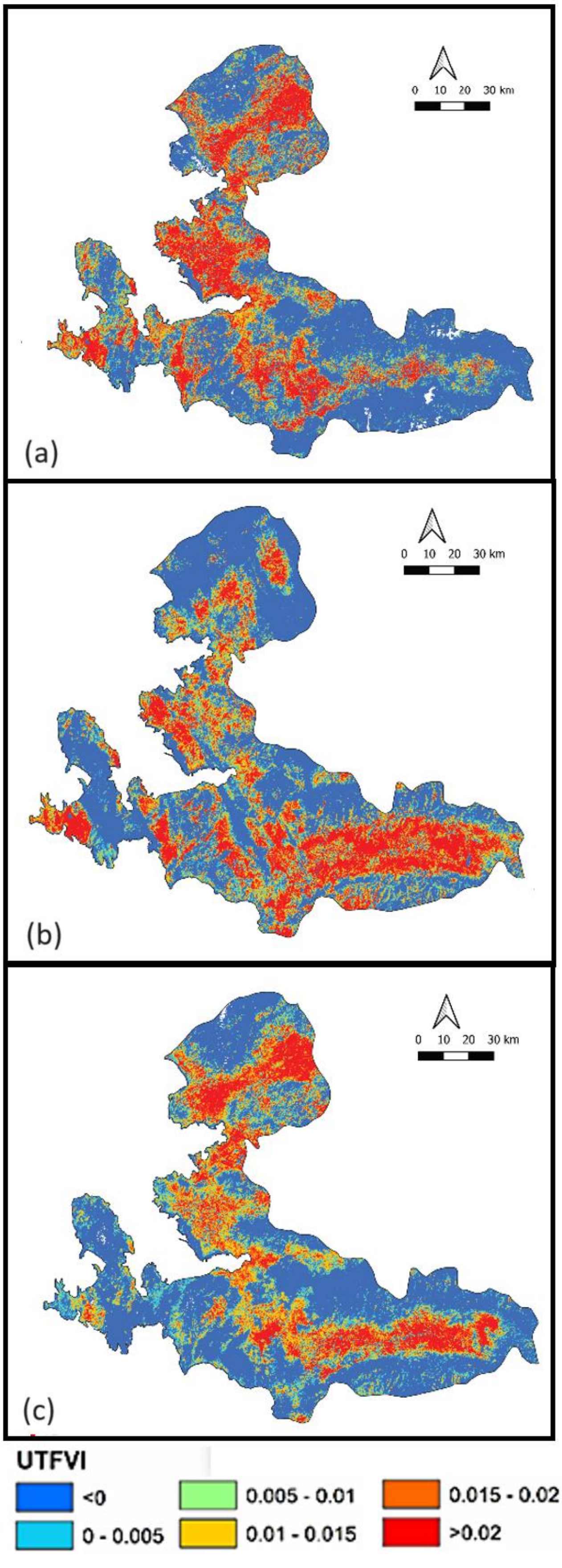

Figure 2. UTFVI maps of Izmir city for (a) 2000, (b) 2009 and (c) 2020.

4. Discussion

Especially in Izmir province, the reflectance values of roofs and the reflectance values of wasteland are mixed, making it very difficult to differentiate in LC classification. Again, in the same province, it was difficult to distinguish between forest and agricultural areas since there is not much difference in reflectance values between them and the transition between climates is smooth. As a solution, by calculating indices on Landsat images, these confused classes can be separated more easily. The higher spatial resolution Sentinel-2 satellite and its Red Edge bands can be useful for differentiation.

Moreover, this study used single image in spring for each year, which raise ambiguities due to seasonal affects both for LC and LST mapping. It is recommended to include multitemporal image set per year to improve the accuracy of findings.

5. Conclusion

This study focused on examining the LC changes in Izmir city of Türkiye for a 20-year period and investigated the effects of urbanization on UHI. Results provided that city continuously urbanized with the expense of destruction in natural lands. When UTFVI maps are examined, it is seen that the UHI effect occurs in urban centers where urbanization is high. Since it is known that human health and future will be negatively affected in places where this effect is intense, it is recommended by the competent authorities to increase afforestation efforts in these areas and to give more space to green lands. If UHI maps are used as a data source to help the preparation of urban plans, especially in metropolitan areas, it will be possible to make climate-sensitive modeling. Thus, urbanization can be ensured with urban land plans made with minimum damage to nature and rural ecosystems.

References

Celik, B., Kaya, Ş., Alganci, U., Seker, DZ. (2019). Assessment of the relationship between land use/cover changes and land surface temperatures: a case study of thermal remote sensing, FEB Fresenius Environ. Bull.,3, 541.

Cevik Degerli, B., Cetin, M. (2023). Evaluation of UTFVI index effect on climate change in terms of urbanization. Environ Sci Pollut Res 30, 75273–75280.

Erdem, F., Derinpinar, M. A., Nasirzadehdizaji, R., Oy, S., Şeker, D. Z., & Bayram, B. (2018). Rastgele Orman Yöntemi Kullanılarak Kıyı Çizgisi Çıkarımı İstanbul Örneği. Geomatik, 3(2), 100–107.

Gillespie, A., Rokugawa, S., Matsunaga, T., Cothern, J. S., Hook, S., & Kahle, A. B. (1998). A temperature and emissivity separation algorithm for Advanced Spaceborne Thermal Emission and Reflection Radiometer (ASTER) images. IEEE Transactions on Geoscience and Remote Sensing, 36(4), 1113–1126.

Jiménez-Muñoz, J. C., & Sobrino, J. A. (2003). A generalized single-channel method for retrieving land surface temperature from remote sensing data. Journal of Geophysical Research: Atmospheres, 108(D22).

Kaya, S., Karaca, M., Basar, U.G., Seker, D.Z. and Weng, D. (2012). Assessment of Urban Heat Islands Using Remotely Sensed Data. Ekoloji, 21, 107-113.

Oke, T. R. (1982). The energetic basis of the urban heat island. Quarterly Journal of the Royal Meteorological Society, 108(455), 1–24.

Qin, Z. H., Zhang, M. H., Karnieli, A., & Berliner, P. (2001). Mono-window algorithm for retrieving land surface temperature from Landsat TM6 data. Acta Geographica Sinica, 56(4), 456–466.

Şekertekin, A.; Kutoglu, Ş.; Kaya, S.; Marangoz, A. Analysing the effects of different land cover types on land surface temperature using satellite data. Int. Arch. Photogramm. Remote Sens. Spat. Inf. Sci. 2015, 40, 665–667.

Sobrino, J. A., Li, Z.-L., Stoll, M. P., Becker, F. (1996). Multi-channel and multi-angle algorithms for estimating sea and land surface temperature with ATSR data. International Journal of Remote Sensing, 17(11), 2089–2114.

Ünal, Y.S., Sonuç, C.Y., Incecik, S. et al. (2020). Investigating urban heat island intensity in Istanbul. Theor Appl Climatol 139, 175–190.

US EPA, O. (2014). Heat Island Impacts [Overviews and Factsheets]. https://www.epa.gov/heatislands/heat-island-impacts

Zhang, Y., Yu, T., Gu, X., Zhang, Y.X., Chen, L.F. (2006). Land surface temperature retrieval from CBERS-02 IRMSS thermal infrared data and its applications in quantitative analysis of urban heat island effect. J Remote Sens-Beijing- 10(5),789.

7th Intercontinental Geoinformation Days

igd.mersin.edu.tr

Examination of earthquake effects in closed reinforced concrete structures

Muhammed Emin Işık[1], Nuri Erdem*[2]

[1]Osmaniye Korkut Ata University, Graduate School of Natural and Applied Sciences, Department of Civil Engineering, Osmaniye, Türkiye
[2]Osmaniye Korkut Ata University, Faculty of Engineering, Department of Geomatics Engineering, Osmaniye, Türkiye

Keywords
Reinforced concrete structures
Collapse
Loss of bearing capacity

Abstract
In this study, the collapse situation, which is one of the factors caused by design errors in reinforced concrete buildings that collapsed or were severely damaged under the influence of an earthquake, was investigated. It has been observed that columns, which are vertical load-bearing elements in buildings with closed cantilevers, are exposed to extra moments and shear forces due to various factors. It has been understood that this situation causes loss of bearing capacity and additional loss of rigidity. According to the results of the review, it has been understood that although closed exits have some economic advantages, their negative effects are much greater.

1. Introduction

One of the most important problems encountered in building designs in our country is the closed cantilevers, which are mostly made to increase the usage area of the building on other floors above the ground floor. In this type of buildings, various negativities occur during an earthquake and the risk of damage increases. Although projects are prepared by calculating the TAKS and KAKS (Precedent) values determined by the Zoning and Urbanization Directorates of the Municipalities, closed cantilever buildings are often projected like others because they do not impose various restrictions (limitation of building height and not specifying h max values). Thus, unlike the ground floor, the building usage areas increase on the normal floors, resulting in an extra gain in architectural and commercial terms. Any residence, office, workplace, etc. Considering that when buying and selling a real estate, pricing is done on a m2 unit price, this is seen as a great financial advantage. However, according to the recently announced data in our country, active faults pass through 45 provincial centers (URL_1) and considering the painful experiences we have had in many major earthquakes, the importance of the issue increases even more. In this context, let alone the construction of closed canopies, our perspective on existing closed canopy buildings has become a top priority issue that threatens not only financial concerns but also the safety of life and property.

Many studies have been conducted in the literature on the structural damages observed in past earthquakes and their sources, the performance of buildings and their structural defects. According to the common results of the studies, the most important causes of earthquake damage to buildings are; These are structural defects and deficiencies such as non- ductile detailing, soft story, short column, weak column-strong beam, closed overhangs and poor concrete quality. In addition, there are thousands of structures that are likely to suffer serious damage in possible medium or large-scale earthquakes (Adalier and Aydingun, 2001; Doğangün, 2004; Inel et al., 2008; Sezen, et al., 2003; Yakut et al., 2005).

2. Method

Approximately 80 percent of the housing stock in our country has covered exits (URL_2). It has been observed in the damage assessment studies in the field that buildings with closed cantilevers received more damage in most earthquakes, especially during the February 6 Kahramanmaraş-centered earthquake, than buildings with regular structures (without closed cantilevers or consoles). Figure 1 shows examples of buildings built with a closed cantilever on the left and without a cantilever on the right. According to the figure, of the two buildings located on the same street opposite each other

* Corresponding Author

(202311330001@ogr.oku.edu.tr) ORCID ID 0009-0006-9590-6957
*(nurierdem@osmaniye.edu.tr) ORCID ID 0000-0002-1850-4616

Cite this study

Işık, M E and Erdem N (2023). Examination of earthquake effects in closed reinforced concrete structures. Intercontinental Geoinformation Days (IGD), 7, 82-85, Peshawar, Pakistan

in Fakıuşağı District of Osmaniye, on island 248, parcel 6 (building on the left) and island 247, parcel 9 (building on the right), the building with a closed exit was damaged, while the building without a closed exit survived the earthquake without any damage. has survived. Of course, it would be incomplete information to say that the damaged buildings were damaged only due to closures. In addition, soft storey irregularity, short column effect, ground liquefaction, inadequacy of ground improvement works, lack of engineering services and workmanship in structures, material quality, technological impossibilities, inadequacy of regulation and inspection mechanism, etc., which are generally examined under the disciplines of civil and geotechnical engineering. Many different factors can be considered.

Figure 1. Buildings with and without Canopy (Archive).

Figure 2: Image of Osmaniye Province 6 February Earthquakes (URL_3).

Figure 2 shows the earthquake-affected view of the site, which consists of 14 blocks and 9 floors, all with closed exits, located on island 2955, parcel 1, in Adnan Menderes District, Adnan Menderes District, Osmaniye Province. In case of a closed exit along with many different factors mentioned above, it is necessary to consider the earthquake effect as a whole. Therefore, if the buildings had been designed and built with a frame system that met the load-bearing system requirements from the ground up, rather than with a closed cantilever, they would have been less affected. Of course, for this purpose, a detailed scan should be made and the existing building data should be processed into the computer environment, earthquake performance analysis should be carried out in the same structure without a closed exit and the results should be compared. Only in this way can reliable data be obtained. Examining the data of previous research on the subject will provide more enlightening and accurate results.

It is known from static calculations that buildings designed and manufactured without column-beam connections are exposed to high amounts of moment and shear forces, which causes irregularities in the load transfer in the carrier system in closed cantilevered sections. Since beam deficiencies cause frame discontinuity, the load transfer mechanism between the column and beam is also negatively affected. In closed cantilevered structures, horizontal load carrying capacity and ductility decrease, causing excessive displacements in the structure (Sarı, 2010).

Figure 3 shows the moment reduction in the column under the effect of cantilever or cantilever (Meral, 2018). In addition, the fact that the difference between the mass and center of rigidity values (eccentricity), which is vital for calculating the buckling of the building during an earthquake, is high and therefore it is prone to receive a high amount of damage, is a situation that should be evaluated separately. It is known that closed overhangs can increase the difference between the centers of gravity and rigidity of the building, and the resulting weight increase will negatively affect the seismic behavior of the building (Özmen, et al., 2011). It has been determined that closed cantilevers, especially on one side, increase the distance between the center of gravity and rigidity of the structure, and that the increase in weight affects the earthquake behavior of the structure. (Meral, 2018). Overhangs in buildings have positive and negative effects on building behavior. First of all, the increase in weight in the structure increases the construction period and causes an increase in displacement demands. In static analysis, the decrease in the moment and shear value carried by the column causes a decrease in the horizontal strength of the building (Özmen, et al., 2011). In his study in 2019, Öz examined existing low and medium height 2, 4 and 6-storey reinforced concrete buildings in 3 different groups according to the number of floors, and 24 earthquakes were affected separately on the buildings by using the SAP 2000 structural analysis program in the modeling. In each separate group, the results of the reference building were compared with the analyzes in case of closed exit.

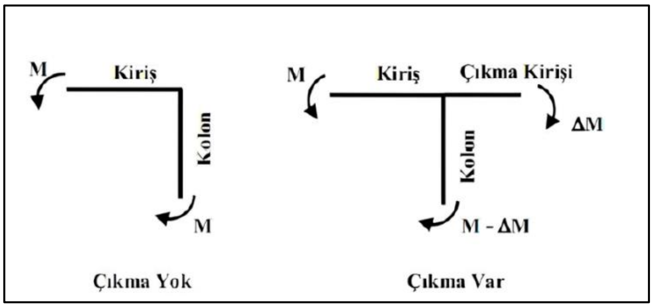

Figure 3: Moment Decrease in the Column in Case of Disconnection.

In her study in 2019, Meral carried out linear performance analyzes of 2, 4 and 7 story buildings designed on the formwork plans in Figure 2, without closed cantilever (reference building), with closed canopy with beams (1.5 m) and with closed cantilever without beams (1.5 m). It was determined by making analyzes in the non-existent time domain.

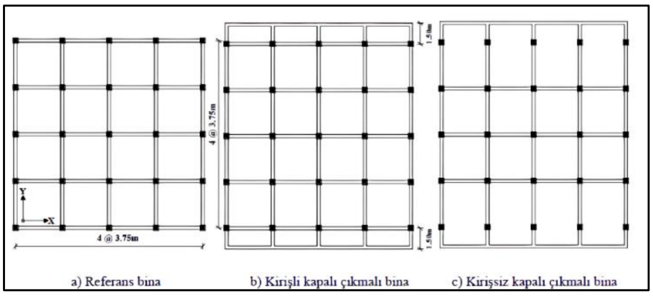

Figure 4: Formwork Plans of Reference and Cantilevered Buildings

3. Discussion

Listing the results obtained by the mentioned researchers in items will contribute to the formation of a final opinion on the subject. According to this the following results were obtained.

1. Base shear force ratio values of closed cantilevered buildings are generally lower than the values of other reference buildings (Öz, 2019).
2. The roof drift ratio of closed cantilevered buildings yielded higher results than other reference building values. Roof drift ratio values increased as the number of floors of the building increased (Öz, 2019).
3. In closed projection modeling, if there is no beam in the console section, it is seen that the earthquake performance is much more negative than the case with beams, especially due to large increases in demand values. (Özmen, et al., 2011).
4. Closed should come out of buildings of the period reference to buildings according to more to be a few accelerations of the record spectral accelerationof its value to fall reason since some results for closed should come out in buildings more low away demands was calculated (Meral, 2018).
5. Generally used earthquake acceleration records include beamless closed cantilevered buildings compared to other reference buildings and other reference buildings.closed beam should come out to buildings according to in terms of demand more negative it affects to say is possible (Meral, 2018).
6. As the number of floors increases, closed cantilevered buildings and reference buildings generally differ in terms of base shear force. The demand gap between the two is increasing. On the other hand, the difference in displacement demands between buildings is similar to 2- and 7-storey buildings. compared to 4 storey It is seen more in the building (Meral, 2018).

4. Conclusion

In line with the detailed analysis data obtained by different researchers, the design features of the structures damaged in earthquakes and the building static calculation values, it is understood that it has some positive and negative effects on buildings with partially-fully closed cantilever or cantilever features. Of course, it would not be correct to describe buildings with closed exits as completely faulty and defective without evaluating them with their features such as correct design, engineering services, workmanship and material quality, and an adequate control mechanism. However, when the positive and negative features of buildings with closed exits are compared, it is seen that their negative features are more. As positive effects; increase in the usage area of the building, an aesthetic appearance away from the appearance of the carrier system in the building, economic advantages, etc. can be sorted. However, since enclosed spaces directly threaten the safety of life and property, it is not even right to compare them with their positive aspects. The best step would be to ban or limit closed spaces in high-rise buildings, especially in cities in the 1st degree earthquake zone, such as Osmaniye province. In this direction;

- Although the Ministry of Environment, Urbanization and Climate Change has made many statements following the February 6 earthquakes and announced that closed areas will be banned up to a certain floor height (4 floors), it has recently stated that indoor areas can be allowed up to 7-8 floors.
- There are still some problems in the construction and inspection mechanism in our country,
- Failure to implement the concept of competent engineering,
- Insufficient quality of materials and workmanship,
- Design errors etc. situations,

Unfortunately, it is a harbinger of similar painful experiences in the future.

References

Adalier, K., & Aydingun, O. (2001). Structural engineering aspects of the June 27, 1998 Adana–Ceyhan (Turkey) earthquake, Engineering Structures; 23(4):343-355.

Dogangun, A. (2004). Performance of reinforced concrete buildings during the May 1 2003 Bingöl earthquake in Turkey, Engineering Structures, 26(6), 841-856.

Inel, M., Ozmen, H. B., & Bilgin, H. (2008). Re-evaluation of building damages during recent earthquakes in Turkey, Engineering Structures, 30, 412-427.

Meral, E. (2019). Kapalı Çıkmalı Betonarme Binaların Deprem Davranışının Değerlendirilmesi. Fırat Üniversitesi Müh. Bil. Dergisi 31(2), 309-318. https://dergipark.org.tr/tr/pub/fumbd/issue/48746/613265

Öz, S. B. (2019). Kapalı Çıkma Düzensizliğinin Betonarme Yapıların Sismik Davranışına Etkilerinin Doğrusal Elastik Olmayan Analizle Belirlenmesi.

Özmen, H. B. & İnel, M. & Çaycı, B. T. (2011). Kapalı Çıkma Düzensizliğinin Betonarme Yapıların Sismik Davranışına Etkilerinin Değerlendirilmesi. Yedinci Ulusal Deprem Mühendisliği Konferansı, İstanbul.

Özmen, H. B. & İnel, M. & Şenel, Ş. (2011). Mevcut Türk Betornarme Yapı Stoğu Dayanım ve Deformasyon Özellikleri. Yedinci Ulusal Deprem Mühendisliği Konferansı, İstanbul.

Sarı, H. (2010). Mevcut Betonarme Yapılardaki Tasarım Olumsuzluklarının Yapı Performansına Etkisi. https://acikerisim.sakarya.edu.tr/xmlui/bitstream/handle/20.500.12619/80509/T04575.pdf?sequence=1&isAllowed=y

Sezen, H., Whittaker, A. S., Elwood, K. J., & Mosalam, K. M. (2003). Performance of reinforced concrete buildings during the August 17, 1999 Kocaeli, Turkey earthquake, and seismic design and construction practice in Turkey. Engineering Structures, 25(1), 103-114.

URL_1: https://www.mta.gov.tr/v3.0/hizmetler/diri-fay-haritalari.

URL_2:https://www.ntv.com.tr/turkiye/konut-stokunun-yuzde-80ini-olusturan-cikmali-binalar-icin-risk-uyarisi,P31vUv0r9kWRwu4grHrT3g

URL_3:https://www.aa.com.tr/tr/asrin-felaketi/depremin-etkiledigi-osmaniyede-en-fazla-yikim-kent-merkezinde-gerceklesti/2868167

Yakut, A., Gulkan, P., Bakır, B. S., & Yılmaz, M. T. (2005). Re-examination of damage distribution in Adapazari: structural considerations. Engineering Structures, 27(7), 990-1001.

7th Intercontinental Geoinformation Days (IGD)

igd.mersin.edu.tr

A tool for basic surveying and geodetic calculations

Muaz Ayran [1], Veli İlçi [1]

[1] Ondokuz Mayis University, Faculty of Engineering, Department of Geomatics Engineering, Samsun, Türkiye

Keywords
Surveying
Geodesy
Education

Abstract

With the rapid development of computer and software technologies, many web-based and mobile applications have been developed in recent years. While these programs can occasionally solve extremely basic problems, they can also solve problems that require a great deal of labour and processing power effortlessly. In the field of geomatics engineering, there are some easy problems as well as challenging and work-intensive calculations. Although there are a few web-based and mobile applications in geomatics, these applications are designed to solve only some professional problems. In this study, a web-based tool has been developed to solve almost all problems encountered in surveying and geodetic applications. All coding is written in C# programming language. User-friendly graphical interfaces (GUI) are designed to be easy to use. Sample images have also been added to the modules so that users can better understand the modules. A total of 35 modules were developed, including 20 surveying and 15 geodetic problem solutions. These modules allow surveying and geodetic problems to be easily solved in both student and professional applications. Thus, it saves both labour and time.

1. Introduction

In recent years, the rapid development of computer, software and sensor technologies has led to rapid changes in many occupations. Geomatics engineering is also trying to keep up with this change as quickly as possible. Specifically, lengthy calculations and time are needed for expert accounting operations, which significantly strains colleagues and increases the probability of errors. Geomatics engineering has also experienced a rapid transformation regarding the solution of these problems. First of all, with the digitalization of calculators and the ability to write mini-programs, performing these complex and long-lasting calculations has become much easier and can be completed quickly. These programs have significantly facilitated and shortened surveyors' calculations in the field. The following change occurred with digitalising measuring devices such as total station and levelling instruments. These instruments initially consisted of purely mechanical systems, have become entirely digital and can automatically perform many desired calculations. In these instruments, calculation operations can be carried out by the mini processors and operating systems, and the desired information is produced by programs using raw measurement data.

Geomatics engineering requires the ability to perform many simple and complex calculations. Nowadays, some commercial programs such as Autocad (Url-1), Microstation (Url-2), and Netcad (Url3-) enable us to perform specific calculation transactions as well as project operations. In addition, there are web-based applications developed by institutions such as the National Oceanic and Atmospheric Administration (NGS) Geodetic Toolkit (Url-4) and General Directorate of Mapping of Turkey (Url-5), which allow us to perform only certain calculations. In addition, within the scope of a few academic studies, web-based tools have been developed to solve specific problems. In Cannavo and Palano (2011), a tool was developed in the Matlab program for Geodetic Reference Frame Identification. This tool calculates the velocity values of any point on the earth. There are also applications for similar purposes that can run on mobile devices and can be easily downloaded from the Apple Store and Google Play Store (Url-6). Delic et al. (2014) developed a mobile application using Augmented Reality (AR). The primary purpose of this application is to display geolocation data representing surrounding land parcels. In the application developed for educational purposes, instant communication with teachers is possible thanks to virtual reality technology. Bednarczyk and Janowski (2014) developed a mobile application for levelling.

* Corresponding Author

*(moazayran@gmail.com) ORCID ID 0009 – 0000 – 3413 – 358X
(veli.ilci@omu.edu.tr) ORCID ID 0000 –0002 –9485 – 874X

Cite this study

Ayran, M., & İlçi, V. (2023). A Tool for Basic Surveying and Geodetic Calculations. 7th Intercontinental Geoinformation Days (IGD), 7, 86-89, Peshawar, Pakistan

With the help of this program, measurements may be taken on the spot and sent to a distant server for processing and report preparation before being stored in a database. A mobile application was developed for coordinate conversion by Hussaini et al. (2023). Additionally, this application also shows instant locations on the map. In Solnyshkova and Dudysheva (2020), a hybrid learning environment, including an interactive virtual teaching tool and mobile application, was developed. As a result, the use of laboratory and field studies in architecture and civil engineering, thanks to the education provided by distance and mobile technologies, was discussed.

The studies above show that web-based or online tools have been developed to solve one or more specific problems. In this study, a tool has been developed that incorporates almost all of the calculations encountered in surveying and geodesy in geomatic engineering. Thanks to this tool, geomatic engineers and surveyors can calculate and check the calculation results to be made and also for our colleagues who forget some calculations or want to do them in a shorter time to access the results quickly.

2. Method

2.1. Coding

Today, many platforms such as C, Python, Java and Matlab are used to create web-based or mobile applications. C is one of the primary programming languages. C++ and C# languages are derived from the C language. Microsoft developed C# in the late 1990s to support the development of the .NET Framework. C# has a rich programming language and is also related to Java.

The entire tools and modules developed within the scope of this study were written in C#. Separate codes were written for all calculations, and a particular module was created for each calculation. All these modules are connected to a single primary tool. An example coding of the developed tool is shown in Figure 1.

```
int N = beta.Length - 2;
double ad1 = alfailk + SUM(beta) - ((N+2) * 200);
double ad = alfason;
double fbeta = ad1 - ad;
double fbetamax = 0.015 * Math.Sqrt(N + 2);
if (fbetamax < fbeta)
{
    double[] h = { 0 };
    System.Windows.Forms.MessageBox.Show("fbeta > fbetamax");
    return h;
}
double hata = -fbeta / (N + 2);
double[] alfa = new double[N+3];
alfa[0] = alfailk;
alfa[N] = alfason;
for (int i = 1; i < alfa.Length - 1; i++)
{
    alfa[i] = alfa[i - 1] + beta[i-1] + hata;

    if (alfa[i] > 200 && alfa[i] < 400)
    {
        alfa[i] = alfa[i] - 200;
    }
    else if (alfa[i] < 200)
    {
        alfa[i] = alfa[i] + 200;

    }
    else if (alfa[i] > 400 && alfa[i] < 600)
    {
        alfa[i] -= 200;
    }
    else if (alfa[i] > 600)
    {
        alfa[i] = alfa[i] - 600;
    }
}
double[] deltay = new double[N+1];
double[] deltax = new double[N+1];
for (int i = 0; i < deltay.Length ; i++)
{
     deltay[i] = S[i] * Math.Sin(alfa[i+1] * Math.PI / 200 );
     deltax[i] = S[i] * Math.Cos(alfa[i+1] * Math.PI / 200 );
}
```

```
double stoplami = SUM ( S );
double deltaytoplami = SUM (deltay);
double deltaxtoplami = SUM (deltax);
double fy = (YN3 - YN2) - deltaytoplami;
double fx = (XN3 - XN2) - deltaxtoplami;
double S1 = Math.Sqrt(Math.Pow(deltaytoplami, 2)
    + Math.Pow(deltaxtoplami, 2));
double fq = 1 / S1 * (fy * deltaxtoplami - fx * deltaytoplami);
double fqmax = 0.05 + 0.15 * Math.Sqrt(S1 / 1000);
if (fqmax < fq)
{

    double[] h1 = { 0 };
    System.Windows.Forms.MessageBox.Show("fq > fqmax");
    return h1;
}
double fl = 1 / S1 * (fy * deltaytoplami - fx * deltaxtoplami);
double flmax = 0.05 + 0.04 * Math.Sqrt(N+2);
if (flmax < fl)
{

    double[] h2 = { 0 };
    System.Windows.Forms.MessageBox.Show("fl > flmax");
    return h2;
}
double yhatadagtimi = fy / N;
double xhatadagtimi = fx / N;
double[] YP = new double[N+1];
double[] XP = new double[N+1];
YP[0] = YN2;
XP[0] = XN2;
for (int i = 1; i < YP.Length; i++)
{
     YP[i] = YP[i-1] + deltay[i-1] + yhatadagtimi;

     XP[i] = XP[i-1] + deltax[i-1] + xhatadagtimi;
}
double[] Q = new double[YP.Length + XP.Length] ;
YP.CopyTo(Q, 0);
XP.CopyTo(Q, YP.Length);

for (int i = 0; i < Q.Length; i++)
{
    Q [i]= Math.Round(Q[i], 3);
}
return Q;
```

Figure 1. Sample code for the built tool

2.2. Design and Implementations

The developed software consists of a leading tool and modules that can be accessed by clicking on this tool. The mathematical calculations in each module were created using the references in the relevant section below and tested using sample data. Modules are supported with figures so that users can understand the variables given in the modules. The developed web-based tool is divided into two primary parts.

The first part consists of 7 main and 20 sub-modules related to surveying calculations (Figure 2). The first module is related to unit conversion. This module allows easy conversion between angle units (degree, grad and radian) (İnal and Baybura, 1998; Yakar et al., 2019a). The second module addresses processes related to fundamental calculations (İnce and Türen, 2016; Yakar et al., 2019b). This module gives the solutions to four fundamental calculations in a single interface. The third module is related to the traverse calculations (Bektas, 2016; Yakar et al., 2019c). This module covers three types of traverse solutions: open traverse, closed connecting traverse, and closed traverse. The other module includes intersection and resection calculations (Atasoy, 2014). The fifth module was created for reduction to ground calculations (Atasoy, 2014). The sixth module includes setting out calculations: setting out with the polar coordinate method, setting out of the road, vertical setting out, and trigonometric setting out (Baykal, 2009a; Baykal, 2009b; Chilani and Wolf, 2012). Calculations for levelling are given in the seventh section: open levelling traverse, closed connecting levelling traverse, closed levelling traverse, vertical angle calculation, trigonometric levelling, and tower height calculation (Yakar et al., 2020).

The second part consists of 3 main and a total of 15 sub-calculation modules related to geodesy (Figure 3). The first module includes calculations made on the sphere surface: calculations on sphere, orthodrome and loxodrome curves, fundamental calculations on sphere, conversions in between cartesian and geographic coordinates, conversion of cartesian coordinates into geographic coordinates, conversion of geographic coordinates into cartesian coordinates, conversion of geographic coordinates into Gauss-Kruger coordinates, conversion of Gauss-Kruger coordinates into geographic coordinates, and spherical triangle calculation (Bektaş, 2005). Geodetic computations performed on the ellipsoid are given in the second section: conversion of geographic coordinates into cartesian coordinates, conversion of cartesian coordinates into geographic coordinates, and UTM projection (Bektaş, 2021; Kahveci et al., 2021). The last module enables conversion operations between different ITRF datums (Url-7).

3. Conclusion

Geomatics engineering is a branch of science that requires the solution of many numerical problems. Solving these problems sometimes requires very long operations and can take a long time. With the web-based tool implemented in this study, many calculations related to surveying and geodesy that our colleagues encounter can be easily solved. The program's user-friendly interface and sample images make it easy to understand and use. It is planned to develop a mobile application containing these calculations and make it available to our colleagues in the future.

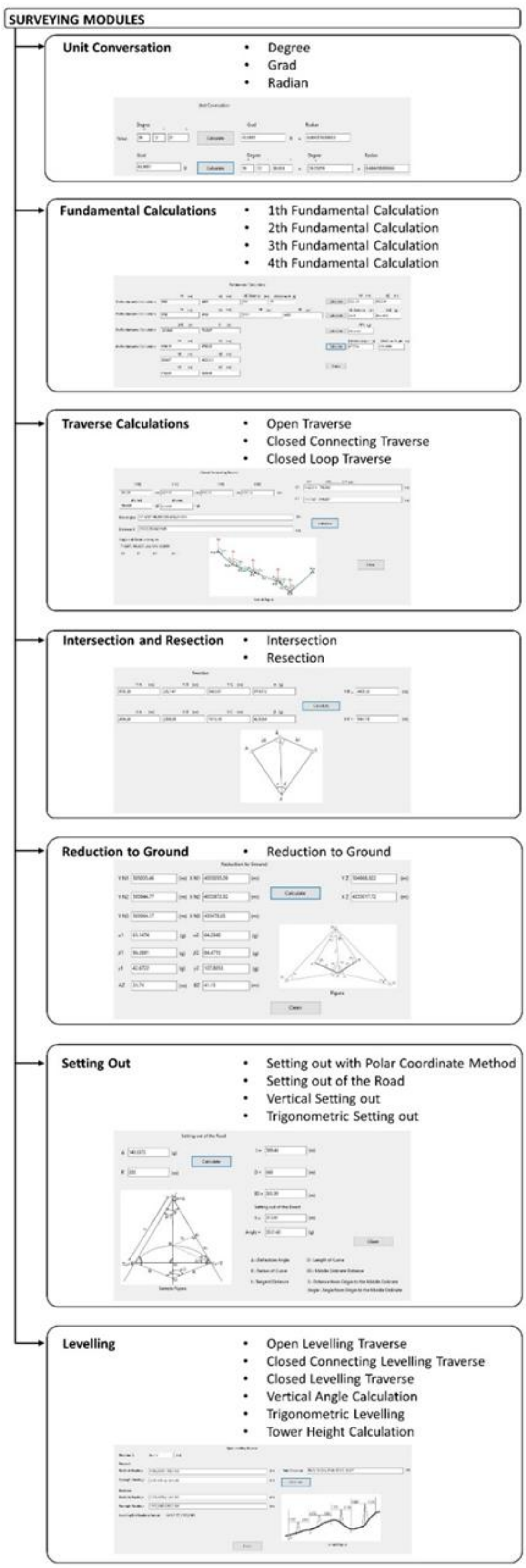

Figure 2. Surveying Modules

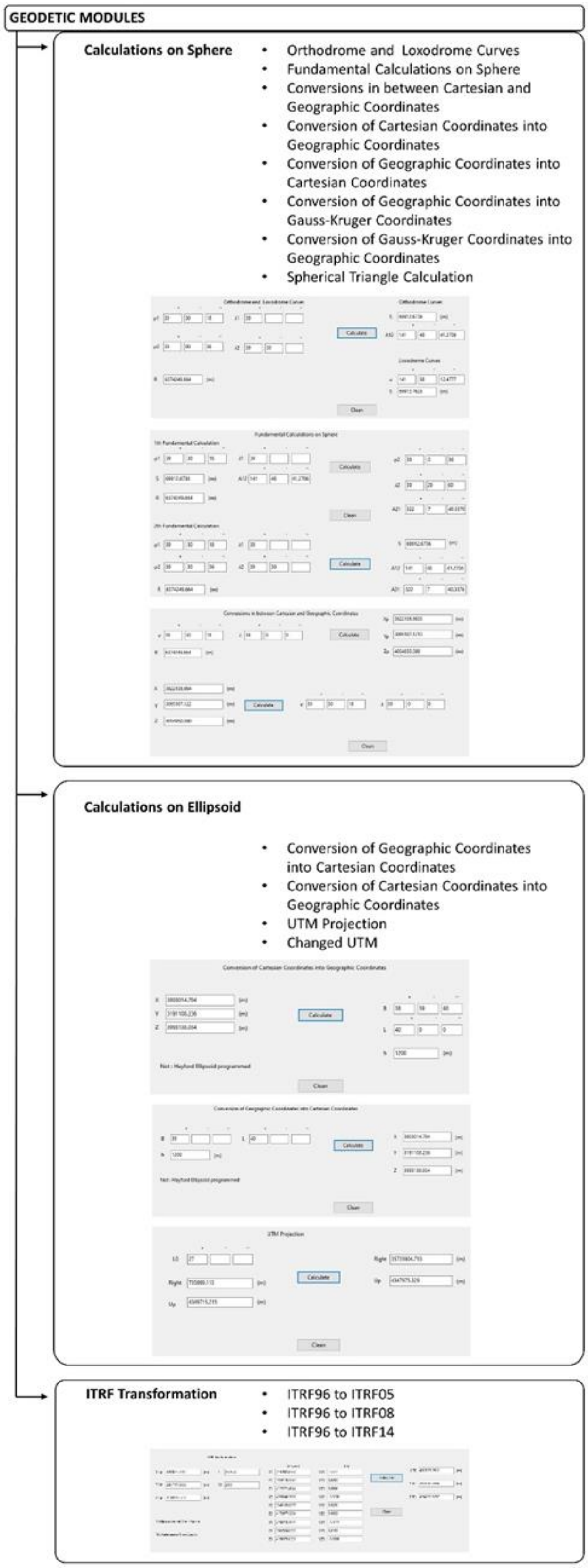

Figure 3. Geodetic Modules

References

Atasoy, V. (2014). Arazi Ölçmeleri, Ekin Basım, Yayın Dağıtım, Bursa, Turkiye.

Baykal, O. (2009a). Mühendislik Ölçmeleri – I, Kara ve Demir Yollarında Geçki Geometrisi Tasarımı ve Aplikasyonu - Metinler, Birsen Yayınevi, İstanbul.

Baykal, O., Tari, E. and Coşkun, Z. (2009b). Mühendislik Ölçmeleri – I, Kara ve Demir Yollarında Geçki Geometrisi Tasarımı ve Aplikasyonu – Sayısal Örnekler, Birsen Yayınevi, İstanbul.

Bednarczyk, M. & Janowski, A. (2014). Mobile Application Technology in Levelling. Acta Geodyn. Geomater, 11(2), (174), 153-157. https://doi.org/10.13168/AGG.2014.0004

Bektaş, S. (2005). Jeodezik Hesap: Düzlemde ve Küre Yüzeyinde Jeodezik Hesaplamalar, Ondokuz Mayıs Üniversitesi, Samsun, Turkiye.

Bektaş, S. (2016). Pratik Jeodezi: Ölçme Bilgisi, Ondokuz Mayıs Üniversitesi, Samsun, Turkiye.

Bektaş, S. (2020). Ölçme Bilgisi: Topoğrafya, Nobel Akademik Yayıncılık, Ankara, Turkiye.

Bektaş, S. (2021). Jeodezi-II: Elipsoid Yüzeyinde Uygulamalar, Atlas Akademi, Konya, Turkiye.

Cannavo, F. & Palano, M. (2011), PlatEMotion: a Matlab Tool for Geodetic Reference Frame Definition, Istituto Nazionale di Geofisica e Vulcanologia.

Chilani, C. D. & Wolf, P. R. (2012). Elementary Surveying: An Introduction to Geomatics. Pearson Education, Inc., Upper Saddle River, New Jersey.

Delic, A., Domancic, M., Vujevic, P., Drljevic, N., & Boticki, I. (2014). AuGeo: A geolocation-based augmented reality application for vocational geodesy education, 56th International Symposium ELMAR-2014, 10-12 September 2014, Zadar, Croatia.

Hussaini, A., Huang, L., & Tang, K. K. W. (2023). Developing Coordinate Conversion Mobile Application for Geomatics Education. 2023 3rd International Conference on Advanced Research in Computing (ICARC). 23-23 February 2023, Faculty of Computing Sabaragamuwa University of Sri Lanka. https://doi.org/10.1109/ICARC57651.2023.10145625

İnal, C. & Baybura, T. (1998). Ölçme Bilgisi 1-2: Problemleri ve Açıklamalı Çözümleri, Lecture Notes No :32, Selçuk Üniversitesi, Konya, Turkiye.

İnce, H. & Türen, Y. (2016). Meslek Yüksekokulları için Haritacılıkta Mesleki Hesaplamalar, Trakya üniversitesi, Edirne.

Kahveci, M., Tuşat, E. & Doğanalp, S. (2021). Jeodezik Koordinat Sistemleri: Teori-Uygulama, Nobel Akademik Yayıncılık, Ankara, Turkiye.

Solnyshkova, O. & Dudysheva, E. (2020). Mobile Technologies in Blended Learning of Engineering Students in Digital Measurements on Geodetic Equipment. 2020 VInternational Conference on Information Technologies in Engineering Education (Inforino), April 14-17, 2020, Moscow, Russia.

Url-1: AutoCad (2023). (Access date: 18.10.2023). https://www.autodesk.com.tr/

Url-2: MicroStation (2023). (Access date: 18.10.2023). https://www.bentley.com/software/microstation/

Url-3: netcad (2023). (Access date: 18.10.2023). https://www.netcad.com/

Url-4: NGS (2023). (Access date: 18.10.2023). https://www.ngs.noaa.gov/TOOLS/

Url-5: Tusaga-Aktif (2023). (Access date: 18.10.2023). https://www.tusaga-aktif.gov.tr/

Url-6: Kocaman, H. (2023). (Access date: 18.10.2023) https://www.hakankocaman.com/tr/kocaman

Url-7: International Terrestrial Reference Frame ITRF, (2023). (Access date: 18.10.2023) https://itrf.ign.fr/en/solutions/transformations

Yakar, M., Ünel, F. B., & Kuşak, L. (2019a). Ölçme Bilgisi I, Atlas Akademi., Selçuklu, Konya.

Yakar, M., Ünel, F. B., Kuşak, L., & Çelik, M.Ö. (2019b). Temel Ödevler, Atlas Akademi., Selçuklu, Konya.

Yakar, M., Ünel, F. B., Kuşak, L., & Çelik, M.Ö. (2019c). Poligon Hesabı, Atlas Akademi., Selçuklu, Konya.

Yakar, M., Kuşak, L., Ünel, F. B., & Kanun, E. (2020). Nivelman Hesabı, Atlas Akademi., Selçuklu, Konya.

7th Intercontinental Geoinformation Days

igd.mersin.edu.tr

Time series analysis of Turkish National Sea Level Monitoring System (TUDES) level data for Amasra Station

Ahsen Çelen*[1], Yasemin Şişman [1]

[1]Ondokuz Mayıs University, Faculty of Engineering, Department of Geomatics Engineering, Samsun, Türkiye

Keywords
Time series analysis
Sea level
TUDES
Minitab

Abstract

The observation and prediction of sea level are crucial for various reasons including the vertical datum determination, crustal movement forecasting, oceanographic modeling, and coastal infrastructure planning. In Turkey, a sea level monitoring system has been established by the General Directorate of Mapping and aims to measure sea level. Through the Turkish National Sea Level Monitoring System (TUDES), sea level is monitored using data collected at 20 tide gauge stations at 15-minute intervals. Time series analysis is considered a highly suitable modeling and forecasting method for data that is periodically measured. In this study, time series analysis models including ARIMA, SARIMA, and Holt-Winter's methods were applied using data from the Amasra tide gauge station within the TUDES for the year 2019. Additionally, a prediction for January 2020 at the same station was performed. The results were compared with the measured tide gauge data to assess the performance of the models. Evaluation criteria included the Mean Absolute Percentage Error (MAPE) for the Holt-Winter's method and the corrected Akaike Information Criteria (AICc) for the ARIMA and SARIMA models. The SARIMA (3,0,0) (0,2,2) model with an AICc value of -1307.83, indicating a seasonality of 12, was observed to be the best-performing model.

1. Introduction

The main objectives of geodesy are to define the shape and size of the earth and to obtain data on the spatial information of points (Vanícek and Krakiwsky, 2015). Due to the inherent impracticality of directly performing mathematical calculations for the Earth's shape, various reference surfaces are employed to acquire positional information. Reference surfaces define the parameters necessary for the mathematical representation of geometric and physical quantities (Drewes, 2009). Depending on the scope and purpose of the study, different reference surfaces such as the sphere, ellipsoid, and geoid can be selected (Jekeli, 2016).

The geoid is an assumed equipotential water surface that extends beneath the continents (Sansò & Sideris, 2013). This equipotential surface used for vertical referencing can be determined through the long-term measurements of the average sea level. The average sea level is defined as the vertical datum (Altamimi et al., 2010). Therefore, the significance and analysis requirement of sea level measurements emerge.

The sensitivity of satellite data over the past few decades, is approximately +3mm per year (Cazenave et al., 2014). For purpose of tracking that change, there is global cooperation to measure sea level. The Intergovernmental Oceanographic Commission (IOC), a subsidiary of UNESCO, addresses this issue on a global scale. The need for long-term monitoring of sea level changes with globally distributed tide gauge stations led IOC to establish the Global Sea Level Observing System (GLOSS). The contact organization of the system in Turkey is the General Directorate of Mapping (https://tudes.harita.gov.tr/).

To extract reliable information from data sets requiring long-term observations of sea level, statistical analysis is necessary. Time series analysis, a type of statistical analysis, is a powerful option for examining sea level data. Time series analyses allow for understanding the stochastic mechanisms of the measured data and gaining insights into future predictions based on past data (Cryer and Chan, 2008).

In this study, the time series analysis in sea level data for the year 2019 at the Amasra tide gauge station was examined using ARIMA, SARIMA, and Holt-Winter's time series analysis methods, and forecasting were made for January 2020. The obtained forecasted values were compared with the actual data, and the best model was observed to be SARIMA (3,0,0) (0,2,2) with a seasonality of 12.

* **Corresponding Author**

*(e-mail) ORCID ID xxxx – xxxx – xxxx – xxxx
(e-mail) ORCID ID xxxx – xxxx – xxxx – xxxx

Cite this study

Çelen, A., & Şişman, Y. (2023). Temporal Analysis of Turkish National Sea Level Monitoring System (TUDES) Level Data (Amasra Example). Intercontinental Geoinformation Days (IGD), 7, 90-93, Peshawar, Pakistan

2. Material and Methods

2.1. Material

The task of monitoring sea level in Turkey is conducted under the General Directorate of Mapping through the Turkish National Sea Level Monitoring System (TUDES) system, there are 20 GNSS-integrated radar sensor tide gauge stations distributed along the coasts of Turkey and the Turkish Republic of Northern Cyprus, adhering to GLOSS standards. These stations record measurements at 15-minute intervals, capturing not only sea level but also meteorological parameters affecting sea level changes, such as atmospheric pressure, wind speed, humidity, and temperature (https://tudes.harita.gov.tr/).

For the purposes of this study, TUDES data was provided by the General Directorate of Mapping, and the sea level data for the Amasra tide gauge station was accessed through the website https://tudes.harita.gov.tr/.

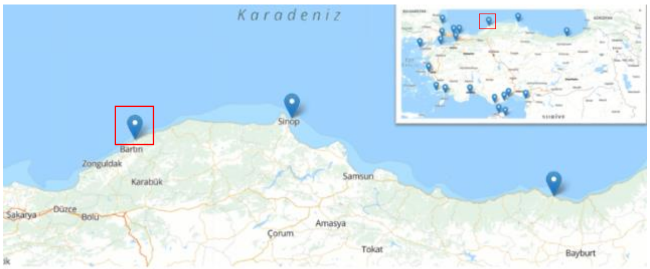

Figure 1. Study area

In the year 2019, a total of 34,921 observation units were obtained for the Amasra tide gauge station. To organize and these data, the code snippet was written using the Python programming language, which calculates daily averages for each day: The organized data was examined for general statistical information using the Minitab program, and tests for normality and outliers were conducted.

2.2. Method

Time series analysis examines the statistical distributions of periodic data within a specific time interval and consists of Autoregressive (AR) and Moving Average (MA) models. In AR models, the dependent variable is considered as a function of its past values. In the AR(p) model, the Zt value is represented as a linear function of the weighted sum of the series' past p values and error terms, as shown in the Equation 1.

$$Zt = \mu + \phi 1\ Zt\text{-}1 + \phi 2\ Zt\text{-}2 + \ldots + \phi p\ Zt\text{-}p + Zt \qquad (1)$$

In this equation, Zt-1, Zt-2, .., Zt-p represent past observed values, μ represents the mean, Zt represents the error term, and φ1, φ2, ..., φp represent the coefficients of past observations. The goal in the model is to obtain the model order that makes the sum of squared errors zero and determine the unknown coefficients (Kara, 2009).

In the MA method, the aim is to reduce the effects of momentary, erroneous, and outlier data on the overall data. There are various types of moving average (MA) methods, such as Simple, Cumulative, Weighted, and Exponential. The equation 2 for the MA method is represented as:

$$Zt = \mu + \alpha t - \theta 1\ \alpha\ t\text{-}1 - \ldots - \theta q\ \alpha t\text{-}q \qquad (2)$$

Here, θ1, ..., θq represents the coefficients of error terms, and αt, α t-1, ..., αt-q represent the error terms. The right side of the equation is expressed in terms of a meaningful q number of errors. The error term in the equation has a mean of zero and a constant variance (Kara, 2009).

2.3.1. ARIMA

It is a method used for performing univariate time series analysis and forecasting, also known as Box-Jenkins models. It represents an integrated model that incorporates operations such as MA, autocorrelation, and differencing. In the model expressed as ARIMA (p, d, q), p denotes the degree of the autoregressive (AR) model, d represents the differencing operation, and q indicates the degree of the MA model (Cryer, 1986). The model is represented as shown in Equation 3.

$$y_t = \alpha_0 + \sum_{t=1}^{p} \alpha_t (y_{t-1} - \mu) + \varepsilon_t \qquad (3)$$

Here, α_0 and α_t represent autoregressive parameters to be estimated, and ε_t represents the random errors with zero mean and finite variances.

2.3.2. SARIMA

For time series data that exhibit seasonality and are non-stationary, ARIMA models often do not yield satisfactory results. Therefore, SARIMA models, which account for seasonality, are employed. In SARIMA models, denoted as SARIMA (p, d, q) (P, D, Q), in addition to the parameters used in ARIMA (p, d, q), there are additional parameters P, D, and Q that represent the seasonal AR order, differencing operation, and seasonal moving average order. These models take into consideration both the non-seasonal and seasonal components, offering a more comprehensive approach to time series modeling (Shumway and Stoffer, 2017).

2.3.3. Holt-Winter's

The Holt-Winter's method is one of the exponential smoothing techniques that involves a three-equation structure, accounting for level, trend, and seasonality. The seasonal equation can be formulated in two ways: multiplicative when trend and seasonality move together, and additive when they do not. (Hafid and Al-maamary, 2011). The model is represented as shown in Equation 4.

$$\text{Level: } L_t = \alpha\frac{Y_t}{S_{t-s}} + (1-\alpha)(L_{t-1} + m_{t-1});$$
$$\text{Trend: } m_t = \beta(L_t - L_{t-1}) + (1-\beta)m_{t-1}$$
$$\text{Seasonal: } S_t(t) = \gamma\frac{Y_t}{L_t} + (1-\gamma)\, S_{t-s}(t) \qquad (4)$$
$$\text{Forecast: } F_{t+\tau} = (L_t + m_t q)\, S_{t-s}(t)$$

Here; α, β and γ are smoothing constants, t is the time period, Y_t is the actual observed values, s is the length of seasonality, L_t is the level component, m_t is the trend component, S_t is the seasonal component and $F_{t+\tau}$ is the forecast for τ periods ahead.

3. Application and Results

For all modeling, the 2021 version of the Minitab program was employed. The model evaluation criterion is based on AICc. AICc is essentially AIC with an extra penalty term for the number of parameters. The smaller AIC is, the better the model fits the data (Minitab, 2021). The AIC is an information-theoretic indicator rooted in Kullback-Leibler Divergence, primarily assessing the information loss incurred by a given model. Consequently, the AIC criterion operates on the premise that the less information a model forfeits, the higher its quality (Kasali and Adeyemi, 2022). On the other hand, the BIC criteria are founded on Bayesian theory, with the goal of maximizing a model's posterior probability given the available data. The Bayesian information criterion (BIC) serves as a pivotal tool in the realm of statistics for model selection from a finite set of options. It maintains a close relationship with the Akaike information criteria and is partly reliant on the likelihood function (AIC) (Kasali and Adeyemi, 2022). Here are the AICc and BIC formulas (Minitab, 2021):

$$\text{AIC} = 2[(\rho + 1) - L_c]\ ;\ L_c(y_i\, \mu_i\, \Phi) = \sum_{i=1}^{n} l_i$$
$$l_i = \ln(f(y_i, \widehat{\mu_i}, \Phi))\ ;\ y_i \ln(\widehat{\mu_i}) + (m_i -)\ln(1 - \widehat{\mu_i})$$

Here; p: the regression degrees of freedom; L_c: the log-likelihood of the current model; y_i: the number of events for the i^{th} row; m_i: the number of trials for the i^{th} row; Φ: 1, for binomial models; $\widehat{\mu_i}$: the estimated mean response of the ith row

$$\text{AICc} = -2\ln(\text{Likelihood}) + 2p + \frac{2p(p+1)}{n-p-1}$$
AICC is not calculated when $n - p - 1 \leq 0$
$$\text{BIC} = -2\ln(\text{Likelihood}) + p\ln(n)$$

The ARIMA model that does not account for seasonality was tested. The optimal parameters for the model were calculated with the assistance of the program, resulting in ARIMA (2,0,2) (Figure 3).

The SARIMA model takes seasonality into account, all combinations of the following values were tested: “3, 4, 12” for seasonality; “0, 1, 2” for differencing; “0, 1, 2” for seasonal differencing. According to the AICc criterion, the models that provided the best results for SARIMA (0,1,0) (1,2,3), SARIMA (0,0,2) (3,2,0), SARIMA (0,1,0) (1,2,3), SARIMA (3,0,0) (0,2,2) and SARIMA (1,2,2) (3,1,0) were given Figure 4a and 4b and Figure 4c according to seasonality “ 3 4 and 12”

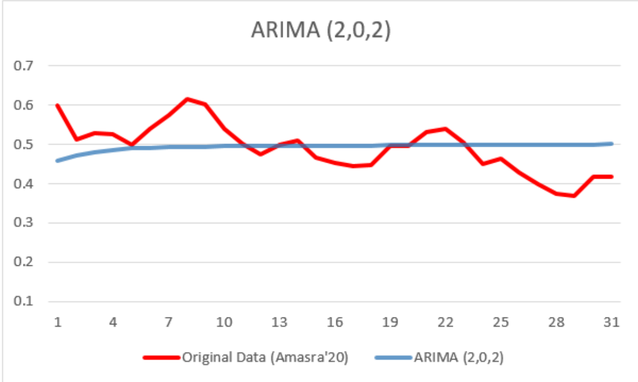

Figure 3. ARIMA (2,0,2) model

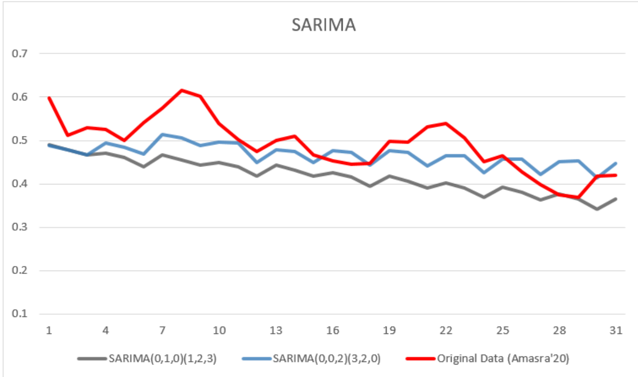

Figure 4a. SARIMA (0,1,0) (1,2,3) and SARIMA (0,0,2) (3,2,0) models

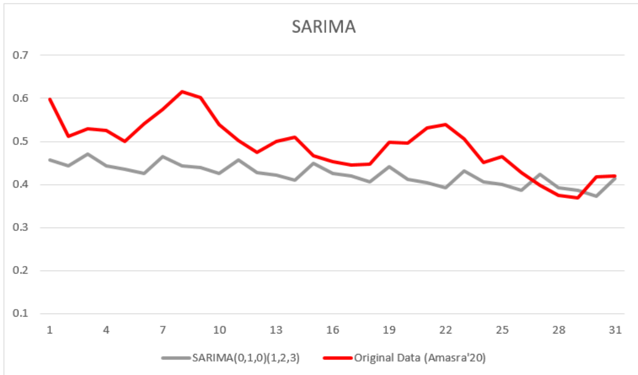

Figure 4b. SARIMA (0,1,0)(1,2,3) model

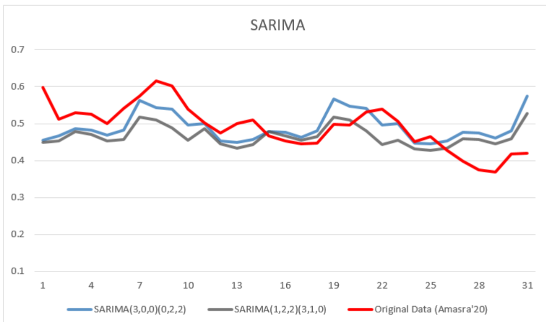

Figure 4b. SARIMA (3,0,0) (0,2,2) and SARIMA (1,2,2) (3,1,0) models

The model performance summaries of ARIMA and SARIMA models were made according to Mean Square Error (MSD), AICc and BIC values, (Table 1).

Table 1. Model Summaries

Model	MSD (Mean Sq. Dev.)	AICc (-)	BIC (-)
ARIMA(2,0,2)	0.0007982	1553.29	1530.13
SARIMA(0,1,0)(1,2,3)$_3$	0.0010915	1389.50	1370.26
SARIMA(0,0,2)(3,2,0)$_3$	0.0010598	1407.44	1384.37
SARIMA(0,1,0)(1,2,3)$_4$	0.0009654	1420.31	1401.10
SARIMA(3,0,0)(0,2,2)$_{12}$	0.0010689	1307.83	1285.09
SARIMA(1,2,2)(3,1,0)$_{12}$	0.0010199	1365.45	1338.75

Here what the abbreviations represent:
MSD: Mean Square Deviation

Finally, the Holt-Winter's method was applied to the data. Sequentially, combinations of α, β, and γ parameters ranging from "0.1 to 0.9" were tested for seasonality values of "3, 4, and 12". The best result was obtained with a seasonality of "4" and α, β, γ parameters set to "0.4", which was adopted in the additive model.

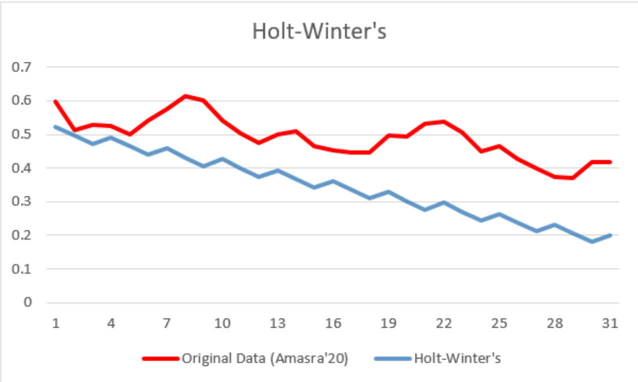

Figure 5. Holt-Winter's model

The obtained outputs to evaluate the model are as follows:

Table 1. Holt-Winter's model accuracy measures

Measures	MAPE	MAD	MSD
Values	6.29203	0.03136	0.00161

MAPE: Mean Abs. Per. Error; MAD: Mean Abs. Dev.

4. Conclusion

In the scope of this study, time series analysis models, including ARIMA, SARIMA, and Holt-Winter's methods, were applied using the 2019 data from the Amasra tide gauge station within the TUDES system. Furthermore, forecasting was made for the same station for the month of January 2020. The obtained results were compared with the measured tide gauge data, and the model's performance was assessed. Evaluation criteria included the MSD for the Holt-Winter's method and the AICc for the ARIMA and SARIMA models. The best model observed was the SARIMA (3,0,0) (0,2,2) model with an AICc value of "-1307.83", indicating a seasonality of "12". And finally, the MSD value of SARIMA (3,0,0) (0,2,2)$_{12}$ method was compared with the MSD value of the Holt Winter's method, revealing that the SARIMA model with the value of "0.0010689" outperformed the Holt-Winter's method with the value of "0.00161".

At the light of these explanation and applications it is said that the SARIMA (3,0,0) (0,2,2)$_{12}$ model is more suitable for these sea level data.

Acknowledgement

The authors thank the General Directorate of Mapping for providing the sea level data.

References

Al-Hafid, Majed, S. (2012). Short term electrical load forecasting using holt-winters method. Al-Rafidain Engineering, 20. 15-22. https://doi.org/10.33899/rengj.2012.63377.

Blewitt, G., Altamimi, Z., Davis, J., Gross, R., Kuo, C. Y., Lemoine, F. G., ... & Zerbini, S. (2010). Geodetic observations and global reference frame contributions to understanding sea-level rise and variability. Understanding sea-level rise and variability, 256-284.

Cryer, J. D. (1986). Time Series Analysis.

Cryer, J. D., & Chan, K. S. (2008). Time Series Analysis with Applications in R (2nd ed.). New York: Springer. http://dx.doi.org/10.1007/978-0-387-75959-3

Drewes, H. (2009). Reference Systems, Reference Frames, and the Geodetic Datum - Basic Considerations. 3-9.

Jekeli, C. (2016). Geometric Reference Systems in Geodesy. 2016 Edition. Ohio State University. USA.

Kara, T. (2009). Sabit GPS istasyonlarında zaman serileri analizi. Yüksek Lisans Tezi, Selçuk Üniversitesi, Konya.

Minitab, LLC. (2021). Minitab. Retrieved from https://support.minitab.com/en-us/minitab/21/help-and-how-to/statistical- modeling/doe/how-to/factorial/analyze-binary-response/methods-and-formulas/model-summary/

Sansò, F., & Sideris, M. (2013). Geoid Determination: Theory and Methods. 10.1007/978-3-540-74700-0.

Shumway, R. H. & Stoffer, D. S. (2017) Time Series Analysis and Its Applications: With R Examples. Fourth Edition, Springer Texts in Statistics, Springer, Cham.

Torge, W., Müller, J., & Pail, R. (2023). Geodesy.

Türkiye Ulusal Deniz Seviyesi İzleme Sistemi. (t.y.). Deniz seviyesi gözlemleri. Harita Genel Müdürlüğü. https://tudes.harita.gov.tr/Portal /Index/32?lang=tr/Deniz%20Seviyesi%20G%C3% Gözlemleri.

Vanícek, P., Krakiwsky, E.J. (2015). Geodesy: The concepts (Revised 2. Edition). North-Holland, Amsterdam. Elsevier.

7th Intercontinental Geoinformation Days

igd.mersin.edu.tr

Examining PPP accuracy in relation to altitude

Emre Akman[*1], **Veli İlçi**[1]

[1]Ondokuz Mayis University, Engineering Faculty, Department Geomatics Engineering, Samsun, Turkiye

Keywords
PPP
Altitude
GNSS

Abstract

Online PPP services are increasing daily due to their user-friendly interfaces, quick turnaround times, the ability to evaluate data from a single GNSS receiver, and their cost-free nature. However, the veracity of the data provided by these services needs to be verified. This study examined the position and height accuracy variation provided by PPP services based on benchmark point altitudes. For this purpose, seven measurement points were established every 200 meters, starting from the sea level. Four-hour static GNSS observations were carried out at each point, and these data were first evaluated with the static post-processing method to obtain the known positions of the points. The static observations were then submitted to the popular online PPP services Trimble-RTX, AUSPOS, and CSRS-PPP, and the received position and height data were compared to the point's known coordinates. When the results were analyzed, it was found that changes in the position data were in the order of cm, while changes in the height data were in the order of 1-2 dm, depending on the altitude of the measurement point.

1. Introduction

Satellite-based positioning systems are evolving with technological developments. The first global positioning system, GPS (Global Positioning Systems), was first used for military purposes. Increasing demands from civilians and the emergence of broad application areas have made satellite systems available for all communities. Following these developments, the concept of global navigation satellite systems (GNSS) emerged as many countries established their positioning systems (GLONASS, GALILEO, BeiDou, QZSS, IRNSS) (Alkan, 2015). Because the absolute positioning approach, which enables position determination with a single GNSS receiver, cannot deliver the required position accuracy, the usage of relative positioning methods has risen.

The developed real-time kinematic (RTK) solution technique uses rover and reference GNSS receivers and provides cm-level position accuracy with an initialization time of a few seconds. The positioning accuracy of this technique varies depending on the base length between the rover and the reference receivers. Position accuracy declines as base length increases due to tropospheric, ionospheric and satellite orbit errors. In addition, carrier phase ambiguities cannot be eliminated sufficiently on long bases (>20km) (İlçi, 2019). Calculated corrections are transmitted through an internet connection or radio link. When correction information is sent via a radio-link connection, the base length is limited to 10-20 km, but this range reaches up to hundreds of km when transmitted via the internet (Alçay vd., 2021).

Due to these drawbacks in the RTK technique, a network-based RTK (NRTK) technique has been developed with continuously operating reference stations (CORS). Today, NRTK systems established by many countries and organizations are actively operating. Correction data is generated in each NRTK system by simulating orbital and atmospheric errors, yielding position data down to the centimeter level (Yurdakul, 2021). In addition to its many advantages, NRTK has disadvantages, such as initial installation cost, complex software and hardware requirements and the need for a GSM connection (Alkan vd., 2020). The system becomes utterly unusable if the work area is outside the GSM operator's coverage (İlçi vd., 2016). With such drawbacks, users seek new, accurate, faster position information acquisition techniques.

The PPP (Precise Point Positioning) technique improves the data collected from only a single GNSS receiver with correction information derived from precise satellite orbit and clock data, products of organizations such as IGS, JPL, and CODE. This technique does not require a radio or internet connection. Position accuracy in the order of centimeters is achieved by processing the observation data gathered in static or kinematic modes with the correction information

* **Corresponding Author**

*(emre.akman.hrt.muh@gmail.com) ORCID ID 0009 – 0008 – 5369 – 4145
(veli.ilci£omu.edu.trl) ORCID ID 0000 – 0002 – 9485 – 874X

Cite this study

Akman, E., & İlçi, V. (2023). Examining PPP accuracy in relation to height. Intercontinental Geoinformation Days (IGD), 7, 94-97, Peshawar, Pakistan

supplied by the services. While the PPP technique offers several benefits, including low cost, easy usability, and position data in a global datum, it also has drawbacks, including long convergence times and access to precise satellite ephemeris data (Alkan, 2020).

In addition to PPP software such as GRAFNAV, PANDA, BERNESE, etc., used for post-process evaluation, there are web-based online services such as CSRS, AUSPOS, TRIMLE-RTX, OPUS, APPS, SCOUT, GAPS, magicGNSS, etc. (Özdemir vd., 2019). AUSPOS, OPUS, and SCOUT services determine the position with a relative method, whereas CSRS-PPP, APPS, GAPS, and magisGNSS services determine the position with an absolute method. Services that employ the absolute method calculate the corrections by obtaining sensitive satellite information from other services, such as IGS, while services that use the relative method make calculations based on IGS or local CORS station coordinates close to the study area (Alkan vd., 2017).

In this study, the accuracy of position and height coordinates from widely used online PPP services were investigated depending on the altitude of the measurement points. Static observation data collected from benchmark points with different altitudes were submitted to TRIMBLE-RTX, AUSPOS, and CSRS-PPP services, and the delivered coordinates were compared with static post-processing outcomes.

2. Method

2.1. Trimble CenterPoint RTX post-processing service

Trimble's CenterPoint RTX (real-time eXtended) service was created in 2011 and made available in 2012 (Richter, 2019). This system monitors GPS, GLONASS, Galileo, BeiDou, and QZSS satellite signals with 120 network stations worldwide and transmits the collected data to the operation center. In order to get high-accuracy position information, real-time observation data and corrections obtained from satellite orbit, satellite time, and atmospheric errors are processed in the operation center using cutting-edge algorithms (Abdulla, 2017; Pirti vd., 2022).

Users can access the service without charge after registering. The process begins with writing the user's e-mail address, selecting the tectonic plate, and uploading GNSS observation data in an appropriate file format (RINEX, DAT, T01, T02, and Quark, etc.) to the service's web portal (Inyurt, 2020). Coordinates derived from GNSS observations are calculated in the ITRF2018 datum if observed before March 23, 2017, and calculated in the ITRF2014 datum if made after that date. Users receive result data through e-mail (URL 1).

2.2. AUSPOS Online GPS Processing Service

AUSPOS service, developed by Geoscience Australia, was first put into service in 2000. The service uses data from IGS and Asia-Pacific (APREF) reference stations closest to the measurement point (Alkan vd., 2017). The service can process at least 1 hour of data (recommended 2 hours) collected in static mode and at 30-second intervals with a dual-frequency GNSS receiver (Konakoğlu, 2020). This service uses the relative solution method (Erol, 2020).

Users do not need to register to utilize the service, which is entirely free to use. The process that uses Bernese software starts by entering the user's e-mail, antenna type and antenna height into the web interface, which allows uploading a maximum of 20 RINEX files (URL 2). Users receive corrected position data in ITRF2014 and Australian datum (GDA) via e-mail (Bahadur, 2014).

2.3. CSRS-PPP

Natural Resources Canada (NRCan) released the Canadian Spatial Reference System Precise Point Positioning (CSRS-PPP) service in 2003. The solution needs IGS and NRCan service data and satellite orbit and time information from the GPS and GLONASS satellite systems (Bülbül vd., 2022). The PPP-AR algorithm was updated to the latest version on October 20, 2020, replacing the previous solution method, which was the classical PPP method. (Bülbül vd., 2022).

Following registration, users can access the service, which is free to use (Yurdakul, 2023). For transaction with the CSRS-PPP service, the RINEX data file is uploaded, the coordinate system (NAD83 or ITRF) and the measurement mode (static or kinematic) is chosen, and the result files are sent to the user via e-mail. The results are available on the measurement epoch (URL 3). Single or dual-frequency GNSS phase measurement data can be processed (Alkan vd., 2017).

2.4. The site selection and data collection

A high-sloping route was determined as a study area in the Atakum district of Samsun, Turkiye. Seven benchmark points with approximately 200 m altitude differences were located along this route, which began at sea level. The locations of the benchmark points and their approximate altitudes above sea level are given in Figure 1. Metal pipes were set up on ground benchmark points for this and future experiments. Point locations suitable for GNSS measurements have been chosen in the study area that won't interfere with the GNSS signals. Four hours of static GNSS observations were conducted at each of the seven benchmark points to determine the known coordinates used for the comparison. GNSS observations were performed with Topcon HyperpPro multi-frequency receivers. GrafNet Post-Processing Software was used to specify the reference positions of the points. One-second RINEX data from the GNSS observation duration of SAM1, SINP, VEZI, and BOYT reference stations in the TUSAGA-AKTIF (CORS-TR) system were used in the Static Post-Processing operations. As a result of processes, high accuracy positions of 7 measurement points were defined in the ITRF96 datum and 2005 measurement epoch. In order to assess the accuracy of the coordinates obtained from online PPP services, they were converted into the ITRF96 datum and 2005 epoch and compared with the reference coordinates.

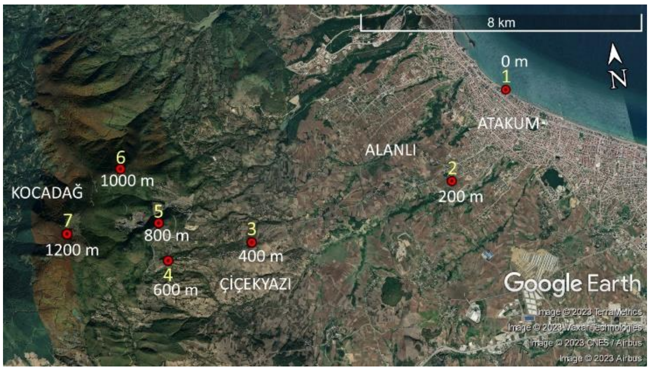

Figure 1. The location and attitudes of benchmark points

3. Results

The number and usage of online PPP services is increasing day by day. The present investigation examined the relationship between point altitude and the coordinate accuracy provided by PPP services. In this study, the use of Trimble CenterPoint RTX post-processing service, AUSPOS Online GPS Processing Service, and Canadian Spatial Reference System Precise Point Positioning (CSRS-PPP) services, all of which have been utilized in numerous academic studies, were preferred.

The 2D position errors of the coordinates supplied by PPP services are displayed in Figure 2. At each benchmark point, three PPP services offered less than 8 cm of error in 2D. The average errors were determined as 5 cm, 5 cm and 4 cm for Trimble, AUSPOS and CSRS services, respectively. However, the position errors gradually increase from point P1, which is closest to sea level, to point P7, which is at the highest altitude.

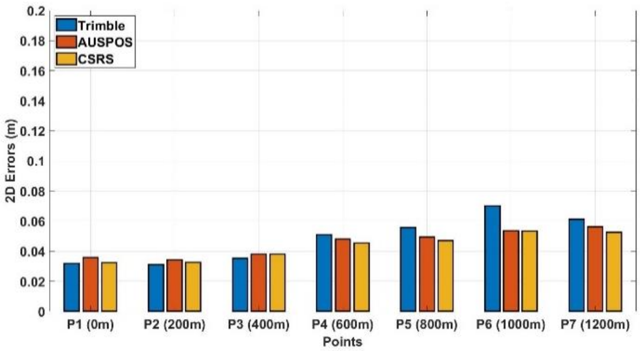

Figure 2. 2D positioning errors

The height errors of the results supplied by the PPP services for seven benchmark points at various altitudes are displayed in Figure 3. Contrary to 2D positioning accuracy, the height errors reach up to 2-dm level. Average height errors are 6 cm in the Trimble service, 6 cm in the AUSPOS service and 12 cm in the CSRS service. Notably, all three PPP services provide 1 cm accuracy at the zero altitude point. Furthermore, there is a noticeable increase in height error values with altitude, especially for the CSRS service.

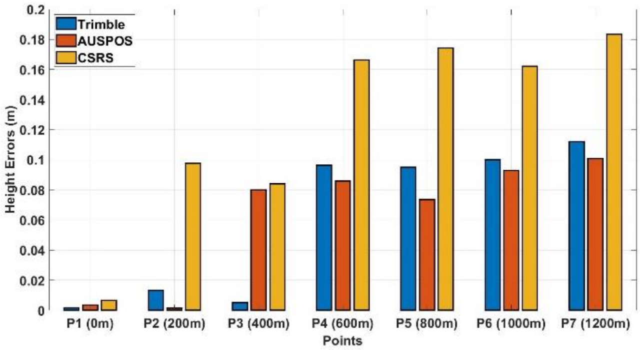

Figure 3. Height errors

4. Conclusion

In this study, the changes in position and height accuracies provided by online PPP services, depending on the altitude of the measurement points, were investigated. One of the main limitations of the use of these services is that the user cannot obtain the desired datum, epoch, or projection information of the output coordinates of the PPP service. Services generally provide results only in the ITRF14 or ITRF20 datum and measurement epoch, and users have to transform this data to the desired datum, epoch, and projection system.

As altitude was increased, a slight increase in 2D position errors was observed in this study. The height errors are observed to reach a 2-dm level and grow noticeably with increasing altitude above sea level. In particular, it has been determined that the height errors provided by the CSRS service are at the highest level. Consequently, it has been noted that point height data acquired from PPP services has less reliability.

References

Abdulla, H. (2017). İnternet tabanlı GNSS veri değerlendirme servislerinin Irak-Duhok bölgesi için kullanılabilirliğinin araştırılması. (Master's thesis, Aksaray Üniversitesi Fen Bilimleri Enstitüsü).

Alçay, S. & Atiz, Ö. (2021). Farklı Yazılımlar Kullanılarak Gerçek Zamanlı Hassas Nokta Konum Belirleme (RT-PPP) Yönteminin Performansının İncelenmesi. Geomatik, 6 (1), 77-83. https://doi.org/10.29128/geomatik.687709.

Alkan, R. M., & Erol, S., & Ozulu, I. M., & Ilçi, V. (2020). Accuracy comparison of post-processed PPP and real-time absolute positioning techniques. Geomatics, Natural Hazards and Risk, 11(1), 178-190.

Alkan, R. M., & Ozulıu, M. İ., & İlçi, V. (2017). Klasik GNSS veri değerlendirme yazılımlarına alternatif olarak web-tabanlı online değerlendirme servisleri. Afyon Kocatepe Üniversitesi Fen ve Mühendislik Bilimleri Dergisi, 17(2), 603-619.

Alkan, R. M., Ozulu, İ. M., & İlçi, V. (2015). Deniz uygulamalarında hassas nokta konumlama tekniğinin (PPP) kullanılabilirliği üzerine bir araştırma. Harita Dergisi, 154(2), 1-8.

Bahadur, B., & Üstün, A. (2014). İnternet tabanlı Gnss veri değerlendirme servisleri. Harita Dergisi, 152(2), 40-50.

Bülbül, S., & İnal, C. & Bilgen, B. (2022). Mevsimsel değişimlerin hassas nokta konumlamaya etkisi.

Konya Journal of Engineering Sciences, 10(2), 274-286.

Erol, S., Alkan, R. M., Ozulu, İ. M., & İlçi, V. (2020). Performance analysis of real-time and post-mission kinematic precise point positioning in marine environments. Geodesy and geodynamics, 11(6), 401-410.

İlçi, V. (2019). Accuracy comparison of real-time GNSS positioning solutions: Case study of Mid-North Anatolia. Measurement, 142, 40-47.

İlçi, V., & Ozulu, İ. M. (2016). PPP yönteminin arkeolojik amaçlı ölçme uygulamalarında kullanılabilirliği: Şapinuva kazı alanı örneği. Harita Teknolojileri Elektronik Dergisi, 8(3), 1-9.

Inyurt, S., & Ulukavak, M. (2020). Web tabanlı GNSS Yazılımlarının (CSRS-PPP, Trimble-RTX) Performansının Araştırılması. Geomatik, 5(2), 120-126.

Konakoğlu, B., & Alper, A. (2020). Elâzığ-Sivrice Depreminin TUSAGA-Aktif (CORS-TR) İstasyonlarının Konumlarına Olan Etkisinin Web Tabanlı GPS Yazılımları ile İrdelenmesi. Erzincan University Journal of Science and Technology, 13(2), 693-718.

Özdemir, E. G., & Gülal, V. E. (2019). İnternet Tabanlı Hassas Nokta Konum Belirleme (PPP) Yazılımlarının İrdelenmesi ve Belirsizlik Analizi, 17. Türkiye Harita Bilimsel ve Teknik Kurultayı, Ankara.

Pirti, A., & Yazici, D. (2022). İnternet tabanlı GNSS yazılımlarının doğruluk açısından değerlendirilmesi. Geomatik, 7(2), 88-105.

Richter, M. (2019). Using PPP corrections in precise real-time applications, GIM Int. 33 (6) (2019) 32e33.

Yurdakul, Ö. (2021). Cors-Tr Ölçmelerinde Glonassin Konum Doğruluğuna Etkisi: Konya Örneği (Doctoral dissertation, Necmettin Erbakan University (Turkey)).

Yurdakul, Ö. (2023). Performance investigation of GLONASS in the static PPP technique with independent short measurement times using online processing services. Survey Review, 1-11.

URL 1. Trimble CenterPoint RTX Post Processing. (Access date: 20.10.2023) http://trl.trimble.com/docushare/dsweb/Get/Document-792295/TAP201606-0017

URL 2. AUSPOS. (Access date: 20.10.2023)
https://www.ga.gov.au/scientifictopics/positioning-navigation/geodesy/auspos

URL 3. CSRS-PPP. (Access date: 20.10.2023)
https://webapp.csrs-scrs.nrcan-rncan.gc.ca/geod/tools-outils/ppp-info.php?locale=en

7th Intercontinental Geoinformation Days

igd.mersin.edu.tr

Assessment of land use land cover changes through remote sensing data in Multan Tahsil

Sajjad Hussain[*1]

[1] COMSATS University Islamabad, Department of Environmental Sciences, Vehari Campus, Vehari, Punjab 61100, Vehari, Pakistan

Keywords
Remote sensing
Land use land cover
GIS
Change analysis

Abstract

Land use land cover (LULC) changes are fundamental aspects of our evolving environment, reflecting the dynamic interplay between human activities and natural processes. Current study, executed to estimate LULC changes in seasonal intervals 2000, 2010 and 2020 to generate an accurate database on LULC changes from 2000 to 2020 in Multan tahsil (Pakistan) using RS data. Data were preprocessed in Arc GIS 10.1 and ERDAS IMAGINE software's for layer stacking, mosaicking, and sub setting. After pre-proceed, the iterative self-organized supervised clustering algorism (ISODATA) of ERDAS IMAGINE software was used to perform the supervised classification. 'Built-up area' in 2000 occupied 15.54 % of all the classes. But in 2020, build-up area increased (911.92 %) as compare to 2020. 'Vegetation area' in 2000 occupied the class with 72.312 %, but in 2020 vegetation area decreased (5.06 %) as compare to 2020 and similarly 'bare soil' decreased (5.77 %). The study shows that building area is increasing from 2000 to 2020. Increase in building area indicates increase in population in this tahsil. Our results about LULC changes are an essential tool for informed decision-making and sustainable land management.

1. Introduction

Land use land cover (LULC) is two terms for describing land. Land use (LU) defines the utilization of any piece of land by humans for one or more purposes (Huet al. 2023). While Land cover (LC) is the bodily matter on the outside of any part of ground which cover the land. LC shows the outside cover on the land, water, vegetation, built-up roads, soil and other. Classification of LC establish the baseline as of which monitor activities able to be perform, and provide the land cover knowledge for baseline thematic map (Hussain et al. 2020a). LU refers to idea about the land supply e.g., recreation, natural environment, or cultivation. LU purposes involve mutually baseline mapping and successive watching. The LULC changes refer to the transformation of the Earth's surface over time, reflecting shifts in how we utilize and occupy land (Karuppasamy et al. 2022). These changes encompass a wide spectrum of alterations, from natural processes like forest succession to the expansion of urban areas and agricultural development driven by human activities (Hussain and Karuppannan, 2023). Remote sensing technology, such as satellite imagery and aerial photography, plays a pivotal role in tracking and analyzing these changes. By classifying and comparing land cover types over different time periods, researchers and policymakers can make informed decisions regarding land management, conservation efforts, and sustainable development strategies (Khaliq et al. 2022; Hussain et al. 2021).

Pakistan is generally an agricultural and sixth most populous country where urban area is very high. Major population in Pakistan is related to agriculture, mainly southern Punjab areas (Majeed et al. 2022). The first challenge is that in temporal LULC change in the region of Mulan. Other challenge is identifying the LULC changes from 2000 to 2020 and its impact of citizen. Using RS data, this study delivers complete LULC changes of the Multan tahsil from 2000 to 2020 to detect changes in LULC. Current study, executed to estimate LULC changes in seasonal intervals 2000, 2010 and 2020 to generate an accurate database on LULC changes from 2000 to 2020 in Multan tahsil (Pakistan) using RS data.

2. Method

2.1. Study Area

The study area is Multan tahsil which lies in Punjab, Pakistan (Fig. 1). It lies approximately between latitude 30.0442° N, 30.6682° N and longitude 72.3441° E, 73.1114° E respectively. Multan District, located in the heart of Pakistan's Punjab province, boasts a unique climate and diverse land characteristics that contribute to its significance in the region. The district's climate is primarily classified as arid to semi-arid, strongly

*Corresponding Author

*(Sp23-pes-018@cuivehari.edu.pk) ORCID ID 0009-0009-5315-4154

Cite this study

Hussain, S. (2023). Assessment of Land Use Land Cover Changes through Remote Sensing Data in Multan Tahsil.Intercontinental Geoinformation Days (IGD), 7, 98-101, Peshawar, Pakistan

influenced by its geographical location and proximity to the Thar Desert. Multan District experiences a hot desert climate, characterized by scorching summers and relatively mild winters. The climate can be divided into three distinct seasons. Summers season (April to September) in Multan are exceptionally hot and dry. Daytime temperatures often soar above 40°C (104°F), with occasional heat waves pushing the mercury even higher.

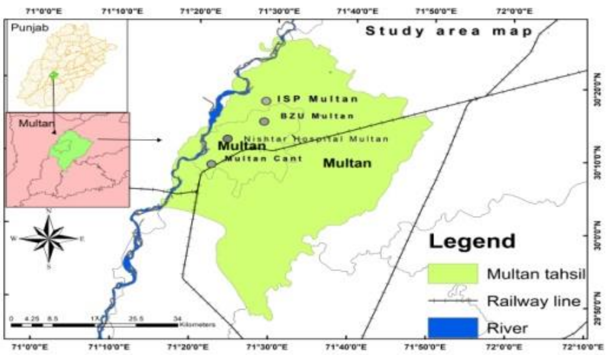

Figure 1. Study area map

2.2. Data Collection

Satellite data and Ancillary data are used in this research. The Landsat data was downloaded freely from official Earth Explorer USGS acquired by National Aeronautics and Space Administration (NASA) website (earthexplorer.usgs.gov). Ancillary data comprised of ground truth data for the LULC classes, topographic maps, aerial images of watershed and its adjacent areas. Ground truth data were collected as data control points using GPS (Geographical Positioning System), used for image analysis and classification, as well as for assessing the accuracy of classification results (Hussain et al., 2022a). Additionally, satellite data comprised of multi-spectral data obtained by Landsat 7 and Landsat 8 OLI (Operational Land Imager) satellite for the month of September (Table 1).

Table 1. Detail of Landsat satellite images

No.	Satellite/ Sensor	Band used	Path/Row	Date
1	Landsat 5	1,2,3,4,56,7	149/039	2000
2	Landsat 7	1,2,3,4,56,7	149/039	2010
3	Landsat 8	1,2,3,4,56,7,9	149/039	2020

2.3. Image classification

Reprocessing satellite images before detecting changes is extremely important and has a unique goal to start a direct connection among the data obtained and biophysical experiences. The data was processed for georeferencing, layer stackin, mosaicking and sub setting of the image in ERDAS IMAGINE 15. All satellite data was investigated by allocating per-pixel signatures and distinguishing five classes based on the definite DN (Digital Number) value of various elements (Hussain et al. 2022 b, c). Digital processing of satellite image provides tools for analyzing the image using various mathematical indices and algorithms. The iterative self-organized supervised clustering algorism (ISODATA) of ERDAS IMAGINE software was used to perform the supervised classification (Hussain et al. 2022d). To create classified LULC maps with a predetermined number of classes (5-24), supervised classifications runs were created on satellite images for 2000, 2010 ad 2020 with step 1 at each subsequent stage, maximum number iterations will be set up to 50% with 0.97 convergence threshold. The signatures were analyzed to acquire minimum and average divergence statistical indicators.

3. Results

A new layer was generating because of all the analysis made on LULC maps. Single layer was generated using weighted overlay tool of spatial analysis. The resulting layer shows the areas of LULC classes in study area. Land Use/Land Cover classes, patterns as well as change over time in the study area were mapped with unsupervised classification methods. Initial level was LC type, 2nd level was LU type and last level was the LULC classes. Final LULC images were used to evaluate areas employed by different LULC classes which were analyzed for variations between and within LULC classes (Table 2). In year 2000 vegetation area was 72.31 % followed by water bodies (1.46 %); the area covered by built-up area was 15.54 % while bare soil covered about 10.69 %. During the year 2020, vegetation area was 67.25 % followed by water bodies (0.36 %); the area covered by built up area was 27.47 % while bare soil covered about 4.92 %.

Change detection plays a pivotal role in understanding the dynamic transformation of landscapes over time. It involves the systematic comparison of satellite or aerial imagery from different time periods to identify and quantify alterations in urban development and natural or cultivated vegetation. 'Built-up area' in 200 occupied 15.54 % of all the classes. But in 2020 build-up area increased (911.92 %) as compare to 2020 (Table 3). However, there is a large increase in 'building area' has experienced a significant increase during 2000 to 2020 (Fig. 2, 3, 4 and 5). 'Vegetation area' in 2000 occupied the class with 72.312 %, but in 2020 vegetation area decreased (5.06 %) as compare to 2020 and similarly 'bare soil' decreased (5.77 %). This result showed that vegetation area converted to residential, commercial area and Road.

4. Discussion

Current study, executed to estimate LULC changes in seasonal intervals 2000, 2010 and 2020 to generate an accurate database on LULC changes from 2000 to 2020 in Multan tahsil (Pakistan) using RS data. The LULC changes are central to addressing some of the most pressing environmental and societal challenges of our time. These changes, driven by a complex interplay of natural processes and human activities, have far-reaching implications that necessitate careful consideration and action. LULC changes are emblematic of the profound impact of human activities on our planet. The expansion of urban areas, agricultural intensification, deforestation, and industrialization has reshaped landscapes, often at the expense of natural ecosystems. These changes are inextricably linked to issues such as habitat loss, biodiversity decline, and alterations in hydrological cycles, posing significant threats to ecological integrity (Hussain et al. 2023a).

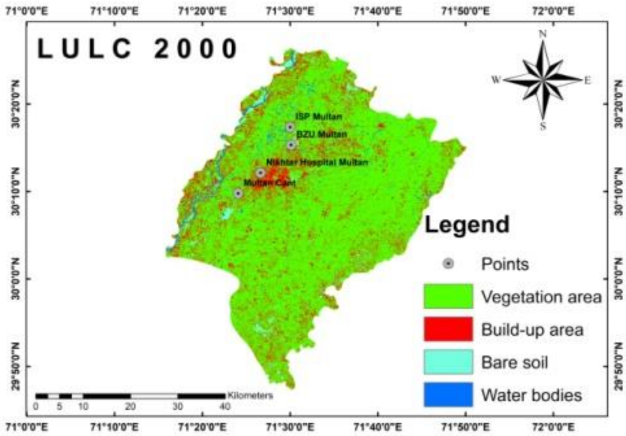

Figure 2. Land Use/Land Cover map for 2000

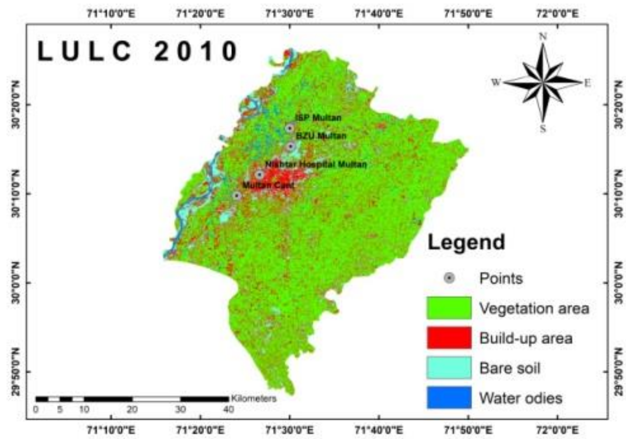

Figure 3. Land Use/Land Cover map for 2010

Moreover, the socio-economic dimension of these changes cannot be understated. Land use alterations directly affect livelihoods, food security, and access to resources for communities around the world. Understanding and mitigating the negative socio-economic consequences, especially for vulnerable populations, is an imperative aspect of addressing LULC changes. Climate change exacerbates the complexities surrounding LULC changes. Altered land cover, such as deforestation or changes in land management, can contribute to greenhouse gas emissions and influence regional climate patterns (Hussain et al. 2023b). Conversely, climate change itself influences land use through factors like altered precipitation patterns, which can impact agriculture and water resources. According to our study, 'Built-up area' in 200 occupied 15.54 % of all the classes. But in 2020 build-up area has increased (911.92 %) as compare to 2020. However, there is a large increase in 'building area' has experienced a significant increase during 2000 to 2020.

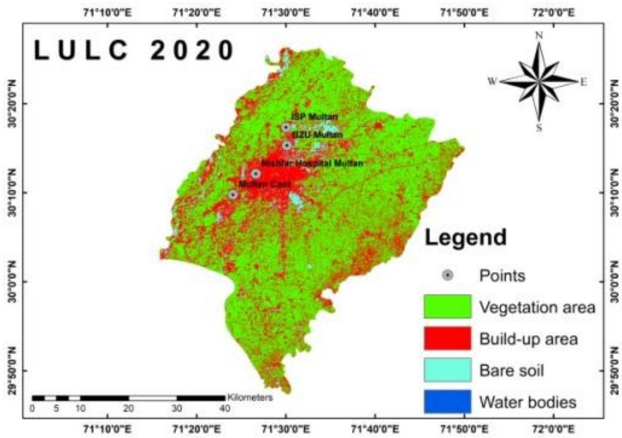

Figure 4. Land Use/Land Cover map for 2020

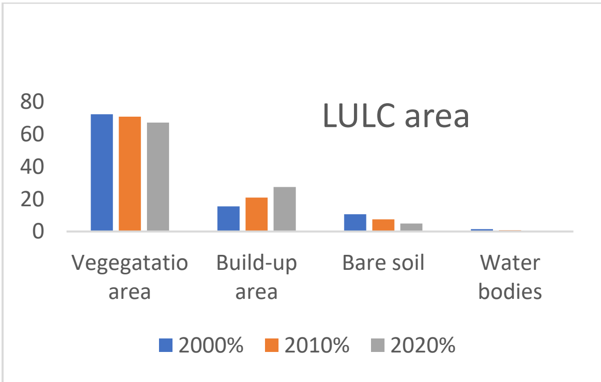

Figure 5. LULC area from 2000 to 2020

Effective policies and international cooperation are vital in addressing these issues on a global scale. Collaborative efforts are essential to conserving biodiversity, promoting sustainable development, and achieving climate goals outlined in international agreements like the Paris Agreement. The findings provide data that can be integrated into land management systems. In conclusion, discussions surrounding LULC changes underscore the intricate relationships between human society, the environment, and climate.

5. Conclusion

Study conducted on Multan tahsil shows that LULC has change over last 20 years. 'Built-up area' in 200 occupied 15.54 % of all the classes. But in 2020 build-up area has increased (911.92 %) as compare to 2020. 'Vegetation area' in 2000 occupied the class with 72.312 %, but in 2020 vegetation area decreased (5.06 %) as compare to 2020 and similarly 'bare soil' decreased (5.77 %). The vegetation trend is on average same from 2000 to 2020 the heavy venations is show in the area. Remarkable changes have shown in building area; it increases from last 20 years vigorously. It is not doubt that the fast population growth in these districts had a maximum effect on LULC. These changes, driven by a myriad of factors including urbanization, agriculture, deforestation, and climate change, have far-reaching consequences that transcend geographical boundaries. In summary, the results of LULC change analyses offer a comprehensive view of how human activities and natural processes are altering our environment. These findings play a pivotal role in guiding sustainable development, conservation efforts, and informed decision-making to address the complex challenges facing in study area.

Reference

Hu, Y., Raza, A., Syed, N. R., Acharki, S., Ray, R.L., Hussain, S., Zubair, M., & Elbeltagi, A. (2023). Land Use/Land Cover Change Detection and NDVI Estimation in Pakistan's Southern Punjab Province. Sustainability, 15, 3572. https://doi.org/10.3390/su15043572.

Hussain, S. & Karuppannan, S. (2023). Land use/land cover changes and their impact on land surface temperature using remote sensing technique in district Khanewal, Punjab Pakistan, Geology, Ecology, and Landscapes, 7:1, 46-58, https://doi.org/10.1080/24749508.2021.1923272.

Hussain, S., Lu, L., Mubeen, M., Nasim, W., Karuppannan, S., Fahad, S., & Aslam, M. (2022a). Spatiotemporal Variation in Land Use Land Cover in the Response to Local Climate Change Using Multispectral Remote Sensing Data. Land, 11(5), 595. https://doi.org/10.3390/land11050595.

Hussain, S., Mubeen, M., & Karuppannan, S., (2022c). Land use and land cover (LULC) change analysis using TM, ETM+ and OLI Landsat images in district of Okara, Punjab, Pakistan, Physics and Chemistry of the Earth, Parts A/B/C, 126, 103117.doi: https://doi.org/10.1016/j.pce.2022.103117.

Hussain, S., Mubeen, M., Ahmad, A., Majeed, H., Qaisrani, S. A., Hammad, H. M., & Nasim, W. (2022b). Assessment of land use/land cover changes and its effect on land surface temperature using remote sensing techniques in Southern Punjab, Pakistan. Environmental Science and Pollution Research, 1-17. https://doi.org/10.1007/s11356-022-21650-8.

Hussain, S., Mubeen, M., Ahmad, A., Masood, N., Hammad, H. M., Amjad, M., & Waleed, M. (2021). Satellite-based evaluation of temporal change in cultivated land in Southern Punjab (Multan region) through dynamics of vegetation and land surface temperature. Open Geosciences, 13(1), 1561-1577. https://doi.org/10.1515/geo-2020-0298.

Hussain, S., Mubeen, M., Nasim, W., Fahad, S., Ali, M., Ehsan, M. A., & Raza, A. (2023a). Investigation of Irrigation Water Requirement and Evapotranspiration for Water Resources Management in Southern Punjab, Pakistan. Sustainability. 15(3), 1768. https://doi.org/10.3390/su15031768.

Hussain, S., Qin, S., Nasim, W., Bukhari, M. A., Mubeen, M., Fahad, S., & Aslam, M. (2022d). Monitoring the Dynamic Changes in Vegetation Cover Using Spatio-Temporal Remote Sensing Data from 1984 to 2020. Atmosphere, 13(10), 1609. https://doi.org/10.3390/atmos13101609.

Hussain, S., Raza, A., & Abdo, H.G. et al. (2023b). Relation of land surface temperature with different vegetation indices using multi-temporal remote sensing data in Sahiwal region, Pakistan. Geoscience Letters. 10, 33. https://doi.org/10.1186/s40562-023-00287-6.

Hussain, S.,Mubeen, M., Ahmad, A., Akram, W., Hammad, H. M., Ali, M., & Fahad, S. (2020a). Using GIS tools to detect the land use/land cover changes during forty years in Lodhran District of Pakistan. Environmental Science and Pollution Research, 27, 39676–39692. https://doi.org/10.1007/s11356-019-06072-3.

Hussain, S.,Mubeen, M., Akram, W., Ahmad, A., Habib-ur-Rahman, M., & Nasim, W., (2020b). Study of land cover/land use changes using RS and GIS: a case study of Multan district, Pakistan. Environmental Monitoring and Assessment, 192(1), p.2. https://doi.org/10.1007/s10661-019-7959-1.

Karuppasamy, M. B., Natesan, U., Karuppannan, S., Chandrasekaran, L. N., Hussain, S., & Abdo, H. G. (2022). Multivariate Urban Air Quality Assessment of Indoor and Outdoor Environments at Chennai Metropolis in South India. Atmosphere, 13(10), 1627. https://doi.org/10.3390/atmos13101627.

Khaliq, M.A., Javed, M.T., & Hussain, S. et al. (2022). Assessment of heavy metal accumulation and health risks in okra (Abelmoschus Esculentus L.) and spinach (Spinacia Oleracea L.) fertigated with wastwater. Food Contamination 9, 11.https://doi.org/10.1186/s40550-022-00097-2.

Majeed, M., Tariq, A., Anwar, M. M., Khan, A. M., Arshad, F., & Shaukat, S. (2021). Monitoring of Land Use–Land Cover Change and Potential Causal Factors of Climate Change in Jhelum District, Punjab, Pakistan, through GIS and Multi-Temporal Satellite Data. Land, 10(10): 1026. https://doi.org/10.3390/land10101026.

Waleed, M., Mubeen, M., Ahmad, A., Habib-ur-Rahman, M., & El Sabagh, A. (2022). Evaluating the efficiency of coarser to finer resolution multispectral satellites in mapping paddy rice fields using GEE implementation. Scientific Reports, 12, 13210. https://doi.org/10.1038/s41598-022-17454-y.

Yang, X., Yang, Q., Zhu, H., Wang, L., Wang, C., Pang, G., & Hussain, S. (2023). Quantitative Evaluation of Soil Water and Wind Erosion Rates in Pakistan. Remote Sensing, 15(9), 2404. https://doi.org/10.3390/rs15092404.

7th Intercontinental Geoinformation Days

igd.mersin.edu.tr

Urban transformation applications

Muhammed Emin Işık [1], Nuri Erdem *[2]

[1]Osmaniye Korkut Ata University, Graduate School of Natural and Applied Sciences, Department of Civil Engineering, Osmaniye, Türkiye
[2]Osmaniye Korkut Ata University, Faculty of Engineering, Department of Geomatic Engineering, Osmaniye, Türkiye

Keywords
Urban transformation
City planning
Disaster
Osmaniye

Abstract

In this study, urban transformation practices are discussed within the scope of renewal, arrangement and development activities of existing buildings under natural disasters and accompanying risks. The problems and deficiencies experienced in practice were examined specifically in Osmaniye city center. Urban transformation has important benefits in terms of public interest and public health. It also increases the comfort levels of city dwellers through urban planning and infrastructure improvements. Despite its many positive effects on disaster-resistant city planning and the priority of life and property safety, it is sometimes possible to encounter very bad examples as a result of incorrect or incomplete applications. When the applications carried out in Osmaniye city center were examined, it was seen that island-based large-scale transformations were more accurate in terms of time, cost and environmental order compared to partially smaller and parcel-based on-site transformations.

1. Introduction

Increasing population rates over the years, needs in line with today's demands, renewal of cities, meeting social and cultural needs, earthquake and natural disaster risks, economic situations, etc. Due to these factors, urban transformation practices have become a necessity rather than a desire. We see that in our country, especially in recent years, practices have been implemented without sufficient planning. Defining urban transformation as only demolishing old and outdated buildings and building new ones in their place means omitting many other parameters, which will bring about negativities in the medium and long term. For this reason, urban transformation applications are based on social, cultural, history, belief, architecture, engineering, aesthetics, safe structures, legal and financial requirements, etc. It needs to be addressed with a multi-disciplinary approach covering many areas and implemented meticulously. Urban transformation includes different application forms such as renewal, rehabilitation, regulation, protection, revitalization and redevelopment (Şişman and Kibaroğlu, 2009). Urban transformation practices, on the other hand, support sustainable development in that they include interventions to protect and develop urban values and ensure socio-economic and socio-cultural developments (Demirkıran, 2008).

It has been observed that there are many factors that negatively affect the sustainable development expected from the urban transformation practices carried out in Turkey to date (İnam and Basarir, 2009). As a solution to the problems experienced in practice, it is of great importance to first define the legal infrastructure and the duties and powers of practitioners. The recently enacted disaster law in our country covers the procedures and principles regarding the improvement, liquidation and renewal of lands and lands where disaster risk areas and risky structures outside these areas are located, in order to create healthy and safe living environments in accordance with science and art norms and standards. The implementation phase of this law is very important because it is far from the goal of generating surplus income in areas at risk of disaster and not only in the physical sense, but also in terms of sustainable planning of the urban space (Bozdağ, et al., 2011).

2. Method

When the applications carried out in Osmaniye city center are examined, it is seen that island-based large-scale transformations are more accurate in terms of time, cost and environmental order, compared to partially

* **Corresponding Author**

202311330001@ogr.oku.edu.tr) ORCID ID 0009-0006-9590-6957
*(nurierdem@osmaniye.edu.tr) ORCID ID 0000-0002-1850-4616

Cite this study

Işık, M. E. & Erdem, N. (2023). Urban transformation applications. Intercontinental Geoinformation Days (IGD), 7, 102-105, Peshawar, Pakistan

smaller and parcel-based on-site transformations. In the visual in Figure 1, it is aimed to demolish a building that has completed its service life in Ümraniye district of Istanbul province and replace it with a new building within the scope of urban transformation. Just like in this example, in many of our cities, urban transformation practices are seen as negative examples where the implementation is not evaluated on a large scale, but on a parcel basis, and the application is inadequately evaluated. Because, in parcel-based on-site transformations, only a limited number of structures will be intervened and the remaining structures in a large area will continue to exist. In this case, the security risk of existing buildings, their incompatibility with new zoning plans, visual pollution, etc. It will appear as an example of incomplete application with its effects. Of course, its transformation on a parcel basis contributes to the renewal and improvement processes. However, when the residential areas are considered as a whole, it is an example of incomplete and inadequate implementation.

In general, one of the most important reasons why parcel-based conversions are widespread is the flat owners and rights holders who are included in the Civil Code, the Law on the Transformation of Areas at Disaster Risk, the Law on Condominium Ownership and related legislation and regulations, which cause difficulties in practice. Parcel-based conversions have become more common due to the factors where disputes between them are frequently encountered. However, the issue of urban transformation, which is directly related to many areas, will help expand the field of application, especially by fulfilling some legal requirements. Finally, the announcement by the Ministry of Justice that the 2/3 requirement between flat owners will be regulated as 50+1 percent and come into force will contribute to making the application easier and broader (URL_1). In this direction, it is aimed to progress the transformation processes more quickly and effectively with the Urban Transformation Directorate, which was announced by the Ministry of Environment, Urbanization and Climate Change and published in the official gazette (URL_2).

Figure 1: Urban Transformation Application Demolition Study (URL_3)

Figure 2 shows the current status of a large-scale area in 2022, specifically in Kocaeli Province, which has completely entered the urban transformation area and is ongoing. It is seen that urban transformation practices are still continuing in the province of Kocaeli, which was exposed to great destruction and damage in the 1999 Gölcük earthquake. Here, island-based large-scale transformations, which have more effective and accurate results compared to parcel-based on-site transformation, and the social, cultural, infrastructural opportunities, economic, spiritual etc. of settlements located in a wide area. Considering its effects, it seems to be a more accurate example of transformation. Based on this example, earthquake, flood, landslide etc. It is understood that cities that have experienced such situations before have implemented urban transformation practices more widely with these bitter experiences. In this regard, an urban transformation planning should be made specifically for Osmaniye province, which is among the 11 provinces affected by the last February 6 Kahramanmaraş earthquakes, and combined with post-disaster urban planning and transformation practices. Because in this way, taking permanent and correct steps in planning the future of the city will be an effective approach.

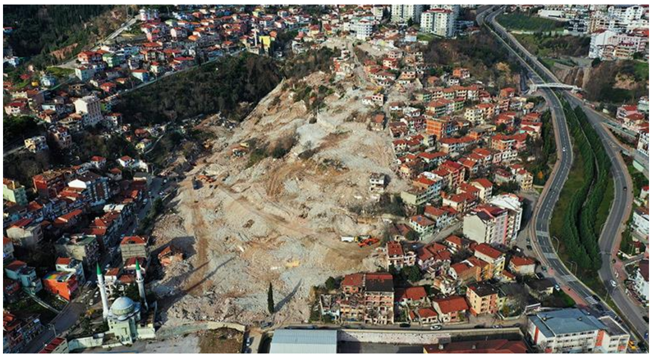

Figure 2: Island Based Transformation in Kocaeli Province (URL_4).

The workplaces, called Shoemakers' Bazaar, which is one of the old settlements in the Central district of Osmaniye province, and also houses various tradesmen's shops, were put into transformation and restoration in line with urban planning and city silhouette in 2022. The necessary infrastructure and project work was completed and it was declared as an application area in the last period of 2022. The areas called Envar-ül Hamit (Great Mosque) and Hamamlar Street, which are located very close to this area and are of historical nature, were considered as a whole and work was started in this context (Figure 3).

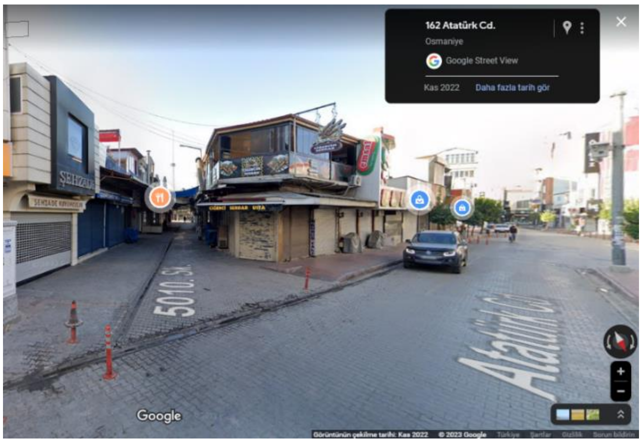

Figure 3: Area Declared for Urban Transformation in Osmaniye Province (URL_5)

Figure 4 shows the details of the development plan published by the Osmaniye Municipality Zoning and Urbanization Directorate in the area where transformation and restoration was declared. The fact that the workplaces, which are currently adjacent and have a maximum of 2 floors, are given as adjacent but 5-storey in the new zoning plan, raises questions about whether it is suitable for the historical, social and cultural spirit of this area. When it comes to urban transformation, the idea of simply demolishing the old building and building a new, multi-storey one in its place is generally not suitable for the needs of the region, as it brings with it some problems.

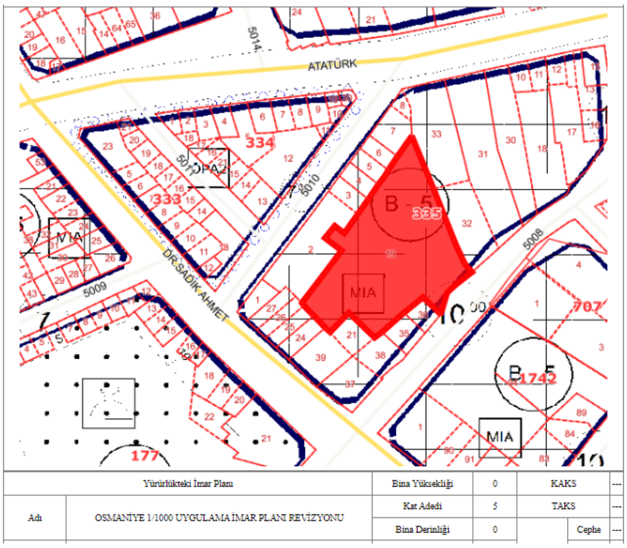

Figure 4: Current Development Plan of the Urban Transformation Area (URL_6)

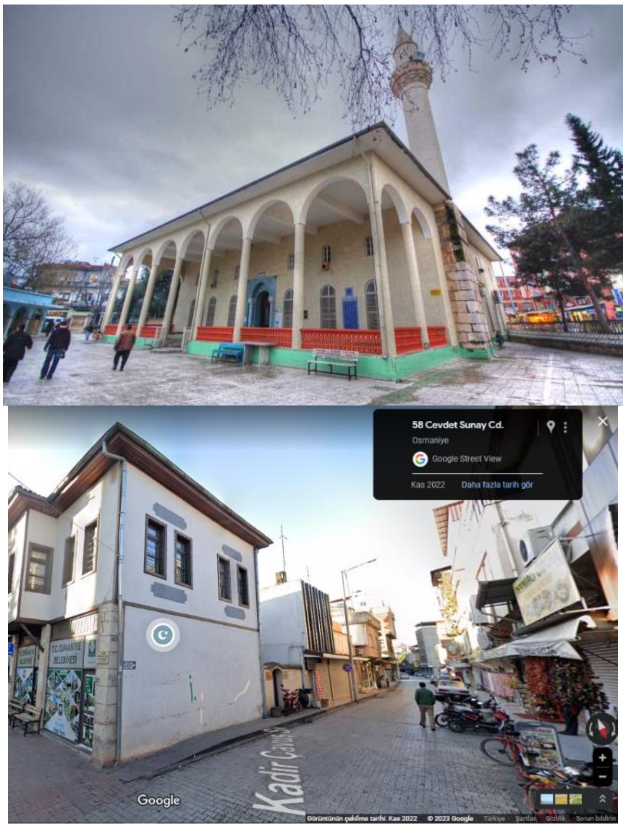

Figure 5: View of the Great Mosque and Baths Street (URL_7)

Figure 5 shows the pre-earthquake images of the 133-year-old historical Grand Mosque and Baths Street, which are located within the transformation and restoration areas. Again, in this area, work was started in the last period of 2022, with the necessary infrastructure works and the part declared as an urban transformation area as a whole. However, in the February 6 Kahramanmaraş earthquakes that occurred at the beginning of 2023, both the Grand Mosque and many workplaces in the area called Shoemakers' Bazaar were severely damaged. Therefore, urban transformation and restoration practices remain unclear until now.

While the necessary arrangements in historical buildings are being considered in coordination with the region declared as an urban transformation area before the earthquake, in accordance with the transformation area, if the restoration of the damaged historical buildings is necessary after the earthquake, it would be a better decision to take a new planning step, including demolition works (Figure 6).

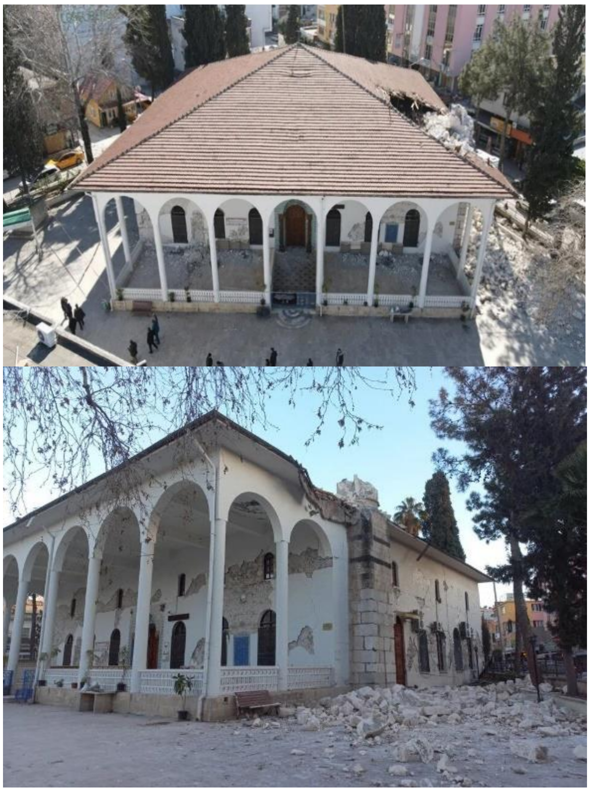

Figure 6: Damage Image After the February 6 Earthquakes (URL_8)

3. Conclusion

Urban transformation practices, examples of which are frequently encountered in the world and in Turkey, are aimed at meeting human life and demands effectively, and positive and negative examples are frequently encountered. Although there are many difficulties in urban transformation applications that involve many disciplines, it is possible to carry out transformation applications based on human health and life safety, taking into account all kinds of disaster risks, especially throughout our country. In fact, taking the necessary precautions with some restrictions and prohibitions, which seem simple but of which we still encounter bad examples in practice, will make very positive contributions. Stream bed of the urban transformation area, landslide and earthquake zone, etc. transformation areas located in risky areas such as:

- Despite the insistence of the local people, it should be completed elsewhere with security-first steps,
- Building structures that will provide uniform use services by imposing floor restrictions in areas with earthquake risk, preventing the design of lower floors as workplaces and upper floors as residences, which are examined under the discipline of civil engineering and causing soft floor irregularities,
- Again, limiting or prohibiting closed projections that increase the square meters of building usage on the ground floor and upper floors,
- Encouraging and supporting island-based large-scale transformations rather than parcel-based transformations,
- To pave the way for more convenient and faster implementation of the disputes that have lasted for many years and led to disagreements between flat owners by taking legal steps,

etc. If the situations are taken into consideration, it will have great effects on public health and development.

References

Bozdağ, A., İnam, Ş., & Durduran, S. S. (2011). Kentsel dönüşüm uygulamalarına çok amaçlı yaklaşım, Bursa (İnegöl) Kenti Örneği. Selçuk Üniversitesi Mühendislik, Bilim ve Teknoloji Dergisi, 26(4), 124-139.

Demirkıran S. (2008). Türkiye'de Kentsel Dönüşüm Uygulamalarında Yerel Yönetimlerin Rolü: Bursa Büyükşehir Belediyesi Örneği, Yüksek Lisans Tezi, Trakya Üniversitesi, Sosyal Bilimler Enstitüsü, Edirne.

İnam, Ş. Başarır, A., (2010). Kentsel Dönüşüm ve Toprak Mülkiyeti Sorunları, Toprak Mülkiyeti Sempozyumu, Editör: Dr. Sonay Bayramoğlu Özuğurlu, Memleket Yayınları, ISBN:978-9944-5435-2-1.

Şişman A. & Kibaroğlu D. (2009). Dünyada ve Türkiye'de Kentsel Dönüşüm Uygulamaları TMMOB Harita ve Kadastro Mühendisleri Odası 12. Türkiye Harita Bilimsel ve Teknik Kurultayı.

URL_1: https://www.ntv.com.tr/turkiye/kentsel-donusum-yasasi-meclise-geliyor-ucte-iki-kurali-yuzde-501-ile-degisecek,2U1BNinPuke3b7t4tpKZZQ

URL_2: https://csb.gov.tr/kentsel-donusum-baskanligi-kuruldu-bakanlik-faaliyetleri-38848

URL_3: https://www.trthaber.com/haber/guncel/umraniyede-kentsel-donusum-kapsaminda-yikim-calismalari-basladi-766343.html

URL_4: https://www.kocaeli.bel.tr/tr/main/news/haberler/3/cseditte-248-binanin-yikimi-tamamlandi/39991

URL_5: https://www.google.com.tr/maps

URL_6:http://kentrehberi.osmaniye.bel.tr:81/Kentrehberiapp/imardurumbelgesi?parselId=109024286

URL_7: https://www.kulturportali.gov.tr/turkiye/osmaniye/kulturenvanteri/enverul-hamt-cam-ve-sehtlk

URL_8: https://www.ntv.com.tr/n-life/gezi/133-yillik-envar-ul-hamit-camii-aslina-uygun-olarak-restore-edilecek,ReSo9EFLmECjMrIC-AuXgA.

Yakar, M., Yılmaz, H. M., & Mutluoglu, O. (2014). Performance of photogrammetric and terrestrial laser scanning methods in volume computing of excavation and filling areas. Arabian Journal for Science and Engineering, 39, 387-394. https://doi.org/10.1007/s13369-013-0853-1

7th Intercontinental Geoinformation Days

igd.mersin.edu.tr

Comparison of machine learning regression methods for mass real estate valuation

Batuhan Kamil Sağlam [*1], **Muhammed Oğuzhan Mete** [1], **Ufuk Özerman** [1], **Reha Metin Alkan** [1]

[1] *Istanbul Technical University, Department of Geomatics Engineering, Istanbul, TÜRKİYE*

Keywords
Real Estate Valuation
Mass Valuation
Machine Learning
Prediction Model
Inverse Distance Weighting

Abstract

Efficient management of real estate requires an objective assessment of their values by using scientific approaches. Valuation is key for value-related applications such as purchase and sale, taxation, expropriation, and urban regeneration. Mass valuation reduces time and costs by evaluating multiple properties simultaneously. Leveraging statistical analysis and predictive capabilities of machine learning enhances accuracy and speed in real estate valuation. This study focuses on applying many regression models for mass valuation of residential properties in Melbourne, Australia, aiming to improve accuracy and efficiency for stakeholders. Evaluating various algorithms, including Linear Regression, Decision Trees, Random Forest, Bagging, AdaBoost, Gradient Boosting, and XGBoost, on Kaggle's open data, performance metrics are calculated. Notably, ensemble methods like Random Forest and XGBoost consistently outperformed others by capturing nonlinear relationships of determinants and predicting the value accurately. Finally, applying the Inverse Distance Weighting (IDW) interpolation method, a real estate value map is generated for the study area. This study aims to uncover machine learning's role and limitations in real estate valuation by comparing the performance of different ensemble learning methods. The findings highlight the significance of advanced regression models in improving valuation practices, supporting decision-making, and enhancing market efficiency.

1. Introduction

Real estate valuation is a comprehensive process crucial for determining the value of a property, serving as a cornerstone for various transactions. Conventionally, methods like sales comparison, income, and cost approaches have been employed. Nevertheless, recent advances in methodologies such as Multiple Regression Analysis (Benjamin, Guttery, & Sirmans, 2020; Yilmazer & Kocaman, 2020), Hedonic Pricing (Lisi, 2019; El Yamani, Ettarid, & Hajji, 2019), Nominal Valuation (Mete & Yomralioglu, 2019; Yomralioglu, 1993), Geographically Weighted Regression (Dimopoulos & Moulas, 2016; Sisman & Aydinoglu, 2022; Wang, Li, & Yu, 2020), Ensemble Learning (Alfaro-Navarro et al., 2020; Aydinoglu, Bovkir, & Colkesen, 2021; Gnat, 2021), and Artificial Neural Networks (Demetriou, 2017; Lee, 2023; Yalpır, 2018) have led more widespread usage of those approaches in mass valuation. In the context of real estate valuation, these modern techniques have been instrumental in providing more accurate estimations and expediting decision-making processes (Doldur & Alkan, 2021). Furthermore, the integration of machine learning has catalyzed a transformative shift in the real estate valuation landscape, promising even greater precision and efficiency for assessments (Ngiam & Khor, 2019). Mass valuation methods can be broadly classified into two groups: hedonic-based regression and machine-learning regression approaches. Hedonic pricing, a prevalent technique for forecasting housing prices, considers both internal and external property characteristics to ascertain value. While known for producing robust predictive results, implementing this approach often requires specialized knowledge in statistical analysis and model specification (Mete & Yomralioglu, 2023). The city of Melbourne, renowned for its dynamic urban landscape and vibrant real estate market, serves as a focal point for this study. Melbourne's diverse property types and market fluctuations provide an ideal ground for testing the robustness and effectiveness of different machine learning regression models. The integration of advanced methodologies in mass valuation processes has facilitated more precise

* **Corresponding Author**

*(saglamba17@itu.edu.tr) ORCID ID 0000-0003-0287-787X
(metemu@itu.edu.tr) ORCID ID 0000-0002-9312-1965
(ozerman@itu.edu.tr) ORCID ID 0000-0001-9812-2185
(alkanr@itu.edu.tr) ORCID ID 0000-0002-1981-9783

Cite this study

Saglam BK, Mete MO, Ozerman MU & Alkan RM (2023). Comparison of Machine Learning Regression Methods for Mass Real Estate Valuation. Intercontinental Geoinformation Days (IGD), 7, 106-110, Peshawar, Pakistan

estimations and informed decision-making processes. Machine learning, in particular, has played a pivotal role in revolutionizing the industry, enabling the analysis of complex data structures and relationships with high accuracy and efficiency (Ngiam & Khor, 2019).

In the study using data from Melbourne, Australia, the power of machine learning was utilized and a comprehensive evaluation of the performance criteria was made, and the contribution of using machine learning methods in the real estate valuation process to the efficiency and accuracy of the valuation processes was tried to be revealed. Within this paper, it is not only prioritized highlighting the accurate machine learning models but also conducting a detailed comparison of performance metrics. By meticulously comparing the results generated from traditional valuation methodologies with those derived from the machine learning algorithms, predictive capability and efficiency of the modern approaches are highlighted.

2. Machine Learning-based Real Estate Valuation

A field of computing algorithms called machine learning is constantly developing and aims to replicate human intelligence by learning from the environment (El Naqa & Murphy, 2015). With the advent of machine learning, data driven approaches have gained prominence in the field, revolutionizing the way real estate professionals evaluate properties. In this article, we explore a range of machine learning algorithms used in real estate valuation, including linear regression, decision trees, random forests, bagging regressor, AdaBoost regressor, gradient boosting regressor, and extreme gradient boosting regressor.

Linear Regression is a statistical modeling technique used in real estate valuation, estimating the relationship between independent variables and the dependent variable as given Eq. (1).

$$\hat{y} = b_0 + b_1X_1 + b_2X_2 + \cdots + b_nX_n \tag{1}$$

where, $\hat{y}$ is dependent variable; X_n is independent variable; b_0 is y-constant value and b_n is coefficients.

It helps predict property prices based on factors like size, location, and amenities. It captures linear trends, aiding in informed decisions and laying the groundwork for advanced modeling techniques in dynamic markets.

Real estate valuation is crucial in property investment and market analysis. Decision trees, a machine-learning model, have revolutionized property assessment and pricing. They provide structured, intuitive predictions based on input variables, allowing for accurate valuation. This paper explores the application and benefits of decision trees in real estate valuation, highlighting their predictive capabilities. The structure of the algorithm is given in Figure 1.

The Bagging Regressor model is a machine learning technique that enhances prediction performance by combining multiple decision trees. It's useful in real estate valuation due to its ability to capture complex interactions and nonlinear relationships, allowing accurate property value predictions. It can handle large datasets and deliver reliable results. The Random Forest Regressor is a machine learning method that combines multiple decision trees to create a decision forest, improving prediction performance. It's particularly useful in real estate valuation, as it can handle complex datasets, non-linear relationships, and noisy data, enhancing accuracy and decision-making.

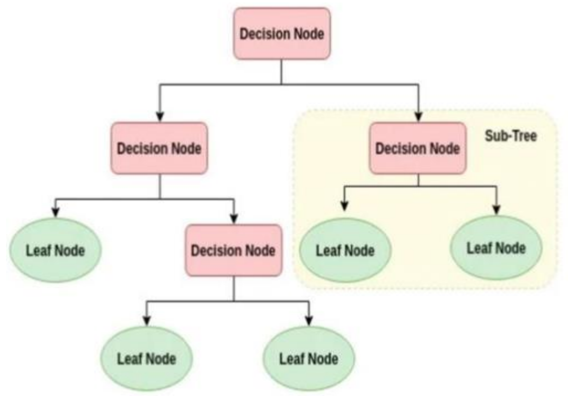

Figure 1. Basic structure of decision tree algorithm

The Gradient Boosting Regressor model is a robust real estate valuation tool that utilizes multiple decision trees to identify significant predictors and make precise property price estimations. XGBoost is a powerful regression tool that uses gradient boosting and regularization techniques to analyze complex data, identify influential variables, and make informed investment decisions. On the other hand, Ada-Boost Regressor is a machine learning strategy that uses boosting to produce highly accurate predictions. Iteratively focusing on misclassified instances and assigning higher weights improves accuracy. This versatile approach helps real estate professionals understand market dynamics, identify influential variables, and estimate property values.

3. Mass valuation with Machine Learning: A case study of Melbourne City, Australia

In this study, different machine learning regression methods such as Linear Regression, Random Forest, Ada-Boost, XGBoost are used for mass valuation of residential properties, and model performances are compared. Mass valuation processes contain data preprocessing, model development, model accuracy assessment, and valuation map production (Figure 2).

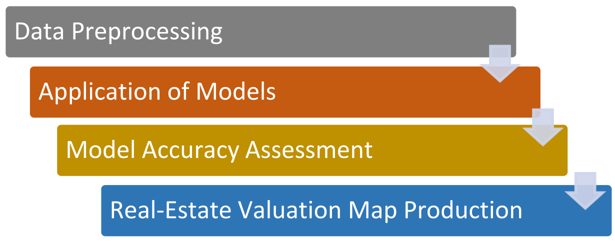

Figure 2. Workflow diagram of the study

While developing mass valuation regression models, The Melbourne Housing Snapshot dataset, which is derived from the Kaggle platform, is used. This dataset can help us understand the general state of the market and predict future trends since it provides valuable insights about the real estate market in the City of Melbourne, Australia. Melbourne is the capital of the Victoria state of Australia. After Sydney, it is the second most crowded city with a 9,993 km^2 metropolitan area.

The key features of the Melbourne Housing Snapshot dataset include the number of rooms, type, price, distance, number of bedrooms, land size, year built, municipality, latitude, longitude, region name, and number of properties. The dataset contains a total of 13,580 samples and the highest price value is determined as 9,000,000 AUD, while the lowest price value is recorded as 85,000 AUD (Figure 3). This range indicates that the real estate market in Melbourne has a fairly wide price range. The standard deviation of price is calculated as 1,075,684 AUD. This shows how volatile housing prices in Melbourne are overall. Visualizing the data on a map helps determine possible price trends, as well as the geographical distribution of housing prices.

Figure 3. Spatially distributed samples of the Melbourne Housing Snapshot dataset

Within the scope of regression analysis, Exploratory Data Analysis (EDA) is first performed to obtain detailed information about the data. EDA is an indispensable step for data science projects, providing a better understanding of the data using statistics and various visualization techniques. At this stage, descriptive statistics (minimum, maximum, mean, standard deviation, etc.) are calculated, null values in the data are checked, correlation matrix, histogram, box plot, scatter plot, and pairwise comparison graphs are created.

Box plot analysis is used to detect and remove outliers. In this method, points outside the limits determined by the quartile range and median of the data distribution are considered outliers, and they are removed from the data set. Then, the 2D graph created by removing these outliers from the data set is shown in Figure 4.

In Figure 5, 3D visualization of the remaining data was performed. This process enabled a more homogeneous and representative visualization of the data set and increased the reliability of the analysis results.

The correlation matrix of determinants is used to establish the relationships between variables in the dataset (Figure 6). The correlation matrix contains the correlation coefficients that show the relationship between each pair of variables. When the correlation matrix is examined, it is seen that the number of rooms, bedrooms, bathrooms, and building area have a high correlation with property prices.

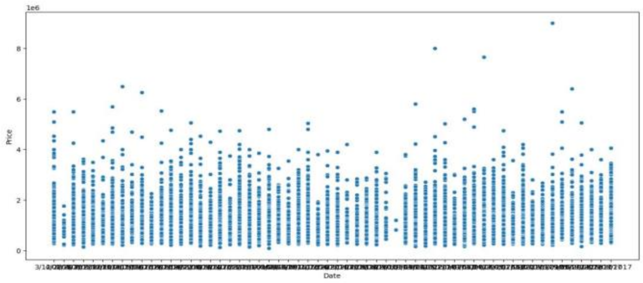

Figure 4. Display of data on graph before outliers are removed

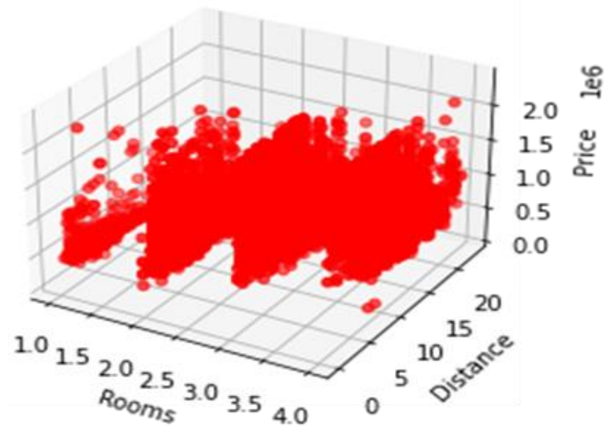

Figure 5. 3D visualization of data after outlier removal

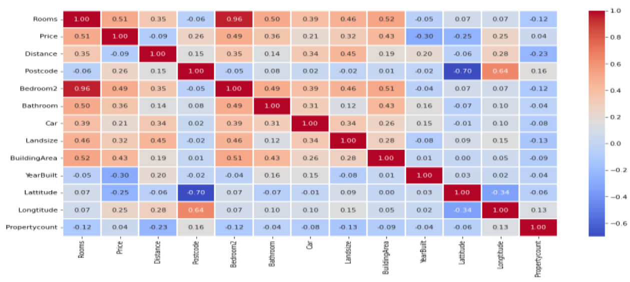

Figure 6. Correlation matrix of the determinants

In the EDA process, a positive correlation is observed between independent variables and property price. However, outliers can significantly affect this correlation. After outliers are removed, a higher correlation is observed between property price and the other determinants.

4. Results

Interpreting the results of the study, Table 1 contains significant metrics used to evaluate the performance of different regression algorithms. Among these metrics, Prediction Score (R^2), Mean Absolute Error (MAE), and Root Mean Square Error (RMSE) stand out. MAE represents the mean value of the absolute differences between actual and predicted values, while RMSE is the square root of the mean value of the squares of these differences. The results were taken into account to determine which model performed best and which model was less suitable for certain datasets.

Table 1. Regression models and performance metrics

Train-Test Split (%)	R^2	MAE	RMSE
Linear Regression			
75 - 25	0.659310	196989.181160	254281.379577
80 - 20	0.657725	197020.394116	254333.875054
85 - 15	0.662422	197041.308263	256050.971488
90 - 10	0.663747	199722.787849	259143.666717
Decision Trees Regressor			
Train-Test Split (%)	R^2	MAE	RMSE
75 - 25	0.627048	188136.539305	266049.036833
80 - 20	0.624262	185960.863014	266476.603100
85 - 15	0.636636	187174.043451	265650.051759
90 - 10	0.628760	187521.209632	272291.957281
Random Forest Regressor			
Train-Test Split (%)	R^2	MAE	RMSE
75 - 25	0.810018	133228.888338	189885.386483
80 - 20	0.811294	132797.522498	188846.789752
85 - 15	0.816629	133367.614061	188714.254893
90 - 10	0.823304	131936.028623	187854.172165
Bagging Regressor			
Train-Test Split (%)	R^2	MAE	RMSE
75 - 25	0.782739	143070.818058	203060.631339
80 - 20	0.794855	134483.965722	196900.253935
85 - 15	0.791527	142722.343037	201216.525166
90 - 10	0.807556	138637.171001	196046.780131
AdaBoost Regressor			
Train-Test Split (%)	R^2	MAE	RMSE
75 - 25	0.554980	244615.349281	290619.562314
80 - 20	0.505043	255277.041956	305843.963484
85 - 15	0.542380	247881.764403	298120.210653
90 - 10	0.541683	253421.545375	302545.302392
Gradient Boosting Regressor			
Train-Test Split (%)	R^2	MAE	R RMSE
75 - 25	0.783971	147336.171724	202484.172220
80 - 20	0.785251	147152.509979	201456.943290
85 - 15	0.794758	146142.888033	199651.220882
90 - 10	0.794952	148050.077514	202365.239109
Extreme Gradient Boosting Regressor			
Train-Test Split (%)	R^2	MAE	RMSE
75 - 25	0.816906	132114.238361	186411.051174
80 - 20	0.817800	133547.754318	185562.469265
85 - 15	0.825908	131702.227114	183877.622347
90 - 10	0.830326	132555.493272	184083.676625

In this study, the performance of different regression algorithms for predicting property prices based on different rates of train-test split is evaluated. Evaluating the results, Linear regression performed good performance, but high Mean Absolute Error and Mean Squared Error values indicated deviation between predicted and actual prices. Decision Trees Regressor showed comparable prediction scores but slightly higher error metrics, suggesting model instability. XGBoost had the highest prediction scores and lower mean absolute and squared errors, indicating better data complexities and improved accuracy. On the other hand, Bagging Regressor yielded satisfactory results, while AdaBoost Regressor had the lowest prediction scores and highest errors, suggesting limitations in capturing underlying patterns. Further analysis and experimentation may be necessary to fine-tune these algorithms.

In order to produce mass valuation map, the Inverse Distance Weighting (IDW) method is used to interpolate estimated real estate prices across the study area using the ArcGIS platform. The IDW calculates the estimated value of a point based on the values of other known points around that point and their distances to those points. The map on the ArcGIS platform shown in Figure 7 visualizes the points predicted by the Extreme Gradient Boosting Regressor model. This visualization shows how close the model's predictions are to actual data. Considering how close the points on the map are to the actual data and how accurate the predictions are overall, it can be concluded that this model is a robust prediction tool applied in the Melbourne property market with high accuracy.

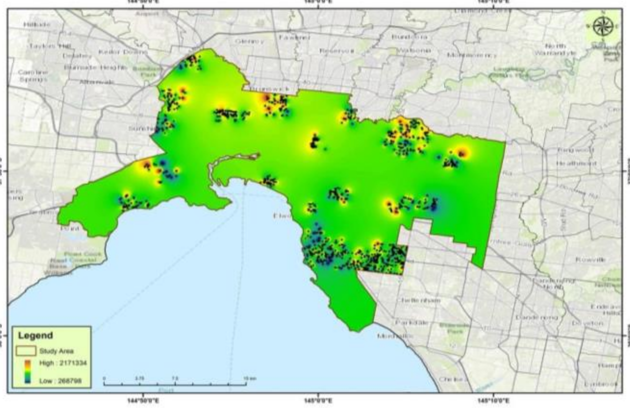

Figure 7. Display of predicted points on the map on the ArcGIS platform

5. Conclusion

Mass valuation is a method used in real estate that involves the assessment of multiple properties at once, typically utilizing statistical models to determine the value based on various factors and characteristics. Regression models for real estate valuation have been analyzed, showing their strengths and limitations. In contrast, machine learning methods, specifically XGBoost, have offered a data-driven and objective approach that leverages the power of algorithms to analyze vast amounts of real estate data, including property characteristics, market trends and location factors, as we see in our study. This allows for the creation of more accurate and reliable property valuations, reducing the risk of overvaluation or undervaluation. Aside from their superior accuracy, machine learning methods also offer several advantages over nominal methods. Machine learning models can be constantly updated and improved as new data becomes available. This ensures that valuations remain updated and reflect current market conditions.

Moreover, machine learning algorithms can identify complex patterns and relationships within real estate data that appraisers cannot see, leading to a more comprehensive understanding of property values. Considering these advantages, it is clear that machine learning methods represent a significant advance in mass valuation applications, as seen in the study. By adopting machine learning techniques, Türkiye can increase the efficiency, accuracy, and transparency of its property valuation system, ultimately benefiting both homeowners and government agencies.

Acknowledgement

This study was carried out as part of the Design Project thesis prepared by B.K. Sağlam at ITU Geomatics Engineering.

References

Alfaro-Navarro, J-L., Cano, E. L., Alfaro-Cortés, E., García, N., Gámez, M., & Larraz, B. (2020). A fully automated adjustment of ensemble methods in machine learning for modeling complex real estate systems. Complexity, Article ID: 5287263, https://doi.org/10.1155/2020/5287263

Aydinoglu, A.C., Bovkir, R., & Colkesen, I. (2021). Implementing a mass valuation application on interoperable land valuation data model designed as an extension of the national GDI. Survey Review, 53(379), 349–365. https://doi.org/10.1080/00396265.2020.1771967

Benjamin, J.D., Guttery, R. S., & Sirmans, C. F. (2020). Mass appraisal: an introduction to multiple regression analysis for real estate valuation. Journal of Real Estate Practice and Education, 7(1), 65–77. https://doi.org/10.1080/10835547.2004.12091602

Demetriou, D. (2017). A spatially based artificial neural network mass valuation model for land consolidation. Environment and Planning B: Urban Analytics and City Science, 44(5), 864–883. https://doi.org/10.1177/0265813516652115

Dimopoulos, T., & Moulas, A. (2016). A proposal of a mass appraisal system in Greece with CAMA system: evaluating GWR and MRA techniques in Thessaloniki municipality. Open Geosciences, 8(1), 675–693. https://doi.org/10.1515/geo-2016-0064

Doldur, M., & Alkan, R. M. (2021). Producing GIS-based land value maps by using nominal valuation method: case study in Avanos/Nevşehir. Afyon Kocatepe Üniversitesi Fen ve Mühendislik Bilimleri Dergisi, 21(4), 846–863 (in Turkish). https://doi.org/10.35414/akufemubid.888502

El Naqa, I., & Murphy, M.J. (2015). What is machine learning? In: El Naqa, I., Li, R., Murphy, M. (eds) Machine Learning in Radiation Oncology. Springer, Cham. https://doi.org/10.1007/978-3-319-18305-3_1

Gnat, S. (2021). Property mass valuation on small markets. Land, 10(4):388. https://doi.org/10.3390/land10040388

Lee, C. (2023). Designing an optimal neural network architecture: an application to property valuation. Property Management. 41(1), 84-96. https://doi.org/10.1108/PM-12-2021-0106

Lisi, G. (2019). Property valuation: the hedonic pricing model-location and housing submarkets. Journal of Property Investment & Finance, 37(6), 589–596. https://doi.org/10.1108/JPIF-07-2019-0093

Mete, M.O., & Yomralioglu, T. (2019). Creation of nominal asset value-based maps using GIS: a case study of Istanbul Beyoglu and Gaziosmanpasa districts. GI_Forum Journal for Geographic Information Science, 7(2), 98–112. https://doi.org/10.1553/giscience2019_02_s98

Mete, M.O., & Yomralioglu, T. (2023). A hybrid approach for mass valuation of residential properties through geographic information systems and machine learning integration. Geographical Analysis, 55(4), 535-559. https://doi.org/https://doi.org/10.1111/gean.12350

Ngiam, K.Y., & Khor, W. (2019). Big data and machine learning algorithms for health-care delivery. The Lancet Oncology, 20(5), e262–e273. https://doi.org/10.1016/S1470-2045(19)30149-4

Sisman, S., & Aydinoglu, A.C. (2022). A modelling approach with geographically weighted regression methods for determining geographic variation and influencing factors in housing price: a case in Istanbul. Land Use Policy, 119(106183). https://doi.org/10.1016/j.landusepol.2022.106183

Wang, D., Li, V.J., & Yu, H. (2020). Mass appraisal modeling of real estate in urban centers by geographically and temporally weighted regression: a case study of Beijing's core area. Land, 9(143). https://doi.org/10.3390/LAND9050143

Yalpır, Ş. (2018). Enhancement of parcel valuation with adaptive artificial neural network modeling. Artificial Intelligence Review, 49(3), 393–405. https://doi.org/10.1007/s10462-016-9531-5

El Yamani, S., Ettarid, M., & Hajji, R. (2019). Building information modeling potential for an enhanced real estate valuation approach based on the hedonic method. WIT Transactions on the Built Environment, 305–316. https://doi.org/10.2495/bim190261

Yilmazer, S., & Kocaman, S. (2020). A mass appraisal assessment study using machine learning based on multiple regression and random forest. Land Use Policy, 99:104889. https://doi.org/10.1016/j.landusepol.2020.104889

Yomralioglu, T. (1993). A nominal asset value-based approach for land readjustment and its implementation using geographical information systems. University of Newcastle upon Tyne.

7th Intercontinental Geoinformation Days

igd.mersin.edu.tr

Spatial clustering of villages: a solution for agricultural area management: Case study of Aghmiyun agricultural area, East Azerbaijan Province, Iran

Javad Ghasemi [1], **Bahman Tahmasi** [*2]

[1]*Agricultural Research Education and Extention Organization, Tehran, Iran*
[2]*University of Tehran, Faculty of Geography, Department of Human Geography, Tehran, Iran*

Keywords
Spatial clustering
Villages
Aghmiyun
Agricultural Area
Agricultural Jihad Center

Abstract

All of the world's basic needs are provided by the agricultural sector, and it also provides the raw materials required for industrial processes. Thus, the appropriate administration and development of agriculture are crucial. Like a number of other countries, Iran faces numerous social, economic, environmental, institutional, and human challenges in the development and administration of its agricultural sector. For managing the agricultural sector, Iran has established many different kinds of organizational structures. The Agricultural jihad centers work at the lowest level of the Iranian agriculture sector's governmental administration hierarchy. Each agricultural jihad center covers one or more rural district and a number of villages. The villages covered by each center are divided among the experts who work in the center. How to divide up villages among experts is a major problem facing agricultural jihad centers. Typically, the number of villages under expert administration is not homogeneous, and the allocation of villages among experts is not done appropriately. In this study, village classification has been investigated utilizing four different spatial clustering techniques: KMeans, KMedians, KMedoids, and Spectral Cluster. The findings indicate that while all of these techniques are capable of spatial clustering of villages, KMeans and KMedians are the most effective and useful techniques for clustering.

1. Introduction

Historically, agriculture has been the most important part of economic activities. And with the occurrence of the industrial revolution, the agricultural sector, in addition to providing the food needed by human societies, also became the supplier of the major part of the raw materials needed by the industry (Pinilla, 2019). For many countries worldwide, particularly developing countries, agriculture provides their main source of income for rural households, employment, added value, exports, addressing poverty, and ensuring food security for a growing population (Atay & Kartal, 2020; Kumar, 2018). Therefore, agricultural development is necessary for the growth of industry and the satisfaction of human population needs (Sabuncu, 2019).

Planning in the agricultural sector for maximizing yields and profit, improving the quality of products, developing agricultural technology and equipment, using new knowledge in agricultural activities, and protecting water and soil resources is very necessary (Margarido & Santos, 2015; Vlad, 2014; Chen, 2018; Kumawat et al, 2020).

agriculture sector faced by challenges such as illiteracy, poor socioeconomic conditions, lack of technical knowledge, small land holdings, land degradation, weather-dependent farming systems and adaptation to climate change (Dwivedy, 2011; Moreddu, 2015; Selvan et al, 2021).

Agriculture is also very important in Iran. About 50% of employment in rural areas of Iran is in the agricultural sector. More than 60 thousand villages and 25.9% of Iran's population live in rural areas that are directly or indirectly related to agricultural activities (Statistical Centre of Iran, 2016). Also, Iran has 5 million farmers in the agricultural sector, about 15 million hectares of agricultural land (Ministry of Agriculture Jihad, 2021) and about 130 million hectares of natural areas (Natural Resources and Watershed Management Organization Of Iran, 2023).

The agricultural sector in Iran is very broad and faces many challenges. Various organizational structures have been established at the national, provincial, county,

* **Corresponding Author**

(javadghasemi710@gmail.com) ORCID ID xxxx – xxxx – xxxx – xxxx
*(bahman.tahmasi@ut.ac.ir) ORCID ID 0000-0002-7742-814X

Cite this study

Ghasemi, J., & Tahmasi, B. (2023). Spatial clustering of villages: a solution for agricultural area management: Case study of Aghmiyun agricultural area, East Azerbaijan Province, Iran. Intercontinental Geoinformation Days (IGD), 7, 111-114, Peshawar, Pakistan

and rural areas levels in Iran to regulate the country's agricultural sector.

Centers of agricultural jihad are engaged at the lowest level of the organizational structure and at the level of rural areas. A number of agricultural experts work inside of each of these agricultural centers, offering advice and instruction to farmers. For this reason, the villages covered by agricultural jihad centers are often divided between the experts based in the agricultural jihad center. Each expert is responsible for managing agricultural activities in a number of villages.

However, the fundamental issue is that, in this field, appropriate indications and methods for zoning and dividing villages between the experts working in the centers have not been developed. Therefore, the dividing of villages between experts is typically not done appropriately and equitably. The spatial clustering method has been attempted to be used in this study as a simple and helpful technique for zoning rural and agricultural areas. In order to improve agricultural area management, the aim of this article is to spatial cluster the villages under the management of the Aghmiyun Agricultural Jihad Center in the province of East Azarbaijan.

2. Method

This study is a type of applied research that was carried out using a quantitative methodology framework. The 48 villages that are under the Aghmiyun Agricultural Jihad Center in the province of East Azarbaijan make up the statistical population for this study. The required statistical data has been collected from the Agricultural Institute of Education and Extension in Iran. Spatial analysis and spatial statistics techniques in Arc Map and GeoDa software have been used for data analysis. Seven indicators in total, which is the number of farmers, the area under irrigation crops, the area under rainfed crops, the area of horticulture crops, the area of greenhouses, the population living in rural areas, and the distance between the villages and the Aghmiyun agricultural Jihad center were used in this study to cluster the villages geographically. Seven steps are involved in discovering and utilizing the index: a review of the literature, indicators identification, indicators validation, data collection, indicators weighting, indicators combination, and village spatial clustering. Based on the opinions of twenty experts in the fields of agriculture and rural development, the indicators have been validated and weighted. Here is how the research process works (Figure 1):

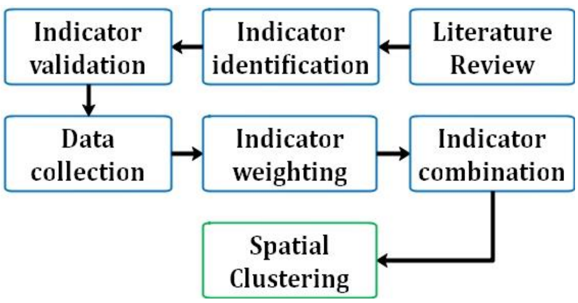

Figure 1. Research Process

2.1. Study Area

The Aghmiyun Agricultural Jihad Center's agricultural fields are included in the research area under study. As to the most recent data, Aghmiyun, Razlig, and Sayin are the three rural districts that are covered by this center. The Aghmiyun Agricultural Jihad Center covers fifty villages in total, two of which are uninhabited and have no agricultural activity. Sayin rural district has twenty-seven villages, Aghmiyun rural district has twenty-two, and Razliq rural district has one village out of a total of forty-eight villages (Ministry of Agriculture Jihad, 2023). Aghmiyun Agricultural Jihad Center is located in the central district of Sarab County, East Azarbaijan Province, northeastern Iran (Figure 2).

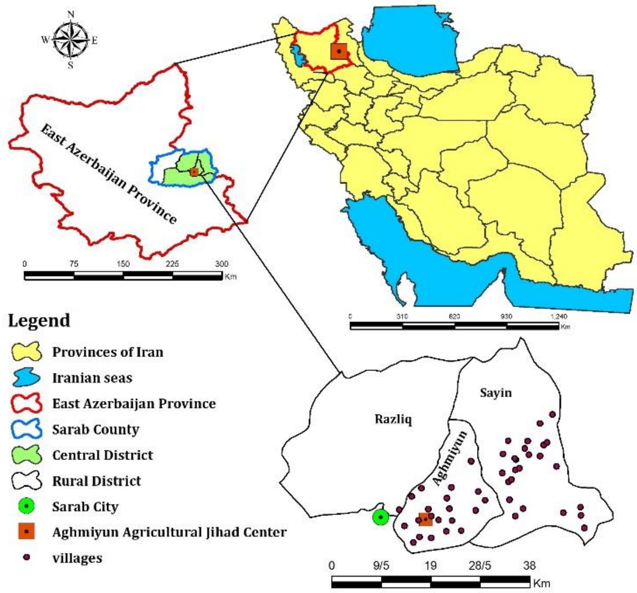

Figure 2. Location of the study area

3. Results

The indicators, their assigned weights, and the values associated with each have been taken into consideration at the beginning of the results section. The Aghmiyun Agricultural Jihad Center covers 12,018 of the rural population, 12,947 hectares of cultivated land, and 3,670 agricultural farmers "Table 1".

Table 1. Weight and values of indicators

Indicator	Weight	Value
Number of farmers (person)	0.2	3670
Area under irrigation crops (hectares)	0.17	9015.25
Area under rainfed crops (hectares)	0.16	3488.6
Area of horticulture crops (hectares)	0.16	442.744
Area of greenhouses (hectares)	0.12	0.24
Rural population (person)	0.14	12018
Average distance between the villages to center (km)	0.05	20
Sum	1	-

Each village's weighted values were calculated separately by multiplying the data of the 48 villages under the Aghmion Agricultural Jihad Center by the indicator's weight.

To find the best method, several techniques for the spatial clustering of villages were evaluated in this section. Given that the Aghmiyun Agricultural Jihad Center employs three experts, it is required to divide the villages under its management into three zones, or three homogeneous clusters. Because of this, there can only be three clusters when applying various clustering techniques. These techniques are all explained below.

Step First: Based on the KMeans technique, the villages were clustered, cluster 1 has 21 villages, cluster 2 has 20 villages, and cluster 3 has 7 villages (Figure 3).

Step Second: Based on Kmedians technique, the villages were clustered, cluster 1 has 19 villages, cluster 2 has 17 villages and cluster 3 has 12 villages (Figure 4).

Step Third: Based on Kmedoids technique, the villages were clustered, cluster 1 has 19 villages, cluster 2 has 18 villages and cluster 3 has 11 villages (Figure 5).

Step Fourth: Based on Spectral Cluster technique, the villages were clustered, cluster 1 has 25 villages, cluster 2 has 14 villages and cluster 3 has 9 villages (Figure 6).

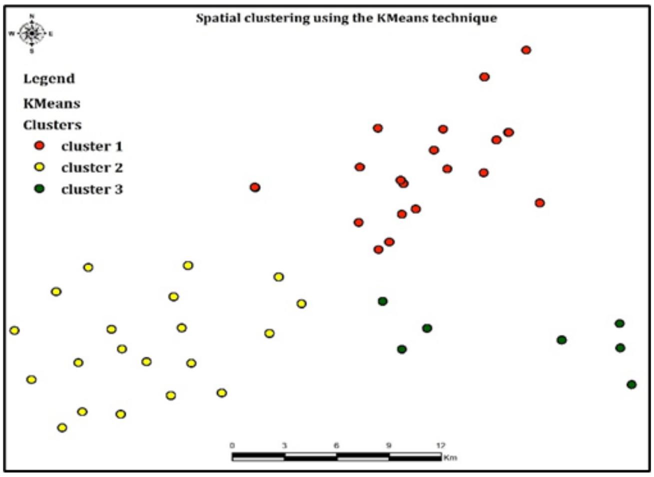

Figure 3. Clustering based on KMeans technique

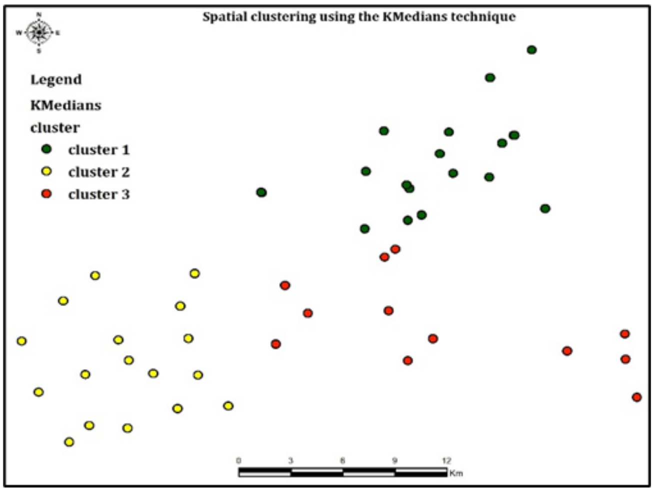

Figure 4. Clustering based on Kmedians technique

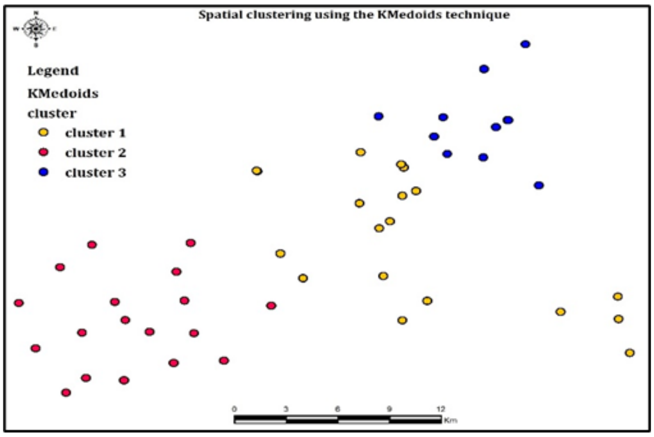

Figure 5. Clustering based on Kmedoids technique

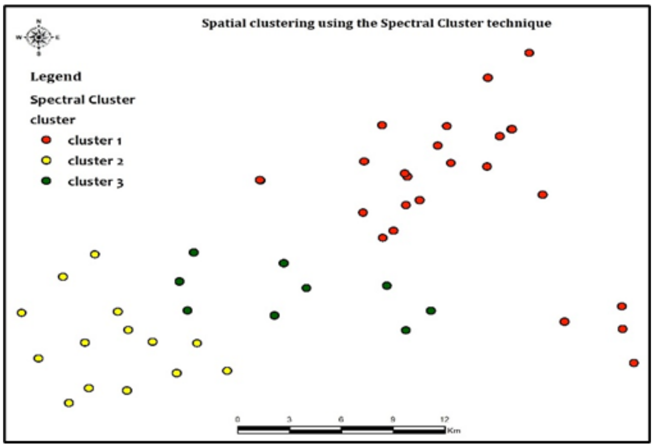

Figure 6. Clustering based on Spectral Cluster technique

4. Discussion

This article discusses the clustering of villages covered by agricultural jihad centers using four simple and helpful techniques. For the purpose of finding homogenous clusters, all four techniques are helpful. In spite of this, the results from the KMeans and Kmedians techniques are better than other techniques in terms of spatial neighborhood and cluster homogeneity.

5. Conclusion

Human societies depend on the agriculture sector for their food security. Furthermore, it meets a significant proportion of the industry sector's needs. Numerous social, economic, environmental, technological, and human resource issues challenge the agriculture sector. Managing human resources as well as providing services to farmers and villages is one of the major issues facing Iran's agriculture sector. In order to better support farmers and promote agricultural development, various types of organizational structures have been established in Iran's agricultural sector at the national, provincial, county, and rural district. In Iran's agricultural sector, the most primitive level of management organizational structure can be observed in agricultural Jihad centers located in rural district. Experts working in agricultural jihad centers are responsible for providing services and managing the villages covered by the center. For this reason, it is necessary to divide the villages effectively and equally among the experts.

The main problem is that, often, experts divide up villages without applying scientific or appropriate methods, which decreases the level of service provided to farmers. For this reason, in this article, an attempt has been made to introduce suitable methods for zoning and spatial clustering of villages. In order to cluster the villages in the Aghmiyun Agricultural Jihad Center, four spatial clustering techniques—KMeans, Kmedians, Kmedoids, and Spectral Cluster—have been examined and tested in this study.

Table 2. Clustering based on different techniques

Clusters	Indicators	KMeans	Kmedians	Kmedoids	Spectral
cluster 1	Number of villages	21	19	19	25
	Number of farmers	599	552	871	871
	Area under cultivation	2293	1991	4039	3241
	Rural population	1676	1530	2220	2452
	Average Distance	30	30	24	30
cluster 2	Number of villages	20	17	18	14
	Number of farmers	3210	3065	3182	2352
	Area under cultivation	10020	9561	9838	7279
	Rural population	10509	10233	10491	7973
	Average Distance	7	6	6	5
cluster 3	Number of villages	7	12	11	9
	Number of farmers	595	787	350	1181
	Area under cultivation	2795	3556	1232	4588
	Rural population	1516	1938	990	3275
	Average Distance	24	21	33	13

The results of spatial clustering show that all four investigated techniques have the appropriate ability to cluster and divide villages into several homogeneous clusters. Despite the reality that each of these techniques produce different results. When it comes to village clustering, the KMeans and KMedians techniques are better than the others. Because of the spatial neighborhood between the villages has been observed in a more appropriate way and the clustering carried out using these two methods has been more homogeneous and equal. With using these two techniques, there is very little difference between the three clusters that are produced in terms of the number of farmers, the cultivated area, the average distance, and the number of villages that are located in each cluster.

Based on these results, the experts working in the agricultural jihad centers are advised to cluster and divide the number of villages among themselves using the KMeans and Kmedians techniques. Efficient rural zoning promotes better agricultural areas management and faster, higher-quality services for farmers.

References

Atay, M. S., & Kartal, C. (2020). Tarımsal ürün pazarlaması ve tarımsal işlemlerin muhasebeleştirilmesi. Süleyman Demirel Üniversitesi İktisadi ve İdari Bilimler Fakültesi Dergisi, 25(2), 185-201.

Chen, G. (Ed.). (2018). Advances in agricultural machinery and technologies. CRC Press.

Dwivedy, N. (2011). Challenges faced by the agriculture sector in developing countries with special reference to India. International Journal of rural studies, 18(2).

Kumar, A. (2018). Issues and prıorıtıes areas of agrıculture ın Indıa. Turkish Journal of Computer and Mathematics Education (TURCOMAT), 9(1), 215-224.

Kumawat, A., Yadav, D., Samadharmam, K., & Rashmi, I. (2020). Soil and water conservation measures for agricultural sustainability. Soil moisture importance, 23.

Margarido, F. B., & Santos, F. (2015). Agricultural planning. In Sugarcane (pp. 1-11). Academic Press.

Ministry of Agriculture Jihad, (2023). Comprehensive system of zoning and management of agricultural data http://poud.maj.ir/ (in Persian)

Ministry of Agriculture Jihad. (2021). Statistical yearbook of Iran's agricultural sector. (in Persian)

Moreddu, C. (2015). Challenges and opportunities for food and agriculture in the 21st Century. Options Méditerranéennes. Série A, Séminaires Méditerranéens, (113), 15-22.

Natural Resources and Watershed Management Organization Of Iran. (2023). https://frw.ir/ (in Persian)

Pinilla, V. (2019). Agricliometrics and agricultural change in the nineteenth and twentieth centuries. Handbook of Cliometrics, 1203-1235.

Sabuncu, H. T. (2019). Tarımın Ekonomi Uzerindeki Etkisi Turkiye Ornegi. Ekonomi Isletme ve Yonetim Dergisi, 3(1), 25-33.

Selvan, S. S., Wahid, A., Patel, A., Kumar, V., & Sahu, P. (2021). Challenges in Indian agriculture. Agricultural Reviews, 42(4), 456-459.

Statistical Centre of Iran. (2016). General population and housing census. (in Persian)

Vlad, M. C. (2014). Use planning analysis on agricultural holdings according to their physical size: Case study. In Agrarian Economy and Rural Development-Realities and Perspectives for Romania. 5th Edition of the International Symposium, November 2014, Bucharest (pp. 163-168). Bucharest: The Research Institute for Agricultural Economy and Rural Development (ICEADR).

7th Intercontinental Geoinformation Days

igd.mersin.edu.tr

The investigation of house value criteria in Atakum-Mimarsinan District Pre- and Post-Pandemic by multiple regression analysis

Simge Anaklı*[1], Yasemin Sisman [2], Mehmet Emin Tabar [3]

[1]Ondokuz Mayıs University, Institute of Graduate Studies, Department of Geomatics Engineering, Samsun, Türkiye
[2]Ondokuz Mayıs University, Faculty of Engineering, Department of Geomatics Engineering, Samsun, Türkiye
[3]Bitlis Eren University, Vocational School of Technical Sciences, Department of Architecture and Urban Planning, Bitlis, Türkiye

Keywords
House Valuation,
Multiple Regression Analysis,
Minitab
Modelling

Abstract

Real estate valuation is the impartial appraisal and determination of the value of a real estate property by evaluating its characteristics such as utility, quality and environment. In recent years, the whole world has faced the Covid19 pandemic. Although the pandemic has actually ended, its impact on human life still continues. It has been observed that living habits have changed in every field due to the pandemic. This study has been prepared by wondering the impact of this change on the importance of the criteria that affect the house valuation. Different methods can be used in real estate valuation. These approaches are categorized under 2 main headings: traditional methods, modern methods and statistical methods. The aim of this study is to analyse the data before and after the pandemic in Atakum-Mimarsinan district of Samsun province using a multiple regression model in the Minitab program and to compare the change in the coefficients of the criteria affecting the house value. As a result of the study, when the coefficients of the criteria affecting the house valuation pre-and post-pandemic are compared, it is concluded that the coefficient of the floor area has decreased, while the number of rooms has become more important.

1. Introduction

In simple terms, real estate is land, which is a physical asset, and structures built on it by people. In legal terms, the term "real estate" is generally defined as fixed assets that cannot be moved such as land, land, buildings and independent sections. There are 5 types of real estate according to their intended use: residential, commercial, industrial, agricultural and special purpose real estate. Residential real estate is that people use to live in safety, to meet one of their most basic needs for shelter or as a means of investment for the future.

Value is defined as, an abstract measure to determine the importance of something. Value is not a tangible data and is an estimate of the price to be paid for goods and services at any given time. In a purchase and sale contract, the price is the amount of money the seller agrees to receive and the buyer agrees to give under certain conditions (International Valuation Standards Council (IVSC)).

There are many methods for real estate valuation. These methods are divided into 2 headings as traditional, modern and statistical methods given in ''Table 1.'' However, for professional real estate valuation, subjective value based on the opinions of individuals it is essential to make use of a mathematical model rather than forecasts (Tabar, et al. 2021).

Table 1. Real Estate Valuation Methods

Traditional Methods	Modern and Statistical Methods	
*Cost Method	*Fuzzy Logic	*Nominal Method
*Income Method	*Structural Equation Modelling	Multiple *Regression Method
*Comparison Method	*Support Vector Machine	*Hedonic Pricing Method
	*Artificial Neural Network	*Spatial Analysis

House valuation is the determination of the value of a real estate by evaluating the benefit provided from a real estate, provided that it is impartial, the characteristics of the real estate such as its quality, environmental assessment and determination (Hışır, 2009). Valuation is the process of determining the value of an asset at a given point in time by collecting data on the asset and analysing them independently and objectively. House valuation requires a comprehensive examination as the other

* **Corresponding Author**

*(simgeanaklii@gmail.com) ORCID ID 0009 – 0002 –0719 – 8876
(ysisman@omu.edu.tr) ORCID ID 0000 – 0002 – 6600 – 0623
(metabar@beu.edu.tr) ORCID ID 0000 – 0002 – 3234 – 5340

Cite this study

Anakli, S., Sisman, Y., & Tabar, M. E. (2023) The investigation of house value criteria in Atakum-Mimarsinan District Pre- and Post-Pandemic by multiple regression analysis. Intercontinental Geoinformation Days (IGD), 7, 115-118, Peshawar, Pakistan

valuation. Because property is very important both in the world and in Türkiye, and throughout history, states have fought with each other to dominate and own land. The aim valuation process is to reach the fairest, most consistent and accurate conclusion possible. The house valuation influenced by many factors such as the community profile of the region, the location, the closeness to natural disaster zone, the structural and environmental features of the real estate. It is understated that the house valuation process is a very detailed and complex.

In recent years, the Covid19 pandemic has affected the whole world. Although the pandemic has actually ended, its impact on our living habits continues. Human life has changed due to the pandemic. This study was prepared by wondering the effect of this change on the importance of the criteria that affect the house valuation.

The aim of this study is to analyse the pre-and post-pandemic data of Atakum-Mimarsinan neighbourhood by multiple regression analysis (MRA) in the Minitab program and to interpret the changes in criteria coefficients by sorting comparing them.

2. Material and Method

2.1 Material

House valuation, many criteria that affect the value of real estate can be identified. In the literature, 17 different local studies were examined (Bulut et al.,2015; Calmasur & Aysin, 2019; Sisman & Sisman, 2013; Sisman & Sisman, 2016; Tabar, 2020; Tabar et al., 2021; Tabar et al., 2021; Uladi & Uladi,2017; Yayar & Gul, 2014; Yilmazel et al.,2018) and 8 different criteria that are most frequently used in these studies and affect the house price were identified. These criteria are area, number of rooms, age of the building, floor, number of floors in the building, heating method, number of bathrooms and balcony. The study was conducted in Atakum-Mimarsinan neighbourhood. The study area is shown in Figure 1. Atakum-Mimarsinan neighbourhood were preferred because they are the most developing district and neighbourhood of the region. A total of 82 data were collected, 32 pre-pandemic ''Table 2'' and 50 post pandemic ''Table 3''. The data were taken from a real estate sales website. While the data of post-pandemic covers the period June-August 2023, the data of pre-pandemic belongs to 2020.

Table 2. Data of Pre-Pandemic (Tabar, 2020)

Area	Room	Building Age (years)	Floor	Building Floor	Heating Method	Bathroom	Balcony	Value (TRY)
135	3+1	11-15	1	4	natural gas	1	yes	275000
120	3+1	11-15	2	5	natural gas	1	yes	260000
120	3+1	11-15	1	6	natural gas	1	yes	190000
150	3+1	5-10	3	5	natural gas	2	yes	375000
...	...	...	...	...	...	...	...	...
140	3+1	5-10	2	5	natural gas	1	yes	300000
120	2+1	5-10	3	3	natural gas	1	yes	240000

Table 3. Data of Post-Pandemic

Area	Room	Building Age (years)	Floor	Building Floor	Heating M.	Bathroom	Balcony	Value (TRY)
130	3+1	5-10	3	9	natural gas	2	yes	3.400.000
115	3+1	16-20	2	4	natural gas	1	yes	2.200.000
125	3+1	21-25	5	6	natural gas	1	yes	1.950.000
130	3+1	5-10	4	4	natural gas	1	yes	2.990.000
...	...	...	...	...	...	...	...	...
100	2+1	16-20	2	4	natural gas	1	yes	1.500.000
100	3+1	16-20	ground floor	5	natural gas	1	yes	990.000

Figure 1. Study Area

2.2 Method (Multiple Regression Analysis)

In general, regression analysis is the analysis of the relationship between two or more variables. it is used to explain whether there is a relation and, if there is a relation, how to demonstrate it. Regression is defined in modern statistics as finding the unknown with the help of the known (Akıs, 2013). Regression analysis aims to make functional sense of the relationship between variables as well as to express the existing relationship as a model.

In MRA, there is one dependent variable and one or more independent variables (Tabar, Basara, Sisman, 2021). MRA is formulated as follows:

$$Y_i = \beta_0 + \beta_1 X_{1i} + \beta_2 X_{2i} + \dots\dots\dots + \beta_n X_{ni} + \varepsilon$$

Here; Y_i: is response variable, X_i: is independent criteria, i = 1, 2, ..., n;, β_0 and β_i are coefficients of criteria (Durmus,2016)

The data given in ''Table 2'' and ''Table 3'' must be normalized before analysis. There are many normalization methods, in this study data of pre- and post-pandemic were normalised according to the minimum-maximum method.

$$Normalized\ data = \frac{(x-\min)}{(\max-\min)}$$

While evaluating the number of floors of the building and the floor where the subject real estate is located, the ratio of each other and quartiles were utilised. Since the region determined as the study area is a region where flood disasters are frequently experienced due to excessive rainfall and inadequate infrastructure, all of the floors below the 1st floor are taken into consideration when scoring as the place that will be most quickly affected by a possible disaster situation. Another issue taken into consideration while scoring is that the houses with (1+1) room number are more in demand due to the high student population in Atakum district. The scores used during normalisation are as in the table below ''Table 4''.

Table 4. The Rating of Normalized Criteria

Criteria	Values		
Area	47: (0) 185: (1)	Building Age	0: (1) 1-5: (0,8889) 5-10: (0,6667) 11-15: (0,4445) 16-20: (0,3333) 21-25: (0,2222) 26-30: (0)
Room	1+1: (0,5) 2+1: (0,25) 3+1: (0,75) 4+1: (1)		
Heating Method	Centralized Heating S.: (1) Natural Gas: (0.75)	Floor Status	1st floor below: (0) Q1: (0.25) Q2: (0.50) Q3-Q4: (1) Top Floor: (0.75)
Bathroom	1: (0) 2: (1)		
Balcony	Yes: (1) No: (0)		

Normalised data pre and post-pandemic are shown in ''Table 5''and ''Table 6''.

Table 5. Normalized Data of Pre-Pandemic (Tabar, 2020)

Area	Room	Age	Floor St.	Heating M.	Bathroom	Balcony
0.75	0.75	0.4445	0.25	0.75	0	1
0.60	0.75	0.4445	0.50	0.75	0	1
0.60	0.75	0.4445	0.25	0.75	0	1
...	...	...	...	...	...	...
0.80	0.75	0.6667	0.50	0.75	0	1
0.60	0.25	0.6667	0.75	0.75	0	1

3. Results

MRA was performed with Minitab program on normalized data. In the process the Analysis of Variance (ANOVA) and the significance test of criteria were realized. The results of applications were given in ''Table 7'' and ''Table 8'' respectively. Since the heating type and balcony criteria were the same in all data pre- pandemic, the analysis was carried out by excluding these criteria.

The P value of ANOVA table shows the possible amount of error that can be made when it is desired to decide that there is a statistically significant difference in comparisons.

Table 6. Normalized Data of Post-Pandemic

Area	Room	Age	Floor St.	Heating M.	Bathroom	Balcony
0.601	0.75	0.67	0.50	0.75	1	1
0.493	0.75	0.33	0.50	0.75	0	1
0.565	0.75	0.22	1	0.75	0	1
...	...	...	...	...	...	...
0.384	0.25	0.33	0.50	0.75	0	1
0.38	0.75	0.33	0	0.75	0	1

Table 7. ANOVA for Pre-Pandemic Data

Criteria	Adj SS	Adj MS	F	P
area	0.21149	0.21149	6.22	0.019
room	0.00069	0.000686	0.02	0.888
buildingage	0.12578	0.125776	3.7	0.066
floorstatus	0.07359	0.073588	2.16	0.153
bathroom	0.12721	0.127212	3.74	0.064

If the P value of criteria is bigger than the significance level (0.05), it is decided that this criterion is affect the house value. In this case, it is concluded that the area criterion affects the value for the pre-pandemic period, while the others do not affect the value as they have values above the significance level. Also, the regression equation can be created from significance test results. The regression equation of pre-pandemic data is as follows;

House Value = -0,273 + 0,547 area + 0,035 room + 0,393 buildingage + 0,204 floorstatus + 0,1841 bathroom

When the weights in the equation are ranked from largest to smallest, the ranking of area, age, floor status, bathroom and number of rooms is obtained.

Table 8. ANOVA for Post Pandemic Data

Criteria	Adj SS	Adj MS	F	P
area	0.16588	0.165878	15.87	0.000
room	0.00436	0.004359	0.42	0.522
buildingage	0.17446	0.174456	16.69	0.000
floorstatus	0.00218	0.002182	0.21	0.650
heatingmethod	0.1107	0.110698	10.59	0.002
bathroom	0.07936	0.07936	7.59	0.009
balcony	0.0267	0.026695	2.55	0.117

When P values for the post-pandemic period ''Table 8''were examined, it was determined that the area, age, heating system and bathroom criteria, which were below the significance level, were effective in the house value. The equation for the after the pandemic MRA is as follows:

House Value = 0.912 + 0.407area + 0.0554 room + 0.2697 buildingage+ 0.0224 floorstatus+ 0.847 heatingmethod+ 0.1217 bathroom+ 0.0924 balcony

When the weights in the equation are sorted from largest to smallest, the order of heating method, area, age, bathroom, number of rooms and floor status is obtained.

4. Discussion

The MRA results for pre-and-post pandemic data can be summaries in the ''Table 9''. The R-sq value indicates the variability of the model that can be explained by the independent variables. R-sq adjusted for degrees of freedom is R sq (adj).

Table 9. Model Summaries

	S	R-sq	R-sq(adj)	R-sq(pred)
Before	0.18443	66.02	59.49	46.59
After	0.102225	78.56	74.99	63.36

According to ''Table 9'', it is seen that the post-pandemic data can be more explained than pre-pandemic. Also, although the accuracy level can be increased with more data after the pandemic, since there was no difference in the pre-pandemic data, the heating method and balcony and post-pandemic data could not be compared. In addition, more accurate results can be obtained by increasing the factors that will affect the value.

5. Conclusion

The conclusions of this study can be taken follows;

- If the ranking is made according to pre-pandemic data it is obtained that area (0,547) > age (0,393) >floor status (0,204) > bathroom (0,1841) >number of rooms (0,035),
- If the ranking is made according to post-pandemic data it is obtained that the heating method (0,847) > area (0,407) > age (0,2697) > bathroom (0,1217) > number of rooms (0,0554) > floor status (0,0224).
- When the coefficient in the equations are compared;
  - ❖ While the area criterion was more effective pre-pandemic (0.547), it was less effective post-pandemic (0.407),
  - ❖ Number of rooms became a more sought-criteria post pandemic (0.035 to 0.0554)
  - ❖ While floor status was a more effective criterion pre-pandemic (0.204), it decreased after the pandemic (0.0224),

There is no significant difference in other criteria. In line with these changes, it can be concluded that people's sensitivity to private space has increased after the pandemic, and the floor status is less effective in housing purchase decisions compared to before the pandemic.

References

Akış, B. (2013). İstatistiki yöntemlerle değer belirleme ve değer haritası üretimi Selçuklu örneği Selçuk Üniversitesi, Yüksek Lisans Tezi, Fen Bilimleri Enstitüsü, Harita Mühendisliği ABD, Konya.

Bulut H., Oner Y., Islamoglu E. (2015). The Investigation of The Factors Affecting On The Prıces Of Real Estates In Samsun Vıa Hedonıc Prıce Model, The Journal of Operations Research, Statistics, Econometrics and Management Information Systems 3(2);121-130

Calmasur G., Emre Aysin M. (2019). Konut Fiyatlarına Etki Eden Faktörlerin Hedonik Modelle Belirlenmesi: TRA1 Alt Bölgesi Üzerine Bir Uygulama, International Journal of Economic and Administrative Studies, 2019(22),77-92.

Durmuş, B. (2016). Konut Fiyatlarını Etkileyen Parametrelerin Çoklu Regresyon Analizi Yöntemiyle İrdelenmesi ve Kentsel Dönüşüme Katkıları. Fen Bilimleri Enstitüsü.

Hışır, M. (2009). Türkiye'de Taşınmaz Değerleme ve Harita Mühendisliği, TMMOB Harita ve Kadastro Mühendisleri Odası, 12. Türkiye Harita Bilimsel ve Teknik Kurultayı, 11-15.

Sisman A. And Sisman Y. (2013). Mesken Değerlemede Faktöriyel Tasarım Uygulaması Samsun İli Örneği, 14. Uluslararası Ekonometri, Yöneylem Araştırması ve İstatistik Sempozyumu.

Sisman, A., & Sisman Y. (2016). Konutun Değerine Etki Eden Faktörlerin Araştırılması.

Tabar, M. E. (2020). Yapay Sinir Ağları ve Bulanık Mantıkla Gayrimenkul Değerleme Modelinin Oluşturulması: Samsun Örneği, Yüksek Lisans Tezi, Ondokuz Mayıs Üniversitesi, Fen Bilimleri Enstitüsü, Harita Mühendisliği ABD, Samsun.

Tabar, M. E., Başara, A. C., & Sisman, Y. (2021) Çoklu Regresyon ve Yapay Sinir Ağları ile Tokat İlinde Konut Değerleme Çalışması, Türkiye Arazi Yönetimi Dergisi, 3(1); 01-07.

Tabar, M. E., Başara, A. C., & Sisman, Y. (2021) Housing Valuation Model in Samsun, Atakum District with Artificial Neural Networks and Multiple Regression Analysis, Advanced Geomatics, 1(1); 27-32.

Uladi, Ş. U. & Uladi, A. İ. (2017). Osmaniye İli Genelinde Konut Özellikleri İle Konut Fiyatları Arasındaki İlişkinin Belirlenmesi, 3(16), 475-480

Yayar, R., Gul, D. (2014). Mersin Kent Merkezinde Konut Piyasası Fiyatlarının Hedonik Tahmini, Anadolu University Journal of Social Sciences 14(3);87-100.

Yılmazel Ö., Afsar A., & Yılmazel, S. (2018). Konut Fiyat Tahmininde Yapay Sinir Ağları Yönteminin Kullanılması, International Journal of Economic and Administrative Studies, 20, 285-30

7th Intercontinental Geoinformation Days

igd.mersin.edu.tr

Detection of collapsed buildings from post-earthquake imagery using mask region-based convolutional neural network

Esra Yildirim*[1], Taskin Kavzoglu [1]

[1] Gebze Technical University, Faculty of Engineering, Department of Geomatics Engineering, Kocaeli, Türkiye

Keywords
Earthquake
Remote sensing
Deep learning
Mask R-CNN
Building detection

Abstract

After large-scale natural disasters such as earthquakes, tsunamis, and floods, the rapid identification of collapsed buildings from high-resolution imagery plays a crucial role in post-disaster damage assessment, reconstruction, and emergency rescue operations. Deep learning (DL) architectures, widely applied across various scientific domains, have also been used for extracting damaged buildings from aerial and satellite images. This study is focused on identifying collapsed buildings using a DL algorithm applied to remotely sensed data collected after the February 6, 2023, Kahramanmaraş earthquake in Türkiye. To achieve this, post-earthquake WorldView-3 image with a spatial resolution of 0.3 m were obtained to establish a building dataset, from which the boundaries of collapsed and intact buildings were manually outlined. The Mask R-CNN model was then trained and validated using various hyperparameter combinations to optimize its performance. Experimental results revealed that the Mask R-CNN model with a ResNet-50 backbone yielded the most accurate results, successfully distinguishing between intact and collapsed buildings with an Average Precision (AP) of approximately 81% and 69%, respectively. The findings of the study illustrate the promising potential of using Mask R-CNN with high-resolution imagery for the detection and mapping of collapsed buildings following earthquake events. This application is particularly significant for post-disaster operations and mitigation studies.

1. Introduction

Earthquakes are considered among the most catastrophic natural calamities, causing extensive damage and resulting in significant loss of life and property. Even though earthquakes are unpreventable, the rapid detection and mapping of collapsed buildings after an earthquake is of utmost significance in emergency response and reconstruction efforts. Moreover, the extent, location, and degree of building damage, as well as the collapsed building rate, reflecting the magnitude of the earthquake, are essential information in supporting the evaluation processes of post-earthquake disasters (Song et al. 2020). While it is possible to obtain an accurate assessment of building damage through field surveys, this conventional method can be time-consuming and costly. It is also inefficient for the rapid evaluation of collapsed buildings during rescue operations (Turker and San 2004).

Due to progress in satellite and sensor technology, remote sensing methods can now capture Earth's surface with incredibly high spatial, spectral, and temporal resolutions. As a result, they have become a potent tool for identifying and tracking the impacts of natural disasters (Rathje and Adams 2008; Dell'Acqua and Gamba 2012; Dong and Shan 2013). A range of studies has been executed aiming to detect building damages triggered by earthquakes through the utilization of aerial and satellite imagery (Serifoglu Yilmaz et al. 2023; Turker and San 2004; Turker and Sumer 2008).

Recent research has explored the application of Convolutional Neural Networks (CNNs) in identifying building damage, displaying their effectiveness in automatically recognizing affected buildings within remotely sensed images. For instance, Moradi and Shah-Hosseini (2020) applied U-Net architecture to pre- and post-imagery of the Haiti earthquake images (WorldView-2) to identify damaged buildings and obtained 68.71% overall accuracy. Zhan et al. (2022) presented an adapted Mask R-CNN model designed for identifying impaired buildings and categorizing these structures based on the severity of their damage. Using the aerial images taken after the Kumamoto earthquake, their proposed model could detect buildings with about 90% accuracy and classified damage levels with about 80% accuracy.

* **Corresponding Author**

*(esrayildirim@gtu.edu.tr) ORCID ID 0000-0002-4951-0488
(kavzoglu@gtu.edu.tr) ORCID ID 0000-0002-9779-3443

Cite this study

Yildirim, E., & Kavzoglu, T. (2023). Detection of collapsed buildings from post-earthquake imagery using mask region-based convolutional neural network. Intercontinental Geoinformation Days (IGD), 7, 119-122, Peshawar, Pakistan

The aim of this research was to detect buildings that collapsed after the February 6, 2023, Kahramanmaraş Earthquake using remotely sensed imagery. To accomplish this, post-earthquake WorldView-3 image were utilized to create a dataset of buildings, and a DL-based Mask R-CNN model was trained and validated with this dataset. The study appraised the efficacy of the model in detecting collapsed buildings and employed the trained model to locate and map damaged structures in a different study zone.

2. Study Area and Dataset

On February 6, 2023, Türkiye was struck by two strong and consecutive earthquakes of magnitude 7.8 and 7.5, causing catastrophic damage to lifelines, facilities and buildings. The first earthquake occurred at 01:17:34 UTC in the Pazarcık district in the Kahramanmaraş province (southern Türkiye). About nine hours later, an aftershock occurred in the Elbistan district of Kahramanmaraş at 10:24:48 UTC (Goldberg et al. 2023).

In this study, the WorldView-3 image acquired on February 7, 2023, just one day after the earthquake, with 0.3 m spatial resolution covering the part of the Islahiye district of Gaziantep province, one of the mostly affected provinces, was employed in the analyses. Building boundaries were manually digitized in ArcGIS Pro 3.03 software in two categories (i.e., "Intact" and "Collapsed") using high-resolution base images of General Directorate of Mapping, a national mapping agency of Turkey, as a reference (Figure 1).

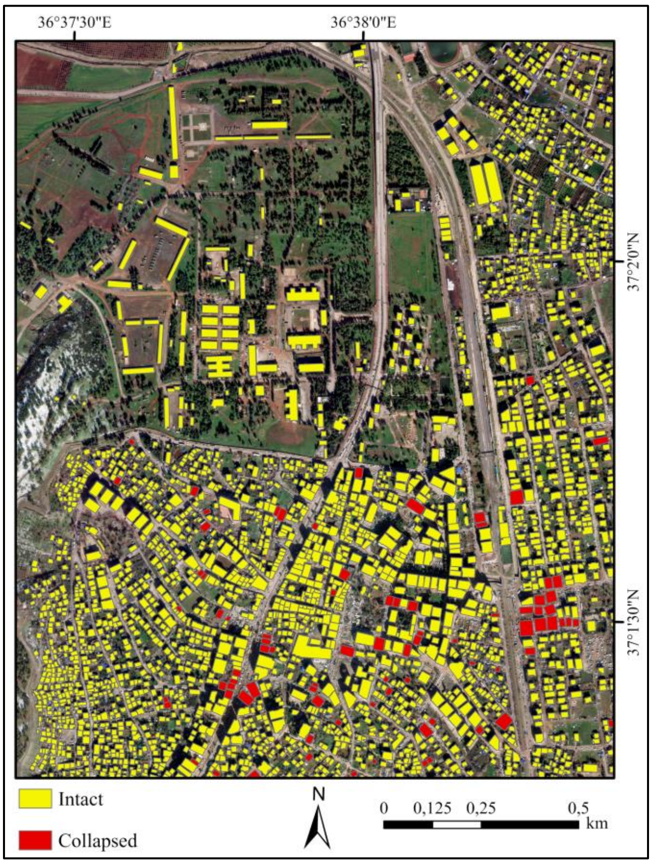

Figure 1. WorldView-3 image in the study area acquired after the 2023 Kahramanmaraş earthquake and locations of intact and collapsed building footprints

To provide training and validation datasets for the DL model, the WorldView-3 image was cropped into 256×256 pixel-sized image chips with a stride of 128×128 pixels (i.e., %50 overlap). The overlap was applied both to expand the dataset and to ensure that each image chip contained at least one building instance of two classes. Besides, the dataset was augmented using 180^0 rotation to increase the number of image samples thus improving the robustness of the model. Consequently, a building dataset containing a total of 3,792 image chips and 31,038 intact and 1,108 collapsed building features was obtained. In addition, corresponding label masks for each image chip were also generated (Figure 2).

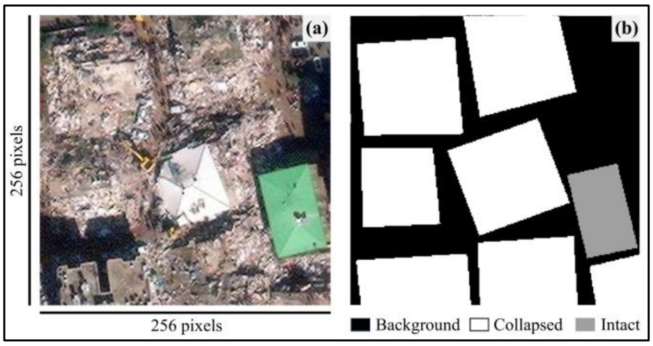

Figure 2. Building dataset, (a) sample of image chip and (b) corresponding ground-truth mask

3. Methods

3.1. Mask Region-Based Convolutional Neural Network (Mask R-CNN)

Mask R-CNN, developed by He et al. (2017), is an enhanced version of Faster R-CNN, capable of predicting both bounding boxes and detailed pixel-wise masks of objects (Figure 3). Mask R-CNN, similar to the Faster R-CNN algorithm, employs a two-stage detection pipeline that starts with the same initial phase, scanning the entire image and generating proposals. In the subsequent phase, while predicting the class and bounding box offsets, Mask R-CNN also generates a segmentation mask for each Region of Interest (RoI). Considering the network architecture of the Mask R-CNN model, it involves: (i) a backbone network (ResNet) responsible for extracting features over a whole image and creating feature maps; (ii) a Region Proposal Network (RPN) for generating regions (RoIs) for areas where objects can be found from feature maps; (iii) a RoI classifier and a bounding box regressor for classifying RoI and refining the bounding box; (iv) a Fully Convolutional Network (FCN) to generate a pixel-wise segmentation mask (Potlapally et al. 2019).

3.1. Design and implementation

The training and validation of the Mask R-CNN model was implemented in ArcGIS API for Python. In order to obtain the best-performing model, different hyperparameter combinations, shown in Table 1, were utilized in the training of the model. Thus, four experiments were conducted using ResNet-50 and ResNet-100 backbone architectures, batch sizes, epochs, and the experimented hyperparameters were adjusted according to the hardware configuration. Additionally, in each model, 90% of the created buildings were used for training and 10% for validation. All experiments were carried out on a Windows 11 laptop with an Intel® Core™ i7-10870H CPU, and a NVIDIA GeForce 3060 RTX GPU, with 32 GB RAM memory.

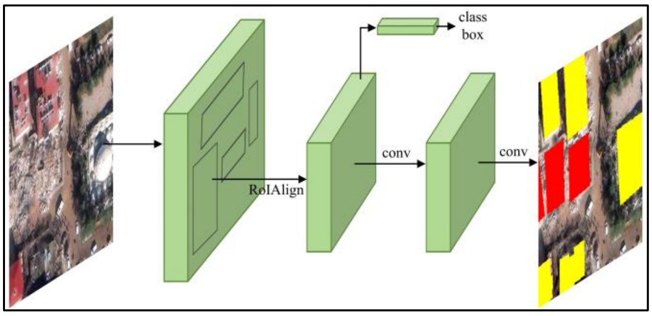

Figure 3. Architecture of the Mask R-CNN algorithm

Table 1. Hyperparameter configuration for Mask-RCNN

	Hyperparameters		
Experiment	**Backbone**	**Batch size**	**Epoch**
1	ResNet-50	2	100
2	ResNet-50	4	100
3	ResNet-100	4	100
4	ResNet-50	2	200

4. Results

The performances of the four trained models were evaluated using the Average Precision (AP) metric calculated for intact and collapsed building classes. The overall accuracy assessments indicated that using Mask R-CNN with a ResNet-50 backbone, trained for 200 epochs across two batch sizes, resulted in the highest AP scores for both intact and collapsed building categories (Table 2). More precisely, it demonstrated improved performance, attaining an AP score of 81.28% for intact or undamaged buildings and 69.26% for collapsed structures. Considering the computational cost of the models, the best-performing model (Experiment 4) required the longest training time of 32 hours and 50 minutes. The model was trained for more than twice the duration of the other models experimented with, owing to the extended training epoch.

Table 2. Performance comparison of Mask R-CNN models trained with different hyperparameters

	Average Precision (AP) (%)		
Experiment	**Intact**	**Collapsed**	**Training Time**
1	80.28	66.61	14 h 2 m
2	79.45	59.24	14 h 45 m
3	74.49	53.72	15 h 35 m
4	81.28	69.26	32 h 50 m

After the training and validation process of the Mask R-CNN model, total loss graphs were generated. It was evident from the loss curves of the most effective Mask R-CNN model that both the training and validation curves exhibited a decreasing trend as the number of epochs increased, reaching their minimum values without overfitting by the end of the process (Figure 4).

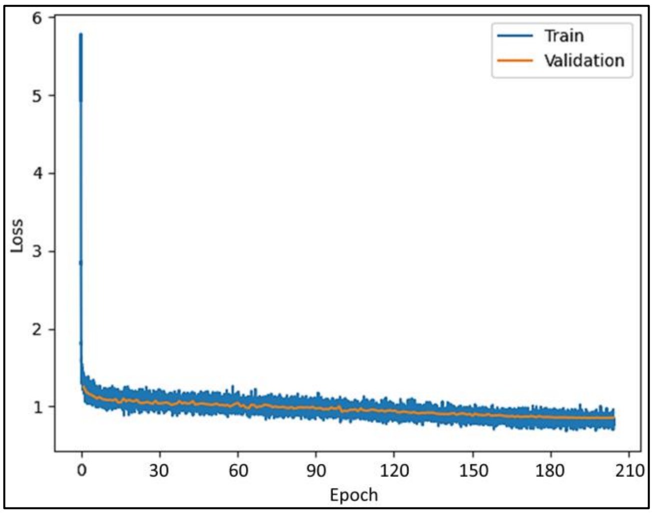

Figure 4. Training and validation loss curves for the Mask R-CNN model

To investigate the transferability of Mask R-CNN combined with best-performing hyperparameters, it was used for the detection and mapping of intact and collapsed buildings on the independent WorldView-3 image, which covers different part of the Islahiye district of Gaziantep province (Figure 5). It was observed that the model was able to accurately distinguish collapsed and intact buildings. However, due to the limited number of collapsed building samples in the training dataset, the model was more robust in identifying and locating intact buildings. Besides, detection errors were observed in collapses due to the viewing angle of the nadir satellite images when the roof of the building did not collapse but the floor collapsed.

5. Conclusion

DL-based algorithms have shown great potential to automatically detect damaged buildings after natural disasters using remotely sensed imagery. In this study, the DL-based Mask R-CNN model was utilized for the identification of collapsed buildings from post-disaster remotely sensed imagery. To meet the objective of the study, a building detection dataset was created using WorldView-3 imagery acquired one day after the February 6, 2023, Kahramanmaraş earthquake. Then, the Mask R-CNN model was trained and validated with the created dataset using different hyperparameter combinations. Experimental results revealed that Mask R-CNN combined with the ResNet-50 backbone and trained with two batch sizes for 200 epochs produced the most accurate results (AP=81.28% for intact buildings, AP=69.26% for collapsed buildings). These results highlighted that the Mask R-CNN model could be an effective solution for detecting and mapping collapsed buildings, which is particularly important for post-earthquake operations. It contributes to the accurate and rapid evaluation of collapsed buildings during emergency rescue operations. However, it should be noted that the main limitation of this study may be attributed to the lack of a high-quality large dataset. To be more specific, the unbalanced instances of collapsed and intact buildings, the constrained spatial resolution, and the use of a single image source were critical issues that influenced the accuracy and generalization ability of the DL model. Given these requirements, the use of an expanded dataset would significantly increase the accuracy and transferability of the study. From this perspective, future research endeavors could emphasize generating a superior building dataset and enhancing the resilience of DL algorithms.

(a)

(b)

Figure 5. Test result, (a) WorldView-3 image of the test site (b) collapsed (red) and intact (blue) buildings detected by the model

References

Dell'Acqua, F., & Gamba, P. (2012). Remote sensing and earthquake damage assessment: Experiences, limits, and perspectives. Proceedings of the IEEE, 100(10), 2876-2890. https://doi.org/10.1109/JPROC.2012.2196404

Dong, L., & Shan, J. (2013). A comprehensive review of earthquake-induced building damage detection with remote sensing techniques. ISPRS Journal of Photogrammetry and Remote Sensing, 84, 85-99. https://doi.org/10.1016/j.isprsjprs.2013.06.011

Goldberg, D. E., Taymaz, T., Reitman, N. G., Hatem, A. E., Yolsal-Çevikbilen, S., Barnhart, W. D., et al. (2023). Rapid characterization of the February 2023 Kahramanmaraş, Türkiye, Earthquake sequence. The Seismic Record, 3(2), 156-167. https://doi.org/10.1785/0320230009

He, K., Gkioxari, G., Dollár, P., & Girshick, R. (2017). Mask R-CNN. IEEE International Conference on Computer Vision, 2961-2969, Venice, Italy. https://doi.org/10.1109/ICCV.2017.322

Moradi, M., & Shah-Hosseini, R. (2020). Earthquake damage assessment based on deep learning method using VHR images. Environmental Sciences Proceedings, 5(1), 16. https://doi.org/10.3390/IECG2020-08545

Potlapally, A., Chowdary, P. S. R., Shekhar, S. R., Mishra, N., Madhuri, C. S. V. D., & Prasad, A. V. V. (2019). Instance segmentation in remote sensing imagery using deep convolutional neural networks. International Conference on Contemporary Computing and Informatics (IC3I), 117-120. https://doi.org/10.1109/IC3I46837.2019.9055569

Rathje, E. M., & Adams, B. J. (2008). The role of remote sensing in earthquake science and engineering: Opportunities and challenges. Earthquake Spectra, 24(2), 471-492. https://doi.org/10.1193/1.2923922

Serifoglu Yilmaz, C., Yilmaz, V., Tansey, K., & Aljehani, N. S. (2023). Automated detection of damaged buildings in post-disaster scenarios: A case study of Kahramanmaraş (Türkiye) earthquakes on February 6, 2023. Natural Hazards, 1-25. https://doi.org/10.1007/s11069-023-06154-z

Song, D., Tan, X., Wang, B., Zhang, L., Shan, X., & Cui, J. (2020). Integration of super-pixel segmentation and deep-learning methods for evaluating earthquake-damaged buildings using single-phase remote sensing imagery. International Journal of Remote Sensing, 41(3), 1040-1066. https://doi.org/10.1080/01431161.2019.1655175

Turker, M., & San, B. T. (2004). Detection of collapsed buildings caused by the 1999 Izmit, Turkey earthquake through digital analysis of post-event aerial photographs. International Journal of Remote Sensing, 25(21), 4701-4714. https://doi.org/10.1080/01431160410001709976

Turker, M., & Sumer, E. (2008). Building-based damage detection due to earthquake using the watershed segmentation of the post-event aerial images. International Journal of Remote Sensing, 29(11), 3073-3089. https://doi.org/10.1080/01431160701442096

Zhan, Y., Liu, W., & Maruyama, Y. (2022). Damaged building extraction using modified Mask R-CNN model using post-event aerial images of the 2016 Kumamoto earthquake. Remote Sensing, 14(4), 1002. https://doi.org/10.3390/rs14041002

7th Intercontinental Geoinformation Days

igd.mersin.edu.tr

Waterbody change detection using Sentinel-3 thermal imagery: A case study of Mighan Wetland, Iran

Maryam Sadat Aghamiri [1], Azadeh Aghamohammadi [1], Zahra Azizi [1*]

[1] *Islamic Azad University, Science and Research Branch, Faculty of Natural Resources and Environment, Department of Remote Sensing and GIS, Tehran, Iran*

Keywords
Change detection
LST
Sentinel3
DTR
wetland

Abstract
The wetland ecosystem is an important indicator of climate change and valuable ecosystems for environment and human being that offer substantial services. This study detects the changes land surface temperature in Mighan wetland in 2018 and 2023 by using Sentinel-3 SLSTR data. Two essential factors were used for detection. LST and DTR factors detect changes in water bodies accurately and correctly. The study finds that in the eastern and southern regions of the wetland, there is a decrease in daily LST, indicating a decrease in water temperature. In the central and western regions, there is a decrease in land temperature. The nightly LST trend shows variations between different regions of the wetland, with the eastern region experiencing lesser changes compared to the central and western regions. Additionally, the article analyzes DTR trends and finds that differences between day and night temperatures decreased over time in the eastern and southern parts of the wetland. These findings contribute to understanding temperature dynamics in wetland ecosystems and their potential implications for climate change impacts.

1. Introduction

Wetlands are valuable ecosystems for both the environment and human beings, offering substantial services (Aghamiri et al., 2022; Alibakhshi et al., 2020). These ecosystems play a significant role in the hydrological cycle, carbon sequestration, ecosystem balance, microclimate stabilization, and the prevention of climate extremes such as droughts, floods, and nutrient imbalances (Mafi et al., 2021; Kattel, 2022; Zhou et al., 2022). Additionally, wetland ecosystems serve as important indicators of climate change and are influenced by climatic factors. They effectively contribute to climate change mitigation at both regional and global scales (Kang et al., 2015).

One of the main factors influencing wetland ecosystems is Land Surface Temperature (LST), which exhibits an inverse relationship with wetland presence (Wang et al., 2022; Pei et al., 2023). LST can be obtained through ground observations, land surface modeling, and satellite remote sensing techniques (Sheffield et al., 2018). In the study of land-atmosphere interactions, relying solely on in situ measurements to meet utility requirements is challenging. Satellite remote sensing technology based on satellite imagery provides a powerful tool for monitoring LST due to its ability to repeatedly observe the same area over time (Hashemi et al., 2022; Qi et al., 2022). The diurnal temperature range (DTR), which represents the difference between daytime and nighttime temperatures in a particular location, is widely used as an important meteorological indicator related to global climate change. DTR trends and variations vary depending on the time scale considered (Bonacci and Đurin, 2023).

It is crucial to assess the impact of climate change on Land Surface Temperature (LST) at both daily and annual time scales. In a study conducted by Musyimi et al (2023), short-term drought in Kenya's lower eastern counties between 2019 and 2021 was analyzed using Sentinel-3 SLSTR data. The researchers derived three essential climate variables: LST, Fractional Vegetation Cover (FVC), and Total Column Water Vapor (TCWV). Their findings revealed that variations in LST were inversely related to vegetation density and soil moisture content. Non-vegetated areas were found to have lower moisture content. Overall, the use of Sentinel-3 SLSTR products proved to be an effective data source for monitoring short-term drought, particularly in situations where in situ measurement data are limited.

* **Corresponding Author**

*(zazizi@srbiau.ac.ir) ORCID ID 0000-0001-8572-7134
(maryam.aghamiri@srbiau.ac.ir) ORCID ID 0009-0008-9659-5809
(azadeh_aghamohammadi@srbiau.ac.ir) ORCID ID 0009 – 0007 – 9486 – 2865

Cite this study

Aghamiri, M. S., Aghamohammadi, A., & Azizi, Z. (2023). Waterbody change detection using Sentinel-3 thermal imagery: A case study of Mighan Wetland, Iran. Intercontinental Geoinformation Days (IGD), 7, 123-126, Peshawar, Pakistan

In another study by Moisa et al (2023), the contribution of forests and wetlands to LST in Yayo district was examined using multi-spectral and multi-temporal satellite Landsat images from 1986, 2003, and 2021. The results indicated that the mean LST increased from 1986 to 2003 but declined over the past two decades due to the protection of forest and wetland ecosystems.

2. Method

2.1. Study area

Meighan wetland is located in of ́49°21 ́ to50°25 ́ east longitude and33°47 ́ to 34°44 ́ north latitude. Meighan wetland is located in 5.8 kilometers northeast of the Arak city in the Farahan Plain and its area is about 100 up to 110 square kilometers and its height is 1660 meter from mean sea level. This wetland is a seasonal saltwater lake and a lowland desert area, and its marginal lands has covered by halophyte bush and shrub plants, sand dunes, alluvial fans and smooth plains.

SLSTR, referring to the Sea and Land Surface Temperature Radiometer, is a dual scan temperature radiometer operating for the ESA Sentinel-3 mission in low Earth orbit as a part of the Copernicus Program. SLSTR products offer highly accurate global and regional Sea and Land Surface Temperatures (SST and LST) for climatological and meteorological applications. In this study, four Sentinel-3 SLSTR Level-2 LST products were downloaded from the Copernicus Open Access Hub. Sentinel-3 SLSTR product generates land surface parameters with a one km spatial resolution.

2.2. Land Surface Temperature (LST)

Land Surface Temperature The radiative temperature of the land in bare soil conditions and the effective emitting temperature of vegetation as determined from a top-view of a canopy determined by infrared radiation are referred to as Land Surface Temperature (LST) (Li et al .,2013) While local modeling relies significantly on field data, remote sensing has become the primary source for LST estimation at different scales (Dar et al .,2019;Meng et al.,2017). The Radiative Transfer Equation (RTE) can be applied to a given thermal IR band to convert radiance observed at a sensor into Land Surface Temperature using Equation (Vlassova et al.,2014)

$$Lsensor = \tau * \varepsilon * LTs + Lu + \tau * (1 - \varepsilon) * Ld \qquad (1)$$

where Lsensor is the top-of-atmosphere radiance; LTs is the radiance related to the surface temperature of a black object as per Planck's law; Ts is the LST; and Lu and Ld are the upwelling and downwelling atmospheric radiances, respectively. τ is the atmospheric transmissivity, while ε is the land surface emissivity. Radiance is expressed in $W \cdot sr^{-1} \cdot m^{-2} \cdot \mu m^{-1}$ (Musyimi et al., 2023).

2.3. Diurnal Temperature Range (DTR)

The daily range of the surface air temperature in a day, i, given as DTRi, represents the difference between the maximum, Tmax ,i, and the minimum, Tmin,i, daily temperature of each day, i, within the analyzed period: (Bonacci and Đurin, 2023).

$$DTRi = Tmax,i - Tmin,i$$

3. Results

3.1. Land Surface Temperature (LST)

LST distribution in Meighan wetland depicted varying spatiotemporal patterns. Figure 1 shows that daily LST estimates ranging between 18 ◦ C and 30 ◦ C in May 2018 and in night LST vary between 18 ◦ C to 26 ◦ C.

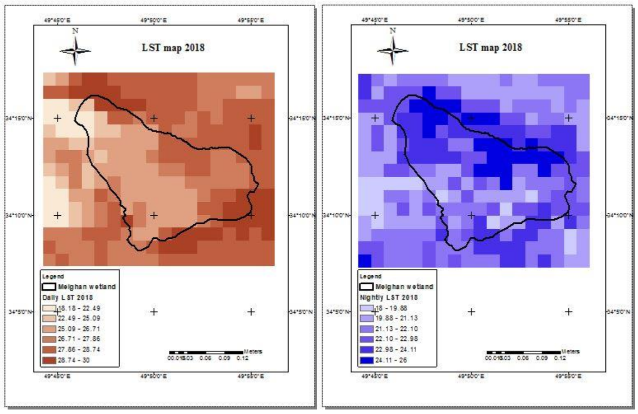

Figure 1. Daily and Nightly LST in 2018

In the same time in May 2023,the daily LST estimates between 19◦ C to 26◦ C and nightly LST estimated ranging between 15 ◦ C and 24 ◦ C (Figure 2).

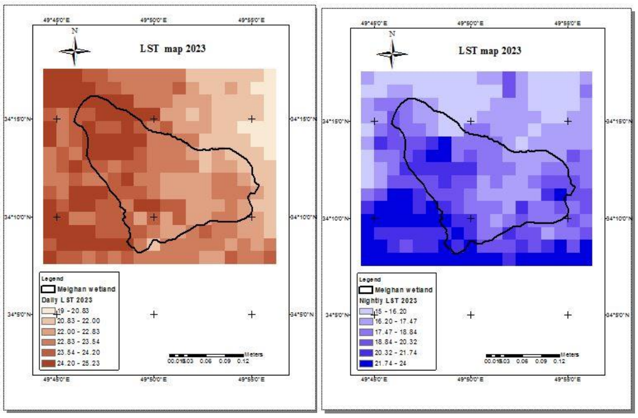

Figure 2. Daily and Nightly LST in 2023

It should be noted that in this study, we aim to monitoring the changes of LST so the LST images were calibrated with true tempreture (Figure 3).

As shows Figure 4 the daily LST and nightly LST trend between 2018 to 2023 is decreasing .

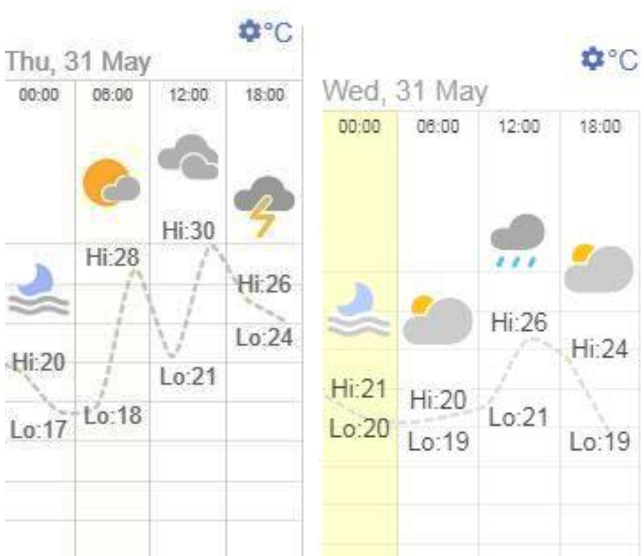

A B

Figure 3. A-real temperature in 31-05-2018
B- real temperature in 31-05-2023

In the East and South of wetland daily LST trend is between -6 ◦ C to -4 ◦ C that shows the water tempreture is decreased.In Central and West of wetland LST trend is between -4 ◦ C to -2 ◦ C in these regions , land tempreture decreased. The nightly LST trend between 2018 to 2023 estimated between -2.96 ◦ C to 0.96 ◦ C in the eastern and between -0.96◦ C to 1.01 ◦ C in western and southern in the Central of wetland it changes between -4 ◦ C to -2.9◦ C.The LST trend is between -9.7◦ C to -6.5 ◦ C in the north of wetland.

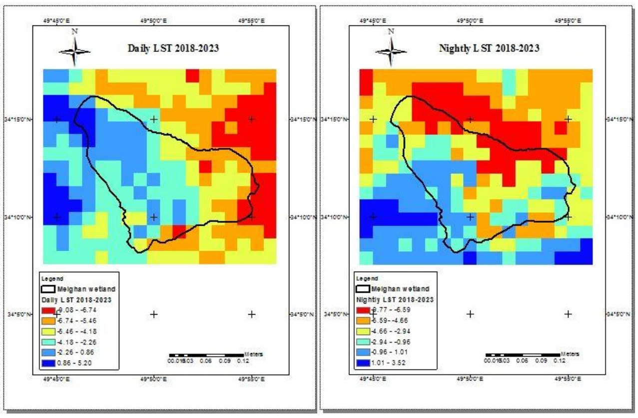

Figure 4. Daily and Nightly LST Map 2018-2023

3.2. Diurnal Temperature Range (DTR)

Figure 5,6 shows a series of DTRs observed at the Meighan Observatory in2018 and 2023. A statistically insignificant downward trend is observed.DTR in 2018 showes a difference between 4◦ C to 8◦ C in the East and South of wetland and in the Central and West ,tempreture is varied between -2 ◦ C to 4.8◦ C. In 2023, DTR changes between -0.3◦ C to 2.88◦ C In the East and South,DTR varies between 2.88◦ C to 7◦ C in the Central and West and in the North is more than 4◦ C .

4. Discussion

Higher daily LST differences in East and South of wetland shows that the water body tempreture deacresed and gets cooler.Although the Center and West of wetland that are covererd by vegetation and land observed few changes in LST.In the East and South nightly LST trend is lesser than the Center and West of wetland.

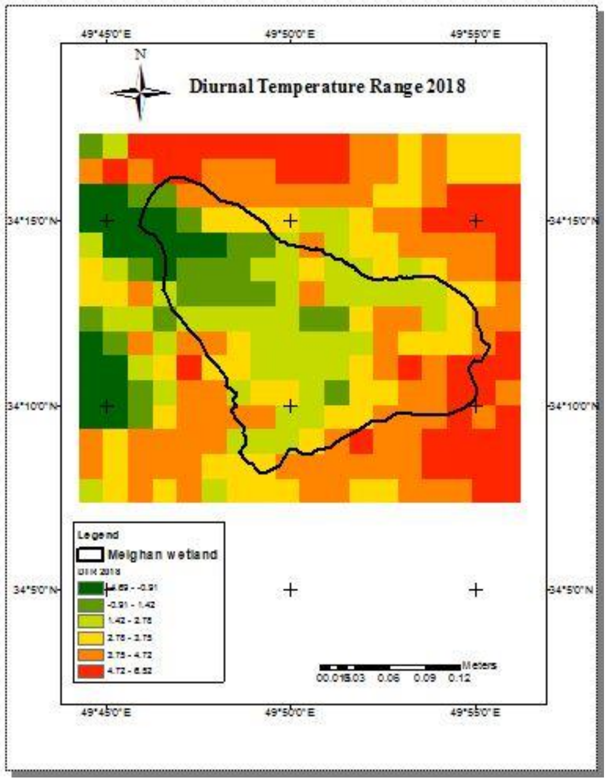

Figure 5. DTR Map 2018

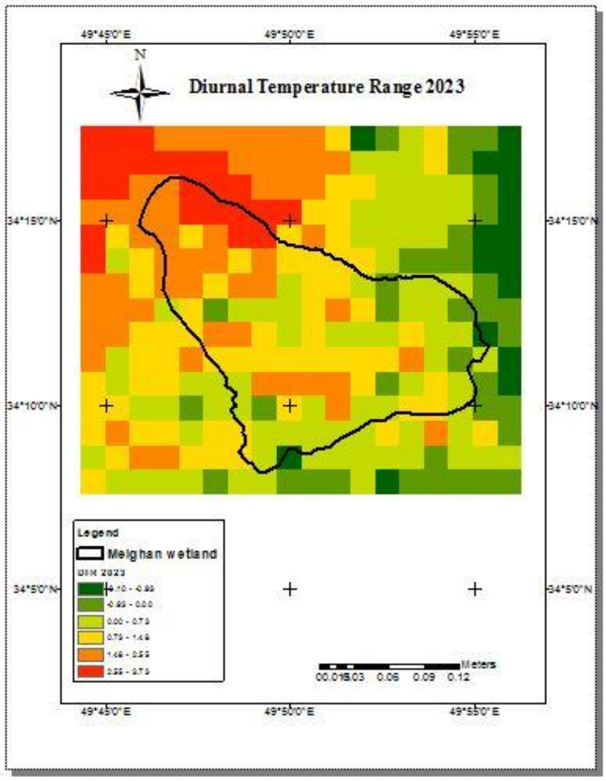

Figure 6. DTR Map 2023

Mustafa et al (2023) showed that LST values over West Africa varied between 20.6 ◦ C and 34.6 ◦ C in

2010, 20.6 ◦ C to 37.6 ◦ C in 2018, and 21.2 ◦ C to 38.7 ◦ C in 2020, which is relatively consistent with the current study. Furthermore, LST increases are associated with changes in land cover from vegetated to non-vegetated surfaces which can be used as an indirect drought indicator.

DTR trend in 2018 and 2023 shows that in the eastern and southern parts the differences between day and night decreased toward to 2023.

An increasing temperature is observed in the western and central parts of the wetland while results show rising temperature in 2023.

5. Conclusion

The results of LST and DTR trend show that the stability of the weather has increased in 2023 and the air temperature has become more moderate.

References

Aghamiri, M., Azizi, Z., & Imani, H. J. (2022). Evaluation of SDI, NDWI, NDMI and AWEI indices in coastline extraction and water body area of Shadegan wetland, Journal of Wetland Ecobiology 14 (2), 61-76.

Alibakhshi, T., Azizi, Z., Vafaeinezhad, A., Aghamohammadi, H. (2020). Survey of Area Changes in Water Basins of Shahid Abbaspour Dam Caused by 2019 Floods Using Google Earth Engine. Iranian Journal of Ecohydrology, 7(2), 345-35.

Bonacci, O., & Đurin, B. (2023). The Behavior of Diurnal Temperature Range (DTR) and Annual Temperature Range (ATR) in the Urban Environment: A Case of ZagrebGriˇc,Croatia.Atmosphere,14,1346.https://doi .org/ 10.3390/atmos14091346

Dar, I., Qadir, J., & Shukla, A. (2019) .Estimation of LST from multi-sensor thermal remote sensing data and evaluating the influence of sensor characteristics. Ann. GIS 2019, 25, 263–281.

Mafi, M., Azizi, Z., Karimi, P., & Alemi, S. P. (2021). Investigating the trend of water level changes in Allahabad wetland by using temporal images. Iranian journal of Ecohydrology, 8(2), 321-329.

Hashemi, Z., Soodaei, Z. H., & Mokhtari, M. H. (2022). Investigation of the Relationship between Land Surface Temperaturewith Vegetation and Surface Moisture in the Land Use of Zahak Area of Sistan Plain Using Landsat Satellite Images. Iranian Remote Sensing & GIS, 14(1), 21-42.

Kattel, G. R. (2022). Climate warming in the Himalayas threatens biodiversity, ecosystem functioning and ecosystem services in the 21st century: is there a better solution? Biodivers Conserv. 31(8–9):2017–2044. https://doi.org/10.1007/s10531-022-02417-6.

Li, Z. L., Tang, B. H., Wu, H., Ren, H., Yan, G., Wan, Z., Trigo, I. F, & Sobrino, J. A. (2013). Satellite-derived land surface temperature:Current status and perspectives. Remote Sens. Environ. 131, 14–37.

Meng, X., Cheng, J., & Liang, S. (2017). Estimating Land Surface Temperature from Feng Yun-3C/MERSI Data Using a New Land Surface Emissivity Scheme. Remote Sens. 9, 1247.

Moisa, M. B., Gabissa, B. T., Wedajo, Y. N., Gurmessa, M. M., Deribew, K. T., Negasa, G. G., Negassa, M. D., & Gemeda, D. O. (2023) Analyzing the correlation of forest and wetland with land surface temperature by using geospatialtechnology: a case of Yayo district, Southwestern Ethiopia. Geocartointernational, VOL. 38, NO.1, 225630.

Musyimi, P. K., Sahbeni, G., Timár, G., Weidinger, T., & Székely, B. (2023). Analysis of Short-Term Drought Episodes Using Sentinel-3 SLSTR Data under a Semi-Arid Climate in Lower Eastern Kenya. Remote Sens. 15, 3041. https://doi.org/10.3390/rs15123041

Pei, Y, Qiu, H., Zhu, Y., Wang, J., Yang, D., Tang, B., Wang, F., & Cao, M. (2023). Elevation dependence of landslide activity induced by climate change in the eastern Pamirs. Landslides. 20(6),1115–1133. https://doi.org/10.1007/s10346-023-02030-w.

Qi, Y., Zhong, L., Ma, Y., Fu, Y., Wang, X., & Li, P. (2023). Estimation of Land Surface Temperature Over the Tibetan Plateau Based on Sentinel-3 SLSTR Data. IEEE Journal Of Selected Topics In Applied Earth Observations And Remote Sensing, 16

Sheffield, J. (2018) Satellite remote sensing for water resources management: Potential for supporting sustainable development in data-poor regions. Water Resour. Res. 54(12), 9724–9758. https://doi.org/ 10.1029/2017wr022437

Vlassova, L., Perez-Cabello, F., Nieto, H., Martín, P., Riaño, D., & De La Riva, J. (2014). Assessment of Methods for Land Surface Temperature Retrieval from Landsat-5 TM Images Applicable to Multiscale Tree-Grass Ecosystem Modeling. Remote Sens. 2014, 6, 4345–4368.

Wang, X., Wang, T., Xu, J., Shen, Z., Yang, Y., Chen, A., Wang, S., Liang, E., & Piao, S. (2022). Enhanced habitat loss of the Himalayan endemic flora driven by warming-forced upslope tree expansion. Nat Ecol Evol. 6(7),890–899. https://doi.org/10.1038/s41559-022-01774-3

Zhou, S., Liu, D., Zhu, M., Tang, W., Chi, Q., Ye, S., Xu, S., & Cui, Y. (2022). Temporal and spatial variation of land surface temperature and its driving factors in Zhengzhou City in China from 2005 to 2020. Remote Sens. 14(17),4281. https://doi.org/10.3390/rs14174281.

7th Intercontinental Geoinformation Days

igd.mersin.edu.tr

Impact of climate change on the assessment of the content of the indicator organic suspended matter and sea surface temperature of the Caspian Sea

Ismayil Zeynalov[*1], **Rena Achmedova** [2]

[1] *Institute of Geography, Caspian Sea Department, Baku, Azerbaijan*

Keywords
Climate change
Sea surface temperature
Radiation balance
Temperature regime
Oil

Abstract

The location of Azerbaijan in relatively low latitudes determines an intense influx of solar radiation and an increased value of the radiation balance (RB) of the underlying surface. The surface of the Caspian Sea causes significant changes in the temperature of the lower atmosphere, thereby affecting the climate of the surrounding areas. Oil pollution of coastal waters and the spread of oil films over large areas have a significant impact on the temperature of the surface layer of air. Consequently, the human factor can influence climate formation and lead to further deterioration of the condition of coastal ecosystems. Limited ground-based observation networks and unreliable calculation methods prevent us from correctly identifying these changes. The application of statistical methods of analysis to study climate on a global scale is unrepresentative due to the limited capabilities of the ground-based observation network. The advantage of space means in studying the climatic characteristics of the territory of Azerbaijan allows, based on the transformation of satellite observation data and interpretation of the resulting time series, to solve these problems, with further presentation of the final information at the nodes of a one-degree regular grid. This allows you to observe changes not at one point in space, as was done, in the traditional vertical column of the atmosphere, but in the zonal profile (horizontal aspect).

1. Introduction

Water is the main essential resource of humanity, which is necessary for its survival. Today the relevance of problems related to water resources has been recognized throughout the world and is intensively studied. Water resources problems are highly interconnected with global climate change, as its influence on the distribution and circulation of water in the environment is observed (Amirgaliev et al. 2022).

A significant portion of the input radiation energy to the ocean is absorbed within a few meters of the surface, increasing the temperature of this ocean layer based on the daily cycle of the solar system. Lack of wind prevents water column mixing and causes the formation of a thermal layer at the ocean surface. Finding climatological variability of sea surface temperatures (SSTs) has been of interest to many researchers. This variability has showed a significant relationship with many factors, including wind, teleconnection indicators, and precipitation. Studies of the critical role of climate change on SST have been conducted in locations around the world (Ghasemifar et al. 2019).

Global warming and climate change are considered as important environmental problems. Environmental security is more pronounced with regard to the Caspian Sea. Due to the geopolitical and geo-economic dimensions on the one hand, and its unique characteristics on the other, this large lake is considerably fragile against environmental challenges. In fact, the innate isolation of the Caspian Sea makes its conditions with regard to global warming unique (Dero et al. 2020).

In the Caspian Sea, increases in the water temperature and air temperature over the water are of great importance. Any increase in water temperature is especially significant, as it decreases the area of winter ice cover in the Northern Caspian, weakens vertical water circulation in the deep sea, increases evaporation and activates chemical and biological processes (2nd State of Environment Report). In the last quarter of the twentieth century, the Caspian Sea has been impacted by global warming, with the air temperature over the water increasing by 0.7–0.8°C and the surface water layer by 0.4 -0.5°C (RPP, 2021).

* **Corresponding Author**

*(ismayil_zeynalov@outlook.com) ORCID ID 0000-0001-9391-583X
(rena.ahmedova.67@mail.ru) ORCID ID xxxx-xxxx-xxxx-xxxx

Cite this study

Zeynalov, I., & Akhmedova, R. (2023). Impact of climate change on the assessment of the content of the indicator organic suspended matter and sea surface temperature of the Caspian Sea. Intercontinental Geoinformation Days (IGD), 7, 127-130, Peshawar, Pakistan

The sea surface temperature is the subsurface bulk temperature in the top few meters of the ocean, measured by ships, buoys and drifters. From ships, measurements of water samples in buckets were mostly switched in the 1940s to samples from engine intake water. Satellite measurements of skin temperature (uppermost layer; a fraction of a millimeter thick) in the infrared or the top centimeter or so in the microwave are also used, but must be adjusted to be compatible with the bulk temperature (Bates et al. 2008).

In the Caspian Sea, long-term changes in water temperature are associated with long-term fluctuations in level. The analysis shows that in 1930...1940 the intense decrease in level had very little effect on the average annual water temperature. Therefore, the long-term norm changed only within 0.1...0.3 °C, but in some months, the change in water temperature was significant (Allahverdiev, 2016).

2. Method

Based on observational data from the NOAA series satellites, below is the accepted algorithm for estimating the albedo of organic suspended matter in water,

The albedo of the ocean-atmosphere system was presented in linearized form (Zeynalov, and Makhmudova, 2021)

$$A_{0.6} = A_{permanent\ 0.6} + A_{atm\ 0.6} + A_{glare\ of\ waves\ 0.6} + A_{org\ 0.6}, \quad (1)$$
$$A_{0.8} = A_{permanent\ 0.8} + A_{atm,\ 0.8} + A_{glare\ of\ waves\ 0.8} + A_{org\ 0.8}, \quad (2)$$

where $A_{permanent\ 0.6}$, $A_{permanent\ 0.8}$, – albedo of pure water in a transparent atmosphere (horizontal visibility range over 100 km), $A_{atm\ 0.6}$ and $A_{atm\ 0.8}$ – atmospheric dust albedo, $A_{glare\ of\ waves\ 0.6}$ and $A_{glare\ of\ waves\ 0.8}$ – albedo of the water surface due to solar glare and waves, $A_{org\ 0.6}$ and $A_{org\ 0.8}$ and organic suspended matter at wavelengths 0.6 and 0.8 mkm.

Based on the identity of the spectral behavior of the quantities A_{atm} and A_{glare} of waves for both wavelengths, that is, from the fact that:

1. the average ratio of changes in the albedo of the cloudless atmosphere at wavelengths of 0.8 and 0.6 µm is 0.92±0.08;
2. the average ratio of changes in albedo of the water surface due to solar glare and waves at wavelengths of 0.8 and 0.6 µm is 0.85 ± 0.15 (authors' estimate based on satellite observations for 5 years);
3. the average ratio of changes in albedo of the water surface due to organic suspensions at wavelengths 0.8 and 0.6 is 0.1±0.02,

the quantities A_{atm} and $A_{glare\ of\ waves}$ can be combined into A_{noise}. After this, the system of equations (1) – (2) is presented in the form (3)-(4):

$$A_{0.6} = A_{permanent0.6} + A_{noise0.6} + A_{org0.6}, \quad (3)$$
$$A_{0.8} = A_{permanent0.8} + A_{noise0.8} + A_{org0.8}, \quad (4)$$

Next, taking into account the above spectral contrasts of the albedo of organic suspensions, the albedo of atmospheric aerosol and the albedo due to solar flare and waves, we present expressions (3) and (4) in the form (5) and (6):

$$A_{0.6} = A_{permanent\ 0.6} + A_{noise\ 0.6} + A_{org\ 0.6}, \quad (5)$$
$$A_{0.8} = A_{permanent0.8} + 0.85 * A_{noise\ 0.6} + 0.1 * A_{org}, \quad (6)$$

Solving this system of equations, we obtain the following expressions for the albedo of organic suspensions and the total albedo due to the atmosphere and waves:

$$A_{org\ 0.6} = (0.85 * (A_{0.6} - A_{permanent\ 0.6}) - (A_{0.8} - A_{permanent\ 0.8}) / (0.85 - 0.1), \quad (7)$$
$$A_{noise\ 0.6} = A_{0.6} - A_{permanent\ 0.6} - A_{noice\ 0.6} \quad (8)$$

The water albedo values for a transparent atmosphere, $A_{permanent}$ 0.6 and $A_{permanent}$ 0.6, were calculated using the LOUTRAN–5 procedure.

The main role is played by the radiation temperature of the underlying surface, estimated from measurement data at wavelengths of 11 and 12 µm.

NOAA offers coefficients for radiation temperatures at 11 and 12 µm, as well as satellite angle considerations, as follows:

$$SST = k_1 * T_{11} - k_2 * T_{12} + k_3 * (T_{11} - T_{12}) * (sec(\tau) - 1) \quad (9)$$

where SST is the radiation temperature of the water surface; T_{11} and T_{12} are radiation temperatures at wavelengths of *11* and *12 µm*, respectively; k_1,k_2 *and* k_3 - weighting coefficients; the values of k1 and k2 are taken equal from 1 to 4, and the value of the coefficient k1 is taken to be approximately one greater than the values of *k2; k3* - 0.7; τ– satellite sensing angle.

3. Results

Surface water temperatures in the Caspian Sea, as in other oceanic waters, are generally determined by air temperature, heat storage, wind properties (mixing) and advection. In different regions of this continental sea area, in addition to the temperature factors common to all regions, various factors dominate.

In the northern part of the Caspian Sea, firstly, the influence of river flow is felt - warmer continental runoff in spring and colder continental runoff in autumn. In the Central Caspian Sea, there is a rise in deep waters off the eastern and western coasts and temperature changes of up to 15°C off the eastern coast. In the southern part of the Caspian Sea, there is a mixing of winter winds and advection of water from the center of the Caspian Sea. During the daytime in spring and summer, sea water temperatures are universally characterized by the presence of areas of warm water exceeding 3°C. Heating and cooling zones are clearly visible in shallow water in spring and autumn, respectively, and the ratio of heating and cooling is higher as the depth of the water area decreases, i.e. less heat is accumulated 8. (Lyushvin P.V. 1996).

Below are maps of the average monthly fields of organic suspended matter albedo (ASSA) and surface water temperature (SST) for 12 months from November 2001 to October 2002, as well as graphs of the course of these variables in individual areas of the sea.

The maps are based on survey data with a spatial resolution of about 1.5 km. In total, the original image has 430 by 700 pixels. In each, the value of the measured quantity is specified: albedo with an accuracy of 0.1%, temperature with an accuracy of 0.2°C. The initial information, which may not be complete everywhere due to cloudiness, ice or non-compliance with information control criteria, is recalculated to a 43 by 35 node grid with a step of 1.4 geographic degrees. Optimal interpolation was used under the assumption that the fields are isotropic. Based on the data received, maps were drawn. The A_{org} and SST maps are equipped with corresponding color scales, the same for all months.

In all figures, on the left are the fields, A_{org}, %, and on the right are the fields, SST, °C. Ice boundaries are shown at the end of the month.

In the graphs presented below, the data was obtained by averaging within ten numbered sections into which the sea is divided. A diagram of sections indicating the number of nodes falling into each of them is shown in the following fig. 1 on the left; a diagram of the numbers of sections and the position of their geographical centers, to which the average values are assigned, is on the right. Initial data are given in tables. All drawings are made in vector graphics formats.

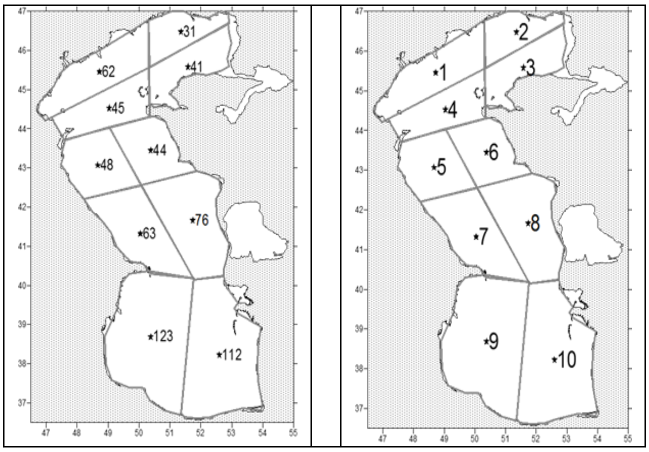

Figure 1. Diagram of sections indicating the number of nodes falling into each of them (on the left) and the numbers of sections with the position of their geographic centers, to which the average values are assigned (on the right).

Table 1. Average monthly values of A_{org} for sections of the Caspian Sea

No	X	Y	111	112	201	202	203	204	205	206	207	208	209	210
1	48,7	45,5	2,3	0,0	0,0	5,1	4,1	4,2	3,4	3,6	3,4	3,4	4,2	4,5
2	51,3	46,4	2,8	0,0	0,0	0,0	6,9	8,3	6,1	6,4	4,2	4,5	5,8	7,5
3	51,6	45,7	2,0	0,0	0,0	7,9	7,3	9,9	7,5	7,5	5,5	5,1	5,6	7,5
4	49,1	44,5	1,9	4,2	3,5	3,2	2,8	2,7	1,9	2,0	1,8	2,0	2,3	2,6
5	48,6	43,0	1,5	2,3	2,5	2,3	2,2	1,6	1,3	1,5	1,5	1,6	1,9	1,9
6	50,4	43,4	1,5	2,6	2,2	1,1	2,2	1,4	1,3	1,5	1,4	1,5	1,7	1,6
7	50,0	41,3	1,3	2,6	2,6	2,0	2,4	1,3	1,5	1,5	1,5	1,4	1,8	1,9
8	51,8	41,6	1,3	2,5	2,4	1,3	2,3	1,5	1,4	1,5	1,5	1,4	1,8	1,7
9	50,4	38,7	1,5	3,2	2,7	1,9	2,4	1,5	1,6	1,6	1,6	1,6	1,9	2,2
10	52,6	38,2	1,3	3,4	2,8	2,2	2,4	2,2	1,9	2,1	2,0	2,1	2,3	2,5

Note to the table. Column No contains the numbers of the sections, columns X and Y contain the longitudes and latitudes of the centers of the sections, the remaining columns are marked with month numbers so that November 2001 is designated as 111, October 2002 as 210, etc.

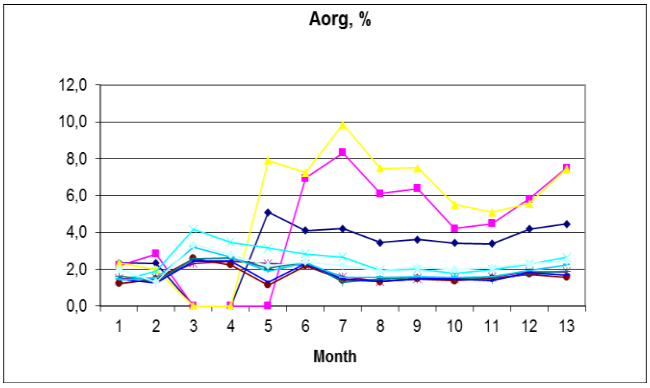

Figure 2. Graphs of the course of average monthly Aorg values for ten sections of the Caspian Sea.

Table 2. Average monthly values of SST by area Caspian Sea

No	x	Y	111	112	201	202	203	204	205	206	207	208	209	210
1	48,7	45,5	9,2	-0,5	-0,5	3,2	7,8	12,8	17,9	23,4	29,0	27,7	22,5	16,9
2	51,3	46,4	9,0	-0,5	-0,5	-0,5	4,5	10,6	16,9	23,2	28,7	27,5	21,6	15,5
3	51,6	45,7	9,4	-0,5	-0,5	1,0	5,9	11,0	17,4	23,5	28,2	27,1	21,3	15,5
4	49,1	44,5	12,7	3,3	1,9	3,5	6,5	11,0	15,5	22,3	27,4	26,9	22,6	19,7
5	48,6	43,0	14,9		7,0	7,1	7,6	10,3	13,9	20,0	26,0	27,1	23,6	21,2
6	50,4	43,4	14,6	7,1	7,9	7,3	8,5	10,2	13,5	19,2	25,5	26,3	22,7	20,1
7	50,0	41,3	15,6	8,9	8,2	8,5	9,0	10,6	14,1	19,7	25,4	26,6	24,1	21,6
8	51,8	41,6	15,5	9,1	9,2	9,0	9,5	11,0	14,4	19,6	25,4	26,1	23,2	20,8
9	50,4	38,7	18,2	12,0	10,8	10,6	11,8	13,4	16,9	22,4	26,9	27,8	25,7	23,9
10	52,6	38,2	18,0	11,3	11,6	11,1	12,5	14,0	17,2	22,9	27,6	28,4	26,6	24,8

Note to the table. Column No contains the numbers of the sections, columns X and Y contain the longitudes and latitudes of the centers of the sections, the remaining columns are marked with month numbers so that November 2001 is designated as 111, October 2002 as 210, etc.

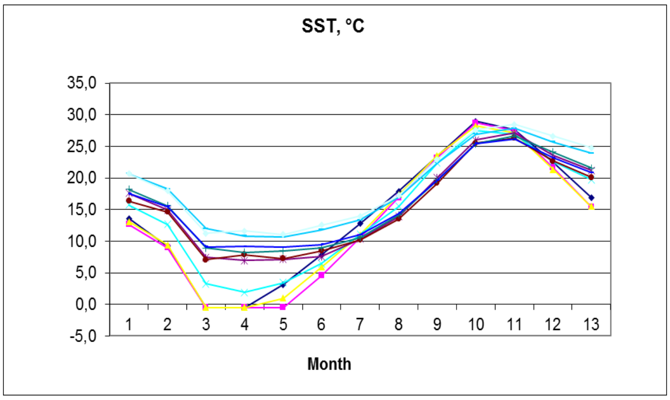

Figure 3. Graphs of the course of average monthly SST values for ten sections of the Caspian Sea.

The resulting graphs show the course of changes in the values of A_{org} and SST according to the retrospective analysis of the Caspian Sea, divided as shown in Fig. 1 for ten test areas, determination of the content of organic suspended matter in the surface waters of the Caspian Sea can give fundamental conclusions on the course of the impact of anthropogenic factors of changes in metrological conditions on the natural factors of the territory of Azerbaijan.

The main systematic data from the Global Hydro meteorological Network's ground stations and satellite monitoring can be received through the National Oceanic and Atmospheric Administration's (NOAA) server network. The National Environmental Satellite, Data, and Information Services (NESDIS) Directorate has a separate division responsible for NOAA satellites and information. As part of NESDIS, the Office of Satellite Data Processing and Distribution (OSDPD) processes and distributes satellite data, enabling data and information from environmental satellites to be processed, systematized, and made available to users in the United States and other countries. The ultimate goal of user maintenance is achieved through appropriate information production through the following three agencies: Satellite Services Department (SSD); Information Processing Department (IPD): Direct Services Department (DSD) (Zeynalov, I., Akhmedova, R., Akhmedova, A., Rustamova, A. 2023).

4. Conclusion

As a result of the studies performed, the possibility of operational monitoring of the state of the studied values of SST and Aorg throughout the entire Caspian Sea was shown. In specially selected areas, a retrospective review of conditions that developed over a certain period of time. The resolution of satellite information and the adopted processing techniques make it possible to recreate the picture of the spatiotemporal variability of these quantities with the degree of detail that cloud conditions only allow.

It is obvious that other means of observation, except artificial earth satellites, are not capable of even approaching the achieved indicators. At the same time, data prepared by specialists in the USA and Europe and published on the Internet are characterized by insufficient detail and methodological shortcomings due to the global nature of the information presented. The method proposed by the authors for monitoring the sea area can be actually tested and reasonably used only after carrying out control sub-satellite observations.

References

Allahverdiev, Z. S. (2016). The impact of climate change on the water surface temperature of the western Caspian Sea (southern territory of Azerbaijan). Hydrometeorology and Ecology, 1, 41-46

Amirgaliev, N. A., Askarova, M., Opp, C., Medeu, A., Kulbekova, R., & Medeu, A. R. (2022). Water quality problems analysis and assessment of the ecological security level of the Transboundary Ural-Caspian Basin of the Republic of Kazakhstan. Applied Sciences, 12(4), 2059. https://doi.org/10.3390/app12042059

Bates, B., Kundzewicz, Z. B., Wu, S., & Palutikof, J. (2008). Climate Change and Water. Intergovernmental Panel on Climate Change.

Dero, Y, Q., Yari, E., & Charrahy, Z. (2020). Global warming, environmental security and its geo-economic dimensions case study: Caspian Sea level changes on the balance of transit channels. Journal of Environmental Health Science and Engineering, 18, 541-557. https://doi.org/10.1007/s40201-020-00481-0

Ghasemifar, E., Farajzadeh, M., Mohammadi, C., & Alipoor, E. (2020). Long-term change of surface temperature in water bodies around Iran–Caspian Sea, Gulf of Oman, and Persian Gulf–using 2001–2015 MODIS data. Physical Geography, 41(1), 21-35. https://doi.org/10.1080/02723646.2019.1618231

Lyushvin P.V. Interpretation of spectral measurements from NOAA satellites over the Caspian Sea // Meteorology and Hydrology. No. 1. 1997. Moscow - pp.75-80.

Regional Programme Proposal (2021). Urbanisation and Climate Change Adaptation in the Caspian Sea Region

Zeynalov, I. M., & Makhmudova, U. Kh. (2021). The role of using data from satellite observation systems in the study of the water surface temperature of the Caspian Sea. International Scientific Conference "Climate Change in the Caspian Sea Region", pp. 97-100

Zeynalov, I., Akhmedova, R., Akhmedova, A., & Rustamova, A. (2023). Analysis of the sea surface temperature (SST) of the Caspian Sea from NOAA Satellites. Intercontinental Geoinformation Days (IGD), 6, 364-367, Baku, Azerbaijan

7th Intercontinental Geoinformation Days

igd.mersin.edu.tr

The impact of climate change on the temperature regime of the Kelbajar and Lachin regions of the Republic of Azerbaijan

Said Safarov *[1], **Arzu Majidzade** [1]

[1]Azerbaijan National Academy of Sciences, Institute of Geography, Baku, Azerbaijan

Keywords
Air temperature
Reanalysis
Climate change
Temperature anomality

Abstract

In an article based on reanalysis data MERRA-2 (Modern-Era Retrospective Analysis for Research and Applications, Version 2) for the period 1980-2022 the general trends in the temperature regime of the Kalbajar and Lachin regions, which are part of the modern East Zangezur economic region, were studied. It has been determined that during the period under review there is a tendency to increase average annual and seasonal temperatures. Temperature trends for all seasons and annual periods were statistically significant at the 5% confidence level. Calculations showed that the average annual air temperature in the period 2001-2022. increased by 0.9 °C compared to the period 1980-2000, which is consistent with the results obtained in other regions of the republic. The largest increase in average monthly temperature was recorded in February (1.7 °C), March (1.8 °C) and October (1.3 °C). The largest increase in the maximum average temperature was observed in March (2.7 °C) and December (1.9 °C), and the minimum average temperature in October (3.5 °C). A decrease of 0.6°C in the minimum average temperature in January was recorded.

1. Introduction

The territory of Kalbajar and Lachin regions belonging to Eastern Zangazur economic region is mainly mountainous. According to the 1961-1990 period data of the Istisu hydrometeorological station located at an altitude of 2257 m above sea level in Kalbajar region, the average annual air temperature is 4,0 ^{0}C. The coldest month is January (-5.2 ^{0}C), and the warmest month is July (13.5 ^{0}C). The average annual precipitation amounts to 506 mm, most of which occurs during the warm half of the year (Khalilov and Safarov, 2001).

According to the data of the Lachin hydrometeorological station for the period 1961-1990, the average annual air temperature is 10 ^{0}C. The coldest month is recorded in January (0 ^{0}C), and the warmest month is July (21.0 ^{0}C). The average annual precipitation is 506 mm, most of which occurs in the warm half of the year. The average annual precipitation is 587 mm, most of which occurs in the warm half of the year (Khalilov and Safarov, 2001). Thunderstorms and fog are very frequent in both areas, continuous snow cover, mountain-valley winds prevail (Климат Азербария, 1968; Museyibov, 1998).

Since the territory was occupied by the Armenian armed forces in 1993-2020, there are no observational materials for those years. For this reason, it is appropriate to use alternative data sources and research methods, including satellite and reanalysis data, to determine the effect of global warming on the temperature regime of the area in recent years.

Thus, the main goal of the research is to determine the changes in the temperature regime in Kalbajar and Lachin regions of East Zangazur economic region in recent years (1991-2022 period).

2. Method

The monthly reanalysis data of MERRA-2 (Modern-Era Retrospective analysis for Research and Applications, Version 2) with a resolution of 0.5º for the period of 1980-2022 was used in the research (https://giovanni.gsfc.nasa.gov). Due to the relatively low resolution, the temperature data was obtained by averaging over the entire area, not individual observation stations. For this purpose, the considered area was marked on the map located on the relevant electronic portal (Giovanni) and with the help of relevant procedures, the time series of the average values of the air temperature in that area for the months of each year

* **Corresponding Author**

*(safarov53@mail.rul) ORCID ID 0000-0002-8447-2843
(masimova1995@gmail.com) ORCID ID xxxx – xxxx – xxxx – xxxx

Cite this study

Safarov, S., & Majidzade, A. (2023). The impact of climate change on the temperature regime of the Kelbajar and Lachin regions of the Republic of Azerbaijan. Intercontinental Geoinformation Days (IGD), 7, 131-133, Peshawar, Pakistan

were obtained. With the help of the obtained series, the trends of temperature change in years and seasons were determined based on the corresponding trend curves. The statistical significance of the trends is determined according to the Equation 1:

$$R/\sigma_R \geq s \qquad (1)$$

where R is the correlation coefficient and σ_R is the random mean squared error (Sikan, 2017). The random mean squared error is calculated by Equation 2:

$$\sigma_R = (1 - R^2)/\sqrt{(n-1)} \qquad (2)$$

where n is the number of terms of the time series. s=2.02 at 5%-significance level and n=40.

3. Results and Discussion

Let's consider temperature changes in Kalbajar-Lachin area. As can be seen from Table 1, compared to the period of 1980-2000, the average annual temperature in the period of 2001-2022 has increased by 0.9 ^{0}C. An increase in average temperature was recorded in all months except April. Larger increases were observed in February, March, June, August, September and October. In April, there was no change in temperature, and in July, November, and December, there were no significant changes.

An increase in the maximum average temperature was recorded in all months, but the highest increases occurred in March and December, and the lowest in February, April and May.

In January and April, the minimum average temperature decreased, while in October it increased sharply (3.5 ^{0}C).

Figure 1 also shows the increasing trend of the annual average temperature in the area during the considered period. According to the formulas (1) and (2), the linear trend showing an increasing trend, as can be seen from the figure, is statistically significant and amounts to 0.4 °C/10 years. The lowest value of the temperature was recorded in 1992, and the highest value was recorded in 2010, which corresponds to the indicators observed in other regions of Azerbaijan. (Safarov et al., 2018; Safarov et al., 2018).

In addition, the temperature series was divided into 2 equal periods and the corresponding temperature anomalies were calculated.

Table 1. The main statistical temperature indicators of the air temperature in the Kalbajar-Lachin area during the years 1980-2000 and 2001-2022, ^{0}C

	Months												Annual
	1	2	3	4	5	6	7	8	9	10	11	12	
	1980-2000												
Average	-5.7	-5.2	-1.0	5.8	10.0	14.6	17.7	17.0	13.2	6.9	1.0	-3.4	5.9
Max.	-2.6	-1.7	2.0	8.6	1.5	17.0	20.2	19.8	15.3	9.0	3.6	-0.3	7.1
Min.	-8.8	-8.7	-4.2	3.2	7.3	12.1	16.1	14.9	11,1	2.5	-4.2	-7.1	4.2
	2001-2022												
Average	-5.0	-3.4	0.8	5.8	10.7	15.5	17.9	17.9	14.2	8.2	1.6	-3.1	6.8
Max.	-2.0	-1.3	4.8	9.0	12.9	18.0	20.7	20.9	16.4	10.1	4.7	1.6	8.2
Min.	-9.5	-7.9	-3.9	3.0	8.2	13.3	16.6	15.0	11.3	6.0	-3.8	-7.1	5.4
	Temperature anomalies												
Average	0.7	1.7	1.8	0.0	0.7	1.0	0.2	0.9	1.0	1.3	0.5	0.4	0.9
Max.	0.6	0.4	2.7	0.4	0.4	1.0	0.5	1.0	1.1	1.1	1.1	1.9	1.0
Min.	-0,6	0.8	0.2	-0.2	0.9	1.2	0.5	0.1	0,3	3.5	0,4	0.0	1.2

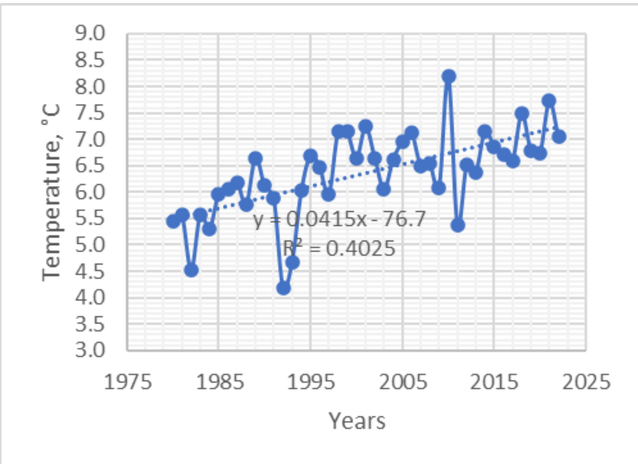

Figure 1. Time course of average annual air temperature in Kalbajar-Lachin area in 1980-2022.

The study of changes in the temperature regime of individual seasons is also of great interest. Figure 2 shows the time course of average temperatures for different seasons. As can be seen from the figure, temperature changes in all seasons have an increasing trend and are statistically significant at the 5% assurance level based on the formulas of the corresponding linear trends (1) and (2).

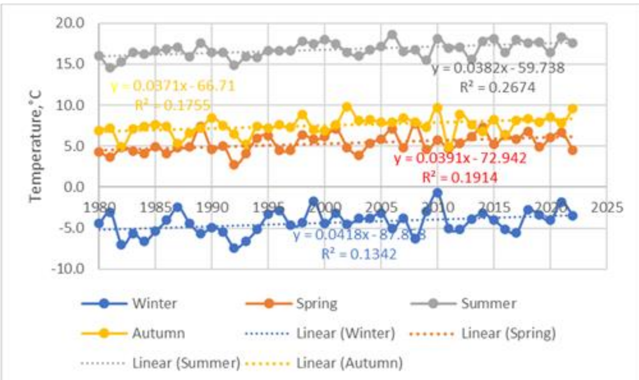

Figure 2. Time course of the average air temperature for separate seasons in the period 1980-2022

Table 2. The difference between the average temperatures of the periods 2001-2022 and 1980-2000 for separate seasons, ^0C

(2001-2022)-(1980-2000)	Winter	Spring	Summer	Autumn
Average	0.9	0.8	0.7	1.0
Maximum	2.7	2.7	1.0	1.1
Minimum	-0.6	-0.2	0.1	0.3

Table 2 shows the average, maximum, and minimum temperature differences in the period 2001-2022 and 1980-2000 for separate seasons. As can be seen from the table, the differences in average temperatures mostly coincided with the cold periods of the year (0.9-1.0 ^0C). The greatest increases are recorded in maximum average temperatures. In winter and spring, this increase is greater (2.7^0C). Changes in minimum average temperatures are not significant.

References

Khalilov, S. H., & Safarov, S. H. (2001). Monthly and annual norms of air temperature and precipitation in the Republic of Azerbaijan (1961-1990). Baku, 109 p. (in Azerbaijani)

Madatzada, A. A. & Shikhlinski, E. M. (1968). Climate of Azerbaijan. Baku. 343 p. (in Russian)

Museyibov, M. A. (1998). Physical geography of Azerbaijan. Baku: "MAARIF" publishing house. 400 p. (in Azerbaijani)

Safarov, S. H., Akhlimanova, I., & Safarov, E. S. (2022). Investigation of temperature and precipitation regimes of Shusha city in 1991-2020 by reanalysis data/ The modern problems of the geography. The integration of science and education. Baku, 26-32.

Safarov, S. H., Huseynov, C. S., & Ibrahimova, I. V. (2018). Characteristics of long-term temperature changes in the western regions of the Republic of Azerbaijan // Scientific Works of the National Aviation Academy, Baku, 1, 108-115. (in Azerbaijani)

Safarov, S. H., Huseynov, J. S., Ibrahimova, I. V., & Safarov, E. S. (2018). The main features of temperature changes, occurring over the territory of Caspian Sea in Azerbaijan /Understanding the problems of inland waters: Case study for the Caspian basin (upcb). Baku. 2018. pp. 85-89.

Sikan, A. V. (2007). Methods for statistical processing of hydrometeorological information. St. Petersburg: RGGMU, 279 p. (in Russian)

7th Intercontinental Geoinformation Days

igd.mersin.edu.tr

Applicability of satellite data in estimating actual evapotranspiration by SEBS algorithm (Mughan plain, Ardabil, Iran)

Mahmoud Sourghali[1], Samaneh Bagheri* [1], Khalil Valizadeh Kamran [1]

[1] *University of Tabriz, Department of Remote Sensing and GIS, Tabriz, Iran*

Keywords
Remote sensing
Evapotranspiration
Landsat 8
Thermal data
SEBS

Abstract

Land surface evapotranspiration (ET) is of importance for environmental applications including optimization of irrigation water use, irrigation system performance, crop dehydration, drought mitigation strategies. In this regard, the SEBS algorithm is one of the most widely used algorithms in the field of calculating real evaporation and transpiration. This algorithm uses satellite equipment observations and meteorological information to estimate the energy flux and includes a tool to determine the land surface (such as albedo, surface emissivity, surface temperature, vegetation index, etc.) from satellite images. In this research, using the spectral data and thermal band of Landsat 8, the actual evapotranspiration rate of Iran's Mughan plain in Ardabil province has been estimated. Also, in order to validate the results of the model, the results were compared with the results of the Penman month. Comparing the results of the SEBS algorithm with FAO-Penman-Monteith shows similar values, so it can be concluded that the SEBS algorithm can be a suitable alternative to the traditional methods of calculating Actual evapotranspiration.

1. Introduction

Evapotranspiration (ET) is the combination of the energy and water cycle and also links the ecological processes of land surface hydrological processes. Accurate determination of regional ET and estimate of the evolution of the climate, water resources planning and management, agricultural water saving crop production simulation and environmental issues have important practical significance.

The surface heat fluxes are the basis for calculating ET using meteorological observations way (Weiqiang et al., 2012).

ET is a key component of the water balance and a major consumptive use of irrigation water and precipitation on farmland. Remote sensing based on field observation and models which rely on land surface energy balance are presently most suited for estimating crop water use at both field and regional scales, such as the Surface Energy Balance Algorithm for Land (SEBAL; Bastiaanssen et al., 1998), the Surface Energy Balance Index (SEBI; Menenti and Choudhury 1993), the Simplified Surface Energy Balance Index (S-SEBI; Roerink et al., 2000), the Surface Energy Balance System (SEBS; Su 2002), and Mapping Evapotranspiration with Internalized Calibration (METRIC; Allen et al., 2007).

The following sections describe the main models in detail. SEBAL (Bastiaanssen et al., 1998) uses hot and cold points within the satellite images to develop an empirical temperature difference equation. It is a single-source model that resolves the energy balance for latent heat flux (λ E) as a residual. Net radiation flux (Rn) and soil heat flux (G0) are calculated based on land surface temperature (Tsfc) and albedo, vegetation variables. Sensible heat flux (H) is estimated using the bulk aerodynamic resistance model. SEBS is based on the Crop Water Stress Index (CWSI; Jackson et al., 1981), idea in which the surface meteorological scaling of CWSI is replaced with planetary boundary layer (PBL) scaling. It uses the contrast between wet and dry areas appearing within a remotely sensed scene to derive ET from the relative evaporative fraction.

SEBS (Su 2002) was coming from the SEBI concept. It uses a dynamic model for aerodynamic roughness length for heat (Su et al., 2001), bulk atmospheric similarity and Monin–Obukhov similarity theories for PBL to estimate regional ET, and atmospheric surface layer scaling for estimating ET at local scale.

Yang et al. (2021) conducted a study to estimate evapotranspiration (ET) by combining Bayesian Model Averaging (BMA) with machine learning algorithms. The objective of this study was to reduce errors and

* **Corresponding Author**

*(samanehbagheri99@gmail.com) ORCID ID 0000-0003-3889-6685
(m.soorghali@gmail.com) ORCID ID 0009-0007-4374-2767
(valizadeh@tabrizu.ac.ir) ORCID ID 0000-0003-4648-842X

Cite this study

Sourghali, M., Bagheri, S., & Kamran, K. V. (2023). Applicability of satellite data in estimating actual evapotranspiration by SEBS algorithm (Mughan plain, Ardabil, Iran). Intercontinental Geoinformation Days (IGD), 7, 134-137, Peshawar, Pakistan

uncertainties among multiple ET models to improve daily ET estimation. The BMA method was used to combine eight ET models using Landsat 8 satellite data, including four energy balance models (e.g., SEBS, SEBAL, SEBI, and SSEB) and four machine learning algorithms (namely, Polynomials, Random Forest, Stacked Regression, and Support Vector Machine). The performance of each model and the BMA method was validated through on-site measurements in a semi-arid region. The results indicated that the BMA method outperformed the eight individual models. Four significant models obtained through the BMA method were ranked based on Random Forest, SVM, SEBS, and SEBAL. The combination of BMA with machine learning can significantly improve the accuracy of daily ET estimation, reduce uncertainties among models, and leverage the distinct advantages of empirical and physical-based models to obtain more reliable ET estimates.

Wang et al. (2017), in the Heihe River Basin, Northwestern China, estimated daily ET using the SEBS algorithm, and assessed its performance with Eddy Covariance and Priestley-Taylor methods. The results revealed that the SEBS model has a relatively accurate performance, particularly for vegetated areas.

Shamloo et al. (2021), evaluated the SEBS algorithm to estimate maize ET and crop coefficient using Landsat 8 images in the Adana Mediterranean Area, Turkey. According to the results, the SEBAL estimated ET values mostly corresponded to the FAO-PM method with $R^2 = 0.91$ and RMSE = 1.14 mm/day. It was also highly correlated with Turc, Hargreaves, and Makkink methods.

Aim of this study was to calculate the actual evapotranspiration using SEBS algorithm for mughan plain.

2. Method

2.1. Case Studies

The study area is located in the northwest of Iran, specifically in Ardabil province, between the cities of Parsabad and Bilasuvar (Moghan Plain), (Figure 1). The area has an average elevation of 100 meters above sea level. The dominant crop in the study area at the time of image acquisition and actual evapotranspiration estimation is wheat.

2.2. Material and Dataset

The used images must be cloud-free. In this research, the OLI sensor images from Landsat 8 satellite were utilized. The Digital Image used corresponds to the date of 04/04/2021, and the local time is approximately 11:00 AM. To calculate evapotranspiration, bands 1 to 7, and also band 10 (thermal band) were utilized.

The climate data used in the model and for calculating the reference evapotranspiration (ETr). In this research, data from two synoptic stations, Parsabad and Pileh Savar, were utilized, and the final values were obtained by averaging the corresponding measurements from these two stations.

The image processing software ILWIS version 7/3 is used.

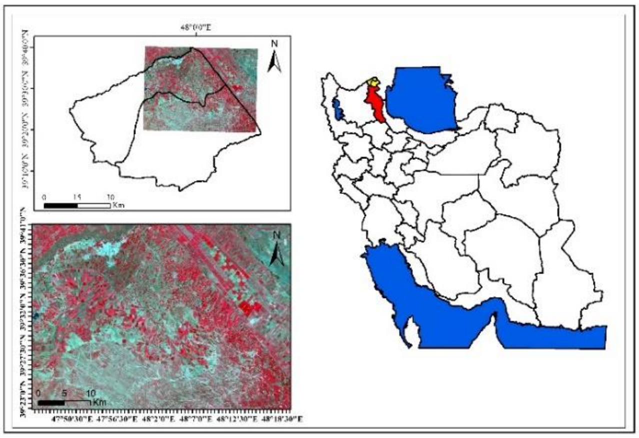

Figure 1. Study area

2.3. Methods

2.3.1. The SEBS Method

SEBS is based on the Crop Water Stress Index (CWSI; Jackson et al., 1981), idea in which the surface meteorological scaling of CWSI is replaced with planetary boundary layer (PBL) scaling. It uses the contrast between wet and dry areas appearing within a remotely sensed scene to derive ET from the relative evaporative fraction.

The basis of this method is to use the energy balance equation and calculate the latent heat flux as the residual of this equation for each pixel. This approach follows similar theoretical principles as the SEBAL algorithm.

The required input data include layers generated from satellite images and data obtained from weather stations. The output of the SEBS algorithm, unlike the SEBAL algorithm, provides daily actual evapotranspiration.

2.3.1.1. Evapotranspiration

The surface energy balance is commonly written as:

$$Rn = G0 + H + \lambda E \quad (1)$$

where Rn is the net radiation flux, G0 is the soil surface heat flux, H is the sensible heat flux, and λE is the latent heat flux. The unit of energy balance terms is watts per square meter.

To estimate the evaporative fraction, SEBS makes use of energy balance at limiting cases at dry limit and wet limit, such that the relative evaporation (ratio of the actual evaporation to the evaporation at wet limit) can be derived as:

$$\Lambda r = 1 - \frac{H - Hwet}{Hdry - Hwet} \quad (2)$$

where the H wet is sensible heat flux at the wet limit and H dry sensible heat flux at the dry limit. The estimations of H wet and H dry were detailed by Su (2002). The evaporative fraction (ratio of latent heat flux to available energy) is estimated by:

$$Rn-G \quad (3)$$

$$\Lambda = \frac{\lambda E}{Rn-G} = \frac{\Lambda r.\lambda E\ wet}{Rn-G} \quad (4)$$

where λE wet is the latent heat flux at the wet limit (i.e., the evaporation is only limited by the available energy under the given surface and atmospheric conditions). The latent heat flux (λE) can then be calculated by:

$$\lambda E = \Lambda(Rn-G0) \quad (5)$$

Finally, the daily actual ET can be written:

$$ET = 8.64 \times 107 \times \Lambda 24 \times \frac{Rn-G0}{\lambda \rho w} \quad (6)$$

where ρw is the density of water (1, 000 kgm-3) and Rn is the average daily net radiation in this equation. Moreover, the soil heat flux G0 for 24 h is normally assumed negligible (G average).

2.3.2. FAO Penman-Monteith Method

Reference crop evapotranspiration according to FAO Penman-Monteith model is:

$$ET0 = \frac{0.408\Delta(Rn-G)+\gamma\left(\frac{890}{T+273}\right)U2(es-ea)}{\Delta+\gamma(1+0.34U2)} \quad (7)$$

where ETo reference evapotranspiration [mm day-1], Rn net radiation at crop surface (MJ m-2 day-1), G soil heat flux density (MJ m-2 day-1), T mean daily air temperature at 2 m height (°C), u2 wind speed at 2 m height (m s-1), es saturation vapour pressure (kPa), ea actual vapour pressure (kPa), es-ea saturation vapour pressure deficit (kPa), Δ slope vapour pressure curve (kPa °C-1), γ psychrometric constant (kPa °C-1).

3. Results

3.1. Daily actual evapotranspiration by SEBS

The results of the daily evapotranspiration calculated by the SEBS algorithm are presented in Figure number 2.

3.2. Daily actual evapotranspiration by FAO Penman-Monteith Method

The amount of daily reference evaporation and transpiration was calculated using FAO by the average of meteorological data of 2 stations and the number is equal to 4.5 mm/day.

4. Discussion

The study aimed to estimate actual evapotranspiration using the SEBS algorithms and spectral data from the OLI and TIRS sensors of the Landsat 8 satellite in the Mughan plain of Ardabil province. The results of the analysis revealed valuable insights into the performance of these algorithms and their applicability in the specific study area.

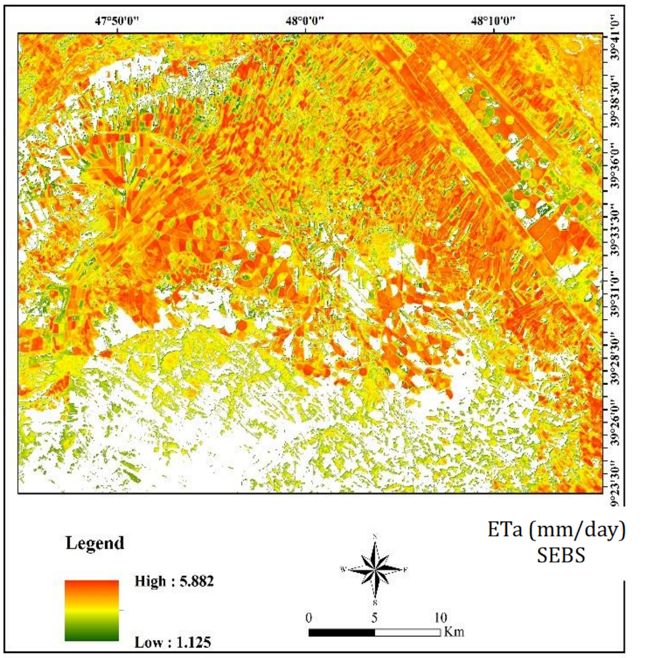

Figure 2. Daily actual evapotranspiration (SEBS)

The paper demonstrates one the first applications of the remote sensing method, SEBS, to determine spatial variation of actual evapotranspiration. Also, in order to validate the calculated evapotranspiration SEBS, reference evapotranspiration using the FAO Penman - Monteith was calculated (Equation 6).

Evapotranspiration estimated by the FAO Penman - Monteith using weather data stations is equal to 4.5 mm per day, A value close to the calculated evapotranspiration SEBS on the same day.

The results indicated that both SEBAL and SEBS algorithms have relatively high capabilities in estimating instantaneous evapotranspiration using spectral data. This finding highlights the potential of satellite data for accurately estimating evapotranspiration for various plant species. However, it is essential to consider the trade-off between the finer spatial resolution and computational complexity when choosing the most suitable algorithm for a particular study.

The results of this research, in comparison with the findings of previous studies such as the calculation of actual evapotranspiration using the SEBS algorithm by Yang and colleagues (2021), Wang et al. (2017) and Shamloo et al. (2021) are consistent.

5. Conclusion

The SEBS algorithm displays the actual Evapotranspiration rate in an equal range (1.125 to 5.88 mm), which shows the ability of this algorithm to separate areas with different evaporation and transpiration rates. Another advantage of SEBS algorithm is the simplicity of its implementation. SEBS algorithm can be very useful for inaccessible areas as well as areas for which weather station data is not available.

References

Allen, R. G., Tasumi, M., & Trezza, R. (2007). Satellite-based energy balance for mapping evapotranspiration with internalized calibration (METRIC)—Model. Journal of İrrigation and Drainage Engineering, 133(4), 380-394. https://doi.org/10.1061/(ASCE)0733-9437(2007)133:4(380)

Bastiaanssen, W. G., Menenti, M., Feddes, R. A., & Holtslag, A. A. M. (1998). A remote sensing surface energy balance algorithm for land (SEBAL). 1. Formulation. Journal of Hydrology, 212, 198-212.

Jackson, R. D., Idso, S. B., Reginato, R. J., & Pinter Jr, P. J. (1981). Canopy temperature as a crop water stress indicator. Water resources research, 17(4), 1133-1138.

Ma, W., Hafeez, M., Ishikawa, H., & Ma, Y. (2013). Evaluation of SEBS for estimation of actual evapotranspiration using ASTER satellite data for irrigation areas of Australia. Theoretical and applied climatology, 112, 609-616. https://doi.org/10.1007/s00704-012-0754-3

Shamloo N, Taghi Sattari M, Apaydin H, Valizadeh Kamran K, Prasad R (2021) Evapotranspiration estimation using SEBAL algorithm integrated with remote sensing and experimental methods. Int J Digit Earth 14(11):1638–1658.

Su, Z. (2002). The Surface Energy Balance System (SEBS) for estimation of turbulent heat fluxes. Hydrology and earth system sciences, 6(1), 85-100.

Wang Q, Blackburn GA, Onojeghuo AO, Dash J, Zhou L, Zhang Y, Atkinson PM (2017) Fusion of Landsat8 OLI and Sentinel2 MSI data. IEEE Trans Geosci Remote Sens 55(7):3885–3899.

Yang, Y., Sun, H., Xue, J., Liu, Y., Liu, L., Yan, D., & Gui, D. (2021). Estimating evapotranspiration by coupling Bayesian model averaging methods with machine learning algorithms. Environmental monitoring and assessment, 193, 1-15.

7th Intercontinental Geoinformation Days

igd.mersin.edu.tr

The modeling and analysis of empirical systems with complex networks

Leyla Naghipour*[1], Khalil Valizadeh Kamran[1], Mohammad Taghi Aalami[2], Vahid Nourani[3]

[1] University of Tabriz, Department of Remote Sensing and GIS, Faculty of Planning and Environmental Sciences, 29 Bahman Blvd., Tabriz, East-Azerbaijan, Iran*
[2] University of Tabriz, Department of Water Resources Engineering, Faculty of Civil Engineering, 29 Bahman Blvd., Tabriz, East-Azerbaijan, Iran
[3] University of Tabriz, Center of Excellence in Hydroinformatics and Faculty of Civil Engineering, 29 Bahman Blvd., Tabriz, East-Azerbaijan, Iran

Keywords
Complex networks
Function
Topology
Collective behavior
Statistical approach

Abstract

Network construction is an acceptable approach for better understanding the behavior of complex system which can be used to reveal the pattern of collective dynamics for realizing physical interactions in the dynamical system. In this case, characterizing functional connectivity of complex networks for studying a broad class of natural and artificial systems from the measures of correlation and causality is of utmost importance to correctly unravel physical phenomena of the system. Many network reconstruction approaches are based on heuristically thresholding the correlation matrices resulting from pairwise correlation analysis according to experimental methods. Other approaches compare the observed correlations against null models in the statistical analyses, obtaining results which are statistically more robust. Different methods were used, including cross-correlation (CC), spectral coherence (SpeCoh), mutual information (MI), transfer entropy (TE), Spearman's rank correlation (SC) and convergent cross-mapping (CCM). The methods were applied to linear and nonlinear collective dynamics by autoregressive moving average (ARMA) and Logistic map (LOG) models, respectively. The dynamics of interconnected units was simulated from different complex topologies widely observed in empirical systems with well-known network models. The methods of MI and CCM were chosen after examining on the artificial cases consisting of desirable features of the real-world systems.

1. Introduction

Complex networks are widely used in many fields throughout the biological, social, information, engineering, and physical sciences to improve our understanding of collective dynamics and function of complex natural and artificial systems evolving in time (Albert and Barabási, 2002; Newman, 2003; Boccaletti et al. 2006).

The networks uncover the system's underlying interaction patterns where a detailed description of dynamics and structure may be impossible due to complex or chaotic behavior. The interconnection between the elements of a real-world complex system should be determined to consider the nature of ongoing interaction. Hence, the intrinsic connectivity between the components needs to be characterized before we can understand the system, and usually this is done by mapping physical (e.g., anatomical) connections onto a network. The effect of that connectivity is frequently investigated by employing the concept of complex networks.

The broad applicability of networks and their success in providing insights into the structure and function of both natural and human-made systems have thus produced considerable excitement across myriad scientific disciplines. For example, transportation networks with airline routes, road and rail networks (Sen et al. 2003; Gastner and Newman 2004; Li et al. 2015); disease containment strategies based on cellular networks data (Lima et al. 2015); characterizing interactions in online social networks (Omodei et al. 2015); understanding the spatio-temporal evolution of an epidemics and infer migration patterns (De Domenico et al. 2013 and Matamalas et al. 2016); organization and functioning of the human's brain (Reis et al. 2014; De

* **Corresponding Author**

*(Naghipour.l@tabrizu.ac.ir) ORCID ID 0000-0001-9000-3851
(valizadeh@tabrizu.ac.ir) ORCID ID 0000-0003-4648-842X
(mtaalami@tabrizu.ac.ir) ORCID ID 0000-0002-5845-9776
(nourani@tabrizu.ac.ir) ORCID ID 0000-0002-6931-7060

Cite this study

Naghipour L, Valizadeh Kamran, K., Aalami, M. T., & Nourani, V. (2023). The modeling and analysis of empirical systems with complex networks. Intercontinental Geoinformation Days (IGD), 7, 138-141, Peshawar, Pakistan

Domenico et al. 2016); good description of protein-genetic interactions (Jeong et al. 2001; Carmi et al. 2006; De Domenico et al. 2015); the modeling of complex climate system (Naghipour et al. 2021 and 2022); analysis of groundwater level (Naghipour et al. 2023).

The quantitative study of networks is fundamental for the characterization of complex systems. Importantly, several features arise in a diverse variety of networks. For example, many networks constructed from empirical data-sets exhibit heavy-tailed degree distributions, the small-world property, and/or modular structures; such structural features can have important implications for information diffusion, robustness against component failure, and many other considerations.

In this study, we will propose a new statistical approach trying to overcome the problems and improve the present understanding of the Earth's climate system and its predictability. This work can also be considered as a comprehensive study for the application of convergent cross-mapping (CCM) method and the evaluation of common methods. Our approach is based on a combination of dynamical systems techniques and statistical analysis. Finally, we show how surrogate models can partially reproduce the nonlinear dynamics.

2. Methodology

In this section, we briefly review the statistical methods most widely adopted for reconstructing the network structure from the observation of collective dynamics. While all the methods differ in the type of correlation, similarity or causality they estimate between two stochastic processes, say X(t) and Y(t), the subsequent steps are the same: i) calculate the same measure for any pair of signals corresponding to the activity in two different nodes; ii) perform a statistical comparison against a null model and, accordingly, iii) keep only the links which reject the null hypothesis of statistically uncorrelated dynamics (see Figure 1).

In the following, a brief description of our procedure is presented by considering two widely used linear correlation statistics, namely Cross-Correlation (CC) and Spectral Coherence (SpeCoh), two widely used information-theoretic correlation measures, namely Mutual Information (MI) and Transfer Entropy (TE), one non-parametric similarity measure, namely Spearman's rank Correlation (SC).

In the next section, we will briefly discuss one method based on the reconstruction of the underlying phase space, namely Convergent Cross-Mapping (CCM), that is widely used to infer causal relationships between two observed dynamics.

According to Figure 1, (a) We generate synthetic network models and correlated dynamics. (b) Methods for inferring correlation, similarity or causality relationships between nodes are used to reconstruct the network connectivity, by performing hypothesis testing for each pairwise interaction. The null hypothesis is that the observed time series are not statistically correlated. (c) The inferred network connectivity is compared against the ground truth and statistical descriptors such as accuracy, negative predictive value, specificity and balanced accuracy are estimated to validate the goodness of the reconstruction (see the study by Naghipour et al. (2021) and (2022) for detailed information).

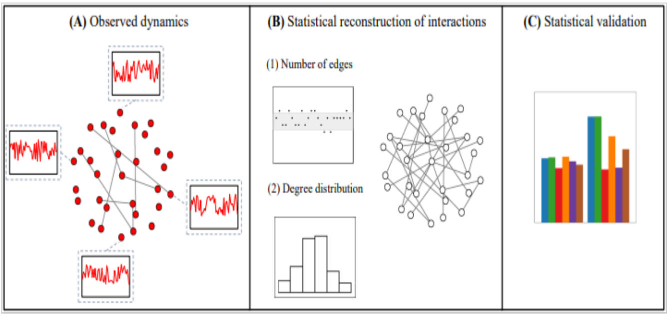

Figure 1. Schematic representation of the procedure used for reconstructing the network connectivity from the analysis of observed collective dynamics.

3. Results

In this work, we simulate 100 independent realizations of different network models -- namely with modular structure (Stochastic Block Model, SBM), scale-free (Barabási-Albert, BA), and small-world (Watts-Strogatz, WS) topology -- for increasing system's size (N=32,64, 128, 256) and time course length (M=64, 128, 256, 512, 1024). This setup allows one to understand the impact on connectivity reconstruction of network size, time series length, as well as the interplay between topology and dynamics. Reconstruction is performed according to the statistical approach previously described and for different correlation measures. The significance level chosen for each analysis in the following is 95%, compatible with a choice of 20 surrogates obtained by using randomly reshuffled series, the null model being the lack of correlation and causality between any pair of dynamics.

In Figure 2, a realization of the Barabási-Albert model, used as ground truth, and networks reconstructed from the observation of linear dynamics with shock propagation. The size of the system is N=32 and the length of temporal measurements is M=64. (B--G) Networks reconstructed with different methods. For each method, three cases are considered: forward dynamics only (1), backward dynamics only (2), and the multiplex network approach obtained from combing forward and backward dynamics (3).

We show in Figure 2 a single realization of a Barabási -Albert network, used as ground truth, simulate linear dynamics with shock propagation and show the resulting reconstructed networks. Once again, all reconstruction techniques described so far are used for forward-only collective dynamics (FOR) and dynamics with time reversal (INT). Methods like cross-correlation and Spearman's rank correlation lead to networks denser than the ground truth, explaining the excess of spurious connectivity observed in previous analyses. Conversely, convergent cross mapping and mutual information lead to networks as sparse as the ground truth, especially the latter. However, mutual information has the undesirable feature to infer edges where they are missing (i.e., high false negative rate), a problem only partially affecting convergent cross-mapping.

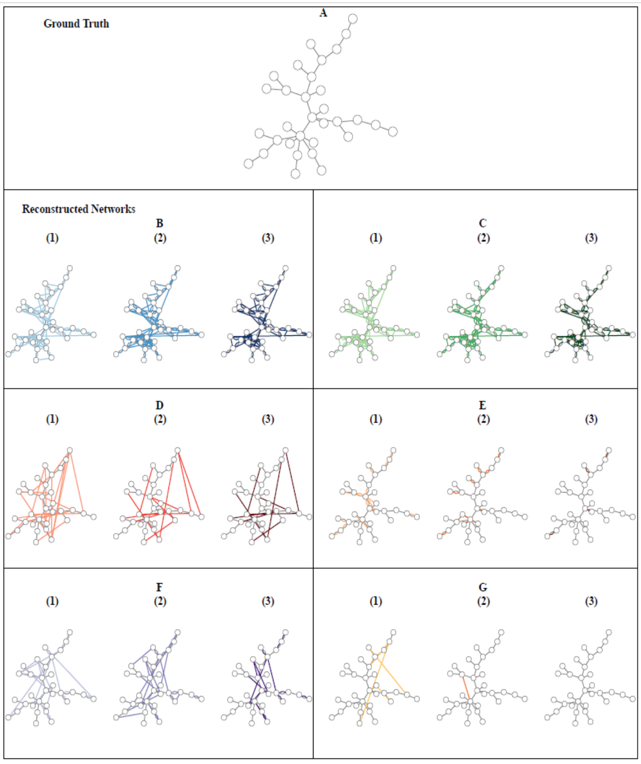

Figure 2. (A) A realization of the Barabási-Albert model with linear dynamics (B--G) Networks reconstructed with different methods, namely (B) cross-correlation, (C) Spearman's rank correlation, (D) spectral coherence, (E) convergent cross mapping, (F) transfer entropy and (G) mutual information.

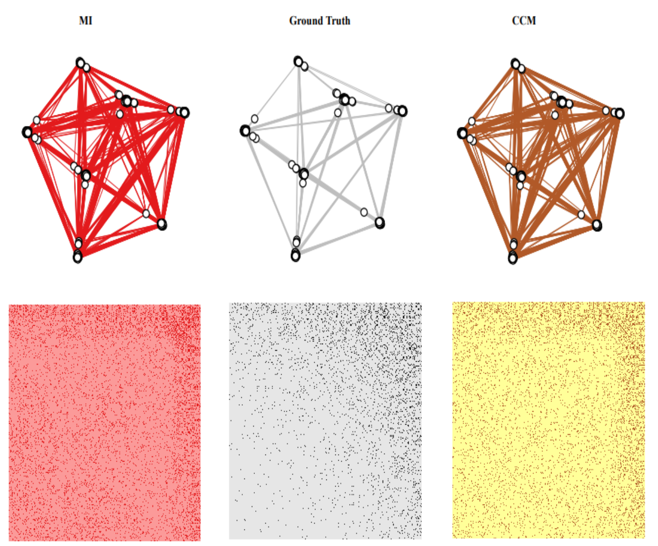

Figure 3. A representation of reconstructed networks and ground truth together with accompanying adjacency matrices.

In Figure 3, topology of the networks follows Lancichinetti-Fortunato-Radicchi model with the simulations from the nonlinearly coupled units with the Logistic map, and one of the network realizations is used as ground truth (gray edges). Inferred connectivity's are represented the reconstructed networks by the selected methods from the analysis presented in Figure 3, namely mutual information (MI) and convergent cross mapping (CCM) with the encoded colors as the previous figures. The dark colors indicate links on the corresponding adjacency matrices of the reconstructed networks. As another representative example, we show in Figure 3, a single realization of Lancichinetti-Fortunato-Radicchi network model, used as ground truth, simulate nonlinear collective dynamics and show the resulting reconstructed networks from the selected methods. Once again, selected reconstruction techniques as satisfied methods, are used, including mutual information and convergent cross mapping. Mutual information leads to networks denser than the ground truth, explaining the excess of spurious connectivity observed in previous analyses with more community detection (not shown in the figure). Convergent cross mapping also leads to networks denser than the ground truth, with less community detection which is desirable in comparison to the reconstructed network by mutual information. However, mutual information and convergent cross mapping have the unpleasant feature to infer edges where they are missing (i.e., high false negative rate), the problem of detecting true communities less affecting convergent cross mapping.

4. Conclusion

We demonstrate the principles of our approach with simple model examples, including BA, WS and SBM, to assess the strengths and weaknesses of the methods by varying system sizes and length of the time-series with performing a robust statistical analysis. The results show that the performance of CCM method is better to model time-series of the deterministic dynamical systems and MI models the stochastic series with high accuracy. In all statistical measures, the ARMA series has less error in compared with the LOG series. In fact, it has been shown that the analysis of collective dynamics might lead to very accurate (or inaccurate) reconstructions depending on the inference approach. However, convergent cross mapping appears to be the most robust, in terms of statistical reconstruction, to the unknown interplay between the structure of an interconnected system and the dynamics of its sites.

Acknowledgement

This study is supported by the research grant of the University of Tabriz (Number 718).

References

Albert, R., & Barabási, A. L. (2002). Statistical mechanics of complex networks. Reviews of modern physics, 74(1), 47.

Boccaletti, S., Latora, V., Moreno, Y., Chavez, M., & Hwang, D. U. (2006). Complex networks: Structure and dynamics. Physics reports, 424(4-5), 175-308.

Carmi, S., Levanon, E. Y., Havlin, S., & Eisenberg, E. (2006). Connectivity and expression in protein networks: proteins in a complex are uniformly expressed. Physical Review E, 73(3), 031909.

De Domenico, M., Lima, A., & Musolesi, M. (2013). Interdependence and predictability of human mobility and social interactions. Pervasive and Mobile Computing, 9(6), 798-807.

De Domenico, M., Nicosia, V., Arenas, A., & Latora, V. (2015). Structural reducibility of multilayer networks. Nature communications, 6(1), 6864.

De Domenico, M., Sasai, S., & Arenas, A. (2016). Mapping multiplex hubs in human functional brain networks. Frontiers in neuroscience, 10, 326.

Gastner, M. T., & Newman, M. E. (2004). Diffusion-based method for producing density-equalizing maps. Proceedings of the National Academy of Sciences, 101(20), 7499-7504.

Jeong, H., Mason, S. P., Barabási, A. L., & Oltvai, Z. N. (2001). Lethality and centrality in protein networks. Nature, 411(6833), 41-42.

Li, D., Fu, B., Wang, Y., Lu, G., Berezin, Y., Stanley, H. E., & Havlin, S. (2015). Percolation transition in dynamical traffic network with evolving critical bottlenecks. Proceedings of the National Academy of Sciences, 112(3), 669-672.

Lima, A., De Domenico, M., Pejovic, V., & Musolesi, M. (2015). Disease containment strategies based on mobility and information dissemination. Scientific reports, 5(1), 10650.

Matamalas, J. T., De Domenico, M., & Arenas, A. (2016). Assessing reliable human mobility patterns from higher order memory in mobile communications. Journal of The Royal Society Interface, 13(121), 20160203.

Naghipour, L., Aalami, M. T., & Nourani, V. (2021). Reconstruction of network connectivity by the interplay between complex structure and dynamics to discover climate networks. Theoretical and Applied Climatology, 143, 969-987.

Naghipour, L., Aalami, M. T., & Nourani, V. (2022). Unravelling the backbone of climate networks from the analysis of collective dynamics and time reversal. International Journal of Climatology, 42(11), 5535-5553.

Naghipour, L., Aalami, M. T., & Nourani, V. (2023). Collective dynamics analysis based on the multiplex network method to unravel the backbone of fluctuations in groundwater level data. Computers & Geosciences, 172, 105310.

Newman, M. E. (2003). The structure and function of complex networks. SIAM review, 45(2), 167-256.

Omodei, E., De Domenico, M., & Arenas, A. (2015). Characterizing interactions in online social networks during exceptional events. Frontiers in Physics, 3, 59.

Reis, S. D., Hu, Y., Babino, A., Andrade Jr, J. S., Canals, S., Sigman, M., & Makse, H. A. (2014). Avoiding catastrophic failure in correlated networks of networks. Nature Physics, 10(10), 762-767.

Sen, P., Dasgupta, S., Chatterjee, A., Sreeram, P. A., Mukherjee, G., & Manna, S. S. (2003). Small-world properties of the Indian railway network. Physical Review E, 67(3), 036106.

7th Intercontinental Geoinformation Days

igd.mersin.edu.tr

Assessing algae accumulation in an artificial pond using UAV-based orthophoto

Seyma Akca*[1], Nizar Polat [1]

[1]Harran University, Engineering Faculty, Geomatics Engineering Department, Sanliurfa, Türkiye

Keywords
UAV
Photogrammetry
Band ratio
Artificial Pond
Algae

Abstract

Artificial ponds serve as critical resources for various human activities, including agriculture, aquaculture, and water management. However, unchecked algae growth in these man-made water bodies can lead to eutrophication, oxygen depletion, and ecological degradation. Monitoring and managing algae accumulation in artificial ponds are essential for environmental sustainability. Traditional assessment methods have limitations in terms of spatial and temporal resolution, making them unsuitable for real-time monitoring. Recent advancements in Unmanned Aerial Vehicles (UAVs) and remote sensing technology have opened new possibilities for environmental monitoring. This study explores the application of UAV-based orthophotos and band ratios for assessing algae accumulation in artificial ponds. Structure from Motion (S*f*M) photogrammetry is used to create high-resolution orthophotos, providing detailed spatial information. Band ratios, derived from spectral information in RGB images, are employed to detect algae presence. Results show that UAV-based photogrammetry generates detailed orthophotos with a ground sampling distance of 1 cm, allowing for the identification of fine-scale features in the pond. The red/green band ratio proves effective in consistently detecting algae presence. The study demonstrates the potential of UAV-based RGB band ratios for accurate algae assessment, enabling informed decision-making and timely interventions to preserve the ecological integrity of artificial ponds. This innovative approach provides a valuable tool for safeguarding water quality and contributing to the sustainability of essential aquatic ecosystems.

1. Introduction

Artificial ponds play a pivotal role in various human activities, including agriculture, aquaculture, and water management (Niemczynowicz, 1999). These man-made bodies of water provide essential resources and services, such as irrigation, fish farming, and recreational opportunities (Popp et al., 2019). However, their ecological health and water quality can be compromised by the unchecked growth of algae, which can lead to eutrophication, oxygen depletion, and the degradation of aquatic ecosystems (Kennish, 2002; Mujere and Moyce, 2018). Monitoring and managing algae accumulation in artificial ponds is thus a critical concern for environmental sustainability.

The monitoring of algae in aquatic environments is a critical aspect of environmental science, given its implications for water quality, ecosystem health, and human activities (Glasgow et al., 2004; Altenburger et al., 2019). Traditional methods for assessing algae levels have included manual sampling, laboratory analysis, and visual inspection, all of which have inherent limitations in terms of spatial and temporal resolution (Peterson et al., 2020; Mozo et al., 2022). Manual sampling, involving the collection of water samples at specific locations and depths, is a well-established method for algae assessment. However, it is labor-intensive, time-consuming, and provides only point-in-time data, making it unsuitable for tracking algae dynamics in real-time (Simpson et al., 2005). Furthermore, manual sampling may introduce biases, especially in heterogeneous aquatic environments. Visual inspection, relying on the subjective judgment of trained observers, is often used for qualitative assessments of algae presence and abundance. While useful for rapid assessments, this method lacks the precision required for quantitative studies and may not be suitable for large-scale or continuous monitoring.

* **Corresponding Author**

*(seymakca@harran.edu.tr) ORCID ID 0000-0002-7888-5078
nizarpolat@harran.edu.tr) ORCID ID 0000-0002-6061-7796

Cite this study

Akça, Ş., & Polat, N. (2023). Assessing algae accumulation in an artificial pond using UAV-based orthophoto. Intercontinental Geoinformation Days (IGD), 7, 142-145, Peshawar, Pakistan

In recent years, advancements in Unmanned Aerial Vehicles (UAVs) and remote sensing technology have revolutionized the field of environmental monitoring (Anderson and Gaston, 2013; Karataş et al. 2022; Kanun et al. 2022). Remote sensing techniques, such as satellite and aerial imagery, offer the advantage of large-scale coverage and frequent data acquisition. Satellites can capture data at regular intervals, providing insights into long-term trends. However, their spatial resolution may limit their ability to detect algae in smaller water bodies or at fine spatial scales. UAVs, have emerged as a powerful tool in environmental science due to their versatility, affordability, and high spatial resolution capabilities. UAVs equipped with various sensors, including RGB cameras, multispectral sensors, and thermal cameras, have been deployed for a wide range of environmental monitoring tasks. In the context of water bodies, UAVs have shown promise in providing detailed and up-to-date information (Mahdavi et al., 2018). RGB cameras onboard UAVs can capture high-resolution orthophotos, which are orthorectified aerial images. These orthophotos can be used to assess water quality, including the presence and distribution of algae. Band ratios, derived from the spectral information in RGB images, have been utilized for detecting the presence of algae in water bodies (Kislik et al., 2018; Alptekin and Yakar, 2020)). Furthermore, UAVs offer the advantage of flexibility in terms of flight altitude and frequency (Karataş et al. 2023). They can be deployed on-demand to capture data at specific times or in response. Thus, it allows for the rapid collection of data on pond health, enabling timely interventions to prevent or mitigate algae-related issues. This paper presents a premise study on the utilization of UAV-based orthophotos for assessing algae accumulation in an artificial pond, focusing specifically on the capabilities of band ratios in algae detection using RGB orthophoto imagery.

2. Method

2.1. Image Processing

Structure from Motion (SfM) is a cutting-edge photogrammetric technique that has revolutionized the way we reconstruct three-dimensional (3D) environments from a series of overlapping 2D images (Calì and Ambu, 2018; Unel et al. 2020; Alptekin and Yakar, 2021). This innovative approach enables the creation of highly accurate and detailed 3D models and orthophotos from aerial photographs, such as those captured by Unmanned Aerial Vehicles (UAVs) or traditional aircraft. SfM works by identifying common features or key points in the overlapping images and then calculating their 3D positions by analyzing the variations in perspective and parallax (Kanun et al.2021; Yılmaz et al. 2022; Yakar et al. 2023). Through this process, SfM can produce a dense point cloud representation of the surveyed area, which can subsequently be used to generate digital surface models, orthophotos, and even textured 3D models (Meneely, 2023). This technology has found applications in a wide range of fields, including geospatial mapping, archaeology, environmental monitoring, and infrastructure assessment, offering a powerful tool for obtaining detailed and accurate spatial information from aerial imagery.

2.2. Band Ratios

Band ratio is a fundamental technique in remote sensing and image analysis that involves the mathematical comparison of two or more spectral bands or channels of remotely sensed data (Tucker, 1979). By dividing the reflectance values in one band by those in another, a band ratio image is created, which highlights specific features or information of interest in the scene (Liu and Mason; 2013). Band ratios are particularly valuable in tasks such as vegetation analysis, mineral identification, and land cover classification. Similarly, mineral exploration often employs band ratios to detect minerals with distinctive spectral signatures in satellite or aerial imagery. Band ratio techniques enhance the interpretability of image data, allowing for the extraction of meaningful information and the identification of specific materials or phenomena within a given area (Shebl et al., 2023).

3. Results and Discussion

In the study, the photogrammetric flight conducted utilizing a UAV at a flight altitude of 30 meters has yielded valuable insights into the artificial lake under investigation. With an 80% overlay rate and a total of 154 aerial photographs captured, our study achieved a remarkable ground sampling distance of 0.7 centimeters. The robust dataset generated during this aerial survey has allowed for the extraction of a dense point cloud comprising an impressive 4,026,467 points, with a point density of 284 points per square meter. These results reflect the effectiveness of UAV-based photogrammetry in producing high-resolution orthophotos and detailed topographic information for our study area. Figure 1 presents a high-resolution (1 cm) orthophoto of the lake under study, captured with remarkable precision during our UAV-based photogrammetric flight.

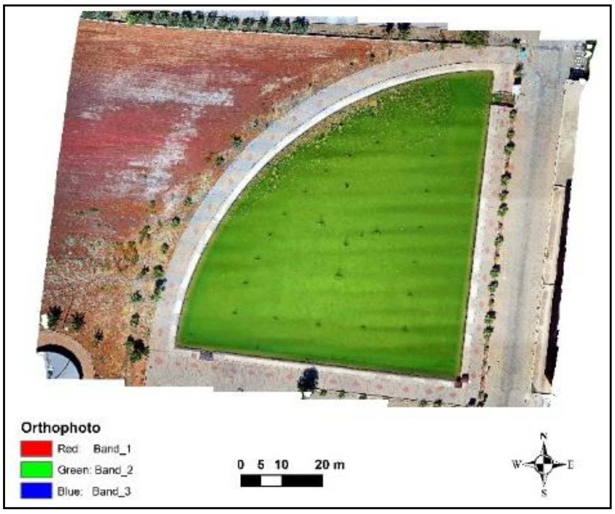

Figure 1. High-resolution (1 cm) orthophoto of the lake

The ground sampling distance of 1 cm highlights the exceptional level of detail attained in this aerial survey. Each pixel in this orthophoto represents an area of just one square centimeter on the ground, providing a clear and vivid visual representation of the lake's features and surroundings. Notably, this orthophoto offers a wealth of spatial information, enabling the identification of fine-scale features such as shoreline characteristics, aquatic vegetation distribution, and even subtle variations in water quality. The vividness of this orthophoto underscores the utility of UAV-based photogrammetry for acquiring high-resolution geospatial data in environmental monitoring, resource management, and scientific investigations. The details depicted in Figure 1 are pivotal for our study's objectives, contributing to a comprehensive understanding of the lake's dynamics and aiding in precise analyses of various factors influencing its health and ecology.

After obtaining the high-resolution orthophoto of the lake, our study delved into further analysis to extract valuable insights regarding water quality and ecological conditions. Apart from visual inspection, the key analytical approach employed was the calculation of band ratios. These ratios serve as valuable tools for identifying specific features and phenomena within the imagery. In this context, we firstly focused on the red/green band ratio, which is known to provide critical information about water quality and the presence of algae. The results of the red/green band ratio analysis are presented in Figure 2.

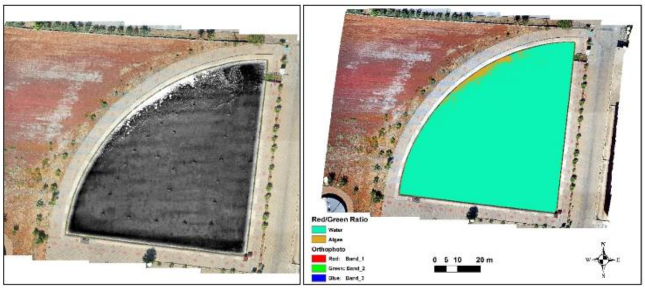

Figure 2. The result of the red/green band ratio (left) and its thematic map (right).

In Figure 2 (left), the red/green band ratio provides valuable insights into the conditions of the lake's water surface. Areas depicting a higher red/green band ratio, indicated by lighter tones in the image, correspond to regions with a greater presence of algae. This result aligns with the greenish tint observed in the water, signifying the accumulation of algae. The distinctive coloration and spatial distribution depicted in the ratio image offer a clear visual representation of the areas affected by algal growth, providing crucial information for our study's assessment of water quality and ecological dynamics (Figure 2 right). Moving beyond the red/green band ratio, we also investigated the red/blue band ratio, as illustrated in Figure 3.

This ratio reveals complementary information about the lake's water quality and the presence of algae. In the context of this ratio, areas exhibiting higher values (figure 3 left), denoted by brighter regions in the image, suggest potentially greenish water. In this case, the dark areas indicate algae accumulated on the water surface. The spatial distribution of algae can be seen in figure 3 right. Finally, Figure 4 presents the green/blue band ratio, which plays a crucial role in our assessment of the lake's water conditions.

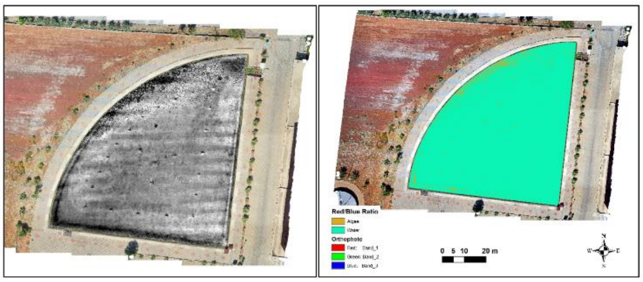

Figure 3. The result of the red/blue band ratio (left) and its thematic map (right).

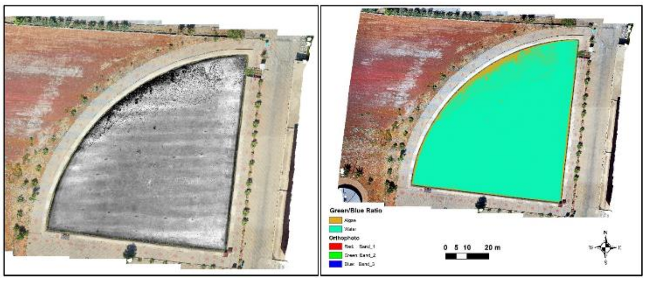

Figure 4. The result of the green/blue band ratio (left) and its thematic map (right).

In this ratio image, areas with elevated green/blue values (left), represented by lighter areas, indicate a greater likelihood of greenish water. The dark areas indicate algae accumulated on the water surface. The spatial distribution of algae can be seen in figure 4 right.
Upon reviewing the band ratio results, it is evident that the red/green ratio provides more consistent and reliable outcomes. However, it's worth noting that in the case of the other two ratios, some instances, such as the fountains within the lake, were mistakenly identified as algae. Furthermore, partial inclusion of shoreline shadows within the algae class was observed. In light of these findings, while all three ratios effectively detect algae accumulation, it is advisable to prioritize the use of the red/green ratio for a more accurate assessment of algae presence and distribution in the lake.

4. Conclusion

In Conclusion, the utilization of UAV-based RGB band ratios presents a powerful and versatile method for investigating water pollution and algae accumulation in artificial lakes. By harnessing the spectral information captured through high-resolution orthophotos, these ratios enable precise identification and mapping of areas affected by algae growth and greenish water. This approach enhances our ability to monitor and manage water quality in artificial lakes with greater efficiency and accuracy. Our study has demonstrated the potential of this innovative technique, specifically highlighting the effectiveness of the red/green band ratio in consistently detecting algae presence and distribution. While the other two ratios occasionally misidentified features such as fountains and shoreline shadows, the red/green ratio emerged as the more consistent and dependable choice for accurate algae assessment.

The integration of UAV technology and band ratio analysis not only provides valuable insights into water quality but also offers a promising pathway toward informed decision-making, timely interventions, and the preservation of the ecological integrity of these vital water bodies. As we continue to explore innovative techniques in environmental science, the UAV-based RGB band ratio approach stands as a valuable tool for safeguarding the health and sustainability of artificial lakes. It empowers us to proactively address water quality challenges and contribute to the preservation of these essential aquatic ecosystems.

References

Alptekin, A., & Yakar, M. (2020). Determination of pond volume with using an unmanned aerial vehicle. Mersin Photogrammetry Journal, 2(2), 59-63.

Alptekin, A., & Yakar, M. (2021). 3D model of Üçayak Ruins obtained from point clouds. Mersin Photogrammetry Journal, 3(2), 37-40.

Altenburger, R., Brack, W., Burgess, R. M., Busch, W., Escher, B. I., Focks, A., ... & Krauss, M. (2019). Future water quality monitoring: improving the balance between exposure and toxicity assessments of real-world pollutant mixtures. Environmental Sciences Europe, 31(1), 1-17.

Anderson, K., & Gaston, K. J. (2013). Lightweight unmanned aerial vehicles will revolutionize spatial ecology. Frontiers in Ecology and the Environment, 11(3), 138-146.

Calì, M., & Ambu, R. (2018). Advanced 3D photogrammetric surface reconstruction of extensive objects by UAV camera image acquisition. Sensors, 18(9), 2815.

Glasgow, H. B., Burkholder, J. M., Reed, R. E., Lewitus, A. J., & Kleinman, J. E. (2004). Real-time remote monitoring of water quality: a review of current applications, and advancements in sensor, telemetry, and computing technologies. Journal of experimental marine biology and ecology, 300(1-2), 409-448.

Kanun, E., Alptekin, A., & Yakar, M. (2021). Documentation of cultural heritage by photogrammetric methods: a case study of Aba's Monumental Tomb. Intercontinental Geoinformation Days, 3, 168-171.

Kanun, E., Alptekin, A., Karataş, L., & Yakar, M. (2022). The use of UAV photogrammetry in modeling ancient structures: A case study of "Kanytellis". Advanced UAV, 2(2), 41-50.

Karataş, L., Alptekin, A., & Yakar, M. (2022). Detection and documentation of stone material deterioration in historical masonry structures using UAV photogrammetry: A case study of Mersin Aba Mausoleum. Advanced UAV, 2(2), 51-64.

Karataş, L., Dal, M., Alptekin, A., & Yakar, M. (2023). The 3D virtual restitution of historical buildings using photogrammetry: A case study of the Dungeon-Cistern structure in the Ancient City of Dara (Anastasiopolis), Mardin. Intercontinental Geoinformation Days, 6, 5-8.

Kennish, M. J. (2002). Environmental threats and environmental future of estuaries. Environmental conservation, 29(1), 78-107.

Kislik, C., Dronova, I., & Kelly, M. (2018). UAVs in support of algal bloom research: A review of current applications and future opportunities. Drones, 2(4), 35.

Liu, J. G., & Mason, P. J. (2013). Essential image processing and GIS for remote sensing. John Wiley & Sons.

Mahdavi, S., Salehi, B., Granger, J., Amani, M., Brisco, B., & Huang, W. (2018). Remote sensing for wetland classification: A comprehensive review. GIScience & Remote Sensing, 55(5), 623-658.

Meneely, J. (Ed.). (2023). 3D Imaging of the Environment: Mapping and Monitoring. CRC Press.

Mozo, A., Morón-López, J., Vakaruk, S., Pompa-Pernía, Á. G., González-Prieto, Á., Aguilar, J. A. P., ... & Ortiz, J. M. (2022). Chlorophyll soft-sensor based on machine learning models for algal bloom predictions. Scientific Reports, 12(1), 13529.

Mujere, N., & Moyce, W. (2018). Climate change impacts on surface water quality. In Hydrology and Water Resource Management: Breakthroughs in Research and Practice (pp. 97-115). IGI Global.

Niemczynowicz, J. (1999). Urban hydrology and water management–present and future challenges. Urban water, 1(1), 1-14.

Peterson, K. T., Sagan, V., & Sloan, J. J. (2020). Deep learning-based water quality estimation and anomaly detection using Landsat-8/Sentinel-2 virtual constellation and cloud computing. GIScience & Remote Sensing, 57(4), 510-525.

Popp, J., Békefi, E., Duleba, S., & Oláh, J. (2019). Multifunctionality of pond fish farms in the opinion of the farm managers: the case of Hungary. Reviews in Aquaculture, 11(3), 830-847.

Shebl, A., Abdellatif, M., Badawi, M., Dawoud, M., Fahil, A. S., & Csámer, Á. (2023). Towards better delineation of hydrothermal alterations via multi-sensor remote sensing and airborne geophysical data. Scientific Reports, 13(1), 7406.

Simpson, S. L., Batley, G. E., Chariton, A. A., Stauber, J. L., King, C. K., Chapman, J. C., ... & Maher, W. A. (2005). Handbook for sediment quality assessment (pp. 126-126). Bangor, NSW: Centre for Environmental Contaminants Research.

Tucker, C. J. (1979). Red and photographic infrared linear combinations for monitoring vegetation. Remote sensing of Environment, 8(2), 127-150.

Ünel, F. B., Kuşak, L., Çelik, M., Alptekin, A., & Yakar, M. (2020). Kıyı çizgisinin belirlenerek mülkiyet durumunun incelenmesi. Türkiye Arazi Yönetimi Dergisi, 2(1), 33-40.

Yakar, M., Ulvi, A., Yiğit, A. Y., & Alptekin, A. (2023). Discontinuity set extraction from 3D point clouds obtained by UAV Photogrammetry in a rockfall site. Survey Review, 55(392), 416-428.

Yılmaz, H. M., Aktan, N., Çolak, A., & Alptekin, A. (2022). Modelling Ozancık village (Aksaray) in computer environment using UAV photogrammetry. Mersin Photogrammetry Journal, 4(1), 32-36.

7th Intercontinental Geoinformation Days

igd.mersin.edu.tr

Classifying unmanned aerial vehicle images for urban vegetation mapping utilizing SVM

Zahra Azizi [1], Payam Alemi Safaval [2]

[1] Islamic Azad University, Science and Research Branch, Faculty of Natural Resources and Environment, Department of Remote Sensing and GIS, Tehran, Iran
[2]Geological Survey & Mineral Exploration of Iran, Iran

Keywords
Maximum likelihood
UAV
GLCM
Karaj
SVM

Abstract

This study focuses on the potential of sUAVs for mapping urban vegetation. The researchers compared the effectiveness of maximum likelihood and SVM algorithms for classification purposes. Additionally, they tested different window sizes to determine the optimal size for calculating textural indices. An ortho-mosaic image was used to analyze the vegetation. A total of 748 images were collected from a height of 100 meters using a low-cost UAV, resulting in a resolution of 2.56 cm per pixel. To ensure accurate results, a high overlap of 90% forward and 80% side overlap was maintained to minimize vegetation masking by tall buildings. Ground control points were collected using GPS RTK technology, and all images were processed using Agisoft PhotoScan v1.27 software with a root mean square error of 0.2 pixels. Eight textural indices, including mean, standard deviation, homogeneity, contrast, dissimilarity, entropy, correlation, and angular second moment were extracted using gray-level co-occurrence matrix (GLCM). These texture indices were calculated using six different window sizes ranging from 3×3 to 45×45. The findings of this study will contribute to the understanding of sUAV-based remote sensing for mapping urban vegetation and provide insights into the most effective classification algorithms and window sizes for calculating textural indices.

1. Introduction

Today, the importance of information is hidden to no one so that the present age can be called the information age, the computer is the symbol of the age, the information is the symbol of wealth and knowledge is the basis of power. Its importance comes from the need for information to make any planning and decision-making.

As a rapidly evolving technology, small unmanned aerial vehicle (sUAV) based remote sensing has received many attentions from researchers and managers recently (Smith et al. 2002; Rasmussen et al. 2016). sUAV is an innovative and flexible technology which is able to collect very high resolution images for both geometric and descriptive purposes (Rasmussen et al. 2016). UAVs collected images offers a unique way to obtain large scale mapping of vegetation cover as well as vegetation canopy attributes (Gini et al. 2012).

From many prospects, urban vegetation plays important roles such as decreasing heat island effect (Chianucci et al. 2016), increasing air quality, reducing sound noises, and promoting quality of life (Fan et al. 2015). Managing and planning urban vegetation establishment and development need accurate timely large-scale spatial data. For many years space born data has been utilized to delineate urban vegetation. However, complex residential area needs high resolution images. Such images aren't usually available and airborne imagery aren't a cost-efficient method. However, sUAV imagery offers a great potential for collecting hyper resolution images with affordable price.

UAV images have been utilized for studying different vegetation aspects such as tree species identification (Miraki and Azizi, 2022), vegetation phenology (Miraki et al., 2021), tree height estimation (Panagiotidis et al, 2017; Sadeghi and Sohrabi, 2019), composition and abundance (Azizi and Miraki, 2021), and etc. Results of these studies showed that using UAV images is highly competitor to other data sources. Despite this, one of the most important drawbacks of such data is low spectral resolution which makes it difficult to delineate vegetation cover using RGB data. In RGB space, it is difficult to separate vegetating from other land classes. Another drawback is shadow which can highly affect the

* Corresponding Author

*(zazizi@srbiau.ac.ir) ORCID ID 0000-0001-8572-7134
(payam.alemi@srbiau.ac.ir) ORCID ID 0000 – 0003 – 4843 – 0782

Cite this study

Azizi Z, Alemi Safaval P (2023). Classifying Unmanned Aerial Vehicle images for Urban Vegetation Mapping utilizing SVM. Intercontinental Geoinformation Days (IGD), 7, 146-148, Peshawar, Pakistan

result of vegetation mapping in residential areas especially where there are many tall buildings.

One solution is to use texture indices instead of spectral data. Some researchers reported better results for estimation of vegetation attributes using textural indices rather than spectral data or indices (Safari and Sohrabi, 2016). However, there are few studied on textural indices derived from very high resolution (VHR) images for urban vegetation mapping. Fan et al (2015) used random forest and textural indices to map the vegetation of an urban area. They concluded that UAV is an efficient and idea platform for mapping urban vegetation.

The aim of this study is to assess the potential of sUAV images for mapping urban vegetation. For classification, we compared maximum likelihood and support vector machine. Also, we tested different window size for calculating textural indices to find the best window.

2. Method

The location of the study area (Karaj City, Alborz Province) and part of the ortho-mosaic is shown in figure1.

For aim of this study, 748 images were collected from 100 meter above sea level using a low-cost UAV resulting in resolution of 2.56 cm per pixel. The forward and side overlap were 90% and 80%, respectively.

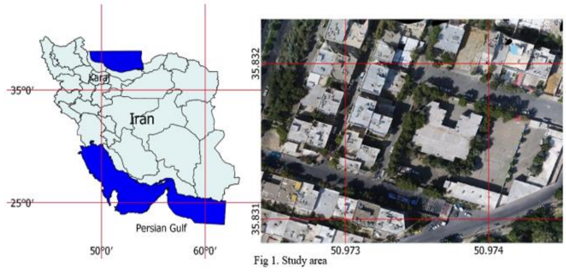

Fig 1. Study area

We considered high overlap to avoid vegetation masking by tall building as much as possible. Using GPS RTK, 24 ground control point has been collected. All images were processes in Agisoft PhotoScan v1.27 with a root mean square error of 0.2 pixel. Based on gray-level co-occurrence matrix (GLCM), eight textural indices including mean (MEA), standard deviation (STD), homogeneity (HOM), contrast (CON), dissimilarity (DIS), entropy (ENT), correlation (COR), and angular second moment (ASM) were extracted. Texture indices were calculated using six different window sizes including 3×3, 9×9, 21×21, 31×31, and 45×45 (Sohrabi et al. 2010).

3. Results

Two frequently used algorithm for classification are random forest (RF) and support vector machine (SVM). However it has been reported by some researchers that SVM performs better than RF (Safari et al. 2017; Piragnolo et al. 2017; Azizi and Miraki, 2022). For classification, we used algorithm. Also, to compare the result of SVM, we used maximum likelihood (ML) classification as well. Three classes were considered including roof, asphalt, and vegetation. Training samples of different classes were randomly chosen in a small polygon block. To assess the accuracy of classification, confusion matrix was used from independent validation samples and Kappa index, overall accuracy (OA), producer accuracy (PA) and user accuracy (UA) were calculated (Figure 2).

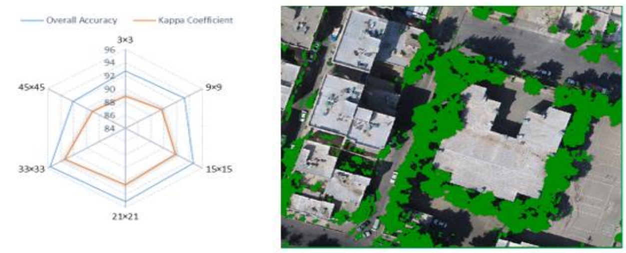

Fig 2. Overall accuracy and Kappa coefficient for different window sizes (left) and classification result (right)

4. Discussion

Results showed that for any window size, SVM resulted better accuracy in comparing to ML algorithm. Also, by increasing the window size for deriving the texture indices the accuracy of classification was increased. But after 31×31 there were rapid decrease in the accuracy of the classification. The best result was for 31×31 by kappa coefficient of 93.4% and overall accuracy of 95.6%. From a visual inspection, using texture with 31×31 windows for classification decreased the drawback of “salt and pepper” effects which is a common problem in spectral based classification.

The smaller the window size, the higher the salt and pepper effect. Also, this problem was higher for ML results. Fan et al. (2015) and Azizi and Miraki (2022) found the same result for comparing ML and RF. Surprisingly, they also reported 31×31 window size as the best window size.

5. Conclusion

The result of accuracy assessment showed that the UAV images and SVM classification can result in green space maps with high accuracy.

Momeni et al. (2016) reported 91% for mapping complex urban land cover from spaceborne imagery. Feng et al. reported 90% accuracy for urban vegetation mapping using random forest and texture analysis. Based on the result using UAV images with the current approach (classifying image texture using SVM) is a promising solution to depict vegetation maps in complex urban areas.

References

Azizi, Z., Miraki, M. (2021). Assessing the accuracy of UAV-captured images used for individual trree crowns delineation in different structures of an urban forest. Scientific- Research Quarterly of Geographical Data (SEPEHR), 30(118), 139-151. doi: 10.22131/sepehr.2021.246146

Azizi, Z., Miraki, M. (2022). Individual urban trees detection based on point clouds derived from UAV-RGB imagery and local maxima algorithm, a case study of Fateh Garden, Iran. Environ Dev Sustain https://doi.org/10.1007/s10668-022-02820-7

Chianucci, F., Disperati, L., Guzzi, D., Bianchini, D., et al. (2016) Estimation of canopy attributes in beech forests using true colour digital images from a small fixed-wing UAV. International Journal of Applied Earth Observation and Geoinformation, 47, pp. 60–68. http://dx.doi.org/10.1016/j.jag.2015.12.005

Fan, C., Myint, Soe W., Zheng, B. (2015) Measuring the spatial arrangement of urban vegetation and its impacts on seasonal surface temperatures. Progress in Physical Geography, 39(2), 199–219. http://journals.sagepub.com/doi/10.1177/0309133314567583

Gini, R., Passoni, D., Pinto, L. and Sona, G. (2012). Aerial Images From an Uav System: 3D Modeling and Tree Species Classification in a Park Area. ISPRS - International Archives of the Photogrammetry, Remote Sensing and Spatial Information Sciences, XXXIX-B1, pp. 361–366. http://www.int-arch-photogramm-remote-sens-spatial-inf-sci.net/XXXIX-B1/361/2012/

Miraki, M., Azizi, Z. (2022). Urban Forest Tree Classification Using UAV-Based High-Resolution Imagery. In: El-Askary, H., Erguler, Z.A., Karakus, M., Chaminé, H.I. (eds) Research Developments in Geotechnics, Geo-Informatics and Remote Sensing. CAJG 2019. Advances in Science, Technology & Innovation. Springer, Cham. https://doi.org/10.1007/978-3-030-72896-0_83

Miraki, M., Sohrabi, H., Fatehi, P., Kneubuehler, M. (2021) Detection of mistletoe infected trees using UAV high spatial resolution images. J. Plant Dis. Prot, 128, 1679–1689.

Momeni, R., Aplin, P., Boyd, D., (2016) Mapping Complex Urban Land Cover from Spaceborne Imagery: The Influence of Spatial Resolution, Spectral Band Set and Classification Approach'. Remote Sensing, 8(2), 88. http://www.mdpi.com/2072-4292/8/2/88

Panagiotidis, D., Abdollahnejad, A.S., Chiteculo, V. (2017). Determining tree height and crown diameter from high-resolution UAV imagery'. International Journal of Remote Sensing, 38(8–10), pp. 2392–2410. 10.1080/01431161.2016.1264028

Piragnolo, M., Masiero, A., Pirotti, F. (2017). Comparison of Random Forest and Support Vector Machine classifiers using UAV remote sensing imagery'. Geophysical Research Abstracts EGU General Assembly, 19(iii), 2017–15692.

Rasmussen, J., Ntakos, G., Nielsen, J., Svensgaard, J., et al. (2016). Are vegetation indices derived from consumer-grade cameras mounted on UAVs sufficiently reliable for assessing experimental plots?' European Journal of Agronomy, 74, 75–92. http://dx.doi.org/10.1016/j.eja.2015.11.026

Sadeghi S, Sohrabi H (2019) The effect of UAV flight altitude on the accuracy of individual tree height extraction in a broad-leaved forest. In: GeoSpatial conference 2019 – joint conferences of SMPR and GI Research, 1168–1173. https://doi.org/10.5194/isprs-archives-xlii-4-w18-1168-2019

Safari, A., Sohrabi, H. (2016). Ability of landsat-8 OLI derived texture metrics in estimating aboveground carbon stocks of coppice Oak Forests'. International Archives of the Photogrammetry, Remote Sensing and Spatial Information Sciences - ISPRS Archives, 41(2011), 751–754.

Safari, A., Sohrabi, H., Powell, S., Shataee, S. (2017). A comparative assessment of multi-temporal Landsat 8 and machine learning algorithms for estimating aboveground carbon stock in coppice oak forests. International Journal of Remote Sensing, 38(22), 6407–6432.

Smith, J.M., Adams, B.A. & Wilson, A. (2002). The Future for Asteroid Exploration.Planet. Space Sci. 285(11), 123–126.

Sohrabi, H., Hosseini, S.M., Zobeiri, M. (2010). Estimation of forest stand volume using textural indices of aerial images. Iranian Journal of Forest and Poplar Research, 18(2), 297–306.

7th Intercontinental Geoinformation Days

igd.mersin.edu.tr

Crack detection for bridge inspection utilizing UAV photogrammetry technique

Abdurahman Yasin Yiğit*[1], Murat Uysal [2,3]

[1]Mersin University, Engineering Faculty, Geomatics Engineering Department, Mersin, Türkiye
[2]Afyon Kocatepe University, Engineering Faculty, Geomatics Engineering Department, Afyonkarahisar, Türkiye
[3]Afyon Kocatepe University, Remote Sensing and GIS Application and Research Center, Afyonkarahisar, Türkiye

Keywords
Photogrammetry
UAV
Bridge Inspection
3D model

Abstract

With the expansion of transportation networks, road networks are also growing, resulting in an increased usage of bridges. Consequently, there will also be an increase in bridge deformations due to increased crossings. Inspecting bridges incurs significant maintenance costs. As a promising strategy to safeguard bridges, a bridge inspection method using UAVs with vision sensors is proposed. Crack identification methods on historic concrete bridges are investigated in this paper using a high-resolution vision sensor attached to a commercial UAV. In the preflight, a photorealistic 3D model based on point cloud is created before detecting cracks on the structural surface and calculating their thicknesses and lengths. A field experiment was performed to authenticate the suggested method, and the scientific findings demonstrated the efficacy of bridge inspection using UAVs in detecting and quantifying cracks in infrastructure.

1. Introduction

Continuous safety monitoring and maintenance of infrastructure such as bridges is essential. Effects such as fatigue, thermal expansion, contraction, and external loads degrade the performance of bridges over time. As bridges age, the number of bridges that need to be inspected increases, resulting in high maintenance costs. If spending on bridge maintenance is delayed, more costs will be required shortly (Kim et al., 2018). Therefore, many countries have established a maintenance plan for bridges. Since a crack directly reflects the condition of structures, it is considered one of the essential parameters for structural health monitoring (Fawzy et al., 2023). Traditional crack detection is performed by human visual inspection (Karataş et al. 2022a). This method has limitations as the performance is dependent on the experience of the inspector, time-consuming, and limited access areas (Unel et al. 2004).

Some approaches include the use of a charge-coupled device (CCD) camera, complementary metal-oxide-semiconductor (CMOS) image sensor, near-infrared (NIR), and hyperspectral camera. In most studies, image processing consists of the following steps: (1) image acquisition; (2) pre-processing techniques, which are efficient image processing methods; (3) image processing techniques such as binarisation and noise removal using a mask filter or morphological processing; and (4) crack measurement, which is a parameter estimation of the crack. Image binarisation methods have converted an RGB image into a binary one.

In recent years, bridge inspection based on unmanned aerial vehicles (UAVs) with high-resolution sensors has attracted much attention in many countries due to its safety and reliability. Using a UAV equipped with a camera to scan the bridge's surface and store the digital images taken during crack detection has many advantages. Due to its efficiency, speed, safety, and cost-effectiveness, local transportation departments are investigating and beginning to implement UAV-based bridge inspection technology (Kim et al., 2018). According to a report by the American Association of State Highway and Transportation Officials (AASHTO), 16 states use UAVs for bridge inspection. However, they roughly assess damage conditions without knowing their size and location (Dorafshan et al., 2017). A GPS-denied environment under a bridge reduces the stability of the UAV platform. Therefore, many flight planning methods using appearance image-based recognition (Han et al., 2015), simultaneous localization and mapping (SLAM)

* **Corresponding Author**

*(ayasinyigit@mersin.edu.tr) ORCID ID 0000-0002-9407-8022
(muysal@aku.edu.tr) ORCID ID 0000-0001-5202-4387

Cite this study

Yiğit, A. Y. & Uysal, M. (2023). Crack detection for bridge inspection utilizing UAV photogrammetry technique. Intercontinental Geoinformation Days (IGD), 7, 149-152, Peshawar, Pakistan

(Munguia et al., 2016), and real-time lidar odometry mapping (LOAM) have been proposed to reduce GPS errors. Other researchers have proposed and investigated a protocol for bridge inspection to overcome the challenges (Kim et al., 2018).

Crack detection methods based on machine learning and deep learning have recently been proposed (Cha et al., 2017). Features are obtained from crack images by training a convolutional neural network. The results of crack detection using these learning methods overcome the limitations of traditional image processing techniques such as drop and edge detection. To locate and visualize the detected crack, it should be supported by 3D models for a photorealistic Building Information Model (BIM) integrated with a UAV process. The advantages of photorealistic models generated by photogrammetry are easy visualization of structural elements and management of maintenance history (Feng et al., 2018). However, many bridges are without BIM, and deriving a new BIM requires much time and effort. Therefore, the UAV-based crack detection system is at an embryonic stage, which needs to solve many challenging problems in its practical applications. In addition, longer flight times and more stable flights are required for stable inspection. When approaching the bridge, it is essential to ensure that the field of view determines the pixel size of the image.

This paper investigates a crack identification method for an aging historic concrete bridge using a 3D model generated from images of a commercial UAV with a high-resolution camera. In such a study, the inspector can create a background model of a bridge without any information. He can also track the damage history by visualizing the cracks on the inspection map. The detailed process of this study is as follows. First, a point cloud-based bridge model was created in a preflight. Next, inspection images were captured by a high-resolution camera mounted on the UAV, and a 3D model was created to scan the structural elements. Finally, the cracks and crack size were estimated. In order to measure the cracks in the captured images, reference marks were previously placed on the structures and analyzed for accuracy.

2. Method

Continuous safety monitoring and maintenance of infrastructure such as bridges are essential issues. Effects such as fatigue, thermal expansion, contraction, and external loading degrade the performance of bridges over time (Fawzy et al., 2023). As bridges age, the number of bridges requiring inspection increases, resulting in high maintenance costs. If we delay spending on bridge maintenance, more costs will be required shortly. Therefore, many countries have established a maintenance plan for bridges (MacGregor et al., 1997). Since a crack is a direct reflection of the condition of a structure, it is considered one of the most essential parameters for structural health monitoring. Traditional crack detection is carried out by human visual inspection. This method has limitations, as the performance depends on the experience of the inspector, time consumption, and limited access areas.

Photogrammetry has been vital for centuries in understanding distant objects and the Earth's surface (Karataş et al. 2022b). Its uses have expanded over the years, and it is a method that uses powerful technologies constantly evolving in sectors such as construction, engineering, medicine, and many more (Karataş et al. 2022c). Photogrammetry can vary, but the general idea revolves around gathering information about an object from photographs (Alptekin and Yakar, 2021). Photographs are taken from different positions and angles to allow precise calculations to be made that help analysts gather the data they are looking for (Yakar, 2011). Typically, they use photo interpretation and geometric relationships to gather measurements. We can create maps and 3D models of real-world scenes with the data collected from photogrammetry (Şasi and Yakar, 2017; Kuşak et al. 2021).

The SfM algorithm is an algorithm that speeds up the photogrammetric process by developing software with technology (Alptekin and Yakar, 2020; Kanun et al. 2022). SfM is a photogrammetric algorithm that automatically solves a 3D target mesh with known scene geometry, camera positions, and orientation without pre-definition (Yakar and Doğan, 2017; Yakar et al. 2023). This algorithm allows self-calibration without pre-calibration (Kanun et al. 2021). Photogrammetric software using the SfM algorithm also uses a block balancing algorithm to optimize the projection errors between the image and the calculated point positions (Yılmaz et al. 2022).

Cracks can be broadly divided into two categories: structural cracks and non-structural cracks. Structural cracks are cracks caused by errors in design, construction, or overloading of the bridge member. On the other hand, non-structural cracks are caused by internal stresses in the bridge member that do not directly affect the structural behavior of the member. It can be referred to as 'direct damage' because the presence of the crack means that moisture reaches the steel reinforcement, corrodes the reinforcement, and eventually causes the bridge element to fail, but this process takes a long time to occur (Arvind, 2016; Chitte et al., 2018). In the study, Bentley Context Capture Centre Ultimate Edition was used to process the aerial images obtained by the UAV. The photogrammetric images were imported into the software. Context Capture was then aligned from the imported images. Finally, the software created a 3D model available in many formats. In this experiment, the 3MX 3D model format was chosen to open the production file obtained from the Context Capture Viewer, a tool for detecting cracks in the Context Capture Centre. Deep learning algorithms were then used to detect cracks in the generated 3D model.

3. Results

All 706 aerial photographs taken for the study were subjected to stabilization, and 696 were stabilized. Figure 1 shows the positional uncertainty of the anchor points, with a minimum uncertainty of 0.00015 m, a maximum uncertainty of 0.0039 m, and a median uncertainty of 0.0045 m. During block balancing, 230791 automatic connection points were created. The 3D model of the bridge used in the study is shown in Figure 1. A visualization of the detailed 3D model is shown in Figure 2.

Figure 1. 3D model of the bridge under study. The entire 3D model of the bridge (top), the part of the bridge studied in detail (bottom).

Figure 2. Detailed 3D model of the bridge

Figure 3. Detected cracks (north view)

Figure 4. Detected cracks (south view)

Cracks were detected using the crack detection algorithm in the artificial intelligence inspection tool provided by the context capture software for inspections of the 3D-modelled bridge. Figures 3, 4, and 5 show the visualizations of the detected cracks.

Figure 5. Detected cracks (east view)

4. Conclusion

Visual inspections for structural damage assessment and analysis are cumbersome, time-consuming, subjective, and difficult to document. Structural analysis from 3D models produced by photogrammetry aims to move towards automated damage assessment for monitoring an asset over its lifetime by developing a methodology to create a twin of individual structures using multiple images taken during inspections as input. It is recognized that this methodology will more efficiently document the information gathered during an inspection, increase objectivity, and reduce operational time. In addition, the 3D models produced are helpful for more detailed damage assessment activities such as mechanical analysis using numerical methods. The end products of the methodology include a 3D reconstructed geometry of a structure with cracks and their characterization. Advances in image capture hardware and artificial intelligence, including deep learning or machine learning and computer vision, make it possible to automate this pipeline using only RGB images. While existing damage assessment methods use techniques from these fields, they are limited to tasks that may require manual intervention, such as detecting damage or creating a 3D model for a specific asset. To do this, combining several state-of-the-art methods to build 3D building models and semantically segment and characterise cracks from images is necessary. The methodology proposed here requires multi-view images of the asset suitable for SfM as input. SfM processes the images, generating camera poses and a point cloud that is used to build a LOD3 model. Deep learning or machine learning trained to detect cracks processes the images used to build the 3D model. The cracks are then characterized by computing their kinematics using a 2D least squares registration algorithm. Finally, the damage information is mapped to the LOD3 model using SfM information to generate the desired DADT output. Looking at the overall results of the research, improvements to the current rapid damage assessment application are being developed. Following rapid assessment using this method, a more detailed analysis of damage characteristics may be required (e.g. crack depth estimation).

Acknowledgment

This study is supported by Afyon Kocatepe University Scientific Research Projects Coordination Unit. Project Number: 23.FEN.BİL.17

References

Alptekin, A., & Yakar, M. (2020). Determination of pond volume with using an unmanned aerial vehicle. *Mersin Photogrammetry Journal*, *2*(2), 59-63.

Alptekin, A., & Yakar, M. (2021). 3D model of Üçayak Ruins obtained from point clouds. *Mersin Photogrammetry Journal*, *3*(2), 37-40.

Arvind, R. (2016). Investigation of cracks in buildings. In *Forensic Structural Engineering a National conference in VIT Chennai, campus* (Vol. 1).

Cha, Y. J., Choi, W., & Büyüköztürk, O. (2017). Deep learning‐based crack damage detection using convolutional neural networks. *Computer‐Aided Civil and Infrastructure Engineering*, *32*(5), 361-378.

Chitte, C. J., & Sonawane, Y. N. (2018). Study on causes and prevention of cracks in building. *International Journal for Research in Applied Science and Engineering Technology*, *6*(3), 453-461.

Dorafshan, S., Maguire, M., Hoffer, N. V., & Coopmans, C. (2017, June). Challenges in bridge inspection using small unmanned aerial systems: Results and lessons learned. In *2017 international conference on unmanned aircraft systems (ICUAS)* (pp. 1722-1730). IEEE.

Fawzy, H. E. D., Kandeel, R., & Farhan, M. (2023). Detection of deformations in reinforced concrete structures using modern surveying techniques. *Alexandria Engineering Journal*, *70*, 191-218.

Feng, C., Liu, M. Y., Kao, C. C., & Lee, T. Y. (2017). Deep active learning for civil infrastructure defect detection and classification. In *Computing in civil engineering 2017* (pp. 298-306).

Han, K., Lin, J., & Golparvar-Fard, M. (2015). A formalism for utilization of autonomous vision-based systems and integrated project models for construction progress monitoring. In *Proc., 2015 Conference on Autonomous and Robotic Construction of Infrastructure*.

Kanun, E., Alptekin, A., & Yakar, M. (2021). Documentation of cultural heritage by photogrammetric methods: a case study of Aba's Monumental Tomb. *Intercontinental Geoinformation Days*, *3*, 168-171.

Kanun, E., Alptekin, A., Karataş, L., & Yakar, M. (2022). The use of UAV photogrammetry in modeling ancient structures: A case study of "Kanytellis". *Advanced UAV*, *2*(2), 41-50.

Karataş, L., Alptekin, A., & Yakar, M. (2022a). Elimination of unqualified additions that distort the silhouette of the historical places: Artuklu example. *Advanced Land Management*, *2*(2), 89-98.

Karataş, L., Alptekin, A., Karabacak, A., & Yakar, M. (2022b). Detection and documentation of stone material deterioration in historical masonry buildings using UAV photogrammetry: A case study of Mersin Sarisih Inn. *Mersin Photogrammetry Journal*, *4*(2), 53-61.

Karataş, L., Alptekin, A., Kanun, E., & Yakar, M. (2022). Tarihi kârgir yapılarda taş malzeme bozulmalarının İHA fotogrametrisi kullanarak tespiti ve belgelenmesi: Mersin Kanlıdivane ören yeri vaka çalışması. *İçel Dergisi*, *2*(2), 41-49.

Kim, I. H., Jeon, H., Baek, S. C., Hong, W. H., & Jung, H. J. (2018). Application of crack identification techniques for an aging concrete bridge inspection using an unmanned aerial vehicle. Sensors, 18(6), 1881.

Kusak, L., Unel, F. B., Alptekin, A., Celik, M. O., & Yakar, M. (2021). Apriori association rule and K-means clustering algorithms for interpretation of pre-event landslide areas and landslide inventory mapping. *Open Geosciences*, *13*(1), 1226-1244.

MacGregor, J. G., Wight, J. K., Teng, S., & Irawan, P. (1997). *Reinforced concrete: Mechanics and design* (Vol. 3). Upper Saddle River, NJ: Prentice Hall.

Munguía, R., Urzua, S., Bolea, Y., & Grau, A. (2016). Vision-based SLAM system for unmanned aerial vehicles. *Sensors*, *16*(3), 372.

Šavija, B., Luković, M., Pacheco, J., & Schlangen, E. (2013). Cracking of the concrete cover due to reinforcement corrosion: A two-dimensional lattice model study. *Construction and Building Materials*, *44*, 626-638.

Şasi, A., & Yakar, M. (2017). Photogrammetric modelling of sakahane masjid using an unmanned aerial vehicle. *Turkish Journal of Engineering*, *1*(2), 82-87.

Unal, M., Yakar, M., & Yildiz, F. (2004). Discontinuity surface roughness measurement techniques and the evaluation of digital photogrammetric method. In *Proceedings of the 20th international congress for photogrammetry and remote sensing, ISPRS* (Vol. 1103, p. 1108).

URL-1 https://tr.wikipedia.org/wiki/K%C4%B1rkg%C3%B6z_K%C3%B6pr%C3%BCs%C3%BC

Yakar, M. (2011). Using close range photogrammetry to measure the position of inaccessible geological features. *Experimental Techniques*, *35*, 54-59.

Yakar, M., & Doğan, Y. (2017). Mersin Silifke Mezgit Kale Anıt Mezarı fotogrametrik rölöve alımı ve üç boyutlu modelleme çalışması. *Geomatik*, *2*(1), 11-17.

Yakar, M., Ulvi, A., Yiğit, A. Y., & Alptekin, A. (2023). Discontinuity set extraction from 3D point clouds obtained by UAV Photogrammetry in a rockfall site. *Survey Review*, *55*(392), 416-428.

Yılmaz, H. M., Aktan, N., Çolak, A., & Alptekin, A. (2022). Modelling Ozancık village (Aksaray) in computer environment using UAV photogrammetry. *Mersin Photogrammetry Journal*, *4*(1), 32-36.

7th Intercontinental Geoinformation Days

igd.mersin.edu.tr

Monitoring shoreline and areal change with UAV data

Adem Kabadayı[1], Yunus Kaya[2]

[1]Yozgat Bozok University, Sefaatli Vocational School, Yozgat, Türkiye
[2]Harran University, Faculty of Engineering, Department of Geomatics Engineering, Şanlıurfa, Türkiye

Keywords
Shoreline
UAV
Change detection
Pond

Abstract

It is important to determine the spatiotemporal changes of wetlands for their sustainable management and effective use. In this study, the shoreline of Topçu Pond used for agricultural irrigation in Yozgat, Turkey in 2022 and 2023 was determined with the help of contour lines. In addition, the maximum capacity elevation of the pond was determined, and its maximum area was calculated. As a result of the study, the water level and pond area for the year 2022 were calculated as 1191.56 m and 99165.58 m^2, respectively, and the water level and pond area for the year 2023 were calculated as 1195.05 m and 142487.95 m^2, respectively. The maximum elevation and area of the pond were determined as 1200.65 m and 279019.94 m^2 respectively.

1. Introduction

Wetlands have vital importance in many areas such as freshwater supply, energy production and agricultural irrigation (Ünel et al. 2020). Wetlands have historically been a hub for a wide range of activities such as transportation, tourism, trade and industry (Duan et al. 2016; You et al. 2018; Zhang et al. 2020). As a result, population growth, destruction and uncontrolled development in coastal areas are occurring (Alptekin and Yakar, 2020). Countries that experience or anticipate the destructive consequences of this uncontrolled development attach importance to sustainable coastal change. However, when we look at the planning processes of coastal lands in Turkey, it is seen that traditional methods are mostly used and sustainable coastal monitoring policies are insufficient (Şahin et al. 2022). Remote sensing techniques have long been successfully used to determine coastlines (Wen et al. 2021). In particular, NASA's Landsat program has been monitoring the contraction and expansion of lakes for nearly 50 years (Jiang et al. 2020). In 2016, Sentinel satellite data, freely shared by ESA, also allowed us to track changes in the Earth's surface with higher spatial and temporal resolution. Many studies have been conducted in the literature using remote sensing data (Dewidar, 2004; Muttitanon and Tripathi, 2005). There are a limited number of studies determining the shoreline change in Turkey. Firatli et al. (2022) determined the 35-year areal change of 27 lakes larger than 2000 hectares in Turkey using Landsat and Sentinel-2 images with Google Earth Engine. Dervisoglu (2022) examined the short and long-term changes of lakes in Ramsar sites in Turkey using Landsat and Sentinel-2 data. Although medium spatial resolution satellite data such as Landsat are effective in determining the areal changes of large lakes or seas, they are not useful for small ponds or dams (Kaiser et al. 2021). UAV data give more successful results in determining small water areas (Kaya et al. 2019). In this study, very high resolution UAV data were used to examine the changes of Topçu pond in 2022 and 2023.

2. Method

2.1. Study area

UAV data obtained in September 2022 and UAV data obtained in September 2023 were used in the study. Flight was made with DJI Mavic 2 UAV in the study area (Figure 1). Information about the UAV flight is given in Table 1.

* **Corresponding Author**

*(adem.kabadayi@bozok.edu.tr) ORCID ID 0000-0002-4891-8131
(yunuskaya@harran.edu.tr) ORCID ID 0000-0003-2319-4998

Cite this study

Kabadayı A & Kaya Y (2023). Monitoring shoreline and areal change with UAV data. Intercontinental Geoinformation Days (IGD), 7, 153-156, Peshawar, Pakistan

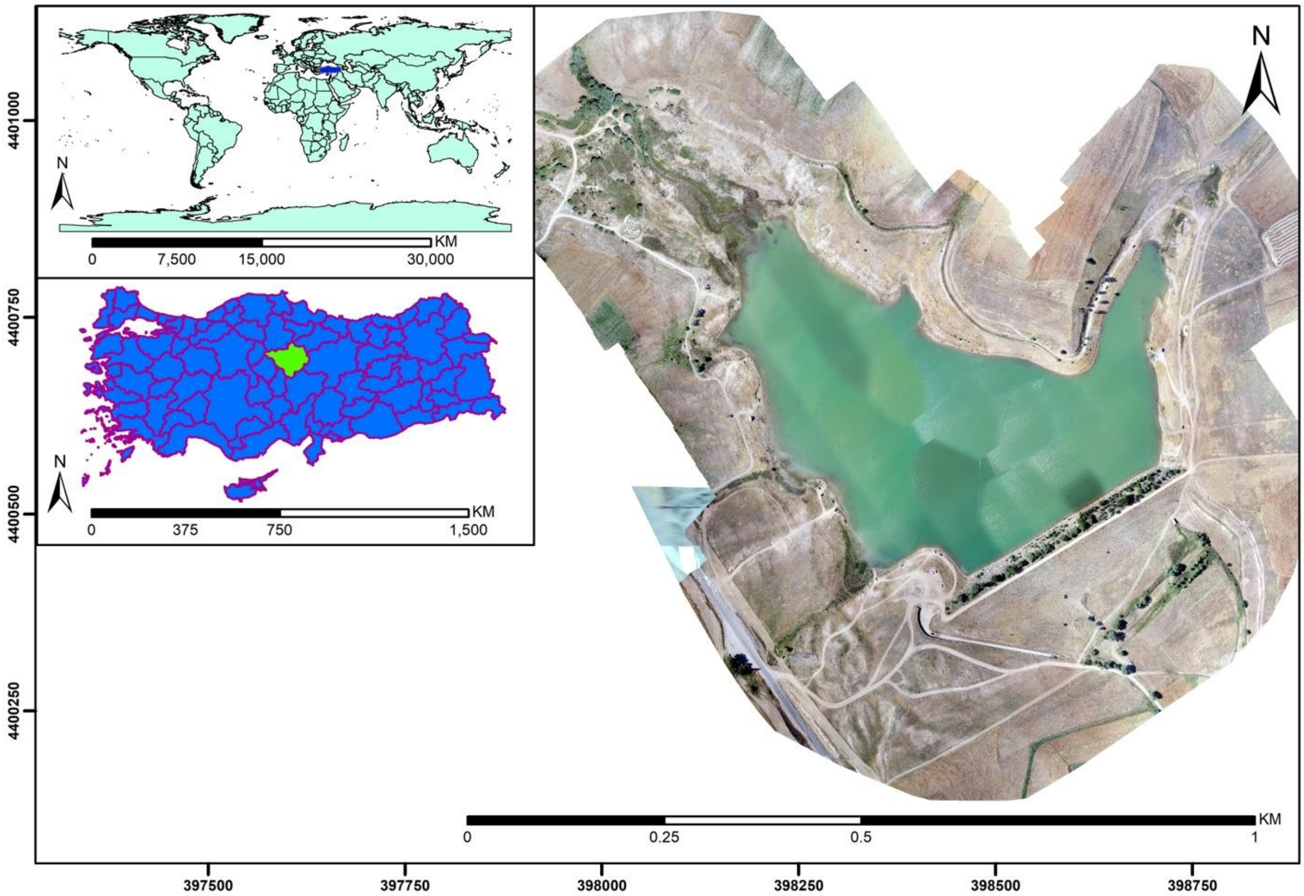

Figure 1. Study area

Table 1. Flight parameters

Parameter	Value (2022)	Value (2023)
Flight Date	10.09.2022	15.09.2023
Flight Time	55 mins	56 mins
Flight Area	656430m^2	702286m2
Overlap	80	80
Camera Angle	90^0	90^0
Planned Altitude	100m	100m
Average Altitude	102m	113m
Number of Photos Taken	490	480
Number of Photos Used	475	464
Planned GSD (cm/pixel)	2.68	2.68
GSD (cm/pixel)	2.95	2.76
DEM Resolution (cm/pixel)	2.54	2.36
Point density (points/m^2)	68	77
Point Cloud Number	7480774	7731599
Dense Point Cloud Number	44762241	50743096

2.2. Method

UAV technology has been used frequently in landslide (Kuşak et al. 2021), rockfall (Yakar et al. 2023) and cultural heritage studies (Yakar and Doğan, 2017; Alptekin and Yakar, 2021; Karataş et al. 2022; Kanun et al. 2022) in the last decade.

In the study, the coordinates of ground control points (GCPs) measured in the field with the photographs obtained from 8 UAV flights performed one year apart were evaluated in Agisoft Photoscan software. One of the most important steps of the photogrammetry method is the determination of camera calibrations. In this study, the photographs were calibrated by self-calibration method using the parameters in the software. The GCP coordinates measured in the field were matched with the points appearing in the software to coordinate the model. Since the quality of the DEM is affected by the dense point cloud produced, the dense point cloud was produced with high accuracy. Then, the orthomosaics and DEMs of the terrain were exported in high quality. The parameters and information used in orthomosaic and DEM generation are given in Table 1. Then, using the contour lines where the shoreline is located, the boundaries of the shoreline and the area covered by the maximum water capacity in the terrain were determined.

3. Results

The shorelines of Topçu pond in 2022 and 2023 were determined by photogrammetric method. Since it is assumed that the water level will be the same at every point of the water surface, contour lines were produced in the coastal areas. From these lines, the shoreline in two different years and the shoreline of the pond at maximum capacity were determined (Figure 2).

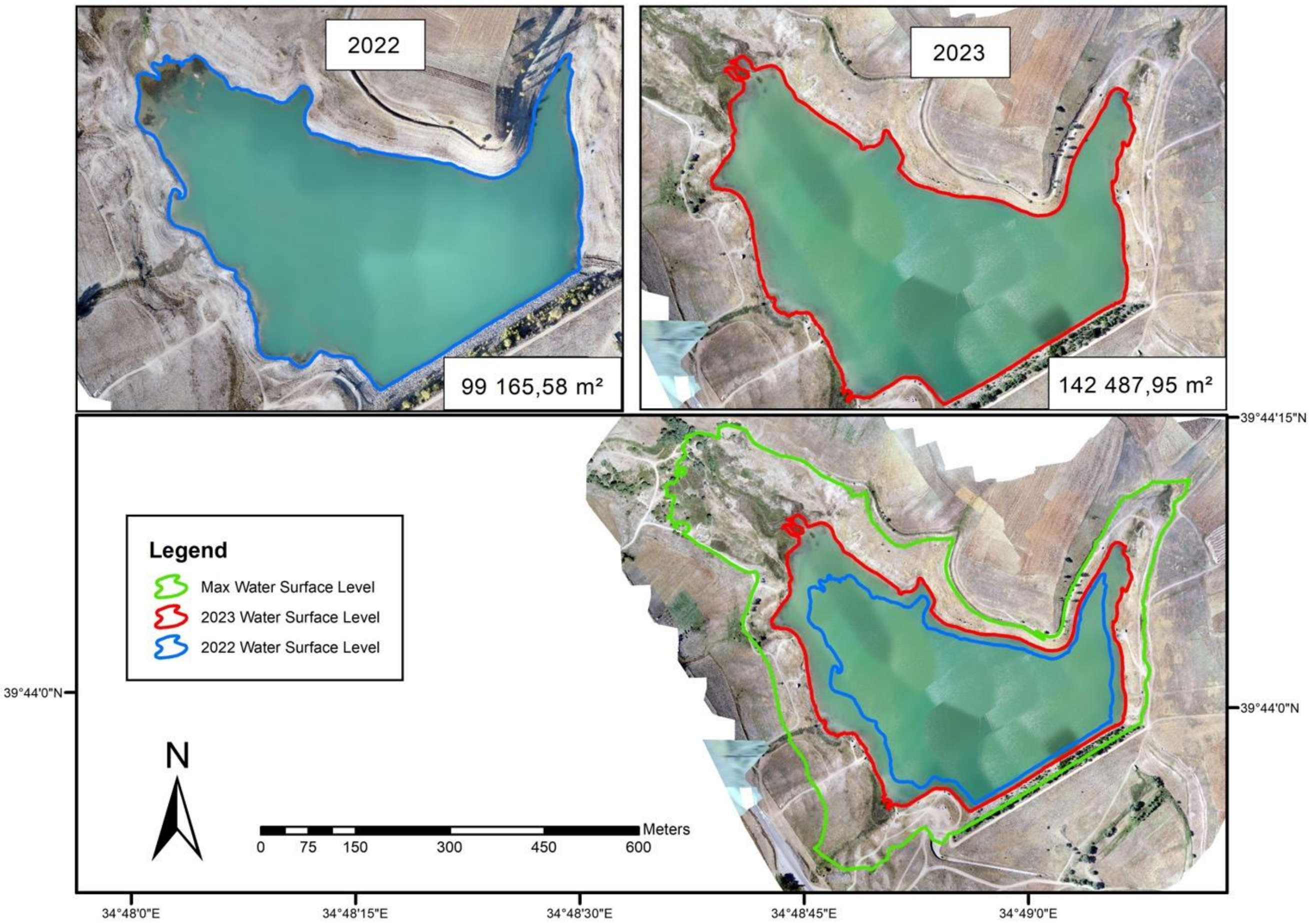

Figure 2. Shorelines in 2022, 2023 and maximum capacity

4. Conclusion

Shoreline monitoring is important for sustainable use of available water and planning for future use. While medium resolution data such as Landsat is effective for determining shoreline changes in large water areas, it is insufficient for determining changes in small water areas. For this reason, UAV technology, which has been used in many different fields in recent years, is also used to determine terrain topography. In this study, the shoreline of Topçu Pond, Yozgat, Turkey, which is used for agricultural irrigation, was determined by high-resolution UAV in 2022 and 2023. In addition, the areas that will be covered by water when the pond reaches its maximum capacity were also determined with UAV data and GCPs. The shoreline in two different years was determined by the average height of the water surface. The water covered areas were also determined with the help of the contour lines at the level of the discharge gate of the pond.

References

Alptekin, A., & Yakar, M. (2020). Determination of pond volume with using an unmanned aerial vehicle. *Mersin Photogrammetry Journal*, *2*(2), 59-63.

Alptekin, A., & Yakar, M. (2021). 3D model of Üçayak Ruins obtained from point clouds. *Mersin Photogrammetry Journal*, *3*(2), 37-40.

Dervisoglu, A. (2022). Investigation of long and short-term water surface area changes in coastal Ramsar Sites in Turkey with Google Earth Engine. ISPRS International Journal of Geo-Information, 11(1), 46.

Dewidar, K. M. (2004). Detection of land use/land cover changes for the northern part of the Nile delta (Burullus region), Egypt. International journal of remote sensing, 25(20), 4079-4089.

Duan, H., Zhang, H., Huang, Q., Zhang, Y., Hu, M., Niu, Y., & Zhu, J. (2016). Characterization and environmental impact analysis of sea land reclamation activities in China. Ocean & Coastal Management, 130, 128-137.

Firatli, E., Dervisoglu, A., Yagmur, N., Musaoglu, N., & Tanik, A. (2022). Spatio-temporal assessment of natural lakes in Turkey. Earth Science Informatics, 1-14.

Heiskanen, W. A., & Moritz, H. (1967). Physical geodesy. Bulletin Géodésique (1946-1975), 86(1), 491-492.

Jiang, L., Nielsen, K., Andersen, O. B., & Bauer-Gottwein, P. (2020). A bigger picture of how the Tibetan lakes have changed over the past decade revealed by CryoSat-2 altimetry. Journal of Geophysical Research: Atmospheres, 125.

Kaiser, S., Grosse, G., Boike, J., & Langer, M. (2021). Monitoring the transformation of arctic landscapes: Automated shoreline change detection of lakes using very high-resolution imagery. Remote Sensing, 13(14), 2802.

Kanun, E., Alptekin, A., Karataş, L., & Yakar, M. (2022). The use of UAV photogrammetry in modeling ancient structures: A case study of "Kanytellis". *Advanced UAV*, *2*(2), 41-50.

Karataş, L., Alptekin, A., & Yakar, M. (2022). Detection and documentation of stone material deterioration in historical masonry structures using UAV photogrammetry: A case study of Mersin Aba Mausoleum. *Advanced UAV*, *2*(2), 51-64.

Kaya, Y., Şenol, H.İ., Memduhoğlu, A., Akça, Ş., Ulukavak, M., & Polat, N. (2019). Hacim Hesaplarında İHA Kullanımı: Osmanbey Kampüsü Örneği. Türkiye Fotogrametri Dergisi, 1(1), 7-10.

Kusak, L., Unel, F. B., Alptekin, A., Celik, M. O., & Yakar, M. (2021). Apriori association rule and K-means clustering algorithms for interpretation of pre-event landslide areas and landslide inventory mapping. *Open Geosciences*, *13*(1), 1226-1244.

Muttitanon, W., & Tripathi, N. K. (2005). Land use/land cover changes in the coastal zone of Ban Don Bay, Thailand using Landsat 5 TM data. International Journal of Remote Sensing, 26(11), 2311-2323.

Sahin, G., Cabuk, S. N., & Cetin, M. (2022). The change detection in coastal settlements using image processing techniques: a case study of Korfez. Environmental Science and Pollution Research, 29(10), 15172-15187.

Ünel, F. B., Kuşak, L., Çelik, M., Alptekin, A., & Yakar, M. (2020). Kıyı çizgisinin belirlenerek mülkiyet durumunun incelenmesi. *Türkiye Arazi Yönetimi Dergisi*, *2*(1), 33-40.

Wen, D., Huang, X., Bovolo, F., Li, J., Ke, X., Zhang, A., & Benediktsson, J. A. (2021). Change detection from very-high-spatial-resolution optical remote sensing images: Methods, applications, and future directions. IEEE Geoscience and Remote Sensing Magazine, 9(4), 68-101.

Yakar, M., & Doğan, Y. (2017). Uzuncaburç Antik Kentinin İHA Kullanılarak Eğik Fotogrametri Yöntemiyle Üç Boyutlu Modellenmesi. 16. *Türkiye Harita Bilimsel ve Teknik Kurultayı. TMMOB Harita ve Kadastro Mühendisleri Odası, Ankara*.

Yakar, M., Ulvi, A., Yiğit, A. Y., & Alptekin, A. (2023). Discontinuity set extraction from 3D point clouds obtained by UAV Photogrammetry in a rockfall site. *Survey Review*, *55*(392), 416-428.

You, S., Kim, M., Lee, J., & Chon, J. (2018). Coastal landscape planning for improving the value of ecosystem services in coastal areas: Using system dynamics model. Environmental Pollution, 242, 2040-2050.

Zhang, X., Song, W., Lang, Y., Feng, X., Yuan, Q., & Wang, J. (2020). Land use changes in the coastal zone of China's Hebei Province and the corresponding impacts on habitat quality. Land use policy, 99, 104957.

7th Intercontinental Geoinformation Days

igd.mersin.edu.tr

Assessing the contribution of RGB VIs in improving building extraction from RGB-UAV images

Richmond Akwasi Nsiah[*1], **Saviour Mantey** [2], **Yao Yevenyo Ziggah** [3]

[1]University of Mines and Technology, Faculty of Geosciences and Environmental Studies, Geomatic Department, Tarkwa, Ghana

Keywords
Building Extraction
UAV
GeoBIA
RGB Vegetative Indices
Random Forest

Abstract

Buildings are a fundamental component of the built environment, and accurate information regarding their size, location, and distribution is vital for various purposes. The ever-increasing capabilities of unmanned aerial vehicles (UAVs) have sparked an interest in exploring various techniques to delineate buildings from the very high-resolution images obtained from UAVs. However, UAV images have limited spectral information, and VIs have been adopted to increase the spectral strength of UAVs for building classification. This study aims to assess the contribution of four VIs, the green leaf index (GLI), red-green-blue vegetation index (RGBVI), visual atmospherically resistant index (VARI), and triangular greenness index (TGI), in improving building classification using geographic object-based image analysis (GeoBIA) approach and random forest classifier. For this purpose, five datasets were created and comprised of the RGB-UAV image and the RGB VIs. The experimental result indicated that the RGB + VARI dataset had the best improvement in the building classification based on four evaluation metrics: overall accuracy (0. 9799), precision (0. 9806), recall (0. 9806), and F1-score (0. 9806). The combination of all the VIs with the RGB image, on the other hand, attained results lower than the standalone RGB image: accuracy (0. 9507), precision (0. 9570), recall (0. 9368), and F1-score (0. 9468).

1. Introduction

Among the myriad of urban features, buildings represent a fundamental component (Schlosser et al., 2020), and obtaining accurate and detailed information on buildings is crucial for urban planning, infrastructure development, disaster management, and other applications (Hu et al., 2021). Recent advancements in unmanned aerial vehicle (UAV) technologies and the sophistication of imaging sensor systems have sparked an interest in exploring various methods to delineate building objects from very high-resolution (VHR) UAV imagery.

One such method is geographic object-based image analysis (GeoBIA), which has emerged as a powerful approach for automating the extraction of objects from remote sensing data (Comert & Kaplan, 2018). GeoBIA integrates machine learning algorithms, spatial information, and spectral characteristics to segment and classify image objects, making it particularly suited for building extraction (Aminipouri et al., 2009; Guo & Du, 2017).

While GeoBIA has shown considerable promise in building classification and segmentation, the spectral limitations of UAV-RGB imagery pose a challenge, especially when distinguishing between building materials and other urban (Li et al., 2022). Researchers have since used various ancillary datasets, such as vegetative indices (VI), to address this drawback in the classification process. VIs can capture subtle spectral variations and, when combined with GeoBIA's spatial context analysis, offer a promising avenue for improving building classification and segmentation urban (Öztürk & Colkesen, 2021; Schlosser et al., 2020).

Although some research works have focused on improving building classification using RGB VIs, a comprehensive comparison of the effect of each VI on classification accuracy has not been conducted. Consequently, the primary objective of this study is to investigate the impacts of integrating RGB-based VIs into the GeoBIA classification pipeline for building extraction. To achieve this objective, four well-established VIs: the green leaf index (GLI), red-green-blue vegetation index (RGBVI), visual atmospherically resistant index (VARI),

* **Corresponding Author**

*(ransiah94@gmail.com) ORCID: 0009-0003-4100-9570
(smantey@umat.edu.gh) ORCID: 0000-0002-8210-3577
(yyziggah@umat.edu.gh) ORCID: 0000-0002-9940-1845

Cite this study

Nsiah, R. A., Mantey, S., & Ziggah, Y. Y. (2023). Assessing the contribution of RGB VIs in improving building extraction from RGB-UAV images. Intercontinental Geoinformation Days (IGD), 7, 157-160, Peshawar, Pakistan

and triangular greenness index (TGI) were employed and combined with UAV-RGB imagery. The efficacy of each amalgamation was assessed using key performance metrics such as overall accuracy (OA), F-1 score, and Kappa coefficient.

2. Method

The methodological framework adopted for this research is presented in the subsequent subsections.

2.1. Study Area

The New Mankessim community is within the administrative jurisdiction of the Tarkwa Nsuaem Municipal Assembly, located approximately 19.30 kilometres southwest of the municipal capital, Tarkwa, in the Western Region of Ghana. Geographically, the community is positioned at latitude 5°5’ 29.45” N and longitude 2°6’ 4.70” W, nestled at an average altitude of 55 meters above mean sea level. A resettlement program initiated by one of the prominent mining companies operating in the region, primarily to accommodate the evolving dynamics of mining activities in the area, led to the relocation of community members from previous dwellings to the current location. As such, a notable feature of the New Mankessim community is the uniformity in architectural designs across the settlement. The community’s well-planned layout is marked by a consistent architectural style, reflecting a cohesive and deliberate approach to urban development. Fig. 1 depicts the UAV Image of the study area.

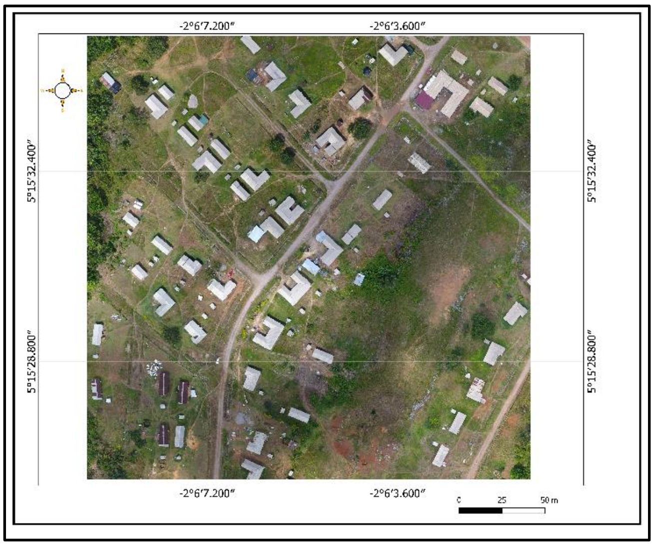

Figure 1. UAV Image of New Mankessim

2.2. Geographic Object-Based Image Analysis (GeoBIA)

GEOBIA is an image analysis approach commonly applied to VHR remote sensing data. It serves various purposes, including land-cover mapping and identifying specific geographic objects like buildings, cars, and trees (Kucharczyk et al., 2020). The workflow of the GeoBIA approach involved image segmentation, feature selection, image classification, and accuracy assessment and was carried out using the Google Earth Engine platform.

2.3 Image Segmentation

This step involved segmenting images into image objects, groups of neighbouring pixels representing objects within the drone image based on spectral and spatial attributes. There are various methods for performing image segmentation. However, the simple linear iterative clustering (SLIC) algorithm (Achanta et al., 2012) was utilised. SLIC is a seed-based clustering technique that effectively utilises a modified k-means clustering strategy to create superpixels with high efficiency. In contrast to prior methodologies, SLIC excels in preserving boundaries while offering improved speed and memory efficiency (Liao et al., 2022).

It also enhances segmentation performance and can be extended for super voxel generation. This method carefully incorporates considerations of both color homogeneity and shape uniformity, achieving a well-balanced trade-off between these aspects (Zhang & Zhu, 2019). Utilising SLIC requires defining several parameters, such as compactness, seed size, and grid type, to obtain optimum and homogenous image objects. For this work, the parameters were determined using a trial-and-error method.

2.4 Feature Selection

The spectral attributes, including the mean values of the red, green, and blue (RGB) bands and VIs within each image object, were selected as the primary features for building extraction. These features capture colour information for distinguishing building objects from other urban features. In total, 916 samples were selected, 456 representing buildings and the remaining non-building objects. These were divided into training (80%) and validation (20%) sets.

2.5 Classification

The step involves using a machine learning classifier to classify the segments into respective classes. For this research, the random forest (RF) classifier proposed by Breiman (2001) was employed to classify the selected features as either buildings or non-buildings. RF is an ensemble machine learning algorithm that combines multiple decision trees to make predictions. Each tree in the forest is trained on a different subset of the data with bootstrapping and random feature selection. The final prediction is determined by a majority vote or averaging of individual tree predictions, making it robust, accurate, and less prone to overfitting, making it robust and effective in handling complex classification tasks (Kumar & Sinha, 2020; Xiao et al., 2020). For this research, the RF classifier was trained using the selected samples, with the mean values serving as input features. Like the image segmentation step, RF also has several parameters that need to be fine-tuned for optimum classification, which were defined using a trial-and-error approach.

2.6 Evaluation Metrics

A comprehensive validation approach is adopted to assess the accuracy of the building classification. The trained RF classifier is applied to the validation data to classify buildings and non-buildings. The results are compared with ground truth data to evaluate classification performance using overall accuracy, precision, recall, and F1-score, which were computed using a confusion matrix—equations (1) to (4) give the mathematical formulations for the evaluation metrics.

$$\text{Recall, R} = \frac{TP}{TP+FN} \quad (1)$$

$$\text{Precision, P} = \frac{TP}{TP+FP} \quad (2)$$

$$\text{Overall Accuracy, OA} = \frac{TP+TN}{TP+FP+TN+FN} \quad (3)$$

$$\text{F1-score, F1} = \frac{2*Precision*Recall}{Precision+Recall} \quad (4)$$

Where TP represents correctly identified building pixels, TN indicates correctly identified non-building pixels, FP represents pixels erroneously classified as buildings but are not, and FN denotes pixels overlooked as non-building despite being so.

2.7 RGB-Vegetative Indices

Vegetation indices (VIs) are derived through mathematical equations applied to two or more spectral bands to highlight specific vegetation attributes (Öztürk & Colkesen, 2021). Several VIs that utilise the RGB bands have been created and developed. The RGB VIs utilised in this research are depicted in Fig. 2, and the formulae are in Table 1.

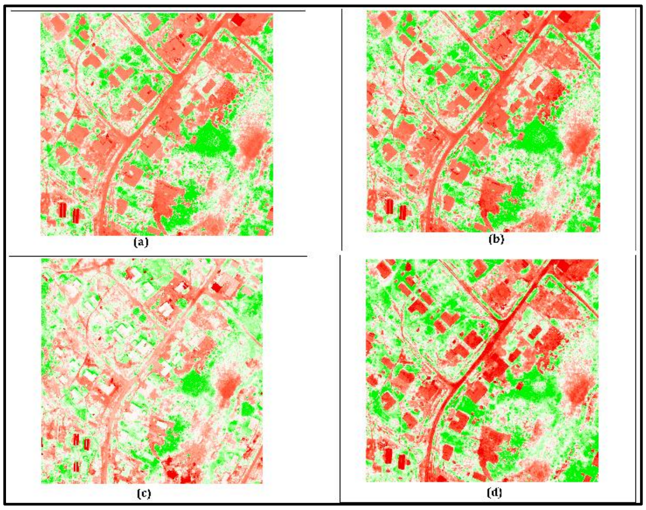

Figure 2. RGB VIs (a)GLI, (b)RGBVI, (c)VARI, and (d)TGI

Table 1. RGB-VIs Utilised

VI	Formula	Reference
Green Leaf Index	GLI = $\frac{(2\times Green)-Red-Blue}{(2\times Green)+Red+Blue}$	Hunt et al. (2012)
Red-Green-Blue Vegetation Index	RGBVI = $\frac{Green^2-Blue\times Red}{Green^2+Blue\times Red}$	Bendig et al. (2015)
Visual Atmospherically Resistant Index	VARI = $\frac{Green-Red-Blue}{Green+Red+Blue}$	Gitelson et al. (2002)
Triangular Greenness Index	TGI = $Green - (0.39 \times Red) + (0.61 \times Blue)$	Louhaichi et al. (2001)

3. Results

For this study, five datasets were created by combining the RGB VIs with the UAV-RGB image. These were RGB and GLI, RGB and RGBVI, RGB and VARI, RGB and TGI, and RGB and all indices. Spectral and spatial information were subsequently selected from each combination and used to train and validate the RF classifier. The evaluation results obtained for each combination, based on the evaluation metrics, are provided in Table 2.

Table 2. Performance of Various Dataset Combinations

Dataset	Metric			
	OA	P	R	F1
UAV-RGB only	0.9565	0.9643	0.9529	0.9586
RGB + GLI	0.9632	0.9897	0.9411	0.9648
RGB +RGBVI	0.9660	0.9671	0.9671	0.9671
RGB + VARI	0.9799	0.9806	0.9806	0.9806
RGB + TGI	0.9714	0.9880	0.9535	0.9704
RGB + All Indices	0.9507	0.9570	0.9368	0.9468

Fig.3. illustrates the extraction results produced by the random forest classifier for each dataset combination.

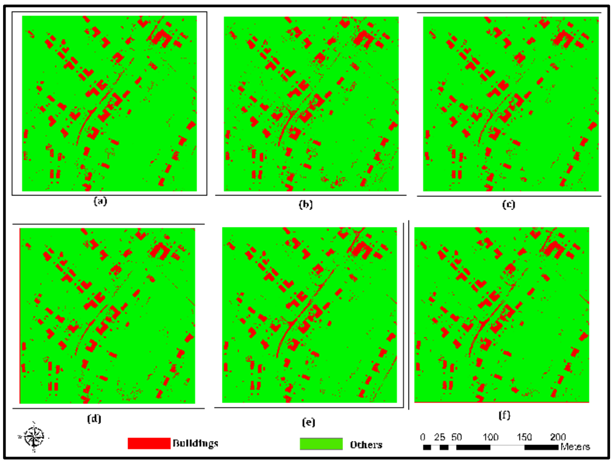

Figure 3. Building Extraction Results RF Classifier (a) UAV Image, (b) RGB + GLI, (c) RGB + RGBVI, (d) RGB + VARI, (e) RGB + TGI, and (f) RGB + All Indices

4. Discussion

The results presented in Table 2 show that the RGB VIs had a significant impact on the building extraction task. All the evaluation metrics were generally improved when the VIs were added to the RGB-UAV image. Notably, the RGB + VARI dataset achieved the highest OA at 0.9799, highest recall at 0.9806, and highest F1 at 0.9806, indicating that the VARI index contributed significantly to accurate building extraction, was influential in capturing most building features and exhibited a strong balance between precision and recall. For precision, however, the RGB + GLI dataset attained the highest precision at 0.9897, indicating minimal false positives.

Surprisingly, combining all available indices, i.e., the RGB + All Indices dataset, resulted in a lower OA and F1 score than some individual index combinations. The thematic maps show that the similar visual outputs were produced by the datasets. Regardless, it is observed that the RGB + VARI dataset had few false positives compared to the others.

5. Conclusion

This study aimed to assess the contribution of four RGB VIs, GLI, RGBVI, VARI, and TGI, in improving building classification tasks from UAV imagery. To that aim, four datasets containing a combination of these VIs and RGB-UAV were created, and a GeoBIA approach was adopted to classify building features from these datasets. In addition, a fifth dataset was created by combining all the RGB VIs and the UAV image. The experimental results highlight the advantages of integrating vegetative indices into building extraction from UAV-RGB imagery. The RGB + VARI dataset emerged as the top-performing combination, achieving the highest overall accuracy, precision, recall, and F1-score levels. However, it is worth noting that the RGB + GLI dataset stood out for its exceptional precision, rendering it particularly suitable for applications where minimizing false positives is paramount. However, combining all the RGB VIs with the RGB image produced lower metric scores than the standalone RGB image.

The consistent performance of RGB + VARI across various metrics accentuates its effectiveness as a standalone index.

References

Achanta, R., Shaji, A., Smith, K., Lucchi, A., Fua, P., & Susstrunk, S. (2012). SLIC Superpixels Compared to State-of-the-Art Superpixel Methods. IEEE Transactions on Pattern Analysis and Machine Intelligence, 34(11), 2274–2281.

Aminipouri, M., Sliuzas, R., & Kuffer, M. (2009). Object-Oriented Analysis of Very High-Resolution Orthophotos for Estimating the Population of Slum Areas, A Case of Dar-Es-Salaam, Tanzania. ISPRS Hannover Workshop 2009 High-Resolution Earth Imaging for Geospatial Information, Hannover Germany, W5.

Bendig, J., Yu, K., Aasen, H., Bolten, A., Bennertz, S., Broscheit, J., Gnyp, M. L., & Bareth, G. (2015). Combining UAV-based plant height from crop surface models, visible and near-infrared vegetation indices for biomass monitoring in barley. International Journal of Applied Earth Observation and Geoinformation, 39, 79–87.

Breiman, L. (2001). Random Forests. Machine Learning - Springer, 45(1), 5–32.

Comert, R., & Kaplan, O. (2018). Object Based Buıldıng Extractıon And Buıldıng Perıod Estımatıon From Unmanned Aerıal Vehicle Data. ISPRS Annals of the Photogrammetry, Remote Sensing and Spatial Information Sciences, 4(3), 71–76.

Gitelson, A. A., Kaufman, Y. J., Stark, R., & Rundquist, D. (2002). Novel algorithms for remote estimation of vegetation fraction. Remote Sensing of Environment, 80(1), 76–87.

Guo, Z., & Du, S. (2017). Mining parameter information for building extraction and change detection with very high-resolution imagery and GIS data. GIScience and Remote Sensing, 54(1), 38–63.

Hu, Q., Zhen, L., Mao, Y., Zhou, X., & Zhou, G. (2021). Automated building extraction using satellite remote sensing imagery. Automation in Construction, 123, 103509.

Hunt, E. R., Doraiswamy, P. C., McMurtrey, J. E., Daughtry, C. S. T., Perry, E. M., & Akhmedov, B. (2012). A visible band index for remote sensing leaf chlorophyll content at the Canopy scale. International Journal of Applied Earth Observation and Geoinformation, 21(1), 103–112.

Kucharczyk, M., Hay, G. J., Ghaffarian, S., & Hugenholtz, C. H. (2020). Geographic object-based image analysis: A primer and future directions. Remote Sensing, 12(12), 1–33.

Kumar, A., & Sinha, N. (2020). Classification of forest cover type using random forests algorithm. In Lecture Notes in Networks and Systems,94, 395–402.

Li, J., Huang, X., Tu, L., Zhang, T., & Wang, L. (2022). A review of building detection from very high-resolution optical remote sensing images. In GIScience and Remote Sensing 59(1), 1199–1225).

Liao, N., Liu, H., Li, C., Ren, X., & Guo, B. (2022). Simple Linear Iterative Clustering with Efficiency. In Smart Innovation, Systems and Technologies, 277, 109–117.

Louhaichi, M., Borman, M. M., & Johnson, D. E. (2001). Spatially located platform and aerial photography for documentation of grazing impacts on wheat. Geocarto International, 16(1), 65–70.

Öztürk, M. Z., & Colkesen, I. (2021). The impacts of vegetation indices from UAV-based RGB imagery on land cover classification using ensemble learning. Mersin Photogrammetry Journal, 3(2), 41–47.

Schlosser, A. D., Szabó, G., Bertalan, L., Varga, Z., Enyedi, P., & Szabó, S. (2020). Building extraction using orthophotos and dense point cloud derived from visual band aerial imagery based on machine learning and segmentation. Remote Sensing, 12(15), 1–28.

Xiao, Y., Huang, W., & Wang, J. (2020). A Random Forest Classification Algorithm Based on Dichotomy Rule Fusion. ICEIEC 2020 - Proceedings of 2020 IEEE 10th International Conference on Electronics Information and Emergency Communication, 182–185.

Zhang, H., & Zhu, Y. (2019). KSLIC: K-mediods clustering based simple linear iterative clustering. In Lecture Notes in Computer Science (including subseries Lecture Notes in Artificial Intelligence and Lecture Notes in Bioinformatics, 1185, 519–529.

7th Intercontinental Geoinformation Days

igd.mersin.edu.tr

The effect of the number and distribution of ground control points (GCP) on map production

Volkan İzci*[1], Ali Ulvi [1]

[1]Mersin University, Department of Remote Sensing and Geographic Information Systems, Institute of Science, Mersin, Türkiye

Keywords
UAV Photogrammetry
Orthophoto
Ground Control Point

Abstract

Thanks to recent advances in data collection technologies from Unmanned Aerial Vehicles (UAVs), very large data sets covering important surfaces with centimeter-scale resolution can be rapidly collected, resulting in the opportunity to analyze areas digitally. With the presence of a regular monitoring program carried out over a wide area, UAVs provide significant advantages in the cost of data collection. Many studies in the literature have focused on finding an effective and sustainable research strategy to limit costs and study times. Unmanned aerial vehicle (UAV) photogrammetry has recently emerged as a popular solution to obtain certain products required in linear projects such as orthoimages or digital surface models. The main reason for this is the ability to provide these topographic products quickly and economically. It is important to know how many ground control points (GCPs) are required to guarantee a certain degree of accuracy and how to distribute them across the work area. The purpose of this study is to determine the number of GCPs for a work area and how to distribute them to provide higher accuracy.

1. Introduction

Unmanned Aerial Vehicle (UAV)-based photogrammetry is becoming a valuable data source for topographic mapping, volume calculations, terrain mapping and creating 3D models. However, using UAVs for any purpose requires basic knowledge of various flight settings. The number and distribution of Ground Control Points (GCPs) are the most important, so the number of GCPs should be used economically. Ground control points (GCPs) are often used to georeference the 3D point cloud created in the photogrammetric process. These control points may be permanent ground features or reference targets scattered on the ground before flight; these need to be examined to obtain their precise coordinates and ensure they can be clearly identified in the raw images. Although it is strongly recommended to increase the number of GCPs to increase the accuracy of photogrammetric products, at least three GCPs are required to perform the georeferencing process (Villi and Yakar, 2022; Kaya et al. 2023). The effect of the GCP number on DSM and the orthoimage accuracies obtained by UAV photogrammetry were examined. Photogrammetric products such as orthoimages and DSM can be obtained from a georeferenced dense point cloud. There are several factors that affect the accuracy of these UAV photogrammetry products, such as the number and distribution of GCPs, flight altitude, examined surface morphology, camera calibration methodology, image overlap, and inclusion of oblique images (Kaya et al. 2021; Şasi and Yakar, 2018).

Considering that the use of GCP directly affects the accuracy of photogrammetric products, many researchers have conducted various studies over the years to evaluate the accuracy of the products obtained from UAV images by changing the number of GCPs. Agüera-Vega, Carvajal-Ramírez and Martínez-Carricondo (Agüera-Vega,2016) investigated the effect of flight altitude, terrain morphology and GCP number on digital surface model (DSM) and orthophoto accuracy. Ruzgiene et al. (Ruzgine et al., 2015) determined the quality of DSMs created using UAV photogrammetry techniques and the impact of GCP number on accuracy. Sanz-Sanz-Ablanedo et al. (Ablanedo et al.,2018) conducted a study on the frequency and accuracy of GCPs in an area of 1200 hectares. Rangel, Gonçalves and Pérez tested the accuracy of DSM and orthophoto maps in their study (Rangel et al., 2018; Yılmaz et al. 2000; Yakar et al. 2015).

* **Corresponding Author**

*(hivizci@hotmail.com) ORCID ID: 0000-0003-4876-423X
(aliulvi@mersin.edu.tr) ORCID ID 0000-0003-3005-8011

Cite this study

İzci, V., & Ulvi, A. (2023). The effect of the number and distribution of ground control points (GCP) on map production. Intercontinental Geoinformation Days (IGD), 7, 161-163, Peshawar, Pakistan

2. Study Area

Mersin University Çiftlükköy campus area was determined as the study area. This area is approximately 700 ha.

Figure 1. General view of the work area

3. Material and Method

Matrice 300 RTK device was used in the study. The general view of this device and the technical specifications of its camera are given in Figure 2 and Table 1.

Figure 2. Matrice 300 RTK rotary wing UAV (URL-1)

Table 1. Zenmuse P1 camera technic specifications

Product Name	ZENMUSE P1
Dimensions	198×166×129 mm
Absolute Accuracy	Horizontal: 3 cm, Vertical: 5 cm *
Sensor size	35.9×24 mm (Full frame)
Effective Pixels	45MP
Pixel size	4.4 µm
Aperture Range	f/2.8-f/16

* Using Mapping Mission at a GSD of 3 cm and flight speed of 15 m/s, with an 75% front overlap rate and a 55% side overlap rate.

The study was carried out in two stages: field work and office work. Field work; Following the establishment and coordination of Ground Control Points (GCP) and Control Points (CHP), the flights were completed with the UAV, and the office work was completed by evaluating the raw data obtained from the field in photogrammetric software and creating an orthophoto map of the area. GCPs were measured in real-time kinematic (RTK) mode before the flight, using virtual reference stations from the permanent global navigation satellite system (GNSS) (Figure 3).

20 GCPs and 30 control points (CP) were used in the study (Figure 4). Photogrammetric evaluation of the images was done in Agisoft Metashape software.

In the study, UAV images were obtained from an altitude of 428 m. A total of 878 pictures were taken.

Camera locations in the working area are shown in Figure 5.

Figure 3. Topcon hiper SR GNSS alıcısı

Figure 4. General view of GCP

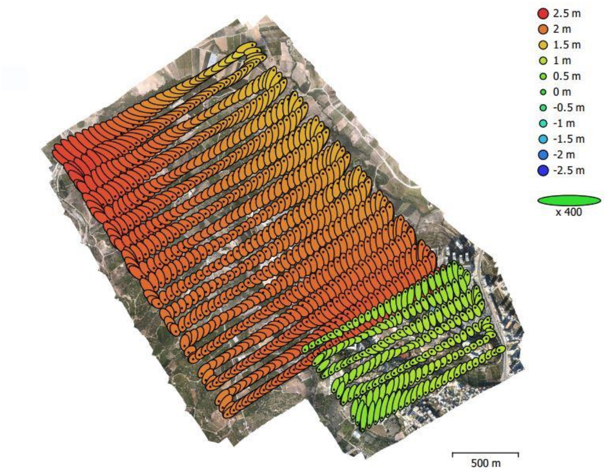

Figure 5. Camera locations and error estimates

The resulting digital elevation model can be seen in Figure 6.

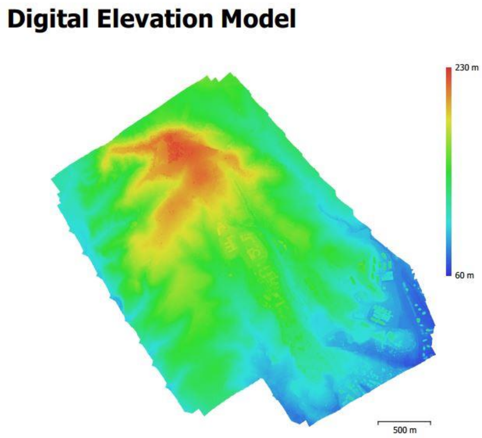

Figure 6. Reconstructed digital elevation model

As a result of the study, the orthophoto map seen in Figure 7 was obtained.

Figure 7. Orthophoto map for study area

4. Results

As a result of the analysis, the locations of GCPs are very important in order to maximize the accuracy obtained in photogrammetric projects. It was envisaged that GCPs should be placed at the edge of the work area to achieve optimum planimetric accuracy. However, this configuration does not mean that it will optimize the results in altimetry. This means that GCPs should be placed in a layered distribution within the study area. This means that as the density of GCPs increases, accuracy will increase until the results are improved. When the GCP reaches a certain number, both planimetric and altimetric accuracy will become stable.

Acknowledgement

This study was supported by Mersin University Scientific Research Projects with project number 2021-2-TP2-4527

5. References

Ablanedo, E. S., J. H. Chandler, J. R. R. Pérez, & Ordóñez. C. (2018). "Accuracy of Unmanned Aerial Vehicle (UAV) and SfM Photogrammetry Survey as a Function of the Number and Location of Ground Control Points Used." Remote Sensing 10 (10), 1606. https://doi.org/10.3390/rs10101606.

Agüera-Vega, F., F. Carvajal-Ramírez, and P. Martínez-Carricondo. (2016). "Accuracy of Digital Surface Models and Orthophotos Derived from Unmanned Aerial Vehicle Photogrammetry." Journal of Surveying Engineering 4016025. https://doi.org/10.1061/(ASCE)SU.1943-5428.0000206.

Kaya, Y., Şenol H.İ., Yiğit A.Y. & Yakar M. (2023). Car Detection from Very High-Resolution UAV Images Using Deep Learning Algorithms. Photogrammetric Engineering & Remote Sensing, Volume 89, Number 2, pp. 117-123(7)

Kaya, Y., Yiğit, A. Y., Ulvi, A. & Yakar, M. (2021). Arkeolojik alanların dokümantasyonununda fotogrametrik tekniklerinin doğruluklarının karşılaştırmalı analizi: Konya Yunuslar Örneği, Harita Dergisi 165, 57-72

Rangel, J. M. G., G. R. Gonçalves, and J. A. Pérez. (2018). "The Impact of Number and Spatial Distribution of GCPs on the Positional Accuracy of Geospatial Products Derived from Low-cost UASs." International Journal of Remote Sensing 39 (21): 7154–7171. https://doi.org/10.1080/01431161.2018.1515508.

Ruzgiene, B., T. Berteska, S. Gecyte, E. Jakubauskiene, and V. C. Aksamitaukas. (2015). "The Surface Modelling Based on UAV Photogrammetry and Qualitative Estimation." Measurements 73, 619–627.

Şasi, A., Yakar M. (2018). Photogrammetric modelling of hasbey dar'ülhuffaz (masjid) using an unmanned aerial vehicle, International Journal of Engineering and Geosciences 3 (1), 6-11

URL-1:https://www.oyuncakhobi.com/dji-matrice-300-rtk-ve-zenmuse-p1-full-frame-fotogrametri

URL-2: https://enterprise.dji.com/zenmuse-p1/specs

Villi, O., Yakar M. (2022). İnsansız Hava Araçlarının Kullanım Alanları ve Sensör Tipleri. Türkiye İnsansız Hava Araçları Dergisi 4 (2), 73-100

Yakar, M., Orhan, O., Ulvi, A., Yiğit, A. Y., & Yüzer, M. M. (2015). Sahip Ata Külliyesi Rölöve Örneği. TMMOB Harita ve Kadastro Mühendisleri Odası, 10.

Yılmaz, H. M., Karabörk, H., & Yakar, M. Yersel fotogrametrinin kullanım alanları. Niğde Üniversitesi Mühendislik Bilimleri Dergisi 4 (1), 1

7th Intercontinental Geoinformation Days

igd.mersin.edu.tr

Delineation of groundwater potential zone and mapping using GIS/Remote Sensing techniques and Analytic Hierarchy Process (AHP) for District Bhimber, Pakistan

Muhammad Shahid Usman*[1], Ghani Rahman[1], Saira Munawar[1]

[1]*University of Gujrat, Faculty of Science, Department of Geography, Gujrat, Pakistan*

Keywords
Groundwater Potential Zones
Analytical Hierarchy Process
Multi-Criteria Decision Analysis
GIS
Bhimber

Abstract

Groundwater plays a critical role in the sustainability of both ecosystems and human activities. This study presents an integrated methodology that combines the Analytic Hierarchy Process (AHP), Multi-Criteria Decision Analysis (MCDA), Geographic Information Systems (GIS), and Remote Sensing (RS) techniques. The main objective is to precisely delineate groundwater potential zones in the Bhimber district, leading to the creation of a comprehensive guide map for optimized groundwater exploration and utilization. This approach aims to promote sustainable resource management and overall development. The methodology involves data collection from diverse sources, including the Shuttle Radar Topography Mission (SRTM) for digital elevation models and remote sensing satellite images for thematic layers like geology, rainfall, slope, soil, drainage density, land use, and lineament density. Integration is facilitated through multicriteria evaluation. Using weighted overlay analysis and AHP-guided weight assignment, potential groundwater zones are systematically identified and mapped. The resulting groundwater potential map is categorized into four classes: Poor, Fair, Good, and Excellent. The findings reveal distinct patterns of groundwater potential in the district. The eastern region stands out with an excellent groundwater potential covering 26 square kilometres, attributed to substantial rainfall and the presence of water bodies. The mid-eastern and western sectors exhibit good potential (512 sq km), influenced by water bodies and consistent rainfall. Elevated terrains correspond to fair potential (779 sq km), while the upper north-east part indicates a Poor potential (24 sq km). This integrated approach enhances informed decision making, boosts resilience, and spurs socioeconomic development. Furthermore, the study contributes to scientific insights on groundwater dynamics, laying the groundwork for future research. The study underscores the effectiveness of GIS, RS and AHP in addressing complex groundwater management challenges, offering valuable information for global water resource management efforts.

1. Introduction

Groundwater stands as a vital natural resource, vital for sustaining human societies and ecosystems across the globe. Its significance lies not only in supporting agriculture, industry, and potable water supply, but also in its role as a lifeline during periods of drought, ensuring socioeconomic stability (Castillo et al. 2022). Particularly in regions where surface water availability is limited or uncertain, groundwater assumes even greater importance. However, effective extraction and management necessitate a thorough understanding of its distribution, potential, and recovery dynamics (Faheem et al. 2023). Nestled in the picturesque landscapes of Azad Kashmir, Pakistan, the Bhimber district stands as an emblematic region where groundwater assumes paramount importance. Characterized by diverse topography and geological formations, the district encounters challenges pertaining to water resource management and sustainable development. Addressing these challenges effectively hinges upon the delineation and mapping of potential groundwater areas. Such delineation empowers informed decision-making and prudent utilization of this finite resource. Traditionally, geological, hydrogeological, geophysical, and photo geological techniques have been employed to identify groundwater potential zones (Ikirri et al. 2023). In recent times, however, the integration of various conventional methods with satellite imagery and

* **Corresponding Author**

*(shahidusmaninfo@gmail.com)

Cite this study

Usman, M. S., Rahman, G., & Munawar, S. (2023). Delineation of Groundwater Potential Zone and Mapping using GIS/Remote Sensing Techniques and Analytic Hierarchy Process (AHP) for district Bhimber, Pakistan. Intercontinental Geoinformation Days (IGD), 7, 164-167, Peshawar, Pakistan

remote sensing (RS) techniques, along with geographical information system (GIS) technology, has gained prominence due to the advent of powerful, high-speed computers. The fusion of GIS and RS tools offers a robust approach for evaluating diverse natural aspects and is particularly effective in delineating groundwater potential zones (Zabihi, M., 2019). A growing body of research suggests that multi-criteria decision-making (MCDM) offers an effective mechanism for water resource management, enhancing decision quality through structure, transparency, and accuracy (Razandi et al. 2015). Notably, the initial structuring of a decision problem, encompassing criteria and decision options, holds paramount importance in the MCDM process. The successful application of AHP in numerous water resource management studies, integrating MCDA with RS and GIS techniques, underscores its utility.

Consequently, this study employs an integration of AHP-coupled MCDA, GIS, and RS techniques, merging hydrogeological, geomorphological, and climatic data. The primary objective is to delineate groundwater potential zones within the District Bhimber, culminating in the creation of a guide map for groundwater exploration and exploitation. This endeavor aims to ensure optimal and sustainable development and management of this vital resource.

2. Data and Methods

2.1. Study Region Description

This research focuses on Bhimber District, a region of vital geographical and strategic importance within Pakistan-administered Azad Kashmir. Covering around 1516 km² (Figure 1), Bhimber District is the southernmost among Azad Kashmir's ten districts. The administrative center is Bhimber town, a bustling hub of local governance and activities. Bordered by Kotli District to the north, Rajouri and Jammu Districts to the east (in Indian-administered Jammu and Kashmir), Pakistan's.

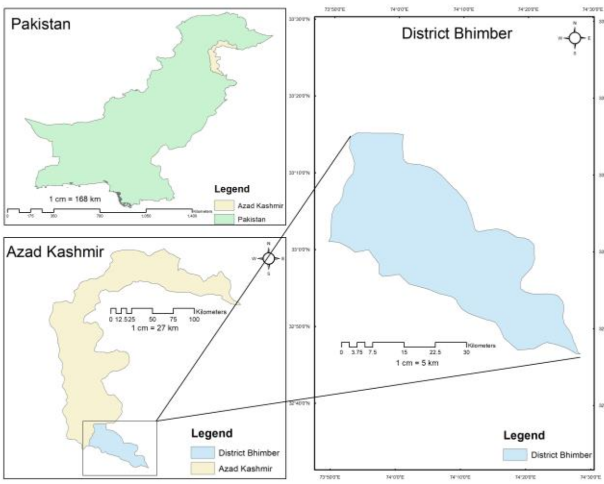

Figure 1. Study area map

2.2. Data

1. THE DIGITAL SOIL MAP FAO/UNESCO, 1995
2. U.S. Department of the Interior Geological Survey
3. CRU TS Version 4.05
4. Remote sensing Dataset

2.3. Methodology

In this study, various types of data were used to delineate groundwater possible areas in the study area. A digital elevation model (DEM) with a 30 m resolution was obtained from Shuttle Radar Topography Mission (SRTM) to derive a slope and drainage density map using the ArcGIS tool. Remote sensing satellite images and the corresponding data have been carried out for the preparation of thematic layers viz., geology, rainfall, slope, soil, drainage density, land use land cover, and lineament density of the study area. All thematic layers were integrated with Multicriteria evaluation technique. The potential zones of groundwater were obtained by overlaying all thematic layers based on weighted overlay method. Weighted overlay index analysis was carried out to give rank for each parameter of each thematic layer. The weight was given for each thematic layer depending on the Analytic hierarchy process (AHP) technique.

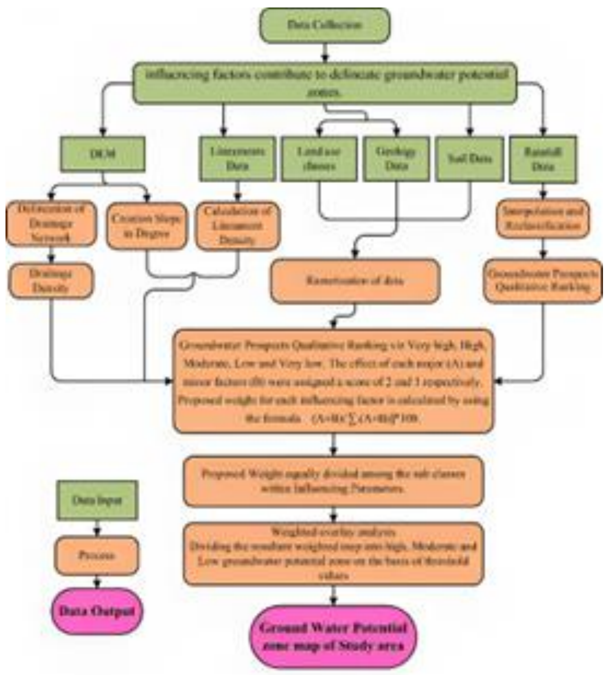

Figure 2. AHP

2.3.1. Multi-criteria decision-making (MCDM)

MCDM methods provide a structured framework to evaluate and compare different alternatives based on multiple criteria, helping decision-makers make more informed and rational choices. These methods aim to find a compromise or optimal solution that best aligns with the decision-maker's prefer.

2.3.2. Preparation of Thematic Layers

In this subsection, we detail the methodology employed for the creation, processing, and integration of the seven thematic layers—geology, rainfall, slope, soil, drainage density, land use land cover, and lineament density. These layers collectively form the foundational dataset for our multi-criteria decision-making analysis.

Infiltration rates, surface runoff, and overall groundwater availability. By integrating this map into our analysis, we enhance the precision of our understanding of how land use impacts groundwater dynamics within the Bhimber district.

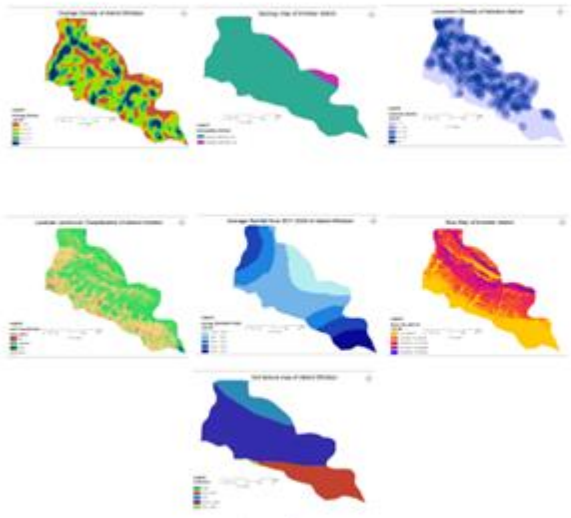

Figure 3. Thematic layers

2.3.3. The Analytic Hierarchy Process (AHP)

The Analytic Hierarchy Process (AHP) is a structured decision-making methodology that helps individuals and groups make complex decisions by breaking them down into smaller, more manageable components. AHP was developed by Thomas L. Saaty in the 1970s and has since been widely applied in various fields, including business, engineering, environmental management, and resource allocation. The Analytic Hierarchy Process (AHP) acts as a methodological framework that facilitates the synthesis of various thematic layers and factors into a cohesive groundwater potential assessment. By providing a structured and transparent approach to assigning weights, AHP empowers you to derive more reliable and robust conclusions regarding the distribution of groundwater potential within the Bhimber district.

Matrix		Rainfall 1	Geology 2	Slope 3	Drainage density 4	LULC 5	Lineament density 6	Soil 7	8	9	10	normalized principal Eigenvector
Rainfall	1	1	3	3	5	5	5	7	-	-	-	38.14%
Geology	2	1/3	1	3	3	5	5	5	-	-	-	24.54%
Slope	3	1/3	1/3	1	1	3	3	5	-	-	-	13.11%
Drainage density	4	1/5	1/3	1	1	1	2	3	-	-	-	8.93%
LULC	5	1/5	1/5	1/3	1	1	1	3	-	-	-	6.61%
Lineament density	6	1/5	1/5	1/3	1/2	1	1	1	-	-	-	5.00%
Soil	7	1/7	1/5	1/5	1/3	1/3	1	1	-	-	-	3.66%
	8	-	-	-	-	-	-	-	1	-	-	0.00%
	9	-	-	-	-	-	-	-	-	1	-	0.00%
	10	-	-	-	-	-	-	-	-	-	1	0.00%

Figure 4. AHP

2.3.4. Overlay analysis

The relative weights derived from the Analytic Hierarchy Process (AHP) were applied to each thematic map, resulting in a cumulative weight for each respective thematic map. The weight value corresponding to the highest or lowest weight was assigned based on field conditions. Furthermore, the normalized and assigned weights for the distinctive features of various thematic layers were summarized, and the consistency ratio for each thematic map was computed and assigned.

The integration of the seven distinct thematic maps was executed using GIS software, specifically ArcMap 10.3. This integration aimed to generate a groundwater potential map (GPM) for the study area, representing an aggregated measure of overall groundwater influence.

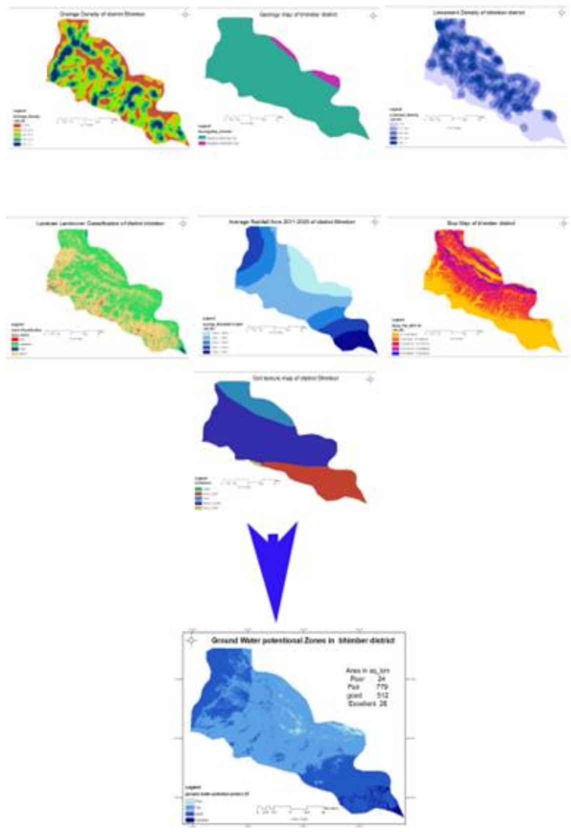

Figure 5. GPM

3. Results & Discussion

After applying all the methodologies, including the weighted overlay analysis of the seven thematic layers, the resulting groundwater potential map was classified into four distinct classes: Poor, Fair, Good, and Excellent. A careful examination of the generated map reveals notable patterns within the Bhimber district, particularly in its eastern region.

The eastern part of Bhimber district demonstrates an Excellent groundwater potential, covering an approximate area of 26 square kilometers. This classification can be attributed to the favorable combination of substantial rainfall and the presence of water bodies within this area. Moving towards the mid-eastern and western regions of the district, a Good groundwater potential is evident, encompassing a total area of approximately 512 square kilometers. This favorable classification is influenced by the proximity of water bodies on both the eastern and western sides. To the south-west, the district is bordered by a river, accommodating the Mangla Dam, while an intricate network of channels is present on the eastern side. Both of these areas receive consistent and substantial rainfall. The elevated terrain, extending over an area of 779 square kilometers, is characterized by a Fair groundwater potential. This encompasses a significant portion of the central district, emphasizing the balanced nature of groundwater potential in these regions. Conversely, the upper north-eastern segment, spanning an area of 24 square kilometers, exhibits a Poor groundwater potential classification.

Despite the relatively limited potential in this specific area, the broader evaluation suggests a diversified distribution of groundwater potential classes across the Bhimber district.

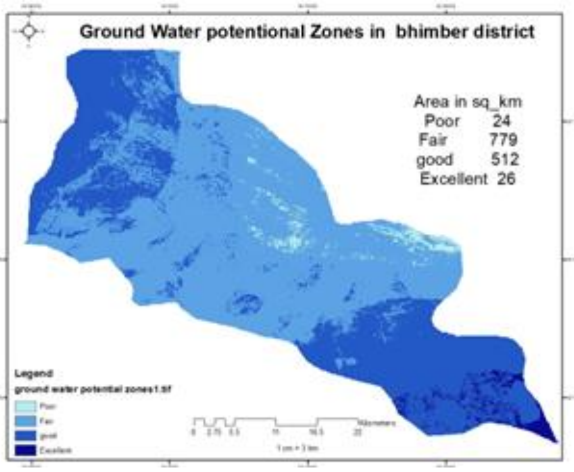

Figure 6. Groundwater potential

In summation, the integrated approach of weighted overlay analysis showcases the intricate relationship between various factors influencing groundwater potential within the Bhimber district. This comprehensive analysis provides essential insights for sustainable water resource management and informed decision-making in the region.

4. Conclusion

In conclusion, this research employs a comprehensive methodology integrating GIS, remote sensing techniques, and the Analytic Hierarchy Process (AHP) to delineate groundwater potential zones in the Bhimber district, Pakistan. The study not only addresses the critical role groundwater plays in sustaining ecosystems and human activities but also offers a practical guide for optimized groundwater exploration and utilization. Through a meticulous analysis of diverse thematic layers, including geology, rainfall, slope, soil, drainage density, land use, and lineament density, the study identifies distinct groundwater potential zones categorized as Poor, Fair, Good, and Excellent.

The findings showcase the effectiveness of the integrated approach, revealing intriguing patterns within the district. The eastern region stands out with an Excellent groundwater potential, attributed to substantial rainfall and the presence of water bodies. The mid-eastern and western sectors exhibit Good potential, influenced by water bodies and consistent rainfall. Elevated terrains correspond to Fair potential, while the upper north-east part indicates a Poor potential. These insights provide valuable information for informed decision-making, sustainable resource management, and overall socioeconomic development.

Acknowledgement

We acknowledged the support of the Departmet of Geography, University of Gujrat for providing us the opportunity and Lab to complete this research work.

Reference

Faheem, H., Khattak, Z., Islam, F., Ali, R., Khan, R., Khan, I., & Tag Eldin, E. (2023). Groundwater potential zone mapping using geographic information systems and multi-influencing factors: A case study of the Kohat District, Khyber Pakhtunkhwa. Frontiers in Earth Science, 11, 1097484.

Ikirri, M., Boutaleb, S., Ibraheem, I. M., Abioui, M., Echogdali, F. Z., Abdelrahman, K., ... & Faik, F. (2023). Delineation of Groundwater Potential Area using an AHP, Remote Sensing, and GIS Techniques in the Ifni Basin, Western Anti-Atlas, Morocco. Water, 15(7), 1436. https://doi.org/10.3390/w15071436

Razandi, Y., Pourghasemi, H. R., Neisani, N. S., & Rahmati, O. (2015). Application of analytical hierarchy process, frequency ratio, and certainty factor models for groundwater potential mapping using GIS. Earth Science Informatics, 8, 867-883. https://doi.org/10.1007/s12145-015-0220-8

Springer, A., Lopez, T., Owor, M., Frappart, F., & Stieglitz, T. (2023). The role of space-based observations for groundwater resource monitoring over Africa. Surveys in Geophysics, 44(1), 123-172. https://doi.org/10.1007/s10712-022-09759-4

Uc Castillo, J. L., Martínez Cruz, D. A., Ramos Leal, J. A., Tuxpan Vargas, J., Rodríguez Tapia, S. A., & Marín Celestino, A. E. (2022). Delineation of groundwater potential zones (GWPZs) in a semi-arid basin through remote sensing, GIS, and AHP approaches. Water, 14(13), 2138. https://doi.org/10.3390/w14132138

Zabihi, M., Pourghasemi, H. R., Motevalli, A., & Zakeri, M. A. (2019). Gully erosion modeling using GIS-based data mining techniques in Northern Iran: a comparison between boosted regression tree and multivariate adaptive regression spline. Natural hazards GIS-based spatial modeling using data mining techniques, 1-26. https://doi.org/10.1007/978-3-319-73383-8_1

7th Intercontinental Geoinformation Days

igd.mersin.edu.tr

Spatial distribution of public services and facilities in the Sahand new city of Iran

Shiva Sattarzadeh Salehi[*1], Firouz Jafari [2]

[1] University of Tabriz, Faculty of Planning and Environmental Science, Ph.D. student of Geography and Urban Planning, Tabriz, Iran.
[2]University of Tabriz, Faculty of planning and Environmental Science, Associate Professor of Geography and Urban Planning, Tabriz, Iran

Keywords
Sahand new city
Sustainability
Moran's spatial autocorrelation
Public services

Abstract
With the increasing growth of urbanization in the world, the cities that are developing, including Iran, with unequal services and population distribution. In this way, its instability is achieved in the form of spatial and social inequality, and it is based on it due to the deprivation of citizens from urban services and the increase of the gap. Therefore, in this research, the new city of Sahand has been investigated for the distribution of urban services and facilities using four indicators of population, electricity and energy, water, and green space. The information needed for the research has been prepared by document-library and field methods. The fuzzy method was used to describe the indicators, and then the mentioned indicators were analyzed in the ArcGIS software environment with Moran's spatial autocorrelation analysis. The results show that the Moran values of population, water, electricity, and green space are 0.17, 0.15, 0.15, and 0.03, respectively, so that the first three indicators follow a strong cluster pattern, while the green space index is scattered in the surface of the city is distributed.

1. Introduction

The rapid growth of the urban population in the last few decades is one of the most important aspects of global change (Xu et al,2007) Also, the rapid growth of the population has provided a prelude to extensive urban growth and development and has also created large changes in land use from local to global scale (Xu and Cho, 2007). Currently, one of the problems of all cities in Iran is the rapid growth of urbanization and the consequent imbalance of urban budgets. Among the most important factors that accelerate the physical-spatial development of cities are the excessive population growth caused by birth, migration, industrialization of cities, development and implementation of economic policies by governments (Sarafi, 2000). The lack of financial, technical and infrastructure facilities to create public and social uses of the city has caused a heterogeneity and imbalance in the distribution of various facilities in the city. It can be said that the population of the cities has increased, but the services that respond to their various needs are not adequately responding to the citizens (Sohel Rana, 2009).

Another important issue that humans face is how to view the use of available energy resources and the interaction between resources and how to exploit these resources (Hosam et al, 2016; Jafari et al, 2022). In this regard, it can be said; Paying attention to urban services and easy access to urban services is one of the basic strategies for establishing social justice in cities, and in order to achieve social justice in the city, these facilities and services must be provided in a way that benefits all classes and social groups of the society. In this regard, urban utilities and services are among the effective and useful factors that respond to the needs of the population, increase the public interest, and pay attention to the merits and merits of people, and can establish the dimensions of spatial, social, and economic justice with a fairer decision (Bezi et al, 2019; Maleki and Rezaei, 2023). In urban planning, these needs include all existing uses, including educational, health, medical, green space, sports, parking, residential, urban infrastructures, etc. are actually services that meet the basic needs in They are urban space. The existing limitations at the level of phases, in order to be successful in providing services at the level of the neighborhoods of the new city of Sahand, the cooperation of city officials and citizens seems to be a vital matter. In the present research, we discuss the spatial distribution of public services and the population of the new city of Sahand.

* **Corresponding Author**

*(Sattarzadeh423@gmail.com) ORCID ID 0000 – 0002 – 9216 – 9326
(F-jafari@tabrizu.ac.ir) ORCID ID 0000 – 0002 – 0294 – 0000

Cite this study

Salehi, S. S., & Jafari, F. (2023). Spatial distribution of public services and facilities in the Sahand new city of Iran. Intercontinental Geoinformation Days (IGD), 7, 168-171, Peshawar, Pakistan

2. Method

The information required for the research was collected by directly referring to the city institutions, such as New Sahand City Municipality, New Sahand City Development Company, Water and Sewerage Department, East Azerbaijan Power Distribution Company, etc., as well as studying documents and electronic library resources, and conducting field studies.

The statistical population of the present study included the citizens of the new city of Sahand. Due to the fact that the statistical blocks were not ready to be obtained in 2022 from the data of the previous years (2011-2016), the population of the city in 2022 was fulfilled. The Public service indicators studied in this research were population (population of 2017 and 2022), water (production and annual water consumption of the Sahand new city in 2022 in cubic meters), electricity (The total number of subscribers in terms of people and energy consumption in 2022) and green space (areas of parks and green spaces based on each phase and number of the existing parks). These 4 indicators were first descaled by the fuzzy method and then, the Moran's spatial autocorrelation were used to analyze the spatial distribution of the public service and population in the Arc GIS 10.8.1 software environment.

2.1. Research models

De-scaling is one of the important steps in multi-criteria decision making and is used to make the decision matrix non-dimensional (Asgharpur, 2016). There is a stochastic process called Moran's process, which describes the changes in the system assuming that the population is constant. Typically, biological systems in which two types of species are competing for expansion in the system are analyzed by this process. It is assumed that each species does not make any mistakes during the reproduction process and only produces its own similar species. In each time step, one person is randomly selected for reproduction and one person for death, and thus the size of the total population remains constant (Talabi Bram, 2013).

Table 1. Formula of models used in research

Model	Formula	Source
Fuzzy de-scaling	$nij = \frac{aij - Minaj}{Maxa\,j - Mina\,j}$ $nij = \frac{Maxa\,j - aij}{Maxa\,j - Mina\,j}$	(Asgharpur, 2016)
Moran	$I = \frac{n}{so}\frac{\sum_{i=1}^{n}\sum_{j=1}^{n}\omega ij(xi - \bar{x})(}{\sum_{i=1}^{n}(xi - \bar{x})}$	(Askari, 2011)

3. Study Area

The new city of Sahand is a newly established city in East Azerbaijan province of Iran, which is located 24 kilometers southwest of Tabriz, in the flow of the Tabriz-Azarshahr communication axis, and in the slopes of south of the Sahand mountain range was built (Sap, 2008).

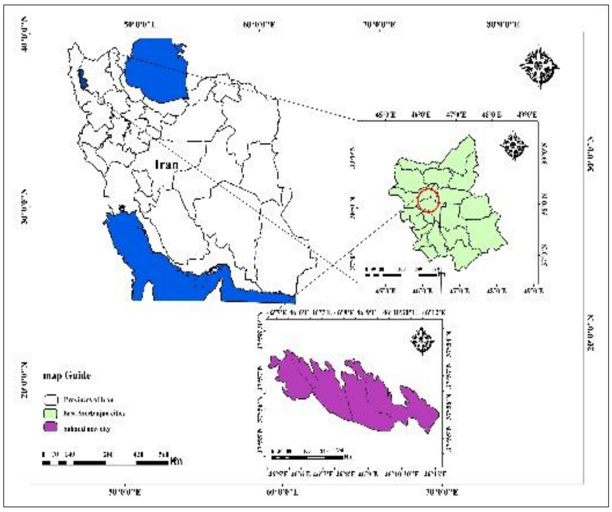

Figure 1. Map of the geographical location of the study area

4. Results

The expansion of the physical dimensions of the cities, the development of the city and the informal settlement of the new urban strata in the suburbs of the big cities of the country, and the increase in the price of land and housing in the area of the cities as well as the metropolis of Tabriz, practically make the provision of housing for the low-income or middle-income strata very difficult and even impossible. made it possible (Sahand New City Development Company, 2019). This has led to an increase in the population of the new city of Sahand, so that according to the population estimate in 2021, it has reached 275,472 people from 82,494 people (Iran Statistics Center, 2015).

Spatial autocorrelation analysis (Moran) has been used for the spatial distribution of the population. Moran's value is equal to 0.17, which shows the spatial distribution of the population of the new city of Sahand, which is distributed in phases two, three, one and four, respectively “Fig. 2”.

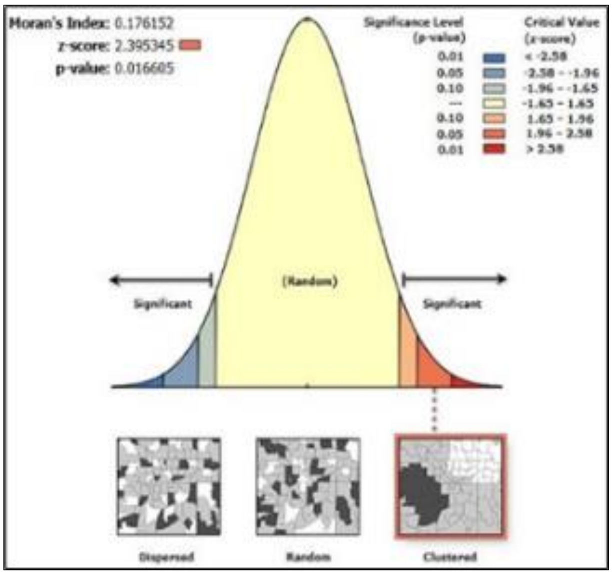

Figure 2. Sahand spatial distribution pattern based on population index

The results of Moran's spatial autocorrelation analysis for water index (production and consumption) showed that Moran's value is equal to 0.15. Considering that the Z calculated for the water index has a positive and large numerical value (2.29), the spatial distribution of this index follows a strong cluster pattern with a high confidence of 97% like the previous index "Fig. 3".

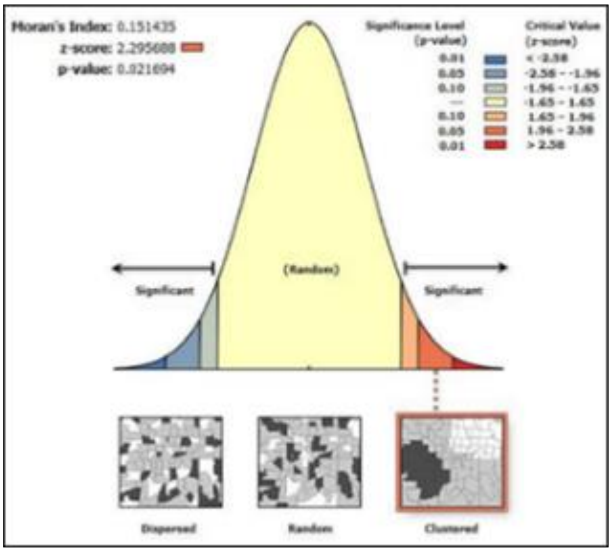

Figure 3. Sahand spatial distribution pattern based on water consumption index

The calculation results of Moran average index of total electricity consumption in New Sahand city show the cluster distribution of this index in the city level. Its Moran coefficient was equal to 0.15, the lowest amount of consumption was in phase four and phase one, and the highest amount was in phase two and three "Fig. 4".

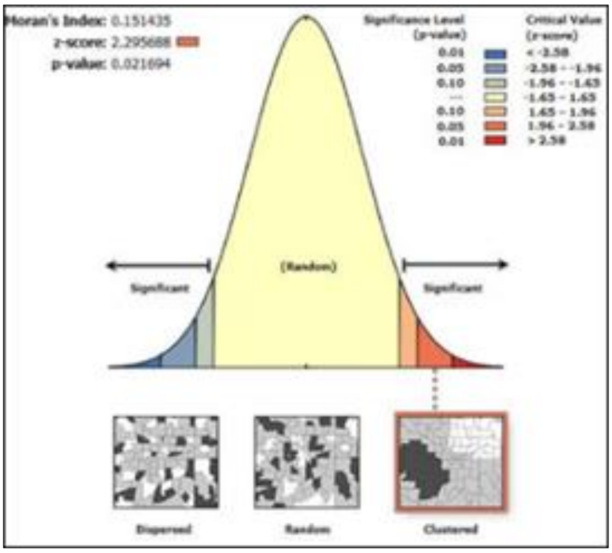

Figure 4. Sahand Spatial Distribution Pattern Based on Energy Consumption Index

The results of Moran's calculation of green space index is equal to 0.03, which indicates the scattered distribution of this use in the new city of Sahand. Also, the concentration of park use is in a part of the city, and as a result, more enjoyment in a certain area and less enjoyment in other areas and their deprivation of this facility "Fig. 5".

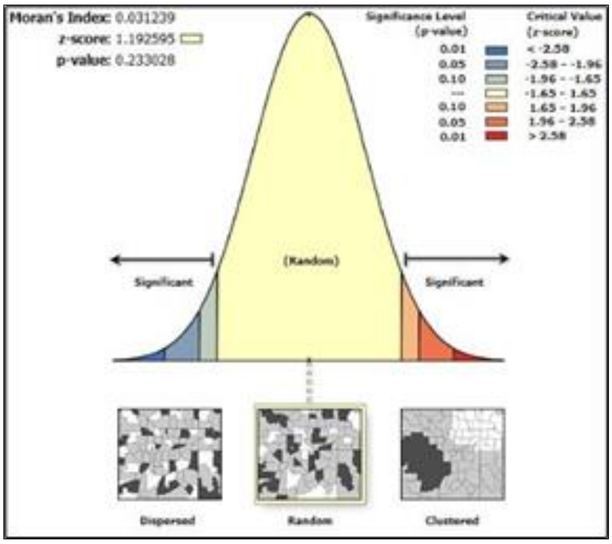

Figure 5. Sahand Spatial Distribution Pattern for Green Space Index

5. Discussion

Moran's spatial autocorrelation analysis is able to measure the spatial difference between all samples.

If the Moran value is close to a positive number of one, the data has spatial autocorrelation and has a cluster pattern, and if the Moran index value is close to a negative number of one, then the data are discrete and scattered. Therefore, this model is one of the best methods for evaluating public uses and services, which has shown us how to distribute them in the city level in the current research.

6. Conclusion

One of the basic problems of cities in recent decades is the unequal distribution of resources in different parts of the city. The disorganization of the distribution system of service centers in urban spaces has become the basis of social inequality of citizens in enjoying these services. Paying attention to the importance of distributing service users in urban areas and providing needed facilities and services is an important factor in improving the standard of living, social justice and sustainability of urban life.

Providing desirable and appropriate services is a suitable platform for social, economic and cultural activities and provides the grounds for citizens' well-being and satisfaction. The well-being and satisfaction of any society depends on making sure that all its members feel that they have a share in it. In this research, we have evaluated the distribution of services and the distribution of the population in the city, that the green space index follows a scattered and random pattern, and the water, electricity and population indices form a strong cluster pattern in phases two and three of the new city OF Sahand is distributed.

References

Asgharpour, M. (2016). Multi-criteria decision making. Tehran: University of Tehran, p. 400.

Askari, A. (2011). Spatial statistics analysis with ArcGIS. Tehran: Publications of the Municipal Information and Communication Technology Organization.

Bezi, K.R., Sayadsalar, Y., and Moamri, A. (2018). Monitoring and tracing the inequality of services and facilities within the city with the approach of spatial justice (case study: Gorgan city). Urban social geography biannual, (1) 6, 29-42.

Hosam, K., El Ghorab, Heidi, I., Shalaby, A. (2016). Eco and Green cities as new approaches for planning and developing cities in Egypt. Alexandria Engineering Journal, 495- 503.

Jafari, F., Asghari Zamani, A. & Sattarzadeh, S. (2022). Evaluation of the new city of Sahand using the urban range capacity system (UCCAS). Spatial Planning, 12(3), 83-108.

Maleki, S. & Rezaei, E. V. S. (2023). Analysis of indicators of social justice and access to urban services (case study: Region 1, Kermanshah city). Geography and development of urban space, 9(4), 75-91.

Sap (2008). Sahand New City Comprehensive Revision Plan, Sabze Andish Paish Consulting Engineers (SAP), first volume, New Cities Construction Company, Tabriz.

Sarafi, M. (2000). The basics of regional development planning, Tehran: Iran Management and Planning Organization.

Sohel Rana, M. (2009). Status of water use sanitation and hygienic condition of urban slums: A study on Rupsha Ferighat slum, Khulna. Desalination, 246(1-3), 322-328.

Talebi Bram, M, Aghababaei Samani, K., & Fazileh, F. (2013). "Study of quasi-stability in evolutionary dynamics on scaleless network using Moran's process", Isfahan University of Technology.

Xi, J., & Cho, N. (2007). Spatial and temporal dynamics of urban sprawl along two urban–rural transects: A case study of Guangzhou, China. Landscape and Urban Planning, 79(1), 96-109.

Xu, C., Liu, M., An, S., Chen, J., & Yan, P. (2007). Assessing the impact of urbanization on regional net primary productivity in Jiangyin County, China. Journal of Environmental Management, 85(3), 597-606.

7th Intercontinental Geoinformation Days

igd.mersin.edu.tr

Geopark Potential of Osmaniye Province

Nuri Erdem[*1]

[1]Osmaniye Korkut Ata University, Faculty of Engineering, Department of Geomatic, Osmaniye, Türkiye

Keywords
Geopark
Geodiversity
Geotourism
Osmaniye

Abstract

Osmaniye province is a city with limited economic opportunities, which was heavily damaged by the earthquakes centered in Kahramanmaraş on February 6, 2023, and where the rural population is predominant. Natural, cultural and geoarchaeological sites with potential for establishing a geopark in the province identifying geosites, protecting them and bringing them into geotourism will make significant economic, social and cultural contributions to the region. The landforms, caves, hot springs, castles and especially the current view of the Lalegölü volcano found in Osmaniye also reflect information about the creation of the world and the change it has undergone. These and similar features increase the potential of a UNESCO-tagged geopark area in the province. Projecting this potential and opening it to geotourism is important for the protection of the geoheritage in the region.

1. Introduction

Typical localities that explain the evolution of the earth's crust are geological elements with a great visual aspect, beautiful representatives of well-known events or processes, very rare formations, and pieces of "geological heritage" that need to be protected. Türkiye is like a “geological park” with its wide variety of formations. If we can protect the elements of this GeoPark and promote them well, we will have dozens of regions similar to Cappadocia and Pamukkale that attract many visitors (URL_1, URL_2).

Geopark: Geographic areas with defined borders that are of international importance in terms of landforms and geological features, where conservation, education and sustainable development activities are carried out and managed from a holistic perspective. Geoparks, which host many geosites, are conservation areas that aim to protect these geosites and transfer them to future generations; They are also sustainable development areas that aim for the social and cultural development of the local people. In addition to protecting geoheritage, Geoparks also aim to raise public awareness on issues such as sustainable use of natural resources, reducing the effects of climate change and reducing risks related to natural disasters. Association for the Protection of Geological Heritage (JEMİRKO) proposes the establishment of the following geoparks in Turkey (URL_1): Nemrut Volcano and Lake Van Geopark, Kula Geopark, Tuz Lake Geopark, Cappadocia Geopark, Karapınar Geopark, Narman Mutluluk Vadisi Geopark, Pamukkale Travertine Geopark, Mut Geopark.

UNESCO Global Geoparks are single, unified geographical areas where areas and landscapes of international geological importance are managed with a holistic concept of conservation, education and sustainable development. The UNESCO Global Geopark uses its geological heritage, in conjunction with all other aspects of the natural and cultural heritage of the region, to raise awareness and understanding of the key issues facing society, such as the sustainable use of our world's resources, mitigation of the effects of climate change, and mitigation of the effects of climate change (URL_3).

UNESCO Global Geoparks empower local communities and give them the opportunity to develop harmonious partnerships with the common goal of promoting important geological processes, features, time periods, historical themes linked to geology or outstanding geological beauty of the region. UNESCO Global Geoparks are established through a bottom-up process involving all relevant local and regional stakeholders and authorities in the region (e.g., landowners, community groups, tourism providers, indigenous people and local organizations). This process requires firm commitment from local communities, a strong local multi-partnership with long-term public and political support, and the development of a comprehensive strategy that will meet the objectives of

* **Corresponding Author**

*(nurierdem@osmaniye.edu.tr) ORCID ID 0000-0002-1850-4616

Cite this study

Erdem, N. (2023). Geopark Potential of Osmaniye Province. Intercontinental Geoinformation Days (IGD), 7, 172-175, Peshawar, Pakistan

all communities while showcasing and preserving the geological heritage of the region (URL_3).

UNESCO started working with geoparks in 2001, and in 2004 the Global Geopark Network (GGN) came together in Paris (Figure 1). In 2015, at the 38th General Conference of UNESCO, it was decided that the status of geoparks changed and became a UNESCO Program with international registration by UNESCO. By adopting the International Geosciences and Geoparks Program (IGGP) Regulation, the concept of UNESCO Global Geopark was formed. There are 177 Geoparks from 46 countries in the UNESCO Global Geopark Network as of 2021 (URL_4).

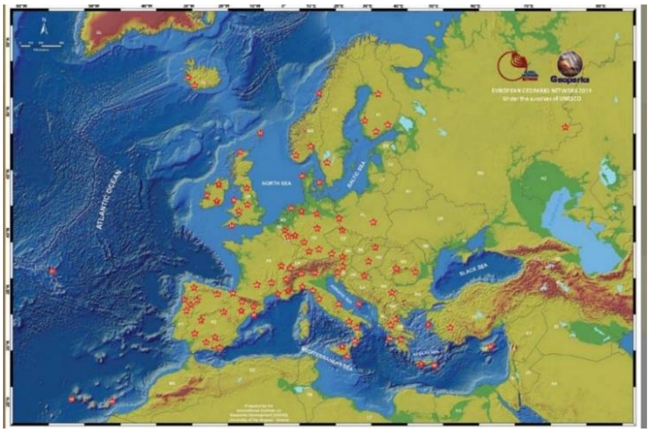

Figure 1. the European Geoparks Network today.

2. Kula Salihli Geopark

Kula-Salihli UNESCO Global Geopark is located in the middle part of the Gediz Graben and the western part of the Inner Western Anatolian Plateaus. The Geopark covers the entire administrative borders of Kula and Salihli districts of Manisa province. The total area of Kula Salihli Geopark is 2320 km2. Kula-Salihli Geopark, located in a region where crustal movements are frequently seen and effective, shows a geologically and tectonically complex and geomorphologically rich structure. The Geopark contains evidence of more than 300 million years of history of the earth, from Paleozoic metamorphic rocks (schist, gneiss) to prehistoric volcanic eruptions, and in this respect, it hosts a very rich geodiversity. Kula Salihli UNESCO Global Geopark is one of the youngest volcanic areas in Turkey. Volcanism, which started in the region approximately 15 million years ago, continued until ancient times. The traces of volcanism in Kula (Katakekaumene) are as fresh as if it happened yesterday. Kula Salihli UNESCO Global Geopark is one of the rare areas in the world where human footprints are found on volcanic tuffs in Salihli. Geological and geomorphological features in the region have led to the development of intensive agriculture, trade and culture since the earliest times of history. For this reason, the geopark area has hosted many civilizations. Sardes, the capital of the Lydian state, where money was first printed and used under state guarantee It is located within the borders of the geopark. The Geopark is Turkey's most important area in terms of geotourism due to its geological, cultural and archaeological richness (Figure 2). Kula-Salihli UNESCO Global Geopark is the first and only UNESCO-labeled geopark of Turkey and the Turkish World. Some photos from https://kulasalihligeopark.com/ (URL_5).

Figure 2. Kula-Salihli UNESCO Global Geopark (URL_5).

3. Features of Osmaniye Province as A Geopark

Osmaniye, located in Upper Çukurova, on the east bank of the Ceyhan River, with its wide hinterland; It is a wetland area due to the Ceyhan River, Hamıs , Karaçay, Kesiksuyu and Sabun Streams, and is in a busy area because it is at the junction of the roads connecting Çukurova to the east. It is a charming province with its rich agricultural lands and large forests unique to Çukurova. Osmaniye; Karatepe is an important tourism center with its Aslantaş Open Air Museum and ancient cities. Osmaniye, located in the east of the Mediterranean Region and Çukurova; It is located between 35^0 52'- 36^0 42' Eastern Meridians (longitudes) and 36^0 57'- 37^0 45' Northern Parallels (latitudes) (Figure 3). It has Gaziantep in the east, Hatay in the south, Adana in the west and Kahramanmaraş in the north. Its surface area is 3,279.9 km2 and it is 121 m above sea level. height and 20 km from the Mediterranean. distance (URL_6).

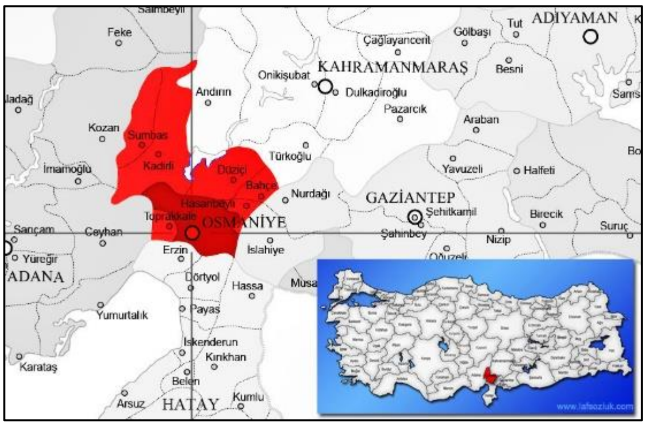

Figure 3. Location of Osmaniye province

Geologically, Osmaniye province is located on the western foothills of the Amanos Mountain (Nur Mountain) range and on alluvial units with poor engineering properties, where large agricultural areas known as Çukurova are located (URL_7; Özgül, 1976).

This region is located in a geography where faults are abundant (Figure 4).

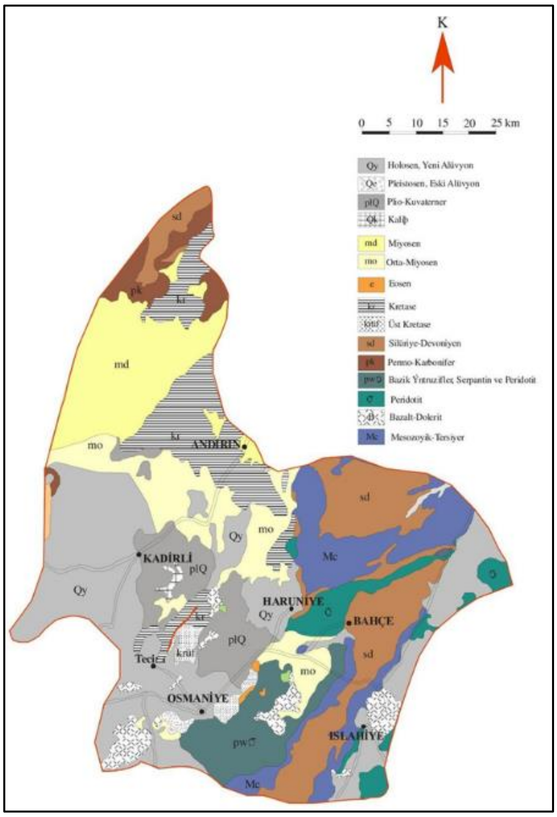

Figure 4. Geological map of Osmaniye province (URL_7).

The main data sources of this research, which deals with landforms that have the potential to become geosites in Osmaniye, are primarily field studies, secondary data collected from various institutions and individuals, and satellite images.

3.1. Lalegölü Volcano

It is thought that if the Lale Lake volcano becomes active again, there will be a significant climate change in Çukurova, and the cities of Osmaniye, Ceyhan and Erzin will probably be affected by this (Figure 5). The current image of the Lale Lake volcano also reflects information about the creation of the world and the change it has undergone. Those who enter the highway from Adana and go towards Ceyhan and Osmaniye can see the pitch-black mountain peak when they approach the Adana-Osmaniye border. When they look a little more carefully, they notice the presence of an area of black stones on the shore of the highway. In popular parlance, this is the " Leçelik " area. In today's parlance, it also means "Volcanic land" (URL_8).

Figure 5. Lalegölü Volcano and Crater Photos (URL_8).

3.2. Toprakkale

Toprakkale Castle is within the borders of Toprakkale district and is at the intersection of Osmaniye, Adana and Iskenderun roads. The history of the castle dates back to 2000 BC. The castle was called Kınık Castle during the Ottoman Period. The castle, built on a masonry hill, was reconstructed with black stones in the 8th century during the time of Abbasid Caliph Harun Reşit (Figure 6). The rectangular planned castle has 12 bastions and outer courtyard walls (URL_9).

Figure 6. There is a lava flow under Toprakkale and the castle, there are cooling cracks on the surface.

3.3. Culture and Tourism

The region where Osmaniye is located, to the east of Çukurova, has preserved its characteristics as a settlement since the earliest periods of history and has been under the influence of many civilizations, and is located in a geography with a significant amount of historical and cultural artifacts. The ruins in Domuztepe and the mounds in Osmaniye belong to the Neolithic, Chalcolithic and Bronze periods. Since ancient times, it has been the scene of the lives of states such as Hittite, Assyrian, Persian, Greek, Roman, Byzantine and some tribes. Later, Turkish tribes came to these lands, where Umayyad and Abbasid people lived, starting from the 1080s with the conquest of Anatolia by the Turks (URL_10).

You should see these: Kastabala (Hierapolis) City, Zorkun Plateau, Karatepe-Aslantaş Open Air Museum, Kadirli Ala Mosque, Karatepe Rugs, Haruniye Thermal Springs, Kırmıtlı Bird Sanctuary, Savrun Canyon, Hamite Castle, Toprakkale Castle, Hamite (Amuda) Castle, Kaypak (Savranda) Castle, Çardak Castle, Karafenk Castle, Babaoğlan Castle, Olukbaşı-Ürün Plateaus, Sumbas -Bağdaş Plateau, Kadirli- Maksutoğlu, Beyoğlu-Savrungözü -Dokurcun and Çığşar Plateaus, Hasanbeyli-Almanpınarı Plateau, Kırmıtlı Bird Sanctuary are other important tourism values (Figure 7), (URL_10).

Figure 7. Important tourism values of Osmaniye (URL_10).

4. Conclusion

Osmaniye; Its location, geological features and landforms need to be preserved as geosites and geoheritage and transferred to future generations. Within the scope of the research, four waterfalls, many caves, two canyons, dialects and cliffs, 30 nearby castles, many 1st, 2nd and 3rd degree archaeological sites and intangible cultural geosites such as Karatepe rugs were identified. These geosites were discussed in terms of their accessibility, number, touristic and scientific features, and were evaluated to determine their geotourism potential. The results are summarized as follows:

- It is thought that these shapes, which are insufficient in terms of tourism on their own, will be important when taken together with other attractions.
- Although the geosites identified in the study area are valuable in terms of geotourism, most of them have not been the subject of academic studies yet. Conducting research on these geosites will contribute to the literature.
- The most important problems of geosites in Osmaniye are their lack of transportation, lack of promotion, lack of tourism investments in general and their lack of protection status. These deficiencies should be corrected as soon as possible. However, natural beauties can suffer great damage when opened to tourism. Great attention should be paid to this.

References

Özgül, N. (1976). Toroslar'ın bazı temel jeoloji özellikleri, TJB, 19, 65-78.
URL_1: https://www.jemirko.org.tr/
URL_2: https://tr.wikipedia.org/wiki/Jeopark
URL_3: https://www.unesco.org.tr/
URL_4: www.europeangeoparks.org
URL_5: https://kulasalihligeopark.com/
URL_6: https://osmaniye.csb.gov.tr
URL_7: Maden Tetkik ve Arama Genel Müdürlüğü Doğu Akdeniz Bölge Müdürlüğü, Osmaniye İli Jeolojik Özellikleri, https://docplayer.biz.tr/20798648-Maden-tetkik-ve-arama-genel-mudurlugu-dogu-akdeniz-bolge-mudurlugu-osmaniye-ili-jeolojik-ozellikleri.html
URL_8: http://cukurovastrateji.blogspot.com/
URL_9: https://www.kulturportali.gov.tr/
URL_10: https://www.osmaniyedeyatirim.com/sektorler/kultur-ve-turizm

7th Intercontinental Geoinformation Days

igd.mersin.edu.tr

Logging methodology decision-making with the new high-resolution DEM of Türkiye

Arif Oguz Altunel*[1], Oytun Emre Sakici[1]

[1]Kastamonu University, Faculty of Forestry, Department of Forest Engineering, Kastamonu, Türkiye

Keywords
DEM
Slope
Topographic roughness
Acreage

Abstract

There are many ways one can decide if an engineering related undertaking would be feasible and productive when the topography is thoroughly and precisely investigated before it takes shape. Forestry is just one profession that proper planning is of the essence when it comes to the logging phase of the entire production process. Logging in Türkiye is primarily handled over an ever-growing forest-road network. Although the specialized equipment e.g. yarders, tractor-winches, are also put into the works, their share and production capacity is limited and confined to certain parts of the country. Thus, timber production primarily revolves around direct tractor-skidding throughout the forest floor, taking the felled log from the stump to the nearest road. Here, topography is the real constraint in production method decision-making. Topographic maps have long been used to extract topographic parameters. However, Türkiye recently announced the completion of first national high-resolution digital elevation model, 5 m DEM. High precision, which would be achieved utilizing this DEM, reemphasized the importance of slope and topographic roughness in primary transport planning. In this study, we calculated the amount of slope and topographic roughness acreages in two forest planning units based on elevation differences. Both yielded enough extreme surface acreages, which would question the expansion of road building and justify the adoption of specialized equipment.

1. Introduction

Digital elevation models (DEM) since the global dissemination of SRTM data in 2005 have come a long way. It was plagued with voids at the beginning, and studies showed how they could effectively be patched (Grohmann et al. 2006; Ling et al. 2007; Gallant and Read, 2009). Announcement of the first version of Aster GDEM in 2009 provided additional support for further strengthening SRTM's later versions (Reuter et al. 2007; Altunel, 2018). As time passed, it proved its worth in every corner of the Earth paving way to devise new methodologies in engineering, hydrology, urban planning, etc. (Alsdorf et al. 2007; Lehner et al. 2008; Altunel, 2023). Although rather satisfactory in spatial positioning and elevation accuracy, they do not provide enough ground resolution for specialty works. Roughly, 30 m (1 arc-second) spatial resolution in each data generalizes the average surface facades excessively to perform precision works. Later, TanDEM-X global DEM of 12 m (0.4 arc-second) and recently Copernicus European DEM of 10 m (0.3 arc-second) raised the bar even further to better represent the surfaces. Although technology has enabled us to further improve the ground resolution to even higher levels with UAV and LIDAR (Akturk and Altunel, 2019; Muhadi et al. 2020), they are most of time not feasible and easily available everywhere. Thanks to its long experience of aerial stereo photo capture, Türkiye recently announced a 5 m national DEM, which means that it provides 36 and 4 times better earth representation than SRTM and new Copernicus DEMs, respectively.

In Türkiye, long-time accepted practices for primary transport are direct tractor skidding, tractor drum winching and yarders in timber production process. The major criteria to decide the primary transport method has been topography of the region and standing volume to be harvested. For instance, 55% gradient or more definitely requires special equipment such as yarders alongside the existing forest road network.

Although the elevation accuracy of a DEM is of the essence in the first glance, practicality of such a high resolution DEM highlighted the importance of topographical parameter extraction (Mukherjee et al. 2013) that is presented in this study as a firm foundation when deciding what type of logging equipment/infrastructure might be preferred while reaching out to the stands to be harvested.

* **Corresponding Author**

*(aoaltunel@kastamonu.edu.tr) ORCID ID 0000-0003-2597-5587,
(oesakici@kastamonu.edu.tr) ORCID ID 0000-0003-4961-2991

Cite this study

Altunel, A. O. & Sakici, O. E. (2023). Logging methodology decision-making with the new high-resolution DEM of Türkiye. Intercontinental Geoinformation Days (IGD), 7, 176-179, Peshawar, Pakistan

2. Method

Kastamonu Regional Directorate of Forestry (RDF) has been the leading contributor in Turkish timber production. The study was devised within Daday Planning Unit in Daday Forest Enterprise (FE) and coastal Doganyurt Planning Unit in Inebolu Forest Enterprise, both within Kastamonu RDF to see the elevation and resulting slope variations (Figure 1). The existence of treacherous topographies due to coast-parallel running mountain ranges throughout Inebolu FE make it a prime candidate for suitable technologies, not only a forest road network. Besides, inland Daday FE was also selected because of the existence of a new generation Tajfun MOZ 500 GR yarder in their machinery park. Although yarders are the preferred specialized equipment used in logging when forests on difficult topographies need to be harvested, they have only been effectively used in Northeast Türkiye, as if the rest of Turkish forests were on favorable grounds.

New 5 m national Turkish DEM, produced by General Directorate of Mapping (GDM), and 2014 geodatabase of Kastamonu RDF were used. DEM was produced utilizing the stereo captured air photos. After Yilmaz and Erdogan (2018) showed over some sample locations placed in various parts of the country that such a national DEM could be generated, GDM with its immense stereo air photography achieve, which have also been used to produce the topographic maps in various scales for 6 decades, actually attempted and successfully produced it. DEM was acquired as elevation values reduced to ortometric heights and projected to UTM-WGS84 projection. DEM was a representation of the land, through which the slope at any given location could be calculated. Later, land forms depicted in 5x5 m grid cells in the DEM were characterized based on the variability of the slope in their surroundings.

Figure 1. Studied planning units

Topographic roughness is just another topographical parameter, which can be added to the long list of what one could produce with an elevation data. Practicality of it was highlighted in this study because DEMs, especially the recently introduced high-resolution ones, have started providing unprecedented detail, which could easily be translated to whatever is intended.

Topographic roughness is another parameter which could be calculated over a DEM, showing if the calculated slope value of a cell is uniform throughout a neighborhood or not. It could very well define not only the slope but also how that slope stays the same or changes in a region (compartments or sub-compartments in a forestry setting). Given the amount of how favorably or steeply slope values are assigned to those 25 m^2 DEM cells and how varied those slope values are, foresters can decide which equipment or infrastructure might be appropriate to effectively manage and harvest the forests. To do this, 5 m DEM was first converted to slope on a projected flat plane using a 2D Cartesian coordinate system, specifying the inclination of the slope as percent rise. Then, the resulting slope map was reclassified defining equal intervals at 1%. Finally, statistics were performed on the reclassified slope map, using a 3x3 cells configuration, calculating the slope varieties (the number of unique values) of the cells within their immediate neighborhoods. The results showed how each and every cell in the finalized map was rated in terms of terrain roughness between 1 and 9 (1-3, rather flat surfaces; 4-6 moderately varied surfaces; 7-9 excessively varied surfaces), depending upon the changing slope values (Figure 2). Analyses were performed by using ArcGIS 10.8.

This study was conceptualized on the existence of both such a DEM, and a known and long-neglected, but reintroduced new machinery to Turkish forestry, yarder. Two forest planning units from Daday and Inebolu FEs, Daday and Doğanyurt were selected based on the elevation differences acquired by subtracting the lowest elevation measurement from the highest one (Table 1).

Table 1. Elevation differences within planning units of Daday and Inebolu and timber production figures of 2022

Forest Enterprise	Planning Unit	Low	High	Difference	Production (m^3)
Daday	Karacaoren	900	1640	740	22299
	Saricam	820	1519	699	20729
	Camkonak	761	1585	824	15331
	Camlibel	889	1491	602	12592
	Yayla	860	1677	817	15856
	Daday	802	1744	942	15212
	Ballidag	896	1739	843	18500
Inebolu	Doganyurt	0	1176	1176	8344
	Gemiciler	0	687	687	14074
	Inebolu	0	415	415	8011
	Ozluce	0	1047	1047	9849
	Altinkum	0	400	400	9855

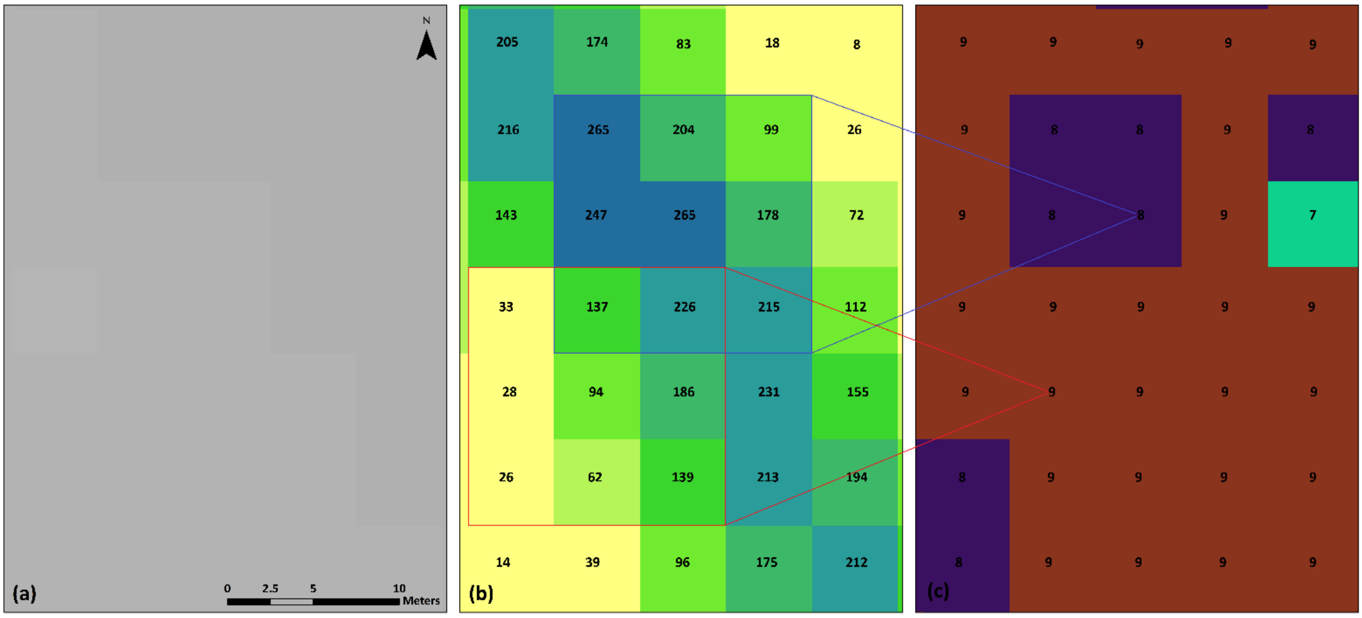

Figure 2. 5 m national DEM (a), reclassified slope map at 1% intervals (b), calculated terrain roughness values (c)

Both Daday and Doganyurt planning units yielded the highest elevation differences among the others in their respected FEs.

3. Results and Discussion

5 m national DEM custom tailored to Daday and Doganyurt planning units' administrative forestlands produced the following acreages. When investigated through the current Kastamonu RDF geodatabase, it was observed that Daday and Doganyurt planning units spanned over 16808 ha and 10228 ha land areas, respectively. Compared to Daday's moderately expanding land area over 55% gradient, 13.2 %, Doganyurt's land area amassed 41.4 %, which was rather steep in a considerably less administrative domain. 2022 production figures showed that Daday planning unit almost doubled the amount produced in Doganyurt. One might think how much of this production was done using ground skidding and winching, and how much using the yarder. In either case, a proper and sufficient road infrastructure is needed for forest management, but a threshold should not ever exceed if proper mechanization is simultaneously integrated. No further detailing was performed, but it was concluded that given the absence of a yarder, Doganyurt's forest land area would have been furnished with forest roads if production were to continue. Roads were regarded as techno-ecosystems, which require in-depth analyses of their would-be effects prior to laying them down (Lugo and Gucinski, 2000). Jordan et al. (2010) stated that risk assessments should be carried out before forest roads are actually placed especially in steep topographies. Thanks to the high-resolution, such assessments could surely be considered and evaluated through the 5 m national DEM, because 5 m width and length of a cell could perfectly align with the proposed road platform of a type-B forest road, and upslope and downslope areas around the platform could be further investigated before the actual road construction begins.

We also checked how the slope values of each 5 m cell varied with respect to the neighboring ones. Grohmann et al. (2010) defined the topographic roughness as a representation of the variability of topographic surfaces, e.g. changing slope values in the surfaces expressed in 5 m cells in this study. DEMs are used to extract numerous topographic parameters (Woodrow et al. 2016; Kruk et al. 2020). High resolution in DEMs provided improved flood inundation predictions (Saksena and Merwade, 2015). We calculated both topographic roughness acreage (ha) and percentage (%) for Daday and Doganyurt planning units (Table 2).

Values affirmed the hardship experienced in Doganyurt with respect to those displayed for Daday. Difficult topography might require specialized equipment to do logging and timber production. Depending upon the findings materialized in this study, there must be many planning units across the country seeking more than ground skidding and excessively and unnecessarily built forest roads to manage their forests. It is also obvious that the new 5 m national DEM of Türkiye is more than capable of producing detailed topographical works, which were impossible to accomplish in the past.

Table 2. Topographic roughness acreage and percentage by planning units

Planning Unit		Flat surfaces	Moderately varied surfaces	Excessively varied surfaces
Doganyurt	ha	162	1684	8382
	%	1.6	16.4	82
Daday	ha	2102	4690	10016
	%	12.5	28	59.5

Acknowledgement

We thank Kastamonu Regional Directorate of Forestry and General Directorate of Mapping for supplying their valuable data.

References

Alsdorf, D. E., Rodríguez, E., & Lettenmaier, D. P. (2007). Measuring surface water from space. Reviews of Geophysics, 45(2), RG2002.

Altunel, A. O. (2018). Suitability of open-access elevation models for micro-scale watershed planning. Environmental Monitoring and Assessment, 190(9), 512.

Altunel, A. O. (2023). The effect of DEM resolution on topographic wetness index calculation and visualization: An insight to the hidden danger unraveled in Bozkurt in August 2021. International Journal of Engineering and Geosciences, 8(2), 165-172.

Akturk, E., & Altunel, A. O. (2019). Accuracy assessment of a low-cost UAV derived digital elevation model (DEM) in a highly broken and vegetated terrain. Measurement, 136, 382-386.

Gallant, J. C., & Read, A. (2009). Enhancing the SRTM data for Australia. Proceedings of Geomorphometry, 31, 149-154.

Grohmann, G., Kroenung, G., & Strebeck, J. (2006). Filling SRTM voids: The delta surface fill method. Photogrammetric Engineering and Remote Sensing, 72(3), 213-216.

Grohmann, C. H., Smith, M. J., & Riccomini, C. (2010). Multiscale analysis of topographic surface roughness in the Midland Valley, Scotland. IEEE Transactions on Geoscience and Remote Sensing, 49(4), 1200-1213.

Jordan, P., Millard, T. H., Campbell, D., Schwab, J. W., Wilford, D. J., Nicol, D., & Collins, D. (2010). Forest management effects on hillslope processes. Compendium of forest hydrology and geomorphology in British Columbia. BC Min. For. Range, pp. 275-329.

Kruk, E., Klapa, P., Ryczek, M., & Ostrowski, K. (2020). Influence of DEM elaboration methods on the USLE model topographical factor parameter on steep slopes. Remote Sensing, 12(21), 3540.

Lehner, B., Verdin, K., & Jarvis, A. (2008). New global hydrography derived from spaceborne elevation data. Eos, Transactions American Geophysical Union, 89(10), 93-94.

Ling, F., Zhang, Q. W., & Wang, C. (2007). Filling voids of SRTM with Landsat sensor imagery in rugged terrain. International Journal of Remote Sensing, 28(2), 465-471.

Lugo, A. E., & Gucinski, H. (2000). Function, effects, and management of forest roads. Forest Ecology and Management, 133(3), 249-262.

Muhadi, N. A., Abdullah, A. F., Bejo, S. K., Mahadi, M. R., & Mijic, A. (2020). The use of LiDAR-derived DEM in flood applications: A review. Remote Sensing, 12(14), 2308.

Mukherjee, S., Mukherjee, S., Garg, R. D., Bhardwaj, A., & Raju, P. L. N. (2013). Evaluation of topographic index in relation to terrain roughness and DEM grid spacing. Journal of Earth System Science, 122, 869-886.

Reuter, H. I., Nelson, A., & Jarvis, A. (2007). An evaluation of void-filling interpolation methods for SRTM data. International Journal of Geographical Information Science, 21(9), 983-1008.

Saksena, S., & Merwade, V. (2015). Incorporating the effect of DEM resolution and accuracy for improved flood inundation mapping. Journal of Hydrology, 530, 180-194.

Woodrow, K., Lindsay, J. B., & Berg, A. A. (2016). Evaluating DEM conditioning techniques, elevation source data, and grid resolution for field-scale hydrological parameter extraction. Journal of Hydrology, 540, 1022-1029.

Yilmaz, A., & Erdoğan, M. (2018). Designing high resolution countrywide DEM for Turkey. International Journal of Engineering and Geosciences, 3(3), 98-107.

7th Intercontinental Geoinformation Days

igd.mersin.edu.tr

Spatial and regression-based missing precipitation data imputation: Western Black Sea region

Seyma Akca*[1], Muhammed Zakir Keskin [2], Ahmad Abu Arra [3] Eyüp Şişman [3]

[1]Harran University, Geomatic Engineering Department, Sanliurfa, Türkiye
[2]Bartın University, Civil Engineering Department, Bartın, Türkiye
[3]Yıldız Technical University, Civil Engineering Department, İstanbul, Türkiye

Keywords
Imputation
IDW
Regression
Black Sea Basin

Abstract

The study of natural phenomena in the environment influences the shaping of human geography. Investigating the occurring physical events is achieved by measuring the magnitudes in nature. These measurements are then structured within certain models, and the resulting outputs are used in engineering applications. However, measurements taken from nature or a system may not provide continuous data due to human and sensor-related errors or inadequacies, resulting in gaps or discontinuities in data acquisition. The success of the method in the missing data completion problem is still an important research topic, as it is influenced by various factors such as the characteristics of the data and the type of missing data. Particularly, the lack of precipitation observation data due to climate change poses serious risks in the planning of water structures. In this study, spatial-based inverse weighted distance (IDW), regression, and statistical methods such as mean and median values are used to fill in and complete missing precipitation data obtained from meteorological stations in the Western Black Sea Region. The results of the study conducted at 10 stations showed that the spatial-based method, IDW, produced more successful results.

1. Introduction

The examination of physical events occurring in nature has an impact on shaping the geography in which humans live. The study of these physical events is achieved through the measurement of quantities in nature. The measurements obtained are structured within specific models and, as a result, the generated outputs are used in engineering applications. However, measurements taken from nature or a system may not be continuous due to human and sensor-related errors or inadequacies, resulting in data gaps or interruptions. When missing data are prevalent in a dataset, they significantly reduce the quality and reliability of that dataset. Effective and accurate planning of water structures and water management require continuous, healthy, and long-term flow data. The success of the missing data completion method depends on various factors, such as the characteristics of the data and the type of missing data, making it an important area of research. Observation data should be complete and extend over many years. In particular, the absence of precipitation observation data related to climate change poses significant risks to the planning of water structures.

Missing data can be categorized into three types: Missing Completely at Random (MCAR), Missing at Random (MAR), and Missing Not at Random (MNAR). MCAR implies that data is missing randomly, unrelated to any observed or unobserved variables, and the probability of data being missing is independent of all other variables. In contrast, MAR occurs when the missing data is related to observed variables but not to unobserved variables, allowing for flexibility in handling it by including relevant observed variables in the analysis. MNAR is the most challenging type as it suggests that missing data is related to both observed and unobserved variables, requiring complex statistical methods or assumptions. The choice of how to handle missing data depends on the mechanism causing the missingness, significantly impacting the validity of the analysis. There are approaches available for completing

* **Corresponding Author**

*(seymakca@harran.edu.tr) ORCID ID 0000–0002–7888–5078
(mkeskin@bartin.edu.tr) ORCID ID 0009-0005-6724-491X
(ahmad.arra@std.yildiz.edu.tr) ORCID ID0000-0001-8679-1752
(esisman@yildiz.edu.tr) ORCID ID 0000–0003–3696–9967

Cite this study

Akça, Ş., Keskin, M. Z., Arra, A. A., & Şişman, E. (2023). Spatial and regression-based missing precipitation data imputation: Western Black Sea region. Intercontinental Geoinformation Days (IGD), 7, 180-183, Peshawar, Pakistan

missing data, including hot and cold deck, listwise deletion, pairwise deletion, mean imputation, regression imputation, last observation carried forward, stochastic imputation, and multiple imputation (Şeker and Eşmekaya, 2017). When studies in the literature on completing missing data are examined; (Yumus et. al.,2020) For the completion of missing data in HCC survival prediction, they employed methods including (median, mode, mean, decision tree-based regression, and linear regression methods), as well as machine learning-based techniques such as Naive Bayes and decision tree-based classifiers. They achieved the best result with a decision tree regression, with an accuracy of 83%. (Albayrak et. al.,2017) They successfully applied clustering and maximum likelihood methods for completing missing data on a health dataset with a 96.5% success rate. Bakış and Göncü (2015) completed the process of filling in missing data in streamflow measurements in the Zap River basin using correlation-based regression analysis and the Drainage Area Ratio method. (Gümüş and Kavşut, 2013) employed feed-forward back-propagation neural network (FFBPNN), radial based artificial neural network (RBANN), and generalized regression neural network (GRNN) artificial neural network models to predict missing discharge values for the station on the Zamanti River. (Erken and Senyay, 2023) compared the performance of fundamental missing data completion methods such as Listwise Deletion, Last Observation Carried Forward, Mean Imputation, along with machine learning methods like Stochastic Regression, Nearest Neighbor Algorithm, Random Forest Algorithm, and Amelia Algorithm to complete missing data on the Hitters dataset.

In this study, missing data in July precipitation records obtained from the stations located in the Western Black Sea basin, including Bartın (17020), Amasra (17602), Ulus (17615), Akçakoca (17015), Çerkeş (17646), Düzce (17072), Cide (17604), Devrekani (17618), İnebolu (17024), KaradenizEreğli (17611), were aimed to be filled using a spatial interpolation method, Inverse Weighted Distance (IDW), unlike statistical methods (mean, mode, median), regression, and other studies. The relevant results are presented in the continuation of the study.

2. Method

2.1. Study Area

The Western Black Sea basin, one of Türkiye's regions, receives a substantial amount of rainfall, as depicted in Figure 1. Encompassing an expanse of 28,855 km^2, this region extends from east to west and is known for its significant precipitation. The information related to the stations used within the study area is provided in Table 1.

Between 2019 and 2022, randomly selected data points from the precipitation data were omitted, and predictions were made using statistical methods (mean and median), regression, and IDW. These predictions were then verified against actual precipitation data using validation metrics to assess their accuracy.

Table 1. Station details

Station Code	Station Name	Lat. (N)	Lon. (E)	Elev. (m)
17020	Bartın	41.62	32.36	33
17602	Amasra	41.75	32.38	73
17615	Ulus	41.58	32.64	162
17015	Akçakoca	41.09	31.14	10
17646	Çerkeş	40.82	32.88	1126
17072	Düzce	40.84	31.15	146
17604	Cide	41.88	32.95	36
17618	Devrekani	41.60	33.83	1050
17024	İnebolu	41.98	33.76	64
17611	KaradenizEregli	41,26	31,43	19

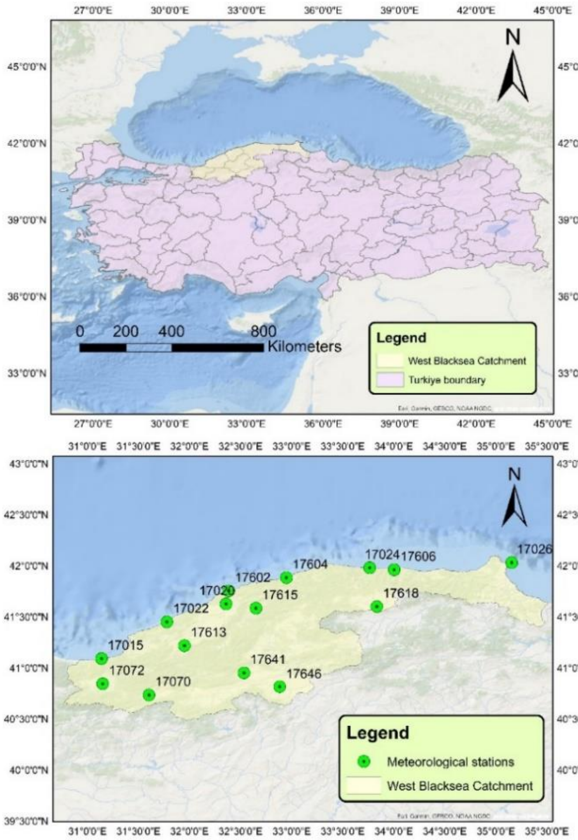

Figure1. The Western Black Sea basin (Türkiye

2.2. Statistical Data Imputation (Mean and Median)

The mean is obtained by summing all the values in the entire series and dividing by the number of data points. The mean of a series is calculated as shown in Equation 1.

$$\bar{x} = \frac{1}{n}\sum_{i=1}^{n} x_i \quad (1)$$

The median (middle) is the value that divides a series or sample data into two equal halves when sorted from lowest to highest.

2.3. Lineer Regression

The direction and degree of the relationship between two numerical variables can be determined through correlation analysis. In the scope of this study, Pearson correlation coefficients were calculated for the annual total rainfall series of the meteorological stations mentioned in the study. The identification of the independent variable for completing missing observations with Regression Analysis was done based on the Pearson correlation coefficient. For the meteorological station with missing observations (Y), the primary station (x) with the highest observed correlation at the same time is determined, and the missing data in the annual total rainfall series can be calculated using the traditional linear regression model provided in Eq. 3. In the research scope, a linear regression model is established between stations with missing data (Y) and meteorological stations without missing data (x). In the traditional regression model, monthly rainfall values observed simultaneously at the stations are used.

$$Y = \beta_0 + \beta_1 x + \xi \tag{3}$$

Where, Y, x, β_1 and ξ epresent the dependent and independent variables (simultaneously observed annual rainfall heights at the stations), regression coefficients, and the error term, respectively.

2.4. Inverse Distance Weighted Enterpolation

Inverse Distance Weighting (IDW) is a common interpolation technique that estimates values for unsampled points by considering nearby sampled points at varying distances. It calculates cell values based on proximity, where closer points hold more influence while points farther away have diminishing impact. IDW assesses data characteristics like distribution, trend, anisotropy, and clustering, making localized comparisons. This deterministic method is popular for weighted moving average interpolation.

The IDW estimator is represented as Equation 4,

$$z_p = \frac{\sum_{i=1}^{n}\left(\frac{z_i}{d_i^p}\right)}{\sum_{i=1}^{n}\left(\frac{1}{d_i^p}\right)} \tag{4}$$

The $z_p$location for predictions depends on neighboring measurements (i = 1, 2, ..., n) with p as the assigned range for each observation at location d. Increasing the exponent reduces the weight of observations farther from the prediction location, making predictions more closely resemble nearby observations (Taylan and Damçayırı, 2016). IDW interpolation is based on the principle that nearby points have a greater influence, performing interpolation from the point of interest by decreasing the weight as it moves away, relying on a weighted average of sample points (İlker et al., 2019).

2.5. Evaluation Metrics

In the validation of the models used, the following criteria have been utilized: proportionality bias (Eq. 5), percentage prediction error (PE%) (Eq. 6), root mean square error (RMSE) (Eq. 7), and mean absolute difference (MAD) (Eq. 8), as described by Ryan and Cryer (2005).

$$\boldsymbol{Bias} = \frac{\sum_{i=1}^{n}\left(\frac{\hat{x}_i - x_i}{x_i}\right)}{n} \; (4), \quad \boldsymbol{PE}_{\%} = \frac{\sum_{i=1}^{n}\left|\frac{\hat{x}_i - x_i}{x_i}\right| \times 100}{n} \quad (5)$$

$$\boldsymbol{RMSE} = \sqrt{\frac{\sum_{i=1}^{n}\left(\frac{\hat{x}_i - x_i}{x_i}\right)^2}{n}} \; (6), \quad \boldsymbol{MAD} = \frac{\sum_{i=1}^{n}|x_i - \hat{x}_i|}{n} \quad (7)$$

The rainfall values obtained from the stations for the month of July between 2019 and 2022 are represented by (x_i) while $\hat{x}_i$ represents the estimated rainfall values. In this context, n represents the number of missing data.

3. Results

The results of the IDW interpolation used to predict missing data between 2019 and 2022 are presented in Figure 2. The results of the accuracy assessment metrics for missing data predicted using statistical, regression, and IDW methods are presented in Table 2.

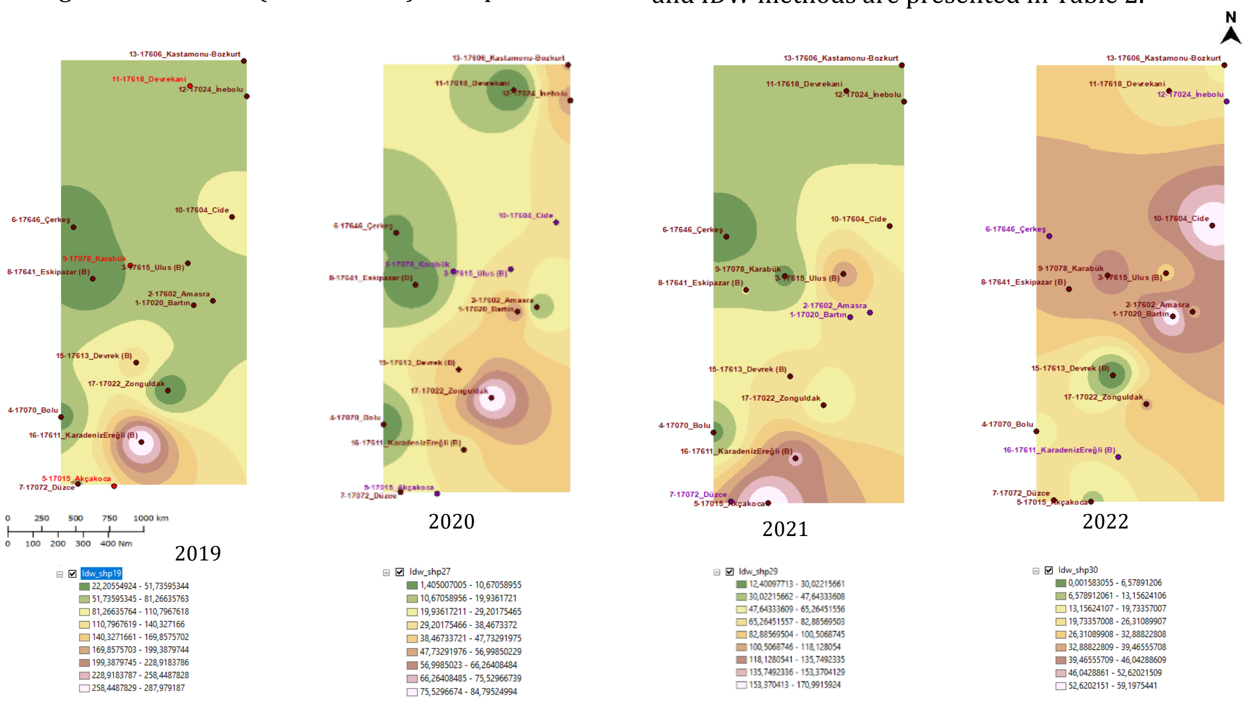

Figure 2. IDW Interpolation results

Tablo 2. Evaluation Metrics Results

Methods	Metrics.	Bartın	Amasra	Ulus	Akça koca	Çerkeş	Düzce	Cide	Devrekani	İnebolu	KaradenizE
Average	**Bias**	-0.40	-0.26	0.84	-0.36	-0.70	-0.73	**0.76**	-0.36	4.40	5.38
	PE%	39.81	25.91	**84.03**	36.34	70.30	73.39	131.16	36.22	439.80	537.80
	RMSE	0.40	0.26	**0.84**	0.42	0.70	0.73	3.13	0.36	4.40	5.38
	MAD	37.9	19.9	**12.1**	57.05	61	115.2	38.8	28.8	28.8	62.5
Median	**Bias**	-0.58	-0.50	2.33	-0.46	-0.75	-0.82	2.55	-0.57	2.94	4.92
	PE%	57.77	50	233.33	45.78	75.50	81.84	255.26	56.69	293.88	492.13
	RMSE	0.58	0.50	2.33	0.49	0.75	0.82	2.55	0.57	2.94	4.92
	MAD	55	38.4	33.6	57.05	61	117.2	38.8	28.8	28.8	62.5
Regression	**Bias**	-0.53	0.35	3.06	**-0.35**	-0.62	-0.78	0.80	**-0.17**	4.38	3.76
	PE%	53.15	34.77	305.56	**35.06**	61.63	77.72	**80.26**	**17.13**	437.76	375.59
	RMSE	0.53	0.35	3.06	**0.35**	0.62	0.78	**0.80**	**0.17**	4.37	3.76
	MAD	50.6	26.7	44	36.65	49.8	111.3	**12.2**	**8.7**	42.9	47.7
IDW	**Bias**	**-0.26**	**0.01**	**1.28**	-0.44	**-0.56**	**-0.14**	0.99	0.35	**1.39**	**0.74**
	PE%	**20.62**	**0.57**	127.85	43.55	**56.05**	**12.00**	99.54	34.76	**138.88**	**74.25**
	RMSE	**0.21**	**0.01**	1.28	0.62	**0.56**	**0.12**	0.99	0.35	**1.39**	**0.74**
	MAD	**19.63**	**0.44**	18.41	**36**	**45.29**	**17.19**	15.13	17.66	**13.61**	**9.43**

4. Discussion

When examining the results presented in Table 2, it can be observed that the best Bias value was obtained using the IDW method for the Bartın, Amasra, Ulus, Çerkeş, Düzce, Cide, İnebolu, and Karadeniz Ereğli station. The best Bias value for the Akçakoca was achieved with the regression method, and for Devrekani, it was also the regression method.

The lowest PE% value was obtained with the IDW method for the Bartın, Amasra, Çerkeş, Düzce, İnebolu, and Karadeniz Ereğli station. For Ulus station, the lowest PE% value was achieved using the average method, and for Akçakoca, Devrekani, and Cide station, it was the regression method.

In terms of RMSE, the IDW method produced the lowest value for the Bartın, Amasra, Çerkeş Düzce, İnebolu, and Karadeniz Ereğli station. The lowest RMSE value for the Ulus station was obtained using the average method, while the Akçakoca and Cide station achieved the lowest RMSE with the regression method, and the Devrekani station also had the lowest RMSE with the regression method.

IDW had the lowest MAD values for several stations, including Bartın, Amasra, Çerkeş, Düzce, İnebolu, and Karadeniz Ereğli, while the Ulus station achieved the lowest MAD using the average method. Akçakoca and Devrekani stations had their lowest MAD values with the IDW method, and Cide station with the regression method. Although the Ulus station performed well with the average method, the IDW method ranked second. Stations like Cide and İnebolu saw better results with the regression model, where IDW was the second-best method. Differences in station results can be attributed to factors such as elevation, rainfall distribution, and inter-station correlations. In general, considering all the results, it has been observed that the IDW method generally produces better results compared to other methods in completing missing data.

5. Conclusion

In this study, for a dataset created by randomly removing rainfall data from 10 different stations in the Western Black Sea Basin between 2019 and 2022, missing data were estimated using statistical methods (mean and median), regression, and IDW techniques. When measuring the accuracy of the models created according to four different evaluation metrics, IDW produced the best results in 6 out of 10 stations. For the other stations, the second-best performing method is again IDW.

References

Albayrak, M., Turhan, K., & Kurt, B. (2017, October). A missing data imputation approach using clustering and maximum likelihood estimation. In 2017 Medical Technologies National Congress (TIPTEKNO), 1-4

Bakış, R., & Göncü, S. (2015). Akarsu debi ölçümlerinde eksik verilerin tamamlanması: Zap Suyu Havzası örneği.

Erken, Ş., & Şenyay, L. (2023). Makine Öğrenmesi İle Eksik Veri Tamamlama Yöntemlerinin Sınıflandırma Performansına Etkileri. Kayseri Üniversitesi Sosyal Bilimler Dergisi, 5(1), 51-71.

Gümüş, V., & Kavşut, M. E. (2013). Zamanti Nehri-Ergenusağı Đstasyonu Eksik Aylık Akım Verilerinin Tahmini. Gazi University Journal of Science Part C: Design and Technology, 1(2), 81-91

İlker, A., Terzi, Ö., & Şener, E. (2019). Yağışın Alansal Dağılımının Haritalandırılmasında Enterpolasyon Yöntemlerinin Karşılaştırılması: Akdeniz Bölgesi Örneği. Teknik Dergi, 30(3), 9213-9219.

Ryan, B. F. & Cryer, J. (2005). Minitab Handbook. Fifth Edition,Regression and Correlation, 313-349, Belmont,California, p.505.

Şeker, Ş. E., & Eşmekaya, E. (2017). Eksik verilerin tamamlanması (imputation). YBS Ansiklopedi, 4(3), 10-17.

Taylan, E. D., & Damçayiri, D. (2016). Isparta bölgesi yağış değerlerinin IDW ve Kriging enterpolasyon yöntemleri ile tahmini. Teknik Dergi, 27(3), 7551-7559.

Yumuş, M., Apaydın, M., Değirmenci, A., & Karal, Ö. (2020, October). Missing data imputation using machine learning based methods to improve HCC survival prediction. 28th Signal Processing and Communications Applications Conference (SIU), 1-4.

7th Intercontinental Geoinformation Days

igd.mersin.edu.tr

Monitoring gully erosion from UAV data

Yunus Kaya*[1], Nizar Polat[1]

[1]*Harran University, Faculty of Engineering, Department of Geomatics Engineering, Şanlıurfa, Türkiye*

Keywords
UAV
Photogrammetry
Gully erosion
Monitoring

Abstract

Gully erosion is recognized as an important process of land degradation. Continuous monitoring of gully erosion is important to determine the damage caused to the land. Terrestrial imaging systems such as handheld cameras are inadequate for monitoring gully erosion damage. Aerial surveys by Unmanned Aerial Vehicles (UAVs) play an important role in monitoring gully erosion. The aim of this paper is to monitor gully erosion with digital photogrammetry technique using UAV data. In this study, Digital Elevation Model (DEM) and orthophoto were produced with UAV data and the directions of gully erosion were determined. This study is also a preliminary study to determine the multi-temporal change of gully erosion.

1. Introduction

Erosion is an important phenomenon that accounts for 9% of disasters in the world (Galli et al., 2008). Erosion is defined as the movement of soil by wind, rain, floods, etc. and is most common in hilly and mountainous areas (Cruden and Varnes, 1996; Roy and Saha, 2019). Gullies are a typical form of erosion in semi-arid and arid landscapes where high morphological activity and dynamics can be observed (Marzolff and Poesen, 2009). Semi-arid and arid climatic conditions increase the risk of soil erosion through low rainfall regimes, low vegetation cover and recurrent heavy rainfall. Low rainfall and irregular rainfall frequency and distribution, deforestation and low biomass lead to very high amounts of runoff. In addition, the transition from traditional agriculture to a more irregular land use accelerates soil runoff, increasing the risk of erosion. In these areas, gullies are the source and carrier of sediment connecting slopes and channels. Poesen et al. (2002) reported that in semi-arid and arid regions gullies contribute between 50% and 80% to sediment production.

A detailed knowledge of landform and topography allows for various geomorphometric characterizations, calculation of different indices, and understanding of the processes that shape the earth's surface (Tarolli et al., 2019). Various new technologies used in geomorphology have developed a new perspective for field research and visualization of findings. Digital photogrammetry and Structure from Motion (SfM), accurate and cost-effective Digital Elevation Model (DEM) production (Uysal et al., 2015), and high-resolution orthophoto generation (Akca and Polat, 2022) have enabled real-scale and photorealistic visualization of terrains and geomorphological structure in a digital environment (Piegay et al., 2015; Viles, 2016; Polat, 2023). DEMs and orthophotos derived from UAV imagery are used in various earth observation surveys due to their sub-meter resolution and relatively high accuracy in representing the terrain structure (Vanmaercke et al., 2016; Passalacqua et al., 2015). High-resolution DEMs and orthophotos are also frequently used to study gully erosion processes (Nagasaka et al., 2005; Niculiță et al., 2020; Wang et al., 2022). Gong et al. (2019) used SfM technology with UAV data to study gully erosion in an open-cast coal mine dumpsite. In the study, they produced high-resolution orthophotos and DEMs and determined the slopes in the gully erosion zones. Kou et al. (2019) examined the erosion of typical gully heads with UAV data to determine rill erosion. They determined the slopes of upland slope, hill slope and vegetation slope using Digital Surface Model (DSM).

In this study, gully erosion in a region northeast of Şanlıurfa city center was monitored with UAV data. The study provides preliminary information for future multi-temporal gully erosion analysis.

* **Corresponding Author**

*(yunuskaya@harran.edu.tr) ORCID ID 0000-0003-2319-4998
(nizarpolat@harran.edu.tr) ORCID ID 0000-0002-6061-7796

Cite this study

Kaya, Y., & Polat, N. (2023). Monitoring gully erosion from UAV data. Intercontinental Geoinformation Days (IGD), 7, 184-186, Peshawar, Pakistan

2. Methods

UAV technology has been used frequently in landslide (Kuşak et al. 2021), rockfall (Yakar et al. 2023) and cultural heritage studies (Şasi and Yakar, 2017; Alptekin and Yakar, 2021; Karataş et al. 2022; Kanun et al. 2022) in the last decade.

In the region selected as the study area, a flight was performed from a height of 110 m with a DJI Mavic 2 Pro UAV. The flights were performed in automatic grid mode and a total of 251 photographs were taken for the entire study area. In addition, Ground Control Points (GCPs) homogeneously located in the study area were established to produce high resolution orthophotos and DEMs. The photographs obtained from UAV flights and GCP coordinates were evaluated using Agisoft Photoscan software. One of the most important steps of the photogrammetry method is the determination of camera calibrations. In this study, the photographs were calibrated with the self-calibration method using the parameters in the Agisoft software. In order to process the images at a scale of 1:1, the align photos step was performed at high quality. Afterwards, the model was georeferenced by matching the points collected from the field with the points appearing in the software. Since the quality of the DEM is affected by the dense point cloud produced, the dense point cloud was produced with high accuracy. Then the orthomosaics and DEMs of the terrain were exported in high quality. The obtained orthophotos and DEMs were combined in Virtual Surveyor software and flow directions were determined.

3. Results

In this study, point cloud and dense point cloud were produced by evaluating 251 photographs obtained with UAV and 6 GCPs together. The parameters of the DEM and orthophoto produced in the study are given in Table 1, orthophoto in Figure 1 and DEM in Figure 2.

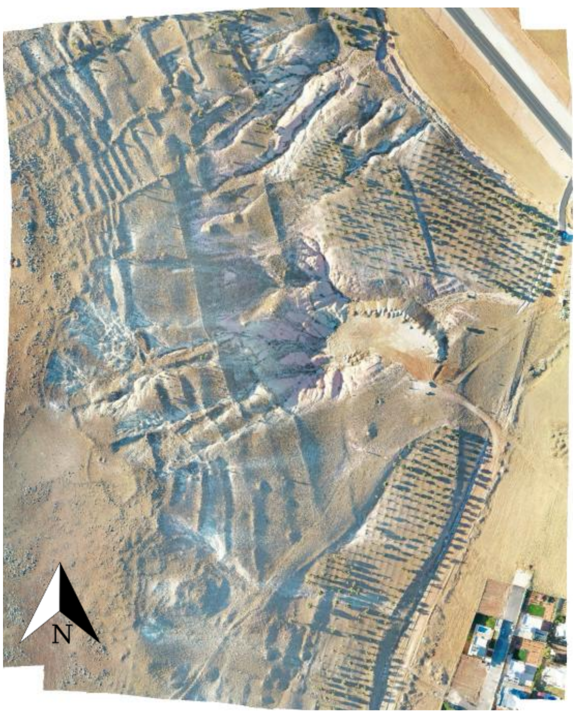

Figure 1. Orthophoto

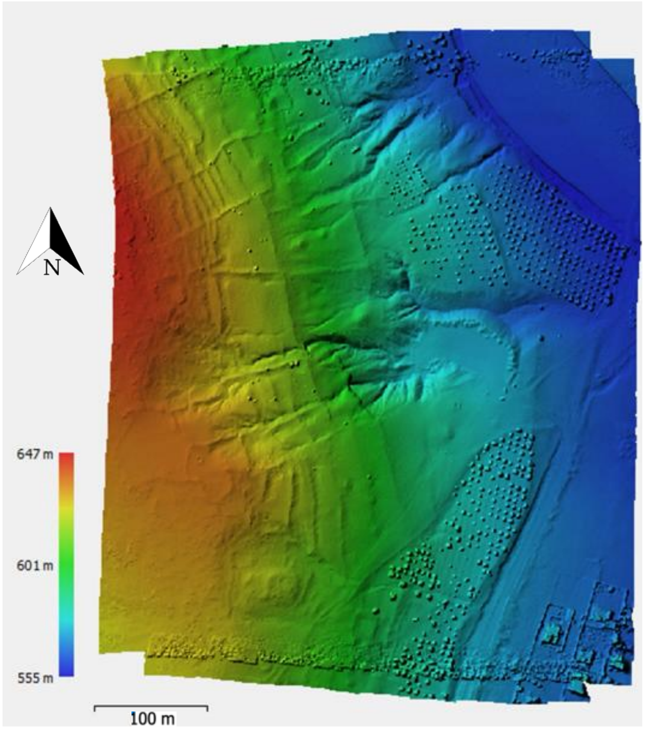

Figure 2. Digital Elevation Model

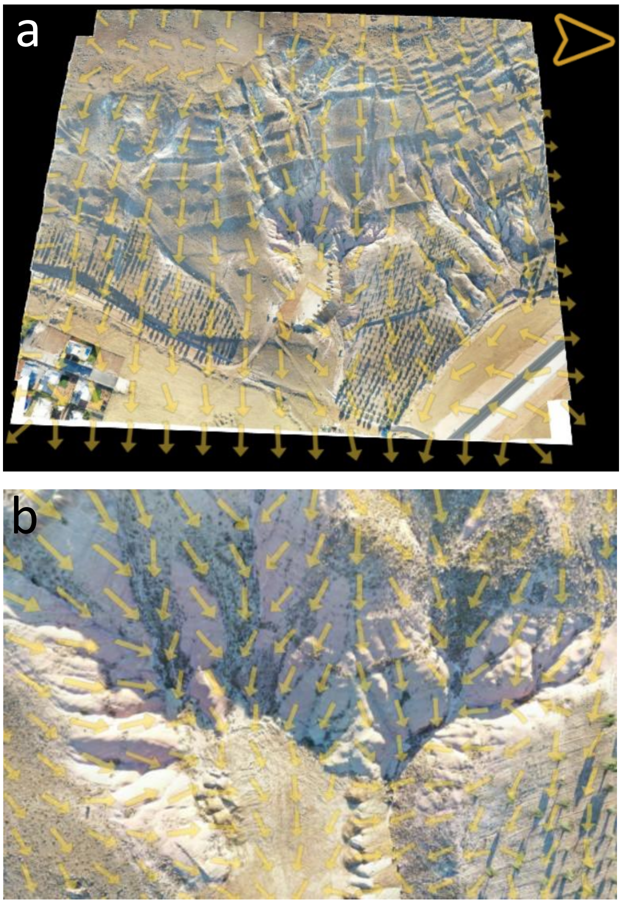

Figure 3. Flow directions, a) General view, b) gully erosion area

Flow directions were determined in Virtual Surveyor software using high resolution orthophoto and DEM (Figure 3).

When Figure 3b is examined, more gully erosion is observed where the flow lines show common orientation. The flow lines have a greater slope in windy areas.

Table 1. Flight and model parameters

Parameter	Value
Flight Area	0.288 km^2
Overlap	80
Camera Angle	90°
Average Altitude	112
Number of Photos Taken	251
Number of Photos Used	251
Planned GSD (cm/pixel)	2.46 cm/pix
DEM Resolution (cm/pixel)	4.91
Point density (points/m^2)	414
Point Cloud Number	4 972 675
Dense Point Cloud Number	135 284 980

4. Conclusion

In this study, monitoring of the erosion zone in the gully erosion region was carried out with UAV photogrammetry. In the study, high resolution DEM and orthophotos were produced from UAV data evaluated together with GCPs. The produced orthophotos and DEMs were visualized in Virtual Surveyor software and flow directions were determined. Since the region is a windy and rainy region, gully erosion is intensely observed in the region. This study includes the first stage of multi-temporal gully erosion analysis. In future studies, the amount of erosion will be determined with measurements made in different seasons and different years and the causes of erosion will be investigated. This study emphasizes the importance of using UAV data in gully erosion areas.

References

Akca, S., & Polat, N. (2022). Semantic segmentation and quantification of trees in an orchard using UAV orthophoto. Earth Science Informatics, 15(4), 2265-2274.

Alptekin, A., & Yakar, M. (2021). 3D model of Üçayak Ruins obtained from point clouds. Mersin Photogrammetry Journal, 3(2), 37-40.

Cruden, D. M., & Varnes, D. J. (1996). Landslides: investigation and mitigation. Chapter 3-Landslide types and processes. Transportation research board special report, (247).

Galli, M., Ardizzone, F., Cardinali, M., Guzzetti, F., & Reichenbach, P. (2008). Comparing landslide inventory maps. Geomorphology, 94(3-4), 268-289.

Gong, C., Lei, S., Bian, Z., Liu, Y., Zhang, Z., & Cheng, W. (2019). Analysis of the development of an erosion gully in an open-pit coal mine dump during a winter freeze-thaw cycle by using low-cost UAVs. Remote Sensing, 11(11), 1356.

Kanun, E., Alptekin, A., Karataş, L., & Yakar, M. (2022). The use of UAV photogrammetry in modeling ancient structures: A case study of "Kanytellis". Advanced UAV, 2(2), 41-50.

Karataş, L., Alptekin, A., & Yakar, M. (2022). Detection and documentation of stone material deterioration in historical masonry structures using UAV photogrammetry: A case study of Mersin Aba Mausoleum. Advanced UAV, 2(2), 51-64.

Kusak, L., Unel, F. B., Alptekin, A., Celik, M. O., & Yakar, M. (2021). Apriori association rule and K-means clustering algorithms for interpretation of pre-event landslide areas and landslide inventory mapping. Open Geosciences, 13(1), 1226-1244.

Marzolff, I., & Poesen, J. (2009). The potential of 3D gully monitoring with GIS using high-resolution aerial photography and a digital photogrammetry system. Geomorphology, 111(1-2), 48-60.

Niculiță, M., Mărgărint, M. C., & Tarolli, P. (2020). Using UAV and LiDAR data for gully geomorphic changes monitoring. In Developments in earth surface processes (Vol. 23, pp. 271-315). Elsevier.

Passalacqua, P., Belmont, P., Staley, D. M., Simley, J. D., Arrowsmith, J. R., Bode, C. A., ... & Wheaton, J. M. (2015). Analyzing high resolution topography for advancing the understanding of mass and energy transfer through landscapes: A review. Earth-Science Reviews, 148, 174-193.

Piégay, H., Kondolf, G. M., Minear, J. T., & Vaudor, L. (2015). Trends in publications in fluvial geomorphology over two decades: A truly new era in the discipline owing to recent technological revolution?. Geomorphology, 248, 489-500.

Polat, N. (2023). An Investigation of Ancient Water Collection and Storage Systems Near the Karahantepe Neolithic Site Using UAV and GIS. Environmental Archaeology, 1-13.

Roy, J., & Saha, S. (2019). Landslide susceptibility mapping using knowledge driven statistical models in Darjeeling District, West Bengal, India. Geoenvironmental Disasters, 6(1), 1-18.

Şasi, A., & Yakar, M. (2017). Photogrammetric modelling of sakahane masjid using an unmanned aerial vehicle. *Turkish Journal of Engineering*, *1*(2), 82-87.

Tarolli, P., Cao, W., Sofia, G., Evans, D., & Ellis, E. C. (2019). From features to fingerprints: A general diagnostic framework for anthropogenic geomorphology. Progress in Physical Geography: Earth and Environment, 43(1), 95-128.

Uysal, M., Toprak, A. S., & Polat, N. (2015). DEM generation with UAV Photogrammetry and accuracy analysis in Sahitler hill. Measurement, 73, 539-543.

Vanmaercke, M., Poesen, J., Van Mele, B., Demuzere, M., Bruynseels, A., Golosov, V., ... & Yermolaev, O. (2016). How fast do gully headcuts retreat?. Earth-Science Reviews, 154, 336-355.

Viles, H. (2016). Technology and geomorphology: Are improvements in data collection techniques transforming geomorphic science?. Geomorphology, 270, 121-133.

Wang, R., Sun, H., Yang, J., Zhang, S., Fu, H., Wang, N., & Liu, Q. (2022). Quantitative evaluation of gully erosion using multitemporal UAV data in the southern black soil region of Northeast China: A case study. Remote Sensing, 14(6), 1479.

Yakar, M., Ulvi, A., Yiğit, A. Y., & Alptekin, A. (2023). Discontinuity set extraction from 3D point clouds obtained by UAV Photogrammetry in a rockfall site. Survey Review, 55(392), 416-428

7th Intercontinental Geoinformation Days

igd.mersin.edu.tr

Evaluating the ground point classification performance of Agisoft Metashape Software

Nizar Polat *1, **Abdulkadir Memduhoğlu** 1, **Yunus Kaya** 1

1Harran University, Faculty of Engineering, Department of Geomatics Engineering, Şanlıurfa, Türkiye

Keywords
UAV
Photogrammetry
Point cloud
Filtering
CSF

Abstract

This paper investigates the complex process of extracting bare land surfaces from point clouds, with a particular focus on filtering out objects such as trees, buildings, and vehicles. It underscores the importance of this task in diverse domains, including cadastral surveying, base mapping, and various geographical sciences, all while excluding specific reference to LiDAR and GIS applications. The research provides an extensive exploration of different algorithms used for point cloud filtering, culminating in a comprehensive evaluation of Agisoft's ground point filtering algorithm in contrast to the well-recognized CSF method. For this comparison, an Unmanned Aerial Vehicle (UAV) flight was performed at Harran University's Osmanbey campus to generate the necessary point cloud. The results of this assessment reveal that a significant portion of the obtained points pertains to ground points, underscoring the efficacy of the filtering process in producing Digital Terrain Models (DTMs). The numerical findings demonstrate that the overall accuracy stands at 0.002, with minimal Type I and Type II errors, reaffirming the robust performance of the filtering algorithms in producing accurate DTMs.

1. Introduction

DTM is a valuable data source for various applications, as noted by Polat and Uysal in (2015). The extraction of bare earth surfaces from point clouds is a multifaceted endeavor. While many studies in surveying, mapping, and topography predominantly focus on natural landscapes, they tend to overlook artificial structures and vegetation. However, in disciplines like cadastral surveying, topographic mapping, and Geographical Information Science (GIS) applications, the imperative to filter out objects such as trees, shrubs, buildings, and vehicles becomes evident.

The creation of a DTM involves the initial step of filtering point clouds to isolate the topography of the bare earth surface. Point cloud filtering entails the removal of points associated with above-ground features like trees, buildings, and bridges, among others. This process is generally challenging, and its success depends on various factors, including topography, the chosen point cloud filtering method, the size and shape of above-ground objects and the expertise of the operator (Yilmaz and Güngör, 2021).

Numerous algorithms have been developed for filtering LiDAR-derived point clouds, with a common goal of distinguishing ground and non-ground points. While these algorithms do not always achieve perfect results, they typically yield accurate filtering outcomes, exceeding 90% accuracy (Zeybek and Şanlıoğlu, 2019). One method involves progressive triangulation to create a sparse TIN iteratively based on the lowest seed points (Axelsson, 2000). The CSF (Cloth Simulation Filter) technique is fundamentally based on the principle of emulating how a fabric-like material behaves when applied to an inverted land surface (Zhang et al., 2016). Mathematical morphology techniques are also employed, utilizing operations like opening, closing, dilatation, and erosion (Liu, 2008; Zhang et al., 2003).

The choice of kernel size is a critical parameter for non-ground point detection. Furthermore, slope-based filtering identifies points with large height differences between neighboring points as non-ground, where high points typically represent non-ground and low points represent the ground (Vosselman, 2000).

The extensive utilization of UAVs has led to a significant increase in the adoption of photogrammetric point clouds as an alternative to LiDAR. To speed up DTM generation from such data, photogrammetric software has begun to incorporate point cloud classification capabilities. Notably, the renowned Agisoft Metashape

* **Corresponding Author**

*(nizarpolat@harran.edu.tr) ORCID ID 0000-0002-6061-7796
(akadirm@harran.edu.tr) ORCID ID 0000-0002-9072-869X
(yunuskaya@harran.edu.tr) ORCID ID 0000-0003-2319-4998

Cite this study

Polat N, Memduhoğlu A. & Kaya Y (2023). Evaluating the Ground Point Classification Performance of Agisoft Metashape Software. Intercontinental Geoinformation Days (IGD), 7, 187-190, Peshawar, Pakistan

software, among other commercial solutions, now provides the ability to classify point clouds generated from aerial images. This study aims to evaluate and compare the performance of Agisoft's ground point filtering algorithm with the well-established CSF algorithm documented in the literature.

UAV technology has been used frequently in landslide (Kuşak et al. 2021), rockfall (Yakar et al. 2023) and cultural heritage studies (Alptekin and Yakar, 2021; Karataş et al. 2022; Kanun et al. 2022) in the last decade.

2. Method

2.1. Agisoft Metashape Ground Points Classification

In the context of ground point classification, Agisoft Metashape introduces an innovative approach designed to enhance the efficiency of manual labor (Kanun et al. 2021). This method is structured as a two-step process. In the initial phase, the point cloud segmentation into cells of predefined dimensions, facilitating the identification of the lowest point within each cell. The triangulation of these identified lowest points culminates in the primary approximation of the terrain model. In the subsequent phase, new points are allocated to the ground class contingent upon two fundamental criteria. Firstly, they must demonstrate proximity to the terrain model within a stipulated range. Secondly, the angle formed between the terrain model and the connecting line between these new points and an existing ground point must not surpass a predetermined threshold angle. This iterative second step endures until all data points have undergone comprehensive evaluation (URL 1).

2.2. Cloth Simulation Filter (CSF)

The Cloth Simulation Filter (CSF) methodology, as detailed by Zhang et al. (2016), is fundamentally grounded in the concept of simulating the behavior of a fabric-like material placed upon an inverted land surface. Within this simulation, the configuration of the fabric effectively serves as the foundation for constructing the DTM corresponding to the specified geographical area.

The initial step in the CSF method involves the inversion of the point cloud dataset. Subsequently, a pivotal user-defined parameter, referred to as the grid resolution, is introduced to determine the quantity of cloth particles to be released onto the dataset. These points and particles are subsequently projected onto a horizontal plane, where each cloth particle is associated with a corresponding point within this plane. The intersection of each cloth particle with the underlying terrain results in the determination of its height, denoted as the 'intersection height value. If the intersection height value exceeds the current height value, the particle is repositioned to align with the intersection height value and is categorized as immovable, as described by Zhang et al., in (2016).

Throughout the iterative process, the CSF method calculates the distances between the point cloud and the cloth particles, with any point exhibiting a distance greater than a user-defined threshold, commonly known as the 'class threshold parameter,' being classified as a non-ground point, aligning with the findings of Zhang et al. (2016). The movement of the cloth particles is influenced by both internal and external forces, with gravity being a significant external force. This movement continues until the desired height variation, or a predefined maximum number of iterations is achieved. In addition to the parameters delineated above, the CSF methodology integrates two further parameters, namely the time step and rigidness: The former parameter governs the control of particle movements, while the latter parameter is instrumental in specifying the terrain type.

2.3. Accuracy Analysis

In this study, an assessment of the filtering methods was conducted, involving the calculation of error type I, error type II, and overall accuracy to gauge their effectiveness.

$$Type\ I = \frac{\alpha}{\mathrm{Ref}_g} ,$$

$$Type\ II = \frac{\beta}{Ref_{ng}}$$

$$Everall\ Accuracy\ = \frac{\alpha+\beta}{\mathrm{Ref}_g\ + Ref_{ng}}$$

In this context, where α represents ground points misclassified as non-ground points, β represents non-ground points misclassified as ground points, and Ref_g and Ref_{ng} indicate the counts of the ground and non-ground reference point sets, the filtering method's performance is assessed by comparing the obtained classification with reference data.

3. Results and Discussion

In the study, a dense point cloud was obtained using aerial photographs. The visualization of the obtained point cloud is given in the Figure 1.

Figure 1. Raw point cloud of the study area.

As can be seen in Figure 1, the ground points, and non-ground objects (such as trees and buildings) points are clearly visible in the dataset. This raw point cloud with points belonging to all objects was filtered with the help of the CSF algorithm. At this stage, grid resolution (grid size) is 0.5 m, iteration 500 and classification threshold is 0.2. Accordingly, the obtained ground points are given in the Figure 2.

Figure 2. Ground points obtained using the CSF algorithm.

As can be seen from the CSF filtering result image given in Figure 2, the above ground points were removed and only the ground points that will form DTM were obtained. This data will be used as a reference. In the continuation of the study, this raw point cloud with points belonging to all objects was filtered with the approach in Agisoft Metashape itself and only ground points were obtained and presented in Figure 3.

Figure 3. Ground points obtained from Agisoft.

According to Figure 3, mostly ground points were obtained succesfully. Raw data, reference data and Agisoft Metashape filtering results are given in Table 1.

Table 1. Raw data and filtering results.

	Data	Points	Min Z (m)	Max Z (m)
	Raw	23 362 221	498.431	522.891
(CSF)	Ground Reference	16 035 473	498.630	509.739
	Non-Ground Reference	7 326 748	498.431	522.891
Agisoft Metashape	Ground	15 996 027	498.431	520.152
	Non-Ground	7 336 194	498.80	522.871

According to Table 1 α (9 446 points) and β (39 446 points) values were obtained. Then type I and type II errors are calculated as 0.0006 error 0.005 respectively. The overall accuracy is found as 0.002.

4. Conclusion

This investigation has revolved around the evaluation of ground point classification techniques, particularly focusing on the performance of Agisoft Metashape software. The significance of DTMs as a fundamental data source for diverse applications was underscored, emphasizing the critical task of extracting bare earth surfaces from point clouds while excluding specific reference to LiDAR and GIS applications.

The study examined Agisoft Metashape and CSF algorithms, designed for filtering point clouds to distinguish between ground and non-ground points, a task that is essential in diverse fields, including cadastral surveying, topographic mapping, and GIS. The research encompassed the renowned Agisoft Metashape software, which has ventured into point cloud classification, to streamline the DTM generation process. Through a thorough evaluation, the performance of Agisoft Metashape's ground point filtering algorithm was compared with the widely recognized CSF methodology. The results illustrated that the Agisoft Metashape algorithm predominantly produced ground points, successfully eliminating above-ground features. The assessment, involving error type I, error type II, and overall accuracy calculations, further substantiated the robustness of the filtering algorithms.

In conclusion, this study contributes valuable insights into point cloud filtering techniques that are instrumental in producing accurate DTMs. The extensive utilization of photogrammetric point clouds, facilitated by software like Agisoft, signifies a promising avenue for DTM generation in various applications, further advancing the field of terrain modeling and point cloud analysis.

References

Alptekin, A., & Yakar, M. (2021). 3D model of Üçayak Ruins obtained from point clouds. Mersin Photogrammetry Journal, 3(2), 37-40.

Axelsson, P. (2000). DEM generation from laser scanner data using adaptive TIN models. International archives of photogrammetry and remote sensing, 33(4), 110-117.

Kanun, E., Alptekin, A., & Yakar, M. (2021). Documentation of cultural heritage by photogrammetric methods: a case study of Aba's Monumental Tomb. *Intercontinental Geoinformation Days*, *3*, 168-171.

Kanun, E., Alptekin, A., Karataş, L., & Yakar, M. (2022). The use of UAV photogrammetry in modeling ancient structures: A case study of "Kanytellis". Advanced UAV, 2(2), 41-50.

Karataş, L., Alptekin, A., & Yakar, M. (2022). Detection and documentation of stone material deterioration in historical masonry structures using UAV photogrammetry: A case study of Mersin Aba Mausoleum. Advanced UAV, 2(2), 51-64.

Kusak, L., Unel, F. B., Alptekin, A., Celik, M. O., & Yakar, M. (2021). Apriori association rule and K-means clustering algorithms for interpretation of pre-event landslide areas and landslide inventory mapping. Open Geosciences, 13(1), 1226-1244.

Liu, X. (2008). Airborne LiDAR for DEM generation: some critical issues. Progress in physical geography, 32(1), 31-49.

Polat, N., & Uysal, M. (2015). Investigating performance of Airborne LiDAR data filtering algorithms for DTM generation. Measurement, 63, 61-68.

URL1:https://agisoft.freshdesk.com/support/solutions/articles/31000160729-parameters-for-ground-point-classification

Vosselman, G. (2000). Slope based filtering of laser altimetry data. International archives of photogrammetry and remote sensing, 33(B3/2; PART 3), 935-942.

Yakar, M., Ulvi, A., Yiğit, A. Y., & Alptekin, A. (2023). Discontinuity set extraction from 3D point clouds obtained by UAV Photogrammetry in a rockfall site. Survey Review, 55(392), 416-428

Yilmaz, Ç. Ş., & GÜNGÖR, O. (2021). The Effect of Point Density on Point Cloud Filtering Performance. Turkish Journal of Remote Sensing and GIS, 2(1), 41-46.

Zeybek, M., & Şanlıoğlu, İ. (2019). Point cloud filtering on UAV based point cloud. Measurement, 133, 99-111.

Zhang, K., Chen, S. C., Whitman, D., Shyu, M. L., Yan, J., & Zhang, C. (2003). A progressive morphological filter for removing nonground measurements from airborne LIDAR data. IEEE transactions on geoscience and remote sensing, 41(4), 872-882.

Zhang, W., Qi, J., Wan, P., Wang, H., Xie, D., Wang, X., & Yan, G. (2016). An easy-to-use airborne LiDAR data filtering method based on cloth simulation. Remote sensing, 8(6), 501.

7th Intercontinental Geoinformation Days

igd.mersin.edu.tr

The effect of segmentation parameters on extracting the crown area of Tehran pine trees (Pinus eldarica)

Ali Hosingholizade *[1], Seyed Kazem Alavipanah [1] Parviz Zeaiean Firouzabadi [2]

[1]*Tehran, Geography, Remote sensing and GIS, Tehran, Iran*
[2]*Kharazmi University, Geography, Remote sensing and GIS, Tehran, Iran*

Keywords
RGB Image
Segmentation
Pine tree
Drone
Bojnord

Abstract

Man_made forests have been created with ecological goals such as preserving water and soil resources and economic goals such as wood production. These forests help reduce pressure on natural forests. Therefore, knowledge of the state of quantitative and qualitative features of the forest has always been of interest to the managers of these types of forests and to help them in future planning and achieving primary goals. The purpose of this research is to compare the crown area of Eldarica pine trees in Pardisan Park, North Khorasan province with the change of density parameters in stages 0.1, 0.3, 0.5, 0.7, 0.9, 1 , scale in stages 0.1,0.5,0.7,0.9 and Shape in stages 25, 50, 100 ,150. The results showed that the change in each of the parameters brings different results in the estimation of the tree's crown surface. Also, the results showed that the best result was obtained in (density=0.5, scale=25, shape=0.1) and the worst result in (shape=0.9, compactness=0.1, scale=150).

1. Introduction

Each of the physical parameters of trees in forests is important for careful monitoring and management. Accurate and efficient measurement of single tree parameters is the basis of man-made forest resource monitoring (Husingolizadeh et al., 2023). With the rapid development of remote sensing technology, it has become possible to obtain information on vast forests and monitor the growth and determine the physical parameters of forest trees with greater speed and efficiency. Remote sensing captures a complete image in its viewing angle by recording the landscape. Therefore, every visible feature, including the position of the complication and the position relative to other complications, is provided for the user. Depending on the conditions and purpose, this complete image can be used together with in_situ measurements to create a valuable perspective on solving some issues on aspects of forest management (Hassingolizadeh et al., 2023). Also, with access to remote sensing data, a wide range of spatial and temporal scales are often available to users. In addition, massive data archives allow us to explore more forest issues from the past to the present (Zhu et al., 2018). Remote sensing images have a high degree of homogeneity and collect data in relatively stable conditions without human intervention in coniferous forests (Duarte et al., 2020). Although the study of forest and trees using remote sensing techniques is considered one of the active areas for research, some physical parameters at the single tree level are problematic (Onishi and Lse., 2021).

With all the capabilities of remote sensing in the forests, sometimes satellite remote sensing cannot observe with proper accuracy due to technical limitations. One of the most important of these limitations and obstacles is the lack of timely data collection in the target areas (Zhang and Jim, 2013). Among them, it can be mentioned that satellite data with medium or low resolution is not suitable for many research fields (Tang and Shao, 2015). On the other hand, height measurement, diameter at breast height and precise measurement of tree crown dimensions are considered as basic physical quantities in forest management (Bukalo et al., 2013).

Despite the valuable research that has been done in the past (Ahmad et al., 2021), so far, no study has been conducted to investigate the effect of segmentation parameters. In this research, the scale parameter is determined to determine the existing objects based on the homogeneity or heterogeneity of the area.

* **Corresponding Author**

*(a.hosingholizade@ut.ac.ir) ORCID ID 0000 – 0001 – 5286 – 1361
(salavipa@ut.ac.ir) ORCID ID 0000-0000-0000-0000
(zeaiean@khu.ac.ir) ORCID ID 0000-0001-8407-5605

Cite this study

Hosingholizade, A, Alavipanah, S. K., & Firouzabadi, Z. P. (2023). The effect of segmentation parameters in RGB images on extracting the crown area of Tehran pine trees (Pinus eldarica). Intercontinental Geoinformation Days (IGD), 7, 191-194, Peshawar, Pakistan

2. Method

2.1. Study area

Pardisan Park of North Khorasan is located at the eighth kilometer of Bojnord-Mashhad road (37° 28 ' 57 N "-57° 25 ' 49 " E, Zone 40 N), at an average altitude of 1080 meters above sea level. This complex is purely covered with Tehran pine (Pinus eldarica). The region is cold semi-arid according to the coupon criteria and has a relatively high slope in terms of topography (altitude range 1112 to 1037 meters). The average rainfall and its temperature according to the statistics of Bojnurd Airport Meteorological Synoptic Station (the closest station to the study area) for a period of 10 years (2011-2021) are 260 mm and 15 ° C, respectively.

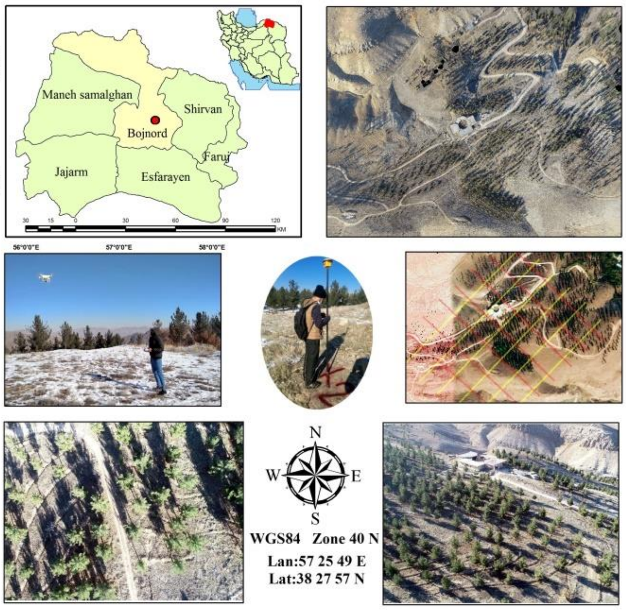

Figure 1. IRAN and Pardisan park

2.2. Research method

In this study, a Phantom 4 Pro was used for the image collection. In the first stage, the planning and design of the flight route was done by visiting the local area and obtaining the necessary permits. In the selection of the flight path, due to the decrease in the number of flight paths and selection of areas with less movement of drone, the design with a longer flight path was considered. In choosing the right day and time of flight, was also considered to control the weather conditions, especially the wind speed of less than one knot.

In order to prevent the stretching of the image and the effect of the intense light of the horizon, the parameters affecting the images, including the opening angle (Field of View<500) and the overall speed of the drone (4 m/s) were adjusted. Before the flight operation, 14 ground control points were established with proper distribution in the area. Then, according to the ups and downs of the ground and control of other effects in the area from a height of 40 meters and the longitudinal and transverse coverage of 80 and 40 percent, flight operations were carried out to receive RGB images. During the entire flight operation, by keeping the bird's balance sensor active (Tilt Sensor<50), taking pictures with a high tilt angle was prevented. In the next step, the images were processed. At this stage, by performing the necessary preprocessing, the three-dimensional model of the Eldarica pine trees of the region was obtained. Then, the images were processed by changing and dividing the parameters including Compactness, Scale Parameter and Shape in Ecognition V9.1. By changing each of the stated parameters, different areas for the tree crown were obtained, which were compared with in situ measurements. Figure 1 shows the location of the research and Figure 2 shows its steps.

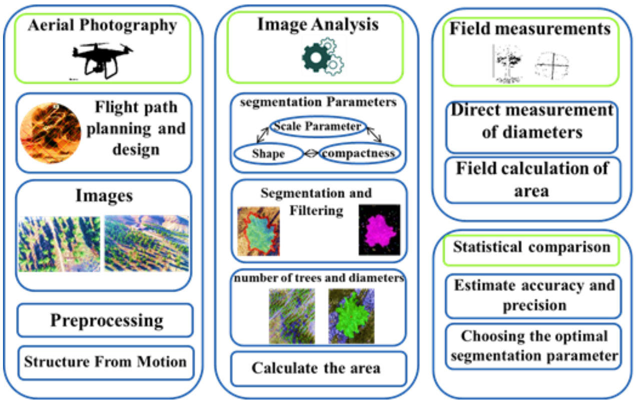

Figure 2. The general steps used to of conduct this research

3. Result

Pine trees with different crown areas were directly measured in the field and photographed by UAV. The field measurements summarized in the study area shown in Table 1.

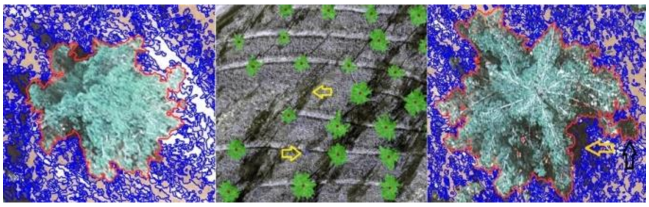

Figure 3. Right side image (black arrow: wrong detection of the shadow instead of the crown, orange arrow: correct detection of the shadow and removing it from the crown area) The middle image (removing the shadow effect and correctly identifying the area of the crown in the top view). The image on the left (a sample of the crown of a tree with the correct recognition of the crown)

The shadow effect misrecognizing a tree crown or not recognizing the real area of the crown (the part that is actually part of the crown area) (Figure 3), the amount of the area has undergone major changes. To solve this problem, the use of cloud points with a suitable filter and imaging at noon (due to the shorter shadow) can partially solve the effect of wrong detection. In Table 1, the red highlight shows the worst result and the green highlight shows the best result.

Table 1. The average area of the canopy of Eldarica pine trees in different parameters (numbers are rounded up)

Average measured value (Square meters)	Crown Area	Scale	Shape	Compactness	Crown Area	Scale	Shape	Compactness	Crown Area	Scale	Shape	Compactness
5106	5556	25	0.1	0.5	6050	25	0.1	0.3	5689	25	0.1	0.1
	5571	50			6140	50			5791	50		
	5620	100			6480	100			5824	100		
	5692	150			6524	150			5836	150		
	5580	25	0.5		6011	25	0.5		6148	25	0.5	
	5598	50			6054	50			6231	50		
	6043	100			6147	100			6480	100		
	6152	150			6349	150			6494	150		
	6004	25	0.7		6033	25	0.7		6124	25	0.7	
	6055	50			6078	50			6176	50		
	6101	100			6128	100			6340	100		
	6247	150			6711	150			6399	150		
	6014	25	0.9		6042	25	0.9		6137	25	0.9	
	6038	50			6088	50			6142	50		
	6079	100			6121	100			6189	100		
	6091	150			6139	150			6508	150		
	4300	25	0.1	1	5702	25	0.1	0.9	6010	25	0.1	0.7
	4381	50			5741	50			6043	50		
	4401	100			5768	100			6085	100		
	4410	150			5831	150			6149	150		
	4204	25	0.5		4501	25	0.5		6044	25	0.5	
	4248	50			4583	50			6055	50		
	4306	100			4598	100			6073	100		
	4409	150			4603	150			6097	150		
	3911	25	0.7		4511	25	0.7		6089	25	0.7	
	3949	50			4562	50			6082	50		
	3980	100			4587	100			6105	100		
	4065	150			4650	150			6119	150		
	3799	25	0.9		4304	25	0.9		6102	25	0.9	
	3855	50			4381	50			6109	50		
	3906	100			4409	100			6157	100		
	4351	150			4207	150			6194	150		

3. Discussion

Due to the presence of a major complication in the region (eldarica pine tree), the comparison of the segmentation in different parameters can be done in better conditions. In this research, steps of 0.1, 0.3, 0.5, 0.7, 0.9, and 1 were used for the Compactness parameter, 0.1, 0.5, 0.7, and 9.0 for the Shape parameter, and 25, 50, 100, and 150 for the Scale parameter. After the necessary processes and with the aim of determining the optimal coefficients for Compactness, Scale and Shape parameters, the results were obtained. According to the results of Table (1), the results showed that a change in each segmentation parameter will result in different areas for the crown of the pine tree. Based on all 96 segmentation executions, the best segmentation was obtained for the only class in the image (Elderica pine tree), in parameters Shape=0.1, Scale=25 and Compactness=0.5. While the worst result was obtained with Shape=0.9, Scale=150 and Compactness=0.1 parameters. In general, the worst segmentation results in this research are when the Shape parameter is set to the maximum value of the research, which is 0.9. In other words, in this case, the color of the images has a full effect on the segmentation, which will bring errors in the result. Including the effect of the color of the bush and the grass at the base of the tree, which are close to each other in the projection of the tree crown in the resulting image, which can have a greater effect on the area estimation error. Regarding the Compactness parameter, the worst results are related to the time when the parameter number is at its maximum value = 1Compactness. In fact, in this case, the shape is considered as a curve with the same radius (circle), which is not in harmony with the irregular, unformulated and varied shape of the pine tree crown. This parameter has the greatest possible effect on the segmentation process compared to the other two parameters. Therefore, more care should be taken in selecting coefficients of parameters, especially Compactness. Also, the results of the analysis in Table (1) show that the quality of appropriate segmentation is obtained if the shape and color have a balanced effect on the creation of parts. In other words, the boundary of the parts should not be too high (Compactness=1) or low (Compactness=0.1). Usually Compactness = 0.5 gives better results because all trees have different shapes with different irregularity, 0.5 can create a more balanced overall effect. Therefore, the total crown area can have better effectiveness. Another result that can be obtained by looking at table 1 is that if only one of the parameters (Compactness, Scale, Shape) is changed and the other two are constant, no regular increase or decrease can be seen in the results. In addition, by increasing each parameter based on the steps determined in the table, this increase or decrease does not take place at the same step, which can be due to various reasons, including the shadow effect in misdiagnosing the shape of the crown and changing the size of the parts in the estimates.

5. Conclusion

Since the crown area of trees is one of the effective parameters in the interpretation of other tree characteristics, such as weight, carbon deposition, growth rate, etc., therefore, its accurate estimation is inevitable. In this research, one of the most irregular crowns (Elderica pine) was selected to estimate its crown area with the help of UAV images in different parameters. In general, the findings of the research showed that Phantom 4 Pro UAV images have the necessary efficiency in estimating the crown area of single pine trees without field data collection. Also, the advantage of this research is the proper spacing of trees and extraction without crown interference. These results will give managers and planners a clear vision to determine general management policies in the forest area. For future research, the parameters of Compactness, Scale and Shape can be evaluated by other trees and the results can be compared with the results of the current research.

References

Ahmad, A., Gilani, H., & Ahmad, S. R. (2021). Forest Aboveground Biomass Estimation and Mapping through High-Resolution Optical Satellite Imagery—A Literature Review. Forests, 12(7), 914.

Bokalo, M., Stadt, K. J., Comeau, P. G., & Titus, S. J. (2013). The validation of the Mixedwood Growth Model (MGM) for use in forest management decision making. Forests, 4(1), 1-27.

Duarte, E., Barrera, J. A., Dube, F., Casco, F., Hernández, A. J., & Zagal, E. (2020). Monitoring Approach for Tropical Coniferous Forest Degradation Using Remote Sensing and Field Data. Remote Sensing, 12(16), 2531.

Hosingholizade, A. (2023). Investigation of linear and logarithmic regression between measured and calculated parameters of Eldarica pine tree. Intercontinental Geoinformation Days, 6, 1-4.

Hosingholizade, A., Erfanifard, Y., Alavipanah, S. K., Latifi, H., & Jouybari-Moghaddam, Y. (2023). Tree Crown Delineation on Uav Imagery Using Combination of Machine Learning Algorithms with Majority Voting. ISPRS Annals of the Photogrammetry, Remote Sensing and Spatial Information Sciences, 10, 287-293.

Onishi, M., & Ise, T. (2021). Explainable identification and mapping of trees using UAV RGB image and deep learning. Scientific reports, 11(1), 1-15.

Tang, L., & Shao, G. (2015). Drone remote sensing for forestry research and practices. Journal of Forestry Research, 26(4), 791-797.

Zhang, H., & Jim, C. Y. (2013). Species adoption for sustainable forestry in Hong Kong's degraded countryside. International Journal of Sustainable Development & World Ecology, 20(6), 484-503.

Zhu, C., Zhang, X., Zhang, N., Hassan, M. A., & Zhao, L. (2018). Assessing the defoliation of pine forests in a long time-series and spatiotemporal prediction of the defoliation using Landsat data. Remote Sensing, 10(3), 360.

7th Intercontinental Geoinformation Days

igd.mersin.edu.tr

Digitization and archiving of Turkish motives by photogrammetric methods

Eda Menekşe [1], Ali Ulvi [*1]

[1] Mersin University, Institute of Science, Department of Remote Sensing and Geographic Information Systems, Mersin, Türkiye

Keywords
Close range
Photogrammetry
Turkish Motives
Digitization
3D Model

Abstract

Individuals bear significant responsibility in carrying out the essential and selfless work that ensures an increased level of knowledge and culture within Turkish society. Additionally, they strive to preserve cultural values that have been harmed or are at risk of disappearing due to various factors. These efforts include documenting and passing along such values to future generations. At this stage, individuals communicated their thoughts through cave art, rock art and woven textiles. Within this context, individuals consider, design, and weave together the events and situations they wish to convey. At this point, motifs play a crucial role and are comparable to the constituent words of a sentence. Understanding the meaning of the motifs allows for grasping and interpretation of the essence of the woven textiles. Carpet and rugs possess artistic characteristics and unravel the socio-cultural context of their era and their makers. Hence, they offer a historical reflection. The patterns on carpets and rugs unveil a spiritual depth and convey meaning by integrating its symbolism with the object on which it is exhibited, through formal connotations, bestowing a unique identity upon it. It could be argued that the symbols and motifs found in traditional carpet and rug weaving are representative of the attitudes and behaviors of their weavers.

1. Introduction

The weaving industry brought to life the natural lifestyle, social, economic, and cultural accumulation of Turkish tribes living across a broad region spanning from East Turkestan to Anatolia. This situation may serve as a means of self-expression or an expression of society. The motifs and colors in textiles are indicative of the differences between tribes and have persevered to the present day. By using dyes inherent to their geography, the weaver showcases the beauty found in objects, situations, and events that have impressed and inspired them. The Turkmen weaver depicts the cultural heritage, traditions, and customs of his tribe by intricately coloring an object, situation, or event that he finds aesthetically pleasing with dyes distinctive to his geographic location. Such weaving is representative of the influence of social constructs and cultural values on aesthetic expression. The symbols and hues expressed in carpets and rugs reveal the culture of the weavers' society (Kayipmaz, 2006). Given the wide geography inhabited by Turks and their historical migrations for various reasons, it can be argued that their ancient culture has been transmitted to different regions. Accordingly, numerous carpets and rugs in Central Asia and Anatolia bear witness to the unique features of Turkish cultural heritage. These artefacts are invaluable resources for illuminating historical developments. Non-verbal communication is an invaluable social tool, complementing verbal communication. Traditional textiles, such as rugs and carpets, hold particular significance as key bearers of nonverbal communication. They achieve this through two factors. Firstly, the motifs use a silent language that conveys meaning. Secondly, rich colours enhance this silent language, further enriching the communication. Overall, traditional textiles silently transport historical stories into the present day. Today, these customary documents, often perceived as mere placemats, actually reflect a vast and intricate cultural, social, and historical process incorporating the anonymous Yoruk aesthetics and Anatolian Turkish ethnography, as pointed out by Okça et al. (2015).

* **Corresponding Author**

*(e-mail) ORCID ID 0000 – 0001 – 8640 – 4804
(aliulvi@mersin.edu.tr) ORCID ID 0000 – 0003 – 3005 – 8011

Cite this study

Menekşe, E, & Ulvi, A. (2023). Digitization and archiving of Turkish motives by photogrammetric methods. Intercontinental Geoinformation Days (IGD), 7, 195-197, Peshawar, Pakistan

Therefore, it is crucial to research them as they provide insight into various periods of our ancient history and are a significant cultural legacy.

Eos Systems Inc. was established as a result of technological advancements in the study's thesis. The Photomodeler (PM) software was utilized to model Turkish motifs, with the objective of documenting these cultural heritage artifacts for preservation and future generations. This was done with consideration to maintaining a balance between protection and use.

2. Material and Methods

The motif can be regarded as a system of cultural values. However, motifs serve multiple functions, notably defining and reflecting cultures, revealing identities, and preserving tradition. Abbreviations for technical terms will be explained upon their initial use. Use high-level, standard language with a formal register, avoiding colloquialisms, jargon and biased language. Avoiding spelling, grammar, and punctuation errors is also crucial for clarity and effectively communicating the written message. Furthermore, it creates a strong connection between art and everyday life. The formation of motifs is shaped by important factors such as geography, social structure, cultural level, animals, and vegetation. It is essential to adhere to consistent citation and formatting features in line with the established style guide. Logical structure is vital to enable information flow and causal connections between statements. Precision in word choice helps to convey the intended meaning, notably by using subject-specific vocabulary where necessary. As anticipated, the designs of societies inhabiting varied geographical regions throughout history are indicative of their cultures. Each textile motif possesses a distinct significance and preserves remnants of the past (Luhmann et al., 2006). Motifs hold a crucial role in the art of weaving Turkish carpets and rugs. According to the Turkish Language Association (TDK), a motif is described as a group of elements that work together to form a decorative piece and provide unity independently. Symbols from everyday life were utilized while weaving motifs in Turkish textiles. For instance, the scorpion, which represents freedom, is the most commonly used pattern. In contrast, the camel's foot symbolizes transportation. Turks living in a vast region encompassing Central and Western Asia portrayed in their woven creations the climate and living conditions of each locale. The woven works are given names based on the motifs and their recounted tales.

- **Elibelinde Motif**

It is the motif that mainly symbolizes femininity. It represents not only maternity or fertility, but also abundance, fortune and joy.

Ram's Horn Motif

As its name suggests, this motif, which resembles a ram, is an expression of heroism, staying strong and masculinity in Turkish history. The ram's horn motif, a symbol of masculinity, symbolizes the male god.

Hairband Motif

It represents the request for marriage. It characterizes birth and reproduction. Young girls who want to get married cut zuluf and make a single braid, while newly married young women make double braids and decorate the ends of their hair with threads of different colors.

Some colours have significant meaning when embroidered onto motifs in weavings.

Red, commonly used in Turkish carpet and rug weaving motifs, is the symbol of life and power. The text does not provide enough context for improvement. It also expresses emotions such as love, passion, and war. Blue, Blue is a symbol of peace, trust and this colour, utilized in motifs for carpet and rug weaving in Turkey, is also associated with the sea and sky. Green: The colour green symbolizes nature and growth, frequently loyalty, often used in Turkish carpet and rug weaving motifs to represent hope, freshness and abundance. Yellow: Although less commonly used in Turkish carpet and rug motifs, yellow is considered a symbol of the sun and light. Therefore, it connotes both opulence and joy, as well as grandeur and prosperity. For these reasons, it is associated with affluence, grandeur, and joy. White: The colour white symbolizes purity, innocence, and sanitation. The colour white symbolizes purity, innocence, and cleanliness. In Turkish carpet and rug weaving motifs, the use of white also signifies death and everlastingness.

2.1. Workflow

Initially, we identified the sources to procure hand-embroidered carpets and rugs for the study. Especially given the observation that Turkmen houses uphold ancient traditions, various designs and motifs are derived from different residences. The aim was to capture textiles with maximum capacity through photography. Sufficient photos were taken to enable 3D modelling and drawing, followed by camera calibration in the PM, and finally automatic balancing was conducted.

Photogrammetric methods have been very efficient in the protection of cultural heritage studies (Kanun et al. 2022; Karataş et al. 2022).

3. Conclusion

As a result of the study, the use of terrestrial photogrammetric techniques in documenting the transfer of cultural patterns to the next generations has provided great benefits in digitalization.

Acknowledgement

This study was supported by Mersin University Scientific Research Projects with project number 2022-1-TP2-4641.

References

Arriaza, M. C., Yravedra, J., Domínguez-Rodrigo, M., Mate-González, M. Á., Vargas, E. G., Palomeque-González, J. F., ... & Baquedano, E. (2017). On applications of micro-photogrammetry and geometric morphometrics to studies of tooth mark morphology: the modern Olduvai Carnivore Site (Tanzania). Palaeogeography, Palaeoclimatology, Palaeoecology, 488, 103-112.

Asri, Ġ. (2005). Üç Boyutlu Modelleme ve Alaeddin Camii Örneği. Y.Lisans tezi, Selçuk Üniversitesi Fen Bilimleri Enstitüsü, Konya.

Asri, İ. ve Çorumluoğlu, Ö. (2007). "Büyük Objelerde Tarihi Dokümantasyon ve Tanıtım Amaçlı GPSSİT Destekli Dijital Fotogrametrik 3B Modelleme." TUFUAB, İTÜ, İstanbul, Türkiye.

Becker, C., Rosinskaya, E., Häni, N., d'Angelo, E., & Strecha, C. (2018). Classification of aerial photogrammetric 3D point clouds. Photogramm. Eng. Remote Sens, 84(5), 287-295. doi: https://doi.org/10.14358/PERS.84.5.287 [Erişim tarihi 15 Kasım 2022].

Çelik, M. Ö., Hamal, S. N. G., & Yakar, İ. (2020). Yersel lazer tarama (YLT) yönteminin kültürel mirasın dokümantasyonunda kullanımı: Alman Çeşmesi örneği. Türkiye Lidar Dergisi, 2(1), 15-22.

Dlesk, A., Uueni, A., Vach, K., & Pärtna, J. (2020). From analogue to digital photogrammetry: Documentation of Padise Abbey in two different time stages. Applied Sciences, 10(23), 8330. https://doi.org/10.3390/app10238330 [Erişim tarihi 7 Şubat 2023].

Geppert, A., C., T., Brandau, D. ve Siebeneichner, T. (2021). Militarizing Outer Space, Palgrave Studies in the History of Science and Technology, Palgrave Macmillan, London, United Kingdom. https://doi:10.1057/978-1-349-95851-1 [Erişim tarihi 18 Şubat 2023].

Gonçalves, J. A., & Henriques, R. (2015). UAV photogrammetry for topographic monitoring of coastal areas. ISPRS journal of Photogrammetry and Remote Sensing, 104, 101-111. https://doi.org/10.1016/j.isprsjprs.2015.02.009 [Erişim tarihi 2 Mart 2023].

Iizuka, K., Itoh, M., Shiodera, S., Matsubara, T., Dohar, M., & Watanabe, K. (2018). Advantages of unmanned aerial vehicle (UAV) photogrammetry for landscape analysis compared with satellite data: A case study of postmining sites in Indonesia. Cogent Geoscience, 4(1), 1498180. https://doi.org/10.1080/23312041.2018.1498180 [Erişim tarihi 16 Mayıs 2023].

Jiang, R., Jáuregui, D. V., & White, K. R. (2008). Close-range photogrammetry applications in bridge measurement: Literature review. Measurement, 41(8), 823-834. https://doi.org/10.1016/j.measurement.2007.12.005 [Erişim tarihi 16 Mayıs 2023].

Kanun, E., Alptekin, A., Karataş, L., & Yakar, M. (2022). The use of UAV photogrammetry in modeling ancient structures: A case study of "Kanytellis". Advanced UAV, 2(2), 41-50.

Karataş, L., Alptekin, A., & Yakar, M. (2022). Detection and documentation of stone material deterioration in historical masonry structures using UAV photogrammetry: A case study of Mersin Aba Mausoleum. Advanced UAV, 2(2), 51-64.

Kayıpmaz, F. (2006). Uluslararası Halı Pazarında Türk Halıcığının Konumu Paneli, Ankara Park Otel, Ankara.

Mapping total suspended matter concentrations in the Black Sea using Landsat TM multispectral satellite imagery. Fresenius Environmental Bulletin, 20(1a), 262-269.

Primicerio, J., Di Gennaro, S., F., Fiorillo, E., Genesio, L., Lugato, E., Matese, A. ve Vaccari, F., P., 2012. A flexible unmanned aerial vehicle for precision agriculture. Precision Agriculture, 13, 4, 517-523.

Ulvi, A. (2015). Metrik olmayan dijital kameraların hava fotogrametrisinde yakın resim çalışmalarda (yere yakın yüksekliklerde) kullanılabilirliği üzerine bir çalışma. PHD Thesis, Selçuk University

7th Intercontinental Geoinformation Days

igd.mersin.edu.tr

3D modeling of a stone sarcophagus at Kanlıdivane Ruins

Aydın Alptekin*[1], Murat Yakar [1]

[1]Mersin University, Department of Geomatics Engineering, Mersin, Türkiye

Keywords
Photogrammetry
3D model
Sarcophagus

Abstract

Türkiye has a wide cultural heritage inventory. Many historical monuments have survived until today without being damaged. However, these historical monuments are destroyed due to natural and human reasons. In order for these works to regain their original state after being worn out, their current condition must be modeled in three dimensions (3D) in a computer environment. In this study, photographs of a sarcophagus, made of stone material, located in Mersin Kanlıdivane Ruins were taken with a mobile phone. Using the photographs obtained, a 3D model of the sarcophagus was created on a computer. The 3D model created can be used both to promote the region in tourism and to restore the sarcophagus when it is damaged in the future.

1. Introduction

Türkiye has hosted many civilizations throughout history. These civilizations have left us many cultural heritages. It is our duty to protect, promote and transmit these heritages to future generations. The original structure of historical monuments is damaged by the materials used, climate, natural disasters, air pollution and the influence of people.

The petrographic and physical properties of the material used affect the life of the structure (Karataş et al. 2022a). The amount of protein, fat, salt and $CaCO_3$, pH value and the ratio of other minerals affect the life of the structure. Physical properties such as loss of ignition, sieve analysis and compressive strength also affect the life of the structure.

The climate of the region, with dry summers and very rainy winters, creates temperature differences on the stone structure. It also causes the salt and moisture in the stone structure to penetrate deeper. In addition, water causes chemical reactions in the stone structure and the development of living things such as fungi and algae.

Natural disasters such as earthquakes, landslides, rock falls and floods have a negative impact on historical buildings. Gaziantep Castle was damaged due to the 06 February Maraş earthquakes (Karataş et al. 2023).

Air pollution creates surface pollution on stone material and causes color change. Factors such as fire, car exhaust and coal stoves cause air pollution.

The unconscious actions of people in the region and the unconscious excavations of treasure seekers have a negative impact.

In this study, a 3D model of the current version of a sarcophagus located in Kanlıdivane was created. Many studies have been carried out on the ruins of Kanlıdivane.

Karatas et al. (2022b) examined the surface degradation of the Aba mausoleum using unmanned aerial vehicle (UAV) photographs. They found that surface contamination, color change, fracture formation, joint deterioration, plant growth, peeling and piece breakage were observed. They stated that UAV photogrammetry is extremely useful in determining surface degradation.

Alptekin et al. (2019) created a 3D model of a mausoleum located in Kanlıdivane Ruins with high resolution and precision using a terrestrial laser scanner (TLS).

Kanun et al. (2022) created a 3D model of a village house in Kanlıdivane Ruins using UAV photogrammetry. The lengths of the village house have been determined.

Kanun et al (2021) created the 3D model of the Aba Mausoleum in Kanlıdivane Ruins using UAV photogrammetry. The length dimensions of the Aba mausoleum have been determined.

* Corresponding Author

*(aydinalptekin@mersin.edu.tr) ORCID ID 0000-0002-5605-0758
(myakar@mersin.edu.tr) ORCID ID 0000-0002-2664-6251

Cite this study

Alptekin, A., & Yakar, M. (2023). 3D modeling of a stone sarcophagus at Kanlıdivane Ruins. Intercontinental Geoinformation Days (IGD), 7, 198-200, Peshawar, Pakistan

2. Study Area

There are many archaeological sites in Mersin province, which is characterized by the typical Mediterranean climate (Alptekin and Yakar 2021). One of the most important among these is Kanlıdivane Ruins located in Erdemli District (Figure 1). There are churches, mausoleums, tombstones, sarcophagi, oil production areas, stone reliefs and a large sinkhole in the ruins, which was an important city of the Olba Empire. The ruins inform us about the religious beliefs and lifestyles of people who lived in the past.

Natural stone, the oldest building material, is observed in many historical buildings. Historical stone structures that carry the living spaces and beliefs of past societies are constantly deteriorating due to environmental and human-related reasons. These stone structures, which are representatives of cultural heritage, need to be protected to be passed on to future generations. The properties of the material in the internal structure of the stone and environmental factors cause the stone material to deteriorate.

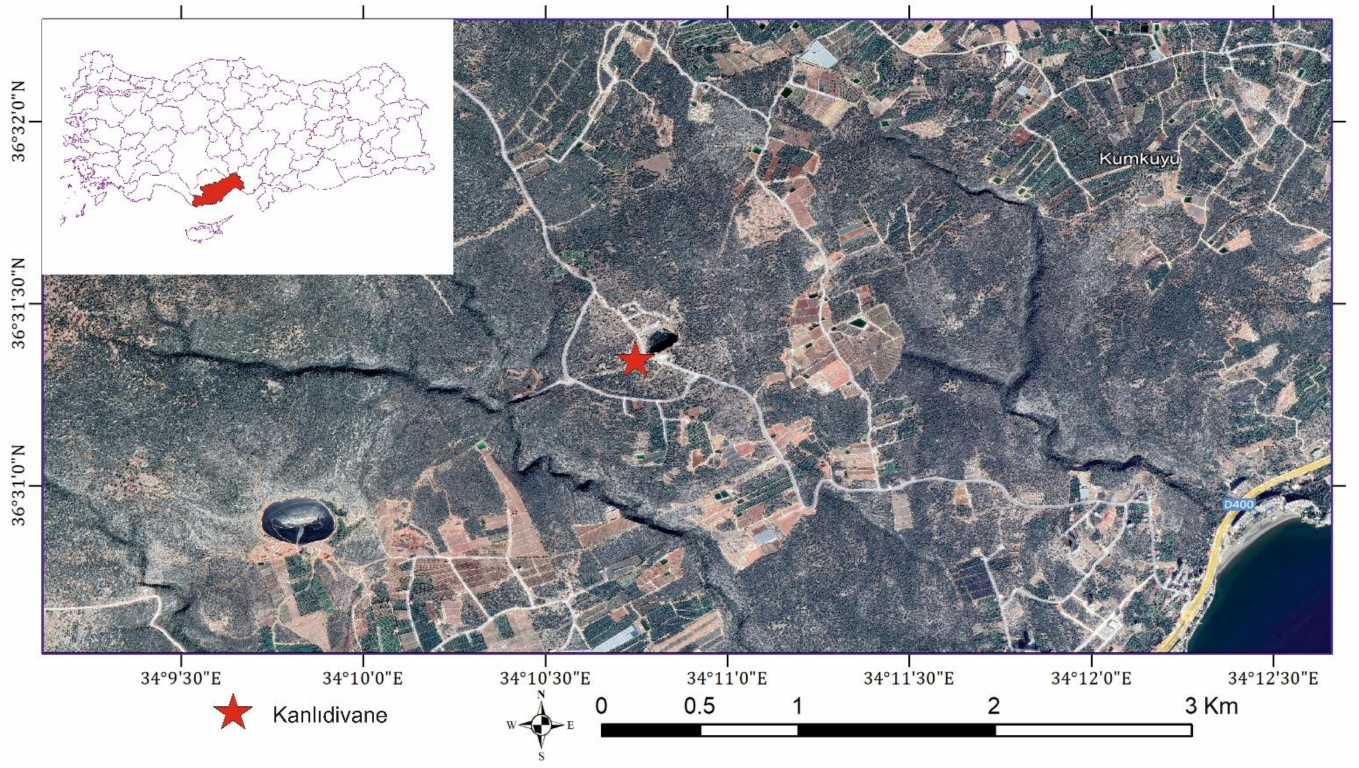

Figure 1. Location map of the study area

3. Method

Remote sensing methods allow us to model objects without damaging them. Unmanned aerial vehicles (UAV) and terrestrial laser scanners (TLS) enable objects to be displayed in detail and with high resolution and precision in a computer environment with the point clouds they obtain.

Karataş and Alptekin (2022) have used photogrammetry, visual inspection and TLS to determine the deteriorations in a stone historical building. Thay suggested restoration proposal for the historical structure.

The photogrammetry method is becoming widespread in cultural heritage studies because it is practical and economical. With photogrammetry, pictures of the works can be taken in high resolution. In this way, the fine details in the work can be seen clearly. By taking images of historical artifacts as overlays, a 3D model can be created from 2D images.

Pictures of a sarcophagus made of stone material found in Kanlıdivane Ruins were taken with a Samsung Galaxy S10 smartphone. The images were modeled in the Agisoft Metashape program. The 3D model of the object has been obtained (Figure 2).

4. Results and Discussion

Known for its strength and durability, the stone was frequently used in ancient times. The cultural heritage consisting of stone materials undergoes various deteriorations over time. The corrosive effect of rainwater and sunlight has been identified in many studies.

Point cloud technology is frequently used in engineering projects. It has been used in determining pond volume (Alptekin and Yakar, 2020), landslide area modeling and mapping (Kuşak et al. 2021), rockfall area modeling (Alptekin et al. 2019), coastal line determination (Unel et al. 2020) and cultural heritage studies (Alptekin and Yakar, 2021).

For the restoration of historical buildings, it is necessary to determine their physical, chemical and mechanical properties as well as their visual models.

Figure 2. 3D model of the stone sarcophagus

5. Conclusion

It can be seen that even the types of material problems can be detected based on the smallest detail. It shows that, as a result of exposure to climate-induced sun and water effects, color change and surface loss and deterioration on the stone surfaces have reached advanced levels. Restoration methods should be attempted to stabilize deterioration and replace the most deteriorated stones. It is recommended to use water-repellent surface coatings to protect natural stone, especially against the intense effects of water on the structure.

References

Karataş, L., Alptekin, A., & Yakar, M. (2022a). Detection of materials and material deterioration in historical buildings by spectroscopic and petrographic methods: The example of Mardin Tamir Evi. *Engineering Applications*, *1*(2), 170-187.

Karataş, L., Ateş, T., Alptekin, A., Dal, M., & Yakar, M. (2023). A systematic method for post-earthquake damage assessment: Case study of the Antep Castle, Türkiye. *Advanced Engineering Science*, *3*, 62-71.

Karataş, L., Alptekin, A., & Yakar, M. (2022b). Detection and documentation of stone material deterioration in historical masonry structures using UAV photogrammetry: A case study of Mersin Aba Mausoleum. *Advanced UAV*, *2*(2), 51-64.

Alptekin, A., Çelik, M. Ö., & Yakar, M. (2019). Anıtmezarın yersel lazer tarayıcı kullanarak 3B modellenmesi. *Türkiye Lidar Dergisi*, *1*(1), 1-4.

Kanun, E., Alptekin, A., Karataş, L., & Yakar, M. (2022). The use of UAV photogrammetry in modeling ancient structures: A case study of "Kanytellis". *Advanced UAV*, *2*(2), 41-50.

Kanun, E., Alptekin, A., & Yakar, M. (2021). Cultural heritage modelling using UAV photogrammetric methods: a case study of Kanlıdivane archeological site. *Advanced UAV*, *1*(1), 24-33.

Alptekin, A., & Yakar, M. (2021). İçel İli jeolojisine ve jeolojik sorunlarına genel bir bakış. *İçel Dergisi*, *1*(1), 27-30.

Alptekin, A., Çelik, M. Ö., Doğan, Y., & Yakar, M. (2019). Mapping of a rockfall site with an unmanned aerial vehicle. *Mersin Photogrammetry Journal*, *1*(1), 12-16.

Alptekin, A., & Yakar, M. (2020). Determination of pond volume with using an unmanned aerial vehicle. *Mersin Photogrammetry Journal*, *2*(2), 59-63.

ÜneL, F. B., Kuşak, L., Çelik, M., Alptekin, A., & Yakar, M. (2020). Kıyı çizgisinin belirlenerek mülkiyet durumunun incelenmesi. *Türkiye Arazi Yönetimi Dergisi*, *2*(1), 33-40.

Alptekin, A., & Yakar, M. (2021). 3D model of Üçayak Ruins obtained from point clouds. *Mersin Photogrammetry Journal*, *3*(2), 37-40.

Kusak, L., Unel, F. B., Alptekin, A., Celik, M. O., & Yakar, M. (2021). Apriori association rule and K-means clustering algorithms for interpretation of pre-event landslide areas and landslide inventory mapping. *Open Geosciences*, *13*(1), 1226-1244.

Karataş, L., & Alptekin, A. (2022). Kagir Yapılardaki Taş Malzeme Bozulmalarının Lidar Tarama Yöntemi ile Belgelenmesi: Geleneksel Silvan Konağı Vaka Çalışması. *Türkiye Lidar Dergisi*, *4*(2), 71-84.

7th Intercontinental Geoinformation Days

igd.mersin.edu.tr

Use of photogrammetry in criminology

Muhammed Emin Bıyık*[1], Murat Yakar [1]

[1]Mersin University, Engineering Faculty, Department of Geomatics Engineering, Mersin, Türkiye

Keywords
Criminology
Photogrammetry
Crime Scene

Abstract

Criminology is a scientific discipline which explains the commission of crime, studies criminal conduct and its origins, and deals with preventing and combating crime. It is widely considered as a field of observation that can play a vital role in promoting a more peaceful society. By identifying a sustainable strategy for a harmonious societal response to crime, criminology can serve as a catalyst for societal transformation. The primary objective of criminology is to guarantee that the evidence found at crime scenes is gathered and documented without incurring any damage or loss. In the traditional approach, police officers and forensic experts take various measurements and photographs of the crime scene. This method consumes a considerable amount of time to resolve the case, and the reconstruction of crime scene drawings is carried out manually. This approach presents various limitations, including time constraints, imprecision, and the restricted view of findings in just two dimensions (2D). However, these drawbacks can be addressed with the implementation of photogrammetry, a scientific method for observing and quantifying objects in 2D or 3D by analyzing photographic data with specific metrics for documentation and interpretation.

1. Introduction

Thorough and accurate documentation of an authentic pre-autopsy situation, perishable findings and the subsequent step of an autopsy enables preservation of forensic evidence and allows other experts to review original results, prevent misdiagnoses and uphold high standards of quality control (Yakar et al., 2013; Polat et al., 2020). Where physical evidence is concerned, this affords a three-dimensional portrayal where all elements are equally represented, without any being overlooked or skewed (Yakar et al 2015b). Three-dimensional surface data is utilized to measure body dimensions and make comparisons across different types of forensic evidence, such as in the analysis of weapons and the examination of how injuries were inflicted by the tool that caused them (Tülüce, 2010). The use of spatial photogrammetry, through photographs taken at the crime scene, enables easy creation of a measurement sketch of the area (Sarıtaş, 2015; Ulvi et al., 2019; Kanun et al., 2021). Photographs taken at the crime scene have the potential to accelerate the interpretation of events, and rectify any mistakes in the measurement sketch. These pictures can also supplement missing or incomplete information.

In the field of criminology, photogrammetric science is employed to resolve and authenticate incidents swiftly and without any loss of physical evidence. Photogrammetry offers swift access to accurate model information at a low cost, while allowing for quick data transfer and computer-based work. It provides a reliable means for criminology to achieve its goals and foster trust among individuals who seek justice (Edelman & Aalders, 2018; Villa & Jacobsen, 2019; Kaya & Yiğit, 2020).

Terrestrial photogrammetry proves a useful forensic documentation tool for homicide cases. Photogrammetry provides more accurate measurements of injuries compared to traditional photography. While traditional methods are still useful for pure documentation purposes, they are outdated and less effective when precise measurements or forensic reconstruction is required (Abate et al., 2017; Sacco & Ricci, 2022). Forensic sciences have already integrated terrestrial photogrammetry in several ways, most notably in crime scene and traffic site documentation. With the use of emerging technologies, it is feasible to determine the height of individuals involved in criminal activities or reconstruct the trajectory of shots fired from a firearm (Ulvi & Yakar, 2010; Ospina-Bohórquez et al., 2023).

* **Corresponding Author**

*(20160011@mersin.edu.tr) ORCID ID 0000-0001-9725-2893
(myakar@mersin.edu.tr) ORCID ID 0000-0002-2664-6251

Cite this study

Bıyık, M. E. & Yakar, M. (2023). Use of photogrammetry in criminology. Intercontinental Geoinformation Days (IGD), 7, 201-204, Peshawar, Pakistan

Terrestrial photogrammetry is a leading method for producing high-quality 3D models (Yakar et al., 2015b; Gonzalez-Aguilera & Gomez-Lahoz, 2019). The archives resulting from 3D documentation studies are more effective documentation tools, both metrically and visually, than digital and classical alternatives (Şasi and Yakar, 2017). In forensic medicine, 3D recording will aid communication among judges, prosecutors, lawyers, and police officers. After the post-mortem, only the autopsy report and 2D images remain once the body is buried. As the report may contain subjective evaluations, 2D images cannot capture sufficient detail regarding angles, depth, and colour. Consequently, 3D recording enables the immortalization of corpses. Employing photogrammetry software, today's mobile device cameras enable cost-effective use of photographs. The research study intends to evaluate whether the initial investment in 3D photogrammetric documentation technology can lead to cost savings for law enforcement agencies by improving efficiency. For this purpose, a cost-benefit analysis was carried out by the research team for the photogrammetry method.

2. Method

Today, three-dimensional (3D) documentation can be achieved using various instruments (Karataş et al. 2022). For human body scanning, lasers, terrestrial photogrammetry, and video imaging are available (Polat et al., 2020).

Laser surface scanners operate by projecting laser beams progressively over the scanned surface and registering their reflection on a light sensor (Karataş and Alptekin, 2022). In general, the scanned object should remain static for an extended period to avoid movement during the scanning process (Yakar and Doğan, 2019). Photogrammetry can be applied within the forensic environment to scan environments such as crime scenes, skeletal remains, corpses, and weapons (e.g., knives, shotguns). However, it is not considered as a preferred method for living persons. In this scenario, a terrestrial photogrammetry technique was employed. To evaluate the quality of the data collected via close-range photogrammetry method, a reference 3D model of a simulated crime scene was photographed from various locations using a camera. Artificial targets were utilized with target marks visible between consecutive photographs to ensure automation and precision in the alignment process. It is important to note that subjective evaluations are excluded unless specifically marked as such. Artificial targets were utilized with target marks visible between consecutive photographs to ensure automation and precision in the alignment process. Artificial targets were utilized with target marks visible between consecutive photographs to ensure automation and precision in the alignment process.

Forensic (often digital) photography has been the traditional method of carrying out homicides by forensic pathologists or police personnel until recently. Forensic photographs may capture the entire body, smaller anatomical regions, or specific organs (Tülüce, 2010; Sarıtaş, 2015). When photographs are taken from various angles or poses, their size or shape may be altered due to optical distortions (Kanun et al. 2021). As each individual possesses distinctive anatomical structures, such differences often result in distortions between photographs. This makes it challenging to comprehend forensic photography, hence it is imperative to furnish a reference for the object of interest's size and location on the body. It is crucial to commence forensic documentation with a scale-less overview photo of the item in focus, followed by more comprehensive shots from varying perspectives with a scale included. The caliber of the evidence can be heavily impacted by common faults in the technical quality of the pictures. To obtain optimal photographic quality, various aspects must be considered, including white balance, exposure, verticality, and especially the sharpness of the intended area. Technical errors in these categories can be minimized by ensuring forensic and specialized police officers receive the appropriate training (Edelman et al., 2018; Villa and Jacobsen, 2019). Viewing a three-dimensional (3D) object on a two-dimensional (2D) photograph always incurs some form of information loss or deformation of the object of interest (Abate et al., 2017; Sacco and Ricci, 2022). This effect becomes more pronounced in areas of high curvature, such as the arms, neck, or hands. It is therefore essential to meticulously photograph these regions when examining forensic images. The visualization of 2D information in forensic photography can be improved by implementing photogrammetry techniques.

Additionally, the application of photogrammetric models to map surface injuries to specific instruments has proven to be an effective technique for reconstructing patterned wounds. It should be emphasised that photogrammetry alone does not provide information regarding subcutaneous medical conditions. The documentation process has a significant impact on the ability to address forensic inquiries. There are several variables that affect the quality of the documentation when photogrammetric methods are involved in measuring the human body. The slightest body movement, such as breathing, may cause problems when attempting to recreate a 3D model.

Here is the workflow employed in this study:

- Location selection (Open space, Closed space)
- Survey (Planning)
- Lifeless Mannequin supply
- Creation of the crime scene
- Photographing the scene of the incident
- Transferring the photographs to the programme
- Creating a three-dimensional model
- Measurement on the model
- Model analysis.

3. Results

Firstly, photographs were taken of the area where the crime scene was staged. A total of 55 photographs were collected for this purpose. These photographs were then 3D modelled using the SfM algorithm. The photogrammetric process was carried out using Context Capture software and took approximately 8 minutes. Data processing took a total of 28 minutes. Consistent citation and footnote style have been followed, with quotes clearly marked, filler words avoided and a logical structure maintained. The figures showcasing the 3D model generated are presented in Figures 1-2 and 3, respectively.

Figure 1. Top view of the 3D model of the crime scene.

Figure 2. Front view of the 3D model of the crime scene.

Figure 3. Bottom view of the 3D model of the crime scene.

Analyses were conducted on the acquired models. For instance, measurements were taken as illustrated in Figures 4 and 5.

Figure 4. The length of the knife at the staged crime scene. The unit is set in cm.

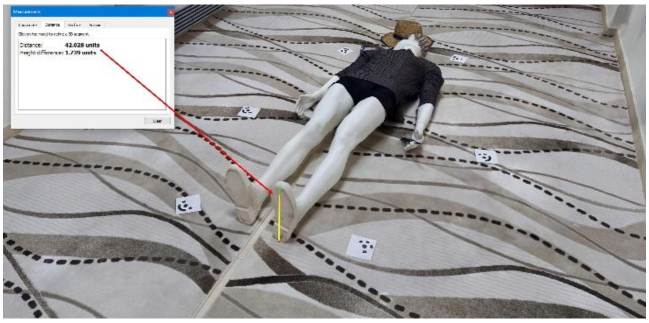

Figure 5. The length of the victim's foot in the staged crime scene. The unit is set in cm.

As demonstrated by the analyses, highly accurate measurements can be obtained from the model, without compromising the integrity of the crime scene.

The study indicates that precise analyses can be conducted on-site at crime scenes and subsequently in digital media. Moreover, institutions may benefit from long-term cost savings. For instance, the photogrammetric software incurs an annual cost of $3500. The remuneration for crime scene investigators is variable. Crime scene police officers and scene experts receive $1000. The classical method offers a pay range of $2000-$4000, depending on the investigator's acumen. Photogrammetric method entails an average salary of $1000 due to less technical skill and sensitivity requirements, unlike crime scene investigation. If the photogrammetry expert is required for future studies, their salary could be adjusted accordingly. The specified prices are solely evaluated for crime scene investigation and modelling purposes.

4. Conclusion

This paper reports on a study analyzing the performance of a handheld camera for crime scene documentation, reconstruction and analysis using photogrammetry. The authors conducted a three-dimensional analysis of a simulated crime scene using data acquired from the sensor. Measurements were extracted from images and 3D point clouds, while point cloud models were generated by applying SfM to 55 multiple images captured from the handheld camera. This study demonstrates that 3D model technology has greatly benefited criminology, particularly in conducting crime scene analyses. Despite this, the use of this technology remains limited in most countries. The primary advantage of 3D modelling is that it improves visualization, interpretation and comprehension. Moreover, the 3D model is a humane approach that prevents damage to the real evidence as it is reconstructed without touching it. Scanned images of the original evidence can be magnified for analysis, printed, and used as explanatory evidence in court. Preliminary study results have demonstrated that this technology provides precise outcomes. Further research, adoption of advanced 3D data collection methods, and sensitization of criminology practitioners have all contributed to the technology's usefulness.

Acknowledgement

This research was funded by project 1919B012211617 as part of the Tübitak 2209-A University Students Research Projects Support Programme.

References

Abate, D., Toschi, I., Sturdy Colls, C., & Remondino, F. (2017, November). A low-cost panoramic camera for the 3d documentation of contaminated crime scenes. In International Society for Photogrammetry and Remote Sensing (Vol. 42, pp. 1-8).

Edelman, G. J., & Aalders, M. C. (2018). Photogrammetry using visible, infrared, hyperspectral and thermal imaging of crime scenes. Forensic science international, 292, 181-189.

Gonzalez-Aguilera, D., & Gomez-Lahoz, J. (2009). Forensic terrestrial photogrammetry from a single image. Journal of forensic sciences, 54(6), 1376-1387.

Kanun, E., Alptekin, A., & Yakar, M. (2021). Documentation of cultural heritage by photogrammetric methods: a case study of Aba's Monumental Tomb. Intercontinental Geoinformation Days, 3, 168-171.

Kanun, E., Alptekin, A., & Yakar, M. (2021). Cultural heritage modelling using UAV photogrammetric methods: a case study of Kanlıdivane archeological site. *Advanced UAV*, *1*(1), 24-33.

Karataş, L., & Alptekin, A. (2022). Kagir Yapılardaki Taş Malzeme Bozulmalarının Lidar Tarama Yöntemi ile Belgelenmesi: Geleneksel Silvan Konağı Vaka Çalışması. Türkiye Lidar Dergisi, 4(2), 71-84.

Karataş, L., Alptekin, A., & Yakar, M. (2022). Detection and documentation of stone material deterioration in historical masonry structures using UAV photogrammetry: A case study of Mersin Aba Mausoleum. Advanced UAV, 2(2), 51-64.

Kaya, Y., & Yiğit, A. Y. (2020). Dijital El Kameraları Kullanılarak Kültürel Mirasın Belgelenmesi. Türkiye Fotogrametri Dergisi, 2(2), 33-38.

Lech, K., Mularczyk, K., Michonski, J., Januszkiewicz, K., & Sitnik, R. (2018, October). Novel active-SfM solution for three-dimensional crime scene documentation. In Counterterrorism, Crime Fighting, Forensics, and Surveillance Technologies II (Vol. 10802, pp. 69-79). SPIE.

Ospina-Bohórquez, A., Del Pozo, S., Courtenay, L. A., & González-Aguilera, D. (2023). Handheld stereo photogrammetry applied to crime scene analysis. Measurement, 216, 112861.

Polat, N., Önal, M., Ernst, F. B., Şenol, H. İ., Memduhoglu, A., Mutlu, S., Mutlu, S. İ., Budan, M., Turgut, M. & Kara, H. (2020). Harran Ören Yeri Arkeolojik Kazı Alanınından Çıkarılan Bazı Küçük Arkeolojik Buluntuların Fotogrametrik Olarak 3B Modellenmesi. Türkiye Fotogrametri Dergisi, 2 (2), 55-59.

Sacco, M. A., & Ricci, P. (2022). E1 The Use of Smart Phone Applications in Crime Scene Analysis: Forensic Advantages and Limitations. Meeeflng and Surpassing TH· E Challuenges OF A 00 E M OD 8 R N, FORE N S· ICSCIE N CE 1 WORLD.\, 281, 525.

Sarıtaş, M. Z. (2015). Adli tıp uygulamalarında 3D (üç boyutlu) teknolojinin kullanımı.

Şasi, A., & Yakar, M. (2017). Photogrammetric modelling of sakahane masjid using an unmanned aerial vehicle. Turkish Journal of Engineering, 1(2), 82-87.

Tülüce, A. R. (2010). Tıp fotoğrafçılığı ve tıp alanındaki uygulamaların fotoğraf sanatında kullanımı (Doctoral dissertation, Marmara Universitesi (Turkey)).

Ulvi, A., & Yakar, M. (2010). An experimental study on preparing photogrammetric rolove plans of antique theatres. International Journal of the Physical Sciences, 5(7), 1086-1092.

Ulvi, A., Yiğit, A. Y. & Yakar, M. (2019). Modelıng of Historical Fountains By Using Close-Range Photogrammetric Techniques. Mersin Photogrammetry Journal, 1 (1), 1-6.

Villa, C., & Jacobsen, C. (2019). The application of photogrammetry for forensic 3D recording of crime scenes, evidence and people. Essentials of Autopsy Practice: Reviews, Updates and Advances, 1-18.

Yakar, M., & Dogan, Y. (2019). 3D Reconstruction of Residential Areas with SfM Photogrammetry. In Advances in Remote Sensing and Geo Informatics Applications: Proceedings of the 1st Springer Conference of the Arabian Journal of Geosciences (CAJG-1), 73-75

Yakar, M., Toprak, A. S., Ulvi, A., & Uysal, M. (2015b). Konya Beyşehir Bezariye Hanının (Bedesten) İHA ile Fotogrametrik Teknik Kullanılarak Üç Boyutlu Modellenmesi. Türkiye Harita Bilimsel ve Teknik Kurultayı, 25, 28.

Yakar, M., Ulvi, A., & Toprak, A. S. (2015a). The problems and solution offers, faced during the 3D modeling process of Sekiliyurt underground shelters with terrestrial laser scanning method. International Journal of Environment and Geoinformatics, 2(2), 39-45.

Yakar, M., Uysal, M., Toprak, A. S., & Polat, N. (2013). 3D modeling of historical doger caravansaries by digital photogrammetry. The International Archives of the Photogrammetry, Remote Sensing and Spatial Information Sciences, 40, 695-698.

7th Intercontinental Geoinformation Days

igd.mersin.edu.tr

The accuracy evaluation of point cloud data generated with iPhone 15 Pro Next Gen LiDAR sensor

Ramazan Alper Kuçak[*1]

[1]*Istanbul Technical University, Civil Engineering Faculty, Geomatics Engineering Department, 34469 Maslak, Istanbul, Türkiye*

Keywords
iPhone 15 Pro
iPad pro
LiDAR
Point cloud

Abstract

Low-cost LiDAR sensors have recently become preferred in many fields by architects, geomatics engineers, industrial design, virtual reality applications, and many other disciplines for rapid 3D model generation. Recently, 3D models created with LiDAR sensors of smartphones (iPhone and iPad LiDAR sensors) have become preferred in many areas for 3D model production. This study discusses the accuracy evaluation of point cloud data automatically generated by the iPhone 15 Pro LiDAR sensor. Therefore, a point cloud was created for the same object with the iPhone 15 Pro LiDAR Sensor, and SiteSCAPE and Scaniverse mobile applications were tested. Our results show that the performance of the iPhone 15 Pro LiDAR Sensor is affected by mobile software technical capabilities. In addition, the results generally concluded that the iPhone 15 Pro LiDAR sensor can be used in many geomatics applications for point cloud generation, but it can be used as auxiliary data for survey studies due to its shortcomings.

1. Introduction

Light Detection and Ranging (LiDAR) is a measurement technique that produces 3D airborne or terrestrial point cloud data. LiDAR systems create a point cloud in 3D space with the intensity values (density value of the reflection energy of the laser reflected from the surface) of the point cloud and RGB values (Kuçak et al.., 2016; Kuçak et al.., 2017; Kuçak et al.., 2020, Kuçak, R. A. 2022, Kuçak et al.., 2023). However, 3D models produced with low-cost LiDAR sensors have recently become preferred for fast 3D model production in many areas.

3D Modeling with point cloud data is essential for archaeologists, architects, or geomatics engineers using smartphones (Such as iPhone Pro sensors). Today's prevalence of smartphones, along with advances in sensor technologies, generation of point clouds, and 3D Modeling, offer new opportunities for scientific applications and low cost. It has been proven that studies can be performed with differences of approximately 10 cm compared to scanning with a hand-held laser scanner (Gollob et al., 2021). Apple Inc., a LiDAR scanner available in consumer-grade devices, will launch the iPad Pro 2020 (11-inch and 12.9-inch displays) on March 25, 2020, and the iPhone 12 Pro and iPhone 12 Pro Max on October 23, 2020 (Luetzenburg et al. 2021). While sensors with the same LiDAR features were preferred in the iPhone 13 and 14 Pro, Apple agreed with SONY for the iPhone 15 Pro and radically changed the LiDAR sensor. While a more efficient ToF (Time of Flight) LiDAR Sensor, first introduced with the iPhone 15 Pro, appeared as Sony IMX591, it was introduced as IMX590 in the iPhone 14 and older series.

Scaniverse and SiteScape programs are mobile applications designed to perform 3D scanning using the LiDAR sensor found in specific iPhone and iPad models. Applications are preferred to produce 3D models by scanning objects and environments with the LiDAR sensor. These apps allow users to create accurate, high-resolution 3D scans directly from compatible iOS devices. Thanks to such applications, Apple iPhone LiDAR is rapidly gaining popularity for the 3D representation of solid objects and surfaces due to its processing capacity, price, size, and versatility (Luetzenburg et al., 2021; Monsalve et al., 2023). Many professional disciplines, including forestry, earth sciences, geology, accident site investigation, documentation of cultural fields, and production of large-scale 3D rapid maps, use point clouds and 3-Dimensional (3D) models created from measurements made using such smartphones, which are

* **Corresponding Author**

*(*kucak15@itu.edu.tr*)

Cite this study

Kuçak, R. A. (2023). The accuracy evaluation of point cloud data generated with iPhone 15 Pro Next Gen LiDAR sensor. Intercontinental Geoinformation Days (IGD), 7, 205-208, Peshawar, Pakistan

relatively less expensive than Professional Terrestrial Laser Scanners. (Çakir et al., 2021; Desai et al., 2021; Gollob et al., 2021; Luetzenburg et al., 2021; Mokroš et al., 2021; Murtiyoso et al., 2021; Plaß et al., 2021; Spreafico et al., 2021; Vogt et al., 2021; Wang et al., 2021; Bobrowski et al., 2022; McGlade et al., 2022; Tavani et al., 2022). This kind of hardware is anticipated to grow and be used more frequently in new application areas because of its many benefits, including ease of use, speed, and accuracy.

This study investigated the accuracy of point clouds obtained using the iPhone 15 Pro new generation LiDAR sensor. Free versions of SiteScape and Scaniverse applications were preferred as software. Additionally, to eliminate sources of error in the comparison, the accuracy comparison of LIDAR systems was made relatively using the distance differences of the points selected from the point clouds.

2. Method

Various Apps are available to create a 3D point cloud model of a surface with the iPhone 15 Pro LiDAR sensor (Such as "Scaniverse," "3D ScannerApp", "Pix4d Catch," "SiteScape"). In this study, Scaniverse and SiteScape Apps were used for scanning (Figure 1). The steel tape measure data was also used as a reference for the accuracy evaluation of İPhone 15 Pro data (Table 2).

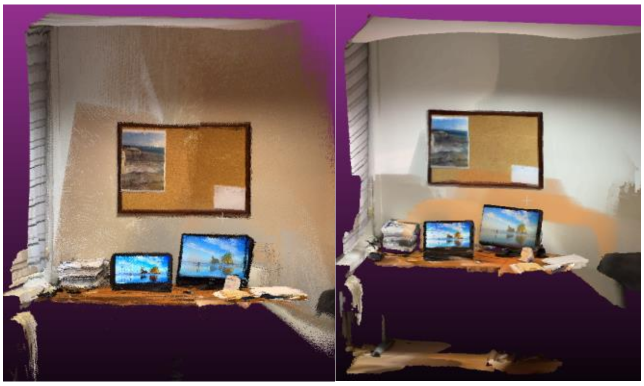

Figure 1. iPad Pro LiDAR sensor SiteScape (Left) and Scanivese (Right) scanning

3. Results

According to the scans obtained, for each point cloud, certain distances were measured with a steel tape measure (Figure 2), and these distances were measured with iPhone 15 Pro (SiteScape, and Scaniverse, software) (Table 1).

The measured distances "a,b,c" are selected as horizontal distances, and "d,e,f" are selected as vertical distances (Figure 2). By taking the differences between these values given in Table 1, standard deviation values were calculated from the distance differences (Table 2).

According to the calculated difference values, it has been observed that Sitescape and Scaniverse values are very close. However, since the steel tape measure is used as a reference in this application, the difference values in Table 2 are calculated according to the steel tape measure values. As can be seen from Table 2, the values obtained from the Scaniverse program were close to the steel tape measure distances, and the most enormous differences were observed to be those obtained from the SiteScape program.

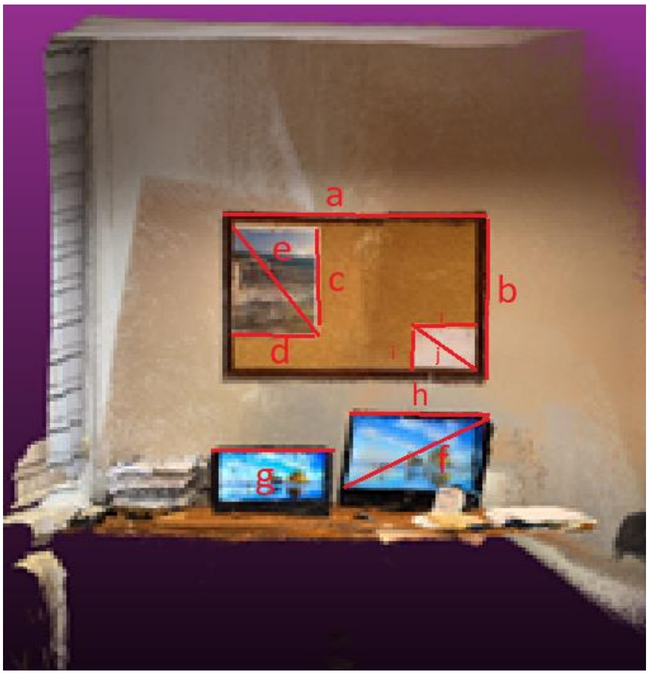

Figure 2. Distances measured with a steel tape

Table 1. Measured distances

(m)	Steel tape measure	SiteScape	Scaniverse
a	0.900	0.904	0.906
b	0.600	0.606	0.601
c	0.420	0.414	0.420
d	0.297	0.295	0.293
e	0.514	0.511	0.510
f	0.558	0.554	0.556
g	0.374	0.375	0.373

Table 2. Calculated differences

(m)	SiteScape	Scaniverse
a	0.004	0.006
b	0.006	0.001
c	-0.006	0.000
d	-0.002	-0.003
e	-0.003	-0.004
f	-0.004	-0.002
g	0.001	-0.001
Std.	0.004	0.003

Overall, the first results from the study showed that LiDAR sensors integrated into portable mobile devices showed promising performance indoors. This study has evaluated that this type of sensor can be an essential alternative to expensive professional-type scanners in many applications with their low cost, portability, speed, and easy usability. However, despite the system's many advantages, it has some disadvantages. The most prominent is that LiDAR sensors integrated into the tablet/phone generally have a limited scanning range. For example, the maximum measurement distance for the iPad Pro used in the study is given as 5 m (Wang et al., 2021). Another issue is that the accuracy of the point clouds obtained as a result of scanning depends on the software used during scanning and the options preferred in the software.

4. Conclusion

According to the calculated values, Scaniverse gave results closer to the steel tape measure with a standard deviation value of 0.003 m. According to this study, SiteScape iPhone 15 Pro data can easily be used in surveying tasks with a standard deviation of 0.004 m. These standard deviations were obtained from approximately 1 meter. When the results obtained according to SiteScape data were examined, it was observed that there may be a need for more detail in obtaining the 3D model of objects with details of up to 2 cm. As seen in Figure 1 from both data sets, it has been observed that although data with sufficient numerical accuracy can be obtained to obtain 3D models, data with the same precision cannot be obtained for all surfaces. The data obtained for SiteScape and Sacaniverse can be collected up to 5 meters indoors, as stated in the user manual of the iPhone 15 Pro and explained in the literature. However, it has been observed that the iPhone 15 Pro LiDAR sensor can collect better data at distances of 3 meters and closer.

When evaluated according to these results, it has been observed that the iPhone 15 Pro LiDAR data can be used in many surveying operations by subjecting it to a proper registration (fine registration) process in areas where terrestrial laser data is incomplete. It can be preferred in projects where an accuracy of approximately 3 cm or more is sufficient, especially in areas such as BIM applications. However, as stated in the literature, it is mentioned that scanning can be done from a distance of 2-3 meters in many applications. In our application, healthy results can be obtained in indoor scanning up to 1-3 meters; A very noisy point cloud could be obtained at distances of 4-5 meters. This situation prevented the data from being used in 3D modeling. However, as seen from the Scaniverse and SiteScape data set, this study has again shown that 3D model data, which can be used as a basis for many applications, can be obtained easily.

References

Bobrowski, R., Winczek, M., Zięba-Kulawik, K., & Wężyk, P. (2022). Best Practices to Use the iPad Pro LiDAR for Some Procedures of Data Acquisition in the Urban Forest. http://dx.doi.org/10.2139/ssrn.4030573

Çakir, G. Y., Post, C. J., Mikhailova, E. A., & Schlautman, M. A. (2021). 3D LiDAR Scanning of Urban Forest Structure Using a Consumer Tablet. Urban Science, 5(4):88. https://doi.org/10.3390/urbansci5040088.

Desai, J., Liu, J., Hainje, R., Oleksy, R., Habib, A., & Bullock, D. (2021). Assessing Vehicle Profiling Accuracy of Handheld LiDAR Compared to Terrestrial Laser Scanning for Crash Scene Reconstruction. Sensors, 21(23):8076. https://doi.org/10.3390/s21238076

Gollob, C., Ritter, T., Kraßnitzer, R., Tockner, A., & Nothdurft, A. (2021). Measurement of forest inventory parameters with Apple IPad pro and integrated LiDAR technology. Remote Sensing, 13, 3129.

Kuçak, R. A., Kiliç, F., & Kisa, A. (2016). Analysis of terrestrial laser scanning and photogrammetry data for documentation of historical artifacts. The International Archives of Photogrammetry, Remote Sensing and Spatial Information Sciences, 42, 155.

Kuçak, R. A., Özdemir, E., & Erol, S. (2017). The segmentation of point clouds with k-means and ANN (artifical neural network). *The International Archives of Photogrammetry, Remote Sensing and Spatial Information Sciences, 42*, 595.

Kuçak, R. A., Erol, S., & İşiler, M. (2020). Comparative Accuracy Analysis of LiDAR Systems. *Turkey LiDAR Journal, 2*, 34–40.

Kuçak, R. A. (2022). An Experimental Approach for The Documentation with Terrestrial Laser Scanning of the 1035 Ad Church of the Redeemer. *Mediterranean Archaeology & Archaeometry*, *22*(3).

Kuçak, R. A., Serdar, E., & Alkan, R. M. (2023). iPad Pro LiDAR sensörünün profesyonel bir yersel lazer tarayıcı ile karşılaştırmalı performans analizi. Geomatik, 8(1), 35-41.

Luetzenburg, G., A. Kroon, and A.A. Bjørk, Evaluation of the Apple IPhone 12 Pro LiDAR for an Application in Geosciences. Scientific reports, (2021). 11(1): p. 1-9.

McGlade J, Wallace L, Reinke K, Jones S. (2022). The Potential of Low-Cost 3D Imaging Technologies for Forestry Applications: Setting a Research Agenda for Low-Cost Remote Sensing Inventory Tasks. Forests, 13(2):204. https://doi.org/10.3390/f13020204

Mokroš M, Mikita T, Singh A, Tomaštík J, Chudá J, Wężyk P, Kuželka K, Surový P, Klimánek M, Zięba-Kulawik K, Bobrowski R & Liang X (2021). Novel Low-cost Mobile Mapping Systems for Forest Inventories as Terrestrial Laser Scanning Alternatives. International Journal of Applied Earth Observation and Geoinformation, 104:102512. https://doi.org/10.1016/j.jag.2021.102512

Monsalve, A., Yager, E. M., & Tonina, D. (2023). Evaluating Apple iPhone LiDAR measurements of topography and roughness elements in coarse bedded streams. *Journal of Ecohydraulics*, 1-11.

Murtiyoso A, Grussenmeyer P, Landes T & Macher H (2021). First Assessments into the Use of Commercial-Grade Solid State LiDAR for Low Cost Heritage Documentation. The International Archives of the Photogrammetry, Remote Sensing and Spatial Information Sciences, Volume XLIII-B2-2021 XXIV ISPRS Congress, 599-604. https://doi.org/10.5194/isprs-archives-XLIII-B2-2021-599-2021

Plaß, B., Emrich, J., Götz, S., Kernstock, D., Luther, C., & Klauer, T. (2021). Evaluation of Point Cloud Data Acquisition Techniques for Scan-to-BIM Workflows in Healthcare. FIG e-Working Week 2021, the Netherlands, 21-25 June 2021.

Spreafico, A., Chiabrando, F., Teppati, L. L., & Giulio, T. F. (2021). The iPad Pro Built-in LiDAR Sensor: 3D Rapid Mapping Tests and Quality Assessment. The International Archives of the Photogrammetry, Remote Sensing and Spatial Information Sciences, XLIII-B1-2021, 63-69. https://doi.org/10.5194/isprs-archives-XLIII-B1-2021-63-2021

Tavani, S., Billi, A., Corradetti, A., Mercuri, M., Bosman, A., Cuffaro, M., Seers, T., & Carminati, E. (2022). Smartphone Assisted Fieldwork: Towards the Digital Transition of Geoscience Fieldwork Using LiDAR-equipped iPhones. Earth-Science Reviews, 227:103969. https://doi.org/10.1016/j.earscirev.2022.103969

Vogt, M., Rips, A., & Emmelmann, C. (2021). Comparison of iPad Pro®'s LiDAR and TrueDepth Capabilities with an Industrial 3D Scanning Solution. Technologies, 9(2):25. https://doi.org/10.3390/technologies9020025.

Wang, X., Singh, A., Pervysheva, Y., Lamatungga, K. E., Murtinová, V., Mukarram, M., Zhu, Q., Song, K., Surový, P., & Mokroš, M. (2021). Evaluation of iPad Pro 2020 LiDAR for Estimating Tree Diameters in Urban Forest. ISPRS Annals of the Photogrammetry, Remote Sensing and Spatial Information Sciences, VIII-4/W1-2021, 105-110. https://doi.org/10.5194/isprs-annals-VIII-4-W1-2021-105-2021

7th Intercontinental Geoinformation Days

igd.mersin.edu.tr

Terrestrial photogrammetry and handheld laser scanning technique in 3D modeling of small objects

Zekeriya Kaçarlar[*1], **Ali Ulvi** [1]

1Mersin University, Department of Remote Sensing and Geographic Information Systems, Institute of Science, Mersin, Türkiye

Keywords
3D Model
Photogrammetry
Handheld Laser Scanning
Small Objects

Abstract

Cultural heritage works are an important tool in shedding light on a society's past to the future and keeping its social values alive at all times. Cultural heritage; We can examine it in three different ways: concrete, intangible and natural heritage. Nowadays, there are many methods and techniques used in 3D modeling of cultural heritage works. In recent years, laser scanning and photogrammetric techniques have been used in 3D modeling of objects of all sizes. In this study, two objects of different sizes were modeled using photogrammetric and hand-held laser scanning methods and the resulting models were examined. 3D models of the objects were created using two different methods, and the lengths of the same places were compared on the resulting models. While the measurements were obtained, the places to be measured were clearly observed in the measurement values obtained from the photogrammetric method, and values close to the measurement value obtained with the electronic caliper were obtained. Since the point cloud density was not sufficient in the measurements obtained by hand-held laser scanning, the image locations obtained from it could not be selected exactly and approximate measurement values could only be taken. Of the two methods, handheld laser scanning was not affected by ambient lighting and the scanning process was completed faster. Handheld laser scanning is not an applicable technique for small-sized objects because it does not create a sufficiently dense point cloud. It has been concluded that the photogrammetry technique is a suitable technique for 3D modeling of small-sized cultural heritage artifacts and that the resulting models can be used safely in studies.

1. Introduction

Cultural heritage works are an important tool for a society to shed light from the past to the future and to keep its social values alive at all times. Cultural heritage; We can examine it in three different ways: tangible, intangible and natural heritage (Ulvi et al., 2019; Döş & Yiğit, 2023). These works are damaged and lose their properties due to reasons such as physical factors, environmental conditions and natural disasters (Cömert et al., 2012; Tercan, 2017; Döş & Yiğit, 2023). For this reason, it is very important to protect, document and record cultural heritage artifacts.

Today, there are many methods and techniques used in 3D modeling of cultural heritage artifacts (Kanun et al. 2022). In recent years, laser scanning and photogrammetric techniques have been used in 3D modeling of objects of all sizes. Common and non-invasive methods have been used in modeling objects from large historical buildings to small sculptures and much smaller objects (Viswanatha et al., 2011). In recent years, photogrammetry has been used for the reconstruction of objects and in architecture. This method can also be applied in areas where it is desired to obtain the spatial shape of an existing object outside of these areas. Laser scanning and point cloud technologies, which are data acquisition methods in documenting cultural heritage, have become quite common.

The photogrammetric method has made significant progress in 3D modeling in terms of obtaining images with lower cost than other methods and with technological developments (Prosdocimi et al., 2017; Karataş et al. 2022a). Photographs of the object to be modeled were taken superimposed from different camera angles and a scaled and coordinated point cloud

* **Corresponding Author**

*(zekeriyakacarlar@gmail.com) ORCID ID: 0000-0003-0232-9574
(aliulvi@mersin.edu.tr) ORCID ID 0000-0003-3005-8011

Cite this study

Kaçarlar, Z & Ulvi, A. (2023). Terrestrial photogrammetry and handheld laser scanning technique in 3D modeling of small objects. Intercontinental Geoinformation Days (IGD), 7, 209-212, Peshawar, Pakistan

and 3D model were created (Kaya et al., 2021; Döş & Yiğit, 2023).

The most important disadvantage of the photogrammetric method is its dependence on an experienced camera operator who can manage the camera parameters and obtain photographs accurately. If the images are not acquired correctly, they will be affected by errors caused by vibration in the 3D model formation (Rodríguez-Martín & Rodríguez-Gonzálvez 2020). If photo capture is not automatic, there will be more user error. Automating image acquisition will eliminate errors caused by the camera operator. The models created with images obtained from automatic systems will be more consistent in terms of accuracy.

Terrestrial laser scanning is a polar measurement system that directly creates 3D object points (Karataş et al. 2022b). Many existing terrestrial laser scanning systems provide color information, but are lacking in modeling small objects due to their minimum acquisition distance and limited distance sensitivity. Thanks to the developed handheld laser scanners, it has become possible to model small objects with laser scanner systems. Handheld laser scanning is a non-contact active measurement technique, just like terrestrial laser scanning. It is used in medical orthoses and prostheses, quality control, and robotic vision technologies in the film production industry. In addition to these areas, it is used to model hollow and very small objects that cannot be scanned with terrestrial laser scanning in cultural heritage documentation studies.

In his master's thesis study, Alvarez (2021) aimed to design a cost-effective photogrammetric 3D Imaging system for small archaeological artifacts. This system aims to produce high-quality 3D artwork with highly detailed textures and color information that is optimized for depth of field and serves many important purposes. The designed system creates higher quality 3D images than other cost-effective solutions. Compared to costly systems, the designed system produced 3D images of comparable quality.

In his undergraduate thesis, Prokop (2022) studied the creation of a 3D model of the Chapel of Our Lady in Brno-Líšeň using images taken from a digital camera Canon EOS 6D Mark II and a low-cost camera Xiaomi Mi 10T Pro. Mobile phone images were combined in two photogrammetric software (Bentley ContextCapture and Agisoft Metashape Professional). The accuracy of the models was analyzed using measured control points and a reference point cloud obtained from a laser scan of the chapel.

In this study, two objects of different sizes were modeled using photogrammetric and hand-held laser scanning methods and the resulting models were examined.

2. Method

In this study, a house figurine with a regular geometric structure (Figure 1a), from which measurements can be easily taken, and a vase object with an irregular geometric structure (Figure 1b), from which measurements cannot be taken (Figure 1b), were modeled using photogrammetric and hand-held laser scanning methods, and the resulting models were examined.

Figure 1a. House figurine **1b.** Vase

In the photogrammetric method, a rotating platform was designed and image acquisition was achieved automatically. The rotating platform was created in software and design. The rotating platform is ready by connecting the camera connections and power adapter. In the photogrammetric method, lighting is important for modeling. Parts with high details, lighting and the image texture of the object affect the number and angle of taking photographs (Arican et al., 2023).

In this study, lighting was provided by a photo shooting tent with a white background and 2*78 LED lights. The camera was positioned appropriately to the object with the help of a tripod (Figure 2).

Figure 2. Location of camera and photo shooting tent

Based on the size and density of the object, the focus waiting time, the number of photos taken, the photo shooting angle, and the number of photos to be taken for each movement were determined from the rotating platform hand unit and the shooting started. In this study, the number of photos taken is 20, focus waiting time; 2 seconds for the household figurine and 3 seconds for the vase object, the photo shooting angle was determined as 20 degrees and the number of photos taken was determined as 1 for each movement. Shooting started under the conditions specified for both objects and was completed without any problems.

The images were transferred to the Context Capture program and a local coordinate system was created with the help of control points on the rotating platform base. Camera positions are formed correctly for both objects. The photogrammetric process was completed with the point cloud and modeling process.

The same objects were used in the handheld laser scanning process, and the objects were placed on a table that the operator could easily turn around.

FARO Freestyle3D was used as the scanner. It is ready with the help of a tablet connected to the scanner in one hand and the printer in the other. Depending on the size of the objects, the distance to the object was determined by making a few attempts. Scanning started by pressing the button on the scanner and the scanning process was completed by making a full tour around the object. The process was repeated for the second object. Scanning data was transferred to the tablet and from there transferred to the special software Scene.

A measurement was taken from both objects with the help of an electronic caliper (Figure 5).

Figure 5. Measurements of objects with electronic caliper

Measurements of the same places were also taken from models obtained by photogrammetric method and models obtained with a hand-held laser scanner.

Lengths obtained by photogrammetric method.

Figure 6. Length measurement obtained from the vase object by photogrammetric method

Figure 7. Length measurement of the house figurine obtained by photogrammetric method

Lengths obtained by handheld laser scanning.

Figure 8. Length measurement obtained from the vase object by hand-held laser scanning method

Figure 9. Length measurement of the house figurine obtained by hand-held laser scanning method

3D models of the objects were created using two different methods, and the lengths of the same places were compared on the resulting models.

When the resulting models were considered, it was observed that the density of point finds in the models obtained by the photogrammetric method was denser than the models obtained by the hand-held laser scanning method. The photogrammetric method gave better results in displaying texture details and colors. Automation of the image acquisition process in the photogrammetric system has increased the accuracy of the obtained model and the sensitivity of the measurement value taken.

While the measurements were being obtained, the places to be measured were clearly observed in the measurement values obtained from the photogrammetric method, and values close to the measurement value obtained with the electronic caliper were obtained. Since the point cloud density was not sufficient in the measurements obtained by hand-held laser scanning, the image locations obtained from it could not be selected exactly and approximate measurement values could only be taken. Of the two methods, handheld laser scanning was not affected by ambient lighting and the scanning process was completed faster.

3. Results

In this study, models were created using the photogrammetric method and hand-held laser scanning method, which are measurement techniques used in modeling small objects in the cultural heritage, and the resulting models were evaluated.

The advantages and disadvantages of the techniques used in the obtained models were discussed and the methods were compared with each other. Handheld laser scanning is not an applicable technique for small-sized objects because it does not create a sufficiently dense point cloud. It has been concluded that the photogrammetry technique is a suitable technique for 3D modeling of small-sized cultural heritage artifacts and that the resulting models can be used safely in studies.

Acknowledgement

This study was supported by Mersin University Scientific Research Projects with project number 2021-2-TP2-4528.

4. References

Alvarez M. (2021). Design of a cost-effective photogrammetric 3D-imaging system for small archaeological artifacts, Delft University of Technology, Delft, Netherlands.

Arican, D., Göksu, F. F., Tunalioğlu, N., & Öcalan, T. (2023). Research on 3D reconstruction of small size objects using structure from motion photogrammetry via smartphone images. Jeodezi ve Jeoinformasyon Dergisi, 10(2), 112-123.

Cömert, R., Avdan, U., & Şenkal, E. (2012). Usage Areas of Unmanned Aerial Vehicles and Future Expectations. IV. Remote Sensing and Geographic Information Systems Symposium (UZAL-CBS 2012), 16-19, Zonguldak.

Döş, M. E., & Yiğit, A. Y. (2023). 3D Modeling and WEB-Based Visualization of Small-Scale Historical Artifacts with Photogrammetry Method. Turkish Journal of Photogrammetry, 5(1), 20-28.

Kanun, E., Alptekin, A., Karataş, L., & Yakar, M. (2022). The use of UAV photogrammetry in modeling ancient structures: A case study of "Kanytellis". Advanced UAV, 2(2), 41-50.

Karataş, L., Alptekin, A., & Yakar, M. (2022a). Detection and documentation of stone material deterioration in historical masonry structures using UAV photogrammetry: A case study of Mersin Aba Mausoleum. Advanced UAV, 2(2), 51-64.

Karataş, L., Alptekin, A., & Yakar, M. (2022b). Determination of Stone Material Deteriorations on the Facades with the Combination of Terrestrial Laser Scanning and Photogrammetric Methods: Case Study of Historical Burdur Station Premises. *Advanced Geomatics*, *2*(2), 65-72.

Kaya, Y., Polat, N., Şenol, H. İ., Memduhoğlu, A., & Ulukavak, M. (2021). Combined use of terrestrial and UAV photogrammetry in documenting archaeological remains. Turkish Journal of Photogrammetry, 3 (1), 9-14. DOI: 10.53030/tufod.899089.

Prokop J. (2022). 3D Model of the Selected Object, Institute of Geodesy, Diploma Thesis, Brno University of Technology.

Prosdocimi, M., Burguet, M., Di Prima, S., Sofia, G., Terol, E., Comino, J. R., Cerdà, A., & Tarolli, P. (2017). Rainfall simulation and Structure-from-Motion photogrammetry for the analysis of soil water erosion in Mediterranean vineyards. Science of the Total Environment, 574, 204-215.

Rodríguez-Martín, M., & Rodríguez-González, P. (2020). Suitability of automatic photogrammetric reconstruction configurations for small archaeological remains. Sensors, 20(10), 2936.

Tercan, E. (2017). Photogrammetric Documentation of the Ancient City and Historical Caravan Route Using Unmanned Aerial Vehicles: Sarıhacılar Example. Journal of Engineering Sciences and Design, 5(3), 633- 642. DOI: 10.21923/jesd.315232.

Ulvi, A., Yakar, M., Yiğit, A. Y., & Kaya, Y. (2019). The Use of Photogrammetric Techniques in Documenting Cultural Heritage. The Example of Aksaray Selime Sultan Tomb. Universal Journal of Engineering Science, 7(3), 64-73.

Viswanatha, V., Patil, N. B., & Pandey, S. (2011). Computation of Object parameter Values based on Reference object embedded in Captured Image. Research Journal of Computer Systems Engineering-RJCSE, 2, 183-191.

7th Intercontinental Geoinformation Days

igd.mersin.edu.tr

A comprehensive study on enhanced accuracy analysis of LiDAR data

Berkan Sarıtaş*[1], Gordana Kaplan[2]

[1]Eskisehir Technical University, Graduate School of Science, Eskisehir, Türkiye
[2]Eskisehir Technical University, Institute of Earth and Space Sciences Institute, Eskisehir, Türkiye

Keywords
Remote sensing
CSF Filter
DTM
LIDAR
Accuracy Analysis

Abstract
LIDAR technology, a prominent remote sensing technology widely employed today, offers a highly reliable means of swiftly and accurately gathering data. This research project aims to generate a Digital Terrain Model (DTM) from a LIDAR dataset featuring urban attributes. The chosen tool for this endeavor is the CSF Filter algorithm within Cloud Compare, an open-source software, with an emphasis on assessing the model's precision. Within the CSF Filter algorithm, we examined the accuracy of the Surface Approximation Mesh (SAM) when various cover values were employed: 0.1, 0.5, 1, 2, and 5. Our investigation primarily revolved around calculating the volume disparity between a manually created reference model within a computer environment and the models generated through filtering. This analysis allowed us to pinpoint the most suitable parameter value for creating an accurate model. The results indicated that opting for a cover value of 0.5 produced the most accurate model. Notably, when a cover value of 5 was chosen for the input parameter, the largest disparities were observed between the resulting model and the reference model.

1. Introduction

Remote sensing techniques have found diverse applications beyond traditional map creation, encompassing the development of 3D city and building models, land use analysis, and the monitoring of natural disasters. Among these applications, the generation of digital elevation models (DEMs) that capture comprehensive elevation data of the Earth's surface is of particular significance. It's essential to distinguish between DEMs, which encompass 3D information pertaining to both natural and man-made structures on the Earth's surface, and digital terrain models (DTMs), which exclusively represent the natural land surface, excluding man-made structures not integrated into the Earth's surface (Uray, 2022).

LIDAR technology, an active sensor technology, plays a pivotal role in numerous domains. LIDAR, an acronym for "light detection and ranging," employs scattered light to gather a wealth of information (Lu et al., 2011). This technology excels in swiftly and accurately acquiring physical data, facilitating the automatic generation of precise 3D models, whether they pertain to man-made or natural objects, without requiring physical contact (Fidan & Fidan, 2021). LIDAR data is often referred to as a "point cloud," a nomenclature attributed to the irregular nature of scanning data resulting from changes in target characteristics and aircraft movements (Lu et al., 2011).

The primary objective of this study is to conduct an accuracy analysis of volume calculations, focusing on the pivotal parameter that determines the ground class within LIDAR data. The data input into the CSF filter of the LIDAR point cloud is provided by different individuals in the context of popular research. The CSF Filter, which facilitates reporting and storage, enables the measurement of accuracy rates when varying parameter values are applied to LIDAR point cloud data. This investigation aims to identify the parameter that yields the most successful filtering outcomes and explores the applicability of alternative methodologies while scrutinizing the accuracy levels in question.

1.1. Point cloud filtering

In the realm of remote sensing, applications extend beyond mapping, encompassing 3D city models, land use analysis, and disaster monitoring. Digital elevation models (DEMs) capture comprehensive elevation data. Notably, DEMs encompass both natural and man-made

* **Corresponding Author**

*(berkansrts@gmail.com) ORCID ID 0000 – 0003 – 1429 – 0304
(kaplangorde@gmail.com) ORCID ID 0000 – 0001 – 7522 – 9924

Cite this study

Sarıtaş, B., & Kaplan, G. (2023). A comprehensive study on enhanced accuracy analysis of LIDAR data. Intercontinental Geoinformation Days (IGD), 7, 213-216, Peshawar, Pakistan

structures, while digital terrain models (DTMs) focus solely on natural land surfaces (Uray, 2022).

LIDAR technology, or "Light Detection and Ranging," is a versatile active sensor technology, enabling swift and precise 3D modeling of both man-made and natural objects without physical contact (Fidan & Fidan, 2021). LIDAR data, often referred to as a "point cloud," reflects the irregularity in scanning data due to varying target characteristics and aircraft movements (Lu et al., 2011).

This study examines the accuracy of LIDAR data filtering using the CSF Filter algorithm, investigating the ground class determination parameter. Different data sources contribute to the LIDAR point cloud within current research, and the CSF Filter aids in measuring accuracy rates with various parameter values. The goal is to identify the most effective parameter for filtering and explore alternative methods while assessing accuracy (Uray, 2022).

2. Method

In the LIDAR point data processing, we start by manually removing noise points using CloudCompare. Then, we experiment with various parameter values in the CSF Filter algorithm to extract soil-class points and create a Digital Terrain Model (DTM). We establish a reference DTM through manual interventions in CloudCompare and Civil 3D for accuracy assessment. To evaluate parameter effectiveness, we calculate the volüme difference between the reference DTM and the filtered DTM data.

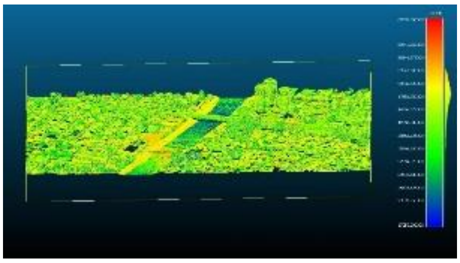

Figure 1. Viewing urban area LIDAR data in CloudCompare software (Sarıtaş and Kaplan, 2023)

2.1. Work area and LIDAR data

The study area is situated in the western part of Skopje, the capital of North Macedonia, encompassing 312 buildings (Figure 1). This region is bisected by the Vardar River, approximately 60 meters wide. On the left side, the area is characterized by a dense grid of low residential buildings with a maximum height of 10 meters, while the right side features taller residential and commercial structures, with a maximum height of 70 meters. The terrain is predominantly flat, with surface elevations ranging from 250 to 327 meters and land elevations between 250 and 325 meters. The study area also includes various trees, bridges, and a 20-meter-wide riverbank (Kaplan et al., 2022).

The primary dataset of the study is LIDAR remote sensing, acquired from the Cadastral Office of North Macedonia. The data collection was conducted using an aerial platform, Cessna 402B, equipped with the Riegl VQ-780i sensor system. The data acquisition took place on May 3, 2019, under clear skies and at an air temperature of 11 °C. The LIDAR data has a point density of 5 points/m² (Kaplan et al., 2022).

In total, the 3D LIDAR point 214ort 214ort he urban area comprises 4,540,667 data points.

2.2. Obtaining the reference model

In the absence of local measurement capabilities, the reference model is manually generated within a computer environment. Initially, an automatic classification process in CloudCompare identifies ground points, and all other points are subsequently removed. However, a closer examination of the ground point class data reveals the necessity for manual filtering. To enhance the precision of this filtering, Google Earth imagery can be leveraged to ascertain whether the processed points are affiliated with the ground or non-ground areas.

Figure 2. Data Obtained by Leaving the Point Cloud of the Soil Class Alone

The consideration of neighborhood relationships to determine the ground class sometimes results in inaccurate selections, particularly in areas with minimal elevation variations. In these cases, data not associated with the ground may be misclassified as ground points, leading to erroneous classifications. To rectify these inaccuracies, Google Earth images of the region are employed to improve the precision of ground point selection.

Figure 3. Google Earth Image of the Study Area (URL-1)

(a) (b)

Figure 4. (a) Google Earth Image of the Area Closely Examined (URL-1), (b) Classified LIDAR Point Cloud Data of the Closely Examined Area

Due to the challenges of identifying the situation from a top-down perspective, thorough examinations are conducted from a side-view angle. These investigations reveal that the point cluster is situated below the actual road level in the real-world context.

Figure 5. Examining the Image of the Area (URL-1)

A comprehensive examination of the entire point cloud, combined with Google Earth images, unveiled visible issues, which were subsequently resolved through manual point deletion. The subsequent step involves utilizing a triangle model to identify problems that might not be apparent to the naked eye, especially those not pertaining to the ground.

In an effort to enhance the reference model's accuracy, another approach is employed, entailing the creation of a triangular model to detect any abrupt surface irregularities. The data initially in ".las" format, generated by CloudCompare, is transformed into ".rcp" format using ReCAP software. Subsequently, it is imported into Civil 3D, where a triangular model is constructed. During the triangular model operations, adjustments are made to address inaccuracies in areas with sudden deviations. These corrections are pivotal in the process of generating the reference Digital Terrain Model (DTM), which includes contour lines and cross-sections analyzed and refined on the triangular model.

2.3. Performing filtering operations with CSF Filter

To assess the accuracy of the CSF Filter algorithm, classifications were conducted by varying the cover value at five different levels: 0.1, 0.5, 1, 2, and 5, respectively.

Table 1. Point numbers of LIDAR data created with CSF Filter (Saritas and Kaplan, 2023)

Cover Value	Number of Off-Ground Points	Number of Points on the Ground
0.1	1.661.947	2.878.720
0.5	2.167.155	2.373.512
1	1.748.797	2.791.870
2	2.643.720	1.896.947
5	2.983.257	1.557.410

2.4. Accuracy Analysis

In the volume calculations conducted between the reference DTM and the DTM data resulting from the filtering process, the model with the smallest calculated volume is regarded as the most accurately filtered model. This conclusion is drawn because of the remarkable similarity between the triangular model created using the reference DTM and the triangular model generated from the filtered DTM. In instances where a substantial disparity is observed, it suggests the presence of deviations in the model and a lower level of data accuracy. Figure 7 visually illustrates the potential differences between these two distinct models.

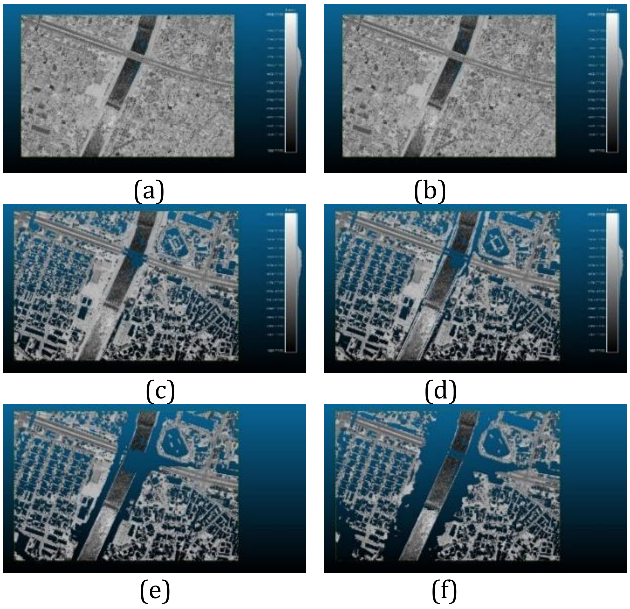

Figure 6. For an urban LIDAR point cloud; (a) The Original Point Cloud, (b) Data Obtained As a Result of Entering the CSF Filter Algorithm Cover Value as 0.1, (c) Data Obtained as a Result of Entering the CSF Filter Algorithm Cover Value as 0.5, (d) Data Obtained As a Result of Entering the CSF Filter Algorithm Cover Value as 1, (e) Data Obtained as a Result of Entering the CSF Filter Algorithm Cover Value as 2, (f) Data Obtained as a Result of Entering the CSF Filter Algorithm Cover Value as 5 (Saritas and Kaplan, 2023)

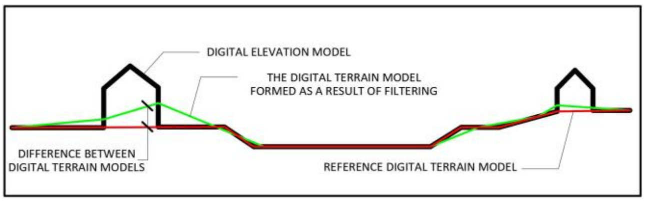

Figure 7. Difference Between Reference DTM and Filtering DTM

In AutoCAD Civil 3D software, a separate triangular model is established for each DTM dataset. This analysis method facilitates volume calculations between the triangular models derived from the DTM data obtained through filtering, individually compared to the triangular model accepted as the reference DTM. These results serve as an indicator of data accuracy. When interpreting the result data, both low and high areas are jointly assessed in relation to the reference model, as illustrated in Figure 8, and the overall discrepancy is taken into account.

This analysis method incorporates volume calculations and also generates a difference surface, highlighting variations between two distinct triangular models. This approach provides a comprehensive evaluation of data accuracy and aids in the identification of optimal parameters.

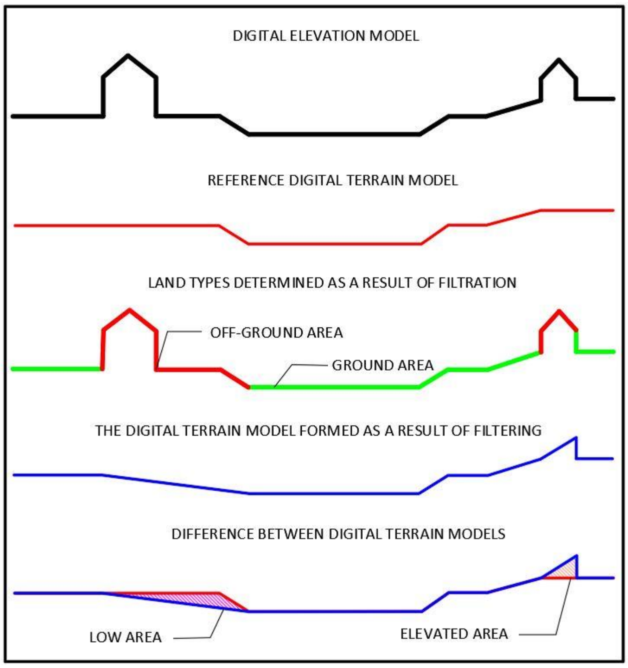

Figure 8. Comparison of DTM

Table 2. Accuracy analysis results of models obtained using the CSF Filter algorithm

CSF Filter Parameter Value	Low Area (m^3)	Elevated Area (m^3)	Total Difference (m^3)
0.1	6563.38	376124.16	382687.54
0.5	24232.04	23732.29	47964.33
1	85385.72	13880.86	99266.58
2	187682.76	9098.31	196781.07
5	493952.45	4434.26	498386.71

3. Results

Upon evaluating the obtained results, it becomes evident that selecting a parameter value of 0.5 for the filtering process yields a Digital Terrain Model (DTM) that closely aligns with reality. Conversely, among the parameter values considered, it is apparent that a value of 5 creates a model that deviates furthest from reality. Even when assessing the models that provide the closest outcomes, it is worth noting that manual interventions can further enhance the accuracy of the results.

4. Discussion

Employing terrestrial measurement methods for crafting the reference model has the potential to significantly enhance its accuracy. In contrast, generating the reference model manually in this particular study may introduce variables that could impact the precision of the subsequent accuracy analysis. The inclusion of terrestrial measurements, characterized by their physical, ground-based nature, can reduce the potential for errors and enhance the overall reliability of the reference model. This approach aligns more closely with the actual topography of the study area, contributing to the accuracy of subsequent comparisons and assessments.

5. Conclusion

By increasing the accuracy of the reference model used in the study by using terrestrial measurement methods, the usability of the cubage calculation, which is the accuracy analysis method investigated in the study, can be determined more accurately.

Acknowledgement

This study was adapted from Berkan Sarıtaş's master's thesis.

References

Fidan, D., & Fidan, Ş. (2021). Yersel lazer tarama teknolojileriyle oluşturulan 3B modellerin akıllı kent uygulamalarında kullanımı: Mersin Süslü Çeşme örneği. Türkiye LIDAR Dergisi, 3(2), 48–57. https://doi.org/10.51946/melid.1021819

Kaplan, G., Comert, R., Kaplan, O., Matci, D. K., & Avdan, U. (2022). Using Machine Learning to Extract Building Inventory Information Based on LIDAR Data. ISPRS International Journal of Geo-Information, 11(10). https://doi.org/10.3390/IJGI11100517

Karasaka, L., & Keleş, H. (2020). CSF (Cloth simulation filtering) Algoritmasının Zemin Noktalarını Filtrelemedeki Performans Analizi. Afyon Kocatepe Üniversitesi Fen ve Mühendislik Bilimleri Dergisi, 267–275. https://doi.org/10.35414/akufemubid.660828

Liu, X. (2008). Airborne LIDAR for DEM generation: some critical issues. Http://Dx.Doi.Org/10.1177/0309133308089496, 32(1), 31–49. https://doi.org/10.1177/0309133308089496

Lu, Y., Wang, X., Zhou, K., & Yang, J. (2011). MATLAB Tools for LIDAR Data Conversion, Visualization, and Processing. In X. He, J. Xu, & V. G. Ferreira (Eds.), International Symposium on LIDAR and Radar Mapping 2011: Technologies and Applications. https://doi.org/10.1117/12.912529

Sarıtaş, B. & Kaplan, G.(2023). Enhancing Ground Point Extraction in Airborne LiDAR Point Cloud Data Using the CSF Filter Algorithm. Advanced LiDAR, 3(2), 53-61.

Uray, F. (2016). Hava LIDAR Nokta Bulutu Verileri Fİltreleme Algoritmalarının Geliştirilmesi ve Performanslarının Karşılaştırılması [Yüksek Lisans Tezi]. Necmettin Erbakan Üniversitesi.

Uray, F. (2022). Derin öğrenme tekniklerini kullanarak hava LIDAR nokta bulutlarının sınıflandırılması [Doktora Tezi]. Necmettin Erbakan Üniversitesi.https://doi.org/10.1515/geo-2019-0038

URL-1: earth.google.com (2023). https://earth.google.com/web/search/Partizanski+Odredi+87,+Boulevard+Partizanski+Odredi,+%c3%9csk%c3%bcp,+Kuzey+Makedonya/@42.00585824,21.3618348,265.50010264a,2966.21743366d,35y,178.08009325h,0t,0r/data=CigiJgokCXBCgJB73ERAEb4DjSnX2kRAGaAp-XmozDVAIdb_99uWwzVAOgMKATA

7th Intercontinental Geoinformation Days

igd.mersin.edu.tr

Investigating the utilization of iPhone lidar sensor in documenting cultural heritage

Emine Beyza Dörtbudak*[1], Şeyma Akça [1]

[1]Harran University, Geomatic Engineering Department, Sanliurfa, Türkiye

Keywords
Photogrammetry
Iphone
LİDAR
Point Cloud
Documentation

Abstract

Historical artifacts and archaeological remains are critical documents that contribute to our understanding of a society's history, culture, and lifestyle. Historical artifacts can be damaged for various reasons. Damages hinder the sustainable preservation of the artwork by complicating the understanding of culture and art. Therefore, documenting the current state of historical artifacts and recording their features helps minimize damage. There are various methods for documenting historical heritage, one of which is photogrammetry, an image-based technique that obtains three-dimensional data by combining two-dimensional images taken from different angles., Another technique that can be employed in the documentation process is Light Detection and Ranging (LIDAR). A Lidar device sends out brief pulses of laser beams to its surroundings. These beams collide with and bounce off objects nearby. Lidar measures distance by detecting these reflected beams. In this study, a 3D point cloud of a relief sculpture in the Kizilkoyun Necropolis was created using photogrammetry and the LIDAR sensor added to smartphones.

1. Introduction

Historical artifacts and archaeological remains are important works that provide information about a society's history, culture, and lifestyles. These works can be damaged by human intervention such as artwork urbanization, warfare, smuggling, or natural disasters like earthquakes and floods. The resulting damages make it difficult for people to connect with the past, understand culture and art, and hinder the sustainable preservation of the artwork. Therefore, documenting the current state of historical artifacts, recording their features, and preserving can assist in passing them on to future generations and minimizing damage.

The efforts made to obtain accurate and reliable data in documenting historical artifacts have led to the emergence of new techniques in the field of documentation (Korumaz et al., 2011). With advancing technology, traditional methods such as hand drawing and photographing with analog cameras have been replaced by modern documentation techniques such as high-resolution digital photography, laser scanning, and photogrammetry for 3D modeling (Yiğit and Uysal, 2021). Photogrammetry is an image-based technique that gathers three-dimensional data from two-dimensional images taken from different angles and positions (Remondino and El-Hakim, 2006). Its ability to determine the characteristics of an object in three dimensions without direct contact and to cover the resulting model with attributes and real textures has contributed to its popularity (Obradović et al., 2020). Due to its speed, low cost, and high-quality data in terms of accuracy, it is frequently preferred for documenting and 3D modeling cultural heritage (Uslu et al., 2016; Zeybek and Kaya, 2020).

Another method that can be employed in the documentation process is LIDAR. A Lidar device sends out brief pulses of laser beams to its surroundings. These beams collide with and bounce off objects nearby. Lidar measures distance by detecting these reflected beams (Polat and Uysal, 2016; Jiang et al., 2005). It has many advantages, such as high accuracy, high point density, and the ability to rapidly collect a large number of point data. Despite the previously perceived high equipment cost, recent technological developments have allowed for the miniaturization of equipment and improvements in sensors, enabling the integration of LIDAR into smartphones. In line with these developments, Apple Inc. released the iPhone 12 and iPhone 12 Pro Max models in

* **Corresponding Author**

*(beyzadbk@gmail.com) ORCID ID 0009-0001-6523-6060
(seymakca@harran.edu.tr) ORCID ID 0000-0002-7888-5078

Cite this study

Dörtbudak, B., & Akca, S. (2023). Investigating the Utilization of iPhone LiDAR Sensor in Documenting Cultural Heritage. Intercontinental Geoinformation Days (IGD), 7, 217-221, Peshawar, Pakistan

2020, the first series of phones equipped with a LIDAR sensor (Aslan and Polat, N 2022). The LIDAR sensor was added to the camera system in these models to provide precise positioning in augmented reality (AR) applications and enhance depth perception (Luetzenburg et al., 2021). In this study, the 3D point cloud of the soldier relief found in the M16 rock tomb of the Kizilkoyun Necropolis, a cultural heritage site, was created using an iPhone 14 Pro Max. The point cloud obtained using the LIDAR sensor was compared with the cloud obtained through terrestrial photogrammetry.

2. Method

2.1. Study area

The chosen study area is the Kizilkoyun Necropolis Archaeological Site. Located at the foothills of the Sanliurfa Tilfindir Hill, the Kizilkoyun Necropolis is bordered to the east by the Yenimahalle archaeological area, to the west by the Haleplibahçe archaeopark area, and to the south by the Sanliurfa Castle and the Balikligöl. Its location within the city center and surrounded by archaeological sites enhances the value of the study area (Tel and Yüksel, 2017). The relief sculpture to be captured in point cloud within the study area is shown in Figure 1.

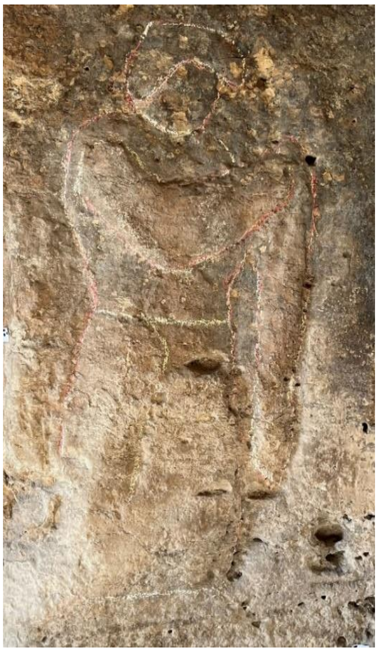

Figure 1. Historical soldier relief

2.2. Equipment

The model production is divided into two stages: fieldwork and office work. The fieldwork stage aims to collect data. For this purpose, photographs of the relief sculpture located north of the rock tomb M16 were taken with a Canon EOS 2000D, as specified in Table 1. Care was taken to ensure that the images were overlapping during the photo shoot. A total of 67 photos were taken with the relevant camera. High-resolution photos from different angles were obtained to capture all the details of the relief. The photos obtained in this stage will constitute the visual data set to be used in the subsequent photogrammetric modeling process. The distance between the markers attached around the relief was measured in meters and recorded.

Table 1. Camera specifications

Camera manufacturer	Canon
Camera model	Canon EOS 200D
F-stop	f/7.1
Exposure time	1/25 sn.
Focal length	18mm

Subsequently, scanning was performed using the iPhone 14 Pro Max mobile device for the point cloud to be created using LIDAR data. The 3D Scanner App application was preferred for scanning. The interface of the LIDAR sensor belonging to the device and the scanning application used is shown in Figure 2.

(a)

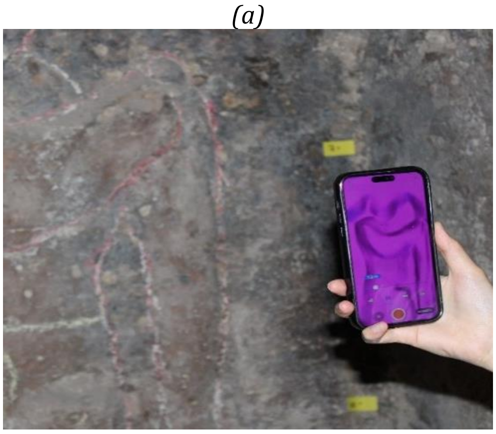

(b)

Figure 2. The LIDAR sensor of the used device *(a)*, Interface of the scanning application *(b)*

2.3. Lidar scanning and S*f*M processing

The scanning parameters were set as follows: resolution 5 mm, distance 1.2 m, processing HD. The Lidar scanning process with the iPhone took an average of 15 minutes. During the scan, the phone was held upright to ensure the sensor's front side could see. Care was taken to avoid creating shadow situations. Lidar sensors have a specific working range, so during the scan, it was ensured that the sensor was at a compatible distance with the target relief sculpture. Attention was paid to avoid areas that were not scanned or had too much overlapping scanning. The fieldwork was completed, and the office work phase began. Special software was used to process the photos at this stage.

The software analyzes the photos, identifies common points, and based on this data, reconstructs the three-dimensional structure. The images obtained from the camera were processed using Agisoft Metashape, an independent software that offers significant capabilities for performing photogrammetric processes on digital images. The software utilizes the Structure from Motion (S*f*M) technique to process the photos. Structure from Motion (S*f*M) refers to the process of creating three-dimensional objects from a series of two-dimensional images. S*f*M is used in various applications such as 3D scanning, augmented reality, visual simultaneous localization and mapping (*SLAM*), and mapping (Korumaz et al., 2011; Yilmaz et al., 2008). S*f*M can achieve faster results compared to other methods, model various objects regardless of size, and is suitable for tasks requiring precise measurements due to its use of high-resolution images (Berra and Peppa, 2020). The evaluation and processing of the images resulted in the creation of a point cloud.

3. Results and Discussion

Using 62 photos, a 3D point cloud was generated with S*f*M. The produced dense point cloud and the locations of the photo captures can be seen in Figure 3.

(a)

(b)

Figure 3. Photo capture locations *(a),* Generated built dense cloud *(b).*

The generated point cloud contains over 2 million colored points.

The generated point cloud contains colored points marked with '80.000' The same relief sculpture was scanned with the iPhone's Lidar Advanced mode. The resulting point cloud is provided in Figure 4.

Figure 4. The point cloud obtained through Lidar scanning

The LiDAR point cloud is sparse than SfM point cloud. It contains over 80-thousand-point cloud.

Both data sets have been scaled using markers. The visual representation of the markers used is shown in Figure 5, and the distances between the markers are provided in Table 2.

Figure 5. The markers on the relief sculpture.

Table 2. Distance between markers

Marker Number	Distance
12-14	95 cm
14-4	190 cm
4-2	106 cm
2-12	189 cm

Both scaled point clouds were registered using markers in the *CloudCompare* software. In CloudCompare, Cloud-to-Cloud Distance module (C2C) was utilized to detect differences between overlapping point clouds after the registration process. In this process, the photogrammetric point cloud was accepted as the reference since it is denser and more comprehensive. The C2C results are provided in Figure 6.

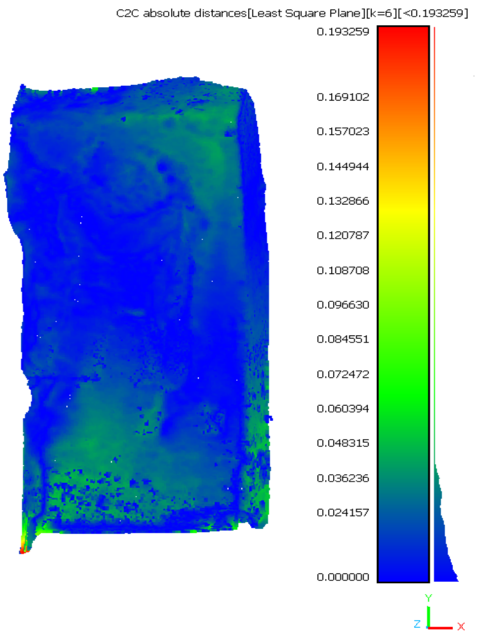

Figure 6. The result of C2C

Upon examination of Figure 6, it is observed that both point clouds overlap significantly. The average difference between the two-point clouds is calculated as 1.5 cm, with the highest difference being 19 cm. The obtained 19 cm difference is not from the relief sculpture but originates from the surrounding wall and floor. In this regard, it can be considered that the overlapping process carried out using markers is successful. Additionally, the point clouds are also usable in terms of the integrity of the object.

4. Conclusion

This study examined the critical endeavor of documenting historical artifacts and cultural heritage, with a specific focus on the utilization of innovative techniques for accurate and reliable data acquisition. The study centered on a cultural heritage site, the Kizilkoyun Necropolis, and employed both photogrammetry and LIDAR techniques for data acquisition. In the photogrammetric process, overlapping high-resolution photos were captured. Simultaneously, LIDAR scanning was performed using the iPhone 14 Pro Max equipped with a LIDAR sensor, making use of a scanning application.

The results revealed successful data acquisition through both methods, with minimal differences in point cloud data. The photogrammetric technique produced a dense point cloud using 62 photos, and the LIDAR scanning generated a point cloud with precise details. The integration of markers in both datasets proved effective in achieving a high level of accuracy and completeness. The comparative analysis showed that the average difference between the two point clouds was only 1.5 cm, with the highest difference being 19 cm, attributed to the surrounding wall and floor rather than the relief sculpture itself. These findings underscore the potential of modern technologies, such as photogrammetry and smartphone-integrated LIDAR, in the documentation and preservation of cultural heritage. They ensure the transfer of knowledge across generations while minimizing the risk of damage to historical artifacts, making it a valuable contribution to the field of cultural heritage documentation.

References

Aslan, İ., & Polat, N. (2022). Availability of Iphone 13 Pro Laser Data in 3D Modeling. Advanced LiDAR, 2(1), 10-14.

Berra, E. F., & Peppa, M. V. (2020, March). Advances and challenges of UAV SFM MVS photogrammetry and remote sensing: Short review. In 2020 IEEE Latin American GRSS & ISPRS Remote Sensing Conference (LAGIRS) (pp. 533-538). IEEE.

Jiang, J., Ming, Y., Zhang, Z., Zhang, J. (2005). Point-based 3D Surface Representation from LiDAR Point Clouds. The 4th ISPRS Workshop on Dynamic and Multidimensional GIS. September 6-8, 2005, Wales, UK, 1-4.

Korumaz, A. G., Dülgerler, O. N., & Yakar, M. (2011). Kültürel Mirasın Belgelenmesinde Dijital Yaklaşımlar. S.Ü. Mühendislik Mimarlık Fakültesi Dergisi, 26(3), 67-83.

Luetzenburg, G., Kroon, A., & Bjørk, A. A. (2021). Evaluation of the Apple iPhone 12 Pro LiDAR for an application in geosciences. Scientific reports, 11(1), 22221.

Obradović, M., Vasiljević, I., Đurić, I., Kićanović, J., Stojaković, V., & Obradović, R. (2020). Virtual Reality Models Based on Photogrammetric Surveys—A Case Study of the Iconostasis of the Serbian Orthodox Cathedral Church of Saint Nicholas in Sremski Karlovci (Serbia). Applied Sciences, 10(8), 2743.

Polat, N., & Uysal, M. (2016). Hava lazer tarama sistemi, uygulama alanları ve kullanılan yazılımlara genel bir bakış. Afyon Kocatepe Üniversitesi Fen Ve Mühendislik Bilimleri Dergisi, 16(3), 679-692.

Remondino, F., & El-Hakim, S. (2006). Image-based 3D modelling: a review. The photogrammetric record, 21(115), 269-291.

Tel, H. Ö., & Yüksel, F. Ş. K. Kızılkoyun Nekropolü Arkeolojik Sit Alanı'nın Koruma-Planlama Kapsamında Değerlendirilmesi. İnönü Üniversitesi Sanat ve Tasarım Dergisi, 7(16), 1-16.

Uslu, A., Polat, N., Toprak A. S., & Uysal, M. (2016). Kültürel Mirasın Fotogrametrik Yöntemle 3B

Modellenmesi Örneği. Harita Teknolojileri Elektronik Dergisi, 8, 2, 165-176.
Yiğit, A. Y., & Uysal, M. (2021). Tarihi Eserlerin 3B Modellenmesi ve Artırılmış Gerçeklik ile Görselleştirilmesi. Bilecik Şeyh Edebali Üniversitesi Fen Bilimleri Dergisi, 8(2), 1032-1043.
Yilmaz, H. M., Yakar, M., & Yildiz, F. (2008). Documentation of historical caravansaries by digital close-range photogrammetry. Automation in Construction, 17(4), 489-498.
Zeybek, M., &Kaya, A. (2020). Tarihi Yığma Kiliselerde Hasarların Fotogrametrik Ölçme Tekniğiyle İncelenmesi: Artvin Tibeti Kilisesi Örneği. Geomatik, 5 (1), 47-57.

7th Intercontinental Geoinformation Days

igd.mersin.edu.tr

Investigation of the usability of handheld laser scanners in reverse engineering applications

Yaren Doğdu *1, **Murat Yakar** 1

[1]Mersin University, Engineering Faculty, Department of Geomatics Engineering, Mersin, Türkiye

Keywords
Reverse Engineering
Handheld Lidar
Prototype

Abstract

Reverse engineering allows for the creation of Computer Aided Design (CAD) models for both new and existing products through surface data capture. CAD is a creative process that utilises computer systems and can be software or hardware based. Typically, CAD data is a software-based tool that is used for design purposes. This process requires computer technology to assist in the creation of technical drawings by incorporating professional concepts. In reverse engineering, prototyping is necessary to quickly fabricate physical parts, assemblies, or models using CAD. Rapid prototyping, a manufacturing technology, enables the creation of physical models directly from 3D CAD drawings. Prototyping enables the design of pre-presentation products before the final product. The aforementioned process involves editing the designed products to create the final product. Therefore, prototyping is a crucial step for ensuring the required quality, accuracy, and precision of the final products in reverse engineering. As such, handheld laser scanners - capable of collecting data at lower densities than their ground-based counterparts - are being evaluated in this field. Although handheld lidar devices are typically preferred for modelling small objects in confined spaces. The study used a handheld lidar device due to its instant and efficient data acquisition, lower cost compared to ground-based lidar, and easy accessibility. Three types of objects were modelled in 3D using handheld laser scanners, which are viewed as an alternative to ground-based laser scanners within the field of reverse engineering. These objects were categorized based on their size, either small, medium, or large scale. For this study, identical models underwent scanning using both a ground-based laser scanner and a handheld laser scanner, followed by a comparative analysis.

1. Introduction

Reverse engineering is the process of obtaining geometric design data of a product in order to replicate or enhance it, in situations where there is no available design information of the original object (Kanun et al., 2021). The need for reverse engineering often arises from prolonged unavailability of an item's component, or from inadequate primary documentation. Furthermore, in situations where the original producer of a product is no longer accessible, but the demand for the product exists, enhancing the favorable features of the product based on its extensive use intensifies the requirement for reverse engineering (Ulvi et al., 2019). The inability or unwillingness of the original manufacturer to provide additional/replacement parts, updating outdated parts or old production processes with current and cheaper technologies are among the most common reasons for the emergence of reverse engineering. In reverse engineering applications, models are commonly measured through traditional methods, drawn digitally and then converted to 3D models However, the accuracy and precision of these models are heavily reliant on the operator and can be time-consuming. To circumvent this issue, rapid prototyping technology has been developed to produce highly realistic products in a shorter timeframe. Rapid prototyping technologies offer solutions to issues encountered in product design and development procedures (Ulvi & Yakar, 2010). By not using rapid prototyping, various steps, including the supply of machines needed to create a prototype of a design, mould manufacturing, and secondary processes, can be expensive and time-consuming. Rapid prototyping technology aims to minimize this problem. Prototyping involves the creation of pre-presentation products to be developed into final products. These

* **Corresponding Author**

*(yarendgd1@gmail.com) ORCID ID 0009-0009-4289-4675
(myakar@mersin.edu.tr) ORCID ID 0000-0002-2664-6251

Cite this study

Doğdu, Y. & Yakar, M. (2023). Investigation of the Usability of Handheld Laser Scanners in Reverse Engineering Applications. Intercontinental Geoinformation Days (IGD), 7, 222-225, Peshawar, Pakistan

products are then refined, culminating in the final product. As such, the prototyping stage is essential to ensure that the final product meets the required standards for reverse engineering in terms of precision, accuracy, and quality. This process can take several days or even weeks when using traditional methods (Kula & Ergen, 2017). During the prototyping phase, generating the desired product via 3D models instead of traditional methods has beneficial outcomes for the project, particularly concerning time efficiency. 3D models produced through the 3D modelling process are frequently used in conjunction with tools that offer a realistic depiction of the product, referred to as 3D rendering. At this point, the Lidar method, which stands out especially in fast and precise data collection, provides a great advantage (Yakar et al., 2015a; 2015b).

LiDAR, an acronym for "Light Detection and Ranging", is a remote sensing technology that employs laser beams to gauge the distance of objects (Çoşkun, 2020). The benefits of LiDAR technology, notably with local laser scanning, lie in its ability to minimize physical touch, promptly digitalize components, provide suitable resolution and accuracy, detect colours, and capture intricate details of the object (Bauwens, 2016). Furthermore, the spatial information in narrow and enclosed areas, which are otherwise inaccessible and challenging to gauge, is made available through the coordinates gathered in the point cloud data structure. Although terrestrial laser scanning has been used for this process for years, it remains a pressing issue today. In this study, a unique handheld laser scanner is used, which is not widely used in this field. Although the handheld laser scanner is not widely used in reverse engineering, if adopted, it could be advantageous in terms of price, cost and time.

2. Method

LiDAR technology, dense point clouds and 3D model production studies are commonly used sources of data (Nex and Remondino, 2012). The edges of the LiDAR model are more advantageous than those produced by photogrammetry when used in reverse engineering, due to the sharp and distinct lines. LiDAR is a popular method of remote sensing for precisely measuring the distance of objects on the earth's surface (Yakar et al. 2010). LiDAR utilizes a pulsed laser for accurately ascertaining the variable distances of an object from the earth's surface, which in turn produces precise 3D information concerning both the earth's surface and the target object (Yakar et al., 2013). The photodetector and optics are other highly important elements central to data collection and analysis (Zeybek, 2019). LiDAR is an extremely beneficial measurement system, providing an exceptionally swift surveying method that can collect substantial point data per second tremendously quickly (Yılmaz and Yakar, 2006). Building interior scans typically require around three minutes, while large-scale measurements can be completed in under an hour- making LiDAR one of the swiftest surveying techniques. In relation to precision, LiDAR systems gather dense data with minimal space between points, resulting in exceedingly accurate outcomes. As for adaptability, there are various alternatives to consider in regards to land surveying with LiDAR. LiDAR systems can be installed on different platforms depending on the application's requirements (Karataş et al. 2022). For small-scale measurements, a fixed tripod may suffice, but aircraft, helicopters, or unmanned aerial vehicles are necessary to gather the data for larger areas. As light is used as the measurement tool, LiDAR data can be collected 24/7. First, LiDAR abbreviation used in this text stands for Light Detection and Ranging. LiDAR systems, in terms of safety, operate at a higher speed than their counterparts and can be controlled from remote locations. This enables their deployment in hazardous locations where extended operator presence may prove risky. LiDAR surveying devices, which have been in use since the 1960s, have transformed into handheld surveying systems. The coordinates in the resulting dense point cloud data structure offer spatial information in areas that are hard to reach and measure, including confined spaces (Nocerino et al., 2017). Handheld LiDAR presents numerous opportunities. It is effortless to operate both outdoors and indoors, lightweight, and handheld, gathering and exhibiting your exact 3D point cloud data in just a few minutes. Thanks to its feature of simultaneous imaging, the scanned or overlooked places in the work area can be viewed, and control can be exercised before completing the scan. Additionally, 3D modelling can be accomplished within minutes (Zeybek, 2021; Özdemir et al., 2022).

The study employed the FARO Freestyle 3D Handheld Laser Scanner. This device boasts high-quality and high-precision features, rapidly and accurately capturing 3D images and generating high-resolution point clouds. It can document rooms, structures, and objects with reliability (Andersson and Hedlund, 2016; Cheng et al., 2018; Rua, 2018; Memduhoğlu et al., 2020). This scanner is a handheld laser scanner that needs to be manually operated and aimed by the user at a maximum distance of 1 meter from the targeted object.

3. Results

In reverse engineering procedures, a product is initially scanned using laser scanning instruments and the resulting data is then sent to a software integrated with the scanning device (Çelebi et al., 2017). The point cloud data captured by the software is later transferred to the computer environment, where they are organised. Finally, the edited point cloud data is used to generate a solid model of the product. If a solid modelled product is to be manufactured, it can be achieved through either rapid prototyping or conventional methods, with reverse engineering processes being necessary. The initial step of this study involves scanning, also termed digitisation, where the model surface is scanned using optical laser scanners. Optical scanning devices are the preferred choice for parts without small holes and fewer surface details, whereas laser scanning devices are more suitable for scanning intricate parts (Yılmaz & Yakar, 2016). A study on the viability of reverse engineering applications in 3D CAD programmes used for design was conducted. Industrially chosen sample components undergo scanning, and the solid model of the point cloud derived from the scan is generated using reverse engineering procedures in design-appropriate software. These applications enable the conversion from a point cloud to a solid model.

The size details of the objects utilized in the research can be found in Table 1. The laser scanning point cloud are presented in Figure 1, alongside the 3D model in Figure 2 and the solid model for reverse engineering in Figure 3.

Through the use of reverse engineering, practical data can be collected to determine detailed and accurate dimensions of parts that may not be available for supply, in development, or currently in production. This information can be directly transferred to the computer environment, allowing for easier analysis and specificity. In addition to the 3D visualization provided by the point cloud, this approach enables designers and technical personnel to extract actual length and measurement values of desired parts from the database. For the reverse engineering study, handheld laser scanners were utilized to scan the selected application objects. Due to the scanner's capacity to record all objects within its 360-degree range, it was discovered that numerous unwanted data were generated. Therefore, purging the 3D point cloud of data contamination was necessary. The importance of cleansing these data cannot be over emphasised, as it ensures simple, high-quality data without contributing to an unnecessary load in file size. The Scene software, a point cloud processing software, was used to conduct this data cleansing.

After discarding excess points, we obtained the point cloud and solid models in ".LAS" format. These models underwent several processing steps in other software. It was established that Geomagic Wrap CAD software's module can be used for reverse engineering operations on scan data of industrial parts obtained via laser scanning devices, also in ".LAS" format. The study showed that CAD data of the parts could be created without difficulty, albeit with minor details (Figure 3).

Table 1. Object dimensions

Scale	Width (cm)	Length (cm)	Height (cm)
Small	0.30	0.20	0.40
Medium	0.40	0.30	0.60
Large	0.60	0.40	1.70

Figure 1. Point cloud of objects on a small, medium, and large scale from left to right.

Figure 2. 3D model of objects on a small, medium, and large scale from left to right.

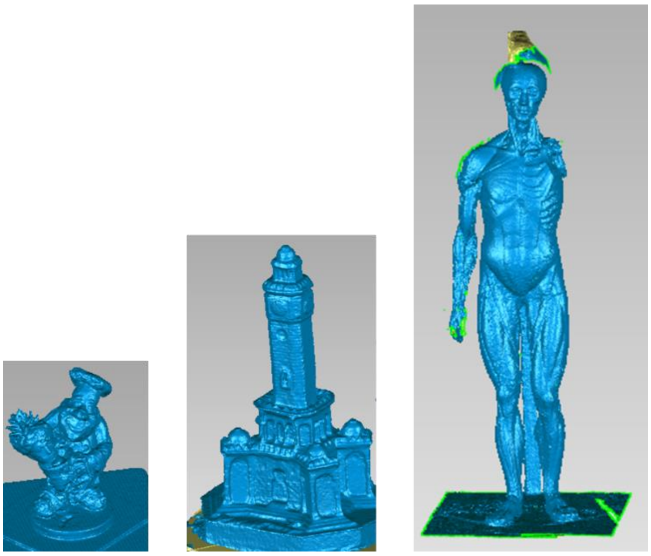

Figure 3. Solid model of objects on a small, medium, and large scale from left to right.

4. Conclusion

The laser scanning method has proved successful in reverse engineering for the design and production of small objects, utilizing three-dimensional modelling. The current study applied this method to objects of varying lengths. The following factors were determined to be crucial for successful implementation using Geomatic Wrap software.

Reverse engineering refers to the method of creating a collection of characteristics following a systematic analysis of a complex hardware system. This procedure is performed by individuals who were not involved in the original design process and must work without the benefit of original drawings, documentation, and operating manuals. Contemporary production methods encompass the procedures that commence with the product's design in a digitized environment, and culminate in the production phase employing industry-appropriate techniques. The deployment of contemporary technology in the data acquisition phase of reverse engineering expedites subsequent stages, culminating in production. Converting objects into CAD models by digitization poses a challenging and intricate issue. Fully automating the creation of a comprehensive and coherent computer-aided design model remains an ongoing research effort. In this regard, besides automation and pace, it is critical to achieve accurate and precise access to the fundamental data. One popular approach to 3D modelling is utilizing the LiDAR method, which is proffered as an alternative solution for acquiring data in reverse engineering applications. The resultant point cloud was then processed in Scene software. The 3D model was transferred to the Geoamgix Wrap software, and technical drawings were carried out on the 3D CAD data. This research investigated the potential of handheld laser scanners as an alternative method for reverse engineering applications. Today's dynamic industrial environment necessitates companies to adopt and integrate new technologies continuously. The utilization of modern communication and information technologies is of great importance, particularly in industries such as automotive manufacturing that cater to large and multinational corporations. Handheld laser scanners confer numerous benefits and enhanced flexibility in reverse engineering applications, such as enabling reproducible measurements and time savings. Handheld laser scanners, according to the authors, may serve as a viable alternative method for data collection in reverse engineering activities.

Acknowledgement

This research was funded by project 1919B012206671 as part of the Tübitak 2209-A University Students Research Projects Support Programme.

References

Agugiaro, G., Nex, F., Remondino, F., De Filippi, R., Droghetti, S., & Furlanello, C. (2012). Solar radiation estimation on building roofs and web-based solar cadastre. ISPRS annals of the photogrammetry, remote sensing and spatial information sciences, 1, 177-182.

Andersson, J., & Hedlund, P. (2016). Undersökning om handhållna laserskannrar vid detaljmätning: En jämförelse mellan multistationen Leica Nova MS50 och den handhållna laserskannern FARO Freestyle X.

Bauwens, S., Bartholomeus, H., Calders, K., & Lejeune, P. (2016). Forest inventory with terrestrial LiDAR: A comparison of static and hand-held mobile laser scanning. Forests, 7(6), 127.

Cheng, L., Chen, S., Liu, X., Xu, H., Wu, Y., Li, M., & Chen, Y. (2018). Registration of laser scanning point clouds: A review. Sensors, 18(5), 1641.

Coşkun, E. (2020). İnsansız hava araçları (İHA) ile halihazır harita üretimi: Ordu ili, Altınordu ilçesi örneği. Master's thesis, Çukurova University

Kanun, E., Alptekin, A., & Yakar, M. (2021). Documentation of cultural heritage by photogrammetric methods: a case study of Aba's Monumental Tomb. Intercontinental Geoinformation Days, 3, 168-171.

Karataş, L., Alptekin, A., & Yakar, M. (2022). Determination of Stone Material Deteriorations on the Facades with the Combination of Terrestrial Laser Scanning and Photogrammetric Methods: Case Study of Historical Burdur Station Premises. Advanced Geomatics, 2(2), 65-72.

Kula, B., & Ergen, E. (2017). Lazer Tarayıcı Teknolojisinin Yapım Yönetiminde Kullanım Alanları. Uluslararası Katılımlı 7. İnşaat Yönetimi Kongresi, 293-302.

Memduhoglu, A., Şenol, H. İ., Akdağ, S., & Ulukavak, M. (2020). 3D Map Experience for Youth with Virtual/Augmented Reality Applications. Harran Üniversitesi Mühendislik Dergisi, 5(3), 175-182.

Nocerino, E., Menna, F., Remondino, F., Toschi, I., & Rodríguez-Gonzálvez, P. (2017, June). Investigation of indoor and outdoor performance of two portable mobile mapping systems. In Videometrics, Range Imaging, and Applications XIV (Vol. 10332, pp. 125-139). SPIE.

Özdemir, E., Erdal, K., Veziroğlu, F., & Ateş, S. S. (2022). Tuz Mağaralarında Sırt Çantası LiDAR Sisteminin 3B Model Üretiminde Kullanılması; Tuzluca, Iğdır Örneği. Türkiye Uzaktan Algılama Dergisi, 4(1), 36-42.

Rua, J. (2018). Exploration of FARO freestyle 3D laser scanners as a method for estimating surface fuel loading for wildland fire management (Doctoral dissertation, Rutgers University-School of Graduate Studies).

Ulvi, A. , Yiğit, A. Y. & Yakar, M. (2019). MODELING OF Hıstorıcal Fountains By Using Close-Range Photogrammetric Techniques. Mersin Photogrammetry Journal, 1 (1), 1-6.

Ulvi, A., & Yakar, M. (2010). An experimental study on preparing photogrammetric rolove plans of antique theatres. International Journal of the Physical Sciences, 5(7), 1086-1092.

Yakar, M., Toprak, A. S., Ulvi, A., & Uysal, M. (2015b). Konya Beyşehir Bezariye Hanının (Bedesten) İHA ile Fotogrametrik Teknik Kullanılarak Üç Boyutlu Modellenmesi. Türkiye Harita Bilimsel ve Teknik Kurultayı, 25, 28.

Yakar, M., Ulvi, A., & Toprak, A. S. (2015a). The problems and solution offers, faced during the 3D modeling process of Sekiliyurt underground shelters with terrestrial laser scanning method. International Journal of Environment and Geoinformatics, 2(2), 39-45.

Yakar, M., Uysal, M., Toprak, A. S., & Polat, N. (2013). 3D modeling of historical doger caravansaries by digital photogrammetry. The International Archives of the Photogrammetry, Remote Sensing and Spatial Information Sciences, 40, 695-698.

Yakar, M., Yılmaz, H. M., & Mutluoğlu, Ö. (2010). Comparative evaluation of excavation volume by TLS and total topographic station based methods. Lasers in Engineering 19, 331–345

Yılmaz, H. M., & Yakar, M. (2006). Yersel lazer tarama Teknolojisi. Yapı teknolojileri Elektronik dergisi, 2(2), 43-48.

Zeybek, M. (2019). El-tipi LiDAR ölçme sistemleri ve 3B veri işleme. Türkiye Lidar Dergisi, 1(1), 10-15.

Zeybek, M. (2021). Indoor mapping and positioning applications of hand-held lidar simultaneous localization and mapping (slam) systems. Türkiye Lidar Dergisi, 3(1), 7-16.

7th Intercontinental Geoinformation Days

igd.mersin.edu.tr

Indoor mapping with wearable laser scanner and iPad lidar

Doğukan Sugölü *1, Abdurahman Yasin Yiğit 1

[1]Mersin University, Engineering Faculty, Department of Geomatics Engineering, Mersin, Türkiye

Keywords
Indoor mapping
SLAM
Wearable laser scanner
iPad LiDAR
LiDAR

Abstract

Efficiently surveying complex indoor environments remains a challenge due to the accuracy demands of interior geometric data. Laser scanning technology in indoor and outdoor mapping has significantly advanced the field, surpassing conventional measuring devices. Indoor and outdoor mapping processes have typically depended on acquiring terrestrial laser scanner point clouds, a time-consuming and costly technique. Alternatively, we present a novel indoor mapping strategy utilizing simultaneous localization and mapping (SLAM) based on a wearable mobile laser scanner and a laser sensor incorporated into portable iPad tablets. This approach has already been successfully tested in mapping processes, offering a more efficient and economical alternative to conventional terrestrial laser scanning point clouds. Indoor scanning is conducted in this methodology. Initially, the specified region is scanned with a ground-based laser scanner, and the resultant data serves as a reference. Subsequently, this area is scanned with wearable and iPad laser scanners, and a comparative analysis is executed. Based on the case study area findings, the proposed technique could be an alternative to the portable and wearable laser scanning method. This alternative provides notable benefits regarding accuracy and time efficiency for point cloud laser scanning at a local level.

1. Introduction

An interior study involves conducting a building survey or extracting detailed plans and models of an existing interior space. Mapping topics have long included developing and planning interior designs (Sırmacek et al., 2016). The availability of maps and plans is beneficial in evaluating existing building conditions against architectural plans or interpreting them in the context of renovation projects. Accurate and precise measurement of geometric properties of enclosed spaces is crucial for numerous studies today (Güleç Korumaz et al., 2011). In the past, classical metric measuring instruments were used for measurement processes. However, the development of precision measuring devices such as total-station has aided in measuring and mapping architectural structures for similar purposes. Advancements in technology and physics have facilitated the proliferation of laser scanning systems, which use laser signals for measurement purposes. The laser scanning technique allows for the direct, accurate, and automated acquisition of three-dimensional (3D) coordinates of objects (Reshetyuk, 2009; Akar, 2017). Using this technology, it is possible to create exact 3D point clouds that contain intricate details of the target object. These clouds offer high-resolution matching and the potential for change monitoring and presentation, all of which can be measured in any metric (Armesto-González et al., 2009).

Laser scanning techniques can be broadly categorized as modern indoor mapping solutions and fall under terrestrial and mobile laser scanners (Ulvi & Yakar, 2014; Tepeköylü, 2016). The terrestrial laser scanner provides highly accurate direct measurements, regardless of illumination conditions. Digital reconstruction of indoor spaces is possible through the main products derived from 3D point clouds (Masiero et al., 2018). When measuring an area, the TLS system allows quick access to highly precise and densely packed X, Y, and Z information. Nevertheless, this situation presents a Big Data issue when analyzing the data (Zheng et al., 2018). While the ground-based laser scanner yields dense and precise data, it poses limitations due to its high cost and static data collection principle, resulting in limited observation points for capturing polymorphic structures (Ulvi et al., 2015; Özdemir et al., 2021).

In large and intricate indoor mapping projects, obtaining adequate data through terrestrial laser

* Corresponding Author

*(sugolud@gmail.com)
(ayasinyigit@mersin.edu.tr) ORCID ID 0000-0002-9407-8022

Cite this study

Sugölü, D. & Yiğit, A. Y. (2023). Indoor Mapping with Wearable Laser Scanner and iPad LiDAR. Intercontinental Geoinformation Days (IGD), 7, 226-229, Peshawar, Pakistan

scanner systems necessitates many scans, prolonging the data collection period. As cited by Ingman et al. (2020), there is a need to evaluate more efficient and economical scanning systems. For the reasons above, scholars (Sanchez Diaz et al., 2022) conducted a recent study, leading to the development of mobile mapping systems that can achieve similar precision as TLS while using less data and in a shorter timeframe (Yaman & Yılmaz, 2020). The latest MLS systems have solved issues related to measuring, documenting, and mapping complex and inaccessible areas or instances where using laser scanning measurement procedures from the ground is unfeasible (Yılmaz & Yakar, 2016). Compared to fixed instruments, this device streamlines and accelerates the measurement process because measuring from multiple points is unnecessary. Although mobile mapping systems' resolution and density are lower than fixed instruments, the values are adequate for structure analysis. According to Di Filippo et al. (2018), errors in these systems have been minimized due to significant developments in the last few years, particularly in managing various sensors. Additionally, these systems enable solutions for complex outdoor and indoor scenarios, making them practical tools for mapping.

Mobile laser scanning methods use a simultaneous localization and mapping (SLAM) algorithm incorporating a Light Detection and Ranging (LiDAR) sensor, as well as complementary sensors such as RGB cameras or thermographic sensors, to expand the captured data of the environment via Inertial Measurement Unit (IMU) integration. The approach is objective and employs clear and concise language while adhering to grammatical and spelling conventions of British English. These new methods can be classified as lightweight wearable, back, or handheld devices in three setups with capture distances and relative accuracies ranging from 5 to 100 meters. Although initially designed to enhance the navigation capabilities of robots, it has also been utilized for mapping objectives. These systems are based on the SLAM algorithm and do not require Global Navigation Satellite Systems (GNSS) support. They are an alternative to the TLS system in indoor mapping studies. Lidar scanners are another method that has begun to be used in iOS-based mobile smart devices. The use of iPad laser scanners in this field has been particularly cost and time-effective. However, wearable and iPad laser scanners generally have inferior positional accuracy, and numerous studies have disclosed significant inconsistencies between various trajectories. Apple disclosed the latest iPad Pro and iPhone 12 Pro/Pro Max iteration, incorporating a sensor in 2020. Such recent technical progression hints at an increase in cost-effective alternatives becoming available shortly, catering to both professional and consumer markets. It may be simpler to gather 3D data on the environment, but the usefulness of such information is still uncertain.

An examination of the literature linked to the study's topic indicates that the laser system employed in local indoor spaces is adequate regarding resolution and sensitivity. Nevertheless, since the TLS system has the abovementioned drawbacks, mobile and iPad LiDAR systems based on SLAM algorithms offer potential substitutes. Within this study, a practical analysis of mobile systems, which propose a new approach to indoor mapping, has been conducted concerning their sensitivity and resolution. For indoor mapping purposes, scans were conducted using wearable and iPad LiDAR devices to produce point clouds. Subsequently, the same area was scanned using local laser scanning as reference data. After the research, a statistical evaluation was carried out on the functionality of the wearable and iPad LiDAR system, presenting a new alternative to the ground-based laser scanner for indoor production. Additionally, recommendations for future studies were proposed.

2. Method

Terrestrial laser scanners fall under the category of laser scanning and produce a 3D point cloud via Light Detection and Ranging (LiDAR) technology. This enables them to gather many points swiftly, leading to their utilization in different fields like project supervision, structure analysis, development monitoring, progress control, change identification, quality control, and creating piecewise and built-in models. TLS is a commendable option for indoor cartography due to its superior point density and precision. However, 3D mapping in large and complex indoor environments can be costly (Green et al., 2014). Terrestrial laser scanners offer not only 3D geometric information about the measured object but also information about the power of the laser beam that is backscattered by the scanned surface. The local laser scanner detects the intensity, a portion of the energy. This measure of intensity, also known as reflection, indicates the proportion of radiated and reflected power in the laser wave. The digital expression of intensity is typically unitless and varies depending on the sensitivity of the laser scanner detector. Ground-based laser scanner detectors generally have an 8 to 16-bit resolution to capture intensity.

Terrestrial laser scanners are typically grouped into three categories based on length measurement principles: time of flight, triangulation, and phase difference scanners (Karataş et al. 2022). Time-of-flight scanners have an extensive scanning range, while phase difference scanners can measure shorter distances with higher precision and accuracy than time-of-flight scanners (Karataş et al. 2023).

The wearable laser scanning system uses the instantaneous positioning and mapping (SLAM) algorithm. This approach permits the mapping of unfamiliar surroundings by passing range sensors while simultaneously establishing the system's position on the map (Di Filippo et al., 2018). This enables capturing point clouds by traveling to diverse areas and surveying from different positions (Yakar et al., 2008). The SLAM-based device obtains data from the Velodyne Puck LITE LIDAR and IMU sensors to locate itself in the surrounding environment. The SLAM algorithm analyzes this data, detecting geometric object variations such as walls, floors, and columns, to create a map of the local coordinate environment and estimate its location. In WMLS devices, the SLAM algorithm forms the foundation for creating maps and models (Kanun et al., 2021).

The iPad Pro tablet (Apple Inc. San Francisco, USA) is the third device to scan the study areas. This particular generation is fitted with an Apple LiDAR sensor capable of scanning the surrounding environment. The sensor is understood to be a distinctly devised LiDAR scanner with direct time-of-flight, which measures depth in addition to employing a camera and motion sensor. Apple has yet to disclose any official information about the device. The scanner can scan objects up to a distance of 5 meters. We utilized the 3D Scanner App (Laan Labs, New York, USA), which has additional features like coloring and exporting mesh and point clouds.

3. Results

Firstly, laser scanning data were collected. The point cloud data of both WMLS and iPad LiDAR are given in Figure 1. Then, ICP and C2C analyses were performed to compare the point clouds of the proposed methods with the reference data, which are ground-based laser scanning data. Firstly, the proximity analyses of the point clouds of wearable laser scanning to the reference data are given in Figure 2. Then, the proximity analyses of the iPad LiDAR point clouds to the reference data are given in Figure 3.

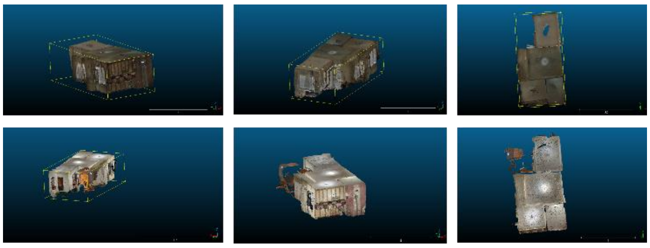

Figure 1. WMLS point cloud (Top), Ipad LiDAR point cloud (Bottom).

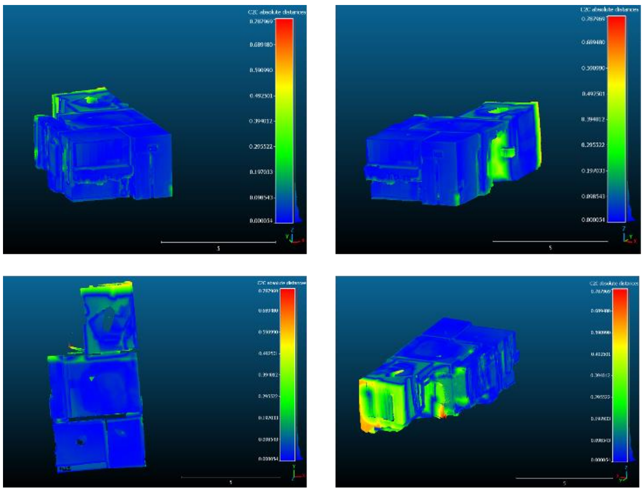

Figure 2. Comparison of WMLS data with reference data

4. Conclusion

Our research indicates that it is feasible to use WMLS and iPad LiDAR point clouds, with SLAM assistance, as an alternative to TLS point clouds in the test region, with an acceptable level of precision. As TLS measurements are costly and time-consuming, mainly when collecting data in corridors between rooms, our study shows that SLAM-based WMLS measurements can reduce data collection time. Additionally, we have found the accuracy of TLS room locations reasonable. Therefore, this study demonstrates that WMLS presents a favorable option, particularly about time, for generating a thorough point cloud that meets the required precision for indoor mapping applications. This method is more efficient than constructing TLS stations for point cloud-based investigations, requiring less labor. The SLAM point cloud is accurately aligned with the reference, with an accuracy of 2.1 cm, while the iPad LiDAR exhibits comparable alignment, with a value of 11.5 cm. Based on the C2C analysis, the TLS measurements show a discrepancy of 3.1 cm compared to the WMLS data. In contrast, the iPad LiDAR exhibits a difference of 11.8 cm, which is deemed acceptable given the intricacies of indoor mapping.

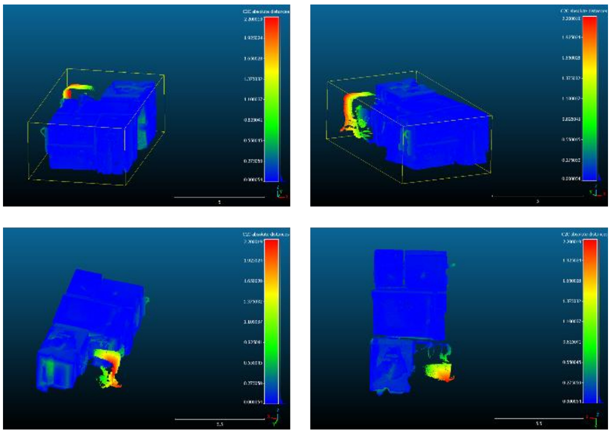

Figure 3. Comparison of Ipad LiDAR data with reference data

However, SLAM-based WMLS and iPad LiDAR incur drawbacks, mainly when operating in long, narrow, or huge environments, in areas with no substantial features such as furniture or other suitable geometric targets for robust mapping, or even in open space. In order to enhance the internal geometric integrity, it is necessary to have features at close intervals, and measurements should be taken through closed-loop paths. Most indoor environments possess adequate geometric features present at short intervals/distances. Meanwhile, the environments that lack adequate geometric features are few. In such situations, it is possible to rectify the deficiencies of WMLS and iPad LiDAR in narrow corridors by incorporating additional features in hindering regions. These features may include furniture or other objects that can enhance perceptible surfaces or even opening doors to draw in supplementary surfaces.

Nevertheless, it is vital to perform operations with well-thought-out planning before mapping the environment due to the abovementioned limitations. Additionally, planning for TLS scanning is more complex than mapping with alternative methods. The collection of point clouds using wearable and mobile LiDARs is a quicker process. The density of mobile LiDAR point clouds relies on the distances between the scanner and the features being measured and the speed at which mapping is conducted. Noisy data is shared, particularly in instances where walking speed is slower. This noise can make recognizing small objects measuring less than

3 cm or displaying window placements complex. However, the research indicates that the noise in the point clouds gathered by the proposed methods has a negligible impact on the accuracy of both registration and 3D mapping compared to TLS point clouds. SLAM-assisted WMLS and iPad LiDAR outperform the TLS method in terms of speed. It takes approximately 1 hour to collect data using WMLS for the studied area compared to 8 hours using individual TLS. Moreover, the WMLS and iPad LiDAR approach can be applied to indoor and outdoor mapping and provide a viable alternative to the TLS system.

Acknowledgment

This research was funded by project 1919B012222231 as part of the Tübitak 2209-A University Students Research Projects Support Programme.

References

Akar, A. (2017). Evaluation of accuracy of dems obtained from UAV-point clouds for different topographical areas. International Journal of Engineering and Geosciences, 2(3), 110–117. https://doi.org/10.26833/ijeg.329717

Armesto-González, J., Riveiro-Rodríguez, B., González-Aguilera, D., & Rivas-Brea, M. T. (2010). Terrestrial laser scanning intensity data applied to damage detection for historical buildings. Journal of Archaeological Science, 37(12), 3037-3047.

Di Filippo, A., Sánchez-Aparicio, L. J., Barba, S., Martín-Jiménez, J. A., Mora, R., & González Aguilera, D. (2018). Use of a wearable mobile laser system in seamless indoor 3D mapping of a complex historical site. Remote Sensing, 10(12), 1897.

Green, S., Bevan, A., & Shapland, M. (2014). A comparative assessment of structure from motion methods for archaeological research. Journal of Archaeological Science, 46, 173-181.

Güleç Korumaz, A., Dülgerler, O. N., & Yakar, M. (2011). Kültürel Mirasın Belgelenmesinde Dijital Yaklaşımlar. Selçuk Üniversitesi Mühendislik, Bilim ve Teknoloji Dergisi, 26(3), 67-83.

Ingman, M., Virtanen, J. P., Vaaja, M. T., & Hyyppä, H. (2020). A comparison of low-cost sensor systems in automatic cloud-based indoor 3D modeling. Remote Sensing, 12(16), Article 2624. https://doi.org/10.3390/ rs12162624

Kanun, E., Metin, A., & Yakar, M. (2021). Yersel Lazer Tarama Tekniği Kullanarak Ağzıkara Han'ın 3 Boyutlu Nokta Bulutunun Elde Edilmesi. Türkiye Lidar Dergisi, 3(2), 58-64. https://doi.org/10.51946/melid.1025856

Karataş, L., Alptekin, A., & Yakar, M. (2022). Determination of Stone Material Deteriorations on the Facades with the Combination of Terrestrial Laser Scanning and Photogrammetric Methods: Case Study of Historical Burdur Station Premises. Advanced Geomatics, 2(2), 65-72.

Karataş, L., Dal, M., Alptekin, A., & Yakar, M. (2023). Architectural documentation with terrestrial laser scanning (TLS) data: Case study of Lutfu Pasa caravanserai (Mathius Caravanserai), Izmir. Intercontinental Geoinformation Days, 6, 143-147.

Masiero, A., Fissore, F., Guarnieri, A., Pirotti, F., Visintini, D., & Vettore, A. (2018). Performance evaluation of two indoor mapping systems: Low-cost UWB-aided photogrammetry and backpack laser scanning. Applied Sciences, 8(3), 416.

Özdemir, S., Akbulut, Z., Karslı, F., & Acar, H. (2021). Automatic extraction of trees by using multiple return properties of the lidar point cloud. International Journal of Engineering and Geosciences, 6(1), 20–26. https://doi.org/10.26833/ijeg.668352

Reshetyuk, Y. (2009). Self-calibration and direct georeferencing in terrestrial laser scanning. Ph.D. Thesis, KTH Royal Institute of Technology, Stockholm, Sweden, 2009.

Sanchez Diaz, B., Mata-zayas, E. E., Gama-campillo, L. M., Rincon-ramirez, J. A., Vidal-garcia, F., Rullan-silva, C. D., & Sanchez-gutierrez, F. (2022). LiDAR modeling to determine the height of shade canopy tree in cocoa agrosystems as available habitat for wildlife. International Journal of Engineering and Geosciences, 7(3), 283–293. https://doi.org/10.26833/ijeg.978990

Sirmacek, B., Shen, Y., Lindenbergh, R., Zlatanova, S., & Diakite, A. (2016). Comparison of Zeb1 and Leica C10 indoor laser scanning point clouds. ISPRS Ann. Photogramm. Remote Sens. Spat. Inf. Sci, 3, 143-149.

Tepeköylü, S. (2016). Mobil lidar uygulamaları, veri İşleme yazılımları ve modelleri. Geomatik, 1(1), 1–7. https://doi.org/10.29128/geomatik.294065

Ulvi, A., & Yakar, M. (2014). Yersel Lazer Tarama Tekniği Kullanarak Kızkalesi'nin Nokta Bulutunun Elde Edilmesi ve Lazer Tarama Noktalarının Hassasiyet Araştırması. Harita Teknolojileri Elektronik Dergisi, 6(1), 25-36.

Ulvi, A., Yakar, M., Toprak, A. S., Mutluoglu, O. (2015). Laser Scanning and Photogrammetric Evaluation of Uzuncaburç Monumental Entrance. International Journal of Applied Mathematics Electronics and Computers, 3(1), 32-36.

Yakar, M., Yılmaz, H. M., & Mutluoğlu, Ö. (2008). Lazer tarama teknolojisi ve fotogrametrik yöntem ile hacim hesabı.

Yaman, A., & Yılmaz, H. M. (2017). The effect of object surface colors on terrestrial laser scanners. International Journal of Engineering and Geosciences, 2(2), 68–74.https://doi.org/10.26833/ijeg.296835

Yılmaz, H., & Yakar, M. (2016). Lıdar (Lıght Detectıon And Rangıng) Tarama Sistemi. Yapı Teknolojileri Elektronik Dergisi, 2(2), 23-33.

Zheng, Y., Peter, M., Zhong, R., Oude Elberink, S., & Zhou, Q. (2018). Space subdivision in indoor mobile laser scanning point clouds based on scanline analysis. Sensors, 18(6), Article 1838. https://doi.org/10.3390/s18061838

7th Intercontinental Geoinformation Days

igd.mersin.edu.tr

Evaluation of point cloud software in terms of 3D architectural drawings

Ali Ulvi[*1]

[1]Mersin University, Department of Remote Sensing and Geographic Information Systems, Institute of Science, Mersin, Türkiye

Keywords
TLS
3D draw
Laser Scanning
Architectural Drawings
Virtual Reality

Abstract
In 3D reconstruction, the point cloud is crucial for preserving the geometric data of the target object. Following the acquisition of data by 3D laser scanner or image-based techniques, several software options are available for analyzing and processing the point cloud. In this investigation, terrestrial laser scanning was employed for point cloud acquisition, with subsequent analysis being carried out using Sketchub and Pointcab software. Ultimately, a web-based application, Sketchfab, was utilized to create a virtual reality simulation.

1. Introduction

Local laser scanning technology is an accelerating field, known for its ability to quickly create point clouds that render realistic 3D models of objects at a low cost. Nowadays, obtaining fast, comprehensive, and cost-effective 3D models and visual information is crucial. Terrestrial laser scanning has introduced a new era in surveying techniques (Atik & Duran, 2020). Thousands of points per second are obtained instantaneously, reflecting the scanned object or object surface (Yakar et al. 2010; Karataş et al. 2022a). These points enable the construction of precise 3D models through careful evaluation of the data (Dustin et al., 2016). The created models allow for access to critical information such as point position, object size, surface area, and volume. Prior to commencing scanning, a measurement plan must be developed, and scanning parameters must be established according to the desired precision. This technique is cost-effective and speedy compared to other measuring methods (Suchocki et al., 2020). The fundamental operating principle is the emission of a light beam (laser) that gets reflected from the object surface and is subsequently detected by the receiver (Yılmaz and Yakar, 2006). Laser scanning systems utilize three distinct measurement principles - Time-of-Flight, Phase Shift, and Triangulation - to assess the sensor-target distance (Ulvi et al. 2014).

The TLS data obtained from terrestrial laser scanning were processed using Scene software. Regular scans are crucial in data processing, allowing automatic merging of scans. The resulting point clouds can be employed to generate precise drawings. Point clouds obtained from laser scanning are more precise and denser than those obtained from photogrammetry, making them more useful (Alptekin et al. 2019).

This study involved using TLS data to create drawings in two different software programs. The resulting drawings were used to generate a 3D model, which was presented in a virtual reality environment. The study highlights the strengths and weaknesses of the software programs used for creating the drawings.

2. Material and Method

The data for the historical building was obtained using the TLS technique (Kanun et al. 2021). Terrestrial laser scanners can be classified into three categories, based on their length measurement principles: time-of-flight, triangulation, and phase difference scanners (Karataş et al. 2022b). Time-of-flight scanners have an extensive scanning range (Alptekin and Yakar, 2020a). Phase-difference scanners can measure shorter distances, but their measurement accuracy is more precise than that of time-of-flight scanners (Alptekin and Yakar, 2020b). Furthermore, while triangulation laser scanners exhibit increased sensitivity and accuracy in comparison to phase-difference laser scanners, they are more suited for smaller objects (Ogawa & Hori, 2019; Karataş et al. 2022c).

The phase difference method was employed in the FARO Focus3D S350 laser scanner used in this research, which boasts a range of 0.6-350 m and a data collection capacity of 976,000 points per second using the phase comparison technique. This laser scanner has the ability to perform scans ranging from 60 cm to 330 m with a

* **Corresponding Author**

*(e-mail) ORCID ID 0000-0003-3005-8011

Cite this study

Ulvi A. (2023). Evaluation of Point Cloud Softwares In terms of 3D Architectural Drawings. Intercontinental Geoinformation Days (IGD), 7, 230-233, Peshawar, Pakistan

precision of ± 2 mm. The scanner is capable of collecting up to 976,000 points per second (Figure 1).

Figure 1. Faro Focus 3D X330 Laser scanner (URL 1)

Point clouds were obtained for the study at a spatial resolution of 1 cm. This resolution was chosen as a suitable balancing point between the final 3D model's level of detail and the computer resources required for data processing. The scans were conducted in 48 sessions on the same day. At the required spatial resolution, a survey design must first establish the locations of the TLS stations to ensure complete object coverage. The laser scanner is capable of generating measurements with an accuracy of approximately 1-2 mm at close range. The quantity of dots on a surface is contingent upon the scanner's resolution (Liscio and Le, 2022). Many manufacturers of laser scanners provide a function that indicates the quantity of dots at a predefined distance. For instance, when the FARO laser scanner is set to a resolution of 14, it produces dots spaced approximately 6 mm apart when scanning at a distance of 10 m. At this resolution, the dot density would be 3 mm on an object that is 5 m away and 0.6 mm on an object that is 1 m away. In contrast, the accuracy of the scanned data is determined by the number of times the spot is sampled. The more samples taken, the closer the data should be to the true value. However, increasing the quality setting leads to longer scanning times. For instance, a ¼ resolution and 1x quality scan takes 1 minute 30 seconds, whereas a scan with the same resolution but 4x quality takes 7 minutes 46 seconds. In this investigation, a ¼ resolution setting and 3x quality setting were utilized (Liscio & Le, 2022). The scanner distance from the wall was approximately 1 meter, resulting in a point spacing of less than 1 mm.

During the positioning of the scanning positions, we ensured a minimum overlap of 60% between the previously scanned area and the subsequent scan region. Some of the test areas featured reflective surfaces. The study aimed to evaluate laser scanning technology efficacy in various areas and we did not take any additional measures designed for reflective surfaces. The study was conducted in four distinct areas, each with its own unique structural features. Relevant details regarding each area have been outlined in the respective sections. The TLS data was collected, and scan data from all locations were merged using a cloud-to-cloud approach before being georeferenced with the aid of target points. Before georeferencing, the point cloud data for each location underwent filtering through the Deviation, Dark-scan and Distance filters. Also, the TLS point cloud data was cleaned and resampled before starting the image processing stage. In the domain of image processing, 3D models can be created and of high quality using Triangular Network and Texture Matching techniques.

3. Results

The point cloud obtained with TLS was transferred to Sketchub software and 3D drawings of the study area (Figure 3) were made.

Drawings of the study area were also made in Pointcab software, a different drawing software (Figure 4).

After the drawings were made, a solid model of the study area (Figure 5) was mounted on the Virtual Reality (VR) system and introduced to the users by offering virtual navigation within the model (Figure 6).

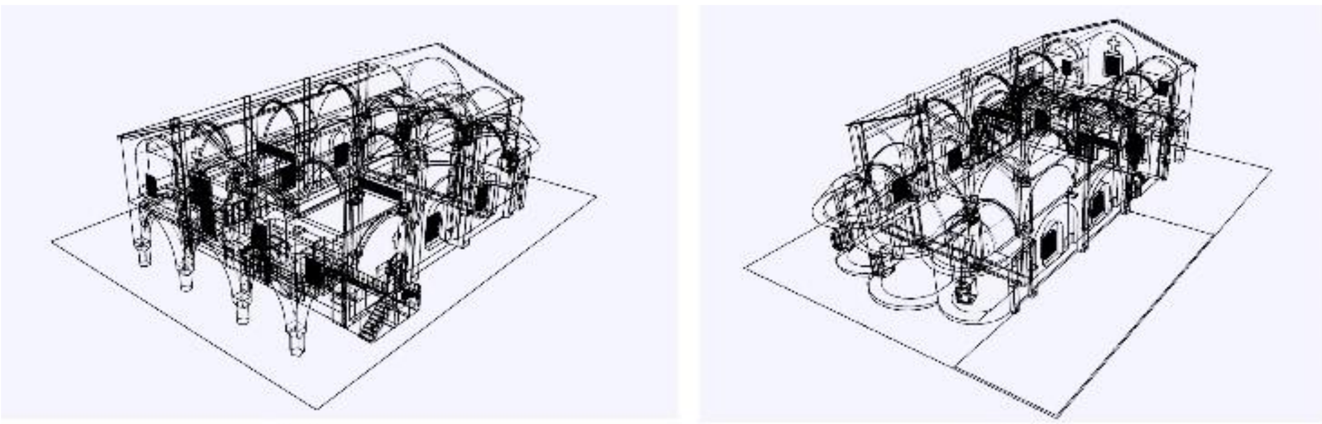

(a) (b)

Figure 3. Sketchhub draws (a) South façades, (b) north façades

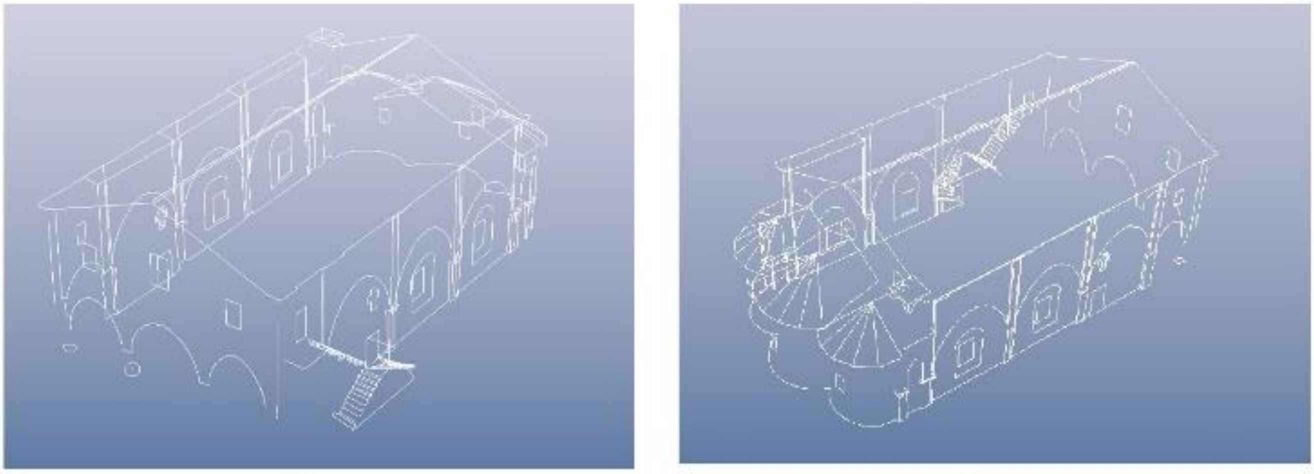

(a) (b)

Figure 4. Pointcab drawings (a) South Facade, (b) North Facade

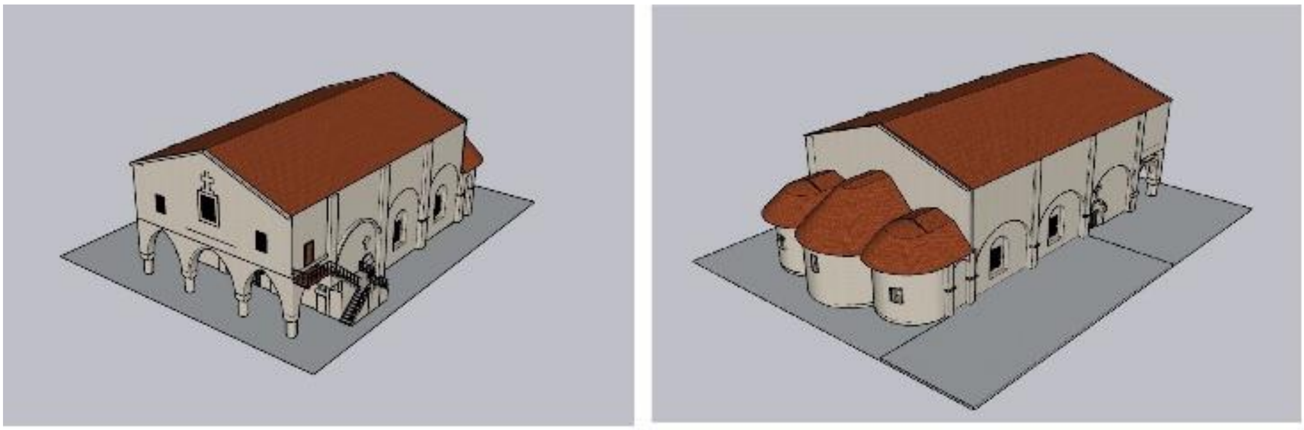

(a) (b)

Figure 5. Solid model. South façade (a), North façade (b)

Figure 6. Virtual Reality through a 3D model

4. Discussion

The accuracy of the local laser scanning in this study is in the range of approximately 0.4-0.7 cm.

The observations obtained as a result of the study are as follows:

Sketchub

- Plans, views, sections can be drawn.
- It provides 3D models for interior spaces.
- It allows use in construction projects.
- It is used in the design of urbanisation and landscape areas.

Pointcab;

- Floor plans and measurements can be made.
- Point cloud data from all commonly used 3D scanners can be processed.
- There is the possibility of output in the extension required by all commonly used CAD software.
- It contains plugins for Autocad, Archicad, Revit and etc. software.

The main advantage of the Laser Scanning technique is the direct generation of point clouds that define the object or scene.

5. Conclusion

Building Inspection has proposed a methodology to establish a comprehensive and accurate data source through Terrestrial Laser Scanning for building inspection, in addition to developing a TLS-derived inspection. The resulting database can be a valuable resource for diverse applications, such as asset management and structural assessment of heritage buildings. The 3D model derived from TLS, which is proposed in this study, has the potential to save time for asset managers and structural engineers as it removes the need for frequent in-person revisits to a structure. Furthermore, it can aid document management through the use of digital models instead of physical ones. Linking additional information, such as structure reports or building inspection data, to a digital copy of a bridge can improve understanding and communication among relevant personnel.

The study area was successfully represented in a 3D model and CAD drawings using TLS point clouds. The study employed two different drawing programs. Both programs have pros and cons that are discussed in detail. Those wishing to undertake similar work should choose their drawing software based on their project requirements. If presenting drawings and solid models in a virtual environment is the aim, VR systems should be utilized. The WEB-based Sketchfab platform, which supports both augmented and virtual reality, was utilized as the VR platform (https://skfb.ly/oNYNq). The use of WEB-based platforms significantly assists with the transfer of such studies to users.

Acknowledgement

This study was supported by Mersin University Scientific Research Projects with project number 2023-1-TP2-4789

References

Alptekin, A., & Yakar, M. (2020a). Kaya bloklarının 3B nokta bulutunun yersel lazer tarayıcı kullanarak elde edilmesi. *Türkiye LİDAR Dergisi*, *2*(1), 1-4.

Alptekin, A., & Yakar, M. (2020b). Mersin Akyar Falezi'nin 3B modeli. *Türkiye Lidar Dergisi*, *2*(1), 5-9.

Alptekin, A., Çelik, M. Ö., Doğan, Y., & Yakar, M. (2019). Illustrating of a landslide site with photogrammetric and LIDAR methods. In *Conference of the Arabian Journal of Geosciences*, 303-305.

Atik, M. E., & Duran, Z. (2021). Lokal özellik temelli yöntemler kullanılarak 3B yüz tanıma ve doğruluk analizi. Gazi Üniversitesi Mühendislik Mimarlık Fakültesi Dergisi, 36(1), 359-372.

Dustin, D., Liscio, E., & Eng, P. (2016). Accuracy and repeatability of the laser scanner and total station for crime and accident scene documentation. J Assoc Crime Scene Reconstr, 20(1), 57-67.

Kanun, E., Metin, A., & Yakar, M. (2021). Yersel Lazer Tarama Tekniği Kullanarak Ağzıkara Han'ın 3 Boyutlu Nokta Bulutunun Elde Edilmesi. *Türkiye Lidar Dergisi*, *3*(2), 58-64.

Karataş, L., Alptekin, A., & Yakar, M. (2022a). Creating Architectural Surveys of Traditional Buildings with the Help of Terrestrial Laser Scanning Method (TLS) and Orthophotos: Historical Diyarbakır Sur Mansion. *Advanced LiDAR*, *2*(2), 54-63.

Karataş, L., Alptekin, A., & Yakar, M. (2022b). Determination of Stone Material Deteriorations on the Facades with the Combination of Terrestrial Laser Scanning and Photogrammetric Methods: Case Study of Historical Burdur Station Premises. *Advanced Geomatics*, *2*(2), 65-72.

Karataş, L., Alptekin, A., & Yakar, M. (2022c). Analytical Documentation of Stone Material Deteriorations on Facades with Terrestrial Laser Scanning and Photogrammetric Methods: Case Study of Şanlıurfa Kışla Mosque. *Advanced LiDAR*, *2*(2), 36-47.

Liscio, E., & Le, Q. (2022). Inter observer errors of cast-off stains using FARO zone 3D. Forensic Science International, 330, 111098.

Ogawa, T., & Hori, Y. (2019). Comparison with accuracy of terrestrial laser scanner by using point cloud aligned with shape matching and best fitting methods. The International Archives of the Photogrammetry, Remote Sensing and Spatial Information Sciences, 42, 535-541.

Suchocki, C., Damięcka-Suchocka, M., Katzer, J., Janicka, J., Rapiński, J., & Stałowska, P. (2020). Remote detection of moisture and bio-deterioration of building walls by time-of-flight and phase-shift terrestrial laser scanners. Remote Sensing, 12(11), 1708.

Ulvi, A., Yakar, M., Toprak, A. S., & Mutluoglu, O. (2014). Laser scanning and photogrammetric evaluation of Uzuncaburç Monumental Entrance. International Journal of Applied Mathematics Electronics and Computers, 3(1), 32-36.

Ulvi, A., Yakar, M., Toprak, A. S., & Mutluoglu, O. (2014). Laser scanning and photogrammetric evaluation of Uzuncaburç Monumental Entrance. *International Journal of Applied Mathematics Electronics and Computers*, *3*(1), 32-36.

Ulvi, A., Yakar, M., Yiğit, A. Y., & Kaya, Y. (2020). İHA ve yersel fotogrametrik teknikler kullanarak Aksaray Kızıl Kilise'nin 3 Boyutlu nokta bulutu ve modelinin üretilmesi. Geomatik Dergisi, 5(1), 22-30.

URL 1: https://gokturkharita.com/

Yakar, M., Yılmaz, H. M., & Mutluoğlu, Ö. (2010). Comparative evaluation of excavation volume by TLS and total topographic station based methods. Lasers in Eng., 19, 331–345

Yiğit, A. Y., Hamal, S. N. G., Yakar, M., & Ulvi, A. (2023). Investigation and Implementation of New Technology Wearable Mobile Laser Scanning (WMLS) in Transition to an Intelligent Geospatial Cadastral Information System. *Sustainability*, *15*(9), 7159.

Yılmaz, H. M., & Yakar, M. (2006). Yersel lazer tarama Teknolojisi. *Yapı teknolojileri Elektronik dergisi*, *2*(2), 43-48.

Zeybek, M. (2019). El-tipi LiDAR ölçme sistemleri ve 3B veri işleme. Türkiye Lidar Dergisi, 1(1), 10-15.

7th Intercontinental Geoinformation Days

igd.mersin.edu.tr

Incorrect use of wearable mobile LiDAR: Example of Mersin Soli Beach and Ankara National Library Underpass

Atila Karabacak[*1], **Murat Yakar** [2]

[1]Mersin University, Vocational School of Technical Sciences, Department of Architecture and Urban Planning, Mersin, Türkiye,
[2]Mersin University, Faculty of Engineering, Department of Geomatics Engineering, Mersin, Türkiye

Keywords
Remote sensing
Wearable Mobile Lidar
Photogrammetry
Laser Scanning
3D

Abstract

Scanning was carried out on the Mersin Soli coast with Wearable Mobile LiDAR (GML) to determine the shore edge line without using a Ground Control Point (GCP) and without creating a closed route. As expected, deviations from the sea and errors up to decimeters were observed since the GCP was not used. In a second study, it was used in the 3D modeling of the Ankara National Library subway underpass. In the study, scanning was carried out using GML without using a Ground Control Point (GCP) and by creating a closed route. The study was unsuccessful as a result of not using GCP and having a symmetrical appearance in the field.

1. Introduction

Mersin has the most beautiful beaches in Turkey. It is important to determine the coastal edge line quickly and accurately with GML. In this study, we know that GML data is corrupted by reflections from water, and it was also determined that the data was corrupted in this study (Karabacak and Yakar, 2023a).

3D modeling of the Ankara National Library subway underpass can be done quickly with GML, of course, this requires using GCP and differentiating the scene. In this study, the scene was not differentiated and it was investigated how to get results without using GCP.

2. Method

Nowadays, the demand for high accuracy 3D data is increasing rapidly. With advances in sensor technology and the continuous improvement of computing power, geo-referenced technologies can today bring unique functionality and flexibility in spatial modeling. Laser scanning is one of the most important technologies in this regard (Yılmaz and Yakar, 2006a; Yılmaz and Yakar, 2006b; Ulvi et al. 2014; Alptekin and Yakar, 2020a; Alptekin and Yakar, 2020b; Karataş et al. 2022a; Karataş et al. 2022b; Yakar et al. 2016; Kanun et al. 2021).

The WML we used in this study is the Gexcel Heron Wearable 3D Mobile Mapping System. The system has been used for 8 years. The system, which uses the SLAM algorithm, can be used anywhere a person can walk. System Building, cave, mine, cultural heritage etc. It is used to measure all kinds of natural and artificial objects. The system can capture 3D point cloud and 5K panoramic images.

The portable Mobile laser scanner tested in this study is the Heron wearable Lidar device produced by Gexcel. It is a 16-channel Velodyne Puck LITE laser scanner that emits infrared laser beams at a wavelength of 903 nm and provides 300,000 dots per second in single rotation mode from 360o horizontal view and 30^{o} vertical view. Range measurements are carried out on the time-of-flight principle with a maximum measurable distance of 100 m. The laser scanner sensor is combined with an XSens MTI, IMU, whose data is used in system orbit estimation. When performing the survey, the scanning head is mounted on a telescopic carbon fiber pole, connected to a battery and a control unit. According to the manufacturer's specifications, the system provides a local accuracy of 3 cm and a final global accuracy of 5 cm. The system is also affected by the presence of loops and closures. features may be affected by the SLAM algorithm and accuracy may decrease to 20-50 cm (Paksoyteknik, 2023; Yakar and Karabacak 2023; Karabacak and Yakar, 2022; Karabacak and Yakar, 2023b; Karabacak and Yakar, 2023c).

* **Corresponding Author**

*(*atilakarabacak@mersin.edu.tr*) ORCID ID 0000-0002-1096-3949
(*myakar@mersin.edu.tr*) ORCID ID 0000-0002-2664-6251

Cite this study

Karabacak, A., & Yakar, M. (2023). Incorrect use of wearable mobile LiDAR: Example of Mersin Soli Beach and Ankara National Library Underpass. Intercontinental Geoinformation Days (IGD), 7, 234-237, Peshawar, Pakistan

2.1. Mersin Soli Beach 3D Modeling Studies

The measurement with GML appears in figure 2 (figure 1). In the route solution given below, the red line appears to be a place where the route is disrupted and goes to different spaces. Here, the SLAM algorithm is affected by the sea (Figure 2).

An attempt has been made to prevent this route disruption with different parameter options.

The 3D model and orthophoto were created with dm precision as shown below. Deviations are greater in the vertical, this was seen as a result of examining the 3D model (Figure 3).

Figure 1. Field study

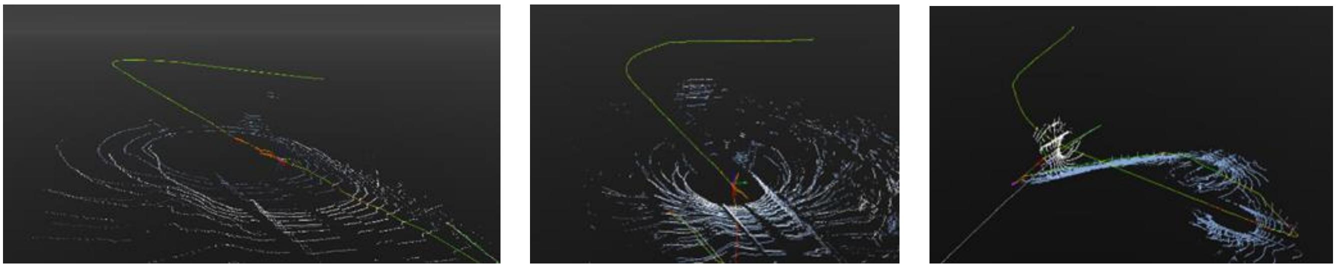

Figure 2. Route distortion

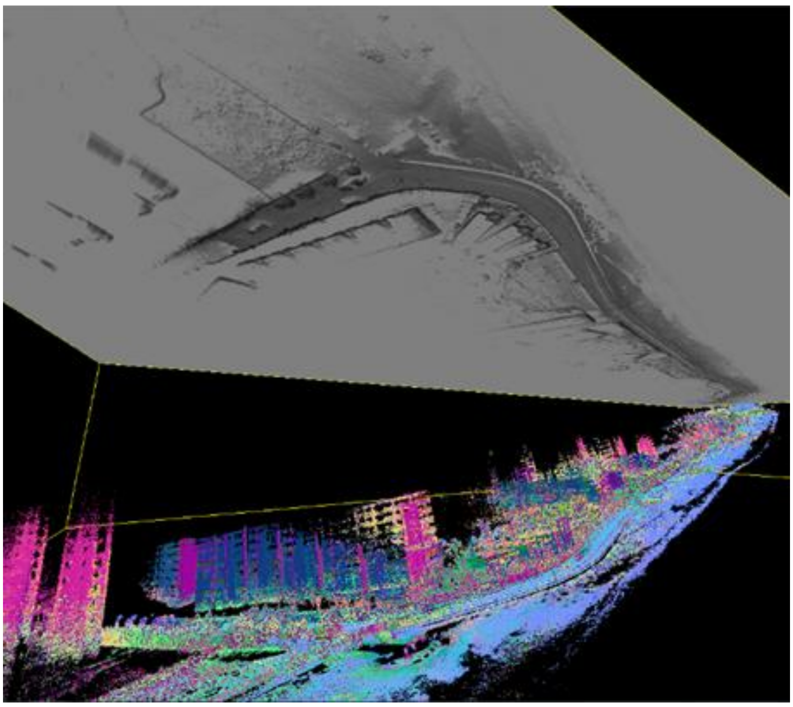

Figure 3. Orthophoto and 3D model

2.2. Ankara National Library Underpass 3D Modeling works

The study was carried out in the Ankara National Library underpass [13]. In the study, GCP was not specifically used and the system was tested without specially differentiating the environment. Working with GML was completed in approximately 9 minutes.

In the study, the SLAM algorithm disrupted the study by going to different spaces since there was no differentiation in the scene. Errors occurred at the meter level [14].

Figure 4. Ankara National Library Underpass

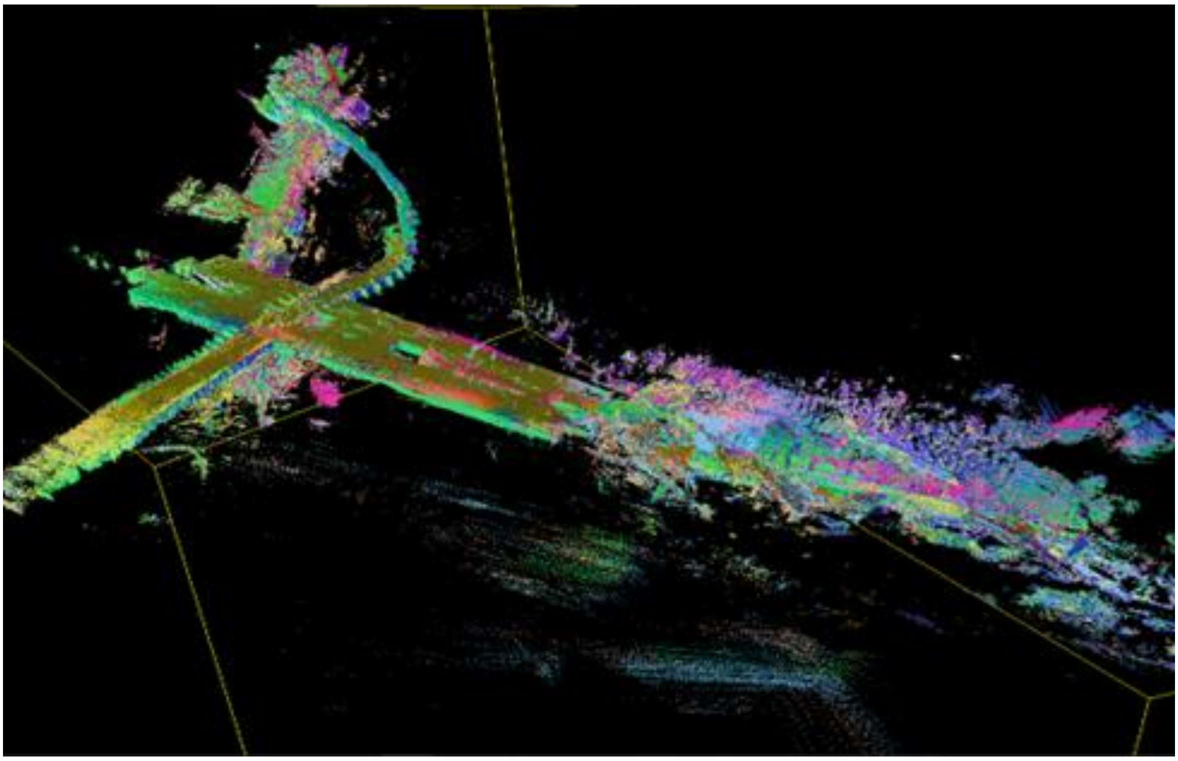

Figure 5. Ortophoto and 3D model

3. Results

In the study carried out on the beach, errors up to dm were observed, corrupting the sea SLAM algorithm. In the study carried out in the underpass, the symmetrical environment disrupted the SLAM algorithm and resulted in errors of many meters.

4. Discussion

Since the GCP point was not used, the SLAM algorithm gave errors in these difficult conditions in both studies. Since different reflections at the seaside disrupt the SLAM algorithm, errors can be reduced by using the GCP point, and it will also reduce the error rate on closed routes.

We tested that since the underpasses were made symmetrically and there were no different objects in the scenes, it made it difficult for the SLAM algorithm to work and distinguish, and it was observed that it confused the direction of the GML route solution. The resulting product is worthless in terms of engineering but valuable in terms of science. Different objects should be placed in places with the same appearance, such as underpasses, and it is necessary to use GCP.

5. Conclusion

As a result, using GML without using GCP is far from giving reliable results since the water surface at water edges disrupts the SLAM algorithm. We recommend using YKN in places such as underpasses etc. and scanning with GML by differentiating the place.

References

Alptekin, A., & Yakar, M. (2020a). Kaya bloklarının 3B nokta bulutunun yersel lazer tarayıcı kullanarak elde edilmesi. Türkiye LİDAR Dergisi, 2(1), 1-4.

Alptekin, A., & Yakar, M. (2020b). Mersin Akyar Falezi'nin 3B modeli. Türkiye Lidar Dergisi, 2(1), 5-9.

Kanun, E., Metin, A., & Yakar, M. (2021). Yersel Lazer Tarama Tekniği Kullanarak Ağzıkara Han'ın 3 Boyutlu Nokta Bulutunun Elde Edilmesi. Türkiye Lidar Dergisi, 3(2), 58-64.

Karabacak, A., & Yakar, M. (2023a). 3D modeling of Mersin Akyar Cliffs with wearable mobile LIDAR. Advanced Engineering Days (AED), 6, 86-89.

Karabacak, A., & Yakar, M. (2023b). 3D modeling of Mersin Sarisih Caravanserai with wearable mobile LIDAR. Advanced Engineering Days (AED), 6, 90-93.

Karabacak, A., & Yakar, M. (2023c). 3D Modeling of Mufti Abdullah Sıddık Mosque using Wearable Mobile LiDAR. Advanced LiDAR, 3(1), 01-09.

Karabacak, A., & Yakar, M. (2022). Giyilebilir Mobil LİDAR Kullanım Alanları ve Cambazlı Kilisesinin 3B Modellemesi. Türkiye Lidar Dergisi, 4(2), 37-52.

Karataş, L., Alptekin, A., & Yakar, M. (2022a). Analytical Documentation of Stone Material Deteriorations on Facades with Terrestrial Laser Scanning and Photogrammetric Methods: Case Study of Şanlıurfa Kışla Mosque. Advanced LiDAR, 2(2), 36-47

Karataş, L., Alptekin, A., & Yakar, M. (2022b). Creating Architectural Surveys of Traditional Buildings with the Help of Terrestrial Laser Scanning Method (TLS) and Orthophotos: Historical Diyarbakır Sur Mansion. Advanced LiDAR, 2(2), 54-63

Paksoyteknik (2023). https://paksoyteknik.com.tr/index.php/paksoy-topcon/lazer-tarama/gexcel-heron

Ulvi, A. Yakar, M., Toprak, A. S., & Mutluoglu, O. (2014). Laser scanning and photogrammetric evaluation of Uzuncaburç Monumental Entrance. International Journal of Applied Mathematics Electronics and Computers, 3(1), 32-36.

Yakar, M., & Karabacak, A. (2023). Giyilebilir Mobil Lidar ve Uygulamaları. Mersin Üniversitesi Harita Mühendisliği Kitapları.

Yakar, M., Ulvi, A., & Toprak, A. S. (2016). The Use of Laser Scanner in Caves, Encountered Problems and Solution Suggestion. Universal Journal of Geoscience, 4(4), 81-88.

Yılmaz, H. M., & Yakar, M. (2006a). Lidar (Light Detection And Ranging) Tarama Sistemi. Yapı Teknolojileri Elektronik Dergisi, 2(2), 23-33.

Yılmaz, H. M., & Yakar, M. (2006b). Yersel lazer tarama Teknolojisi. Yapı teknolojileri Elektronik dergisi, 2(2), 43-48

7th Intercontinental Geoinformation Days

igd.mersin.edu.tr

Assessing the vulnerability of residential lands against earthquakes and ways to reduce vulnerability using spatial analysis: Case study of Tabriz city

Sana Foroughi *1, **Farzad Rezaei** 1, **Faezeh Khoshkhoy** 1

1University of Tabriz, Faculty of Planning and Environmental Sciences, GIS Department, Tabriz, Iran

Keywords
Residential users
Tabriz city
Vulnerability

Abstract

Earthquakes are known as one of the most important and dangerous natural hazards in earthquake-affected areas and can lead to severe physical, economic and social damage in cities. Based on the information and data collected about Tabriz city, this article evaluates the vulnerability of urban uses against earthquake risk. The current research was carried out with a descriptive-analytical method and by using the GIS environment as well as the zoning of earthquake-prone areas, an appropriate estimate of the vulnerability of residential uses in Tabriz city was made using spatial and descriptive data. Based on the analysis of spatial data, the residential lands near the faults were examined, and by using appropriate methods, weak points and high-vulnerability uses are identified. Then, solutions to improve and strengthen urban uses are provided and suggestions are provided to reduce vulnerability and increase resistance against earthquakes. The results showed that a significant percentage of Tabriz city is in high and very high vulnerability classes. According to the seismic vulnerability zoning of the city and the distribution of vulnerable classes in Tabriz city, it can be concluded that most of the area is vulnerable to earthquakes.

1. Introduction

Earthquakes are considered as one of the powerful natural phenomena that threaten the safety and health of humans and the environment. Due to dense population, structure of buildings, complex infrastructure and economic and social sensitivities, cities are considered as very sensitive places against earthquakes, especially in densely populated areas like Tabriz city. The purpose of this article is to investigate and evaluate the vulnerability of residential use in Tabriz city against earthquakes. Vulnerability of residential use refers to the vulnerability of different sectors. This evaluation identifies the weaknesses and strengths of the existing systems and can be used as solutions to increase the security and resistance of the city against earthquakes. To do this evaluation, analytical methods are used in this article. At first, the city of Tabriz is studied completely and (buildings) are examined. Then, using (spatial data analysis such as: identifying the location of faults and earthquake-prone points in the GIS environment) the vulnerability of residential use is evaluated. The purpose of assessing the vulnerability of residential use is to identify and evaluate the weak points of different parts of the city against earthquakes. This assessment can help city managers, urban planners and relevant organizations to take measures to increase the city's resistance and security against earthquakes. Also, the results of this evaluation can be used as a way to increase public awareness and educate people about appropriate behaviors in case of an earthquake. Finally, this article provides suggestions and solutions to improve the vulnerability of urban use against earthquakes. These suggestions can include strengthening buildings, improving infrastructure, improving telecommunication networks, equipping public places with safety equipment and earthquake training. By implementing these suggestions, the vulnerability of urban use against earthquakes will be reduced and the city of Tabriz can be improved in facing future earthquakes. In the end, this article refers to related sources and studies in the field of urban use vulnerability assessment and earthquake risk management. And it can be used as a basis for future research in this field.

* **Corresponding Author**

*(e-mail) ORCID ID : Sanaforouqi@gmail.com

Cite this study

Foroughi, S., Rezaei, F., & Khoshkhoy, F. (2023). Assessing the vulnerability of residential lands against earthquakes and ways to reduce vulnerability using spatial analysis: Case study of Tabriz city. Intercontinental Geoinformation Days (IGD), 7, 238-240, Peshawar, Pakistan

2. Method

According to the purpose of the study, the type of research is based on descriptive-analytical method. Argument has been used in document review and library study and then using the extracted principles in presenting the proposed method and checking the studied area based on it. For the division of the earthquake zone, the multring buffer tool is used to obtain information. Vulnerability from the tabulate intersection tool and also to generate vulnerability maps, this software is also used.

2.1. Theoretical

Earthquake means strong shaking of the earth (Dakhkhoda dictionary), which usually causes the earth to break under the pressure. This rupture fluctuates from a few millimeters to tens of meters, and the released energy is released from the rock and becomes terrestrial. These are ruptures (Ebrahimzadeh et al., 2015). Earthquake as a natural hazard has a direct and indirect impact on the society and is considered as an important challenge in the development process (Johnson, 2004).

Vulnerability is a situation that begins in historical, cultural, social processes that use them and limit the response of individuals and groups to crisis. This view sees vulnerability as "a product of characteristics such as: race, religion, social base, gender, age that affect access to power and resources" (Winsor, Blahi, Cannon, & Davis, 2004) and harm Acceptability is somehow related to social and economic status

2.1 Understanding the study area

The city of Tabriz with a population of 1 million 693 thousand 42 people is bounded from the north by Warzghan city, from the south by Maragheh city, from the east by Haris and Bostan Abad cities, from the west by Esko city and northwest by Shabstar city. The area of Tabriz city is approximately 1781 square kilometers. This city is located at 46.25 east longitude and 38.2 north latitude from the Greenwich Peninsula and its approximate altitude varies from 1300 to 2100 meters above sea level.

Figure 1. Map of the study area

2.1. Fault range

The Tabriz fault is one of the linear structures of Iran, which can be traced with a length of 100 km from Misho mountains (in the west) to Bostanabad (in the east). The best effect of this fault can be seen in the north of Tabriz and that is why it is named Tabriz fault. Its general trend is north of 115 degrees east and its slope is vertical. From Sufiyan to the west, this fault passes through Khoi city towards Mako and then reaches the Ararat mountains in Turkey. Its southeastern continuation is the Soltanieh Mountains in southeastern Zanjan, which may reach the Qom-Zafrah fault.

North Tabriz fault is one of the old faults of Iran, which passes through Zanjan_Abhar depression, north of Tabriz and northwest of Azerbaijan and continues to the Caucasus. During the previous Devonian, this fault divides the Azerbaijan region into two blocks. The northeastern block has sunk and the southwestern block has been underground until the end of the Carboniferous; Therefore, the activity of this fault may have started from the Devonian period; Although its older age is probable.

Figure 2 shows the area of Tabriz fault as well as residential areas located in that area.

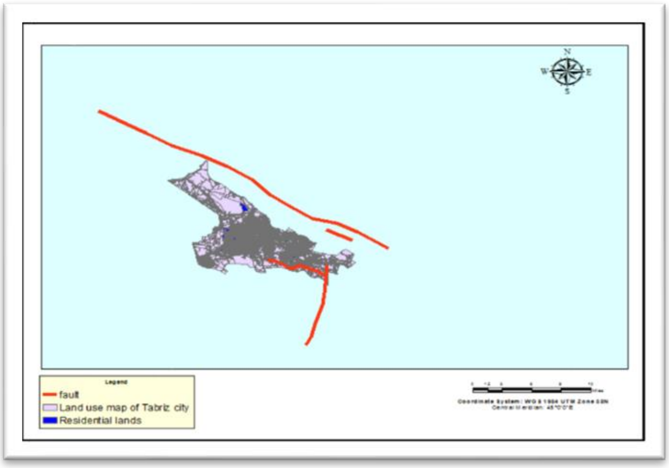

Figure 2. Fault map

3. Results

Based on the evaluation done, the residential lands located in the south of Tabriz city in the range of 300-500 meters from the South Tabriz fault (Figure 2) are more vulnerable. And in the northern fault of this city, the lands located at a distance of 5 kilometers are more vulnerable.

The lands in the western and southwestern parts, which are located at a distance of 10-15 km from the fault, are relatively less vulnerable.

In the southeastern part of the lands that are located at a distance of 500 meters and 1 kilometer from the fault, they are exposed to medium and high vulnerability. The central part is also very vulnerable.

As it is clear in Figure 3, the northern fault has the greatest potential risk on buildings, so engineers and relevant authorities should pay more attention to this area in terms of retrofitting. Lands that are in the danger zone of the fault line should be placed on resistant formations. . As the evidence of historical earthquakes shows, the relative resistance of the earth has never shown adequate tolerance against destructive earthquake waves (Rustaei, 2010).

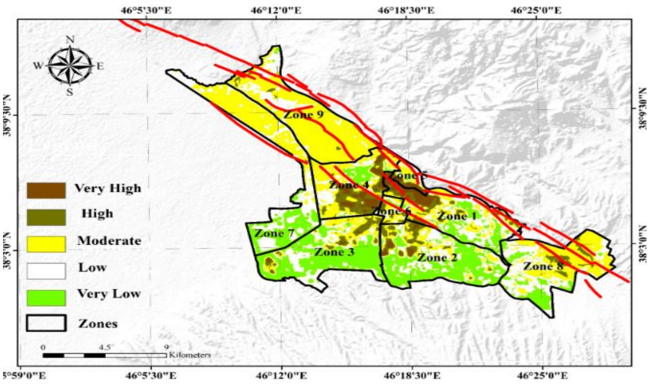

Figure 3. Earthquake line zoning map

4. Discussion

Planning solutions aimed at reducing vulnerability:

First step: Identifying vulnerable areas and vulnerability indicators

The second stage: creating complete information about buildings and how they resist earthquakes and using the collected information in order to strengthen the city and manage the crisis.

The third step: drawing a map of vulnerability to earthquakes as a tool for prevention planning

The fourth stage: conducting extensive studies regarding the reduction of earthquake risk and damage, in various fields such as: economic, social, physical studies, etc.

The fifth stage: continuous monitoring of the relevant officials, especially the municipality, on the way of construction and development of the city to prevent the continuation of the process of building the vulnerability of the city.

The sixth stage: the strength of the social structures of the society is an important step in reducing vulnerability; Because when an earthquake occurs, the weak performance of social organization in formal and informal societies increases the level of vulnerability.

The seventh stage: providing legal facilities; Such as residential loans, giving loans for renovations, strengthening houses, etc.

5. Conclusion

The assessment is for Tabriz city. It includes areas with very high, high, medium, low, very low and no risk. It can be seen from the assessment in Figure (3) that most of the residential lands in the north of Tabriz are in the area with the danger is high. Bagh Misheh town and Valiasr area are in the dangerous ring in terms of faults. Bagh Misheh town is located on a fault system. The greatest possible danger comes from the movement of faults. Therefore, civil engineers should pay attention to this point. The results of spatial vulnerability assessment using spatial data analysis in GIS environment showed that a significant percentage of residential lands and neighborhoods in Tabriz city are in high and very high vulnerability class. Even the parts that are within 10 kilometers of Baghsal are at moderate risk. According to the vulnerability zoning of Tabriz city, it can be concluded that most of the residential lands of this city are vulnerable to earthquakes.

Acknowledgement

Special thanks to Dr. Valizadeh Kamran for helping to carry out this project.

References

Ebrahimzadeh et al. (2014) Vulnerability assessment of urban neighborhoods against earthquakes - Case example: Piranshahr city, Sistan and Baluchistan, Spatial Planning Scientific-Research Quarterly (Geography), 5(1).

Lalepour et al. (2022). Vulnerability assessment of urban areas against earthquake crisis - Case example: Warzaghan city areas, Maragheh, Scientific Research Journal of Natural Environment Hazards No. 31

Manocherhotbibian and Nagin Mozafari (2018), Vulnerability assessment of residential contexts and strategies to reduce vulnerability - case study: District Six of Tehran Municipality, Tehran, Scientific-Research Quarterly No. 27

Shahram Rootaee (2010), risk zoning of Tabriz fault for different urban land uses, Tabriz, Geography and Development Quarterly No. 21

Jila Kalali Moghadam (2015), evaluating the vulnerability of marginal and informal settlements against earthquakes - case study: Mashhad city outskirts, Neishabur, Rural Research and Planning Magazine No. 4

Geological map 1:25000 sheet of Tabriz. https://en.wikipedia.org/wiki/Wikipedia Wikipedia

https://www.irna.ir/news

7th Intercontinental Geoinformation Days

igd.mersin.edu.tr

Evaluation of the quality of climate time series maps extracted from GEE: A case study of Arasbaran Region - Iran

Sajjad Moshiri [1], Khalil Valizadeh Kamran *[1], Omid Rafieyan [2] Ahmad Nikdel Monavvar [1], Mohammad Ebrahim Ramazani [2]

[1] University of Tabriz, Department of Remote Sensing and GIS, Tabriz, Iran
[2] Islamic Azad University, Department of Environmental Engineering, Tabriz Branch, Iran - Sustainable Development Management Research Center of Urmia Lake basin and Aras River, Tabriz Branch, Islamic Azad University, Tabriz, Iran

Keywords
Climate
Meteorological station
Remote sensing
GEE
Arasbaran

Abstract

As one of the 13 biosphere reserves of Iran, the precious forests of Arasbaran are exposed to damage caused by climate change. For its protection, management and continuous monitoring, it is necessary to obtain accurate, correct and timely environmental data and information, including climate data. Due to the insufficient number and inappropriate distribution of meteorological stations in the region, the use of (RS&GIS) data in the GEE platform to extract climatic parameters was put on the agenda. These data were prepared either in the form of existing products or by applying valid formulas on satellite images. Daily minimum, daily maximum and daily average temperatures, along with the temperature of the earth's surface every 16 days (resulting from Landsat 8) as well as daily precipitation, monthly cumulative precipitation and daily maximum wind speed, related to the first six months of the year 1400, are from both sources of information mentioned (GEE and the aforementioned meteorological station) were extracted and compared. Examining the relationship between these climate maps (produced in GEE) with the meteorological data recorded at the Jolfa meteorological station (for example), except for the maximum daily wind speed parameter, other parameters of daily cumulative precipitation, minimum, maximum and daily average temperature, showed a good correlation and the data can be trusted.

1. Introduction

Arasbaran forest is a complex and dynamic ecosystem, in which its constituent parts are always in balance. These valuable forests, which were registered in 1977 as one of the 13 biosphere reserves of Iran in the UNESCO Man and Planet Earth program, when they are affected by natural or artificial destructive factors, depending on the type and intensity of the destructive factors, the state of equilibrium or its self-regulation get weak and gradually disappears may be reached. Therefore, it is necessary to protect and support these valuable forests against various environmental and human factors.

For this, we need to obtain accurate, correct and timely environmental data and information for continuous monitoring and optimal management of this unique ecosystem. Collecting the required ecological and climatic data with field methods has been very expensive and time-consuming, and among them, climatic information is of special importance due to its variable and dynamic nature. The use of meteorological climate stations faces serious limitations due to the insufficient number and inappropriate distribution at the regional level (Rahimi and Esmaili, 2009; Kerr and Stroskai, 2003). In this connection, remote sensing and geographic information system (RS&GIS), especially with today's satellites with spatial, temporal, production and radiometric resolution, are suitable for selecting climatic stations with acceptable accuracy and reliability and independent of Geology data is presented.

The important challenge in using satellite images is the huge volume, especially in studies that require downloading multiple and voluminous time series data and heavy processing due to the multitude of parameters required for studies related to forest fires. This problem is well solved by Google Earth Engine (GEE). This system enables users to perform calculations on a large amount of data (from a spatial resolution of 10 meters to several kilometers) without the need for high-powered systems. This system hosts a huge database of satellite image data, which includes images from more than forty years ago.

* **Corresponding Author**

*(valizadeh@tabrizu.ac.ir) ORCID ID ORCID ID 0000-0003-4648-842X
(Sajjadmoshiri@gmail.com) ORCID ID 0009-0007-7148-5948
(o_rafieyan@yahoo.cam) ORCID ID 0000-0002-2660-3593
(ahmadnikdel21@gmail.com) ORCID ID 0000-0003-2354-1187
(ramazani@iaut.ac.ir) ORCID ID 0000-0003-2777-7349

Cite this study

Moshiri, S., Kamran, K. V., Rafieyan, O, Monavvar, N. A., & Ramazani, M. E. (2023). Evaluation of the quality of climate time series maps extracted from GEE: A case study of Arasbaran Region – Iran. Intercontinental Geoinformation Days (IGD), 7, 241-245, Peshawar, Pakistan

These images, which are captured daily, include a searchable data catalog including the entire Landsat satellite catalog (USGS/NASA), multiple MODIS sensor data sets, Sentinel-1 satellite data, NAIP (National Agriculture Imagery Program) data, Rainfall data, sea surface temperature data, weather data ,CHIRPS (Climate Hazards Group InfraRed Precipitation with Station) and altitude data (Gurlik et al., 2017).

The purpose of the research is to use the remote sensing technology and the technical capabilities of the GEE system in order to compensate for the lack of climatic data resulting from meteorological stations in a cold semi-humid forest area in the middle latitude of the earth.

2. Method

In order to include the climatic parameters in this research, due to the limited number and long distance of the stations on the one hand and the extreme topography and diverse land covers of the region on the other hand, which has caused the creation of different microclimates in the region. Practically, the use of interpolation and zoning methods to apply climatic parameters to the entire region will not be logical and reality.

Therefore, in this research, the use of hourly, daily or monthly climate data resulting from telemetry data in the GEE was considered. These data were prepared in two ways; In the form of ready data available on reliable sites (Product) or by applying accepted scientific formulas and relationships (citing reliable articles and sources) on different bands of satellite images and achieving the desired climate parameter which is applied to each pixel according to the dimensions and reflection of each pixel (spatial and spectral resolution).

Therefore, regardless of the type of topography and land cover, the climate parameter is applied to each pixel independently of other pixels. The type of climatic data extracted from the telemetry data used in this research and the source of their preparation are shown in the following tables.

Table 1. The type of climate data extracted from telemetry data used in the research

Dataset Availability	period	Image level	Satellite OR product
2013-04-11 - 2021-12-11	7:37:48 AM	Level 2, Collection 2, Tier 1	Landsat 8
1979-01-02 - 2020-07-09	Daily	Climate Reanalysis Produced by ECMWF / Copernicus Climate Change Service	ERA5
1981-01-01- 2021-09-29	Hourly	Land Hourly - ECMWF Climate Reanalysis	ERA5
1958-01-01 - 2020-12-01	Month	Monthly Climate and Climatic Water Balance for Global Terrestrial Surfaces, University of Idaho	TerraClimate
1981-01-01 - 2021-11-30	Daily	Climate Hazards Group InfraRed Precipitation with Station Data (Version 2.0 Final)	CHIRPS
2009-01-01 - 2021-11-11	10 days	Actual Evapotranspiration and Interception	WAPOR

2.1. Study area

Arasbaran or Qara Dagh is a vast mountainous area in the north of East Azarbaijan province in the northwest of Iran. In 1976, UNESCO registered 72,460 hectares of the region's land as a biosphere reserve. UNESCO's general description is as follows; This biosphere reserve is located in the Caucasian mountains of Iran near the country's border with the Republic of Azerbaijan and Armenia. The region, being located between the Caspian, Caucasian and Mediterranean regions, includes high mountains, alpine meadows, semi-arid plains, pastures and forests, rivers and springs. An area equal to 634,719 hectares (about 4 times the pure area of Arasbaran forests) was selected according to Figure 1, including the uses of forest, pasture, agriculture, residential and water areas. Arasbaran and Dizmar National Park and Protected Area and parts of Kental National Park and Kiamaki Wildlife Sanctuary are included in the study area. The altitude range of the study area ranges from 187 meters in the northeast of the region in Larijan to 3254 meters in the Kantal peak in the west of the region. The most important river is Aras in the northern border of the region, where Selenchai, Kaleybarchai, Setenchai, Ilganehchai, Mardanqomchai and Hajilerchai rivers flow into Aras River from east to west respectively.

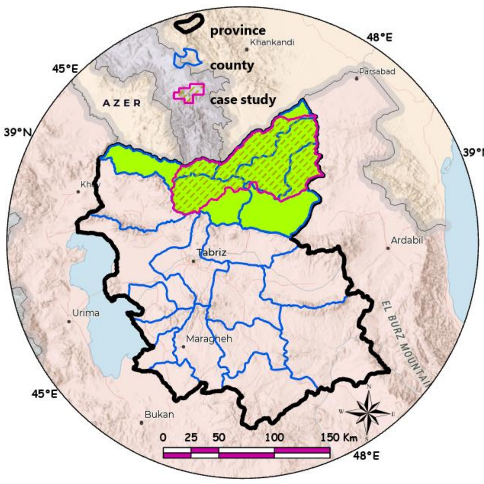

Figure 1. Case study

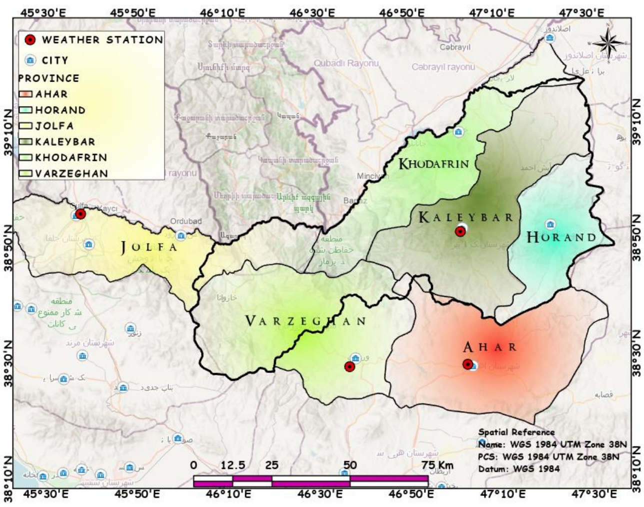

Figure 2. The location of the closest meteorological stations to the study area

3. Results

In this research, climate maps were produced from Landsat 8 and Sentinel 2 satellite images, which are available in the GEE database, by applying known and confirmed formulas and Indicators. As an example, some of the maps produced for the entire study area are given below (**Figure 3-7**).

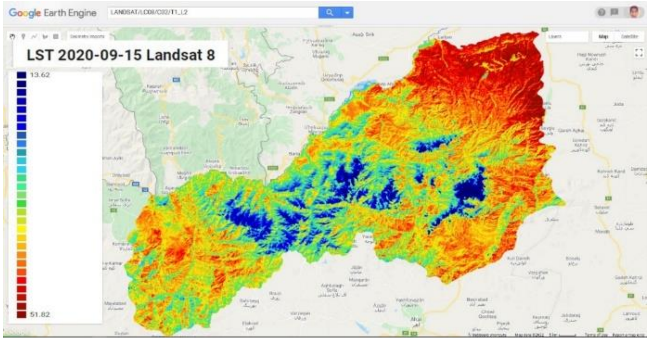

Figure 3. Land surface temperature (LST) .prepared in GEE based on Landsat 8

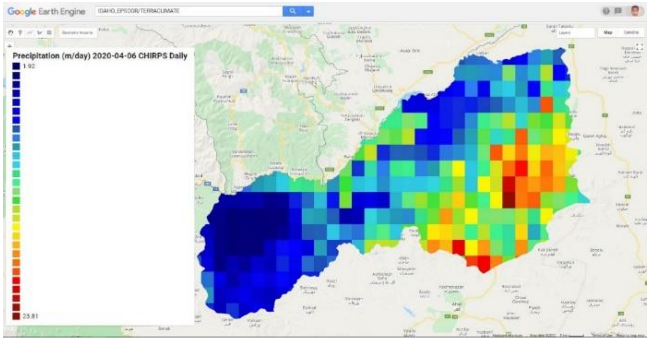

Figure 4. Daily rainfall, prepared in GEE.

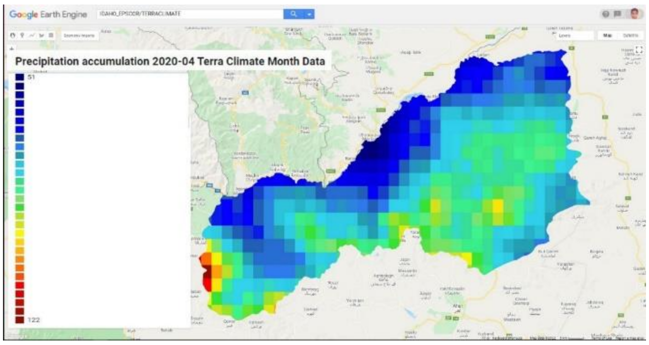

Figure 5. Cumulative monthly rainfall map, prepared in GEE.

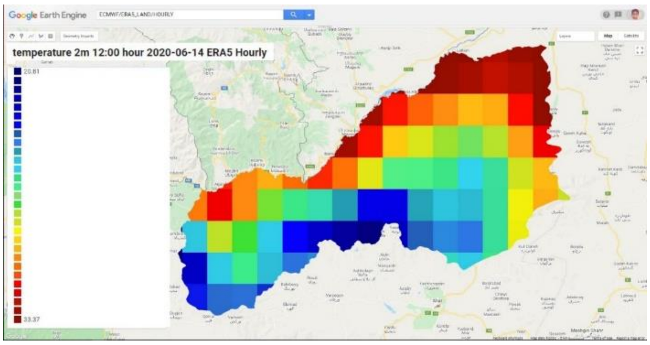

Figure 6. Hourly temperature map, prepared in GEE.

3.1. Evaluation of climatic data extracted from GEE in comparison with meteorological station data

In order to validate the mentioned data, one of the meteorological stations (Jolfa meteorological station) and the climate data downloaded or produced based on the formulas and relationships compiled with the hourly and daily data of the existing meteorological stations were compared and assessed for accuracy. For this purpose, the data: daily minimum, daily maximum and daily average temperatures, along with the temperature of the earth's surface every 16 days (extracted from Landsat 8) as well as daily rainfall, monthly cumulative rainfall and daily maximum wind speed, related to the first six months of 2021 was extracted and compared from both mentioned sources of information (GEE and the mentioned meteorological station). The comparison of these statistics actually showed how much the climate maps extracted from remote sensing in the GEE can be trusted.

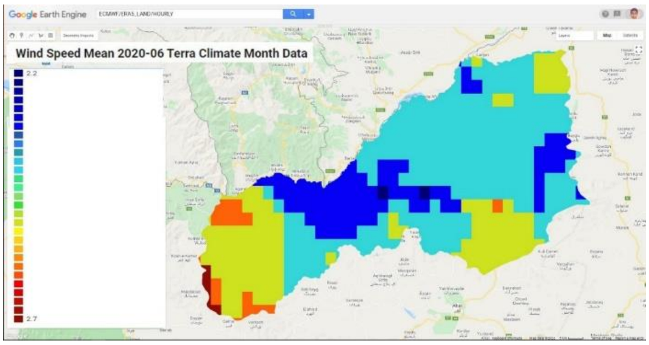

Figure 7. Average monthly wind speed map, prepared in GEE.

According to Figure 8 there is a very strong correlation between the temperature of 10 specific days in the first six months of 2021, obtained from the Landsat 8 satellite image, and the temperature of the meteorological station on the same days. With the explanation that the temperature obtained from the satellite image is higher than the temperature of the station during the days, which will be applied when entering the temperature map in the process of the necessary calibration. Figure 8 shows the relationship between the daily maximum wind speed between the original data from the ERA5 product site and the meteorological station, that the fluctuations of the meteorological station data are more intense and with more details, while the data from GEE has less fluctuations and a lower amount. Although the data of the meteorological station is more precise and accurate in point form, but if the goal is to produce a climate parameter map for the entire region and each pixel of the image, the accuracy and precision of the map obtained from the meteorological data is definitely lower due to the long distance and low density in the area will not be reliable and dependable.

According to Figure 8, the relationship between the daily cumulative precipitation of telemetry data and meteorological station is strong and it shows the appropriate accuracy of telemetry data. Figures 8, which respectively deal with the relationship between the minimum, maximum and daily average temperature of telemetry data with meteorological station, also shows a good correlation.

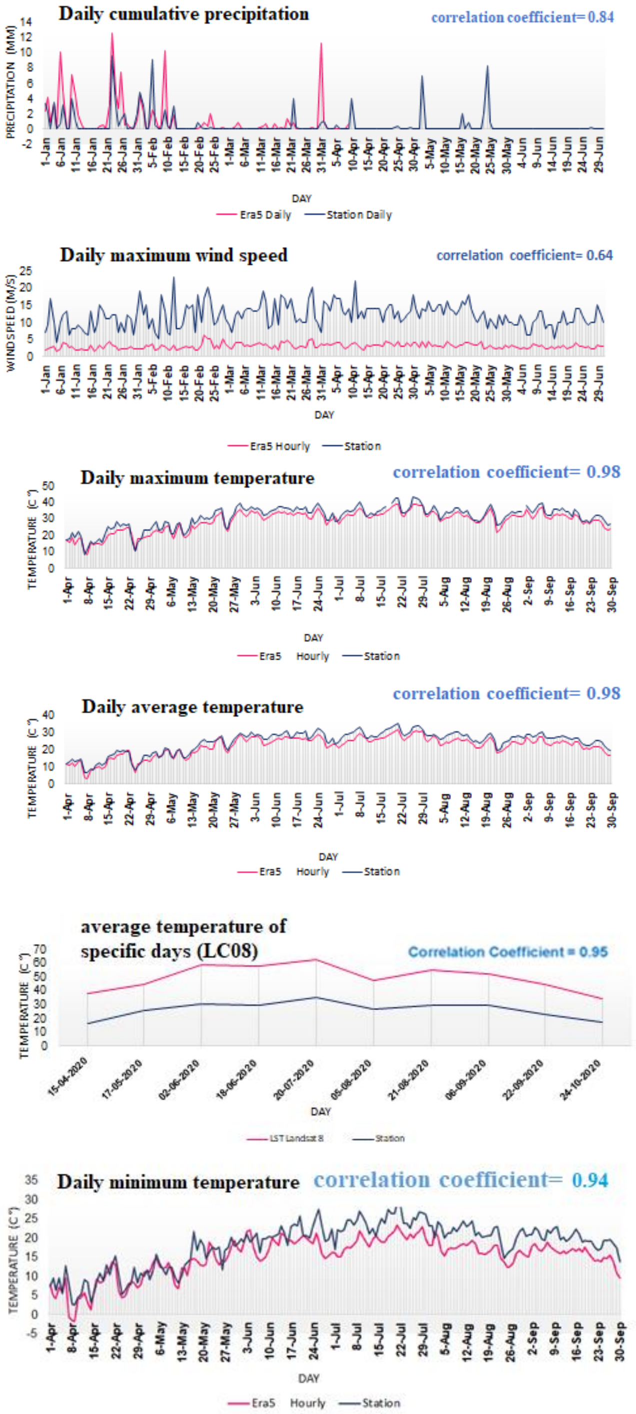

Figure 8. The relationship between the telemetry and the meteorological stations data.

4. Conclusion

The precious Arsbaran forest is a complex and dynamic ecosystem, in which its components are always in balance. When it is affected by natural or artificial destructive factors such as fire, according to the type and severity of the destructive factors, its balance or self-regulation may weaken and gradually disappear.

Preparing a map of burnt areas in the forest and pasture, as well as collecting the ecological and climatic data needed to study the fire, with field methods is very costly and time-consuming and the use of climate data from weather stations faces serious limitations in terms of using interpolation and zoning methods due to the insufficient number and inappropriate distribution in the region. In this connection; remote sensing and geographic information system (RS&GIS) are useful tools.

The purpose of the present research; The use of RS&GIS technology and the technical capabilities of the GEE system was aimed at compensating for the lack of climatic data extracted from meteorological stations in the forests of Arasbaran.

Therefore, in this research, the use of hourly, daily or monthly climate data resulting from telemetry data in the GEE was considered. Examining the relationship between these climate maps (produced in GEE) with the meteorological data recorded at the Jolfa meteorological station, except for the maximum daily wind speed parameter, other parameters of daily cumulative precipitation, minimum, maximum and daily average temperature of the telemetry data showed a good correlation with the meteorological station and can trust these datas.

References

Almedia, (1994). Forest fire risk areas and definition of the prevention priority planning actions using GIS, Proceedings of the fifth European conference and exhibition on Geographic Information System, EGIS 94. Utrecht: EGIS Foundation, 2,1700- 1706.

Amani, M., Salehi, B., Mahdavi, S., Masjedi, A. & Dehnavi, S. (2017). Temperature-Vegetation-soil Moisture Dryness Index (TVMDI). Remote Sensing of Environment. 197:1-14.

Assaker, A. (2011). Use of Remote Sensing and GIS to Assess the Anthropogenic Science Journal, Vol. 13, No. 1.

Auret, L. & Aldrich, C, (2012). Interpretation of nonlinear relationships between process variables by use of random forests. Minerals Engineering, 35:27-42.

Avdan, U. and Jovanovska, G., (2016). Algorithm for automated mapping of land surface temperature using LANDSAT 8 satellite data. Journal of Sensors, 2016, 1–8.

Bajocco, S; Rosalti, L; Ricotta, C, (2009). Knowing fire incidence through fuel phenology. A remotely sensed approach. Ecol. Model. 59- 66.

Banazountas, M; Kallidromitou, D; Kassamenos, P; Passes, N, (2006). A decision support system for managing forest fire casualties. Journal of Environmental Management. 1-7.

Barnes, B. V., Zak, D. R., Denton, S. R., & Spurr, S. H. (1998). Landscape assessment: Remote sensing of severity, the normalized burn ratio; and ground measure of severity, the composite burn index. Forest Ecology.

Chuvieco, E, (1996). Fundamentos de Teledetección Espacial - 3ª Edición revisada REF.REVISTA/LIBRO: Madrid, Rialp, 568 pags. ISBN 84-321-3127.

Chuvieco, E., & Congalton, R. (1989). Application of remote sensing and Geographic Information System to forest fire hazard mapping. Remote Sens. Environ. 29:47-159.

Chuvieco, E., D. Cocero, D. Riano, et al, (2004). Combining NDVI and surface temperature for the estimation of live fuel moisture content in forest fire danger rating, Remote Sensing of Environment, 92:322–331.

Chuvieco, E; Sales, J, (1996). Mapping the spatial distribution of forest fire danger using GIS. International Journal of Geographical Information Systems. 10(3):333-345.

Dong, X; Shao, G; Li-min, D; Zhang, H; Lei, T, (2006). Mapping forest fire risk zones with spatial data and principal component analysis. Sciences china: Series E Technological Sciences. I140- 149.

Drisya, J. and Roshni, T., (2018). Spatiotemporal variability of soil moisture and drought estimation using a distributed hydrological model. In Integrating Disaster Science and Management, 451-460. Elsevier.

FAO (2001). International handbook on forest fire protection. Technical guide for the countries of the Mediterranean basin.163p.

Garcia, J; Alhaddad, B; Cladera, J, (2007). Remote sensing analysis to detect fire forest locations, Geo Congress of Using Remote Sensing For Forest Fires Effects Analysis, Quebec, Canada.

Gorelick, N., Hancher, M., Dixon, M., Ilyushchenko, S., Thau, D., & Moore, R. (2017). Google Earth Engine: Planetary-scale geospatial analysis for everyone. Remote Sensing of Environment.

Jaiswal, R; Mukerjee, S; Raju, K; Saxana, R, (2002). Forest fire risk zone mapping from satellite imaging and GIS. International Journal of Applied Earth Observation And Geoinformation, 4:1-10.

Kerr, J, Ostrovsky, M., (2003), From space to species: ecological applications for remote sensing. Trends Ecol. Evol. 18(6):299- 305.

Kaufman, Y., and L. Remer. (1994). Detection of Forests Using mid-IR Reflectance: An Application for Aerosol Studies. IEEE Transactions on Geoscience and Remote Sensing. 32: 672-683.

Kogan, F. N. (1995). Droughts of the late 1980s in the United States as derived from NOAA polar-orbiting satellite data. Bulletin of the American Meteorological Society, 76(5):655–668.

Konkathi, P. & Shetty, A, (2021). Inter comparison of post-fire burn severity indices of Landsat-8 and Sentinel-2 imagery using Google Earth Engine Earth Science Informatics, 14,645–653

Lasaponara, R. (2006). Estimating Spectral Separability of Satellite Derived Parameters for Burned Areas Mapping in the Calabria Region by Using SPOT-vegetation Data. Ecological Modelling. 196: 265–270.

Mallinis, G., Mitsopoulos, I., & Chrysafi, I. (2018). Evaluating and comparing sentinel2A and landsat-8 operational land imager (OLI) spectral indices for estimating fire severity in a mediterranean pine ecosystem of Greece. GIScience and Remote Sensing, 55(1):1-18.

Mao, K. B., Z. H. Qin, & J. C. Shi, (2005). Retrieval of land surface temperature of Shandong Peninsula using MODIS image and split window algorithm" Jouranlof China University of Minning & Technology, vol. 34(1): 46–50.

Meguela, S; Huescal, M; Gonzalez, F, (2010). MODIS reflectance and active fire data for burn mapping and assessment at regional level. Ecological Modeling. 67-74.

Miller, J., E. Knapp, C. Key, C. Skinner, C. Isbell, R. Creasy, and J. Sherlock. (2009). Calibration and Validation of the Relative Differenced Normalized Burn Ratio (rdNBR) to Three Measures of Fire Severity in the Sierra Nevada and Klamath Mountains, California, USA. Remote Sensing of Environment. 113: 645–656.

Nayaka. R., Srinivas, R., Krishnaswamy, V., (2014). Fire and grazing modify grass community response to environmental determinants in savannas: Implications for sustainable use. Agriculture, Ecosystems and Environment.

Patah, N; Mansor, S; Mispan, M, (1999). An application of remote sensing and Geographic Information System for forest fire risk mapping. Bulletin of Malaysian Ceter for Remote Sensing: 54- 67.

Pereira, J. (1999). A Comparative Evaluation of NOAA/AVHRR Vegetation Indexes for Burned Surface Detection and Mapping. IEEE Transactions on Geoscience and Remote Sensing 37:217–226.

Peng, G. X., J. Li, Y. H. Chen, and N. Abdul-patah, (2007). A forest fire risk assessment using ASTER images in Peninsular Malaysia. Journal of China University of Minning & Technology, vol. 17(2):232–237.

Rogan J. & S. R. Yool, (2001). Mapping re-induced vegetation depletion in the peloncillomountains, Arizona and New Mexico, Int. J. Remote Sens., vol. 22: 3101–3121,

Roy, P, (2003). Forest fire and degradation assessment using satellite remote sensing and Geographic Information System. Satellite Remote Sensing and GIS Application In Agricultural Meteorology. 361- 400.

Roy, D. P., Giglio, L., Kendall, J. D., Justice, C. O. (1999). Multi-temporal active-fire based burnscar detection algorithm. Int. J. Remote Sens., 20:1031–1038.

Sakr, G; Elhajj, I; Mitri, G, (2011). Efficient forest fire occurrence prediction for developing countries using two weather parameters. Engineering Applications of Artificial Intelligence. 24:888 -894.

Swarvanu Dasgupta, John Jianhe Qu, Xianjun Hao, (2006). Design of a Susceptibility Indexfor Fire Risk Monitoring IEEE geoscience and remote sensing letters, 3(1):234-245.

Veraverbeke, S., Lhermitte, S., Verstraeten W., and Goossens, R. (2010). The Temporal Dimension of Differenced Normalized Burn Ratio (Dnbr) Fire/Burn Severity Studies: The Case of the Large 2007 Peloponnese Wildfires in Greece. Remote Sensing of Environment. 114: 2548-2563.

Veraverbeke, S., S. Lhermitte, W. Verstraeten, and R. Goossens. (2011). Evaluation of Pre/Post-Fire Differenced Spectral Indices for Assessing Burn Severity in a Mediterranean Environment withLandsat Thematic Mapper. International Journal of Remote Sensing 32: 3521–3537.

Veneros, J. E. and García, L. (2022). Application of the Standardized Vegetation Index (Svi) and Google Earth Engine (Gee) for Drought Management in Peru. Tropical and Subtropical Agroecosystems, 25(1):1–13.

Yebra, M., E. Chuvieco, and D. Rian, (2008). Estimation of live fuel moisture content from MODIS images for fire risk assessment, Agriculture and Forest Meteorology, 148:523-536.

7th Intercontinental Geoinformation Days

igd.mersin.edu.tr

Estimation of land subsidence using DInSAR and SBAS techniques

Mojdeh Miraki[*1], **Hormoz Sohrabi** [2], **Siavash Bakhtiarvand Bakhtiari** [2]

[1]Tarbiat Modares University, Faculty of Natural Resources, Department of Forest Science and Engineering, Tehran, Iran.
[2]Mobarakeh Steel Company, Esfahan

Keywords
Land subsidence
Interferometry
SBAS technique
Sentinel-1
Mobarakeh Steel Company

Abstract

Land subsidence is one of the few environmental hazards that has received much less attention than other hazards due to low human casualties. However, subsidence over time causes irreparable damage to cities and adjacent areas and facilities, and infrastructure. In the present research, land subsidence in Isfahan province in Iran and specifically in the area of Mobarakeh Steel Company (MSC) using the traditional interferometric method by two images related to the years 2016 and 2021 and time series analysis using the SBAS method by 621 Interferometer and 178 epochs and 159 Sentinel satellite images were used in the ascending direction. The maximum subsidence rate was about -83 mm per year and -28 cm in 5 years for Isfahan City, after processing with time series and traditional interferometric method, respectively. The results of the two methods were close to each other, which can confirm the correctness of the estimated subsidence. Also, the obtained maps were matched with the subsidence maps of the National Cartographic Center of Iran, and it was found that the land subsidence areas are located in the two hotspots of Isfahan and Mahyar plains. Subsidence has expanded in a trend of Isfahan, Shahreza, and Mobarakeh, Iran.

1. Introduction

Subsidence of the earth's surface, as one of the destructive geological phenomena, is a sinking of the ground that occurs on a large scale (UNESCO). Land subsidence can be caused by natural geological and geotechnical phenomena such as ice, compaction of deposits, dissolution of soluble materials and rocks, slow movements of the crust, and the release of lava from the solid crust of the earth. Or it is due to human activities such as mining and tunneling, civil constructions, and compaction caused by loading, subsidence of waste landfills, and subsidence caused by underground fluids such as oil and gas and extraction of underground water.

In the meantime, excessive extraction of water from underground aquifers is one of the main causes of subsidence all over the world. Extracting underground water and not replacing it causes a decrease in pore water pressure and an increase in effective soil stress in the lower layers. The increase of the effective stress ultimately leads to the compression of the compressible layers that are located in the underground water. These layers are mainly made of clay and silt sediments, whose density will lead to subsidence on the earth's surface. Subsidence changes are investigated using ground and remote sensing methods. The high frequency of observations in remote sensing methods (radar interferometry), as well as time and cost saving compared to other methods, provides the user with a comprehensive view of changes in the shape of the earth (Declercq et al. 2017; Du, 2017; Zhu, 2015).

The change in the process and amount of subsidence can cause serious damage to the facilities and also the buildings located on them, which is considered a threatening risk, especially for industrial and residential areas. The subsidence is detected in most areas only when it affects the surface morphology, especially in the facilities and equipment, and causes a lot of damage and destruction. Considering the extensive facilities and infrastructure of Mobarakeh Steel Company in the center of Iran, the investigation of the process and position of subsidence in Mobarakeh Plain is more needful than before.

2. Method

To estimate subsidence in this study, two methods of DInSAR and SBAS techniques.

* **Corresponding Author**

*(mojde.miraki@gmail.com) ORCID ID xxxx – xxxx – xxxx – xxxx

Cite this study

Miraki, M., Sohrabi, H., & Bakhtiari, S. B. (2023). Estimation of land subsidence using DInSAR and SBAS techniques. Intercontinental Geoinformation Days (IGD), 7, 246-249, Peshawar, Pakistan

2.1. DInSAR method

Radar interferometry uses the phase difference of the radar image with high spatial resolution to produce a digital elevation model of the area and estimate the deformation and displacement of the earth's crust.

In this section, the subsidence was calculated using the phase difference of two images in the years 2016 and 2021 from the Sentinel-1 satellite images in the Snap software in the following steps.

- Split
- aplay orbit
- co-registration
- Interferogram
- Deburst tops
- topographic phase removal
- Goldstein phase filtering
- phase unwrapping
- snaphu import
- phase to displacement
- Geometric
- Export

In this method, the lack of temporal and spatial correlation between the images causes almost every interferometer to include large areas where the correlation is low, and the measurements made in these areas are not reliable or cannot be performed at all. These limitations cause the interferometric method alone to not be a complete tool for monitoring and measuring ground surface distortions and topographical changes.

2.2. Time series analysis using SBAS interferometric method

The SBAS method for interferometric time series analysis was proposed by Berardino et al. (2002). In the SBAS time series analysis, only image pairs are used whose vertical component of the baseline is less than the critical value of the baseline, and their time baseline is also minimal at the same time. In this way, only interferograms that have a suitable quality are formed. After that, a grid of images is created, then the displacement value of each pixel is estimated using the least squares method.

The stages of time series processing and analysis were performed in the LiCSBAS package as follows:

- Identify frame ID
- Download GeoTIFF from COMET-LiCS Web
- Convert (and Downsample)
- GACOS Correction
- Mask Unwrapped Data
- Clip Unwrapped Data
- Quality Check
- Loop Closure
- Small Baseline Inversion
- Calculate STD of Velocity by Bootstrap
- Mask Time Series
- Filter (& Deramp) Time Series
- Display results
- Export results

3. Results

Fig 1 shows the map of land surface changes using the traditional interferometry (DInSAR) method between 2016 and 2021 in Isfahan province. In this map, the amount of subsidence in two images with a time difference of 6 years is 28 cm, which is observed in Isfahan City and even near the studied area of Foolad Mobarakeh.

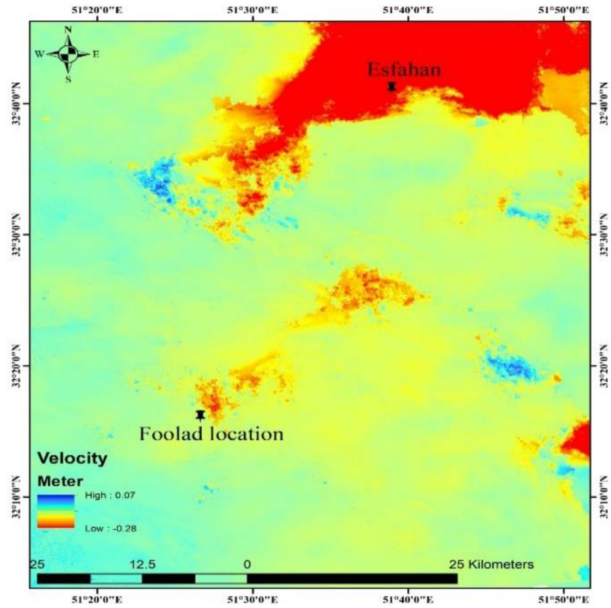

Figure 1. Land surface changes Map in 2016-2021 using the DInSAR method.

Spatial and temporal inconsistency causes noise and limitations in the phase of interferometry, and this noise created in the phase can be called inconsistency in the phase between two radar images taken from the same area at two different times under the title of coherence between two images. The coherence value ranges from 0 (all information is related to noise) to 1 (information is free from noise). As seen in the coherence map in Fig 2, many regions have low coherence. For this reason, the SBAS method was used in the time series analysis, which has more acceptable results than the PS method in areas with low coherence.

The result of annual land surface changes using 621 images between 01/01/2016 to 01/12/2022 using SBAS time series analysis is shown in Fig 3. The highest annual rate of subsidence with the value of 83 mm per year is related to the Isfahan City.

After the coherence value determination in each pixel, the values with low coherence were removed. Also, the low-pass filter in place and the high-pass filter in time were included in the final results.

Finally, after the completion of the time series analysis, the changes of the land surface can be extracted from each pixel of the output map with a spatial resolution of 90 meters. In the current study, 3 points in the study area were considered as pilots and the graph of land surface changes was prepared for the mentioned points, which is shown in Fig 4.

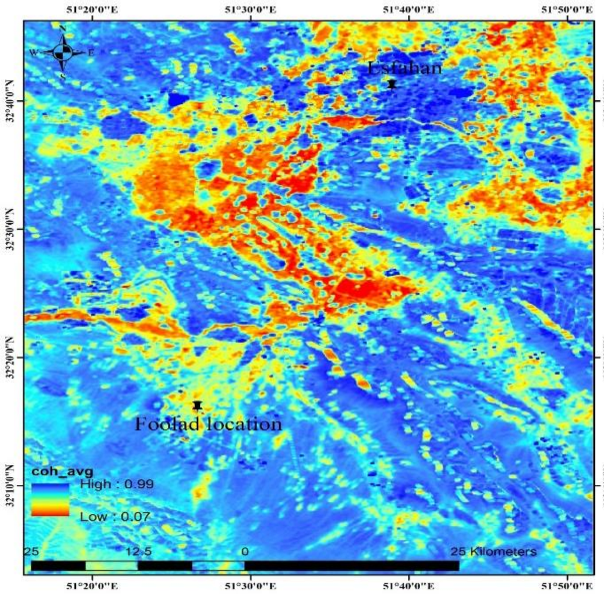

Figure 2. Coherence map in the study area

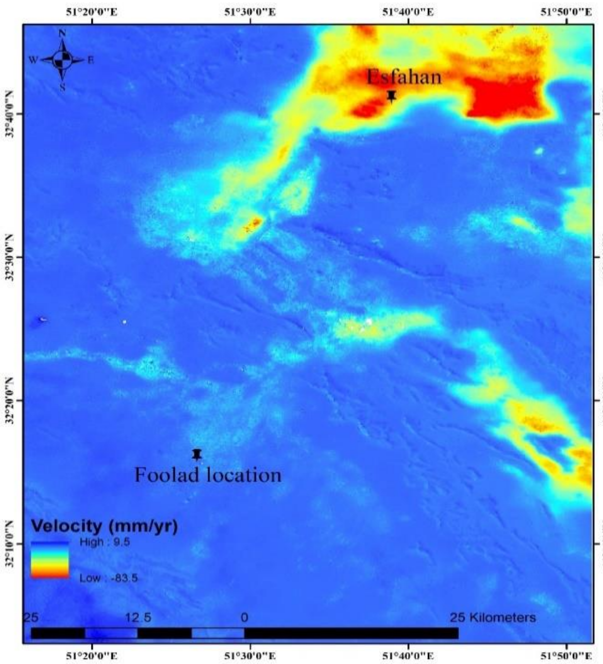

Figure 3. Velocity Map of displacement in 2016-2022 using time series analysis.

4. Discussion

As expected, after processing the radar images using the SBAS interferometric time series technique, a large area of Isfahan province had subsidence in the period between 2016 and 2022.

In Fig 4, sinusoidal fluctuations can be seen, which may be related to the lowering of the aquifer level and its re-feeding in the rainy season and the type of soil texture. The graph generally shows a decreasing trend with a low slope, which requires careful monitoring of the area and preventing the occurrence and consequences of subsidence in the future.

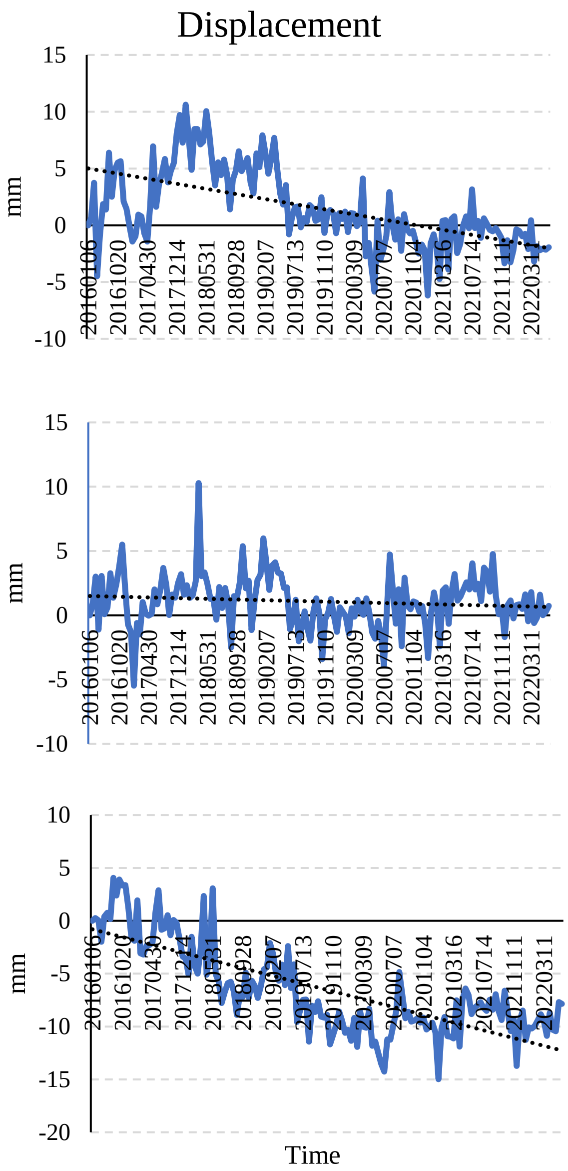

Figure 4. Displacement changes at the three pilot points

The maximum subsidence rate obtained after processing with time series and traditional interferometric method was approximately -83 mm per year and -28 cm in 5 years for Isfahan City, respectively. The results of the two techniques were in close agreement with each other, which can confirm the correctness of the subsidence obtained. Also, according to Fig 5 and the relatively good overlap of the resulting maps with the subsidence maps of Iran National Cartographic Center, it is clear that the determined areas of subsidence are located in the two hotspots of Isfahan and Mahyar plains. Subsidence in Mahyar Plain has passed through Isfahan City, Shahreza, and Mobarakeh in a certain process.

According to the two production maps and the map obtained from the Iran National Cartographic Center, subsidence is expanding with a certain trend, which according to the necessary investigations and the correspondence of the map with the ground reality in the areas of subsidence, agriculture, and water pumping. Underground are more abundant than the adjacent areas

(Fig 6). This process started in Isfahan City and extended to Shahreza and Mobarakeh cities, which requires the investigation of piezometric wells and groundwater level changes in the study area.

According to the mentioned cases, it is necessary to check the underground water and the changes in the water level of the piezometric wells and establish the subsidence monitoring system in the study area.

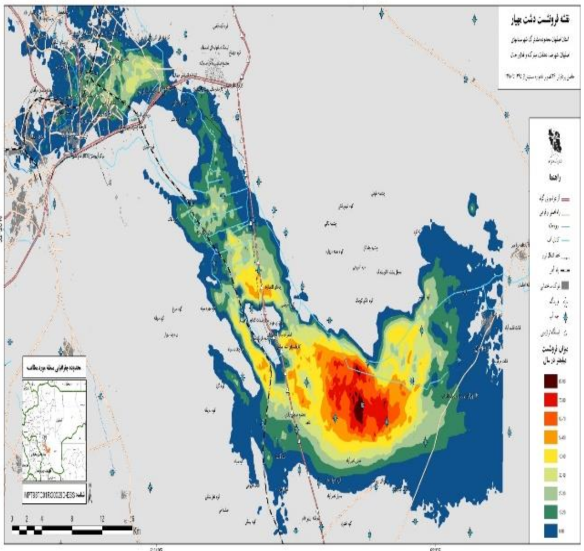

Figure 5. Subsidence map of Mahyar Plain (downloaded from the website of Iran National Cartographic Center)

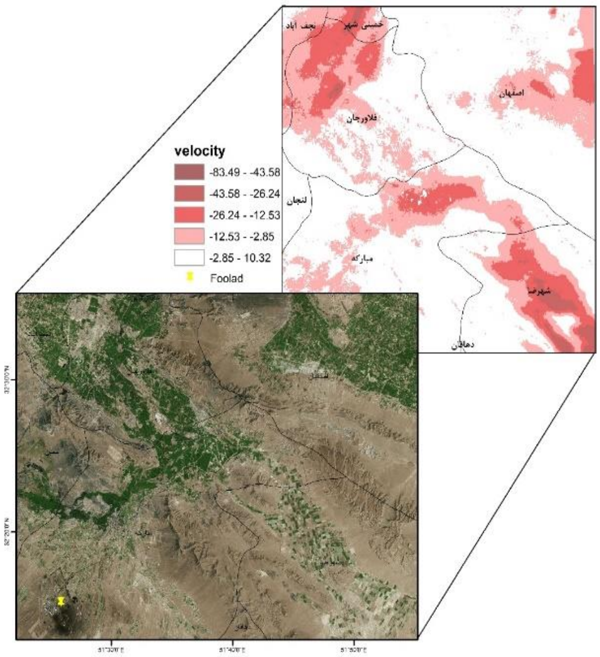

Figure 6. Correspondence of annual subsidence rate (mm) with ground reality image

References

Berardino, P., Fornaro, G., Lanari R., & Sansosti, E. (2002). A new algorithm for surface deformation monitoring based on small baseline differential SAR interferograms, in IEEE Transactions on Geoscience and Remote Sensing, 40(11), 2375-2383, Nov. 2002, https://doi.org/10.1109/TGRS.2002.803792.

Declercq, P. Y., Walstra, J., Gérard, P., Pirard, E., Perissin, D., Meyvis, B., & Devleeschouwer, X. (2017). A study of ground movements in brussels (Belgium) monitored by persistent scatterer interferometry over a 25-year period. Geosciences, 7(4), 115. https://doi.org/10.3390/geosciences7040115

Du, Y., Feng, G., Peng, X., & Li, Z. (2017). Subsidence evolution of the Leizhou Peninsula, China, Based on InSAR observation from 1992 to 2010. Applied Sciences, 7(5), 466. https://doi.org/10.3390/app7050466

Zhu, L., Gong, H., Li, X., Wang, R., Chen, B., Dai, Z., & Teatini, P. (2015). Land subsidence due to groundwater withdrawal in the northern Beijing plain, China. Engineering Geology, 193, 243-255. https://doi.org/10.1016/j.enggeo.2015.04.020

7th Intercontinental Geoinformation Days

igd.mersin.edu.tr

Comprehensive temperature analysis of Türkiye between 2013 and 2023 using Google Earth Engine and ERA5 Dataset

Abdullah Sukkar*[1], Ugur Alganci [2], Dursun Zafer Seker[2]

[1]ITU, Istanbul Technical University, Graduate School, Geomatics PhD Program, Istanbul, Turkiye
[2]ITU, Istanbul Technical University, Civil Engineering Faculty, Department of Geomatics Engineering, Istanbul, Turkiye

Keywords
Google Earth Engine
ERA 5
Temperature
Türkiye

Abstract

The climate system involves complicated interactions among diverse atmospheric and environmental elements, and it is essential to comprehend prolonged temperature trends for evaluating the consequences of climate change. In this study, an analysis of temperature changes in Türkiye over the period from 2013 to 2023 was realized. Employing advanced geospatial technology, specifically Google Earth Engine, and utilizing the ERA5 dataset, this study seeks to delve deeply into temperature trends throughout Türkiye. The incorporation of satellite imagery and detailed climate data with high resolution facilitates a detailed exploration of temporal and spatial fluctuations, enhancing a nuanced comprehension of climate dynamics. As climate change continues to exert its influence globally, a focused analysis of Türkiye's temperature trends becomes a necessity for informed decision-making in areas such as agriculture, water resource management, and urban planning. This study aimed to contribute valuable insights into the evolving climate change of Türkiye, considering the relationship between the changing environment and societal considerations. Results indicated a 0.20 Celsius degree increment over Türkiye during this ten-year period, while the Southeastern Anatolia Region faced the highest warming.

1. Introduction

"Global warming," as defined by Oxlade (2002) in its simplest form, is described as "an increase in the temperature of the Earth's atmosphere." On the other hand, "climate change" can be understood as significant alterations occurring over many years in the average conditions of climate (such as temperature, precipitation, or wind), regardless of the cause. Climate research has entered a new era marked by technological advancements that facilitate in-depth analyses of temporal and spatial climate patterns (Kocoglu and Gokalp, 2021).

Recent years have witnessed a paradigm shift in climate data analysis with the emergence of Google Earth Engine, a cloud computing platform that enables the processing of vast geospatial datasets (Gorelick et al., 2017). Simultaneously, the ERA5 dataset, developed by the European Centre for Medium-Range Weather Forecasts (ECMWF), has gained prominence for its high spatiotemporal resolution and accuracy in representing climate variables (Hersbach et al., 2020).

The urgency of understanding and mitigating climate change impacts has prompted an influx of research, especially focused on regional climate dynamics. Recent publications highlight the significance of high-resolution datasets like ERA5 in capturing fine-scale climate variations (Jones et al., 2019). Moreover, studies emphasizing the integration of satellite-derived information, such as those conducted with Google Earth Engine, underscore its efficacy in monitoring and understanding climate trends (Smith et al., 2021).

As Türkiye grapples with the implications of a changing climate, the need for localized, up-to-date analyses becomes imperative. Recent works explain the importance of region-specific climate assessments for informed decision-making and adaptive strategies. This study contributes to this body of knowledge, offering a comprehensive examination of geographic regions of Türkiye's temperature trends over the past decade. However, climate change, including global warming, has begun to manifest its effects on Turkey. Rising temperatures and increased aridity have heightened the demand for water resources in agricultural areas, leading to a reduction in water availability. Drought issues are

* **Corresponding Author**

*(sukkar20@itu.edu.tr) ORCID ID 0000-0002-8258-3734
(alganci@itu.edu.tr) ORCID ID 0000-0002-5693-3614
(seker@itu.edu.tr) ORCID ID 0000-0001-7498-1540

Cite this study

Sukkar, A., Alganci, U., & Seker, D. Z. (2023). Comprehensive Temperature Analysis of Türkiye between 2013 and 2023 Using Google Earth Engine and ERA5 Dataset. Intercontinental Geoinformation Days (IGD), 7, 250-253, Peshawar, Pakistan

particularly prominent in the Southeastern Anatolia region. This situation adversely affects agricultural production and may result in economic challenges.

Additionally, climate change poses threats to coastal areas due to rising sea levels. The coasts of the Marmara, Aegean, and Mediterranean regions are vulnerable to erosion and flooding as a consequence of sea-level rise. This situation threatens ecosystems and settlements along the coastline of the country.

Due to Turkey's distinct geographic location and vulnerability to climatic fluctuations, in-depth climate research is necessary. This study endeavors to conduct an exhaustive analysis of Türkiye's temperature dynamics between 2013 and 2023, leveraging state-of-the-art tools such as Google Earth Engine and the ERA5 dataset.

2. Method

2.1. The study area and data set

The selected study region is Türkiye, which is situated at the intersection of Southeast Europe and Southwest Asia, east of the Mediterranean, north of the Aegean Sea, and south of the Black Sea. This strategic location permits a wide range of geographical characteristics and climate types. Turkey is divided into seven geographical regions: Marmara, Aegean, Mediterranean, Central Anatolia, Black Sea, Southeastern Anatolia, and Eastern Anatolia (Figure 1).

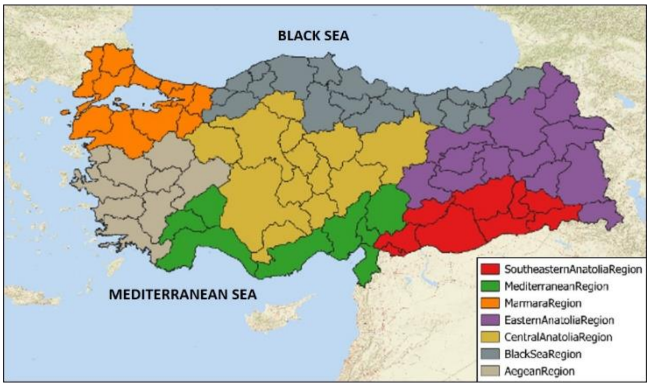

Figure 1. The geographic regions of Türkiye

Each region exhibits distinct characteristics in terms of climate, vegetation, and agricultural activities. The Mediterranean region is characterized by a hot and dry climate, while the Aegean region typically experiences a mild climate. Central Anatolia has an inland climate, whereas the Black Sea region receives abundant rainfall, resulting in lush green vegetation. This diversity contributes to Türkiye's richness in agriculture and natural resources.

In response to these challenges, Türkiye is actively working to combat climate change and promote a sustainable future. Initiatives include a shift towards renewable energy sources, strengthening water management policies, and increasing awareness about environmental issues. These efforts aim to enhance the country's resilience to climate change and contribute to global sustainability.

The 2m temperature component of the ERA5-Land dataset was analyzed for each geographical region of Türkiye using the Google Earth Engine (GEE) platform. The ERA5-Land-Landset is an enhanced edition of ERA5, provided by the European Center for Medium-Range Weather Forecasts (ECMWF). It has a finer spatial resolution of 0.1° compared to 0.25° for ERA5 (Tan et al., 2023). The 2 m temperature parameter is measured at a height of 2 meters above sea level or land.

ERA5 stands for the Fifth Generation of the European Centre for Medium-Range Weather Forecasts (ECMWF) Reanalysis dataset. It is a comprehensive global atmospheric reanalysis dataset, providing a detailed and consistent record of the Earth's climate from 1940 to the present. ERA5 offers a high spatial resolution of approximately 31 km globally, allowing for detailed analysis of weather and climate phenomena. It provides hourly data, enabling a more granular understanding of climate variability and trends. Additionally, it covers a wide range of meteorological variables, including temperature, precipitation, wind speed, and more, facilitating diverse research applications.

3. Methodology

Climate change is a pressing global concern with far-reaching implications for ecosystems, economies, and human well-being. Thorough studies of regional climate patterns are crucial as countries work to comprehend and lessen the effects of climate change. This study focuses on Türkiye, a region situated at the crossroads of Europe and Asia, and endeavors to provide a thorough examination of its temperature dynamics over the decade spanning from 2013 to 2023.

In recent years, advancements in geospatial technology have revolutionized our capacity to analyze large-scale environmental datasets. Google Earth Engine, a cloud-based platform for planetary-scale environmental data analysis, and the ERA5 dataset, a high-resolution reanalysis dataset developed by the European Centre for Medium-Range Weather Forecasts (ECMWF), offer unprecedented opportunities for detailed and accurate climate studies. By leveraging these tools, our research aims to unravel the intricacies of Türkiye's temperature trends, employing a combination of satellite imagery, climate modeling, and ground-based observations.

The significance of such a study is underscored by Türkiye's unique geographic and climatic characteristics, which render it vulnerable to the impacts of a changing climate. Understanding how temperatures have evolved over the past decade is crucial for anticipating future climate scenarios and developing adaptive strategies. This analysis contributes to the broader scientific discourse on regional climate change impacts, providing valuable insights that can inform policy decisions, resource management, and societal resilience.

As we delve into this comprehensive temperature analysis, we draw upon a range of authoritative sources, including the ERA5 dataset, which has become a cornerstone in climate research for its accuracy and high spatiotemporal resolution. Additionally, insights from peer-reviewed scientific literature and international climate reports form the foundation of our investigation, ensuring the reliability and validity of our findings. Through this research, we aim to contribute to the growing body of knowledge on regional climate dynamics, fostering a deeper understanding of the challenges posed by a changing climate in Türkiye and beyond.Google Earth Engine (GEE) is a cloud-based platform for planetary-scale geospatial analysis that brings Google's massive computational capabilities to bear on a variety of high-impact societal issues including deforestation, drought, disaster, disease, food security, water management, climate monitoring, and environmental protection (Gorelick et al., 2017). It is one of the most widely used tools in the field as an integrated platform designed to empower not only traditional remote sensing scientists but also a much wider audience needed to utilize traditional supercomputers or large-scale commodity cloud computing resources.

Through the GEE, the air temperature of Türkiye and its different geographical regions was analyzed between 2013 and 2023. First, the daily temperature of October 2023 was analyzed. Then the October months for the last decade were investigated, and finally, the average annual temperature over the past decade was analyzed and plotted.

4. Results and Discussions

Globally, October 2023 was the warmest October ever recorded. In addition, it was the fifth consecutive month of record-warm temperatures. However, in Türkiye, it was not the highest October, it is the 3rd in the last decade and the 7th in Türkiye's record (MGM, 2023). The average temperature of October 2023 was 14.4° C. while in 2019 and 2020 was 15.1° C and 16.3° C respectively (Figure 2).

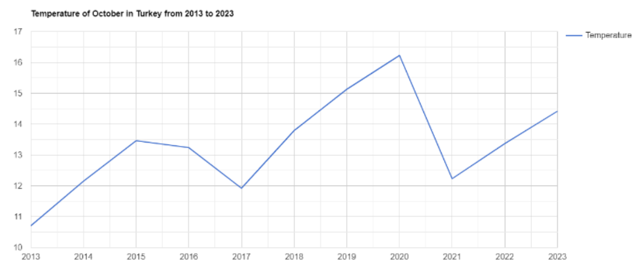

Figure 2. The monthly average temperature of October months in Türkiye (2013-2023).

The highest temperature observations of October months through the last decade were seen in the Southeastern Anatolia region (Figure 3), followed by the Mediterranean, Aegean, and Marmara regions.

The lowest and highest average annual temperatures during the last decade occurred in 2013 and 2018, respectively. The average annual temperature in 2013 was 11.15 degrees Celsius, whereas it was 12.5 degrees Celsius in 2018. However, the year 2023 is almost guaranteed to be the warmest on record (Figure 4). Moreover, the highest and lowest annual temperatures were recorded in the Southeastern Anatolia and Eastern Anatolia regions respectively (Fig. 5).

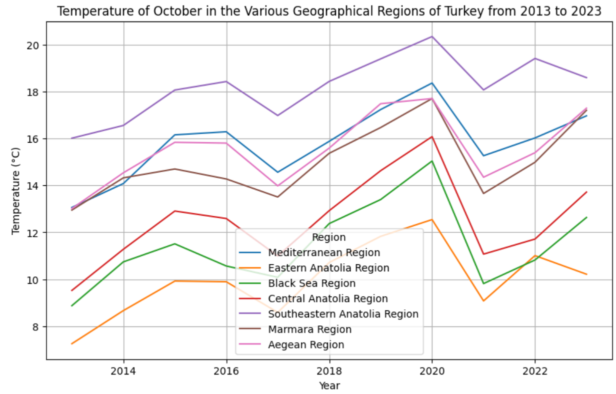

Figure 3. The monthly average temperature of October months in Türkiye's geographical regions (2013-2023).

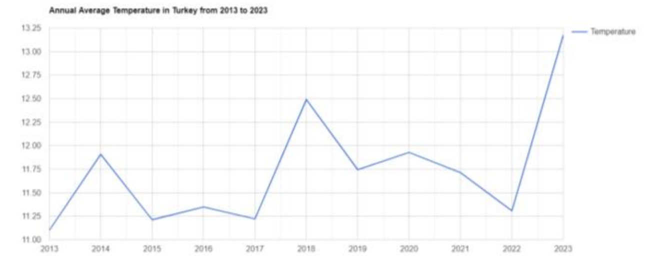

Figure 4. The annual average temperature of Türkiye (2013-2023).

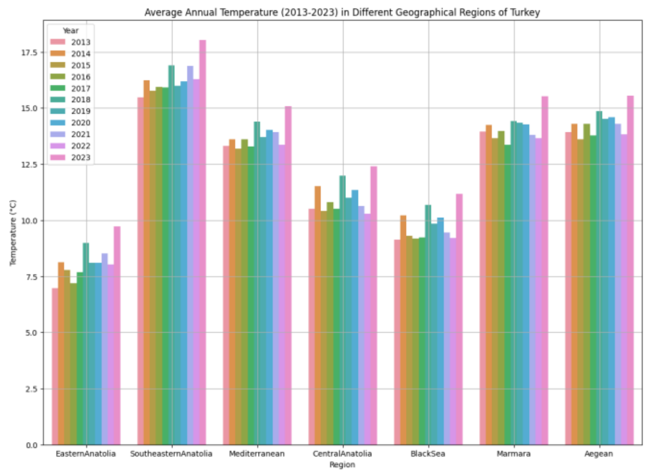

Figure 5. The annual average temperature of Türkiye's geographical regions (2013-2023).

3. Discussion

ERA5 and ERA5 Land datasets were validated and applied in several studies for several purposes in Türkiye. In all of these studies, the datasets have shown very high correlation levels with the ground truth data (Hisam et al., 2023; Karaman, & Akyürek, 2023). Through the last decade (2013-2022), the average annual temperature in Türkiye has been raised by 0.20° C. The same results also were obtained by (Güler & Erlat, 2023), which is almost 3 times the global average. The peak annual average temperatures were recorded in 2018, and 2020, with an average of 12.49° and 11.93° C respectively. The observational temperature of the Southeastern Anatolia region was, on average, higher during of the 10-year periods than in the other six regions. Also, it was the highest between 1951 and 2020 (Yilmaz, 2023).

4. Conclusion

This study investigated the temperature change trends in Türkiye between 2013 and 2023 using Google Earth Engine platform and ERA5 Dataset. When examining the average temperature from January to October for the calendar year and comparing it to the corresponding periods of previous years, it is evident that the worldwide average temperature for 2023 is the highest ever recorded. The average temperature of October 2023 in Türkiye was the 3rd highest October over the past decade. The annual average temperature in Türkiye has risen and fallen and reached its maximum in 2018 when the temperature was 12.5° C. Southeastern Anatolia is the warmest region in Türkiye in the last 10 years, there is a significant difference in terms of temperature between Southeastern Anatolia and other regions exceed 2 degrees. It is highly probable that the current year, specifically 2023, will establish a new record as the warmest year ever documented in both Türkiye and worldwide. Especially, with the current record levels of greenhouse gases in the atmosphere.

References

Güler, H. & Erlat, E. (2023). Türkiye'de 1950-2022 Döneminde Ortalama Hava Sıcaklıklarında Gözlenen Değişim ve Eğilimler. Ege Coğrafya Dergisi , 32 (1) , 1-17 . https://doi.org/10.51800/ecd.1281319

Hisam, E., Danandeh Mehr, A., Alganci, U., & Seker, D. Z. (2023). Comprehensive evaluation of Satellite-Based and reanalysis precipitation products over the Mediterranean region in Turkey. Advances in Space Research, 71(7), 3005-3021. https://doi.org/10.1016/j.asr.2022.11.007

Karaman, H. Ç., & Akyürek, Z. (2023). Evaluation of near-surface air temperature reanalysis datasets and downscaling with machine learning based Random Forest method for complex terrain of Turkey. Advances in Space Research, 71(12), 5256-5281. https://doi.org/10.1016/j.asr.2023.02.006

Koçoğlu, E., & Gökalp, L. (2021). Türkiye'de küresel ısınma alanında yapılan lisansüstü tezlerin analizi: Bir meta sentez çalışması (Analysis of the Graduate Thesis Made Global Warming Areas in Turkey: A Meta Synthesis Study). Doğu Coğrafya Dergisi, 26 (46), 129-142. https://doi.org/10.17295/ataunidcd.927150

Oxlade, C. (2002). Global warming, Minnesota: Bridgestone Books an Imprint of Capstone Press.

Tan, M. L., Armanuos, A. M., Ahmadianfar, I., Demir, V., Heddam, S., Al-Areeq, A. M., Abba, S. I., Halder, B., Cagan Kilinc, H., & Yaseen, Z. M. (2023). Evaluation of NASA POWER and ERA5-Land for estimating tropical precipitation and temperature extremes. Journal of Hydrology, 624, 129940. https://doi.org/10.1016/J.JHYDROL.2023.129940

Turkish State Meteorological Service (MGM). (2023). State of the Climate in October 2023, Ankara. https://www.mgm.gov.tr/eng/Monthly-Climate/State_of_the_Climate_in_October_2023.pdf

Yilmaz, M. (2023). Accuracy assessment of temperature trends from ERA5 and ERA5-Land. Science of The Total Environment, 856, 159182. https://doi.org/10.1016/j.scitotenv.2022.159182

7th Intercontinental Geoinformation Days

igd.mersin.edu.tr

PM10 air pollutant prediction using deep learning LSTM Model: A case study of Istanbul, Türkiye

Omar Wisam Alqaysi*[1], Dursun Zafer Şeker[2]

[1] Istanbul Technical University, Graduate School, Applied Informatics Department, GIT Program, Istanbul, Türkiye
[2] Istanbul Technical University, Civil Engineering Faculty, Department of Geomatics Engineering, Istanbul, Türkiye

Keywords
Deep learning
LSTM
Air pollution
PM10
GRU

Abstract

Accurate forecasting of PM10 concentrations is crucial for air quality management and public health protection. This study proposes a deep learning-based model for predicting PM10 concentrations in Istanbul, Türkiye, utilizing a combination of Long Short-Term Memory (LSTM) and Gated Recurrent Unit (GRU) models. Historical air pollution data from the Ministry of Environment, Urbanization, and Climate Change of Turkey and meteorological data from NASA for the period of January 2018 to August 2023 were employed for model development. Ümraniye district was selected as the study area due to its comprehensive air quality data availability. An extensive model development process involved identifying the optimal input sliding window, input features, and model architecture through parameter tuning. The LSTM+GRU model resulted in the best metrics, achieving an RMSE of 6.71, R2 of 0.86, and MAPE of 15.9%. The model demonstrated strong generalization capabilities when tested on data from eight different stations in Istanbul. While the proposed model exhibited promising performance, certain limitations warrant further investigation. The effectiveness of the model for air pollutants other than PM10 remains unexplored. Additionally, an evaluation of feature importance ranking for the input parameters is necessary to identify the most influential factors contributing to PM10 concentrations. Future research endeavors will address these limitations and refine the model for broader applicability.

1. Introduction

Air pollution, especially PM10 and PM2.5, is a major health and environmental hazard. PM air pollution causes cardiovascular and respiratory diseases, according to numerous studies. (Anderson et al., 2011; Liang et al., 2014). In addition, there are a number of important environmental effects of air pollution, such as the greenhouse effect, acid rain, ozone layer alterations, decreased visibility, and lower-quality products. (Lehadus et al., 2019).It is widely regarded as a primary concern for the environment and public health on a global scale. It is considered one of the main problems for the environment and public health globally (Estuardo-Moreno et al., 2022). Particulate matter also impacts climate and precipitation, making it a crucial issue associated with air pollution (Kamarehie et al., 2017).

Understanding the effects of PM10 and PM2.5 on the environment and public health is essential for developing effective strategies to mitigate air pollution and protect human well-being.

1.1 Machine Learning & Deep Learning Prediction Models

Machine learning and deep learning methods have become effective tools for predicting air pollutants because they can comprehend intricate connections among many components and provide precise forecasts. Machine learning methods such as Extreme-Gradient Boosting (XGBoost), Random Forest (RF), and Deep Neural Networks (DNNs) have effectively been utilized for PM10 prediction RF has been used to estimate daily concentrations of pollutants in Sweden (Stafoggia et al., 2020), while XGBoost has been applied to assess the role of atmospheric circulation in PM10 in urban areas with complex topography (Sekula et al., 2022) DNNs have demonstrated their effectiveness in comprehensive air-quality index prediction, incorporating multiple variables and factors (Kim et al., 2022). These machine learning and deep learning models offer promising solutions for air quality monitoring and forecasting, enabling timely interventions and mitigating the adverse health and environmental impacts of air pollution.

* **Corresponding Author**

*(alqaysi21@itu.edu.tr) ORCID ID 0009-0009-1085-9621
(seker@itu.edu.tr) ORCID ID 0000-0001-7498-1540

Cite this study

Alqaysi O & Şeker D Z (2023). PM10 Air Pollutant Prediction Using Deep Learning LSTM Model: A Case Study of Istanbul, Türkiye. Intercontinental Geoinformation Days (IGD), 7, 254-257, Peshawar, Pakistan

1.2 Long-Short Term Memory (LSTM)

LSTM (Long Short-Term Memory) recurrent neural network (RNN) architecture overcomes typical RNNs' shortcomings in learning long-term dependencies (Kratzert et al., 2018). Since 1995, it has been employed in natural language processing, time series forecasting, and trajectory prediction (Dai & Li, 2019; Greff et al., 2017).

Due to its ability to capture and store data across lengthy sequences, LSTM is useful for processing and predicting. Gates and memory cells control network information flow (Gers et al., 2000). Each LSTM memory cell has input, forget, and output gates. These gates control information flow into, out of, and within each memory cell, allowing the network to recall or forget information at specific time steps. (Gers et al., 2000).

Studies show that LSTM is an effective and accurate PM10 prediction model. W. Li & Jiang (2023) suggested a TCN-BiLSTM-DMAttention model with strong prediction accuracy and generalization performance to help prevent air pollution. Istiana et al. (2022) evaluate deep learning applications, notably LSTM, for PM2.5 concentration prediction, emphasizing their efficiency and cost-effectiveness.

1.3 Gated Recurrent Unit (GRU)

Recurrent neural networks (RNNs) like the Gated Recurrent Unit (GRU) capture dependencies and patterns in sequential input. It has gating techniques to keep long-term dependencies and solve the vanishing gradient problem in traditional RNNs. Reset and update gates allow the GRU model to adaptively acquire and interpret sequential information, making it ideal for time series data and sequential modeling. The GRU model has been used to predict PM10 and PM2.5 air pollution in several studies. Dairi et al. (2021) used deep learning models using RNN, LSTM, and GRU architectures to forecast air quality using the AirNet dataset, which comprises meteorological time series and air quality data. Qing et al. (2019) suggested a deep learning-based short-term PM2.5 concentration forecasting model using convolutional-based bidirectional gated recurrent unit (CBGRU) neural networks and 1D convents. Yang et al. (2020) also evaluated CNN—LSTM and CNN—GRU with different stand-alone PM concentration prediction algorithms in Seoul.

2. Method

This study tests the performance of both LSTM & GRU deep learning models on PM10 concentrations forecasting concentrations. The LSTM model, inspired by the human brain, processes and learns sequential data well, making it suited for modeling air pollution data's temporal patterns and correlations. The study's methodology includes data collecting, preprocessing, model construction, and evaluation.

2.1 Study area & Data collection

Istanbul, a heavily populated megacity on the European and Asian continents, is a vital air pollution forecast research hub. For air quality assessments, Istanbul's comprehensive air pollution monitoring station network provides valuable data. Air pollution from heavy traffic, industrial activities, and high population density makes the city a good air quality research site. Istanbul map with metrological and air quality stations is in Figure 1.

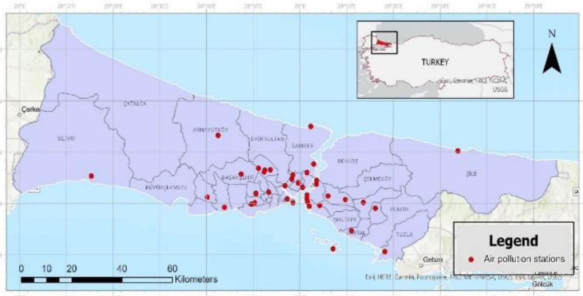

Figure 1. Air pollution stations across Istanbul.

Ümraniye district was chosen for model training because it had the most consistent PM10 data. Hourly time series data of air quality for 38 stations in Istanbul from January 2018 to August 2023 was obtained from the Ministry of Environment, Urbanization and Climate Change of Turkey (SIM, 2023). Eight air pollutants were monitored: PM10, PM2.5, SO2, CO, NO, NOX, NO2, and O3. However, subsequent inspection revealed that not all stations measured all contaminants.

Meteorological data was obtained from NASA's MERRA2 satellite data using its Earth Science research program. The following abbreviations were used to denote wind speed at 10 m, wind direction, surface pressure, specific humidity, and temperature at 2 m: WS10M, WD10M, PS, QV2M, and T2M. (NASA, 2023).

2.2 Data preprocessing

After exploring the data, missing values and outliers were detected thus data cleaning and missing data imputation were done in the following steps. Figure 2 shows the missing data for PM10 in white areas.

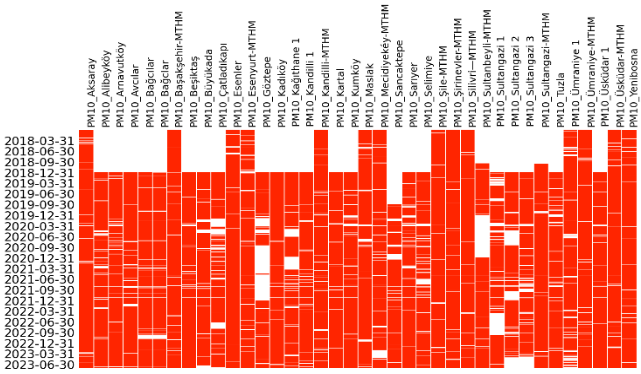

Figure 2. PM10 Data availability.

Imputation of missing values follows outlier removal. Outliers were identified using the Python ADTK library's InterQuartileRangeAD detector (Arundo, 2023). This detector utilizes historical data to compare time series values with the 1st and 3rd quartiles. Anomalous data points are identified when their differences exceed the product of the interquartile range (IQR) and a user-defined factor c.

The data was standardized using StandardScaler after outlier elimination. After that, "Fancyimpute" (Rubinsteyn & Feldman, 2016) was used to fill in the missing data. Before modeling, the dataset was split into 60% training, 20% validation, and 20% testing sets.

2.3 Model development

A variety of LSTM and GRU model architectures were trained and evaluated then the best-performing model was selected based on evaluation metrics. The study utilizes five criteria to evaluate the models' predictive performance and ascertain the effectiveness of the suggested strategy.

Sliding window inputs were made which is a common technique used in time series analysis and is often used in conjunction with LSTMs. The sliding window technique involves splitting a time series into smaller windows of fixed length and using these windows as input to a model. Many trials were done until the best window size was selected.

Prior to training, it is necessary to normalize the dataset. Applying data normalization can enhance the efficiency of deep learning models and enhance their resilience to fluctuations in the input data.

The model development was conducted in three steps, which involved determining the optimal input size by utilizing all input features. Then choose input features alternatively. Finally, adjusting the number of hidden layers and neurons in the model architecture until optimal results are achieved.

Table 1. Parameters used during model development.

Model Architecture	Input Features	Input window(hr)	Hidden units
LSTM	Metrological data	50	32
LSTM,LSTM	Metrological data + NO	30	32,32
LSTM,LSTM,LSTM,LSTM	Metrological data + NO2+NOX+PM2.5	20	64,64
GRU		10	64
GRU,GRU		5	16,16,16,16
GRU,GRU,GRU			
GRU,LSTM			
LSTM,GRU			

The assessment measures employed include Root Mean Square Error (RMSE), Mean Square Error (MSE), Mean Absolute Error (MAE), Mean Absolute Percentage Error (MAPE), and Coefficient of Determination (R2). Figure 3 illustrates the sequence of steps followed in our study. The parameters that were examined to determine the optimal combination are illustrated in Table 1.

3. Results & Discussion

Experimental trials were done to get the lowest MSE & RMSE by changing the combination of parameters used for model training. Table 2 shows some of the trials and their respective evaluation metrics.

As mentioned in the model development section, the first step is finding the best input window size, and trials showed that 10 hours of input data performed best. Using metrological data and (NO) pollutants improved feature selection predictions.

Finally, choosing the model architecture, hidden layers, and neurons. After testing, one-layer LSTM and one-layer GRU with 32 neurons in each layer produced the most accurate prediction model with an RMSE of 6.71 and R2 of 0.86. Figure 4 shows PM10 predictions vs. actual PM10 values.

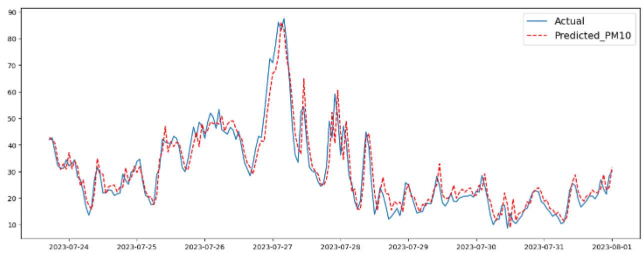

Figure 4. Predicted PM10 vs. Actual concentrations.

The best model generalization ability was tested on other stations and the results is shown in table 2. Although the model would predict more accurately if PM2.5 data were used. But using PM2.5 data would limit our model's usability on other stations. Since not all stations have data for PM2.5 it was not added for our model.

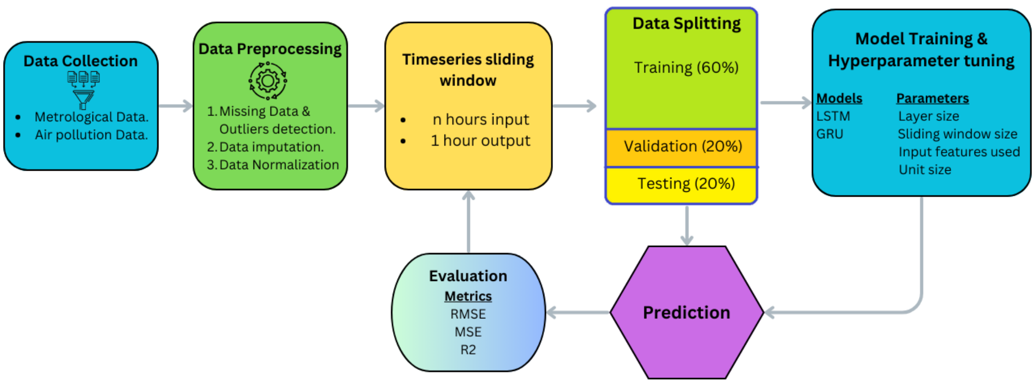

Figure 3. PM10 prediction workflow.

It's worth noting that usage of other outlier detectors or other station's data for modeling may yield better results and that can be performed on later research.

Table 2. PM10 prediction trials with different parameter combination.

Features	input window	Model Architecture	Hidden units	RMSE	MSE	MAE	MAPE	R2
Metrological data	10	BatchNorm, LST	32,32	7.67	58.89	5.15	20.16	0.82
Metrological data + NO	10	BatchNorm, LST	32,32	7.25	52.61	4.79	17.6	0.84
Metrological data + NO	10	LSTM,LSTM	32,32	6.73	45.34	4.35	16.58	0.86
Metrological data + NO	10	LSTM	32	6.84	46.72	4.34	15.66	0.86
Metrological data + NO	10	LSTM,LSTM,LST	16,16,16,1	6.92	47.95	4.51	17.69	0.85
Metrological data + NO	10	GRU	32	6.88	47.31	4.54	17.45	0.85
Metrological data + NO	20	LSTM,LSTM	32,32	6.77	45.78	4.33	15.71	0.86
Metrological data + NO	30	GRU,GRU	32,32	6.93	48.03	4.42	16.02	0.85
Metrological data + NO	10	GRU,GRU,GRU	32,32,32	6.86	47.07	4.43	16.81	0.85
Metrological data + NO	10	GRU,LSTM	32,32	6.88	47.37	4.35	15.79	0.85
Metrological data + NO	10	LSTM,LSTM	32,32	6.97	48.53	4.58	17.96	0.85
Metrological data + NO	**10**	**LSTM,GRU**	**32,32**	**6.71**	**45.06**	**4.31**	**15.89**	**0.86**

Table 3. Model's PM10 prediction performance on other stations.

Station	RMSE	MSE	MAE	R2
Aksaray	10.87	118.12	8.37	0.81
Alibeyköy	7.69	59.1	6.58	0.66
Arnavutköy	8.79	77.23	6.07	0.74
Avcılar	13.1	171.52	7.44	0.6
Bağcılar	10.94	119.62	6.71	0.76
Başakşehir	9.01	81.1	5.87	0.89
Beşiktaş	10.07	101.31	7.55	0.63
Çatladıkapı	5.37	28.87	3.61	0.87

4. Conclusion

This study constructed a deep-learning model utilizing LSTM and GRU deep-learning algorithms to estimate PM10 concentrations on an hourly basis.

Compared to earlier models, the LSTM+GRU model has demonstrated great predictive capabilities across all the models that have been built. In addition, the model that was created was tested on data from eight distinct areas and showed strong generalization abilities.

Nevertheless, this study has specific constraints. The efficacy of the suggested model has not been investigated for air pollutants other than PM10. Moreover, there has been no assessment of the ordering of the input parameters in terms of their relevance. Subsequent investigations will focus on overcoming these constraints.

References

Anderson, J. O., Thundiyil, J. G., & Stolbach, A. (2011). Clearing the Air: A Review of the Effects of Particulate Matter Air Pollution on Human Health. Journal of Medical Toxicology. https://doi.org/10.1007/s13181-011-0203-1

Dai, S., & Li, L. (2019). Modeling Vehicle Interactions via Modified LSTM Models for Trajectory Prediction. Ieee Access. https://doi.org/10.1109/access.2019.2907000

Estuardo-Moreno, H., Gomez-Alvarez, A., Lucero-Acuña, J. A., Almendariz-Tapia, F. J., Esparza-Ponce, H. E., & Ramirez-Leal, R. (2022). Physical and Chemical Morphology of Organic Compounds at PM10 by TEM-EDS and GC-SM. Microscopy and Microanalysis. https://doi.org/10.1017/s1431927622011977

Greff, K., Srivastava, R. K., Koutník, J., Steunebrink, B. R., & Schmidhuber, J. (2017). LSTM: A Search Space Odyssey. Ieee Transactions on Neural Networks and Learning Systems. https://doi.org/10.1109/tnnls.2016.2582924

Istiana, T., Kurniawan, B., Soekirno, S., & Prakoso, B. (2022). Deep Learning Implementation Using Long Short Term Memory Architecture for $PM_{2.5}$ Concentration Prediction: A Review. Iop Conference Series Earth and Environmental Science. https://doi.org/10.1088/1755-1315/1105/1/012026

Kamarehie, B., Ghaderpoori, M., Jafari, A., Karami, M. A., Mohammadi, A., Azarshab, K., Ghaderpoury, A., & Noorizadeh, N. (2017). Estimation of Health Effects (Morbidity and Mortality) Attributed to PM10 and PM2.5 Exposure Using an Air Quality Model in Bukan City, From 2015-2016 Exposure Using Air Quality Model. Environmental Health Engineering and Management. https://doi.org/10.15171/ehem.2017.19

Kim, D., Han, H., Wang, W., Kang, Y., Lee, H.-Y., & Kim, H. S. (2022). Application of Deep Learning Models and Network Method for Comprehensive Air-Quality Index Prediction. Applied Sciences. https://doi.org/10.3390/app12136699

Kratzert, F., Klotz, D., Brenner, C., Schulz, K., & Herrnegger, M. (2018). Rainfall–runoff Modelling Using Long Short-Term Memory (LSTM) Networks. Hydrology and Earth System Sciences. https://doi.org/10.5194/hess-22-6005-2018

Lehadus, M. P., Nedeff, V., Barsan, N., Sandu, A. V., Mosnegutu, E., Tomozei, C., Irimia, O., Andrioai, G., & Sandu, I. (2019). Monitoring the Particulate Matter (PM10) Emissions from Bacau City Termo-Energetic Industry. Revista De Chimie. https://doi.org/10.37358/rc.19.8.7446

Liang, Y., Fang, L.-Q., Pan, H., Zhang, K., Kan, H., Brook, J. R., & Sun, Q. (2014). PM2.5 in Beijing – Temporal Pattern and Its Association with Influenza. Environmental Health. https://doi.org/10.1186/1476-069x-13-102

Rubinsteyn, A., & Feldman, S. (2016). fancyimpute: An Imputation Library for Python. https://github.com/iskandr/fancyimpute

7th Intercontinental Geoinformation Days

igd.mersin.edu.tr

Estimation of chlorophyll concentration on surface water bodies from hyperspectral satellite data

Martina Frezza*[1], Valeria La Pegna [1], Davide De Santis [1], Dario Cappelli [1], Fabio Del Frate [1]

[1]Tor Vergata University of "Rome", Faculty of Engineering, Civil Engineering and Computer Science Engineering Department, Rome, Italy

Keywords
PRISMA
Sentinel-3
Water Quality
Trophic level
Neural Networks

Abstract

This research contributes to advancing the measurement and monitoring of crucial biogeophysical parameters, serving as both qualitative and quantitative indicators for the assessment of natural surface conditions. Leveraging hyperspectral satellite sensors, the primary objective is to enhance the management of natural resources. A key focus of this investigation is the concentration of chlorophyll, a pivotal indicator for assessing phytoplankton abundance and algal biomass in aquatic environments. Chlorophyll concentration emerges as a valuable metric for gauging water quality, understanding the biophysical state of water bodies, discerning trophic levels, and evaluating the eutrophication status of water. The imperative to estimate chlorophyll concentration through satellite-derived data stems from inherent limitations in in-situ measurements. Traditional field measurements conducted by pertinent Regional Environmental Protection Agency entities are labor-intensive, allowing for only a sparse sampling frequency, typically limited to a few measurements annually. Furthermore, these in-situ measurements offer data at specific points, potentially overlooking the spatial variability of chlorophyll concentration across water bodies. By leveraging hyperspectral satellite technology, this research aims to overcome these limitations, providing a more comprehensive and spatially distributed understanding of chlorophyll concentration. This holistic approach not only enhances the efficiency of resource management but also contributes to a more nuanced comprehension of the dynamic ecological processes within aquatic ecosystems.

1. Introduction

The term "pollution," as defined by Legislative Decree 152/06 Article 74, refers to the "direct or indirect introduction, as a result of human activity, of substances or heat into the air, water, or soil, which can harm human health or the quality of aquatic ecosystems or terrestrial ecosystems directly depending on aquatic ecosystems, disrupting, defacing, or deteriorating recreational values or other legitimate uses of the environment". According to the Department of Civil Protection website, pollution sources can be categorized into three types:

- **Civil**: Originating from urban discharges when water flows without any treatment into rivers or directly into the sea.
- **Industrial**: Comprising various substances dependent on industrial production.
- **Agricultural**: Linked to the excessive and improper use of fertilizers and pesticides, which, being generally water-soluble, penetrate the soil and contaminate aquifers.

Polluted waters pose a serious risk to human health and ecosystem quality, as pollutants enter the food chain, causing diseases and deformities. Sustainable water availability and management are among the sustainable development goals. Specifically, Goal 6.3 aims to improve water quality by 2030, reducing pollution, chemical releases, and increasing wastewater treatment before discharge into water bodies. Goal 6.6 focuses on protecting water-related ecosystems. Freshwater ecosystems underpin global water security but face threats from human activities and climate change. The European Water Framework Directive (2000/60/EC) urges member states to achieve good status in water

* **Corresponding Author**

*(martina.frezza@uniroma2.it) ORCID ID 0009-0000-9868-9667
(valeria.la.pegna@uniroma2.it) ORCID ID 0009-0009-1541-6627
(davide.de.santis@uniroma2.it) ORCID ID 0000-0002-5123-8161
(dario.cappelli@uniroma2.it) ORCID ID 0009-0000-9918-9728
(fabio.del.frate@uniroma2.it) ORCID ID 0000-0002-1655-0643

Cite this study

Frezza M, La Pegna V, De Santis. D, Cappelli D. & Del Frate F (2023). Estimation of Chlorophyll Concentration on Surface Water Bodies from Hyperspectral Satellite Data. Intercontinental Geoinformation Days (IGD), 7, 258-261, Peshawar, Pakistan

bodies by 2027, necessitating the reduction of anthropogenic pollution and the restoration of ecosystems. Goal 14 also aims to reduce or prevent all forms of marine pollution, particularly from nutrients, and to sustainably manage and protect the marine and coastal ecosystem. To gauge progress, continuous monitoring of key biological, physical, and chemical parameters is crucial for understanding the ecological state of water bodies.

This work contributes to the measurement and monitoring of biogeophysical parameters using hyperspectral satellite sensors. These sensors provide both qualitative and quantitative indicators of natural surface conditions. Advanced space technologies, such as the PRISMA satellite in the European Copernicus project, play a vital role in studying Earth, offering real-time and non-intrusive monitoring capabilities.

The study focuses on estimating water quality parameters in lagoon and marine surfaces, specifically chlorophyll concentration in the Venice lagoon (Italy) and nearby marine zones from 2019 to 2022. Utilizing hyperspectral data processed by a neural network, inspired by the biological function of the human brain, overcomes challenges associated with in-situ chlorophyll concentration estimation.

In this research, neural networks significantly enhance chlorophyll concentration monitoring, addressing the limitations of in-situ measurements and providing a more comprehensive understanding of water body dynamics.

2. Method

A neural network is created to estimate chlorophyll concentration from PRISMA satellite data.
The network comprises layers: the Input layer receives external data, the Hidden layer processes information, and the Output layer collects results.
Neural networks can be Single Layer Perceptron (SLP) or Multi-Layer Perceptron (MLP). SLP is simple, offering binary output, while MLP, with hidden layers, uses non-linear transformations and backpropagation.
The activation function adds non-linearity; common ones include sigmoid and hyperbolic tangent functions.
Neural networks generalize learning, vital for complex tasks. Designing a network involves defining inputs/outputs, generating training data, determining structure, and training. The training phase employs backpropagation to adjust weights iteratively.

2.1. Dataset creations

The dataset integrates Sentinel-3 and PRISMA data. Sentinel 3 chlorophyll data was used as ground truth; using the Water Full Resolution product, 22 Sentinel-3 products between 2019 and 2022 were selected.

The PRISMA (PRecursore IperSpettrale della Missione Applicativa) satellite, a groundbreaking initiative by the Italian Space Agency (ASI), represents a significant milestone in the field of Earth observation. Successfully launched on March 22, 2019, PRISMA carries with it a state-of-the-art hyperspectral sensor, setting new standards for high-resolution imaging across numerous spectral bands. This hyperspectral capability empowers PRISMA to unravel intricate details in electromagnetic signatures, facilitating comprehensive analyses of Earth's diverse surfaces and dynamic atmosphere. The satellite's advanced technology enhances our ability to study and understand environmental changes, monitor vegetation health, and investigate variations in mineral composition. PRISMA's contributions extend across diverse domains, from agriculture to water quality, making it a crucial asset in the realm of Earth observation.

The Sentinel-3 Ocean and Land Colour Instrument (OLCI) leads the forefront of the European Space Agency's Sentinel-3 mission, epitomizing state-of-the-art capabilities for Earth observation. Integral to the Copernicus program, Sentinel-3 OLCI assumes a pivotal role in surveilling the well-being of Earth's oceans and land surfaces. Deployed alongside the Sentinel-3A satellite in February 2016, and later complemented by the Sentinel-3B in April 2018, OLCI serves as a medium-resolution imaging spectrometer specifically crafted to capture a diverse array of spectral bands. With its adeptness in recording radiance and reflectance from the Earth's surface, OLCI facilitates the tracking of crucial environmental parameters, spanning ocean color and surface water quality.

For PRISMA data relevant reflectance values were downloaded. Selecting bands crucial for chlorophyll estimation involved referencing absorption spectra and literature. Ten VNIR bands were chosen.

The final dataset structure includes a random set of points on the selected dates, their S3 chlorophyll values and PRISMA reflectance values for selected bands. This data set was divided 60% for the training phase and 40% for the validation phase, which in turn was divided by 55% for the validation phase and 45 % for the testing phase.

2.2. Network structure

By doing a several simulations, also varying the number of intermediate layers, the configuration that reports the minimum error value is shown in Figure 1.
The performance metrics used on validation and test set are the Mean Absolute Error (MAE) and Root Mean Square Error (RMSE).

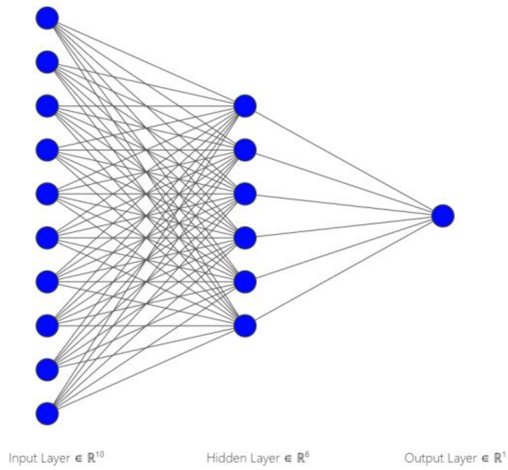

Figure 1. Neural network configuration

3. Results

The neural network created was applied to PRISMA images over the Venice lagoon for determination of chlorophyll concentration maps.
The areas of greatest interest within the lagoon are the city of Venice (1) and Venice Marco Polo airport (2).

Figure 2. Area of interest

Figure 3. Venice Marco Polo airport

The following results were obtained for the date of August 2, 2021.

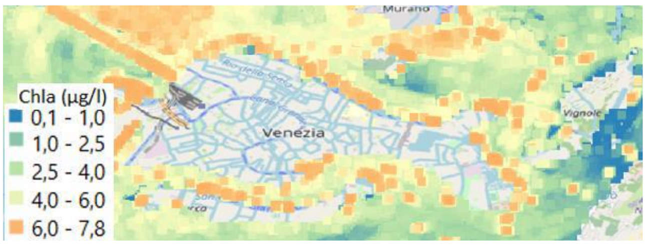

Figure 4. Trend in chlorophyll concentration on 12 August 2021 in the city of Venice

The highest concentrations for the city of Venice are found along the coasts, reaching approximately 8 µg/l. This demonstrates how anthropogenic presence can alter the normal chlorophyll concentration. In the central zone of the lagoon, characterized by limited water exchange, the concentration varies between 2 µg/l and 6 µg/l. In the area where the lagoon connects to the Adriatic Sea, the concentration reaches a maximum value of 1 µg/l. The Mediterranean Sea, in fact, is considered an oligotrophic basin due to its very low chlorophyll concentrations.

Figure 5 confirms what was said previously, there is an increase in the concentration of chlorophyll along the coast of the airport. The concentration reaches a maximum value of approximately 8 µg/l and decreases as the distance from the coasts increases, where concentration values even lower than unity are recorded.

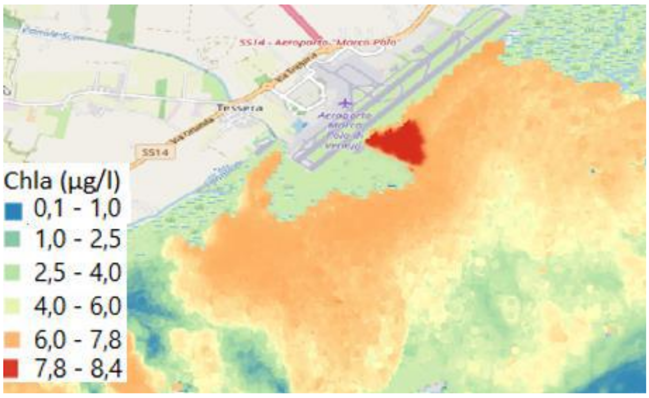

Figure 5. Trend in chlorophyll concentration on 12 August 2021 near the airport

4. Discussion

The analyses conducted unveiled a pronounced issue of eutrophication in the examined waters. During the winter period, the extent of the area impacted by elevated chlorophyll concentration is more substantial. The transition from winter to spring marks the occurrence of phytoplankton "blooms." In contrast, during the summer season, the combination of vertical stratification, leading to diminished nutrient supply in deeper layers, and elevated temperatures results in lower chlorophyll concentrations. This observation contributes valuable insights to the understanding of seasonal variations in phytoplankton dynamics, emphasizing the significance of environmental factors in shaping chlorophyll levels in aquatic ecosystems.

5. Conclusion

In exploring the proposed study, we initially addressed the concern of pollution in surface water bodies, a prevalent issue affecting numerous water systems. Our specific focus centered on the eutrophic condition of these bodies, resulting from the excessive and uncontrolled discharge of nutrients. To meet the objectives outlined in Directive 2000/60/EC, meticulous monitoring of various biophysical parameters becomes imperative for enhancing resource management and quality. The conducted experiments underscored the substantial relevance of neural networks in both the study and surveillance of resources, often relying on specific and constraining observations.

Of particular note is the potential offered by remote sensing in environmental monitoring and the remarkable adaptability of neural networks, making them applicable to a wide array of distinct case studies.

Through the application of the network to various cases of interest, criticalities in chlorophyll concentration were identified, particularly in the coastal regions, characterized by an ecologically poor-sufficient state and zones exhibiting a pronounced eutrophic condition.

The capability to generate, nearly in real-time, a map illustrating the trend in chlorophyll concentration for the designated area holds significant importance. This information proves valuable for the implementation of strategies and measures directed at safeguarding and enhancing the available resources.

Acknowledgement

The authors would like to thank the Italian Space Agency (ASI) for providing the PRISMA data used for this work.

References

Antoine, D. (2010). OLCI Level 2.

Bresciani, M., Rossini, M., Morabito, G., Matta, E., Pinardi, M., Cogliati, S., ... & Giardino, C. (2013). Analysis of within-and between-day chlorophyll-a dynamics in Mantua Superior Lake, with a continuous spectroradiometric measurement. Marine and Freshwater Research, 64(4), 303-316.

Burkholder, J. M., Tomasko, D. A., & Touchette, B. W. (2007). Seagrasses and eutrophication. Journal of experimental marine biology and ecology, 350(1-2), 46-72.

Chen, J., Chen, S., Fu, R., Wang, C., Li, D., Peng, Y., ... & Zheng, Q. (2021). Remote sensing estimation of chlorophyll-A in case-II waters of coastal areas: three-band model versus genetic algorithm–artificial neural networks model. IEEE Journal of Selected Topics in Applied Earth Observations and Remote Sensing, 14, 3640-3658.

Giardino, C., Bresciani, M., Fabbretto, A., Ghirardi, N., Mangano, S., Pellegrino, A., ... & Tzimas, A. (2021, July). Hyperspectral prisma products of aquatic systems. In 2021 IEEE International Geoscience and Remote Sensing Symposium IGARSS (pp. 1229-1232). IEEE.

Gilerson, A., Gitelson, A., Zhou, J., Gurlin, D., Moses, W., Ioannou, I., A. Ahmed, S. (2010). Algorithms for remote estimation of chlorophyll-a in coastal and inland waters using red and near infrared bands. Opt. Express 18, 24109-24125

Keiner, L. E., & Yan, X. H. (1998). A neural network model for estimating sea surface chlorophyll and sediments from thematic mapper imagery. Remote sensing of environment, 66(2), 153-165.

Marzano, F. S., Iacobelli, M., Orlandi, M., & Cimini, D. (2020). Coastal water remote sensing from sentinel-2 satellite data using physical, statistical, and neural network retrieval approach. IEEE Transactions on Geoscience and Remote Sensing, 59(2), 915-928.

Nguyen, T., Nguyen, P., Katsuaki, K., Mai, T. (2017). Selecting the best band ratio to estimate chlorophyll-a concentration in a tropical freshwater lake using sentinel 2A images from a case study of lake Be Be (Northern Vietnam). ISPRS Int. J. Geo.Inf, 6(9), 290. https://doi.org/10.3390/ijgi6090290

Vilas, L. G., Spyrakos, E., & Palenzuela, J. M. T. (2011). Neural network estimation of chlorophyll a from MERIS full resolution data for the coastal waters of Galician rias (NW Spain). Remote Sensing of Environment, 115(2), 524-535.

Zilioli, E., Brivio, P. A., & Lechi, G. M. (Eds.). (1992). Il telerilevamento da aereo e da satellite. Delfino.

7th Intercontinental Geoinformation Days

igd.mersin.edu.tr

Spatial analysis of the vulnerability of rural housing to earthquakes (case study: rural settlements in the Tehran metropolitan area)

Bahman Tahmasi *[1], **Hassan Ali Faraji Sabokbar** [1], **Seyed Ali Badri** [1]

[1]*University of Tehran, Faculty of Geography, Department of Human Geography and planning, Tehran, Iran*

Keywords
Spatial analysis
Vulnerability
Rural housing
Earthquake
TMA

Abstract
Natural disasters are one of the main factors in the destruction of human settlements and cause much damage to human societies. An earthquake is one of the most destructive natural disasters that can destroy settlements in just a few seconds. Iran is located in an earthquake-prone region where many earthquakes occur every year. Also, the Tehran metropolitan area is one of the most prone to earthquakes in Iran. This area has a high risk of earthquake due to the high population density, high residential density and the existence of many faults. Rural settlements located in the Tehran metropolitan area have a high potential for vulnerability to earthquakes due to their high population density, low-quality housing, and unique socio-economic conditions. This is the reason this paper analyzes the vulnerability of housing of rural settlements in the Tehran metropolitan area. The statistical population in this research was the rural settlements located in the TMA region. For data analysis, several spatial analysis methods, including IDW interpolation, hotspot analysis, and KMeans spatial clustering, have been used. The results of this study show that the rural settlements located in the central area of TMA have more resistant housing and less vulnerability, and the peripheral areas have more non-resistant housing and more vulnerability.

1. Introduction

Natural disasters have a negative impact on human society. natural disasters can lead to substantial damages to human capital, including nutrition, education, and health. The impacts are often long-lasting and disproportionately affect the poorest socioeconomic groups (Baez et al, 2010; Felbermayr, & Groschl, 2014; Cavallo et al,2013; Khan et al, 2020; Murat & Sozen, 2021). Each year, natural disasters cause a large number of deaths as well as significant economic losses. The number of deaths and the amount of damages from natural disasters can be highly variable from year-to-year; some years pass with very few deaths and damages before a large disaster event claims many lives. If we look at the average over the past decade, approximately 45,000 people globally died from natural disasters each year. This represents around 0.1% of global deaths (Global Change Data Lab, 2023).

Among the natural hazards, earthquakes are one of the most destructive hazards and have many negative effects. Earthquakes can have devastating impacts in a matter of seconds. Their unpredictable nature and the potential scale of their impact make them one of the most lethal of all disasters, claiming an average of 27,000 lives a year worldwide since the 1990s (Guha-Sapir, 2010).

Earthquake has different effects in social, economic and physical dimensions (Alizadeh et al, 2021; Minos-Minopoulos, 2017). Therefore, seismic vulnerability can be classified into physical, social and economic components. But in practice, physical vulnerability, especially of buildings, is the most important and has attracted the most attention in evaluations, because so far the most deaths and casualties in earthquakes have been caused by building collapse (Gao & Ji, 2014). And this issue is more evident in developing countries (Kenny, 2009). For this reason, in this article, physical vulnerability to earthquakes in rural settlements has been considered the most important component of vulnerability to earthquakes.

Iran is located in one of the world's most seismically active areas. The Tehran metropolitan area (TMA) is one of the areas with a high risk of earthquakes in Iran due to the history of earthquakes and the presence of numerous and active faults. Rural settlements located in this area are vulnerable to earthquakes due to high population density and low quality of housing. The important issue is that the quality of rural houses and their vulnerability

* **Corresponding Author**

*(bahman.tahmasi@ut.ac.ir) ORCID ID 0000-0002-7742-814X
(hfaraji@ut.ac.ir) ORCID ID 0000-0002-5470-4287
(sabadri@ut.ac.ir) ORCID ID 0000-0001-7422-7281

Cite this study

Tahmasi, B., Faraji Sabokbar, H. A., & Badri, S. A. (2023). Spatial analysis of the vulnerability of rural housing to earthquakes (case study: rural settlements in the Tehran metropolitan area). Intercontinental Geoinformation Days (IGD), 7, 262-265, Peshawar, Pakistan

to earthquakes are not the same in the entire the Tehran metropolitan area (TMA), but some rural settlements have low-quality houses and higher vulnerability, and some other rural settlements have high-quality houses. and are less vulnerable to earthquakes. Therefore, the aim of this article is to spatially analyze the vulnerability of rural dwellings and clustering rural settlements located in the Tehran metropolitan area (TMA) based on the degree of vulnerability.

2. Method

This study is a type of applied research that was carried out using a quantitative methodology framework. The study's statistical population consists of 1519 rural settlements situated inside the Tehran metropolitan area (Statistical Centre of Iran, 2016). Among these, a statistical sample of 928 rural settlements with data on the types of building materials available was examined. The data used in this research was collected from the general census of population and housing, Statistical Centre of Iran. Data analysis was done using spatial analysis methods, spatial statistical techniques, and spatial clustering, including the IDW interpolation technique, HotSpot analysis, and the KMeans clustering technique. ArcMap and GeoDa software have been used for data analysis. The three variables used in this research include; The number of buildings built with metal materials, the number of buildings built with concrete materials, and the number of buildings built with low-quality materials such as wood, stone, brick, clay, etc.

2.1. Study area

The study area of this research includes the Tehran metropolitan area. The capital city of Iran is located in this region and almost 20% of the total population of Iran lives in this region. The two provinces of Alborz and Tehran are included in the Tehran metropolitan area. Tehran Province has an area of about 13842 square kilometers. Tehran province is divided into 16 counties, 46 cities, and 1048 villages. Also, Tehran province has a population of 13267637 people. Alborz province has an area of about 5182 square kilometers. Alborz province comprises 6 counties, 17 cities, and 471 villages. Also, Alborz province has a population of 27124000 people (Statistical Centre of Iran, 2021).

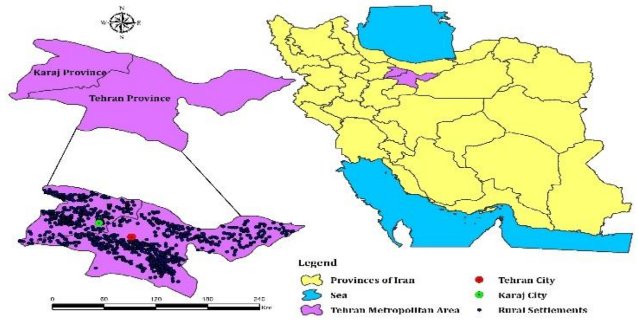

Figure 1. The location of the Tehran metropolitan area

The provinces of Mazandaran in the north, Qazvin in the west, Markazi in the southwest, Qom in the south, and Semnan in the southeast encircle the Tehran metropolitan area (Fig 1).

3. Results

The overall number of buildings in the 928 villages under study comes to 286,889, based on the information that was gathered. Among them, 145,664 (50.77%) were constructed using metal materials, 35,253 (12.29%) using concrete materials, and 105,083 (36.63%) using low-quality materials including clay, stone, brick, wood, etc. Furthermore, the type of materials in 889 (0.31%) rural buildings is also unknown “Table 1”.

Table 1. The number of rural buildings by type of materials

Variable	All buildings	Metal materials	Concrete materials	Low quality materials	Unknown
Number	286889	145664	35253	105083	889
Percent	100	50.77	12.29	36.63	0.31

The utilization of metal materials is higher in TMA's center regions and less common in its other peripheral locations, according to the spatial distribution of the different types of materials utilized in rural buildings. Concrete materials are similarly distributed spatially in the same pattern. However, throughout the whole TMA range, the geographical distribution of low-quality materials is visible. Therefore, the number of housing built with metal and concrete materials is more in the central areas of TMA (Fig 2).

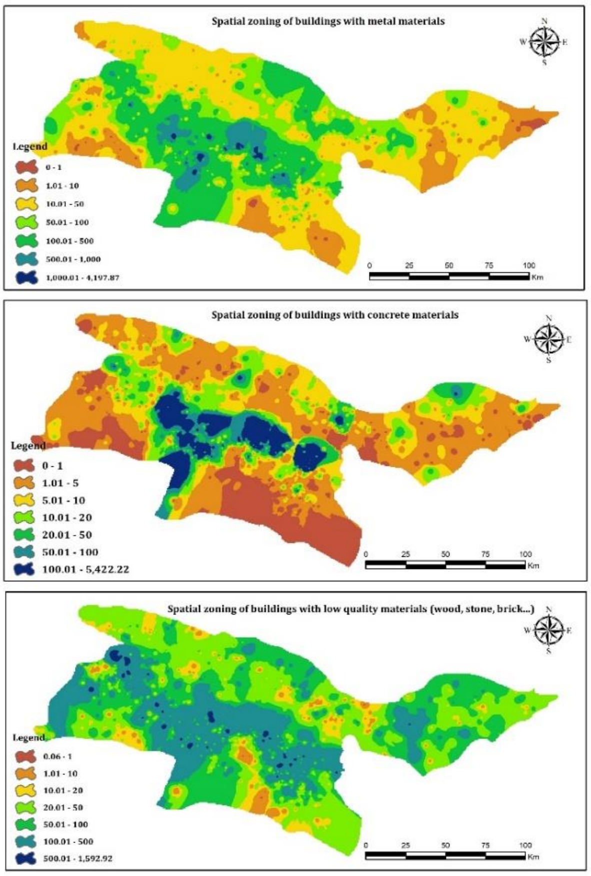

Figure 2. Spatial distribution of types of materials in rural buildings

At this stage, the ratio of buildings with resistant materials and the ratio of buildings with non-resistant materials has been calculated. For this action, the number of metal and concrete buildings have been added together and defined as resistant buildings. Also, buildings with low-quality materials (such as wood, stone, brick, clay, etc.) are defined as non-resistant buildings. Next, by dividing the number of resistant and non-resistant buildings by the total number of buildings, the ratio of each of them is obtained "Table 2".

Table 2. The ratio of resistant and non-resistant buildings

Variable	Ratio of resistant buildings	Ratio of non-resistant buildings	Ratio of unknown buildings	Total
Number	180917	105083	889	286889
Ratio (%)	63.06	36.63	0.31	100

The spatial distribution of the ratio of resistant and non-resistant buildings in the Tehran metropolitan area shows that the ratio of resistant buildings is higher in the center, south, north, and northeast of the TMA. Also, the proportion of non-resistant buildings is higher in the west, southwest, east, and southeast of TMA (Fig 3).

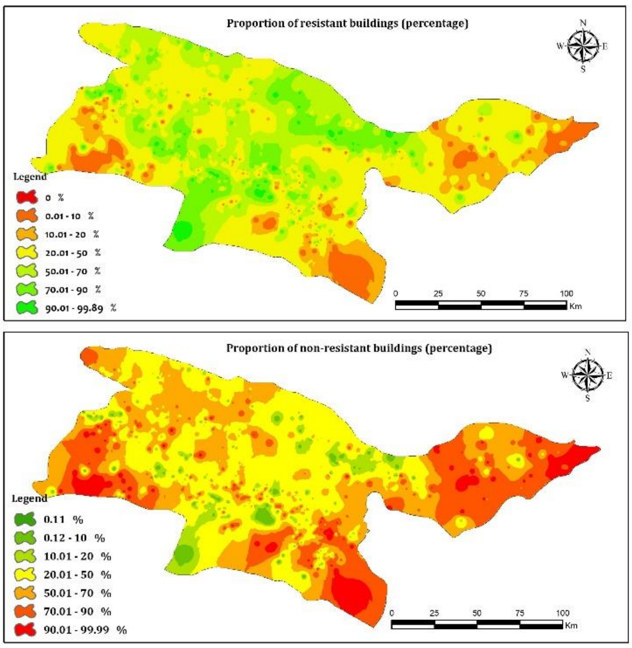

Figure 3. Spatial distribution of the ratio of resistant and non-resistant buildings

In the following, hotspots analysis has been used to identify the location of the concentration of hot and cold spots related to the ratio of resistant and non-resistant buildings. The hotspots analysis of the ratio of resistant buildings shows that a hot spot has been identified in the center of TMA. This spot shows the concentration of high values related to the proportion of resistant buildings. This spot is also statistically significant. In addition, three cold spots related to the proportion of resistant buildings have been identified in the southwest, south, and east of the TMA area. This spot shows the low value of the proportion of resistant buildings. These spots are statistically significant.

The hotspots analysis of the ratio of non-resistant buildings shows that a cold spot has been identified in the center of TMA. This spot shows the concentration of low values related to the proportion of non-resistant buildings. As well as, three hot spots related to the proportion of non-resistant buildings have been identified in the southwest, south, and east of the TMA area. This spot shows the high value of the proportion of non-resistant buildings (Fig 4).

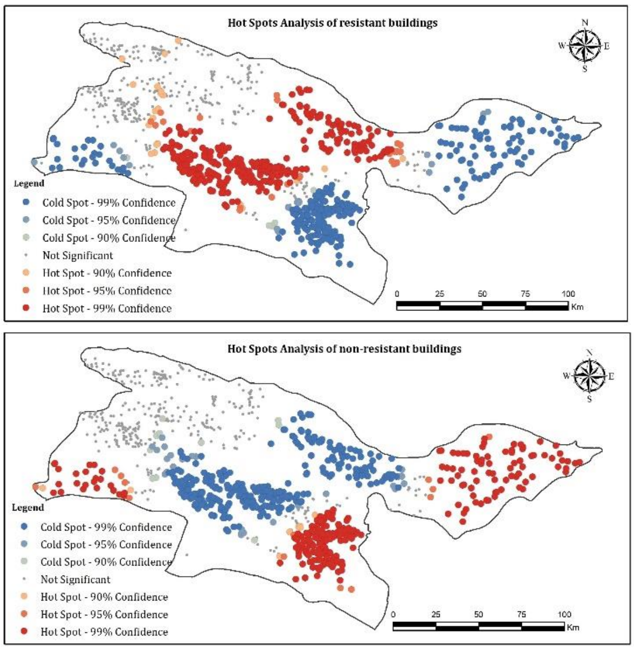

Figure 4. Hotspots analysis of the ratio of resistant and non-resistant buildings

Finally, based on the level of vulnerability of housing to earthquakes, rural settlements are clustered in TMA. Based on the level of housing vulnerability, rural settlements located in TMA are divided into 5 clusters. Cluster 1 in the north and northeast of TMA has more resistant housing and less vulnerability to earthquakes. Cluster 5 in the east of TMA has more non-resistant houses and more vulnerability to earthquakes. Three other clusters are located between these two clusters (Figure 5).

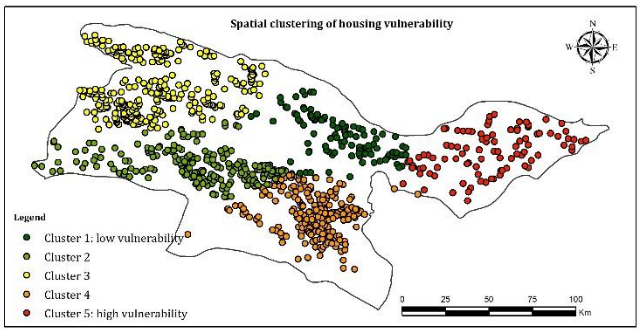

Figure 5. Spatial clustering of rural settlements based on KMeans

4. Discussion

Vulnerability to earthquakes has a direct relationship with the type of materials used in buildings and the level of resistance of housing. In this study, different dimensions of housing quality and their vulnerability to earthquakes in TMA were analyzed. And finally, rural settlements were divided into five categories according to physical vulnerability “Table 3”.

Table 3. Clustering of rural settlements

cluster	Resistant materials	Non-resistant materials	Number of rural
1	48.35	50.25	111
2	54.80	44.20	224
3	39.36	57.43	278
4	64.75	32.17	220
5	27.30	72.32	95

5. Conclusion

In this article, the spatial analysis of the vulnerability of rural housing in TMA to earthquake is discussed. The results of this study show that about one-third of the rural houses located in the Tehran metropolitan area are built using non-resistant materials such as wood, stone, brick, clay, etc. These results show that a significant number of rural housing units located in the Tehran metropolitan area are of low quality, which causes their destruction and severe vulnerability against a possible earthquake.

The spatial pattern related to the type of building materials shows that more resistant materials are used in the central areas of TMA, and low-quality and non-resistant materials are used more in the peripheral areas of TMA. Based on the hotspots analysis, it was also found that the focus of hot spots related to resistant houses is located in the central area of the TMA, and the focus of hot spots related to non-resistant houses is located in the peripheral area of the TMA.

The results of the spatial clustering of Kamenez divided the villages into five categories based on the vulnerability of the houses. Based on this method, the villages located in the central area of the TMA are less vulnerable, and the villages located in the peripheral area of the TMA are more vulnerable.

In this study, three IDW interpolation methods, hotspot analysis and cluster analysis—were used for the spatial analysis of the vulnerability of rural housing. The results of this study show that the output of different methods used for zoning and spatial clustering of the physical vulnerability of rural settlements to earthquakes is consistent.

References

Alizadeh, M., Zabihi, H., Rezaie, F., Asadzadeh, A., Wolf, I. D., Langat, P. K., ... & Pradhan, B. (2021). Earthquake vulnerability assessment for urban areas using an ANN and hybrid SWOT-QSPM model. Remote Sensing, 13(22), 4519.

Baez, J., De la Fuente, A., & Santos, I. V. (2010). Do natural disasters affect human capital? An assessment based on existing empirical evidence.

Cavallo, E., Galiani, S., Noy, I., & Pantano, J. (2013). Catastrophic natural disasters and economic growth. Review of Economics and Statistics, 95(5), 1549-1561.

Felbermayr, G., & Groschl, J. (2014). Naturally negative: The growth effects of natural disasters. Journal of development economics, 111, 92-106.

Gao, X., & Ji, J. (2014). Analysis of the seismic vulnerability and the structural characteristics of houses in Chinese rural areas. Natural hazards, 70, 1099-1114.

Global Change Data Lab. (2023). Natural Disasters Data. https://ourworldindata.org/natural-disasters

Guha-Sapir, D., & Vos, F. (2010). Earthquakes, an epidemiological perspective on patterns and trends. In Human casualties in earthquakes: progress in modelling and mitigation (pp. 13-24). Dordrecht: Springer Netherlands.

Kenny, C. (2009). Why do people die in earthquakes? The costs, benefits and institutions of disaster risk reduction in developing countries. The Costs, Benefits and Institutions of Disaster Risk Reduction in Developing Countries (January 1, 2009). World Bank Policy Research Working Paper, (4823).

Khan, A., Chenggang, Y., Khan, G., & Muhammad, F. (2020). The dilemma of natural disasters: Impact on economy, fiscal position, and foreign direct investment alongside Belt and Road Initiative countries. Science of the Total Environment, 743, 140578.

Minos-Minopoulos, D., Dominey-Howes, D., & Pavlopoulos, K. (2017). Vulnerability assessment of archaeological sites to earthquake hazard: an indicator based method integrating spatial and temporal aspects. Annals of Geophysics, 60(4), S0445-S0445.

Murat, G. E. N. Ç., & Sozen, E. (2021). The sustainable scale of earthquake awareness, development, validity and reliability study. International Electronic Journal of Environmental Education, 11(1), 24-41.

7th Intercontinental Geoinformation Days

igd.mersin.edu.tr

The effect of smart mobility performance in mitigation of climate change, the experiences of European cities

Parinaz Badamchizadeh[1], Iraj Teymuri *[1], Ali Oskouee Aras [1], Fereidoun Babaie Aghdam [1]

[1]Tabriz University, Faculty of Planning and Environmental Sciences, Tabriz, Iran

Keywords
Smart mobility
Urban development
Smart city
Climate Change mitigation

Abstract

Smart and sustainable urban improvement is the current priority. Mobility is one of the most difficult topics to face within the urban regions. Great mobility for citizens and businesses incredibly increases the attractiveness and competitiveness of cities. The transport sector is one of the biggest contributors of CO2 emissions and other greenhouse gasses. In order to decreasing the global average temperature by CO2, critical and transformative activities in urban portability are required. As a sub-domain of the smart-city concept, smart-mobility-solutions integration at the municipal level is thought to have environmental, financial and social benefits, e.g., decreasing air pollution in cities, giving modern markets for alternative mobility and ensuring widespread get to to open transportation. Therefore, this article points to analyze the significance of smart mobility in creating a cleaner environment and provide strategic and practical illustrations of smart-mobility services in four European cities: Berlin (Germany), Kaunas (Lithuania), Riga (Latvia) and Tartu (Estonia). The paper presents a systematized writing review approximately the potential of smart-mobility services in reducing the negative natural affect to urban situations in different cities.

1. Introduction

Climate change mitigation requires transformative changes in cities. Rapid urban population growth, traffic congestion and related air pollution, as well as ageing infrastructure and energy usage put cities at the center of the climate mitigation agenda. In 2018, 4.2 billion of the world's population lived in cities. This number is expected to reach 6.5 billion by 2050(United.Nations, 2023).

Environmental implications are highly related to the consumption of natural resources for energy production and greenhouse gas emissions (GHG), which contribute to climate change. Currently, cities are responsible for 60 to 80% of all energy consumption and approximately 70% of carbon emissions in the world(United.Nations, 2023). The transport sector is one of the main contributors to greenhouse gas emissions. At the global scale, transportation accounted for 28% of the global final energy demand and 23% of global energy-related CO2 emissions in 2014 (Masson-Delmotte. el 2018). The transport sector's emissions, such as particulate matter (PM10 and PM2.5), nitrogen dioxide (NO2), carbon monoxide (CO) and other gases, mostly depend on the type of fuel used, with diesel and gasoline being the most popular. (World Urban Forum, 2014).

In the early 1990s the phrase "smart city" was coined to signify how urban development was turning towards technology, innovation and globalization (Schaffers and all, 2018). The World Foundation for Smart Communities advocated the use of information technology to meet the challenges of cities within a global knowledge economy. However, the more recent interest in smart cities can be attributed to the strong concern for sustainability, and to the rise of new Internet technologies, such as mobile devices (e.g., smart phones), the semantic web, cloud computing, and the Internet of Things (IoT) promoting real world user interfaces. (Komninos, 2002 and 2008).

2. Method

The study is based on the literature sources analysis and data regarding of smart urban development with a special regard to smart mobility indicators.

* **Corresponding Author**

(p_badamchi98@ms.tabrizu.ac.ir) ORCID ID 0000-0002-7038-173X
*(Iraj-teymuri@tabrizu.ac.ir) ORCID ID 0000-0002-3167-5583
(ali.oskouee.aras@tabrizu.ac.ir) ORCID ID 0000-0002-8897-5237
(Fbabaei@tabrizu.ac.ir)

Cite this study

Badamchizadeh, P., Teymuri, I., Oskouee Aras, A., & Babaie Aghdam, F. (2023). The effect of smart mobility performance in mitigation of climate change, the experiences of European cities. Intercontinental Geoinformation Days (IGD), 7, 266-270, Peshawar, Pakistan

2.1. Role of Smart-Mobility in Urban Environment Improvement

Smart-city discourse and its concept application is widely analyzed in scientific literature.

The smart-city concept is placed at the center of the urban agenda and is used as a tool for ensuring competitiveness and sustainability in urban areas. In a broad sense, it means a long-term vision, which includes usage of intelligent solutions and knowledge (Zawieska & Pieriegud, 2018), information and communication technologies, for efficient natural resource management, environmental impact reduction and better quality of life creation for citizens (Torre, T.; Braccini, A.M.; Spinelli, 2016).

In sustainability concept, urban mobility needs to consider improvement of natural environment condition, increase of social cohesion and economic competitiveness. Therefore, specific measures such as transport optimization, co-modality between public and private transport, and development and implementation of sustainable mobility plans could contribute in addressing these sustainability goals (Strulak-Wójcikiewicz & Lemke, 2019). Therefore, smart-mobility services are a complementary layer to conventional transport systems (Figure 1). It includes integrated ICT infrastructures, sustainable transport systems, and logistics to support better urban traffic and mobility (Cledou et al., 2018). Smart urban mobility uses technology for data generation and sharing; information and knowledge for decision-making; enhancement of vehicles, infrastructure and services; and improvement of transport system operators, users, and stakeholders (Lyons, 2018). Moreover, the term "smart mobility" is not only related to sustainable and efficient transport systems based on contemporary technology, but it also contributes to cleaner mobility pattern changes and decision effectiveness in the transport sector.

Mobility is also a necessary element in creating more resilient cities, which could be able to deliver natural and manmade shocks. The reduction of negative environmental impact of transportation during the COVID-19 pandemic crisis by improving air quality was proved by Feiferyt ˙ e-Skirien ˙e and Stasiškien ˙e (Skirienė & Stasiškienė, 2021), and Pepe et al. (Pepe et al., 2020). During the same crisis, smart-city systems, IoT sensors and Machine learning were used for timely insights provision, based on a real-time data, for assessing pedestrian levels and traffic volumes, as well as for effective decision making (James et al., 2020).

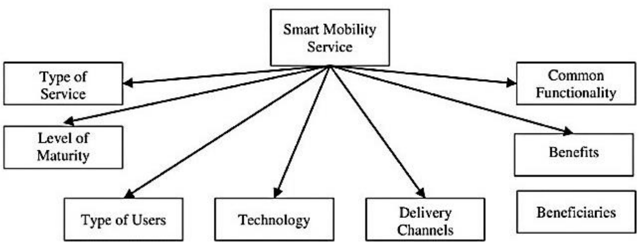

Figure 1. A smart-mobility service taxonomy (Cledou et al., 2018).

2.2. Smart-Mobility Strategies for Climate Mitigation

This analysis focuses on four main European cities—Berlin, Kaunas, Riga and Tartu—where the main strategic documents of these cities are analyzed in order to highlight sustainable mobility objectives, which were/are planned for making the mobility sector in urban areas smarter.

Public transport in Berlin is regulated at the State of Berlin and federal levels. There are a number of types of public transport modes such as buses, tram, subway, ferries and ridesharing. When comparing air-quality data in the four selected cities, we see that Berlin has the highest rates of air pollution from NO_2 and PM2.5. According to the municipality, NO_2 emissions were caused by traffic, heating and industry; PM2.5 was mainly caused by traffic (diesel vehicles and tire abrasion), heating, industry, the building sector. Due to COVID-19 pandemic restrictions, the emissions from the main pollutants decreased in 2020.

In Kaunas, public transport is regulated by national law acts, for example, the Law of the Republic of Lithuania on the Framework of Transport Activities. Buses, trolleybuses (electric) and buses are publicly operated transport modes, which currently exist in the city. Kaunas has the highest PM10 levels, it was the third from the four cities in NO2 emissions' concentrations.

Riga is a city in Northeastern Europe and the capital of Latvia. In Latvia, public transport is regulated by the Law on Public Transport Services. Currently, public transport modes in the city include buses, tram, trolleybuses (electric) and microbuses. Comparing all selected cases, Riga was the second city according to air emission rates (NO2, PM2.5 and PM10) in 2019. A majority of residents prioritize private transport for travelling inside the city, therefore, it could be presumed that the emissions could be caused by vehicles, which are powered by diesel and have a long period of use. However, it is not possible to indicate air-quality changes in 2020, as the data are not provided.

Tartu is the second largest city in Estonia, located in Northeastern Europe. Types of publicly operated public transport modes include buses, tram, subway, ferries and ridesharing. Tartu is the most environmentally-friendly city taking the lowest rates or main air emissions used in the study. Since the beginning of 2020, public transportation vehicles were fully powered by renewable fuel—biomethane—produced by recycled bio-waste.

Figure 2. Publicly operated smart-mobility services in Germany and the Baltic countries.

3. Results

3.1. Berlin "Urban Development Plan for Mobility and Transport" (2021–2030)

The report highlights the significance of mobility for inclusion, the financial sector and social cohesion. It too outlines that mobility has negative impacts on air quality, noise, wellbeing and the climate. Appropriately, the arrange characterizes overarching objectives related to a change of transport (82% ecomobility by 2030, with 23% cycling, 30% walking and 29% public transport), climate mitigation (42% CO2 reduction of the transport sector in comparison to 1990), wellbeing (decrease NOx and other air pollutions, as well as noise). Building on these objectives, the plan defines specific targets, related to characteristic assets, global environment and city-compatible traffic. The advancement arrange moreover sets target to decrease energy consumption related to traffic by 34% in 2030.

3.2. Sustainable Urban Mobility Plan in Kaunas City (2019–2030)

There are two main documents which address smart-mobility-concept integration in Kaunas City—Strategic Development Plan of Kaunas City Municipality Up to 2022 and Sustainable urban mobility plan in Kaunas city.

High quality and safe transport infrastructure is one among the long-term priorities in the city of Kaunas.

Table1. Specific targets and detailed measures for this plan implementation

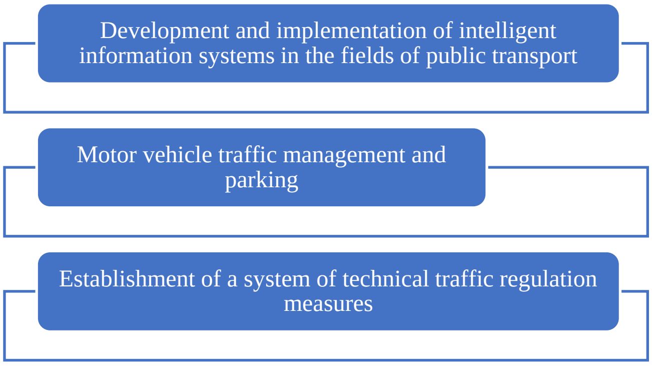

3.3. Riga Sustainable Development Strategy Until 2030 (2014–2030)

Development of a "smart" traffic control system and facilitation of the development of the latest technologies, economically effective transport services are the targets of the strategy. A number of the measures are set in order to achieve the latter targets such as reconstruction and construction of modern traffic infrastructure, development pedestrian traffic infrastructure, pedestrian street network and network of mobility points, improvement of parking service, modernization of public transport, provision of a flexible ticketing system, integration of public transport into a single network of bus and train routes, improvement of the operation of the traffic management center and introduction of smart traffic lights.

Table 2. Priority sequence in the development of transport infrastructure is formed as follows.

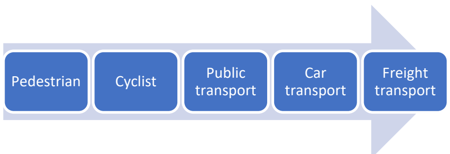

3.4. The Development Strategy "Tartu 2030+" (2006–2030)

One of the targets are related to the increase of public transport capacity and environmentally friendly public transport vehicles. The Strategy also highlights the importance of the completion of the construction of main streets, bridges and different level streets and road crossings to guarantee smooth traffic, the organization of an efficient parking system and the development of public and light transport.

Table 3. The priorities for long-term transport system development in Tartu city until 2030

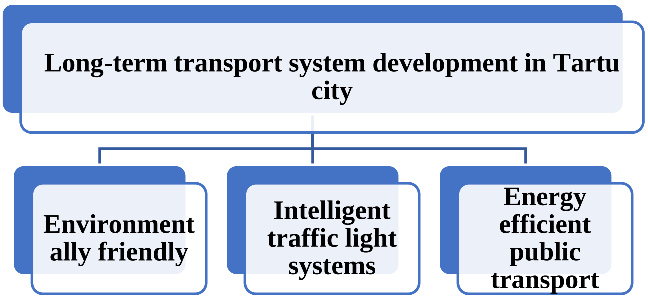

4. Discussion & Conclusion

The results of the literature review showed that smart mobility is an important component of the smart-city concept. Smart mobility is a vision, based on the smart-city concept, and could result in a more sustainable future of cities. The installation of new smart-mobility innovations may reduce the negative environmental impact from the transport system; stimulate new (healthier and cost-effective) citizens' mobility patterns; and contribute to more efficient decision-making, urban-mobility policy planning and implementation. The involvement of decision-makers, public transport companies, private companies, citizens, experts, researchers and innovators is a necessary component in the planning process (both in top down and bottom-up initiatives) to form realistic and clear goals, targets and measures.

Intelligent transport systems installation, intelligent parking systems, traffic management systems, the importance of public transport services and integration of new technologies for smart-mobility development are important parts for rendering smart cities sustainable. The cities already integrate smart technologies such as intelligent transport systems installation, smart-mobility management platform, intelligent parking system, telematics systems, traffic management system, pollution control and transport air pollution- control-system sector speedometers. Even if the real impact of smart technologies is not assessed, smart technologies must provide the value and solutions, based on real-time data, in order to achieve global, the EU and municipal goals. The European Green Deal is a promising financial tool for cities to integrate more additional intelligent technologies in urban areas in the future.

The analysis of four selected cities—Berlin, Kaunas, Riga and Tartu—provided examples of different smart-mobility services in European cities. Modal split results in the cities revealed a high citizens' dependence on private cars in Kaunas, Riga and Tartu, non-motorized transport modes (walking, cycling) are more preferred in Berlin. It also showed that public transport is one of the preferred modes of mobility. Regarding these findings, the examples of smartphone application, mobile ticketing app, smart bike-sharing and mobility point provided by the public sector could change these mobility patterns in a more sustainable way. Moreover, the data are not yet accessible that could be used for real contribution to CO2 and greenhouse gas reduction assessment. Therefore, it is necessary not only to provide smart-mobility services, but also use the beneficial output generated from/by these services in an intelligent way, to further benefit the smart-city system. The air-pollution data showed that, when comparing the four selected cities, Berlin had the highest levels of NO2 and PM2.5 emissions, while Kaunas had the highest rates of PM10 emissions. The best air-quality results were found in Tartu.

In particular, sustainable mobility strategies should focus on aligning ambitious climate mitigation with pandemic recovery measures, by investing in environmentally friendly mobility, i.e., biking, walking and public transport infrastructure, as well as ensuring universal and affordable access to urban mobility services. Furthermore, emphasis should be placed on rendering public transport more resilient for future crisis situations. Smart-mobility solutions should be integrated within overall mobility decarbonization to ensure that solutions that minimize transport's climate footprint in cities are replicated.

References

Beratung GmbH. (2013). Requirements. The Preparation and Implementation of the Sustainable Urban Mobility Plan. Prepared on behalf of the European Commission. World Urban Forum, 2014.

Burns, L. D. (2013). Sustainable mobility: A vision of our transport future. Nature 497. https://doi.org/10.1038/497181a.

Cepeliauskaite, G., Keppner, B., Simkute, Z., Stasiskiene, Z., Leuser, L., Kalnina, I., Kotovica, N., Andiņš, J., & Muiste, M. (2021). Smart-mobility services for climate mitigation in urban areas: Case studies of baltic countries and Germany. Sustainability (Switzerland), 13(8). https://doi.org/10.3390/su13084127

Charles A. (2017). Community Lead, Infrastructure and Urban Development, World Economic Forum, https://www.weforum.org/press/2017/02/global-rise-of-cities-poses-challenge-tosustainable- urban-development/, 2017-03-14.

Cledou, G., Estevez, E., & Soares Barbosa, L. (2018). A taxonomy for planning and designing smart mobility services. Government Information Quarterly, 35(1), 61–76. https://doi.org/10.1016/j.giq.2017.11.008

Giffinger R., Fertner C., Kramar H., Kalasek R., Pichler-Milanovic N. (2007). MEIJERS E., Smart Cities – Ranking of European Medium-Sized Cities, Research Re-port, Vienna University of Technology, Vienna.

Girard L. F. (2010). Creative Evaluations for a Human Sustainable Planning, in: Making Strategies in Spatial Planning, Cerreta M., Concilio G., Monno V. (eds.), Springer, Dordrecht, Heidelberg, London, New York, p. 305-328.

Guidelines Developing and Implementing a Sustainable Urban Mobility Plan. (2013). Rupprecht Consult, European Union.

James, P., Das, R., Jalosinska, A., & Smith, L. (2020). Smart cities and a data-driven response to COVID-19. Dialogues in Human Geography, 10(2), 255–259. https://doi.org/10.1177/2043820620934211

Jason Chang S.K., Hsu Y.T. (2014). Smart Travel and Sustainable Mobility for Green Transport Cities in Re-imagining Urban Mobility, New Cities Foundation, Geneva.

Komninos, N. (2002). Intelligent Cities: Innovation, knowledge systems and digital spaces. Taylor & Francis, London and New York

Komninos, N. (2008). Intelligent Cities and Globalisation of Innovation Networks. Routledge, London and New York.

Lopez-Ruiz H., Panayotis Ch., Demirel H., Kompi M. (2013). Quantifying the Effect of Sustainable Urban Mobility Plans. European Commission Joint Research Center, p. 1-85. DOI:10.2791/2187.

Lyons, G. (2018). Getting smart about urban mobility – Aligning the paradigms of smart and sustainable. Transportation Research Part A: Policy and Practice, 115, 4–14. https://doi.org/10.1016/j.tra.2016.12.001

Masson-Delmotte, V.; Zhai, P.; Pörtner, H.-O.; Roberts, D.; Skea, J.; Shukla, P.R.; Pirani, A.; Moufouma-Okia, W.; Péan, C., & Pidcock, R. et al. (2018). Global warming of 1.5°C. An IPCC Special Report on the impacts of global warming of 1.5°C above pre-industrial levels and related global greenhouse gas emission pathways, in the context of strengthening the global response to the threat of climate change. Ipcc - Sr15, 2(October), 17–20.

Mobility&Transport, Retrived April 5, 2018, from: https://smartcitiesinfosystem.eu/technologies/mobility_transport

Pepe, E., Bajardi, P., Gauvin, L., Privitera, F., Lake, B., Cattuto, C., & Tizzoni, M. (2020). COVID-19 outbreak response, a dataset to assess mobility changes in Italy following national lockdown. Scientific Data, 7(1). https://doi.org/10.1038/s41597-020-00575-2

Przybylowski A. (2017). Port cities smart&sustainable development challenges – Gdynia case study, Safety of sea transportation: marine navigation and safety of sea transportation, edited by Weintrit A.& Neumann T., Taylor&Francis Group, London, UK.

Schaffers H., Komninos N., Pallot M., Trousse B., Nilsson M., Oliveira A., Smart Cities and the Future Internet: Towards Cooperation Frameworks for Open Innovation Hans, Retrived April 5, 2018, from: https://link.springer.com/chapter/10.1007/978-3-642-20898-0_31

Skirienė, A. F., & Stasiškienė, Ž. (2021). COVID-19 and air pollution: Measuring pandemic impact to air quality in five European countries. Atmosphere, 12(3). https://doi.org/10.3390/atmos12030290

Strulak-Wójcikiewicz, R., & Lemke, J. (2019). Concept of a simulation model for assessing the sustainable development of urban transport. Transportation Research Procedia, 39, 502–513. https://doi.org/10.1016/j.trpro.2019.06.052

Studzieniecki T. (2016). The development of cross-border cooperation in an EU macroregion – a case study of the Baltic Sea Region, Elsevier, Procedia Economics and Finance 39. Sustainable urban mobility and the smart citypolis. Cities and regions networking for innovative

Sustainable Urban Mobility and the Smart City, Retrived April 5, 2018, from: http://www.fifrontiercities.

Torre, T., Braccini, A. M., & Spinelli, R. (2016). Empowering Organizations: Enabling Platforms and Artefacts. 11, 315. https://doi.org/10.1007/978-3-319-23784-8

United Nations. (2014). Department of Economic and Social Affairs, Population Division, World Urbanization Prospects: The 2014 Revision, Highlights, New York.

United.Nations. (2023). Goal 11: Sustainable Cities and Communities. https://www.undp.org/content/undp/en/%0Ahome/sustainable-development-goals/goal-11-sustainable-cities-and-communities.html

Wefering F., Rupprecht S., Bührmann S., & Böhler-Baedeker S (Rupprecht Consult — Forschung

Zawieska, J., & Pieriegud, J. (2018). Smart city as a tool for sustainable mobility and transport decarbonisation. In Transport Policy (Vol. 63). https://doi.org/10.1016/j.tranpol.2017.11.004

7th Intercontinental Geoinformation Days

igd.mersin.edu.tr

Evaluating land use plans in line with climate change adaptation policies in the Semnan Urban Region

Vahid Isazade *1, Abdul Baser Qasimi 2, Taher Parizadi 3 , Esmail Isazade 4

1Kharazmi University, Faculty Geographical Sciences, Department of Urban planning, Tehran, Iran
2Samangan University, Faculty Education, Department of Geography, Aibak, Afghanistan
3 Kharazmi University, Faculty Geographical Sciences, Department of Urban planning, Tehran, Iran
4 Tarbiat modares University, Faculty Humanities, Department of Urban planning, Tehran, Iran

Keywords
Climate Change
Governance
Adaptation
Urban Planning
Multi-Level

Abstract

Climate change in developing countries is more exposed to the risks of climate change due to lack of adaptation capacity, economy dependent on climate-sensitive sectors, gaps in policies caused by central governments, weak institutions and lack of learning adaptation strategies. This article examines the relationship between land use systems as one of the intervention areas of multi-level climate governance and the policy of adapting to different governance methods in this area. This article also introduces the conceptual model of the compatibility of the land management system and the multi-level climate governance framework, from the documentary research method and the systematic review of texts in the form of documents, laws and programs prepared for urban and suburban development in Semnan urban complex in two decades. Examines the latter. The results showed that Regulating the development process of Semnan city based on climate, and environmental considerations, considering natural hazard management and climate change, improving the level of development sustainability through comprehensive ecological management based on a participatory approach, emphasizing desertification control, water conservation, and protection of Soil, air and vegetation, its optimal use, especially in the northern margin of Iran, The climate change fact is intensive among the Middle Eastern countries and especially Iran

1. Introduction

The history of development planning in Iran is more than six decades and planning in general and land use planning in particular at this time under the influence of economic, social, and political conditions has always been associated with the changes (Ghanbari et al., 2022; Akbari, 2016; Attarchi et al., 2020). In this regard, the realization of local governance as a new concept in rural-urban management is very important (Isazade et al., 2021). Local governance and the formation of new scales over the last few decades have caused local governance to face new challenges (Isazade et al., 2021; Qasimi et al., 2023).

The increasing availability of geo-referenced data on subnational entities provides a unique opportunity to link geographical features of local areas in resource-rich countries to administrative, household, and individual data (Isazade et al., 2022; Qasimi et al., 2023).

The literature touches upon urban climate goals indirectly, and mostly by pointing to the gap between intentions and practices in current urban governance (vander Heijden, 2019; Isazade et al, 2023), recent studies have shown that climate change, including changes in precipitation and temperature patterns, has caused hydrological changes in Iran (Heidari et al., 2018; Qasimi et al., 2023; Isazade et al., 2022; Ghanbari et al., 2022).

The Semnan urban complex is also exposed to the consequences related to vulnerabilities of temperature changes and changes in precipitation in this category and according to the forecast of the Intergovernmental Panel on Climate Change, by 2100 AD, Iran will increase the average temperature above 5 degrees Celsius and Will experience a 10 to 20 per cent decrease in rainfall. The international level should act as an integrated mechanism to the local level, providing a wide range of possible vertical and horizontal interactions in different parts of the governance framework. In the meantime, what is the basis of this research is to establish the relationship between land use systems as one of the areas of intervention of multilevel climate governance and adaptation policy and different methods of governance in this area. According to the research

* **Corresponding Author**

*(Vahidisazade75@gmail.com) ORCID ID 0000-0002-6348-4028
(qasimi.abdul.a@gmail.com) ORCID ID 0000-0001-9180-831X
(tparizadi@khu.ac.ir) ORCID ID 0000-0001-8303-1723
(ismailisazadeh75@gmail.com) ORCID ID 0000-0002-3825-7739

Cite this study

Isazade, V., Qasimi, A. B., Parizadi, T., & Isazade, E. (2023). Evaluating land use plans in line with climate change adaptation policies in the Semnan Urban Region. Intercontinental Geoinformation Days (IGD), 7, 271-274, Peshawar, Pakistan

literature, research has been done in line with this research; for example.

Stehle et al. (2020) in the article entitled Urban Climate Politics in Emerging Economies: A Multi-Level Governance Perspective article explores the vertical and horizontal integration of cities' climate actions in the multi-level climate governance landscapes in Brazil, India, Indonesia, and South Africa.

Vedeld et al. (2021) Drawing upon two strains of climate governance and collaborative governance literature, respectively, this article adopts a polycentric approach to the analysis of Oslo's urban climate governance. It unpacks the relationships between urban leadership, climate goal-setting, and institutional design, and reveals how these variables condition the employment of a combination of integrative and interactive governing instruments that foster both self-governance and co-creation in climate responses.

2. Method

In this study, the method of documentary research and the technique of systematic review of texts in the form of documents, laws, and programs prepared for urban and suburban development in the Semnan urban complex during the last two decades were used. In this regard, after extracting, classifying, and reducing the data in the mentioned projects, the data were analyzed and the compliance of the explained programs with the climate change adaptation policies was investigated. The scale of measurement in the method was the Likert spectrum and the degree of adaptability was done in 5 levels (fully compliant, relatively compliant, partially compliant, relatively non-compliant, and completely non-compliant).

The validity of the answers is based on the audit method and the expert opinions of experts. Among the documents and plans related to the subject under study and at national, regional, and regional levels in the last decade, we obtained 3 documents (Table 1) which were reviewed.

Table 1. Documents examined in documentary analysis

Approval reference	Operational level	Year of plan approval	Documents reviewed
Supreme Council of Land Management	National	2020	Iran land use document
Iran Program and Budget Organization	Regional	2019	Semnan land use document
Supreme Council of Urban Planning and Architecture of Iran	District	2012	Semnan Urban Complex plan

2.1. Study Area

Semnan urban area, including the urban complex formed from the links of urban structure between the cities of Sorkheh, Semnan, Darzin, Mahdishahr, and Shahmirzad - the city of Semnan, has provincial, national and transnational functions. Semnan is one of the cities of Iran, the capital of the province, and the city of Semnan (Figure 1). This city is located in the south of the Alborz Mountain range and north of the central desert plain of Iran, at a distance of 216 km from Tehran (the capital of Iran). And is located 34 minutes away. The city is bounded on the north by the cities of Darjazin, Mahdishahr on the west by the city of Sorkheh, and on the east by the city of Dam Ghan.

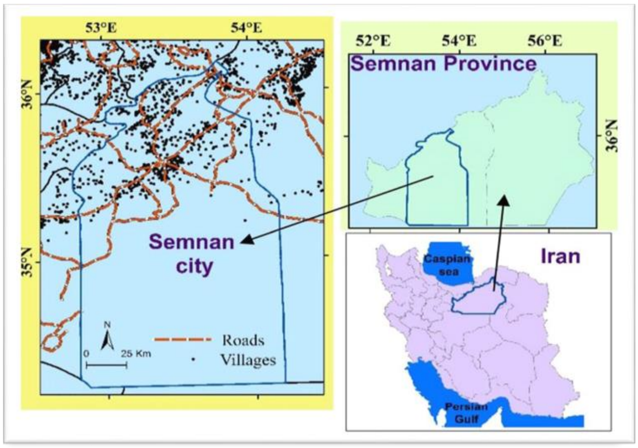

Figure 1. Range and location of the study area

2.2. Land use planning in IRAN

Iran enjoys the experience of six decades of development planning. During this period, planning in general and land use in particular have gone through many changes and modifications due to the economic, social, and political circumstances of the country (Figure 2). In the land management plan of Iran, Semnan province, the policy of attracting surplus population and overflow of Tehran, Mazandaran and Golestan provinces has been emphasized by undertaking part of the industrial and service activities of these provinces (Isazade et al., 2022).

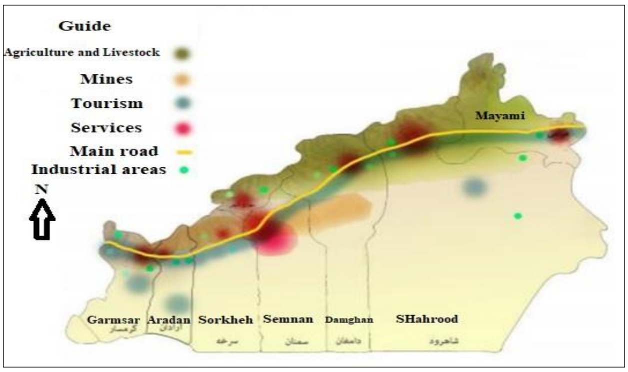

Figure 2. Optimal space organization on the horizon 2045

3. Results

The results showed that the document contains 24 territorial strategies and 254 territorial policies. The territorial strategy determines the main and long-term direction of the spatial development of the territory by considering the capabilities, opportunities and limitations in facing challenges to achieve the desired spatial development goals of the territory, and the territorial policy reflects the policy of implementing the spatial development strategies. It is a land. (Figure 3). Based on the topics studied, this document has considered different roles for this area in the study area (Semnan urban area), which are:

• Logistics center
• The region is prone to producing renewable energy (wind and solar).
• Level one and two level service axis of the city in the residential system Areas prone to special strategic and industrial development.
• Located at 4 communication crossings North-South, East-West, Trisica and Echo
• Managed areas affected by dust
• Establishment of industrial activity in the field of production of electronic, computer and optical machines and pharmaceutical products.

Also, out of 24 land strategies, 8 strategies were related to environmental issues, land use, and land use-related activities. Below these 8 territorial strategies, 21 territorial policies related to the mentioned topics have been identified and are listed in (Table 2). The compatibility of the policies extracted in this document with the policies of adaptation to climate change was examined (Figure 3).

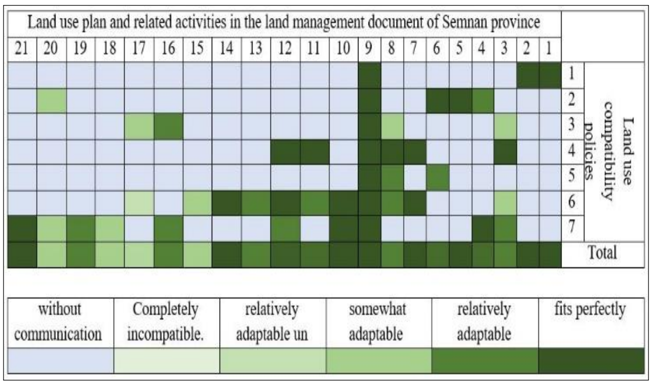

Figure 3. Assessing the Conformity of Compatibility Plans and Policies and Land Use Plan and Related Activities in the National Land Use Document

Based on the results, the degree of compliance of the program in the field of land use and climate change adaptation policies was estimated to be relatively consistent, indicating the high degree of compliance of this document in the field of land use, environment, and related activities. With climate change adaptation policies. Policy No. 9 in the National Land Use Management Document, which refers to the formulation and implementation of climate change adaptation programs in various fields, including water, agriculture and food security, health, tourism, natural ecosystems, etc., specifically states It focuses on adaptation to climate change, which shows the importance of this issue in legislation.

4. Discussion

The objectives identified in the land management document of Semnan province have been formulated in several sections: the objectives of the upstream documents, the objectives of the problem, and the objectives of the value, the basic objectives of the planning of Semnan province are as follows:

1. Improving connectivity and strengthening the joint role of the province in the trans-regional transport network

2. Upgrading and transitioning from corridor spatial development to spatial spatial development 3. Promoting spatial and inter-territorial justice in the development process of the province

4. Improving the rate, diversity and productivity of productive and sustainable employment

5. Development of institutional capacities Development and planning of the main actors of the province

6. Reducing and refining the intensity and quality of dependence of economic activities on natural and climatic resources

7. Promoting the sustainability of natural resources, especially water, soil, and desert resources 8. Control and reduce the risk of residential, activity and communication areas against natural hazards (Qasimi et al., 2023).

This document contains 11 territorial strategies and 86 territorial policies. Territorial development policies of the province are based on the strategies developed for the development of the province, which focus on redefining the system of population and activity in the province and form the policy framework for the development of service and production infrastructure. Semnan province planning research studies and utilizing the achievements of physical plan research in Semnan province, the zoning of planning areas in Semnan province; including two macro-western planning areas, to the center of the east, to the center of the city, it is located in the center of Shahroud city. The province has two prominent populations this document has considered different roles and specializations for this area in the study area (Semnan urban area) based on the studied subjects (Figure 4).

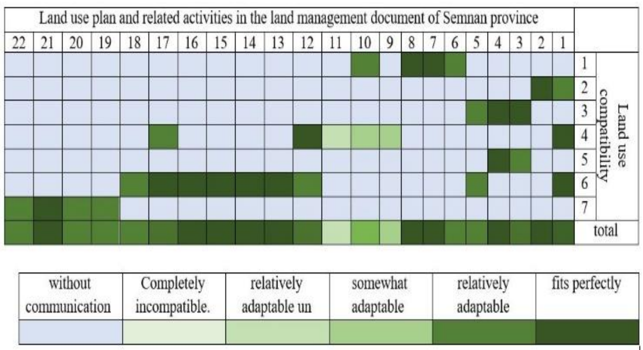

Figure 4. Assessing the compliance of adaptation programs and policies and land use program and related activities in the land management document of Semnan province

5. Conclusion

Regulating the development process of Semnan city based on climatic and environmental considerations with regard to the management of natural hazards and climate changes, improving the level of development sustainability through comprehensive ecological management based on a collaborative approach, emphasizing desertification control, water conservation and soil protection. Air and vegetation, its optimal use, especially in the northern border of Iran, the reality of climate change among the countries of the Middle East and especially Iran is severe. Considering the characteristics of multi-level governance and due to the weakness in the body of the land development system, whether in the field of policy making and performance in the urban area of Semnan in general or the weakness in facing climate changes in the city of Semnan in particular, using New management approaches in this field, such as multi-level climate governance, can be helpful.

The establishment of such a system requires the identification of effective actors and stakeholders and the examination of the capacities and governance methods that can be used in this region and its compatibility with the land development system. Considering the current situation of the Semnan urban area and also because land preparation is considered the most important tool of city managers and policy makers in facing climate changes in the Semnan urban area.

Acknowledgement

The authors are grateful to the reviewers of the article.

References

Akbari, Y., Imani Jajarmi, H., & Rostamalizadeh, V. (2016). Analysis of land use barriers in Iran. Science and Technology Policy Letters, 6(3), 5-13.

Attarchi, S., Poorrahimi, M., & Isazade, V. (2020). Comparison of spectral indices and object-based classification for built-up area extraction in different urban areas. Geographical Urban Planning Research (GUPR), 8(1), 23-43.

Ghanbari, A., Isazade, V., & Alibeigy, Z. (2022). Analysis of Spatial Justice in Dealing with Urban Facilities Using Quantitative, Spatial and Moran Correlation Models (Study Area: Isfahan). Journal Research and Urban Planning, 13(50), 240-254.

Ghanbari, A., Isazade, V., Isazade, E., & Seraj, K. (2022). Modeling of access and spatial mobility changes associated with floods in the field of transportation and movement of vehicles in areas 3, 6 and 7 of Tehran. Intercontinental Geoinformation Days, 4, 62-67.

Heidari, M., Khazaei, M. R., & Akhtari, A. A. (2018). Impacts of Climate Change on climate variables and catchment stream-flow, using HBV model under BCM2 Scenarios. Irrigation and Water Engineering, 8(2), 129-139.

İsazade, V., Ghanbari, A., & Kamran, K. V. (2022). Evaluation of spectral indices and extraction of constructed and non-constructed urban features and its comparison with ground surface temperature using Landsat 7 and 8 satellite images (Study area, Tehran). Geographical Planning of Space, 11(42), 23-39. doi: 10.30488/gps.2021.243118.3283.

Isazade, V., Qasimi, A. B., & Kaplan, G. (2021). Investigation of the effects of salt dust caused by drying of Urmia Lake on the sustainability of urban environments. J. Clean WAS, 5(2), 78-84. http://doi.org/10.26480/jcleanwas.02.2021.78.84.

Isazade, V., Qasimi, A. B., Seraj, K., & Isazade, E. (2022). Spatial modeling of air pollutant concentrations using GWR And ANFIS Models in Tehran city. Environ Contam Rev, 5(2), 72-78. https://doi.org/10.26480/ecr.02.2022.78.84.

Isazade, V., Qasimi, A. B., & Isazade, E. (2023). Environmental dust effect phenomenon on the sustainability of urban areas using remote sensing data in GEE. Safety in Extreme Environments, 5(1), 59-67. https://doi.org/10.1007/s42797-022-00067-z.

Isazade, V., Toomanian, A., & Isazade, E. (2021). The Effect of Drought Phenomenon on the Surface of Groundwater Aquifer in Qazvin Plain in Iran. Journal of Geoinformatics & Environmental Research, 2(02), 103-112.

Qasimi, A. B., Isazade, V., Enayat, E., Nadry, Z., & Majidi, A. H. (2023). Landslide susceptibility mapping in Badakhshan province, Afghanistan: A comparative study of machine learning algorithms. Geocarto International, 38(1), 2248082.

Qasimi, A. B., Isazade, V., & Berndtsson, R. (2023). Flood susceptibility prediction using MaxEnt and frequency ratio modeling for Kokcha River in Afghanistan. Natural Hazards. https://doi.org/10.1007/s11069-023-06232-2.

Qasimi A., Isazade V., Kaplan G., Nadry Z. (2023). Spatiotemporal and multi-sensor analysis of surface temperature, NDVI, and precipitation using google earth engine cloud computing platform. Russian Journal of Earth Sciences. (6), 1-12. DOI: https://doi.org/10.2205/2022ES000812 Retrived from (Date of access 25.11.2023).

Qasimi, A. B., Toomanian, A., Nasri, F., & Samany, N. N. (2023). Genetic algorithms-based optimal site selection of solar PV in the north of Afghanistan. International Journal of Sustainable Energy, 42(1), 929-953.

Stehle, F., Hickmann, T., Lederer, M., & Höhne, C. (2022). Urban climate politics in emerging economies: a multi-level governance perspective. Urbanisation, 7(1_suppl), S9-S25.

Vedeld, T., Coly, A., Ndour, N. M., & Hellevik, S. (2016). Climate adaptation at what scale? Multi-level governance, resilience, and coproduction in Saint Louis, Senegal. Natural Hazards, 82, 173-199.

Vedeld, T., Hofstad, H., Solli, H., & Hanssen, G. S. (2021). Polycentric urban climate governance: Creating synergies between integrative and interactive governance in Oslo. Environmental policy and governance, 31(4), 347-360.

7th Intercontinental Geoinformation Days

igd.mersin.edu.tr

Preventive measures in disaster management can make the difference

Lucrezia Vittoria Natale[1], **Donato Abruzzese** [2]

[1]University of Rome "Tor Vergata", Department of Economy and Finance, Rome, Italy
[2]University of Rome "Tor Vergata", Department of Civil Engineering and Computer Sciences, Rome, Italy

Keywords
Natural Disaster
Disaster management
Flooding
Disaster prevention
Economy of Disaster

Abstract

Coping with the consequences and losses caused by natural disasters is one of the most pressing issues that humanity is often facing. Addressing this challenge involves different strategies, from prevention and reaction plans to adaptation and mitigation projects. Preventive measures can be seen as the most effective way to prevent loss of life and damage to property. These encompass building codes, land use, and environmental conservation efforts, as well as less tangible activities linked to education and awareness. The paper shows some of the possible ways to create effective natural disaster management, with a set of ex-ante measures which are particularly focused on prevention methods. Highlighting their importance does not mean denigrating ex-post activities. Rather, an impactful approach should integrate these two typologies of measures and avoid an excessive reliance on insurance alone. Indeed, by investing in prevention, communities can substantially reduce their vulnerability and exposure. Examples drawn from experience with flooding events are also provided for a more concrete understanding.

1. Introduction

The damage caused by natural disasters can be examined from different perspectives: environmental damage, economic repercussions, and the disruption of livelihoods and lives.

The graph below can give insights into the overall damages caused by such phenomena. Indeed, it shows the financial value losses given by natural disasters by GDP (with normalisation) in Europe.

Natural disasters may never be eliminated, but their risk can be reduced or mitigated through risk management. From an ex-ante perspective, risk prevention, financial protection, and preparedness are crucial. Conversely, from an ex-post perspective, what matters most is the possibility of resilient reconstruction, socio-economic recovery, and response.

During the past decades, the intensity of natural disasters appears to have increased with dramatic consequences. In their Global Assessment Report (GAR2022), the United Nations reveal *"…that between 350 and 500 medium-to-large-scale disasters took place every year over the past two decades."* Moreover, the report predicts that, by 2030, this number will reach 560 events a year, meaning a frequency of 1.5 disasters a day. This data shows the urgency surrounding natural disasters management and the paramount importance of learning how to cope with their increasing prevalence and scale.

Decision-makers typically employ two types of approaches when creating public policies addressing these concerns. The first one may be referred to as a "passive" protection for communities which are encouraged to rely on insurance coverage to face natural disaster recovery. The other, which is more comprehensive and complete, includes investing on the territorial assets before the disaster occurs, thus embodying a proactive and preventive approach.

Given the rise in frequency and intensity of natural disasters, coping measures must primarily focus on mitigating potential damages before they occur. Creating an effective risk management strategy implies the use of both approaches, since taking into account that the sole reliance on ex-post measures and insurance is insufficient to address the problem.

2. The Role of Citizens and the Government

2.1. The Impact on Exposure and Vulnerability

In the field of natural disaster prevention, promoting useful preventive practices is one of the main tasks of governments, at the national and at the local levels. Their overall objective is to reduce the vulnerability and the exposure of communities. The

* **Corresponding Author**

(lucrezia.natale@icloud.com) ORCID 0009-0004-7160-9232
(abruzzese@uniroma2.it) ORCID ID 0000-0003-0798-5239

Cite this study

Natale, L. V. & Abruzzese, D. (2023). Preventive measures in disaster management can make the difference. Intercontinental Geoinformation Days (IGD), 7, 275-278, Peshawar, Pakistan

latter element of risk can be defined as the people and elements which are present in hazard zones, and which are, therefore, subject to potential losses. As stated by the World Health Organisation (WHO), "*Populations and societies need to be exposed to a hazard to be affected by it.*" Moreover, vulnerability must also be considered: according to the United Nations Office for Risk Reduction (UNDRR), *vulnerability* refers to *"…the conditions determined by physical, social, economic and environmental factors or processes which increase the susceptibility of an individual, a community, assets or systems to the impacts of hazards.*" Ultimately, understanding the role and level of vulnerability and exposure in each area is key to envisaging the right type of preventive measures to implement.

Vulnerability depends on a range of factors. As affirmed by the WHO, these include physical, social, economic, and environmental elements such as the proximity to a potentially hazardous event, public education and awareness of the hazard, building codes and land use, and public infrastructures. This is why it is the responsibility and duty of public authorities to enforce measures and laws that prevent, as for instance thinking to the floodings and earthquakes, the misuse of land and resources while promoting natural disaster education.

2.2. The role of citizens: choosing where to build and where to live

Since some areas are more vulnerable than others, it is crucial that citizens carefully select the places where they build and live. Recently, increased urbanisation has become ever more evident. According to The World Urbanisation Prospect, in their 2014 revision, 54% of the world population lives in urban areas, and the United Nations estimate this number to increase to between 60% and 70% by 2050. Also, according to the World Bank, urbanisation is one of the factors increasing exposure and vulnerability to natural disasters.

The first reason is the case is that urban sprawl does not always consider the vulnerability and exposure of certain areas. Indeed, some towns may be near rivers prone to flooding in case of heavy rain or on steep slopes subject to landslide risk. It is important for citizens to be informed about the specific risks and the types of disasters affecting a given territory, opting for safe areas where to work and live.

However, people do not always have the privilege and the chance to choose where to live. This is the case especially in low-income countries, where, according to the European Commission, one billion people live in hazardous areas, equivalent to 42% of the total population. These findings highlight the need for enhanced public awareness campaigns and government incentives to prevent the persistence of this situation.

2.3. The Role of the Government: Regulate Urbanisation and Spread Awareness

While completely avoiding disasters may not always be possible, citizens can take action to be ready for when disasters strike. These preparatory measures significantly contribute to limit the negative aftermath of disasters, containing injuries and casualties.

Governments have a central role in this: they should provide adequate knowledge and tools to prepare for disasters. Without their resources, the efforts of individual citizens would not have enough impact to make a difference.

The most evident field in which their role can have an impact is urbanisation and urban planning. Indeed, while it is true that citizens should be conscious when choosing where to reside, governments should also forbid to building in areas which are defined as risk-prone by experts such as geologists. According to a paper published by UNDRR, "*Weak regulation, for instance the lack of enforcement of building codes, planning permission and regulatory investment, often linked to corruption, allow the transfer of risk from construction companies to those who live and work in the buildings*." The same paper reveals alarming figures relating to this problem: 90% of low-income families in urban areas live in unsafe and exposed housing.

Governments can actively coordinate and take action in the urban planning process, which involves a diversified series of actors, including investors, landowners, and regulators. The development of an adequate urban project, documentation and analysis of sites, and post-completion maintenance are key. Laws regulating and setting limits to soil consumption and building are essential.

3. The Role of Excessive Urbanisation

3.1. The Risks Linked to a Misuse of Soil

The soil has the capacity to store CO^2 and absorb water. This is why artificially changing soil characteristics is risky and can exacerbate the negative outcomes of natural disasters. Urbanisation needs to replace natural land cover with impermeable materials such as asphalt, reducing the soil's capacity to store water. This is how floods can take place: either due to a stagnation of water or due to the destructiveness of excessive water runoff in steep slopes.

Pakistan is an example of this dramatic tendency: only 5% of land is currently covered in forests (Shahbaz et al., 2007). Just as worrying is the fact that, according to The World Bank, this country has the highest deforestation rate in South Asia.

3.2. A New Approach to Urban Contexts

Despite the alarming data regarding urbanization and deforestation, some innovative solutions to reduce natural disaster risk in urban contexts are possible. In particular, when it comes to geo-hydrological risk, Nature-Based Solutions (NBS) can have a positive impact. These integrate natural elements into urban water management. Typical examples of NBS alternatives are green roofs, gardens, dry retention ponds, and permeable pavements (Vojinovic et al., 2021). Governments may be reticent to this kind of approach and may want to invest in interventions that generate shorter-term results. Since their adoption is not widespread, further research on the topic is needed

However, there are some studies have already been made which highlight their benefits. To this regard, the SaferPaces project is an interesting global platform that can be used as a model. Co-funded by the EIT Climate-KIC, a European Innovation and Technology Institute section, and coordinated by different entities, universities, GECOsistema srl, and other private companies, it is already working in Milan (Italy), Pamplona (Spain), Cologne (Germany), and Rimini (Italy).

This project has contributed to the creation of the project "Parco del Mare", based on NBS, on Rimini's coasts, whose building works have started in autumn 2023. The pictures, which show the impact the Parco del Mare will have in preventing town flooding, clearly demonstrate the potential of this innovation.

Figure 1. Scenario of foreseen floodings by 2050 without and with the Parco del Mare project in Rimini, Source: Legambiente, Italy

4. Insurance as a Means of Protection

4.1. The Role of Insurance for Natural Disasters

Nowadays, trends seem to emphasise funds and insurance for natural disasters, focusing less on concrete prevention plans. Funds and insurance play a crucial role when it comes to efficiently starting a recovery process in the aftermath of a natural disaster. Although some studies do portray funds and insurance as the most suitable solutions, it is nonetheless crucial to recognise the complexity of the issue.

It is, however, true that citizens residing in high-risk zones frequently express a willingness to rely on insurance to mitigate the uncertainties associated with losses generated by natural disasters. India is an example of this trend: according to a record published in 2009 by the World Wide Fund for Nature (WWF) and Allianz, due to climate change, insurance claims have surged, reaching a peak during the 2005 unprecedented rainfall in Mumbai (Lenton et al., 2009).

While beneficial for recovery, funds and insurance, are not a solution by themselves. They neither substitute the lack of legislative measures supporting prevention, nor do they reduce the vulnerability of the population. In other words, they do not offer practical solutions to fixing the consequences of natural disasters or prevent them; preventive measures remain the most effective solution.

4.2. The Limits of Insurance

Indeed, insurance presents a series of criticalities. For example, given the unprecedented frequency and scale of disasters, in the coming years, insurance companies might have to raise their rates. This increase may make insurance premiums so expensive as to become increasingly unaffordable for many. Secondly, the possibility of an increase in dishonest (fraudulent) insurance claims, possibly stemming from a rise in poverty as one of the consequences of climate change, should also be considered. What is more, insurance provides a temporary solution only at an individual level, and cannot compensate collective damages. This means that while an individual or a family may receive financial assistance to rebuild their personal property after a natural disaster, their broader community and environment will nonetheless remain adversely affected, making it difficult for the individual household to recover and for local economy to restart in any significant way.

5. Conclusion

Natural disasters pose a significant challenge to humanity. During the past decades, people and authorities have underrated problems related to them: for example, irresponsible urbanization policies have, if anything, exacerbated them. Natural land cover was replaced by surfaces made by concrete and asphalt which reduced soil drainage capacity, thus increasing the risk of floods in many areas, and a bad construction policy can lead to seismic potentially vulnerable buildings and infrastructures.

Insurance is a crucial means to start an efficient recovery stage after the disaster occurs, but the sustainability of this system, in the long run, is unfeasible and it does not eradicate the underlying risk.

However, there is still an opportunity to take preventive measures: testing NBS in urban environments and conducting further research is crucial to highlight their benefits as local governments may be persuaded to implement them. Governments, and various organisations, as well as local institutions, also need to spread disaster prevention and reaction awareness and knowledge to citizens. Ensuring that populations are well-informed about the risks they face is essential enable them to make informed decisions when aware and facing natural disasters.

References

European Commission, "The Future of Cities." urban.jrc.ec.europa.eu/thefutureofcities/the-resilien-city#:~:text=One%20billion%20

GAR2022: (2022). Our World at Risk (GAR) | UNDRR."Www.undrr.org, 26 Apr. 2022, www.undrr.org/gar/gar2022-our-world-risk-gar#container-downloads.

Lenton, T., Footitt, A. & Dlugolecki, A. (2009). Major Tipping Points in the Earth's Climate System and Consequences for the Insurance Sector. people%20live%20in.

Shahbaz, B., T. Ali, and A. Q. Suleri. (2007). A Critical Analysis of Forest Policies of Pakistan: Implications for Sustainable Livelihoods. Mitigation and Adaptation Strategies for Global Change 12: 441–453. doi: 10.1007/s11027-006-9050-9

UNDRR. "Poorly Planned Urban Development". Www.preventionweb.net, 2013,

UNDRR. Vulnerability. www.undrr.org. Available at: https://www.undrr.org/terminology/vulnerability.

United Nations. "68% of the World Population Projected to Live in Urban Areas by 2050, Says UN. "United Nations Department of Economic and Social Affairs, United Nations, 16 May 2018, www.un.org/ development/ desa/en/news/population/2018-revision-of-world-urbanization-prospects.html.

United Nations. "World Urbanization Prospects-Population Division- United Nations. "Un.org, 2018, population.un.org/wup/.

Vojinovic, Z., Alves, A., Gómez, J.P., Weesakul, S., Keerakamolchai, W., Meesuk, V. and Sanchez, A. (2021). Effectiveness of small- and large-scale Nature-Based Solutions for flood mitigation: The case of Ayutthaya, Thailand. Science of The Total Environment, 789, p.147725. 10.1016/ j.scitotenv.2021.147725

Wahba Tadros, S. N., et al. "Demographic Trends and Urbanization", World Bank, 2021, documents. worldbank.org/en/publication/documents-reports/documentdetail/260581617988607640/demographic-trends-and-urbanization.

World Bank. (2013). Forest Carbon Relationships. Washington, DC: World Bank.

World Health Organization. (2021). "Guidance on Research Methods for Health Emergency and Disaster Risk Management". 3.2 Disaster Risk Factors -Hazards, Exposure and Vulnerability.

World Urbanization Prospects – (2018). Population Division- United Nations. Un.org, 2018, population.un.org/wup/.

7th Intercontinental Geoinformation Days

igd.mersin.edu.tr

Utilizing photogrammetry for forest rehabilitation assessment: Remote sensing techniques applied to Mt Rubavu in Rubavu District, Rwanda

Sabato Nzamwita [1], Isaac Nzayisenga *[1], Patience Manizabayo [1]

[1] *University of Rwanda, Urban Planning, Spatial Planning, Kigali City, Rwanda*

Keywords
Forest Rehabilitation
Photogrammetric Images
GIS and Remote sensing
Spatiotemporal Change
Forest Management

Abstract

Forest rehabilitation has gained popularity in an era of unprecedented rapid urban growth for sustainable development. Monitoring forest restoration using geospatial technologies has recently attracted many researchers' attention. In Rwanda, GIS and remote sensing have been proven to be useful tools in monitoring rehabilitated forest landscapes. The current work assumes to monitor the spatiotemporal change of the rehabilitated artificial forest of Mount Ruvubu near Rubavu city using advanced photogrammetric images and Geographic Information System (GIS) techniques across three distinct time periods: 2005, 2010, and 2015. The results revealed that forest encroachment increased from 23.5 hectares in 2005 to 23.9 in 2010, followed by a significant reversal of this trend in 2015. The NDVI imagery provides a visual representation of these changes, highlighting encroachment in the western and southwest parts of the forest in 2005 and 2010, and successful rehabilitation in the central and western regions in 2015. All in all, the study demonstrates the effectiveness of remote sensing and GIS in monitoring forest cover and rehabilitation efforts. These technologies are essential in sustainable forest management, offering valuable insights into areas that require immediate attention. GIS and remote sensing are crucial for protecting forest benefits for society and the environment.

1. Introduction

Globally, forests are vital natural assets that support biodiversity, provide food for the human population, and contribute to economic livelihoods(Kinoti & Mwende, 2019). Urban forests are often called "the green lungs" of city ecosystems, providing substantial social, economic, and environmental benefits to urban dwellers. However, rapid urbanization has led to the rapid decline of urban forests and environmental degradation in pursuing socio-economic growth(Kojo & Paschal, 2018).

In the early 21st century, forest conservation has gained substantial attention globally. The United Nations Millennium Development Goals and the United Nations Framework Convention on Climate Change (UNFCCC) have underlined the essential role of forest preservation in pursuing sustainable development. Moreover, introducing Sustainable Development Goals (SDGs), particularly Goal 15 and the Aichi targets, has reinforced the efforts (Duguma et al., 2019).

Recently, researchers have turned their attention to monitoring the dynamic of spatiotemporal land use and land cover (LULC) change using geospatial technology. Several studies have emphasized the essential role of GIS and Remote Sensing in monitoring forest rehabilitation programs to ensure their effectiveness. Geospatial data, GIS and Remote Sensing techniques create meaningful thematic forestry maps, yielding quantitative evidence on forest cover, deforestation, and biophysical aspects (Avtar et al., 2017).

In Rwanda, GIS and remote sensing have been useful in monitoring forest cover changes and restoration outcomes, specifically in Gishwati-Mukura National Park. However, no study has been done to monitor the artificial forest of Mt. Ruvavu adjacent to Rubavu City following the relocation of the encroached forest rehabilitation practices in 2010 for forest management. Therefore, this work aims to utilize photogrammetric images and GIS techniques to monitor forest cover change on Mount Rubavu in three-time series: 2005, 2010, and 2015.

* **Corresponding Authors**

*(nzayisaac85@gmail.com) https://orcid.org/0009-0009-2284-9834
(manizabayopatience08@gmail.com) https://orcid.org/0009-0000-5283-5358
(nzamwitasabbath@gmail.com) https://orcid.org/0009-0004-7138-0386

Cite this study

Nzamwita, S., Nzayisenga, I., & Manizabayo, P. (2023). Utilizing photogrammetry for forest rehabilitation assessment: Remote sensing techniques applied to Mt Rubavu in Rubavu District, Rwanda. Intercontinental Geoinformation Days (IGD), 7, 279-281, Peshawar, Pakistan

2. Method

2.1. The study area description

Rubavu District is situated within a high-altitude mountainous area, predominantly in volcanic terrains, and is a constituent part of the Western Province. It is located approximately 145 kilometers from Kigali, the primary gateway to the Democratic Republic of Congo(Kubwimana, 2020). The region encompasses a total land area of 388.3 square kilometers, comprising 12 sectors, 80 cells, and 525 villages. The population density is recorded at 1,614 individuals per square kilometer, with a population count of 546,683 as of 2022(NISR, 2023). The choice of Mountain Rubavu, situated within the Gisenyi sector, was deliberate, and its approximate boundary encompassing an area of 20 square kilometers was meticulously digitized.

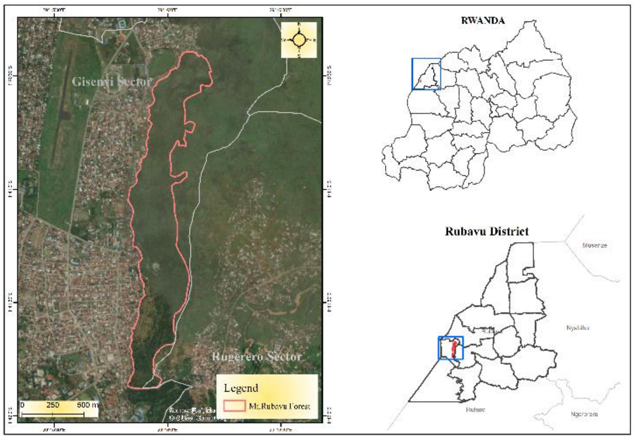

Figure 1. Location map of Mt Rubavu

2.2. Data source

The data employed in this work was meticulously acquired by integrating photogrammetric and remote sensing techniques facilitated by Google Earth Pro. These advanced methodologies were instrumental in bridging critical information gaps and enabling comprehensive geospatial analysis (NISR, 2023). Administrative shapefile data were sourced from DIVA-GIS, enriching the dataset with crucial administrative boundaries and geospatial information. This addition enhances the precision and contextual relevance of the dataset, ensuring a comprehensive understanding of Rubavu District's geographical and administrative landscape.

Figure 1. Data source table

Data	Time	Source
High-resolution images	2005, 2010, 2015	Google Earth Pro 7.3.6.9345 (64-bit)
NDVI	2005, 2010, 2015	https://ladsweb.modaps.eosdis.nasa.gov/
Administrative shapefiles	-	https://www.diva-gis.org/gdata

2.3. Data processing

The forest boundary on Mt. Rubavu was meticulously delineated through digitization using Google Earth Pro, ensuring precise demarcation. Additionally, the level of population encroachment onto the mountain was also digitized using the same tool, capturing data from three distinct time points: 2005, 2010, and 2015. Furthermore, Normalized Difference Vegetation Index (NDVI) values were derived by multiplying 0.0001 with the MOD13Q1 Vegetation Indices for each time frame. This NDVI data was subsequently compared with the encroachment levels to discern correlations or patterns. This comprehensive approach leverages advanced geospatial techniques to gain insights into forest cover dynamics and population impact on Mt. Rubavu over time.

3. Results

3.1. Forest encroachment results for 2005, 2010 and 2015

The forest encroachment rate increased from 2005 to 2010 but decreased significantly in 2015. In 2005, 23.5 hectares of forest were converted to other land uses, particularly informal residential, while 62 hectares remained unconverted. In 2010, the converted area increased to 23.9 hectares, while the unconverted area decreased to 61.6 hectares. However, in 2015, the converted area decreased sharply to 0 hectares, while the unconverted area increased to 85.5 hectares.

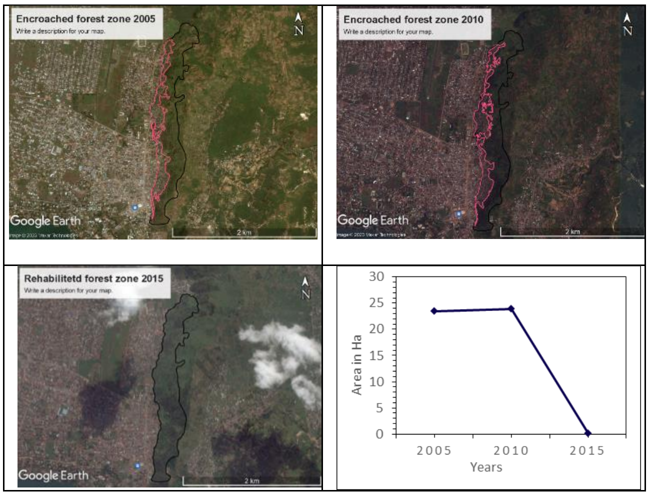

Figure 2. Forest encroachment level

3.2. NDVI change due to forest encroachment.

The NDVI image shows the study area in three different years: 2005, 2010, and 2015. The NDVI values range from -0.2 to 0.9995, with higher values indicating more vegetation cover. The NDVI image-based visualization is valuable for monitoring forest encroachment and rehabilitation. It can identify areas where the forest is at risk and where rehabilitation efforts are successful.

The following observations can be made from the NDVI image-based visualization: The encroachment in 2005 and 2010 is most evident in the western and southwest parts of the forest. However, the rehabilitation in 2015 is most evident in these parts of the forest where encroachment was prevalent. The rehabilitation efforts have restored the forest cover to its pre-encroachment levels.

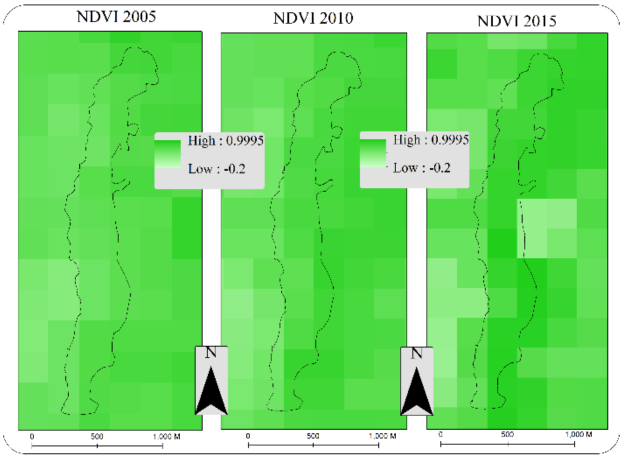

Figure 3. NDVI changes due to forest encroachment

4. Discussion

In the study area, the NDVI image-based visualization and accompanying table indicating forest encroachment trends point to a noteworthy shift toward sustainable forest management (Molnár & Király, 2023). The data emphasizes a substantial reduction in the rate of forest encroachment in recent years attributed to successful restoration initiatives. This positive trajectory indicates a shift towards a more environmentally sound management approach. Current monitoring and proactive measures to mitigate future encroachment are imperative to sustain this progress (Hallegatte et al., 2020). These may encompass heightened law enforcement, incentivizing conservation through economic means, and heightening awareness regarding the significance of sustainable forest management (Malik et al., 2020). By undertaking these measures, the stakeholders responsible for forest management can ensure its continued provision of societal and environmental benefits in the years ahead.

5. Conclusion

Remote sensing data can monitor changes in forest cover and tree health over time. This information can be used to identify areas where encroachment occurs and areas where rehabilitation efforts are needed. The successful implementation of sustainable forest management in the study area is a testament to the power of GIS and remote sensing. By integrating these technologies, forest managers have better understood the forest and make more informed decisions about managing it sustainably.

As we continue to face challenges such as climate change and population growth, the role of GIS and remote sensing in sustainable forest management will only become more important. By investing in these technologies and developing the skills to use them effectively, we can help ensure that our forests can provide their many benefits to society and the environment for generations to come.

References

Avtar, R., Kumar, P., Oono, A., Saraswat, C., Dorji, S., & Hlaing, Z. (2017). Potential application of remote sensing in monitoring ecosystem services of forests, mangroves and urban areas. Geocarto International, 32(8), 874–885.

Duguma, L. A., Atela, J., Minang, P. A., Ayana, A. N., Gizachew, B., Nzyoka, J. M., & Bernard, F. (2019). Deforestation and forest degradation as an environmental behavior: unpacking realities shaping community actions. Land, 8(2), 26.

Hallegatte, S., Rentschler, J., & Rozenberg, J. (2020). Adaptation principles.

Kinoti, K. D., & Mwende, K. M. (2019). Spatial-temporal assessment of forest rehabilitation along Mt. Kenya east forest buffer zone using remote sensing and GIS. Int J Environ Plann Dev, 5(1).

Kojo, R., & Paschal, N. (2018). Urban population growth and environmental sustainability in Nigeria. Journal of Empirical Studies, 5(1), 12–19.

Kubwimana, J. J. (2020). Risk Analysis of Vegetables Marketing in Rwanda, A case of carrots and cabbages produced in Rubavu District and supplied across the country. Journal of Agribusiness and Rural Development, 56(2). https://doi.org/10.17306/j.jard.2020.01326

Malik, S. Y., Cao, Y., Mughal, Y. H., Kundi, G. M., Mughal, M. H., & Ramayah, T. (2020). Pathways towards sustainability in organizations: Empirical evidence on the role of green human resource management practices and green intellectual capital. Sustainability, 12(8), 3228.

Molnár, T., & Király, G. (2023). Forest Monitoring Based on Sentinel-2 Satellite Imagery, Google Earth Engine Cloud Computing, and Machine Learning.

NISR. (2023). The Fifth Rwanda Population and Housing Census, Main Indicators Report. https://statistics.gov.rw/file/13787/download?token=gjjLyRXT

7th Intercontinental Geoinformation Days

igd.mersin.edu.tr

Groundwater analysis and management plan using integrated community perception and geo-spatial techniques in Wana, South Waziristan

Saddam Hussain *1, **Shakeel Mahmood** 1

[1]Government College University, Department of Geography, Lahore, Pakistan

Keywords
Ground water
GIS
NRCS
Wana
Dams

Abstract

Groundwater is one of the most valuable natural resources supporting human health and economic development. Globally, there has been an enormous stress on groundwater. In Pakistan, water shortage and decreasing groundwater level is one of the major issues. The groundwater assessment and management study has been conducted in Wana, South Waziristan using field survey and geospatial techniques. To achieve objectives, both primary and secondary data sources were used. The secondary data were acquired from concerned governmental departments. Primary data were collected through questionnaire survey, personal observations and Global Positioning System (GPS). Landsat ETM+ images were extracted to derive the land use land cover (LULC) of the area with four classes i.e., (Barren land, vegetation, built up and water bodies) through maximum likelihood (ML) technique. Soil map of the study area was digitized in Arc GIS 10.5. Inverse Distance Weighted (IDW) technique was applied to interpolate rainfall. Different parameters include rainfall analysis, land cover, soil group and geology were used to generate NRCS model. NRCS hydrological and watershed modeling were applied to calculate the estimation of surface runoff and stream network order. Forestation, check dams and embankments have been proposed in the management plan. The results show groundwater level in Wana has declined 13 feet in the last five years. There are multiple factors that led to water depletion. The groundwater level drops sharply in the areas where there are high population and where there is large agricultural land. The need of construction of large and small dams to maintain the cultivation of water intensive crops in Wana South Waziristan, which will be helpful in augmenting the groundwater level, stabilizing the climate and will also prevent the land from flooding. The results and findings of this study can assist researchers for future research and decision makers.

1. Introduction

The Groundwater is one of the most valuable natural resources supporting human health and economic development (Wang et al., 2020). Globally, there has been an enormous stress on groundwater. The over-exploitation of water resources is threatening the ecosystem (Khare et al., 2018; Harini et al., 2018). Unfortunately, the excessive use and mismanagement of groundwater resources have led to water shortages (Jackmen et al., 2016; Shen, 2015). The consequences of groundwater unsustainability are becoming evident and the concern is the maintenance of long-term yield from aquifers (Singh, 2013; Moore & Fisher, 2012). Groundwater extraction for agricultural and domestic uses in areas such as South Asia and other countries has depleted the aquifer system (Chatterjee et al., 2009; Amore, 2012).

Groundwater is poorly known and understood by the general masses and decision makers (Famiglietti, 2014). Globally, there has been an enormous stress on groundwater resources (Riemann et al., 2012). This stress has also been noted in Pakistan and specifically in Tehsil Wana, district South Waziristan. The local residents of Wana, South Waziristan use the water reservoirs for multi-purposes, i.e., irrigational purposes, domestic purposes, municipal uses, recreational purposes and fishing. This will help in the development of the local community (Zektser, 2004). The water availability fluctuates throughout the year. As the main source of income of the residents of the Wana is agriculture and horticulture therefore, it is imperative to store rainwater so that it can be used as a substitute for groundwater (Rahman & Parvin, 2009).

This research will address the following objective, to assess the spatio- temporal variation in groundwater table, to identify the groundwater recharging zones using NRCs hydrological model and finally to identify suitable sites for micro-level multipurpose dams.

* **Corresponding Author**

*(shakeelmahmoodkhan@gmail.com) ORCID ID 0000-0001-6909-0735

Cite this study

Hussain, S., & Mahmood, S. (2023). Groundwater analysis and management plan using integrated community perception and geo-spatial techniques in Wana, South Waziristan. Intercontinental Geoinformation Days (IGD), 7, 282-285, Peshawar, Pakistan

2. Method

In the research both primary and secondary data sources were used to achieve the desired objectives. The secondary data were acquired from concerned government departments and other private organizations. Primary data were collected through questionnaire, personal observations and Global Positioning System (GPS). Prior to field survey, field visits and meeting with local people were arranged to understand the problem of declining groundwater. Based on the initial visits, micro- level investigations and analysis of the severe affected areas were carried out.

Global positioning system (GPS) was used to acquire the geo-location of the well, the respondents and the distance between points.

Following software was used for this purpose, Google Earth, Arc GIS 10.1.

2.1. Watershed Modelling

Stream network was created within the watershed of study area. Stream and watershed lines throughout the entire watershed were determined. Different streams orders were generated to propose potential sites for construction of check dams and embankments.

Surface run-off depth (mm) was estimated by applying NRCS hydrological model and implemented in Arc GIS environment. The main inputs spatial layers in the NRCS hydrological model were land cover, hydrological soil group, and geology and rainfall pattern. Rainfall events (annul & monthly) of 29 years (1990-2019) were processed by applying Inverse Distance-Weighted Technique (IDW) to interpolate event rainfall. The CN value is extracted by combining hydrological soil groups and land cover spatial layers to quantify the surface run-off potential. The mathematical expression of NRCS hydrological model is shown in the Equation 1.

$$Q = \frac{(P - Ia)\ 2 + S}{P - Ia} \quad (1)$$

Where P is total rainfall (mm), Ia is initial abstraction, F is cumulative infiltration excluding Ia, Q is direct surface runoff (mm), S is potential maximum retention after rainfall begins. Ia is assumed to be correlated to S through the Equation 2.

$$Ia = 0.2\ S \quad (2)$$

The maximum retention is further related to the soil and land cover condition of the processed study area through CN by the Equation 3.

$$S = \frac{25{,}400 - 25}{CN} \quad (3)$$

Descriptive Statistical Analysis was performed on the data which was acquired primarily during field survey.

The management plan for groundwater has also been design in the study. Different input parameters were considered in designing the management plan. It includes rainfall analysis, land cover, soil group and geology of the study area. These input parameters were then put in GIS environment to generate NRCS model.

3. Results

3.1. Ground water Assessment

Age of water pumps installed is mentioned in (table 2). 41% water pumps were newly installed and 24.7% were installed the past 5 to 10 years. The remaining installed pumps are even older than 10 years which makes the percentage of the 32%.

Table 1. Age of water pump installation.

Serial No.	Categories	Frequency	Percentage
1	>5 Years	70	41.17
2	5-10 Years	42	24.7
3	>10 Years	58	32.11
	Total	170	100

Table 2. Capacity of water Pump.

Serial No.	Water Pump Capacity (Inches)	Frequency	Percentage
1	1	12	7.05
2	2	36	21.17
3	2.5	16	9.41
4	3	76	44.7
5	4	27	15.88
	Total	170	100

The data in Table 3 shows the diameter of the pipeline of the water pumps and the capacity of these water pumps. 44% pumps had the capacity of the 3 inches. 16% were having the 4 inches diameter of the pipe. 22% pumps were those which had the capacity of the only 2 inches. 9 % of the water pumps have the capacity of 2.5 inches and 7 % have 1 inches capacity which mostly falls in hand pumps category.

Table 3. Domestic Water Consumption.

Serial No.	Water Consumption Per-day (Liter)	Frequency	Percentage
1	<50	54	31.76
2	50-100	35	20.58
3	>100	81	47.64
	Total	170	100

Data in (table 4) is about the daily domestic water consumptions. It is evident from the tabular data that about half of the population had the daily domestic usage of more than 100 liters of water per day. The other percentage was 31% of the people who use the average water less than 50 liters. And the percentage of the people which lies in between 50 to 100 liters was 20%.

The agricultural data of the respondents reveals that majority of the population has the land ranging between 25 to 50 Kanals and that is about 40%. Remaining 25% had the agricultural land ranging less than 25 Kanals. And about 1/3rd kept the land more than 50 Kanals (Table 5).

Table 4. Agricultural land of the respondents.

Serial No.	Land (Kanals)	Frequency	Percentage
1	<25	53	31.17
2	25-50	68	40
3	>50	49	28.82
	Total	170	100

Table 5. Groundwater pumping in the study area.

Serial No.	Groundwater Pumping	Frequency	Percentage
1	Electric Motor	102	60
2	Solar Pump	43	25.29
3	Tube well	17	10
4	Hand Pump	08	4.17
	Total	170	100

Table 6 describes the ground water pumping in the region. It is evident in the tabular data that majority of the pumps are electric pumps which makes 60%. The other major use is of solar pumps. Solar pumps make 26% of the total pumps in the region. 10% are the tube well. The data also reveals that hand pumps were only 4% and these hand pumps are mainly used for domestic purposes only.

Table 6. Community's perception regarding Groundwater level.

Serial No.	Decrease in Groundwater Level (Feet)	Frequency	Percentage
1	5	42	24.7
2	5-10	32	18.82
3	10-15	41	24.17
4	>15	66	38.82
5	Dried	07	4.11
	Total	170	100

Table 7. Groundwater Level Variations in Villages.

Village Nmae	Groundwater Level (Average)	Drop in Groundwater Level (Feet)	Average of drop
Speen Kalai	250	15	15
Tanaye	250	15	15
Tiarza	180	15-20	17.5
Wacha-Khwara	150	15-20	17.5
Mughalkhel-Kalai	150	5	5
Doag Village	120	10-15	12.5
Daabkot	170	5-10	7.5
Karikot	200	15-20	17.5
Sherana	270	10-15	12.5
Sheen-Warsak	350	10	10
Ghwa Khwa	300	10	10
Azam-Warsak	450	15-20	17.5
Sholam	370	5	5
Inzar	500	20	20
Total	265		13.03571

In Table 7, the community perception about groundwater level is mentioned in the statistical manner. 38% people were of the view that groundwater level has been decreased more than 15 feet. 24% people were of the view that the decrease in the groundwater level is between 10 to 15% and the other majority had the perception that decrease is only 5 feet.

Groundwater in Wana is decreasing because of several prevailing problems. First and foremost; there is inordinate dispersion of tube well that has excessive use and immensely impacted the groundwater. Second underscored reason is owing to climate change, there is less rainfall; water level has declined 13 feet in previous five years. The results show that there are multiple factors that led to water depletion.

3.2. Groundwater Management

Different input parameters were considered in designing the management plan. It includes rainfall analysis, land cover, soil group and geology of the study area. These input parameters were then put in GIS environment to generate NRCS model. Forestation, check dams and embankments have also been proposed in the management plan.

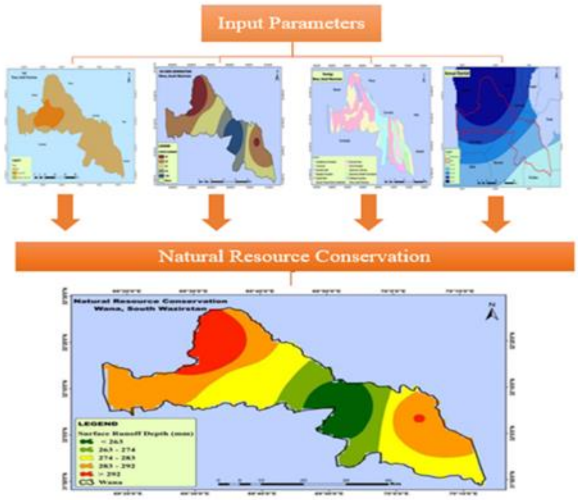

Figure 1. Flow Diagram of Natural Resource Conservation Service (NRCS)

3.3. Groundwater Management Plan

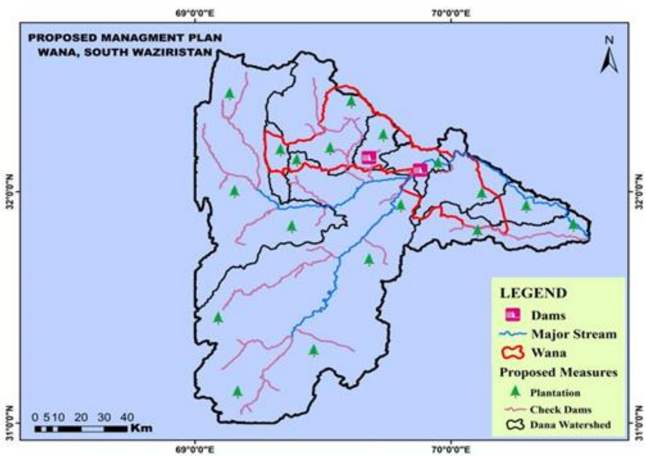

Figure 2. Groundwater management plan for Wana, South Waziristan.

The sustainability of groundwater is closely linked with some micro and macro management which influences land use and surface water and becomes one of the major challenges in natural resource management. Watershed management approach is basically used to manage groundwater. It is highly important to increases the retention capability of the watershed.

4. Discussion

Groundwater in Wana is decreasing because of several prevailing problems. First and foremost; there is inordinate dispersion of tube well that has excessive use and immensely impacted the groundwater. Second underscored reason is owing to climate change, there is less rainfall; water level has declined 13 feet in previous five years as mentioned earlier. The third reason is, as pointed out, is lack of government policy and inefficiency toward ground water management which severely affected the local people including their agriculture land. According to elders of the concerned region, the crop production has been decreased, and one of the indispensable issues is the migration of people, since when the water level started decreasing, many tribes migrated to other settled region to seek jobs as there are less or no water available in Wana to irrigate their own lands. It was also reported that the major tribe of Marwat had migrated in the past from Wana just because of water shortages. According to government institutions, they had and still have inadequate qualitative instruments for ground water to be measured. The lack of effective utilization of rainwater has put tremendous pressure on the groundwater. The over abstraction of groundwater for agricultural and domestic purposes has lowered the water table. It is found out from the study that during the past five years, the average drop in the groundwater level is 13 feet which means 2.6 feet drop per annum. It was also revealed from people perception that about 4 percent of the wells have dried completely in the last five years. Furthermore, the level of groundwater has lowered beyond the level of 550 feet in some areas. The most vulnerable areas to this declining groundwater in the study area are Azam Warsak, Sheen Warsak, Sholam and Inzar.

5. Conclusion

The study concludes that Wana is prone to the decreasing groundwater level. If the issue is not taken seriously, it will have dire consequences in the near future. The construction of small and medium reservoirs under the present conditions is the only possible way to meet the impeding water crisis. The construction of Dam will not only provide water for the agricultural activities but will also raise the groundwater level.

References

Ahmed, A., El Ammawy, M., Hewaidy, A. G., Moussa, B., & Hafz, N. A. (2019). Mapping of lineaments for groundwater assessment in the desert fringes east El-Minia, eastern desert, Egypt. Environmental monitoring and assessment, 191(9), 1-22.

Amore, L. (2012). The United Nations World Water Development Report–N 4–Groundwater and Global Change: Trends, Opportunities and Challenges (Vol. 1). UNESCO.

Barthel, R., Foster, S., & Villholth, K. G. (2017). Interdisciplinary and participatory approaches: the key to effective groundwater management. Hydrogeology Journal, 25(7), 1923-1926.

Bredehoeft, J. D. (2002). The water budget myth revisited: why hydrogeologists model. Groundwater, 40(4), 340-345.

Burke, J. J. (2002). Groundwater for irrigation: productivity gains and the need to manage hydroenvironmental risk.

Changming, L., Jingjie, Y., & Kendy, E. (2001). Groundwater exploitation and its impact on the environment in the North China Plain. Water international, 26(2), 265-272.

Chatterjee, R., Gupta, B. K., Mohiddin, S. K., Singh, P. N., Shekhar, S., & Purohit, R. (2009). Dynamic groundwater resources of National Capital Territory, Delhi: assessment, development and management options. Environmental Earth Sciences, 59(3), 669-686.

Chenini, I., Zghibi, A., & Kouzana, L. (2015). Hydrogeological investigations and groundwater vulnerability assessment and mapping for groundwater resource protection and management: state of the art and a case study. Journal of African Earth Sciences, 109, 11-26.

Chowdary, V. M., Rao, N. H., & Sarma, P. B. S. (2003). GIS-based decision support system for groundwater assessment in large irrigation project areas. Agricultural Water Management, 62(3), 229-252.

7th Intercontinental Geoinformation Days

igd.mersin.edu.tr

Mapping Covid-19 incidence hotspots in Pakistan using spatial-statistical approach

Shakeel Mahmood *1, Zara Tariq 1

[1]Government College University, Department of Geography, Lahore, Pakistan

Keywords
Covid-19
GIS
Hotspot
Pakistan

Abstract

COVID-19 pandemic is a top-level global emergency which has reduced the coping capacity several developed nations. The infected cases are growing very rapidly. The social interaction and travelling of people have further intensified the situation. Therefore, in this paper an attempt has been made to identify and assess COVID-19 hotspot in Pakistan and public health department to decelerate the exponential growth of patients. Point-level geo-coding technique is applied on patient's record (25/03/2020 to 20/04/2020) and the relative location was converted into absolute location. A total 468 confirmed cases were geo-coded. Getis-OrdGi* statistical model is applied in ArcGIS10.2 to calculate Z-score and P-values for each location representing the COVID-19 incidence intensity. Then Inverse distance weighted (IDW) technique of spatial interpolation was applied on Z-score and spatial clusters of confirmed cases were geo-visualized in the form hotspot and cold spot. The spatial extent of hotspots and age group of infected persons is alarming. The study provides a suitable methodological framework for identification and analysis infectious disease hotspots. The results can also facilitate public health department and related authorities to win war against COVID-19 lethal outbreak. Similarly, it can help policy makers to restrict travelling and social interaction in hotspots.

1. Introduction

Human history is observing a very strange time fighting an invisible enemy; the novel corona virus infectious disease 2019 (COVID-19). Initially observed in, now spreading swiftly around the world. In Pakistan, first case was reported on February 25, 2020. The main cause of COVID-19 pandemic in Pakistan is the entry of infected pilgrims from Iran, pilgrims and migrants from Saudi Arab. Similarly, infected people from UAE, Malaysia and China have also transmitted the virus. These infected migrants travelled and meet different people over different locations and transmit corona virus to healthy people. This transmission continues till the complete lock down. Currently, lock down has minimized the interaction of infected and healthy persons. Similarly, the quarantine facility across the country has decrease the exposure of healthy citizens. But still, the entire population in Pakistan is at high risk due to COVID-19 outbreak across the country (Mahmood 2022).

Globally, corona virus disease 2019 (COVID-19) pandemic became a biological disaster and tens of thousands of people have lost their lives; millions are infected and quarantined. Man has experienced various pandemics throughout the history with different intensity and impact (Remuzzi & Remuzzi, 2020; Mahmood, 2022). Today we are observing and experiencing a very tough time by fighting once again with an invisible enemy; the COVID-19 (Sah et al. 2020; Bastola et al. 2020). As of today, 28th April, 2020, there are 3.06million confirmed Coronavirus cases, with 0.213 million deaths while 0.907million has been recovered. In the total Coronavirus patients died, very interestingly the highest number belongs to Italy i.e., 4,032 deaths. The death toll is followed by China (3,248), Iran (1,433) and Spain (1,044) Corona virus (COVID-19) started spreading in December 2019 and was noticed in early January 2020. It started spreading in China in mid- to late-January (The Economist, 2020). The impact of this public health emergency has affected countries and communities in terms of economic, socio-psychological issues, as well as international relations (Hua and Shaw, 2020).

Currently, a variety of human diseases is prevailing with unknown etiology (Rodriguez-Morales et al. 2020; Callaway 2020; Li et al. 2020). Viruses have been considered as cause of these diseases which has increased the continuous search for new viruses

* **Corresponding Author**

*(shakeelmahmoodkhan@gmail.com) ORCID ID 0000-0001-6909-0735

Cite this study

Mahmood, S., & Tariq, Z. (2023). Mapping Covid-19 incidence hotspots in Pakistan using spatial-statistical approach. Intercontinental Geoinformation Days (IGD), 7, 286-289, Peshawar, Pakistan

(Stohlman & Hinton, 2001; Jubelt and Berger, 2001; Shingadia et al. 2002; Rota et al. 2003). There are four human coronaviruses known to exist: human coronavirus 229E (HCoV-229E), HCoV-OC43, severe acute respiratory syndrome (SARS)-associated coronavirus (SARS-CoV) and Coronavirus. The coronaviruses have been identified in mice, rats, chickens, turkeys, swine, dogs, cats, rabbits, horses, cattle and humans, and can cause a variety of severe diseases including gastroenteritis and respiratory tract diseases (Martina et al. 2003; Harapan et al. 2020). Van der Hoek et al. (2004) reported the identification of a fourth human coronavirus, HCoVNL63, using a new method of virus discovery. The virus was isolated from a 7-month-old child suffering from bronchiolitis and conjunctivitis. Coronavirus has caused an ongoing outbreak of viral pneumonia in China. Person-to-person transmission has been demonstrated, but, to our knowledge, transmission of the novel coronavirus that causes coronavirus disease 2019 (COVID-19) (Bai et al. 2020; Leung and Wuhttps 2020). It spreads by the mucous containing liquid present in the human body mainly droplets of saliva or discharge of nose. At this crucial time, vaccines or any obvious treatment had developed to cure COVID-19. After the first three months of this pandemic multiple epidemiological assessments in different countries from Asia, Europe, and North America have been published (Sah et al. 2020; Bastola et al. 2020). Nevertheless, there are countries, with a rapid increase and a high number of cases, with a lack of studies (Rodriguez-Morales et al. 2020; Arab-Mazar et al. 2020).

In early December 2019, an outbreak of coronavirus disease 2019 (COVID-19), caused by a novel severe acute respiratory syndrome coronavirus 2 (SARS-CoV-2), occurred in Wuhan City, Hubei Province of China (Harapan et al. 2020). The World Health Organization (WHO) declared COVID-19 as Public Health Emergency of International Concern (PHEIC) on 31th of January 2020, and finally a pandemic on 11th March 2020 (Li et al. 2020). As of March 24th, 2020, the virus has caused a casualty of over 16,600 people worldwide with more than 380,000 people confirmed as infected by it, of which more than 10,000 cases are serious. Then on April 28th, 2020, there were 3.06million confirmed Coronavirus cases, with 0.213 million deaths while 0.907million has been recovered. In the total Coronavirus patients died, very interestingly the highest number belongs to Italy i.e., 4,032 deaths. The death toll is followed by China (3,248), Iran (1,433) and Spain (1,044) Corona virus (COVID-19) started spreading in December 2019 and was noticed in early January 2020. Worldwide, the impact of this pandemic has affected countries and communities socially, economically and psychologically as well as international relations (Hua and Shaw, 2020). At present, COVID-19 pandemic is hot topic globally.

In Pakistan, first case was reported on February 25, 2020. As of 28th April, 2020. The total confirmed cases are 14612, active cases 11067, deaths 312 and recovered cases 3233 (NIH, 2020). The main cause of COVID-19 pandemic in Pakistan is the entry of infected pilgrims from Iran, pilgrims and migrants from Saudi Arab. Similarly, infected people from UAE, Malaysia and China have also transmitted and spread the virus. These infected migrants travelled and meet different people over different locations and transmit corona virus to healthy people. This transmission continues till the complete lockdown. Currently, lockdown has minimized the interaction of infected and healthy persons. Similarly, the quarantine facility across the country has decrease the exposure of healthy citizens. The COVID-19 is still a biological hazard and the entire population is at high risk in Pakistan. Therefore, the aim of this pioneer study is to summarize the current situation of COVID-19 and model incidence hotspot using spatio-statistical approach.

2. Method

This study is based on secondary data. The data regarding registered COVID-19 confirmed cases were acquired from National Institute of Health (NIH) of Pakistan website. The data were classified in MS Excel. Point-level geo-coding technique is applied to geo-code 492 confirmed COVID-19 cases of past 30 days i.e. 15/03/2020 to 15/04/2020. The hotspots is determined by applying Getis-OrdGi* (G-i-star) statistical model in GIS environment to quantify Z-score and P-values. Finally, Inverse Distance Weighting (IDW) technique of spatial interpolation is implemented to generate a spatial layer depicting hotspots and coldspot zones by utilizing Z-score as input data. In the current study, Getis-OrdGi* geo-statistical model has utilized due to its better predictive validity and spatial clustering that fits the study area as definition of hotspot than other models. The Gi* statistic is more interested in assessing incident intensity than in analyzing the spatial clustering of any particular value associated with COVID-19 incidence. Similarly, Gi* statistic examines the individual locations, enabling hotspots to be identified based on a comparison with the neighboring samples and has been successfully applied in hotspot identification and mapping.

2.1. Hotspot Analysis

The geo-coded COVID-19 cases records were imported into ArcGIS10.2 and geo-visualized in the form of point feature class as spatial layer (Fig. 2). The layer was added as input data to perform hotspot analysis. The hotspot analyst, identifies spatial clusters of high values (hotspots) and low values (cold spots) by implementing Getis-OrdGi* statistical model. It converts the geo-coded COVID-19 cases record into a new output feature having attributes of the z-score, p-value, and Gi-Bin confidence level ranging from -3 to +3. High counts of cases close together have +ve z-score indicating hotspot and vice versa. The z-score range +/-3 reflect statistical significance with 99-percent confidence level, +/-2 bins reflect 95-percent confidence level, and +/-1 bins reflect 90-percent confidence level, whereas 0 bin is not significant (Fig. 3). Then the IDW technique of spatial interpolation is implemented to generate the raster spatial layer depicting COVID-19 cases intensity as hotspot or coldspot. The z-score values are utilized as input data in spatial interpolation. The COVID-19 incidence intensity is categorized into five classes namely very low (-2.1 to -3), low (-1.1 to -2), moderate (+1 to -1), high (1.1 to 2) and very high (2.1 to 3). Linear regression analysis is applied on daily COVID-19 confirmed cases.

3. Results and Discussion

The results obtained from processed data are explained in the following sections.

3.1. Spatial Analysis

The spatial pattern of COVID-19 confirmed cases is variable across the country. The number of confirmed cases decreases towards north. The province Sindh becomes hotspot whereas northern areas including northern parts of Khyber Pakhtunkhwa and GB form coldspot. The spatial extent of hotspot seems to extend towards Punjab. In this regard, research on emergency bases is highly needed to minimize the spread of COVID-19 pandemic.

The spatial pattern of COVID-19 confirmed cases is variable across the country. The number of confirmed cases decreases towards north. Currently (26/03/2020) province Sindh is the hotspot whereas northern areas including northern parts of Khyber Pakhtunkhwa and GB form a coldspot (Fig. 1). The spatial extent of hotspot seems to extend towards Punjab. In this regard, research on emergency bases is highly needed to minimize the spread of COVID-19 pandemic.

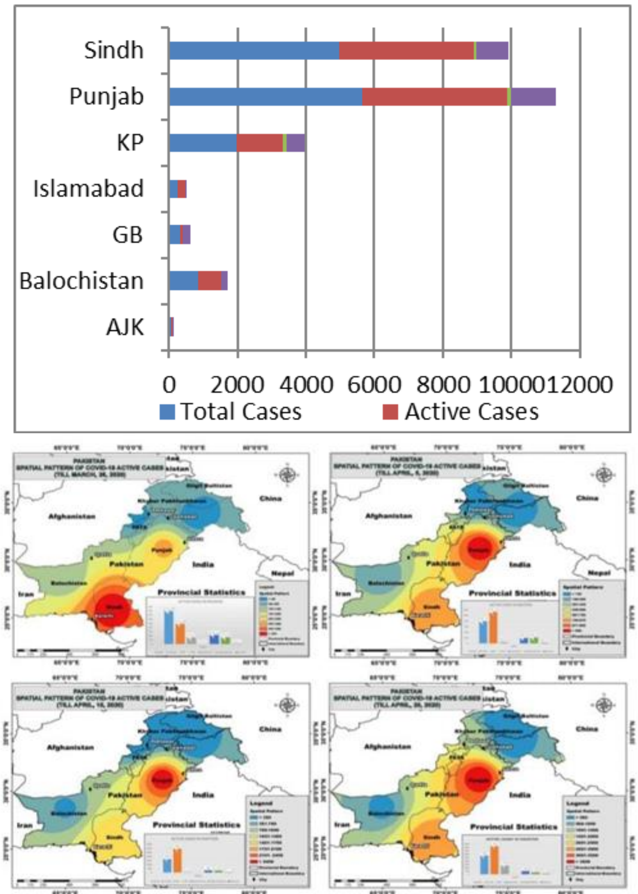

Figure 1. Hotspots and coldspots of COVID-19 active cases from 26/03/2020 to 20/04/2020 in Pakistan

Moreover, this study attempts to investigate the spread of corona Virus, a deadly pandemic infectious disease. The Province Sindh has highest concentration of infected patients due to several reasons. Karachi is the capital of Province Sindh and largest city of Pakistan. Karachi has the largest stock exchange market in Pakistan, which attracts the world international economist.

It is also the hub of international businesses around the world. Moreover, Jinnah International Airport is one of the Pakistan's largest and busiest international and domestic airports. The passengers coming from international flights such as students of Pakistan's went over to other countries to seek knowledge might be already infected. These are reasons from which international people attract towards the Sindh. Karachi has a port, which is South Asia's largest and busiest deep-water seaports.

Almost Pakistan's 60% cargo is hand by this port, which means it can also be the major hotspot region of this infectious virus. It is because goods are being imported from the world and there is a probability that these goods are already had infected by the corona virus. Political instability in Sindh region and poverty rate can also be a major reason of this pandemic spread.

After Sindh Province, Punjab leads because the carelessness of people. Mostly the people who had infected by this virus are in age group of 21 -50 years. Lahore is second largest city of Pakistan's and hub of many industrial and domestic level markets. A large proportion of commuters daily travel this and infect other people.

Figure 1. demonstrated the spatial distribution of COVID-19 in Pakistan's province. Moreover, this study attempts to investigate the spread of corona Virus, a deadly pandemic infectious disease. The province Sindh has highest concentration of infected patients due to several reasons. Karachi is the capital of Province Sindh and largest city of Pakistan. Karachi has the largest stock exchange market in Pakistan, which attracts the world international economist.

3.2. Temporal Analysis

On February 25, 2020, first case was reported in Pakistan. The total number of confirmed cases in in Pakistan are 1,415 in which 1,374 are active cases. Total deaths from corona Virus in Pakistan are 13. The seven patients are critical in their health. Only 29 patients had recovered from this deadly disease. It has been estimated that the probability of number of cases per 1 Million population is 6 whereas, Deaths in per million population is 0.05.

In 31 days from February 25, 2020 to March 26, 2020, 915 patients caught by deadly disease of Corona Virus. The Sindh province having the total area of 140,914 km2 and considered second largest province by population (47.88 M). The province Sindh is leading with the 399 patients found with the COVID-19 and Punjab Province is on second number having 246 patients. Other provinces including Baluchistan, Gilgit Baltistan and Khyber Pakhtunkhwa have 110, 81 and 78 patients respectively.

4. Conclusion

It is concluded from the study that Pakistan is still in a good position than many other countries to react to the current outbreak. The aggressive and systematic approach taken by the Government of Pakistan has played a crucial role in lockdown, quarantine facilities and awareness campaigns across the country. Similarly, care of the critically COVID-19 patient has recovered more than 2500 infected persons. The existing health system is responding under enormous pressure and accommodating the new cases. The established quarantine centers are supporting the health system. It is predicted in the study that if the exponential trend continues for the next few weeks, then the health system will be not able to respond. The measures taking by the government in the right direction, but prediction tells us that they need to be implemented without delay. Otherwise, a substantial number of unnecessary deaths will become inevitable.

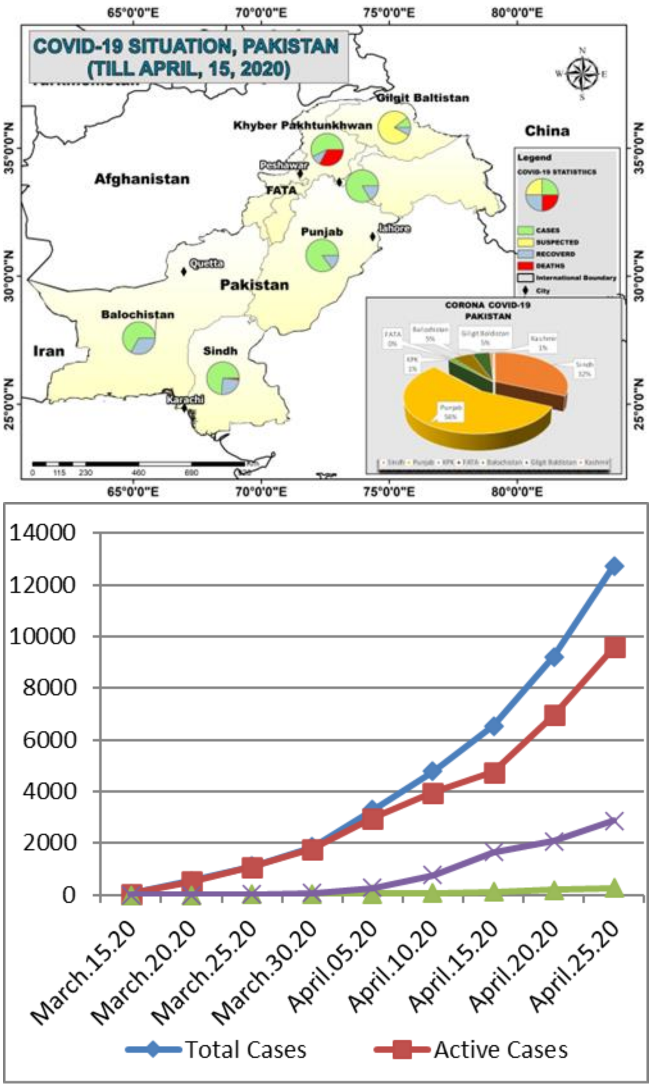

Figure 2. COVID-19 Situation, Pakistan (till April, 15, 2020).

Spatially, the COVID-19 incidence is very high (Hotspot) in central and south west of district Lahore whereas the surrounding of hotspots are covered by high incidence areas. The incidence is moderate in the south and west. Towards north incidence is decreasing forming cold spot with low incidence of COVID-19. The spatial extent of hotspot seems to extend towards the borders of Lahore. In this regard, research on emergency bases is highly needed to minimize the spread of COVID-19 pandemic.

Most importantly, the prediction suggests that maximum number of infected persons that will be reached in Pakistan. The maximum number of patients will require intensive health care units. The spatio-temporal pattern and prediction of COVID-19 is of crucial importance to plan for new facilities in Pakistani hospitals and to calculate the time period in which they need to be available. Finally, lock down has minimized the interaction of infected and healthy persons. Similarly, the quarantine facility has decreased the exposure of healthy citizens to COVID-19. But still, the entire population in main cities particularly in Lahore is at high risk due to the rapidly growing COVID-19 confirmed cases. Identification of hotspot is highly needed for all major cities because the incidence is very high in all capital cities of Pakistan. This will provide a base for policy regarding people traveling and interaction.

References

Arab-Mazar, Z., Sah, R., Rabaan, A. A., Dhama, K., & Rodriguez-Morales, A. J. (2020). Mapping the incidence of the COVID-19 hotspot in Iran–Implications for Travellers. Travel Medicine and Infectious Disease. https:///do.org/10.1016/j.tmaid.2020.101630

Bai, Y., Yao, L., Wei, T., Tian, F., Jin, D. Y., Chen, L., & Wang, M. (2020). Presumed asymptomatic carrier transmission of COVID-19. Jama, 323(14), 1406-1407.

Bastola A, Sah R, Rodriguez-Morales AJ, Lal BK, Jha R, Ojha HC, et al. (2020). The first 2019

Callaway E. (2020). Time to use the p-word? Coronavirus enter dangerousnew phase. Nature; 579, 12.

Harapan, H., Itoh, N., Yufika, A., Winardi, W., Keam, S., Te, H., ... & Mudatsir, M. (2020). Coronavirus disease 2019 (COVID-19): A literature review. Journal of Infection and Public Health.

Hua, J. & and Shaw, R. (2020). Corona Virus (COVID-19) “Infodemic” and Emerging Issues through a Data Lens: The Case of China. International Journal of Environmental Research and. Public Health, 17, 2309; https://doi.org/10.3390/ijerph17072309.

Jubelt, B. & Berger, J.R. (2001). Does viral disease underlie ALS? Lessons from the AIDS pandemic. Neurology 57, 945–946.

Li Q, Guan X, Wu P, et al. Early transmission dynamics in Wuhan, China, of novel coronavirus-infected pneumonia. N Engl J Med 2020; published online Jan 29. https://doi.org/10.1056/NEJMoa2001316.

7th Intercontinental Geoinformation Days

igd.mersin.edu.tr

Multi-sensorial data-based assessment of artificial surfaces and vegetation index for the response to population expansion: A case study of Musanze Secondary City, Rwanda

Katabarwa Murenzi Gilbert [1], Yishao Shi *[1], Isaac Nzayisenga [2]

[1] Tongji University, College of Surveying and Geo-Informatics, Shanghai 200092, China
[2] University of Rwanda, Urban Planning, Spatial Planning, Kigali City, Rwanda

Keywords
Remote sensing
Vegetation Index
Population Expansion
Forest Conservation
Musanze City

Abstract

Rapid population growth impacts land use, especially in Musanze, a secondary city. Therefore, our research aims for spatial analyses of the time series change in artificial surfaces and NDVI from 2000 to 2020. A multi-sensorial data-based analysis method assessed the changes and their effects on sustainability. Mathematical expression results reveal that (1) cultivated land increased from 64.6% to 68.9%, signifying a 4.3% rise. Conversely, forested areas decreased from 30.9% to 25.4%, reflecting a notable reduction of -5.5%. Water bodies saw a marginal uptick from 3.4% to 3.5%, a modest increase of 0.1%. Notably, artificial surfaces nearly doubled, soaring from 1.1% to 2.2%, representing an approximate 1.1% expansion in total coverage. (2) In 2000, sampled points demonstrated elevated vegetation indices, signifying that artificial areas were notably smaller than natural ones. Fast forward to 2020, after artificial surfaces had completely covered the sampled area, a significant and notable decrease in the vegetation index was observed, effectively halving the initial value recorded in 2000. In summary, urbanization can foster well-coordinated development; however, it poses a significant threat to natural areas as people migrate to urban centers. Therefore, to ensure a sustainable future for the population, we recommend enforcing zoning plans and building upward, using taller residential buildings instead of spreading out horizontally.

1. Introduction

Rapid urbanization in Africa, driven by population growth, creates complex and fragmented city landscapes, causing environmental degradation and urban poverty (Asabere et al., 2020). Primarily, People move to cities seeking better economic opportunities, improved access to services, and a higher quality of life. This rural-to-urban migration leads to urban expansion, resulting in the conversion of agricultural and forest land. As cities grow, they encroach upon surrounding rural areas, transforming once fertile agricultural land into urban developments. Additionally, the demand for resources such as timber and land for construction contributes to deforestation. This dual pressure of urban expansion and resource extraction accelerates agricultural and forest land reduction, ultimately impacting ecosystems and livelihoods dependent on these natural resources (Petrişor et al., 2020; Romano et al., 2017; Sumari et al., 2020).

Rwanda has experienced rapid urbanization driven by population growth and economic opportunities. This has led to the conversion of agricultural and forested land due to urban expansion (Aboh & Mutabazi, 2020; Gilbert & Shi, 2023; Nduwayezu et al., 2021). Remote sensing technologies, particularly GIS and NDVI analysis, have been instrumental in monitoring this transformation. GIS allows for the integration and analysis of spatial data, providing valuable insights into the spatial patterns and dynamics of urban growth. NDVI, a satellite-derived measure of vegetation health, has been crucial in assessing the impact of urban expansion on vegetation cover and health (Mugabowindekwe & Rwanyiziri, 2020; Rushema et al., 2020).

Various analyzed and cited studies have utilized Landsat data for monitoring purposes; however, it is worth noting that the outcomes can be influenced by the specific areas selected for supervised classification. To address this knowledge gap, this research has two primary objectives. First, it aims to track the two-decade

*Corresponding Authors

(hata2020@tongji.edu.cn) ORCID ID 0009-0005-4789-275X
*(shiyishao@tongji.edu.cn) ORCID ID 0000-0002-0048-6958
(nzayisaac85@gmail.com) ORCID ID 0009-0009-2284-9834

Cite this study

Gilbert, K. M., Shi, Y., & Nzayisenga, I. (2023). Multi-sensorial data-based assessment of artificial surfaces and vegetation index for the response to population expansion: A case study of Musanze Secondary City, Rwanda. Intercontinental Geoinformation Days (IGD), 7, 290-293, Peshawar, Pakistan

urban expansion in Musanze City, from 2000 to 2020, using the latest classified data from Globe Land 30. Secondly, it seeks to establish a mathematical and visual correlation between urban expansion and the indices related to natural areas and vegetation cover. This comprehensive approach aims to provide a more robust understanding of urban growth dynamics and its impact on the environment in Musanze city.

2. Methods

2.1. Study area

Musanze is a phase I secondary city located in northern Rwanda, with its proximity to five dormant volcanoes. The district covers an area of 5,302 square kilometers and is divided into 15 sectors(Hirwa et al., 2023; Nzayisenga & Nzamwita, 2023). According to the detailed findings of the Fourth and Fifth Rwanda Population and Housing Census, from 2012 to 2022, its population grew from 368,267 to 476,522, increasing population density from 694 to 1,157 people per square kilometer. 68.9% of the total population are engaged in agriculture. Among them, 62.6% are engaged in crop farming, and 50.4% are engaged in Livestock husbandry (NISR, 2023; NISR & MINECOFIN, 2012).

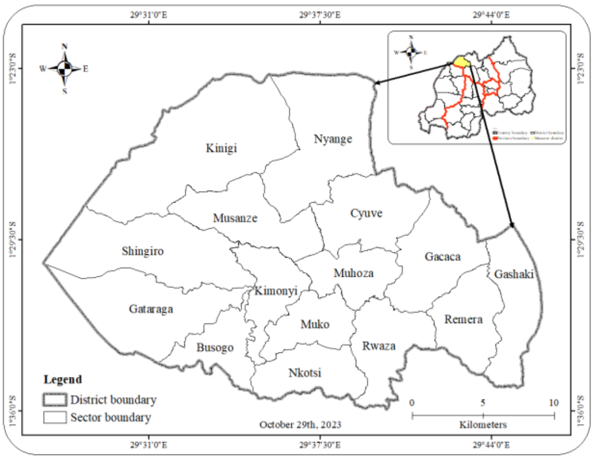

Figure 1. Administrative map of Musanze district

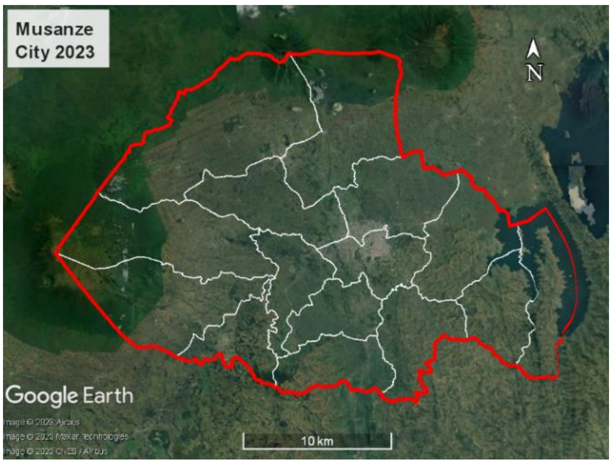

Figure 2. Google Earth image of Musanze (2023)

The topography of Musanze sets it apart from other secondary cities in Rwanda, as it is conducive to dense forests and receives higher levels of rainfall(Nakato et al., 2023; Twahirwa et al., 2023). This is attributed to its elevation range, which ranges from 4507 meters to 1535 meters above sea level. This geographical feature not only facilitates agriculture practices but also attracts a diverse range of people to the district, as it is known for its abundance of food resources compared to other areas.

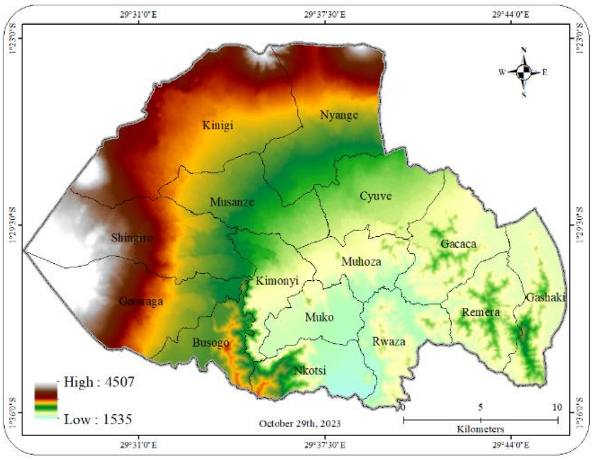

Figure 3. Elevation (meter) map of Musanze city

2.2. Data source and processing

This research has used only secondary data from different websites, as they are detailed in Table 1.

Table 1. Data source table

Data	Resolution	Source
LU/LC Data (GL30)	30 m	http://www.globalland cover.com
MOD13Q1 Vegetation Indices (NDVI)	250 m	https://ladsweb.moda ps.eosdis.nasa.gov/
SRTM Tile (DEM)	30 m	https://dwtkns.com/sr tm30m/
High-Resolution Image (2023)	-	Google Earth Pro 7.3.6.9345 (64-bit)

2.3. Data pre-processing and processing

Globeland30 is a 30-meter global land cover dataset that provides detailed and accurate information about land cover and land use on Earth(Wang et al., 2018). Regarding the nature and use of the study area, two maps of four classes (LU/LC) each were made using ArcMap 10.8 software.

The MOD13Q1 Vegetation Indices is a product of the Moderate Resolution Imaging Spectroradiometer (MODIS) sensor aboard NASA's Terra and Aqua satellites used to generate the Normalized Difference Vegetation Index (NDVI)(Peng et al., 2021). It provides information on the density and health of vegetation across the Earth's surface by measuring the reflectance of photosynthetically active radiation. To generate NDVI maps for 2000 and 2000, using a raster calculator tool in ArcMap 10.8, an adjustment of 0.0001 was applied to each tile to standardise the values within a range of -1 to +1.

SRTM stands for Shuttle Radar Topography Mission, a space shuttle-based mission that collects topographic data on the Earth's surface(Mahmood et al., 2021). An SRTM Tile, often called a Digital Elevation Model (DEM), is a specific section of this data representing a geographical area. The tile was subject to a masking procedure specifically tailored to cover the Musanze area, and this same process was systematically implemented for all the data utilised in this research.

Under the guidance of ArcMap, a specific tool known as "Extract Multi Values to Points" was employed to gather data from 371 sample points. The attribute table subsequently established the correlation between NDVI and Globeland30 data. However, for this study, only 8 sample points representing areas converted to artificial surfaces were deliberately selected for analysis. It is worth noting that Globeland30 encompasses various land use classes, each distinguished by a unique code. For this study, the following codes were utilized: artificial surfaces (code 80), cropland (code 10), forest (code 20), and waterbodies (code 60). These codes will play a pivotal role in the subsequent analysis.

3. Results

Based on the analyzed data showing changes in land use over the past two decades, it is evident that there have been significant shifts in various land categories. Specifically, forested areas have experienced a reduction, while agricultural land and built-up areas have increased.

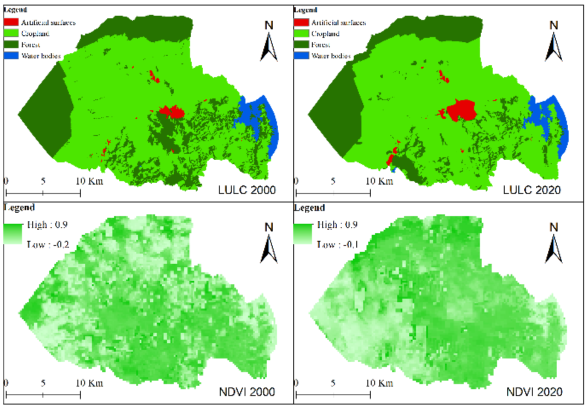

Figure 4. LULC and NDVI changes between 20 years

In terms of mathematical representation, the alterations in land use from 2000 to 2020 can be summarized as follows: The proportion of cultivated land rose from 64.6% to 68.9%, indicating a percentage increase of 4.3%. Meanwhile, forested areas experienced a decrease from 30.9% to 25.4%, accounting for a total reduction of -5.5%. Water bodies, on the other hand, exhibited a marginal increase from 3.4% to 3.5%, resulting in a slight overall uptick of 0.1%. Artificial Surfaces nearly doubled, surging from 1.1% to 2.2%. This equates to an approximate 1.1% surge in total coverage over two decades. Table 2 shows the change in square kilometers between two decades ago.

Table 2. LULC change from 2000 to 2020

Class name	2000 km²	2020 km²	Change km²
Cultivated land	341.21	363.61	22.39
Forest	163.48	134.23	-29.24
Water bodies	17.81	18.55	0.74
Artificial Surfaces	5.5	11.61	6.11

Figure 5 illustrates the percentage shift in land use within the Musanze district, presenting a comparative and visual representation of the changes over time.

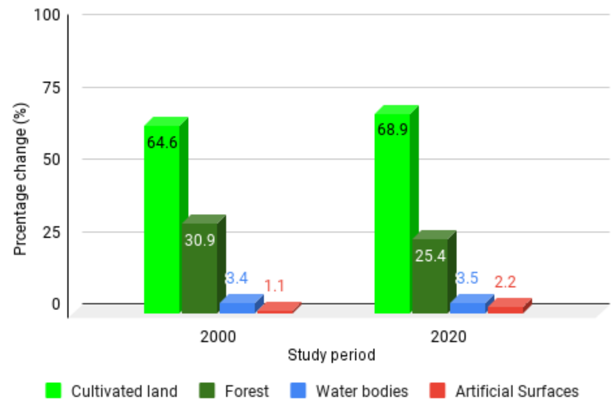

Figure 5. Comparative representation of the changes

4. Discussion

This study has revealed significant forest conversion around -29.24 km^2, which accounts for a total reduction of -5.5%, which is the source of increased severe effects of climate variability and climate change, specifically rising temperature and decrease of rainfall(Twahirwa et al., 2023). Therefore, 8-point samples from artificial areas were taken to increase the extraction accuracy for built-up areas and their influence on vegetation cover(Zheng et al., 2021). Half of the transitioned land to artificial surfaces (coded as 80) originated from agricultural areas (coded as 10), with 25% originating from forests (coded as 20). The remaining 25% remained consistent with its original coding (80).

Table 3. Correlation between LULC and NDVI

GL30_2000	NDVI_2000	GL30_2020	NDVI_2020
10	0.730	80	0.380
10	0.718	80	0.538
10	0.665	80	0.304
10	0.735	80	0.417
20	0.410	80	0.330
20	0.729	80	0.332
80	0.597	80	0.392
80	0.176	80	0.456

In 2000, Table 3 illustrates that most sampled points exhibited high vegetation indices, indicating that artificial areas were considerably smaller than natural ones. However, by 2020, after artificial surfaces had enveloped the entire sampled area, there was a stark and noteworthy reduction in the vegetation index, approximately halving the initial value recorded in 2000.

5. Conclusion

In summary, urbanization can foster development when well-coordinated; however, it currently poses a significant threat to natural areas as people migrate to urban centers, leading to an expansion of artificial surfaces for survival. Our study, utilizing globeland30 data spanning from 2000 to 2020, has unveiled adverse effects on forests due to the simultaneous increase in artificial surfaces and agriculture. Consequently, the region is now experiencing heightened temperatures and reduced rainfall. This alteration in land use also impacts vegetation cover, evident in the significant disparity in reflectance index between 2000 and 2020 in areas converted to artificial surfaces. To ensure sustainable livelihoods for the population, it is imperative to curtail horizontal urban sprawl. Instead, there should be a shift towards vertical housing solutions such as high-rise residential buildings. Equally important is the need for rigorous inspection and enforcement of zoning plans. Furthermore, it is crucial to provide support and incentives to encourage the adoption of sustainability measures. This multifaceted approach is essential to balance urban development and the preservation of natural ecosystems.

Acknowledgement

We extend our sincere gratitude to the proprietors of the data utilized, the authors referenced in this research, and lastly, the reviewers and organizers whose invaluable contributions were instrumental in facilitating the publication of our study.

References

Aboh, B., & Mutabazi, A. (2020). Satellite Imagery Analysis for Land Use, Land Use Change and Forestry: A Pilot Study in Kigali, Rwanda. Proceedings of the 3rd ACM SIGCAS Conference on Computing and Sustainable Societies, 127–135.

Asabere, S. B., Acheampong, R. A., Ashiagbor, G., Beckers, S. C., Keck, M., Erasmi, S., Schanze, J., & Sauer, D. (2020). Urbanization, land use transformation and spatial-environmental impacts: Analyses of trends and implications in major metropolitan regions of Ghana. Land Use Policy, 96, 104707. https://doi.org/https://doi.org/10.1016/j.landusepol.2020.104707

Gilbert, K. M., & Shi, Y. (2023). Assessing land use/land cover change in Kigali City, Rwanda. Intercontinental Geoinformation Days, 6, 396–399.

Hirwa, H., Ngwijabagabo, H., Minani, M., Tuyishime, S. P. C., & Habimana, I. (2023). Geospatial Assessment of Urban Flood Susceptibility Using AHP-Based Multi-Criteria Technique: Case Study of Musanze, Rwanda. Rwanda Journal of Engineering, Science, Technology and Environment, 5(1).

Mahmood, S. A., Shahzad, M., Batool, S., Amer, A., Kaukab, I. S., & Masood, A. (2021). Neotectonics from Geomorphic Indices: Highlights from Main Mantle Thrust (Pakistan). Geotectonics, 55(4), 563–583.

Mugabowindekwe, M., & Rwanyiziri, G. (2020). Comparative assessment of homogeneity differences in multi-temporal NDVI strata and the currently used agricultural area frames in Rwanda. South African Journal of Geomatics, 9(1), 89–107.

Nakato, G. V., Okonya, J. S., Kantungeko, D., Ocimati, W., Mahuku, G., Legg, J. P., & Blomme, G. (2023). Influence of altitude as a proxy for temperature on key Musa pests and diseases in watershed areas of Burundi and Rwanda. Heliyon, 9(3).

Nduwayezu, G., Manirakiza, V., Mugabe, L., & Malonza, J. M. (2021). Urban growth and land use/land cover changes in the post-genocide period, Kigali, Rwanda. Environment and Urbanization ASIA, 12(1_suppl), S127–S146.

NISR. (2023). The Fifth Rwanda Population and Housing Census, Main Indicators Report. https://statistics.gov.rw/file/13787/download?token=gjjLyRXT

NISR, & MINECOFIN. (2012). Rwanda Fourth Population and Housing Census. Thematic Report: Population size, structure and distribution.

Nzayisenga, I., & Nzamwita, S. (2023). Assessıng Women's Access to Credıts Usıng Land Lease Certıfıcates: A Case Study of Cyabagarura Cell, Musanze Sector, Musanze Dıstrıct. https://doi.org/10.13140/RG.2.2.15720.65280/1

Peng, Z., Yang, K., Luo, Y., & Yang, J. (2021). Based on MOD13Q1 data to analyze the characteristics of vegetation changes in central Yunnan from 2000 to 2019. IOP Conference Series: Earth and Environmental Science, 658(1), 012007.

Petrişor, A.-I., Hamma, W., Nguyen, H. D., Randazzo, G., Muzirafuti, A., Stan, M.-I., Tran, V. T., Aştefănoaiei, R., Bui, Q.-T., & Vintilă, D.-F. (2020). Degradation of coastlines under the pressure of urbanization and tourism: Evidence on the change of land systems from Europe, Asia and Africa. Land, 9(8), 275.

Romano, B., Zullo, F., Fiorini, L., Marucci, A., & Ciabò, S. (2017). Land transformation of Italy due to half a century of urbanization. Land Use Policy, 67, 387–400. https://doi.org/https://doi.org/10.1016/j.landusepol.2017.06.006

Rushema, E., Maniragaba, A., Ndihokubwayo, L., & Kulimushi, L. C. (2020). The Impact of Land Degradation on Agricultural Productivity in Nyabihu District-Rwanda, A Case Study of Rugera Sector. IJOEAR, 6(7), 49–63.

Sumari, N. S., Cobbinah, P. B., Ujoh, F., & Xu, G. (2020). On the absurdity of rapid urbanization: Spatio-temporal analysis of land-use changes in Morogoro, Tanzania. Cities, 107, 102876.

Twahirwa, A., Oludhe, C., Omondi, P., Rwanyiziri, G., & Sebaziga Ndakize, J. (2023). Assessing Variability and Trends of Rainfall and Temperature for the District of Musanze in Rwanda. Advances in Meteorology, 2023.

Wang, Y., Zhang, J., Liu, D., Yang, W., & Zhang, W. (2018). Accuracy assessment of GlobeLand30 2010 land cover over China based on geographically and categorically stratified validation sample data. Remote Sensing, 10(8). https://doi.org/10.3390/rs10081213

Zheng, Y., Tang, L., & Wang, H. (2021). An improved approach for monitoring urban built-up areas by combining NPP-VIIRS nighttime light, NDVI, NDWI, and NDBI. Journal of Cleaner Production, 328, 129488.

7th Intercontinental Geoinformation Days

igd.mersin.edu.tr

Flood vulnerability assessment using geographical information system: Case study of Mpazi Sub-catchment, Kigali

Patience Manizabayo *1, Hyacinthe Ngwijabagabo 1, Isaac Nzayisenga 2, Sabato Nzamwita 2, Laika Amani 1, Eugene Uwitonze 1

[1] University of Rwanda, Environmental Planning, Spatial Planning, Kigali City, Rwanda
[2] University of Rwanda, Urban Planning, Spatial Planning, Kigali City, Rwanda

Keywords
Flood Vulnerability
GIS
Natural Disasters
Spatial Overlay
Climate Change

Abstract

Floods in the Mpazi sub-catchment pose significant and recurring threats to the community and environment. This study utilized GIS technology to assess flood vulnerability by integrating spatial data on land use, elevation, and rainfall patterns. The results revealed a high susceptibility to flood hazards, particularly during the rainy season. This information is invaluable for stakeholders in formulating effective flood management strategies to mitigate the devastating impact of these recurrent floods on society and essential infrastructure. The study identifies the most vulnerable areas: very high risk 39.74% (353.34 ha), high risk 13.02% (115.73 ha), moderate risk 30.22% (268.62 ha), low risk 5.12% (45.51 ha), very low risk 11.9% (105.77 ha). Infrastructure, such as residential and commercial buildings, is impacted by flooding. This study offers valuable insights for decision-makers and stakeholders, supporting the development of effective flood management plans in the Mpazi sub-catchment.

1. Introduction

Globally, climate change makes many people highly vulnerable to natural disasters and other environmental changes (Wali et al., 2013). This is because the climate has changed and is continuously changing globally. As a result, there are natural increases in the frequency and severity of natural disasters (Hu et al. 2017). The most common natural disasters occur when the river channel receives much more water than it can (Andrews, Babb, and Barber 2017). Excessive rainfall results in the rivers rising, and a flood develops because the river cannot handle the extra water, causing flooding everywhere along the river's path. Excessive rainfall results in the rivers rising, and a flood develops because the river cannot handle the extra water, causing flooding everywhere along the river's path. This implies that all elements at risk, such as population, are highly affected by floods, i.e., the more vulnerable a population is, the more likely they are to suffer the consequences of a flood event (Cutter et al. 2008).

Nyabugogo watershed, particularly the Mpazi Sub catchment that is the focus of our research, has experienced flooding in several incidents. This is mostly because the Mpazi sub-catchment is located at a low altitude relative to its surroundings and the peculiarities of the Kigali city drainage system convergence zone, which has frequently experienced flooding. When flooding happens in this region, the damaged materials and the soil eroded from the upper stream flow with the water through the river channel. As a result, they are deposited downstream, ultimately closing the drainage channels (Manyifika, 2015). All the materials and eroded soil cause the channel to be blocked, and the water cannot flow as it should, which causes the surrounding area to flood. Mpazi channel, which receives upstream rainwater, is one of the main causes of flooding in this area. Since the channel is blocked by debris, eroded soil, and damaged materials, the water cannot flow as it should, which suddenly causes the surrounding areas to flood. The Nyabugogo River, especially the Mpazi channel, which receives rainwater from upstream, is one of the main causes of flooding in this area.

* Corresponding Author

*(manizabayopatience08@gmail.com) https://orcid.org/0009-0000-5283-5358
(ngwijabagabohyacinthe@gmail.com) https://orcid.org/0000-0003-1530-9302
(nzayisaac85@gmail.com) https://orcid.org/0009-0009-2284-9834

Cite this study

Manizabayo, P., Ngwijabagabo, H., Nzayisenga, I., Nzamwita, S., Amani, L., & Uwitonze, E. (2023). Flood vulnerability assessment using geographical information system: Case study of Mpazi Sub-catchment, Kigali. Intercontinental Geoinformation Days (IGD), 7, 294-297, Peshawar, Pakistan

Vulnerability refers to the degree of loss to a given element at risk resulting from the occurrence of a natural phenomenon of a given magnitude and expressed on a scale from 0 (no damage) to 1 (total damage) damage (United Nations, 2018). In the context of flooding, vulnerability refers to the degree to which elements at risk are susceptible to the negative impacts of flooding, such as property damage, displacement, or loss of life. Various factors can influence vulnerability, including socioeconomic status, geographic location, infrastructure, and environmental conditions (De Brito, Evers, and Delos Santos Almoradie, 2018). According to (Hoque et al. 2019), the vulnerability is expressed using the Equation (1):

$$\textit{Vulnerability} = (\textit{Exposure}) + (\textit{Resistance}) + \textit{Resilience} \qquad (1)$$

This study aims to bridge a critical knowledge gap by utilizing GIS-based analysis, specifically the GIS-AHP method, to map flood-prone areas within the Mpazi sub-catchment comprehensively. Past research has highlighted the inadequacy of previous GIS technology in this regard.

2. Materials and Method

2.1 Study Area

The study is concentrated on the Mpazi sub-catchment, which is wholly enclosed inside the Nyarugenge district. One of the Nyabugogo catchment sub-catchments, the Mpazi sub-catchment, lies between 10 56'15" and 10 58'45"S and between 300 02'00'E and 300 03'45"E. This sub-sub-catchment is found in Nyarugenge District in western Kigali City and covers an area of 888.90 ha.

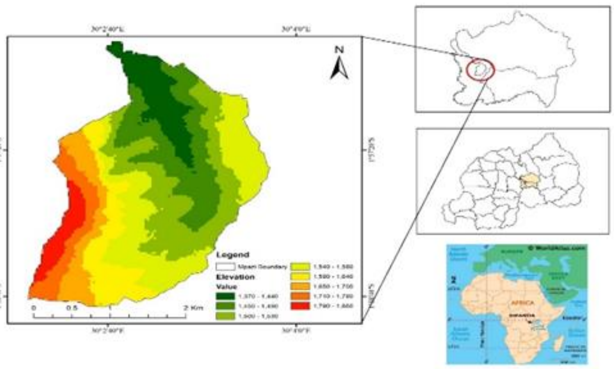

Figure 1. Study Area

Figure 2. Mpazi sub-catchment downstream (Source: Photo from Google Earth Pro, 2023)

2.2 Data Processing Methods

Choosing the right factors or criteria is crucial for a detailed flood vulnerability assessment. This is particularly important in identifying and mapping natural hazards such as landslides, floods, and cyclones, which rely on various factors for their occurrence. To create an accurate flood vulnerability map for a particular catchment area, it is imperative to carefully select the most appropriate factors (Rimba et al., 2017; Roy & Blaschke, 2015; Shivaprasad et al., 2018). However, this can be challenging, as selecting parameters that consistently produce accurate susceptibility maps requires careful consideration and attention to detail. The selection of criteria and alternatives for flood vulnerability assessment in the Mpazi sub-catchment was based on a detailed literature review, data availability, and their relevance and impact on flood vulnerability. The analysis of vulnerability in this study focuses on the physical and natural factors that control and influence it. These factors have been identified and selected as criteria for the analysis. The study has identified five vulnerability criteria from different sources. The land use and cover map of the study area was delivered from data produced by Rwanda GeoPortal 2020. Slope data and elevation map were generated from Digital Elevation Model (DEM) data obtained from the United States Geological Survey portal (USGS). The precipitation map of the study area was delivered from the interpolation of data from Meteo Rwanda. To process and prepare the numerous spatial criterion layers, ArcGIS software (version 10.8) was used. The Analytical Hierarchy Process (AHP) technique is a GIS-based decision-making method and was delivered to weigh the criteria based on the information gathered during the field survey and literature review. This enabled the development of a more accurate and comprehensive assessment of flood vulnerability in the Mpazi sub-catchment.

2.3 Identification of Criteria

Land use, particularly the built-up areas, is a critical factor that influences flooding in the study area. When natural surfaces such as vegetation and soils are replaced by impervious surfaces such as concrete and asphalt, the surface runoff increases, leading to more flooding. In the Mpazi sub-catchment, built-up areas also reduce the amount of infiltration, causing more water to flow into the streams and rivers, increasing the volume of water, which causes flooding, especially in low-lying sub-catchment areas. Generally, low-lying areas with gentle slopes are more susceptible to flooding than those with higher elevations and steeper slopes (Hu et al. 2017).

Another important flood risk factor is distance from the river channel. The lower the distance from the river, the higher the flood risk level. Precipitation is crucial to flood risk. When the precipitation increases, the flood risk also is higher (Rimba et al. 2017). The Topographical Wetnex Index is another important factor that contributes to flood vulnerability. The topographic wetness index (TWI) is crucial in flood vulnerability assessment. TWI measures the land's capability to retain water and indicates areas of potential water accumulation during flooding events. Considering the TWI in flood vulnerability assessments, it is possible to identify low-lying areas with poor drainage and higher flood susceptibility. Areas with high TWI values are likely to have higher water saturation, resulting in increased vulnerability to flooding. Additionally, TWI can help prioritize flood mitigation efforts and inform land use planning by identifying areas where development should be avoided or proper water management measures should be implemented. The study area with level >2-7 tend to be wet and more vulnerable to risk compared to areas with low wetness (Figure 3d).

The influence of slope and elevation in flood vulnerability assessment is significant. Slope affects the speed and direction of water flow during floods, impacting the intensity and spread of flooding. Areas with steeper slopes tend to channel water more rapidly, increasing flood hazards. Elevation is crucial in flood vulnerability, as low-lying areas are more prone to inundation. Higher elevations offer natural protection from flooding.

Table 2. Flood risk classes and weights

Criteria	Unit	Very High	High	Moderate	Low	Very Low	Weights
LULC	Level	Waterbody	Agricultural Land	Built-Up	Bare Land	Vegetation	0.178
Precipitation	mm	0.26 – 0.31	0.2 – 0.25	0.14 – 0.19	0.1-0.13	<0.1	0.262
Slope	%	0 – 7.2	7.3 – 13	14 – 20	21 – 30	31 - 53	0.145
Topographical Wetnex Index	Level	2 - 7	-1 – 1	-3 - -2	-5 - -4	-8 - -6	0.09
Elevation	m	>1370 – 1490	1500 – 1560	1570-1650	1660 - 1750	1760 - 1860	0.1
Distance from River	m	<129	>130 – 257	>258 – 386	>387 – 515	>516 - 644	0.225

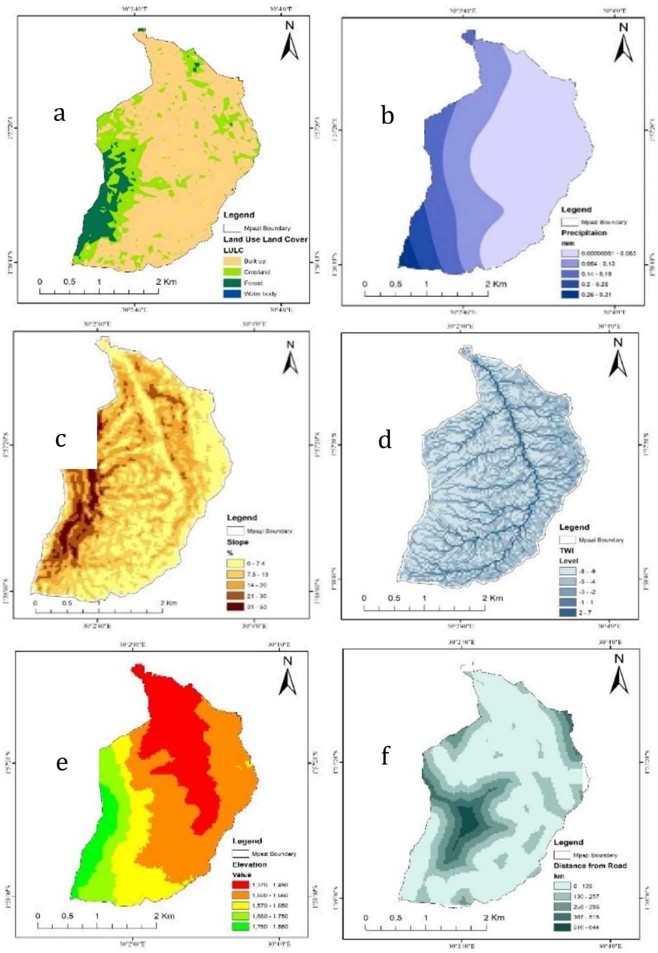

Figure 3. Flood risk criteria maps (a) Land Use Land Cover (b) Precipitation (c) Slope (d) Topographical Wetness Index (e) Elevation (f) Distance from River

3. Results

By comparing the criteria weighted with the highest influence on flooding risk in the study area were calculated, precipitation (0.262); distance from the river (0.225); LULC (0.17); slope (0.145); elevation (0.1); TWI (0.09).

The flood vulnerability map identifies the most vulnerable areas to flooding in the study area, very high risk 39.74% (353.34 ha), high risk 13.02% (115.73 ha), moderate risk 30.22% (268.62 ha), low risk 5.12% (45.51 ha), very low risk 11.9% (105.77 ha) as shown in Table 3. According to the field survey, infrastructures such as residential houses, trading centers, roads and bridges are frequently affected by flooding.

Table 3. Flood risk areas in Mpazi Sub-catchment

Flood Risk Classes	Area (Km^2)	Rate (%)
Very Low	105.77	11.9
Low	45.51	5.12
Moderate	268.62	30.22
High	115.73	13.02
Very High	353.34	39.74

4. Discussion

The areas which are more vulnerable to flooding are those very close to the active river channel. Also, the lowlands (low elevated areas) areas are at high risk because of overflow of water as shown in Figure 4 (a). The reverse is true, which means the areas with high elevation are likely to have vegetation cover and this place is not more vulnerable to flooding as shown in Figure 4 (c).

A combination of engineering measures and nature-based solutions is essential to reduce flood risk effectively. Constructing retaining walls and planting vegetation cover are vital components of flood risk reduction, as they help to manage water flow and prevent erosion. However, in addition to these conventional approaches, developing nature-based solutions like Natural Water Retention Measures (NWRM) and Natural Flood Management (NFM) is becoming increasingly crucial. NWRM enhances natural features like wetlands and forests to absorb excess water, while NFM focuses on working with the landscape to slow down and naturally store floodwaters. By integrating these nature-based approaches with developed infrastructure, a more resilient and sustainable flood management system is created, safeguarding communities and the environment from the growing threat of floods.

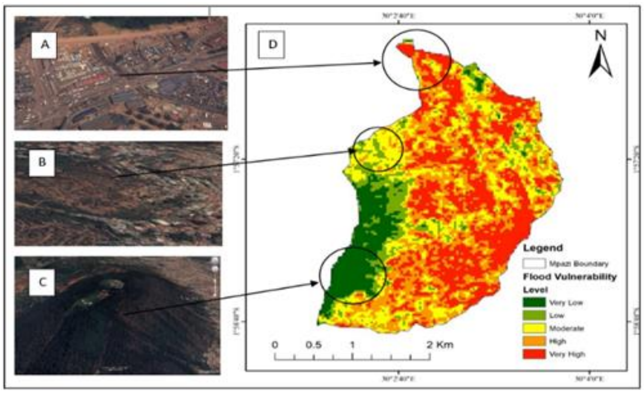

Figure 4. Flood Risk Map of Mpazi Sub-catchment

5. Conclusion

Flooding can have a wide-ranging and severe impact on various sectors and communities. Human settlements and shelters are vulnerable to damage or displacement, threatening people's safety, and well-being. Health and nutrition, water and sanitation, education, agriculture, and infrastructure can all be disrupted or damaged, affecting the basic needs and services of the affected population. Small and medium-sized enterprises suffer losses and can struggle to recover. Moreover, flooding threatens human life, carries health risks from contaminants, and causes long-term environmental effects through erosion and habitat disruption. The economic impact can be substantial, affecting both the government and private sector. To address these issues, utilizing GIS for flood vulnerability assessment is essential. This approach helps identify high-risk areas and informs strategies for reducing the impacts through better preparedness, improved infrastructure, and sustainable land use planning.

Acknowledgment

This study was extracted from the first author's bachelor's degree graduation project.

References

Andrews, J., David, B., & David, G. B. (20179. Climate Change and Sea Ice: Shipping Accessibility on the Marine Transportation Corridor through Hudson Bay and Hudson Strait (1980-2014). Elementa, 5. https://doi.org/10.1525/elementa.130.

De Brito, Mariana, M., Mariele, E., & Adrian, D. S. A. (2018). Participatory Flood Vulnerability Assessment: A Multi-Criteria Approach. Hydrology and Earth System Sciences 22(1), 373–90. https://doi.org/10.5194/hess-22-373-2018.

Cutter, S. L., Lindsey, B., Melissa, B., Christopher, B., Elijah, E., Eric, T., & Jennifer, W. (2008). A Place-Based Model for Understanding Community Resilience to Natural Disasters. Global Environmental Change 18(4), 598–606. https://doi.org/10.1016/j.gloenvcha.2008.07.013.

Hoque, M. Al A., Saima, T., Naser, A., & Biswajeet, P. (2019). Assessing Spatial Flood Vulnerability at Kalapara Upazila in Bangladesh Using an Analytic Hierarchy Process. Sensors (Switzerland) 19(6). https://doi:.org/10.3390/s19061302.

Hu, S., Xiangjun, C., Demin, Z., & Hong, Z. (2017). GIS-Based Flood Risk Assessment in Suburban Areas: A Case Study of the Fangshan District, Beijing. Natural Hazards 87(3), 1525–43. https://doi.org/10.1007/s11069-017-2828-0.

Manyifika, M. (2015). Diagnostic Assessment on Urban Floods Using Satellite Data and Hydrologic Models in Kigali, Rwanda.

Rimba, A., Martiwi, S., Abu, S., & Fusanori, M. (2017). Physical Flood Vulnerability Mapping Applying Geospatial Techniques in Okazaki City, Aichi Prefecture, Japan. Urban Science 1(1),7. https://doi.org/10.3390/urbansci1010007.

Roy, D. C., & Thomas, B. (2015). Spatial Vulnerability Assessment of Floods in the Coastal Regions of Bangladesh. Geomatics, Natural Hazards and Risk 6(1), 21–44. https://doi.org/10.1080/19475705.2013.816785.

Shivaprasad, S. S. V., Parth, S. R, Chakravarthi, V., & Srinivasa, R. G. (2018). Flood Risk Assessment Using Multi-Criteria Analysis: A Case Study from Kopili River Basin, Assam, India. Geomatics, Natural Hazards and Risk 9(1),79–93. https://doi.org/10.1080/19475705.2017.1408705.

United Nations. (2018). UNDRO, Natural Disaster and Vulnerability Analysis (2018). Natural Disaster and Vulnerability Analysis.

Wali, U., Garba, O. M., Yves, K. N., & Umaru, G. W. (2013). Hydraulic Structures Design for Flood Control in the Nyabugogo Wetland, Rwanda, 6.

6th Intercontinental Geoinformation Days

igd.mersin.edu.tr

Land surface temperature and urban heat island analysis using remote sensing and GIS: A case study in Mersin, Türkiye

Mehmet Özgür Çelik*1, Murat Yakar1

1Mersin University, Engineering Faculty, Department of Geomatics Engineering, Mersin, Türkiye

Keywords
LST
UHI
RS
GIS

Abstract

Global urbanization is rapidly increasing. This situation shifts land use/land cover (Lu/Lc) quickly. It also puts pressure on the land. Mersin, the study area, is also experiencing an increase in urbanization pressure. It is critical to assess the effects of urbanization on land. The calculation of remote sensing (RS) and geographic information system (GIS)-based Land surface temperature (LST) and urban heat island (UHI) aids in detecting impacts. LST and UHI maps were constructed for this purpose, and the most recent changes in the study area were monitored.

1. Introduction

Rapid and ongoing urbanization as a result of the world's expanding population is currently putting pressure on the land and causing the land use/land cover (Lu/Lc) to shift rapidly (Mishra et al., 2021). The fact that nearly 56% of the global population lives in cities, with the pace gradually increasing, demonstrates the strain [2]. The relationship between Lu/Lc and Land Surface Temperature (LST) and Urban Heat Island (UHI) is direct. LST and UHI can be used to calculate changes in Lu/Lc over time.

With sustainable urban management, places under urbanization pressure can grow in a planned and ecologically sound manner (Çoruhlu & Çelik, 2022; Coruhlu et al., 2021; Coruhlu and Toludan, 2019). This requires determining the Lu/Lc change caused by urbanization. LST and UHI based on remote sensing (RS) and Geographic Information Systems (GIS) are gaining attention as metrics to be used in assessing variations in Lu/Lc (Kusak & Kucukali, 2023; Rahman et al., 2022; Dewan et al., 2021; Doğan & Yakar, 2018).

The application was carried out in Mersin, which is located in the Mediterranean Region and has seen a growth in population in recent years. The current LST and UHI of the study area were computed using November 2023 Landsat 8-OLI satellite images. Thus, the consequences of urbanization pressure were attempted to be exposed in the study area.

2. Study Area

Mersin province is located in Turkey's southern region, between 36-37° North latitudes and 33-35° East longitudes (Figure 1). It has a land area of 15853 km^2 and a population of 1,916,432 (TÜİK, 2023).

3. Material and Method

Land surface temperature (LST) and urban heat island (UHI) were calculated in the study area, where the pressure on the land is growing due to urbanization, to examine the Lu/Lc change. A four-stage technique was used for this goal (Figure 2). Firstly, USGS EarthExplorer was used to retrieve Landsat 8-OLI images dated November 13-15, 2023 (USGS, 2023). Secondly, the LST calculation was performed. Radiance (Equation 1), Brightness Temperature (BT) (Equation 2), Normalized Difference Vegetation Index (NDVI) (Equation 3), and Land Surface Emissivity (LSE) (Equation 4) were estimated for this purpose. LST was eventually discovered (Equation 5). Finally, UHI (Equation 6) was estimated. Finally, it was generated LST and UHI.

* Corresponding Author

*(mozgurcelik33@gmail.com) ORCID ID 0000-0003-4569-888X
(myakar@mersin.edu.tr) ORCID ID 0000-0002-2664-6251

Cite this study

Çelik, M. Ö., & Yakar, M. (2023). Land surface temperature and urban heat island analysis using remote sensing and GIS: A case study in Mersin, Türkiye. Intercontinental Geoinformation Days (IGD), 7, 298-301, Peshawar, Pakistan.

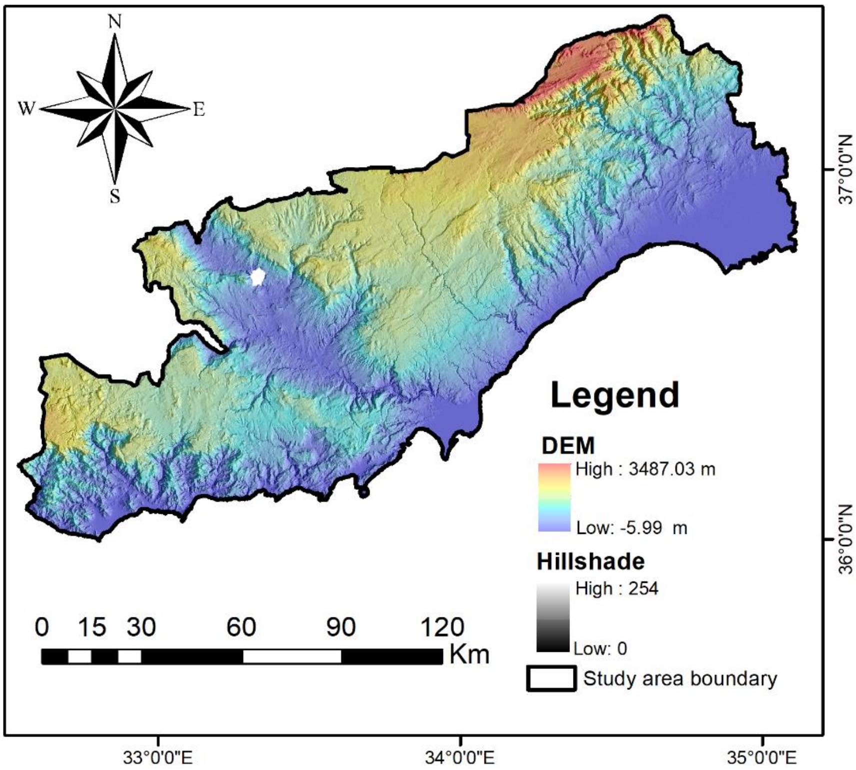

Figure 1. Study area

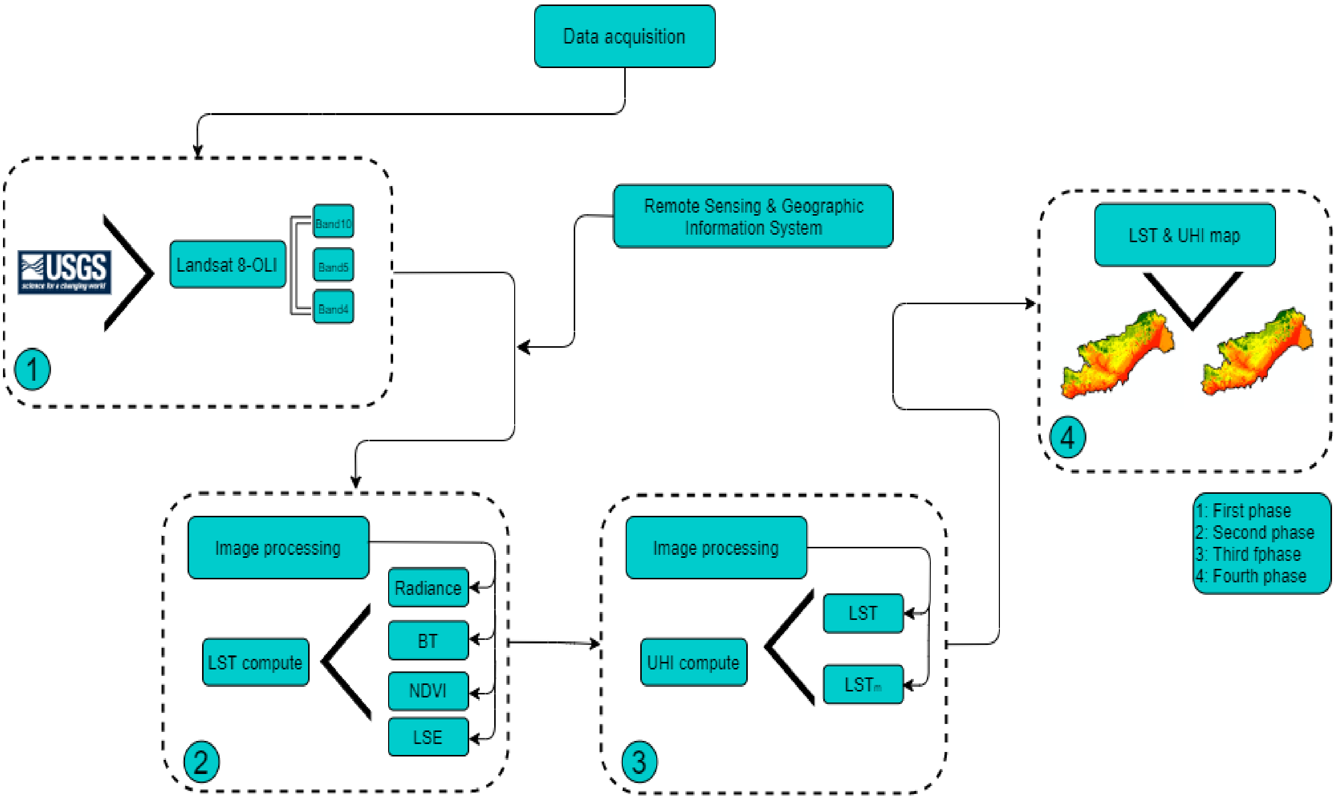

Figure 1. Flowchart of methodogy

$$L_\lambda = M_L * Q_{cal} + A_L - Q_i \quad (1)$$

Where L_λ is top of atmosphere spectral radiance (TOA), Q_{cal} is quantized and calibrated standard product pixel values, M_L is radiance multiplicative band number, A_L is radiance band ve Q_i is correction value for band 10 (0.29).

$$BT = K_2 / ln\,(K_1/L_\lambda + 1) - 273.15 \quad (2)$$

Where represents BT TOA brightness temperature, K_1 constant band, and K_2 constant band.

$$NDVI = (NIR - RED)/(NIR + RED) \quad (3)$$

Where NIR is near infrared band (Band5), and RED is red (Band4).

$$P_V = (NDVI - NDVI_{min}) / (NDVI_{max} - NDVI_{min})^2$$
$$LSE = 0.004 * P_V + 0.986 \quad (4)$$

Where LSE presents land surface emissivity, P_V symbolize the proportion of vegetation.

$$LST = (BT/1 + 0.00115 * BT/1.4388) * ln\,(LSE) \quad (5)$$

Where LST is land surface temperature.

$$UHI = (LST - LST_m)/SD \quad (6)$$

Where UHI is urban heat island, LST_m is the mean temperature of the land surface temperature in the study area, and SD is standard deviation of temperature.

4. Results

LST and UHI were calculated and maps were created as part of a study that determined the effects caused by urbanization and land construction. Initially, LST was calculated and a map of it was created using Equations 1-5 (Figure 3a). Following that, UHI was calculated using Equation 6, and a map of it was constructed (Figure 3b).

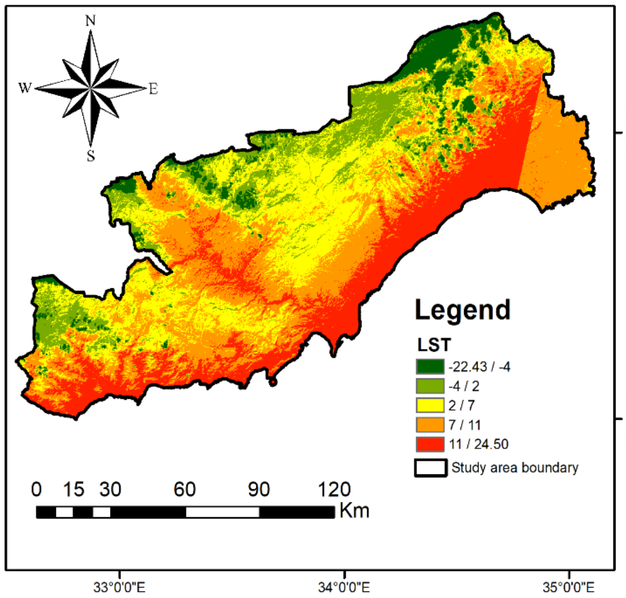

(a)

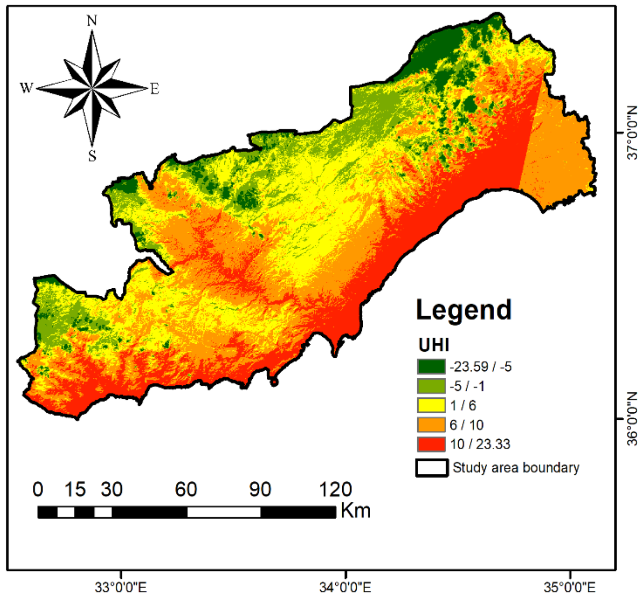

(b)

Figure 3. (a) LST, (b) UHI

5. Conclusion

Following the growth in urbanization in Mersin, the study's area, considerable changes have occurred in Lu/Lc. The consequences of urbanization concentrated in the city center can be reached using both the LST and UHI maps. In this context, it would not be incorrect to say that the maps developed are consistent. The study is expected to help decision-makers understand the importance of sustainable land management and use.

References

Çelik, M. Ö., & Yakar, M. (2023). Monitoring Land Use and Land Cover Change Using Remote Sensing and GIS: A Case Study in Mersin, Türkiye. Turkish Journal of Geographic Information Systems, 5(1), 43-51. https://doi.org/10.56130/tucbis.1300704

Çoruhlu, Y. E., & Çelik, M., Ö. (2022). Protected area geographical management model from design to implementation for specially protected environment area. Land Use Policy, 122, 106357. https://doi.org/10.1016/j.landusepol.2022.106357

Coruhlu, Y. E., & Toludan, T. (2019). Data model development for 'buying and selling' transactions as a real estate acquisition method. Survey review, 403-414. https://doi.org/10.1080/00396265.2019.1626585

Coruhlu, Y. E., Baser, V., & Yildiz, O. (2021). Object-based geographical data model for determination of the cemetery sites using SWOT and AHP integration. Survey Review, 53(377), 108-121. https://doi.org/10.1080/00396265.2020.1747843

Dewan, A., Kiselev, G., & Botje, D. (2021). Diurnal and seasonal trends and associated determinants of surface urban heat islands in large Bangladesh cities. Applied Geography, 135, 102533. https://doi.org/10.1016/j.apgeog.2021.102533

Doğan, Y., & Yakar, M. (2018). GIS and three-dimensional modeling for cultural heritages. International Journal of Engineering and Geosciences, 3(2), 50-55. https://doi.org/10.26833/ijeg.378257

Kusak, L., & Kucukali, U. F. (2023). Investigating the relationship between COVID-19 shutdown and land surface temperature on the Anatolian side of Istanbul using large architectural impermeable surfaces. Environment, Development and Sustainability, 1-38. https://doi.org/10.1007/s10668-023-03397-5

Mishra M, Santos C. A. G., do Nascimento, T. V. M., Dash, M., K, da Silva, R. M., Kar, D., & Acharyya, T. (2022). Mining impacts on forest cover change in a tropical forest using remote sensing and spatial information from 2001–2019: A case study of Odisha (India). Journal of Environmental Management, 302, 114067. https://doi.org/10.1016/j.jenvman.2021.114067

Rahman, M. N., Rony, M. R. H., Jannat, F. A., Chandra Pal, S., Islam, M. S., Alam, E., & Islam, A. R. M. T. (2022). Impact of urbanization on urban heat island intensity in major districts of Bangladesh using remote sensing and geo-spatial tools. Climate, 10(1), 3. https://doi.org/10.3390/cli10010003

TÜİK (2023b). TÜİK Statistics Data Portal Urban-Rural Population Statistics, [Retrieved 10.11.2023], https://data.tuik.gov.tr/Bulten/Index?p=Kent-Kir-Nufus-Istatistikleri-2022-49755

USGS (2023). USGS EarthExplorer, Retrieved 15.11.2023], https://earthexplorer.usgs.gov/

MERSIN UNIVERSITY

ISBN: 978-605-72800-6-0

https://igd.mersin.edu.tr/